МС 13

ТРИНАДЦАТЫЙ
МОСКОВСКИЙ
МЕЖДУНАРОДНЫЙ
СИМПОЗИУМ
ПО ИССЛЕДОВАНИЯМ
СОЛНЕЧНОЙ СИСТЕМЫ

10–14 ОКТЯБРЯ 2022
ИНСТИТУТ
КОСМИЧЕСКИХ
ИССЛЕДОВАНИЙ
МОСКВА

THE THIRTEENTH
MOSCOW
SOLAR SYSTEM
SYMPOSIUM

10–14 OCTOBER 2022
SPACE RESEARCH
INSTITUTE
MOSCOW

ИКИ
ИНСТИТУТ КОСМИЧЕСКИХ ИССЛЕДОВАНИЙ РАН

ГЕОХИ

BROWN

ТРИНАДЦАТЫЙ МОСКОВСКИЙ СИМПОЗИУМ ПО ИССЛЕДОВАНИЯМ СОЛНЕЧНОЙ СИСТЕМЫ 13M-S^3

октябрь 10-14, 2022
ИНСТИТУТ КОСМИЧЕСКИХ ИССЛЕДОВАНИЙ
РОССИЙСКОЙ АКАДЕМИИ НАУК
МОСКВА, РОССИЯ

THE THIRTEENTH MOSCOW SOLAR SYSTEM SYMPOSIUM 13M-S^3

october 10-14, 2022
SPACE RESEARCH INSTITUTE
OF RUSSIAN ACADEMY OF SCIENCES
MOSCOW, RUSSIA

спонсоры:
- Институт космических исследований РАН
- Институт геохимии и аналитической химии им. Вернадского РАН
- Брауновский университет (США)

sponsored by:
- Space Research Institute RAS
- Vernadsky Institute of Geochemistry and Analytical Chemistry RAS
- Brown University, USA

ISBN: 978-5-00015-057-3
DOI: 10.21046/13MS3-2022

TABLE OF CONTENT

THE THIRTEENTH MOSCOW SOLAR SYSTEM SYMPOSIUM 13M-S^3

SPACE RESEARCH INSTITUTE
MOSCOW, RUSSIA
october 10–14, 2022

Starting from 2010, the Space Research Institute holds annual international symposia on Solar system exploration. Main topics of these symposia include wide range of problems related to formation and evolution of Solar system, planetary systems of other stars; exploration of Solar system planets, their moons, small bodies; interplanetary environment, astrobiology problems. Experimental planetary studies, science instruments and preparation for space missions are also considered at these symposia.

The Thirteenth Moscow international Solar System Symposium (13M-S^3) will be held from October 10 till 14, 2022.

THE FOLLOWING SESSIONS WILL BE HELD DURING THE SYMPOSIUM:

OPENING SESSION

- Session. MARS
- Session. VENUS
- Session. MOON AND MERCURY
- Session. SMALL BODIES (INCLUDING COSMIC DUST)
- Session. GIANT PLANETS
- Session. EXTRASOLAR PLANETS
- Session. ASTROBIOLOGY

Space Research Institute holds this symposium with participation of the following organizations:

- Vernadsky Institute of Geochemistry and Analytical Chemistry RAS, Russia
- Brown University, USA
- Schmidt Institute of Physics of the Earth RAS, Russia
- Keldysh Institute of Applied Mathematics RAS, Russia
- Kotelnikov Institute of Radio-engineering and Electronics RAS, Russia
- Sternberg Astronomical institute, Moscow State University, Russia

Symposium website: **https://ms2022.cosmos.ru**
Contact email address: **ms2022@cosmos.ru**

PROGRAM COMMITTEE

chair:
acad. **ZELENYI L.M.** IKI RAS

members:
BAZILEVSKIY A.T. GEOHI RAS
BIBRING J.-P. IAS,CNRS, France
BOROVIN G.K. Keldysh AMI RAS
HEAD III J. Brown University, USA
KORABLEV O.I. IKI RAS
KOSTITSYN Y.A. GEOHI RAS
MAROV M.Ya. GEOHI RAS
MITROFANOV I.G. IKI RAS
RODIN A.V. IKI RAS
SHEVCHENKO V.V. GAISH MSU
SMIRNOV V.M. IRE RAS
TAVROV A.V. IKI RAS
VAISBERG O.L. IKI RAS
VOROBYOVA E.A. MSU
ZAKHAROV A.V. IKI RAS
ZASOVA L.V. IKI RAS

secretary:
ROSTE O.Z. IKI RAS, ms3@iki.rssi.ru

overview 13M–S^3 program
THE THIRTEENTH MOSCOW SOLAR SYSTEM SYMPOSIUM

Space Research Institute, 10–14 October 2022

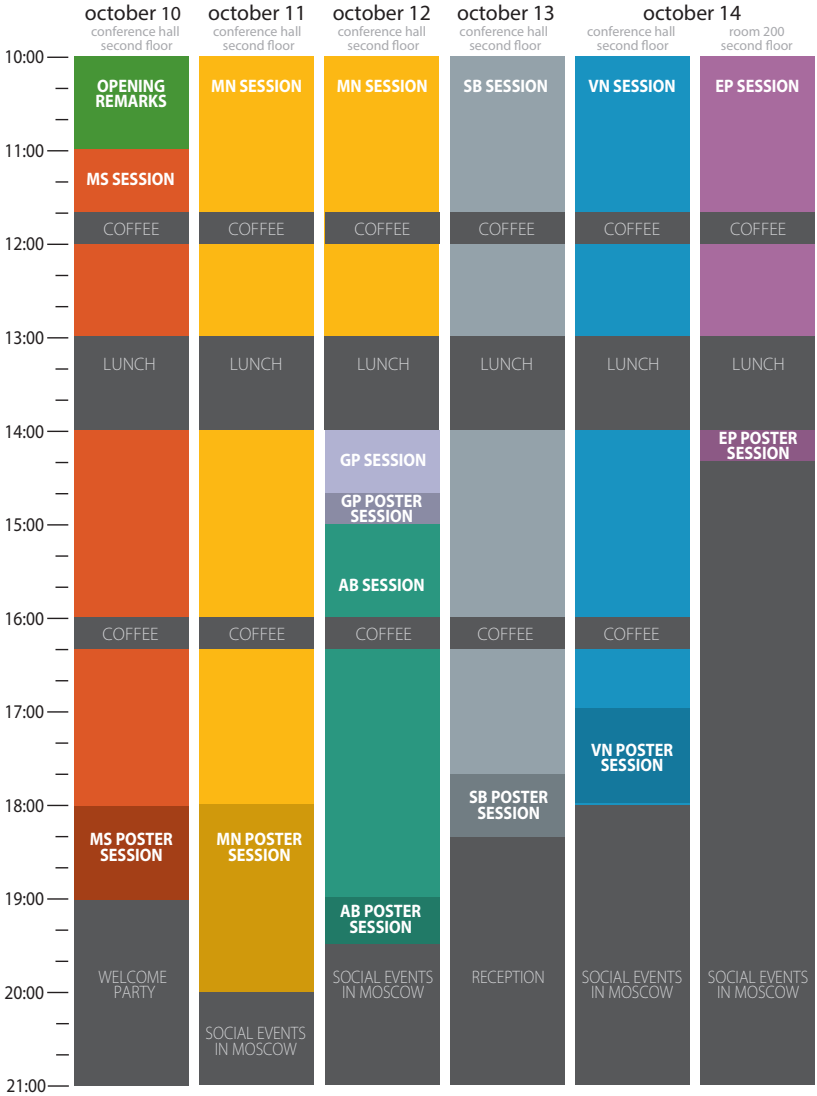

- **MS SESSION**: MARS SESSION
- **MN SESSION**: MOON AND MERCURY SESSION
- **GP SESSION**: GIANT PLANETS SESSION
- **AB SESSION**: ASTROBIOLOGY SESSION
- **SB SESSION**: SMALL BODIES SESSION (INCLUDING COSMIC DUST)
- **VN SESSION**: VENUS SESSION
- **EP SESSION**: EXTRASOLAR PLANETS SESSION

13M-S³ SCIENTIFIC PROGRAM

MONDAY, 10 OCTOBER 2022

10.00–11.00

OPENING REMARKS

Convener: **Lev ZELENYI**
conference hall, second floor

Lev ZELENYI (IKI)
James HEAD (Brown University)
Alexander BASILEVSKY (GEOKHI)
Mikhail SACHKOV (INASAN)

11.00–18.45

1 MARS SESSION

Convener: **Oleg KORABLEV**
conference hall, second floor

11.00–11:20	**Denis BELYAEV et al**	Thermal structure of the middle and upper atmosphere of Mars as seen by ACS MIR spectroscopy	13MS3-MS-01
11.20–11.40	**Ekaterina STARICHENKO et al**	Gravity wave statistics in the Martian atmosphere from the ACS/TGO solar occultation experiment	13MS3-MS-02
11.40–12.00		COFFEE-BREAK	
12.00–12:20	**Anna FEDOROVA et al**	A two-Martian year survey of the water vapor saturation state on Mars based on ACS NIR/TGO occultations	13MS3-MS-03
12.20–12.40	**Pavel VLASOV et al**	Overview of Martian Year 34 atmospheric thermal structure and dust distribution from ACS TIRVIM nadir observations onboard ExoMars TGO	13MS3-MS-04
12.40–13.00	**Mikhail LUGININ et al**	Observations of 2.7 micrometer CO_2 ice band on Mars from ACS solar occultations onboard TGO/ExoMars	13MS3-MS-05
13.00–14.00		LUNCH	
14.00–14.20	**Valery SHEMATOVICH et al**	Kinetic modeling of hot fraction in the extended hydrogen corona of Mars	13MS3-MS-06
14.20–14.40	**Artyom SHESTAKOV and S. SHUVALOV**	Planetary ions acceleration inside Martian hot flow anomaly	13MS3-MS-07
14.40–15.00	**Jordanka SEMKOVA et al**	Radiation environment in ExoMars TGO Mars orbit during solar energetic particle events in July 2021–March 2022	13MS3-MS-08
15.00–15.20	**Victor BENGHIN et al**	Comparison of the flux and dose rate measured by the Liulin-MO device aboard ExoMars TGO with calculated estimations	13MS3-MS-09
15.20–15.40	**Alexey MALAKHOV et al**	Global map of water abundance in the upper regolith layer of the equatorial region on Mars	13MS3-MS-10

15.40–16.00	**James HEAD et al**	When did Mars become bipolar? Outstanding issues in a conceptual model of a Noachian-Amazonian climate transition from an altitude-dominant temperature environment (ADD) to a latitude-dominant temperature environment (LDD)	13MS3-MS-11
16.00–16.20		COFFEE-BREAK	
16.20–16.40	**Benjamin BOATWRIGHT and James HEAD**	Constraining Early Mars Glacial Conditions from Paleodischarge Estimates of Intracrater Inverted Channels	13MS3-MS-12
16.40–17.00	**Elena PODOBNAYA et al**	Fragmentation model for impact clusters on Mars	13MS3-MS-13
17.00–17.20	**Ekaterina FABER et al**	Mineralogical variations of deposits in the Utopia Planitia region of Mars measured by CRISM and OMEGA spectrometers	13MS3-MS-14
17.20–17.40	**Jun CHU et al**	Lateral extension of layered deposits in S-W portion of Holden crater, Mars	13MS3-MS-15
17.40–18.00	**Egor KULIK and Tamara GUDKOVA**	On model values of Chandler wobble period for Mars	13MS3-MS-16
18.00–18.45	**POSTER SESSION, SESSION MARS** 9 posters * 5 min		
	Oleg VAISBERG	Mars magnetopause	13MS3-MS-PS-01
	Sergei KULIKOV et al	Study of wave phenomena in the plasma environment of Mars: simultaneous observations at ground and on orbits	13MS3-MS-PS-02
	Inna STEPANOVA et al	Combined approach in finding analytical continuations of the Mars magnetic field from satellite data	13MS3-MS-PS-03
	Ekaterina MELIKHOVA et al	The activity of the young Sun and isotopic composition evolution of the atmospheres of Mars and Venus	13MS3-MS-PS-04
	Daria EVDOKIMOVA et al	Upper limits of Mars atmospheric trace gases from the thermal spectra by ACS–TIRVIM/ExoMars	13MS3-MS-PS-05
	Vladimir OGIBALOV	Radiative transfer in the Martian atmosphere taking account line-mixing in the 15 μm CO_2 band	13MS3-MS-PS-06
	Vladimir OGIBALOV	Modelling of the non-equilibrium emissions of the Martian atmosphere in the near-IR CO_2 bands taking account aerosol extinction	13MS3-MS-PS-07
	Alexey BATOV et al	On model crust thickness variations of Mars and Venus with love numbers	13MS3-MS-PS-08
	Nikolai KASATIKOV et al	Using neural networks to search for information about Mars remotely	13MS3-MS-PS-09
19.00–20.00		WELCOME PARTY	

10.00–20:00

2 MOON AND MERCURY SESSION

Conveners: **Igor MITROFANOV, Maxim LITVAK**
conference hall, second floor

MERCURY			
10.00–10.20	**Johannes BENKHOFF**	BepiColombo Status	13MS3-MN-01
10.20–10.40	**James HEAD et al**	Mercury magmatic, tectonic and geodynamic history a comparative planetology analysis	13MS3-MN-02
10.40–11.00	**Alexander LAVRUKHIN et al**	Mercury's magnetosphere variations	13MS3-MN-03
11.00–11.20	**Alexander KOZYREV et al**	A comparative analysis of neutron flux data measured by MGNS/BepiColombo experiment for Venus and Mercury flybys	13MS3-MN-04
THE STUDIES OF THE MOON AS CELESTIAL BODY			
11.20–11.40	**Lionel WILSON et al**	Modeling the eruption and the cooling times of the lavas sampled by the Chang'e 5 mission	13MS3-MN-05
11.40–12.00		COFFEE-BREAK	
12.00–12.20	**Sergey KRASILNIKOV et al**	Northern oblique impact formation of the South Pole-Aitken basin	13MS3-MN-06
12.20–12.40	**Ksenia KOCHUBEY and Mikhail IVANOV**	Degradation of fresh-looking craters in Mare Fecunditatis, Moon	13MS3-MN-07
12.40–13.00	**Alexander BASILEVSKY et al**	Surface morphology inside the PSR area of polar crater Shoemaker in comparison with that of the sunlit areas	13MS3-MN-08
13.00–14.00		LUNCH	
14.00–14.20	**Evgeny SLYUTA et al**	Site selection problems of the Moon research station	13MS3-MN-09
14.20–14.40	**Mikhail IVANOV et al**	Absolute model age estimates of the Fecunditatis basin and Mare Fecunditatis in the region of Luna-16 landing site	13MS3-MN-10
14.40–15.00	**Chunyu DING et al**	Yutu-2 Radar sounding over the Chinese Chang'E–4 landing site on the far-side of the Moon	13MS3-MN-11
15.00–15.20	**Sergey VOROPAEV and Artem KRIVENKO**	Some features of the early Moon' degassing	13MS3-MN-12
15.20–15.40	**Alexader GUSEV et al**	Geological exploration of the Moon III: water ice in near polar regions of the Moon	13MS3-MN-13
15.40–16.00	**S. MEGALA and Tirtha Pratim DAS**	Salient results from Chandrayaan-2 mission	13MS3-MN-14

16.00–16.20		COFFEE-BREAK	
		THE EXPERIMENTS ON THE MOON	
16.20–16.40	**Andrey SHUGAROV et al**	The concept of Moon-based UV survey to study transients and variables	13MS3-MN-15
16.40–17.00	**Huijuan WANG et al**	Science of the lunar-based UV–OPTICAL–IR telescope for ILRS	13MS3-MN-16
17.00–17.20	**Ilia KUZNETSOV et al**	Investigation of the lunar dusty plasma and electric field dynamics with lunar dust monitoring instrument	13MS3-MN-17
17.20–17.40	**Andrey KIM et al**	Testing SLM technology with simulants of lunar regolith: applications to Lunar Printer experiment	13MS3-MN-18
17.20–18.00	**Maxim MOKROUSOV et al**	Space gamma-ray spectroscopy experiment with tags of Galactic cosmic rays	13MS3-MN-19
18.00–20:00		**POSTER SESSION , SESSION MOON AND MERCURY** 31 posters * 4 min	
	Maxim LITVAK et al	Experiment MGNS onboard ESA BepiColombo mission	13MS3-MN-PS-01
	Yongliao ZOU et al	Studying lunar evolution based on comprehensive physical field exploration for International Lunar Research Station program	13MS3-MN-PS-02
	Shaopeng HUANG et al	Heat flow measurement a priority for upcoming lunar missions	13MS3-MN-PS-03
	Bingxian LUO et al	Moon-based space weather station for Sun-Earth-Moon environment interaction monitoring and research	13MS3-MN-PS-04
	Jiajie FENG and Hong LIU	Key Scientific Questions of Lunar Life Sciences	13MS3-MN-PS-05
	Zhiguo MENG et al	Probing surface deposits in heavily ejecta-contaminated Mare Frigoris using CE–2 MRM data	13MS3-MN-PS-06
	Xuelei CHEN	Low Frequency Radio Interferometry from the Lunar Orbit	13MS3-MN-PS-07
	Mikhail PODZOLKO and Vladimir KALEGAEV	Suggestion of an experiment for measuring the fluxes of energetic galactic and solar protons and nuclei onboard future lunar station	13MS3-MN-PS-08
	Andrey TURUNDAEVSKIY et al	The Neutronium experimental complex for the Russian Lunar Scientific Observatory	13MS3-MN-PS-09
	Maya DJACHKOVA et al	The water abundance at Artemis landing sites	13MS3-MN-PS-10
	Natalia KOZLOVA et al	Availability of LROC NAC stereo images for construction of detailed DEMS at the south subpolar region of interest for Russian lunar missions	13MS3-MN-PS-11

Svetlana PONOMAREVA et al	Drilling of Ice-rich Regolith: Vibration and Blocking Issues	13MS3-MN-PS-12
Olga SHEVALDYSHEVA et al	Stationary and mobile lunar gravimeters	13MS3-MN-PS-13
Olga TURCHINSKAYA and Evgeny SLYUTA	Development of routes for the heavy rover «Lunar Robot-Geologist» on the territory of the volcanic province of Mons Rumker	13MS3-MN-PS-14
Anatoly MANUKIN et al	The SEISMO–LR is a three–coordinate seismometer for measurements on the Moon	13MS3-MN-PS-15
Vladimir CHEPTSOV et al	Applicability of LASMA–LR mass-spectrometer for the water ice detection within lunar regolith	13MS3-MN-PS-16
Kirill ZAKHARCHENKO et al	Durable diamond detector of cosmic radiation	13MS3-MN-PS-17
Egor SOROKIN et al	Natural lunar test site on Earth	13MS3-MN-PS-18
Alexandra UVAROVA	Consideration of ashes from the Kamchatka peninsula as lunar soil- analogues on the basis of physical and mechanical properties	13MS3-MN-PS-19
Ivan AGAPKIN	The Kamchatka volcanic ashes as a lunar soil analogue (physical properties)	13MS3-MN-PS-20
Alexandr KRASILNIKOV and Mikhail IVANOV	Estimates of the Local/Foreign Material Mixing on the Moon: the Crater Langrenus Case	13MS3-MN-PS-21
Alexandr KRASILNIKOV et al	Geological Structure of the Main Landing Ellipses of Luna-25	13MS3-MN-PS-22
Vladimir AFANASYEV and G. PECHERNIKOVA	The new analytical approach for calculation of craters ejecta thickness	13MS3-MN-PS-23
Ekaterina KRONROD et al	Thermal evolution of the Moon with geophysical constraints	13MS3-MN-PS-24
Mikhail IVANOV and Evgeniya GUSEVA	Automatic method to estimate the steepness of walls of small impact craters on the Moon	13MS3-MN-PS-25
Ekaterina FEOKTISTOVA et al	Morphological features of craters in the polar regions of the Moon	13MS3-MN-PS-26
Ekaterina FEOKTISTOVA et al	Hermite A crater as a cold trap near the north pole of the Moon	13MS3-MN-PS-27
Nadezhda CHUJKOVA et al	Dynamics of the Moon-Earth system and its impact on climate	13MS3-MN-PS-28
Boris EPISHIN and Michael SHPEKIN	Autonomous electronic Yearbook for observations from the surface of the Moon	13MS3-MN-PS-29
Gennady KOCHEMASOV	Moon-Earth' comparable fine wave structures created by equal orbits (around Sun and in Galaxy)	13MS3-MN-PS-30
Gennady KOCHEMASOV	Moon-dichotomous as other cosmic bodies (from asteroids to Universe)	13MS3-MN-PS-31

10.00–13.00

2 MOON AND MERCURY SESSION

Conveners: **Igor MITROFANOV, Maxim LITVAK**
conference hall, second floor

THE EXPERIMENTS ON THE MOON			
10.00–10.20	**Vladislav YAKOVLEV et al**	The ground tests of Lunar Manipulator Complex for Luna-25	13MS3-MN-20
10.20–10.40	**S. MEGALA and Tirtha Pratim DAS**	Indian Lunar exploration program – an Overview	13MS3-MN-21
10.40–11.00	**Mikhail MALENKOV et al**	Discussion of the concept of mobile robotic complexes for the International Lunar Research Station	13MS3-MN-22
11.00–11.20	**Guang LIU et al**	Developing the Lunar-based Earth observation platform	13MS3-MN-23
LUNAR EXPLORATION PROGRAMS/PERSPECTIVES			
11.20–11.40	**Chi WANG et al**	Preliminary scientific objectives of the International Lunar Research Station program	13MS3-MN-24
11.40–12.00		COFFEE-BREAK	
12.00–12.20	**Anatoly PETRUKOVICH et al**	The International Lunar Research Station from science perspective	13MS3-MN-25
12.20–12.40	**Lev ZELENYI et al**	Scientific objectives of lunar exploration	13MS3-MN-26
12.40–13.00	**Igor MITROFANOV et al**	The "Korvet" Program: Integrated Human and Robotic Missions to Moon	13MS3-MN-27
13.00–14.00		LUNCH	

14.00–15.00

3 GIANT PLANETS SESSION

Convener: **Valery SHEMATOVICH**
conference hall, second floor

14.00–14.20	**Nikolai SLODARZH et al**	Hyperion (C7): control point network and shape model. Difficulties and solutions	13MS3-GP-01
14.20–14.40	**Anatoly ZUBAREV et al**	Updated Ganymede control point network based on JUNO mission data	13MS3-GP-02
14.40–15.00	**POSTER SESSION, SESSION GIANT PLANETS**	4 posters * 5 min	
	Anna DUNAEVA et al	Organic matter in the structure of partially differentiated Titan	13MS3-GP-PS-01
	Victor KRONROD et al	Convection in the rock-ice mantle of partially differentiated Titan	13MS3-GP-PS-02
	Margarita MELNIKOVA et al	New global mosaic of Ganymede, detailed DEMs and maps	13MS3-GP-PS-03
	Azariy BARENBAUM	Measuring the precession period of Solar System ecliptic plane using Galactic model	13MS3-GP-PS-04

15.00–19.35

4 ASTROBIOLOGY SESSION

Convener: **Oleg KOTSYURBENKO**
conference hall, second floor

15.00–15.20	**Sohan JHEETA**	Electron irradiation of a homogeneous mixture of ammonia and carbon dioxide (NH_3:CO_2) ice at simulated planetary temperatures	13MS3-AB-01
15.20–15.40	**Martin DOMINIK**	The cosmic context of planet Earth – Don't buy a roadmap that only shows a single road	13MS3-AB-02
15.40–16.00	**Oleg KOTSYURBENKO et al**	Life on Venus: different concepts of its origin and evolution	13MS3-AB-03
16.00–16.20		COFFEE-BREAK	
16.20–16.40	**Dmitry SKLADNEV et al**	The simplest Lab-on-Chip for detecting living cells in the acidic environment of Venusian clouds	13MS3-AB-04
16.40–17.00	**Anatoliy PAVLOV et al**	The effects of nearby Supernova and solar superflares on Earth biosphere evolution: mass extinctions and "flash of mutations"	13MS3-AB-05
17.00–17.20	**Valery SHEMATOVICH et al**	Kinetic Monte Carlo model of the auroral electron precipitation into the N_2–O_2 planetary atmosphere	13MS3-AB-06
17.20–17.40	**Iren KUZNETSOVA et al**	Application of acoustoelectronic techniques to registration microbial objects in liquid	13MS3-AB-07
17.40–18.00	**David SMITH**	The Functioning Microbiome as Link between Genes and Microbial Environment	13MS3-AB-08
18.00–18.20	**Ahya REZAEI**	Remote Sensing in Agriculture	13MS3-AB-09
18.20–18.40	**Nikita DEMIDOV and Mikhail IVANOV**	Speculaitive history of life on Mars	13MS3-AB-10
18.40–19.00	**Daniil MIRONOV**	Geochemical indication of desert overgrowth (by the example of the Sarykum sand complex)	13MS3-AB-11
19.00–19.35	**POSTER SESSION, SESSION ASTROBIOLOGY** 7 posters * 4 min		
	Viacheslav ILYIN et al	Prospects for the application of microbial fuel cells in regenerative biological life support systems	13MS3-AB-PS-01
	Savio Torres DE FARIAS	Life on Mars: What can the use of biosignatures tell us?	13MS3-AB-PS-02

Vladimir CHEPTSOV et al	Peptides preservation under high-dose irradiation with accelerated electrons	13MS3-AB-PS-03
Andrey BELOV and Vladimir CHEPTSOV	Biodiversity of drought-tolerant bacteria: Astrobiological concern	13MS3-AB-PS-04
Denis VEDENEV et al	Influence of perchlorates on water crystallization temperature and bacterial survivability in mechanical simulants of Mars regolith	13MS3-AB-PS-05
Daniil BARBASHIN et al	Tolerance of arid ecosystems bacteria to sodium perchlorate: implications for Mars' habitability	13MS3-AB-PS-06
Daniil BARBASHIN and Daniil MIRONOV	Growing pea plants in Martian soil analogue with the addiction nitrogen fixer bacteria	13MS3-AB-PS-07

10.00–18.20

5 SMALL BODIES SESSION including cosmic dust

Conveners: **Alexander BASILEVSKY**, **Alexander ZAKHAROV**
conference hall, second floor

10.00–10.20	**Vladimir BUSAREV et al**	Only a quarter of newly observed primitive asteroids are active	13MS3-SB-01
10.20–10.40	**Boris SHUSTOV et al**	Collisions as a possible reason of sublimation-dusty activity of main belt asteroids	13MS3-SB-02
10.40–11.00	**Thomas DUXBURY and Natalia SEREGINA**	ESA MEX astrometric observations of the asteroid Psyche: the target of a NASA mission	13MS3-SB-03
11.00–11.20	**Anton KOCHERGIN et al**	Motion of dust in comet C/2021 A1 (Leonard)	13MS3-SB-04
11.20–11.40	**Maxim ZHELTOBRYUKHOV et al**	Microphysics of dust in comet C/2021 A1 (Leonard) inferred by means of polarimetry	13MS3-SB-05
11.40–12.00		COFFEE-BREAK	
12.00–12.20	**Tatiana SALNIKOVA et al**	On the conjecture of formation of the Martian moons Phobos and Deimos	13MS3-SB-06
12.20–12.40	**Sergey POPEL et al**	Electrostatically produced dusty plasmas near the surface of Mercury	13MS3-SB-07
12.40–13.00	**Vladimir TCHERNYI and S. KAPRANOV**	Role of Magnetism in the Separation of the Particles of the Saturn's rings	13MS3-SB-08
13.00–14.00		LUNCH	
14.00–14.20	**Yulia REZNICHENKO et al**	Dusty clouds evolution in the Martian atmosphere	13MS3-SB-09
14.20–14.40	**Irina NADEZHDINA et al**	Hyperion (C7) cartography: challenges and the first surface map	13MS3-SB-10
14.40–15.00	**Sergei IPATOV**	Probabilities of collisions of bodies ejected from the Earth with the terrestrial planets and the Moon	13MS3-SB-11
15.00–15.20	**Dmitry GLAZACHEV et al**	Assessing the consequences of asteroid and comet impacts on the Earth	13MS3-SB-12
15.20–15.40	**Tatyana GALUSHINA et al**	Modification of technique of asteroid observations on Terskol observatory	13MS3-SB-13
15.40–16.00	**Ilia KUZNETSOV et al**	Experimental investigation of the dust particles lofting processes	13MS3-SB-14
16.00–16.20		COFFEE-BREAK	
16.20–16.40	**Ekaterina CHORNAYA et al**	The 10-micron silicate feature in heterogeneous dust particles	13MS3-SB-15

16.40–17.00	**Anna KARTASHOVA et al**	The mass estimations of faint meteors	13MS3-SB-16
17.00–17.20	**Roman ZOLOTAREV and Boris SHUSTOV**	On the mass indices of meteor bodies	13MS3-SB-17
17.20–17.40	**Dominik BELOUSOV and Anatoliy PAVLOV**	Energy accumulation in icy bodies during long-term irradiation	13MS3-SB-18
17.40–18.20	**POSTER SESSION, SESSION SMALL BODIES (INCLUDING COSMIC DUST)** 8 posters * 5 min		
	Stanislav KUZNETSOV and Vladimir BUSAREV	Statistic analysis of dynamic parameters and sizes of asteroids of the Adeona Family	13MS3-SB-PS-01
	Tatiana MOROZOVA and Sergey POPEL	Influence of meteor flares on the development of modulation instability of electromagnetic waves in meteoroid tails	13MS3-SB-PS-02
	Dmitry PETROV and E. ZHUZHULINA	Influence of the internal structure of dust on the light-scattering properties of comet 29P/Schwassmann-Wachmann 1	13MS3-SB-PS-03
	Mariia VASILEVA and Eduard KUZNETSOV	Age estimation of Brugmansia asteroid family	13MS3-SB-PS-04
	Yulia IZVEKOVA and Sergey POPEL	Drift turbulence in dusty plasma near the Moon	13MS3-SB-PS-05
	Elena PETROVA and Vladimir BUSAREV	Properties of particles in the exospheres of active asteroids: estimates based on the spectral features in the UV–Visible range	13MS3-SB-PS-06
	Habibullo ABDUSSAMATOV	Lunar observatory aimed at monitoring and study of energy imbalance and climate of the Earth, near-Earth asteroids and comets, exoplanets, supernovae, and novae	13MS3-SB-PS-07
	Alexander SAMOKHIN and M. SAMOKHINA	About the 11th edition of the global trajectory optimization competition held in 2021 – "Dyson sphere" building	13MS3-SB-PS-08
18.30–21.00	**RECEPTION**		

10.00–18.05

6 VENUS SESSION

Convener: **Ludmila ZASOVA**
conference hall, second floor

10.00–10.20	**Vadim ROZHIN et al**	Geological history of the north region of Polik-mana Mons, Venus	13MS3-VN-01
10.20–10.40	**Arina SHIMOLINA et al**	Mapping of lava flows of Theia Mons, Beta regio, Venus	13MS3-VN-02
10.40–11.00	**Danil MALYSHEV et al**	Geological history of Samodiva Mons region, Devana Chasma Quadrange V–29, Venus	13MS3-VN-03
11.00–11.20	**Dargilan OLIVEIRA AMORIM and Tamara GUDKOVA**	PREM-based models of Venus' interior structure	13MS3-VN-04
11.20–11.40	**Tamara MENSHCHIKOVA et al**	Model stress values for Venus: elastic case	13MS3-VN-05
11.40–12.00		COFFEE-BREAK	
12.00–12.20	**Boris IVANOV**	Footprints of asteroid atmospheric explosions at the surface of Venus	13MS3-VN-06
12.20–12.40	**Piero D'INCECCO et al**	Idunn Mons as the landing site of the Venera-D mission: scientific relevance and possible operational tests on Mount Etna	13MS3-VN-07
12.40–13.00	**Dmitry GORINOV et al**	Winds in the lower cloud level on the nightside of Venus from IR2 (AKATSUKI) 1.74 μm images	13MS3-VN-08
13.00–14.00		LUNCH	
14.00–14.20	**Mikhail ZOLOTOV et al**	Exploration of Venus atmosphere and surface with the upcoming NASA DAVINCI mission	13MS3-VN-09
14.20–14.40	**Ludmila ZASOVA et al**	The Venera-D mission: progress in study	13MS3-VN-10
14.40–15.00	**Gaurav SETH et al**	Case study of Venus Surface Studies using PolSAR	13MS3-VN-11
15.00–15.20	**Elias CHATZITHEODORIDIS et al**	New instruments, methods, and experiments in astrobiology research: Venus and Mars	13MS3-VN-12
15.20–15.40	**Vladislav ZUBKO et al**	Mission scenario of flight to Venus with landing at desired location on its surface	13MS3-VN-13
15.40–16.00	**Mikhail GERASIMOV and JSD Team**	Scientific Goals of the Venera-D Lander	13MS3-VN-14
16.00–16.20		COFFEE-BREAK	
16.20–16.40	**Imant VINOGRADOV et al**	Study of sulphurous and other components of the Venus atmosphere by laser absorption spectroscopy at the Venera-D mission	13MS3-VN-15

16.40–17.00	**Denis BELYAEV et al**	Venus Infrared Atmospheric Gases Linker (VIRAL): scientific concept for solar occultation experiment on board Venus Orbiter Mission	13MS3-VN-16
17.00–17.20	**Vladimir GUBENKO and I. KIRILLOVICH**	Reanalysis of internal waves in the Venus's atmosphere by using Magellan radio occultation data	13MS3-VN-17
17.20–18.05	**POSTER SESSION, SESSION VENUS** 9 posters * 5 min		
	Igor KHATUNTSEV et al	Winds from the visible (513 nm) images obtained by the Venus Monitoring Camera onboard Venus Express	13MS3-VN-PS-01
	Marina PATSAEVA et al	From VMC/Venus Express to UVI/Akatsuki. long-term and longitude variations of zonal wind speed at the cloud top level near noon	13MS3-VN-PS-02
	Denis BELYAEV et al	Descent in the atmosphere of Venus with the Ultraviolet Spectrometer (DAVUS): scientific concept for a landing mission	13MS3-VN-PS-03
	Vladimir GUBENKO et al	Diffraction phenomena in radio occultation studies of the atmosphere of Venus by the satellites Venera-15 and -16	13MS3-VN-PS-04
	Evgeniya GUSEVA and Mikhail IVANOV	The spatial-genetic relationships of coronae, lobate plains and rift zones on Venus	13MS3-VN-PS-05
	Carlos BRAGA et al	Detailed mapping of large shield volcanoes on Venus – challenges and perspectives based on the study of Atira Mons, BAT region, Venus	13MS3-VN-PS-06
	Ekaterina ANTROPOVA et al	Characterization of the elongate cluster of "splotches" in the Phoebe Regio, Venus	13MS3-VN-PS-07
	Valery KOTOV	Motion of the Sun, Earth and Venus	13MS3-VN-PS-08
	Natalia BULATOVA	The role of Russian science in the development of planetary science of the Solar System(from the XVIII century to the present day)	13MS3-VN-PS-09

10.00–14.20

7 EXTRASOLAR PLANETS
SESSION

Convener: **Alexander TAVROV**
room 200, second floor

10.00–10.20	**Oleg YAKOVLEV et al**	Transiting exoplanet detection project at SAO RAS	13MS3-EP-01
10.20–10.40	**Shingo KAMEDA et al**	Upper atmospheres of Earth-like exoplanets around low-temperature stars	13MS3-EP-02
10.40–11.00	**Marina RUMENSKIKH et al**	Insights from a Non-detection of HeI 23S Absorption of GJ436b	13MS3-EP-03
11.00–11.20	**Valery SHEMATOVICH and A. AVTAEVA**	Non-thermal atmospheric loss for hot Neptune GJ3470 b	13MS3-EP-04
11.20–11.40	**Igor SAVANOV**	Activity of the young star KEPLER–1627 with exoplanet	13MS3-EP-05
11.40–12.00		COFFEE-BREAK	
12.00–12.20	**Ildar SHAIKHISLAMOV et al**	Space weather around hot exoplanets inferred from transit observations	13MS3-EP-06
12.20–12.40	**Artem SHEPELIN et al**	Simulation of Aeronomy and Transit Absorption of Trace Elements in Atmosphere of Hot Exoplanets: Development of General Kinetic non-LTE Model	13MS3-EP-07
12.40–13.00	**Sergei IPATOV**	Scattering of planetesimals from the feeding zone of Proxima Centauri c	13MS3-EP-08
13.00–14.00		LUNCH	
14.00–14.20		**POSTER SESSION, SESSION EXTRASOLAR PLANETS** 4 posters * 5 min	
	Artem BEREZUTSKY et al	Possible transit features of the TOI-421b and TOI-421c in Lyα and HeI 10830 A lines	13MS3-EP-PS-01
	Sergei IPATOV	Mixing of planetesimals in the TRAPPIST-1 exoplanetary system	13MS3-EP-PS-02
	Mikhail EFIMOV et al	On the transit spectroscopy features of warm mini-Neptunes in the HD–63433 system, revealed with their 3D numerical simulations	13MS3-EP-PS-03
	Eduard KUZNETSOV and Alexander PERMINOV	Search for chains of resonances in the compact planetary system K2–72	13MS3-EP-PS-04

SESSION 1. MARS (MS)
ORAL SESSION

THERMAL STRUCTURE OF THE MIDDLE AND UPPER ATMOSPHERE OF MARS AS SEEN BY ACS MIR SPECTROSCOPY

D.A. Belyaev[1], A.A. Fedorova[1], A. Trokhimovskiy[1], J. Alday[2], O.I. Korablev[1], F. Montmessin[3], A.S. Patrakeev[1]
[1] *Space Research Institute, Moscow, Russia; bdenya.iki@gmail.com*
[2] *School of Physical Sciences, The Open University, Milton Keynes, UK*
[3] *LATMOS/IPSL, CNRS, Guyancourt, France*

KEYWORDS:
Mars atmosphere, thermal structure, CO_2 density, solar occultation, infrared spectroscopy

Temperature and density in the upper Martian atmosphere, above ~100 km, are key diagnostic parameters to study processes of the species' escape, investigate the impact of solar activity, model the atmospheric circulation, and plan spacecraft descent or aerobraking maneuvers. In this paper, we report vertical profiling of carbon dioxide (CO_2) density and temperature from the Atmospheric Chemistry Suite (ACS) solar occultations onboard the ExoMars Trace Gas Orbiter (TGO). A strong CO_2 absorption band near 2.7 μm observed by the middle infrared spectrometric channel (ACS MIR) allows the retrieval of the atmospheric thermal structure in an unprecedentedly large altitude range, from 20 to 180 km. We present the latitudinal and seasonal climatology of the thermal structure for 1.5 Martian years (MYs), from the middle of MY 34 to the end of MY 35.

The results [1] show the variability of distinct atmospheric layers, such as a mesopause and homopause. The mesopause altitude rises from 70–90 km in the high-winter latitudes to 130–150 km in the summer season for both hemispheres. The homopause altitude varies from 90 km at aphelion to 130 km at perihelion in the Martian years 34 and 35, and it depends on dust activity. The homopause is generally located above the mesopause at low-middle latitudes, and below the mesopause near polar regions. A few near-equatorial observations reveal the mesopause subfreezing temperatures, below CO_2 frost point.

ACKNOWLEDGEMENTS:
The analysis of temperature and density profiles at IKI are funded by the grant No. 20-42-09035 of the Russian Science Foundation.

REFERENCES:
[1] Belyaev D.A. et al. Thermal structure of the middle and upper atmosphere of Mars from ACS/TGO CO2 spectroscopy // J. Geophysical Research: Planets (under review). 2022. https://doi.org/10.1002/essoar.10510820.2.

GRAVITY WAVE STATISTICS IN THE MARTIAN ATMOSPHERE FROM THE ACS/TGO SOLAR OCCULTATION EXPERIMENT

E.D. Starichenko[1], D.A. Belyaev[1], A.S. Medvedev[2], A.A. Fedorova[1], O.I. Korablev[1], F. Montmessin[3], A. Trokhimovskiy[1]

[1] *Space Research Institute, Moscow, Russia*
[2] *Max Planck Institute for Solar System Research, Göttingen, Germany*
[3] *LATMOS/IPSL, UVSQ Université Paris-Saclay, UPMC Univ. Paris 06, CNRS, Guyancourt, France*

KEYWORDS:
Gravity waves, Martian atmosphere, Trace Gas Orbiter, Atmospheric Chemistry Suite, solar occultation

INTRODUCTION:
Gravity waves (GWs) are omnipresent in planetary atmospheres and originate from displacements of air parcels. Since they re-distribute energy and momentum between atmospheric layers, GWs greatly affect atmospheric dynamics. In this work, we study the activity of GWs in the Martian atmosphere from solar occultation experiments conducted by the infrared spectrometers of Atmospheric Chemistry Suite (ACS) [1] on board the Trace Gas Orbiter (TGO).

OBSERVATIONS:
ACS is a part of the TGO, which represents the ESA-Roscosmos ExoMars 2016 collaborative mission. The instrument consists of three infrared channels [1]: near-IR (NIR, 0.73–1.6 μm), middle-IR (MIR, 2.3–4.2 μm) and thermal-IR (TIRVIM, 1.7–17 μm). In this work, we use the data obtained from the MIR and NIR instruments, operating in solar occultation mode since April 2018. ACS-MIR is a cross-dispersion echelle spectrometer that allows for retrieving temperature and density vertical profiles in the strong 2.7 μm CO_2 absorption band covering the broad altitude range of 20–180 km [2, 3]. ACS-NIR, an echelle spectrometer combined with an acousto-optic tunable filter, measures the atmospheric structure in the 1.57 μm CO_2 band at altitudes from 10 to 100 km [4, 5]. Both ACS channels possess a high resolving power, exceeding ~25000, signal to noise ratio more than 1000, and sound the atmosphere with the vertical resolution of 0.5–2.5 km. During simultaneous occultations, the instruments lines of sight target identical tangent points that provide confidential cross validation between the retrieved atmospheric profiles. Presently, we report the observations for 1.5 Martian years (MY), from the middle of MY34 (April 2018) to the end of MY35 (January 2021), counting ~600 occultations of MIR and ~6200 occultations of NIR. Fig. 1 and 2 show MIR and NIR data coverages respectively.

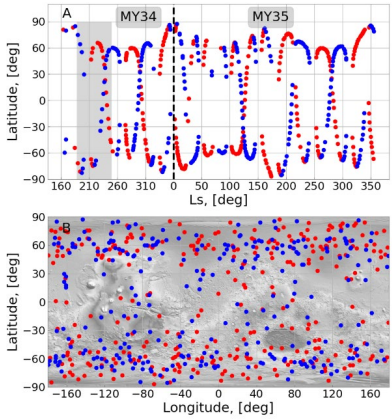

Fig. 1. Latitudinal coverage of ACS-MIR occultations versus Solar longitude (Ls) (a) and Martian longitude (b). Grey area in (a) depicts the global dust storm (GDS) period in MY34.

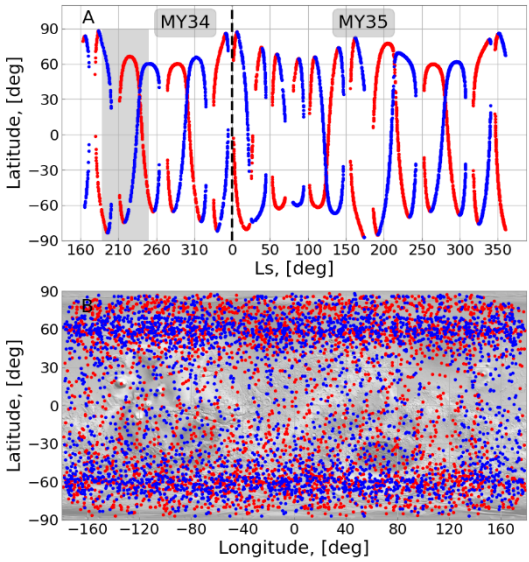

Fig. 2. The same as in Fig. 1 but for ACS-NIR

RESULTS:

In order to derive the parameters of GWs, we use the method described in [6]. We determine and analyze such characteristics of GWs as the acceleration (wave drag), vertical flux of horizontal momentum, potential energy and Brunt-Väisälä frequency, which characterizes the stability of GWs propagation. Fig. 3 shows the analysis of the single vertical temperature profile. First, from the vertical temperature profile (Fig. 3a, solid black line) we reveal the background temperature profile (Fig. 3a, red dashed line). From these two, we find their difference T' and the amplitude (envelope of T') of GW packets (Fig. 3b, solid black and red dashed lines respectively). Then we calculate the Brunt-Väisälä frequency, vertical flux of horizontal momentum and acceleration by GWs (Fig. 3c, d). In addition, we find GW potential energy, which we use as a measure of GW activity in this study.

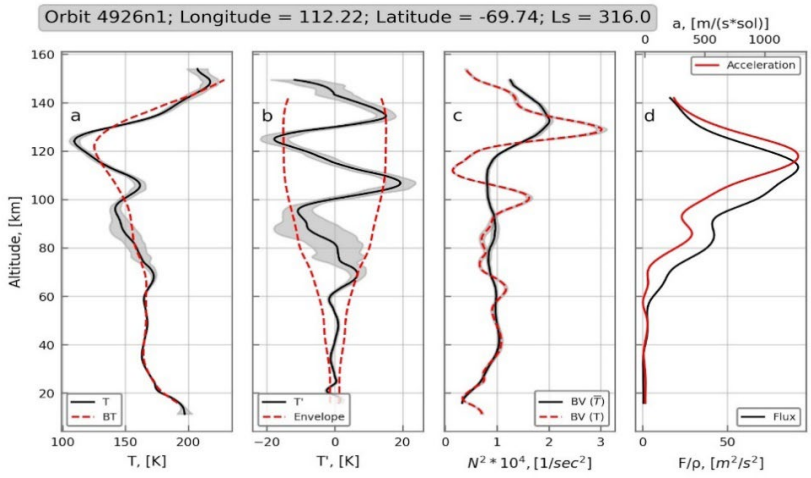

Fig. 3. Vertical profiles for the orbit 4926n1: a) the measured (solid black) and fitted mean temperature (red dashed); b) wave temperature disturbance (solid black) and envelope (red dashed); c) Brunt-Väisälä frequency calculated for the mean (black) and net temperature (red dashed); d) momentum flux (black) and mean flow acceleration ("wave drag", upper axis, red). Shading denotes observational uncertainties

In many cases we observe the mechanism of GW saturation and breaking (Fig. 3b), where the wave amplitude increases with altitude and stops grow-

ing at ~110 km. At the same altitude, the Brunt-Väisälä frequency of the net temperature tends to zero (Fig. 3c), which means that the temperature gradient is approaching the adiabatic lapse rate, and dissipation process takes place. This process, when the GW transfers its energy to the ambient flow, can be seen in the behavior of the momentum flux profile, which has steep drops, and an increase of acceleration (see Fig. 3d).

In this work we present the climatology of GWs and its parameters since the start of the ACS-MIR operations (April 2018, Ls –165̊ MY34) till the end of the MY35 (January 2021).

ACKNOWLEDGMENTS:
The data analysis in IKI is supported by the RSF grant #20-42-09035.

REFERENCES:

[1] Korablev O., Montmessin F. and ACS Team. The Atmospheric Chemistry Suite (ACS) of three spectrometers for the ExoMars 2016 Trace Gas Orbiter // Space Sci. Rev.2018. V. 214. Art. No. 7. 62 p. DOI 10.1007/s11214-017-0437-6.
[2] Belyaev D. et al. Revealing a high water abundance in the upper mesosphere of Mars with ACS onboard TGO // Geophysical Research Letters. 2021. V. 48. Art. No. e2021GL093411. DOI: 10.1029/2021GL093411.
[3] Belyaev D. et al. Thermal Structure of the Middle and Upper Atmosphere of Mars from ACS/TGO CO_2 Spectroscopy // J. Geophysical Research: Planets. 2022. 26 p. Under Review. DOI:10.1002/essoar.10510820.1.
[4] Fedorova A. et al. Stormy water on Mars: The distribution and saturation of atmospheric water during the dusty season // Science. 2020. Art. No. eaay9522. DOI: 10.1126/science.aay9522.
[5] Fedorova A. et al. A two-Martian year survey of the water vapor saturation state on Mars based on ACS NIR/TGO occultations // J. Geophysical Research: Planets. 2022. DOI:10.1002/essoar.10511229.1.
[6] Starichenko E. et al. Gravity wave activity in the Martian atmosphere at altitudes 20-160 km from ACS/TGO occultation measurements // J. Geophysical Research: Planets. 2021. V. 126. Art. No. e2021JE006899. DOI: 10.1029/2021JE006899.

A TWO-MARTIAN YEAR SURVEY OF THE WATER VAPOR SATURATION STATE ON MARS BASED ON ACS NIR/TGO OCCULTATIONS

A.A. Fedorova[1], F. Montmessin[2], A. Trokhimovskiy[1], M. Luginin[1], O. Korablev[1], J. Alday[3], D. Belyaev[1], J. Holmes[3], F. Lefevre[2], K. Olsen[4], A. Patrakeev[1], A. Shakun[1]

[1] *Space Research Institute, Moscow, Russia; fedorova@iki.rssi.ru*
[2] *LATMOS/CNRS, Guyancourt, France*
[3] *The Open University, Milton Keynes, UK*
[4] *Department of Physics, University of Oxford, Oxford, UK*

KEYWORDS:
Mars, atmosphere, temperature profiles, water vapor, saturation state

Recent measurements of water and temperature profiles in the Martian atmosphere showed that water can be strongly supersaturated at and above the level where clouds form [1, 2]. The near-infrared spectrometer NIR of the Atmospheric Chemistry Suite (ACS) onboard the Trace Gas Orbiter (TGO) has measured H_2O and temperature profiles using solar occultation in the infrared from below 10 km to 100 km of altitude. These observations provide the first long-term monitoring of the water saturation state for about two Martian years from Ls = 163° of MY34 to the Ls = 180° of MY36 and contain about 8500 water vertical profiles with simultaneous retrieval of CO_2 density and temperature. The latter was obtained from 1.43 and 1.57 μm CO_2 bands (orders 49 and 54 of the spectrometer) in the range of altitudes from 0 to 110 km. The H_2O mixing ratio was retrieved from the 1.38 μm water band (order 56 of the spectrometer) in the range of altitudes from 0 to 100 km. We also used the aerosol extinction at 1.4 μm from the same ACS NIR observations and H_2O ice extinction from simultaneous ACS MIR observation at 3.3 μm H_2O ice band.

Here we present the first detailed analysis of the vertical distribution of water vapor saturation state and studied the seasonal, latitudinal and local time variations. We found that the supersaturation is nearly ubiquitous above aerosol layers especially during the dust season, thereby promoting water escape. Water vapor abundance and its saturation state was found to vary between evening and morning terminators in response to temperature modulation imparted by thermal tides. Although water vapor is more abundant in the evening, colder morning temperatures induce a daily peak of saturation. The comparison of MY34 and MY35 with SPICAM IR observations on Mars-Express in MY29 has shown a good consistency which means the supersaturation is repeatable state of water vapor in the Martian atmosphere from year to year.

REFERENCES:

[1] Maltagliati L., Montmessin F., Fedorova A., Korablev O., Forget F., Bertaux J.-L. Evidence of Water Vapor in Excess of Saturation in the Atmosphere of Mars // Science. 2011. V. 333. 1868-1871.
[2] Fedorova A.A., Montmessin F., Korablev O., Luginin M., Trokhimovskiy A., Belyaev D.A. et al. Stormy water on Mars: The distribution and saturation of atmospheric water during the dusty season // Science. 2020. V. 367(6475). P. 297-300.

OVERVIEW OF MARTIAN YEAR 34 ATMOSPHERIC THERMAL STRUCTURE AND DUST DISTRIBUTION FROM ACS TIRVIM NADIR OBSERVATIONS ONBOARD EXOMARS TGO

P. Vlasov[1], N. Ignatiev[1], S. Guerlet[2], D. Grassi[3], O. Korablev[1], A. Grigoriev[4], A. Shakun[1], D. Patsaev[1], I. Maslov[1], L. Zasova[1], M. Luginin[1], A. Trokhimovskiy[1], E. Millour[2], F. Forget[2], R. Haus[5], G. Arnold[5,6], F. Montmessin[7]

[1] *Space Research Institute, Moscow, Russia, pavel.vlasov@phystech.edu;*
[2] *LMD/IPSL, Sorbonne Université, PSL Research Université, École Normale Supérieure, École Polytechnique, CNRS, Paris, France;*
[3] *Istituto di Astrofisica e Planetologia Spaziali – Istituto Nazionale di Astrofisica, Rome, Italy;*
[4] *Research School of Astronomy and Astrophysics, Australian National University, Canberra, Australia;*
[5] *DLR, Berlin, Germany Institute of Planetary Research, DLR, Berlin, Germany;*
[6] *Institute of Geoscience, University Potsdam, Potsdam, Germany;*
[7] *LATMOS, Guyancourt, France*

KEYWORDS:
ExoMars TGO, ACS TIRVIM, nadir observations, MY 34, Martian atmosphere, thermal structure, dust variability

The ExoMars Trace Gas Orbiter (TGO) is a mission by ESA and Roscosmos, which started its operational scientific phase in March 2018 [1]. The Atmospheric Chemistry Suite (ACS) is a set of three spectrometers (NIR, MIR, and TIRVIM) designed to observe the Martian atmosphere in solar occultation, nadir and limb geometry [2]. The Thermal InfraRed channel (TIRVIM) is a Fourier-transform spectrometer capable of operating in nadir and occultation modes in the spectral range of 1.7–16.7 μm [3]. The main scientific goal of TIRVIM is long-term monitoring of temperatures and aerosols (dust and water ice) distribution in Martian atmosphere in nadir mode of observations in the 7.7–16.7 μm spectral range with the spectral resolution 1.17 cm^{-1}. The nadir spectra of thermal radiation emitted by Mars in this spectral range contain deep 15 μm CO_2 absorption band which carries information about the temperature of the atmosphere at different altitudes and aerosols absorption bands which provides information about dust particles and water ice clouds loading in Martian atmosphere. Vertical temperature profiles from the surface up to 60 km of altitude, surface temperatures, column dust and water ice optical depths at 1075 and 825 cm^{-1} respectively are retrieved by statistical regularization method [4].

We present an overview of Martian Year (MY) 34 atmospheric thermal structure from the surface up to 60 km of altitude along with column dust optical depth evolution from L_s = 142.8° to 357.3° (Solar Longitude) from ACS TIRVIM nadir observations onboard ExoMars TGO. The considered dataset includes: atmosphere before the northern autumnal equinox (L_s = 142.8°–166.5°); onset and peak of the global dust storm (GDS) of MY 34 (L_s = 182.2°–211.8°); atmosphere around northern winter solstice (L_s = 241.7°–255.1°, 272.7°–317.2°); the entire regional dust storm (C-storm) (L_s = 320.2°–341.8°); and atmosphere before northern spring equinox (L_s = 344.7°–357.3°). We retrieved the thermal structures of Martian atmosphere at various local times, diurnal and seasonal contrasts of temperature, seasonal and spatial maps of surface temperature and column dust optical depth evolution. The obtained results are compared to MCS/MRO observations [5] and GCM simulations for MY 34 [6].

ACKNOWLEDGMENTS:
Science support in IKI is funded by the RSF grant #20-42-09035.

REFERENCES:

[1] Vago J., Witasse O., Svedhem H., Baglioni P., Haldemann A., Gianfiglio G. et al. ESA ExoMars program: The next step in exploring Mars // Solar System Research. 2015. V. 49(7). P. 518-528.
[2] Korablev O., Montmessin F., Trokhimovskiy A. et al. The Atmospheric Chemistry Suite (ACS) of Three Spectrometers for the ExoMars 2016 Trace Gas Orbiter // Space Science Reviews. 2018. V. 214(1). Art. No. 7. 62 p.
[3] Shakun A., Ignatiev I., Luginin M., Grigoriev A., Moshkin B., Grassi D. et al. ACS/TIRVIM: Calibration and first results // Proc. SPIE. V. 10765. Infrared Remote Sensing and Instrumentation XXVI. 2018. Art. No. 107650E. 9 p.
[4] Rodgers C.D. Inverse methods for atmospheric sounding: Theory and practice. River Edge, NJ: World Scientific, 2000.
[5] Lee C., Lawson W.G., Richardson M.I., Heavens N.G., Kleinböhl A., Banfield D. et al. Thermal tides in the Martian middle atmosphere as seen by the Mars Climate Sounder // J. Geophysical Research. 2009. V. 114. Art. No. E03005.
[6] Forget F., Hourdin F., Fournier R., Hourdin C., Talagrand O., Collins M. et al. Improved general circulation models of the Martian atmosphere from the surface to above 80 km // J. Geophysical Research. 1999. V. 104. P. 24155-24175.

OBSERVATIONS OF 2.7 MICROMETER CO_2 ICE BAND ON MARS FROM ACS SOLAR OCCULTATIONS ONBOARD TGO/EXOMARS

M. Luginin[1], N. Ignatiev [1], A. Fedorova[1], A. Trokhimovskiy[1], D. Belyaev[1], A. Grigoriev[2,1], A. Shakun[1], F. Montmessin[3], O. Korablev[1]
[1] *Space Research Institute, Moscow, Russia, mikhail.luginin@phystech.edu;*
[2] *Australian National University, Canberra, Australia;*
[3] *LATMOS-UVSQ, Guyancourt, France*

KEYWORDS:
Mars, aerosols, CO_2 clouds, ACS, TGO

Martian atmosphere is primarily composed of carbon dioxide. Its seasonal cycle plays an important role in atmospheric dynamics and climate of Mars. Seasonal formation of CO_2 frost deposits in the Martian polar regions results in up to 30 % of atmospheric pressure variations. Another case of carbon dioxide condensation is formation of a CO_2 clouds that are still poorly studied, despite the fact that they have been observed by a number of instruments [1–6] on the orbit of Mars.

Three types of aerosols are observed on Mars: mineral dust, water ice and carbon dioxide ice. To distinguish CO_2 ice from other types of aerosols, one can analyze CO_2 ice absorption features. In this work, we use data from the Atmospheric Chemistry Suite (ACS) onboard the Trace Gas Orbiter (TGO) and analyze spectra in the 2.7 μm region. This spectral region contains CO_2 absorption feature which consists of two aerosol absorption peaks: combination modes $2\nu_2+\nu_3$ and $\nu_1+\nu_3$ located at 3599.5 cm^{-1} and 3708.0 cm^{-1} respectively [7].

ACS is a set of three infrared spectrometers: Near InfraRed (NIR), Mid-InfraRed (MIR), and Thermal InfraRed (TIRVIM). Spectral coverage of MIR and TIRVIM allows observations of 2.7 μm CO_2 ice band and retrieval of microphysical properties of aerosols such as particle size and number density; NIR spectra are used to better constrain them. In Fig. 1, transmission spectra in the spectral region 3700–3740 cm^{-1} is shown in blue and recorded by MIR instrument during the ingress occultation #9192 at altitude 56 km. Recorded transmission is produced both by CO_2 gas (black lines) and by aerosols (red lines) that consist of CO_2 ice particles with effective radius of ~1 μm.
In this work, we will present results of CO_2 ice clouds observations using 2.7 μm absorption band the from ACS solar occultation data received in the period from May 2018 to June 2022.

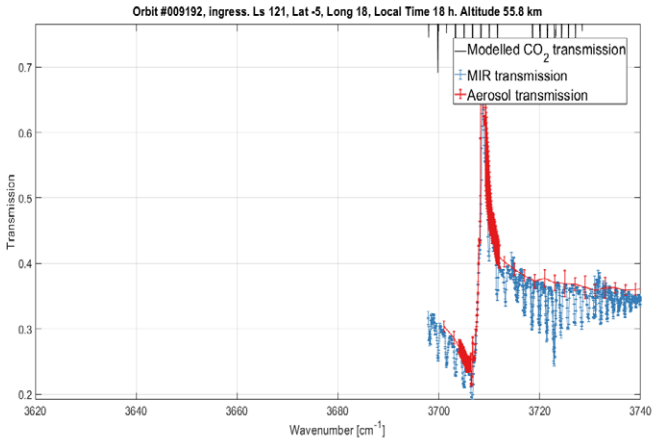

Fig. 1. Transmission data in the spectral region 3700–3740 cm^{-1} recorded by MIR instrument during the ingress occultation #9192 at altitude 56 km. Blue: transmission produced both by CO_2 gas and by aerosols. Black: gaseous transmission. Red: aerosol transmission produced by CO_2 ice particles with effective radius of ~1 μm.

ACKNOWLEDGMENTS:
This work was funded by Russian Science Foundation, grant number 20-42-09035.

REFERENCES:

[1] Montmessin et al. Subvisible CO_2 ice clouds detected in the mesosphere of Mars // Icarus. 2006. V. 183. P. 403-410. https://doi.org/10.1016/j.icarus.2006.03.015.
[2] Määttänen et al. Mapping the mesospheric CO_2 clouds on Mars: MEx/OMEGA and MEx/HRSC observations and challenges for atmospheric models // Icarus. 2010. V. 209. P. 452-469. https://doi.org/10.1016/j.icarus.2010.05.017.
[3] McConnochie et al. THEMIS-VIS observations of clouds in the Martian mesosphere: Altitudes, wind speeds, and decameter-scale morphology // Icarus. 2010. V. 210. P. 545-565. https://doi.org/10.1016/j.icarus.2010.07.021.
[4] Vincendon et al. New near-IR observations of mesospheric CO_2 and H_2O clouds on Mars // J. Geophysical Research. 2011. V. 116. Art. No. E00J02. https://doi.org/10.1029/2011JE003827.
[5] Jiang et al. Detection of Mesospheric CO_2 Ice Clouds on Mars in Southern Summer // Geophysical Research Letters. 2019. V. 46(14). P. 7962-7971. https://doi.org/10.1029/2019GL082029.
[6] Liuzzi et al. First Detection and Thermal Characterization of Terminator CO2 Ice Clouds with ExoMars/NOMAD // Geophysical Research Letters. 2021. https://doi.org/10.1029/2021GL095895.
[7] Isokoski K., Poteet C.A., Linnartz H. Highly resolved infrared spectra of pure CO_2 ice (15-75 K) // Astronomy and Astrophysics. 2013. V. 555. Art. No. A85. https://doi.org/10.1051/0004-6361/201321517.

KINETIC MODELING OF HOT FRACTION IN THE EXTENDED HYDROGEN CORONA OF MARS

V.I. Shematovich[1], D.V. Bisikalo[1], D. Bhattacharyya[2], J.T. Clarke[3]
[1] *Institute of Astronomy of the Russian Academy of Sciences, Moscow, Russia; shematov@inasan.ru*
[2] *Laboratory for Atmospheric and Space Physics, University of Colorado Boulder, Boulder, CO, USA*
[3] *Center for Space Physics, Boston University, Boston, MA, USA*

KEYWORDS:
Mars, hydrogen corona, suprathermal H atoms, kinetic modeling, UV observations

INTRODUCTION:
The ballistic motion of hydrogen atoms over the exobase leads to the formation of an extended exosphere or corona of Mars, observed in the scattered solar ultraviolet (UV) radiation in the Lyman-α line [1–3]. This corona has been repeatedly observed both by the Mars Express and MAVEN spacecraft [1, 2] and the Hubble Space Telescope [3]. Recent analysis of the MAVEN data, from the Imaging Ultraviolet Spectrograph's (IUVS) Echelle channel [4], has raised the likelihood of an energetic population of atomic hydrogen in the extended corona of Mars. Energetic H atoms were recently discovered in the exosphere of Mars with HST [5]. Understanding energetic atoms has become the key to understanding present-day water loss and the enhanced D/H ratio in the water at Mars.

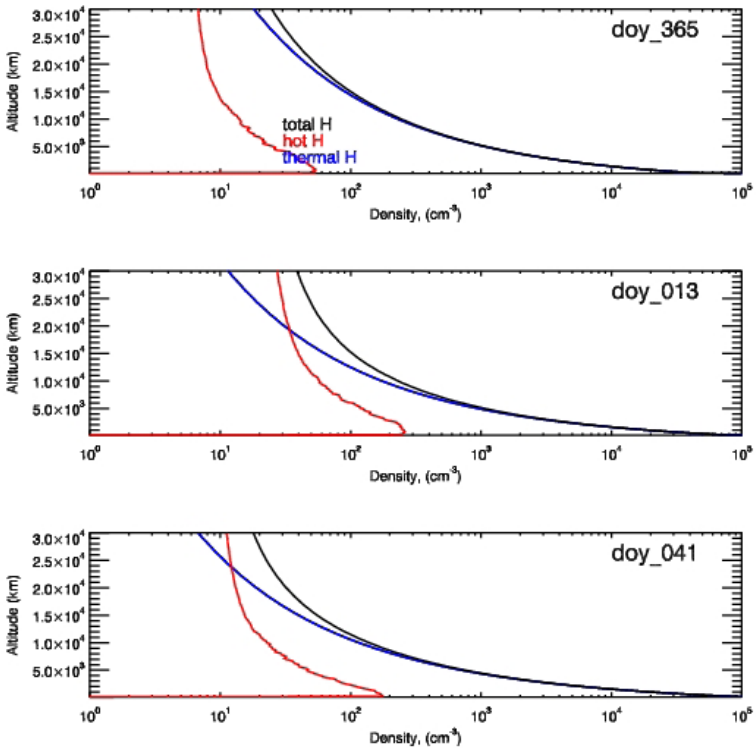

Fig. (top panel) Height profiles of the thermal (blue lines) and hot (red lines) fractions of atomic hydrogen in the extended corona at Mars. Total H concentrations are shown by black lines. Calculations were done for the dates December 31, 2017 (upper panel), January 13, 2018 (middle panel), and February 10, 2018 (bottom panel) when the HST observations of the hydrogen corona at Mars were made.

To calculate the distribution of hot H fraction in the extended hydrogen corona of Mars the kinetic Monte Carlo model [6, 7] of solar wind interaction with the Martian atmosphere was used. This model allowed us to estimate the charge exchange efficiency in the range 4–8 % depending on the total hydrogen content in the Martian corona. It was also found that the energy spectrum of hydrogen atoms penetrating into the Martian atmosphere does not change and remains identical in structure to the spectrum of undisturbed solar wind protons. These estimates, combined with the developed kinetic Monte Carlo model of the proton and hydrogen atom precipitation into the planetary atmosphere [7], provided the possibility to trace all the stages of the penetration of the undisturbed solar wind protons into the dense layers of the Martian atmosphere, as well as interpret the observed characteristics of the extended hydrogen corona depending on the variations of atomic hydrogen content. One of the important outputs are the calculated height profiles of hot hydrogen fraction in the Martian corona (see Figure). It is seen that the concentration of hot fraction of H atoms formed due to the forcing of the solar wind onto the Martian atmosphere becomes comparable with the thermal fraction in the most upper region of the hydrogen corona at Mars. These profiles were calculated for the dates — December 31, 2017, January 13, 2018, and February 10, 2018 — when the HST observations of the hydrogen corona at Mars were conducted [5].

ACKNOWLEDGMENTS:
VIS and DVB are grateful to the Government of the Russian Federation and the Ministry of Higher Education and Science of the Russian Federation for grant support No. 075-15-2020-780 (GA No. 13.1902.21.0039).

REFERENCES:

[1] Chaffin M.S., Chaufray J.Y., Deighan J. et al. Elevated atmospheric escape of atomic hydrogen from Mars induced by high-altitude water // Nature Geoscience. 2017. V. 10. P. 174-178. DOI: 10.1038/ngeo2887.
[2] Chaffin M.S., Chaufray J.Y., Deighan D. et al. Mars H escape rates derived from MAVEN/IUVS Lyman alpha brightness measurements and their dependence on model assumptions // J. Geophysical Research: Planets. 2018. V. 123. Iss. 8. P. 2192-2210. DOI: 10.1029/2018JE005574.
[3] Bhattacharyya D., Clarke J.T., Bertaux J.-L. et al. Analysis and modeling of remote observations of the Martian hydrogen exosphere // Icarus. 2017. V. 281. P. 264-280. https://doi.org/10.1016/j.icarus.2016.08.034.
[4] Clarke J.T., Mayyasi M., Bhattacharyya D. et al. Variability of D and H in the Martian upper atmosphere observed with the MAVEN IUVS echelle channel // J. Geophysical Research: Space Physics. 2017. V. 122. Iss. 2. P. 2336-2344. https://doi.org/10.1002/2016JA023479.
[5] Bhattacharyya D., Clarke J., Mayyasi M. et al. Evidence of hot hydrogen in the exosphere of Mars // EPSC-DPS Joint Meeting. 15-20 Sept. 2019, Geneva, Switzerland. 2019. V. 13. Art. No. EPSC-DPS2019-960. 2 p.
[6] Shematovich V.I., Bisikalo D.V., Zhilkin A.G. Effects of column density variations of extended hydrogen corona of Mars on the charge exchange efficiency with solar wind protons // Astronomy Reports. 2021. V. 65. Iss. 3. P. 203-208. DOI:10.1134/S1063772921030033.
[7] Shematovich V.I., Bisikalo D.V. Kinetic calculations of the charge exchange efficiency between solar wind protons and extended hydrogen corona of Mars // Astronomy Reports. 2021. V. 65. Iss. 9. P. 869-875. https://doi.org/10.1134/S106377292110036X.

PLANETARY IONS ACCELERATION INSIDE MARTIAN HOT FLOW ANOMALY

A.Yu. Shestakov[1], S.D. Shuvalov[1]
[1] *Space Research Institute, Moscow, Russia, sartiom1@yandex.ru, shuvalovsergei@gmail.com*

KEYWORDS:
Hot flow anomaly, HFA, Mars, solar wind, foreshock transient, bow shock

INTRODUCTION:
Hot Flow Anomalies (HFAs) are among the most common foreshock transients, non-stationary events that occur in planetary foreshocks. They are a flow of heated plasma directed from the planetary shock observed in the vicinity of its intersection region with the interplanetary current sheet. Observations of HFAs at the Earth by MMS mission have shown that protons can be effectively accelerated inside these structures to nearly 1 MeV under certain conditions via first-order Fermi acceleration process. This suggests that HFA play an important role in cosmic rays emissions on astrophysical shock waves throughout outer space [1].

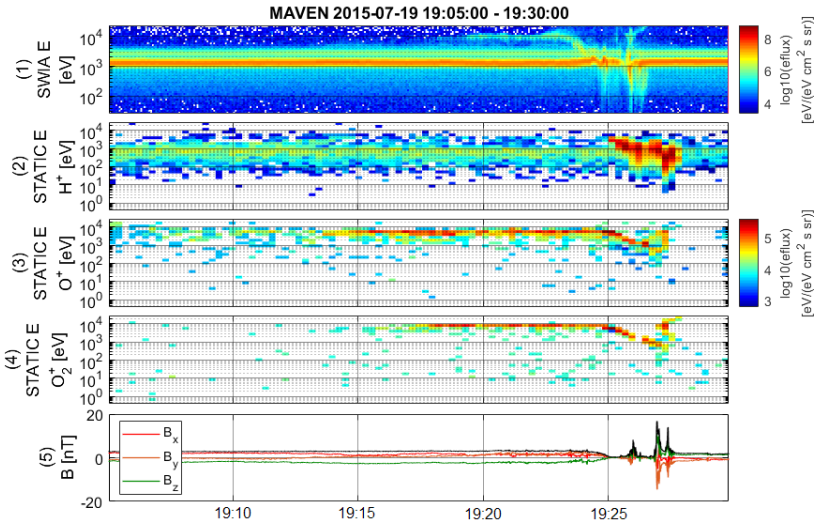

Fig. (1) — ion energy spectra of all masses; (2)–(4) — H+, O+, O2+ energy spectra; (5) — magnetic field vector and magnitude.

Current study focuses on the analysis of a single HFA from the list presented in our previous paper [2] registered at Mars by MAVEN spacecraft. The event is characterized by the presence of accelerated O^+ and O_2^+ ions of ionospheric origin on both sides from the current sheet, associated with an event. Ions with energies up to ~10 keV are detected before the current sheet crossing, and over 30 keV after the current sheet crossing. There is a relationship between the ion mass and the maximum energy to which acceleration occurs, which is consistent with the above-described Fermi acceleration process [1].

The presence of heavy ions inside the HFA is apparently possible only near planets without own global intrinsic magnetic field, since their bow shocks are close enough (~1 radius of the planet) to the ionosphere, which allows planetary ions to reach the shock when it undergoes serious disturbances. The acceleration of planetary ions in HFAs can also form another channel of Martian atmospheric losses.

ACKNOWLEDGEMENTS:
The research is conducted within the framework of the Russian Science Foundation grant №. 21-42-04404.

REFERENCES:

[1] Turner D.L., Ergun R., Schwartz S.J. et al. Autogenous and efficient acceleration of energetic ions upstream of Earth's bow shock // Nature. V. 561. P. 206-210. Art. No. 30209369 DOI: 10.1038/S41586-018-0472-9.
[2] Shuvalov S.D., Ermakov V.N., Zorina V.O. et al. Propagation properties of Hot Flow Anomalies at Mars: MAVEN observations //Planetary and Space Science. 2019. V. 179. Art. No. 104717. DOI: 10.1016/j.pss.2019.104717.

RADIATION ENVIRONMENT IN EXOMARS TGO MARS ORBIT DURING SOLAR ENERGETIC PARTICLE EVENTS IN JULY 2021 – MARCH 2022

J. Semkova[1], R. Koleva[1], V. Benghin[3], K. Krastev[1], Y. Matviichuk[1], B. Tomov[1], N. Bankov[1], S. Maltchev[1], T. Dachev[1], I. Mitrofanov[2], A. Malakhov[2], A. Kozyrev[2], D. Golovin[2], M. Mokrousov[2], A. Sanin[2], M. Litvak[2], S. Nikiforov[2], D. Lisov[2], A. Anikin[2], V. Shurshakov[3], S. Drobyshev[3]

[1] *Space Research and Technology Institute, Bulgarian Academy of Sciences, Sofia, Bulgaria; jsemkova@stil.bas.bg*

[2] *Space Research Institute, Moscow, Russia; mitrofanov@np.cosmos.ru*

[3] *State Scientific Center of Russian Federation, Institute of Biomedical Problems RAS, Moscow, Russia; v_benghin@mail.ru*

KEYWORDS:

The dosimetric telescope Liulin-MO for measuring the radiation environment onboard the ExoMars TGO is a module of the Fine Resolution Epithermal Neutron Detector (FREND).

Here we present results from the observation of solar energetic particle (SEP) events in July, September and October 2021, February and March 2022 and their effects on the radiation environment on TGO during the corresponding periods. Shown are the results from the measurements of the SEP charged particle fluxes, dose rates and estimation of dose equivalent rates provided by Liulin-MO. Compared are the time profiles of the particle fluxes and count rates measured by Liulin-MO and the neutron detectors of FREND during the most important SEP events in October 2021 and February 2022. The data for SEP events on TGO in July 2021 – February 2022 contribute to the details for the solar activity at a time when Mars is on the opposite side of the Sun from Earth.

The results of the radiation measurements on TGO are of importance for benchmarking of the space radiation environment models and for assessment of the radiation risk to future manned missions to Mars.

COMPARISON OF THE FLUX AND DOSE RATE MEASURED BY THE LIULIN-MO DEVICE ABOARD EXOMARS TGO WITH CALCULATED ESTIMATIONS

V. Benghin[3], J. Semkova[1], R. Koleva[1], K.Krastev[1], Y. Matviichuk[1], B. Tomov[1], N. Bankov[1], S. Maltchev[1], T. Dachev[1], I.Mitrofanov[2], A. Malakhov[2], A. Kozyrev[2], D. Golovin[2], M. Mokrousov[2], A. Sanin[2], M. Litvak[2], S. Nikiforov[2], D. Lisov[2], A. Anikin[2], J. Guo[4], V. Shurshakov[3], S. Drobyshev[3]

[1] *Space Research and Technology Institute, Bulgarian Academy of Sciences, Sofia, Bulgaria; jsemkova@stil.bas.bg*

[2] *Space Research Institute, Russian Academy of Sciences, Moscow, Russia; mitrofanov@np.cosmos.ru*

[3] *State Scientific Center of Russian Federation, Institute of Biomedical Problems, Russian Academy of Sciences, Moscow; Russia, v_benghin@mail.ru*

[4] *University of Science and Technology of China, Hefei, China, 3CAS Center for Excellence in Comparative Planetology; jnguo@ustc.edu.cn*

INTRODUCTION:

We present results of comparisons the flux and dose rate measured by the Liulin-MO device aboard ExoMars TGO with calculated estimations. The Liulin-MO device is a module of the Fine Resolution Epithermal Neutron Detector (FREND). The calculation was carried out using On-Line Tool for the Assessment of Radiation in Space (OLTARIS) developed by NASA.

An analysis of the ExoMars TGO spatial orientation effect on Liulin-MO detectors count rate was carried out. It was taken into account galactic cosmic rays and Mars albedo radiation. We had assessed the sensitivity of the Liulin-MO device semiconductor detectors to neutron and gamma radiation. It is shown that the contribution of albedo radiation can be about 10%. A significant part of the albedo contribution to the detectors count rate is introduced by neutron radiation. However, the main role in the detectors counting rate changing when the orientation of the ExoMars TGO changes is played by the contribution made by the direct effect of the galactic cosmic rays on the Liulin-MO detectors. The effect of orientation on the measured dose rate is weaker than on the particle flux.

GLOBAL MAP OF WATER ABUNDANCE IN THE UPPER REGOLITH LAYER OF THE EQUATORIAL REGION ON MARS

A.V. Malakhov[1], I.G. Mitrofanov[1], M.L. Litvak[1], A.B. Sanin[1], D.V. Golovin[1], M.V. Djachkova[1], N.V. Lukyanov[1]
[1] *Space Research Institute, Moscow, Russia, malakhov@np.cosmos.ru*

KEYWORDS:
Mars, hydrogen, water, neutron, regolith

INTRODUCTION:
FREND [1] is a neutron telescope onboard ESA's Trace Gas Orbiter [2], and is a collimated neutron telescope capable of mapping Mars' hydrogen content in the upper 1 m of regolith with a high spatial resolution, up to 200 km globally.

After performing measurements for two martial years, we present in this study a map of water content in the equatorial regions showing many new details and water-rich locations that were not previously observable [3]. A brief analysis of this map reveals about 20 areas in the equatorial area where water content is unusually high, reaching 20 weight percent. These areas were studied in more detail to explain the possible source of the observed water abundance in them.

ACKNOWLEDGEMENTS:
This study is performed under the Russian Science Foundation Grant No. 19-72-10144.

REFERENCES:
[1] Mitrofanov I.I., Malakhov A., Bakhtin B. et al. Fine Resolution Epithermal Neutron Detector (FREND) onboard the ExoMars Trace Gas Orbiter // Space Science Reviews. 2018. V. 214. Art. No. 86. 26 p. DOI: 10.1007/s11214-018-0522-5.
[2] Vago J., Witasse O., Svedhem H. et al. ESA ExoMars program: The next step in exploring Mars // Solar System Research. 2015. V. 49. Iss. 7, P. 518-528. DOI:10.1134/S0038094615070199.
[3] Malakhov A.I., Mitrofanov I.G., Golovin D.V. et al. High Resolution Map of Water in the Martian Regolith Observed by FREND Neutron Telescope Onboard ExoMars TGO // J. Geophysical Research: Planets. 2022. V. 127. Iss. 5. Art. No. e2022JE007258. 16 p. https://doi.org/10.1029/2022JE007258.

WHEN DID MARS BECOME BIPOLAR? OUTSTANDING ISSUES IN A CONCEPTUAL MODEL OF A NOACHIAN-AMAZONIAN CLIMATE TRANSITION FROM AN ALTITUDE-DOMINANT TEMPERATURE ENVIRONMENT (ADD) TO A LATITUDE-DOMINANT TEMPERATURE ENVIRONMENT (LDD)

J.W. Head[1], R.D. Wordsworth[2], J.L. Fastook[3]
[1] *Brown University, Providence, USA*
[2] *Harvard University, Cambridge, USA*
[3] *University of Maine, Orono, USA; james_head@brown.edu*

KEYWORDS:
Mars, climate, atmosphere, valley networks, lakes, warm and wet, cold and icy, Noachian, Hesperian, Amazonian, climate change, altitude-dependent, latitude-dependent

INTRODUCTION:
The nature of the evolution of the Mars atmosphere and climate from its early history to that of today (Fig. 1) is one of the most fundamental questions in planetary science [1, 2]. What were the initial conditions? What were the characteristics of the Noachian atmosphere and climate ('warm and wet', rainfall and runoff, P_{atm} 1 bar or more, MAT >273 K supported by greenhouse gases [3, 4]; or 'cold and icy', P_{atm} 1 bar (?), MAT ~226 K, icy highlands) [5–7]? What were the factors that led from the Noachian ambient climate to the currently observed ambient late Amazonian climate conditions (extremely low 6 mbar P_{atm}, hyperarid, hypothermal MAT ~213 K) [8]?

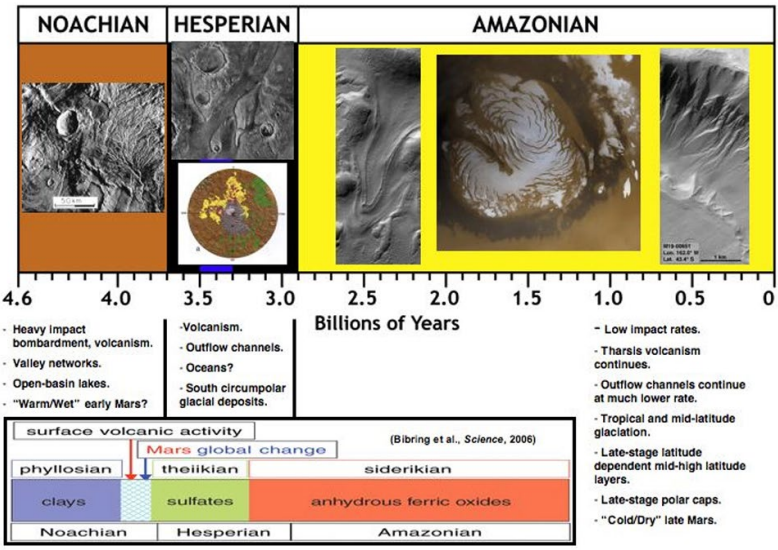

Fig. 1. Diagrammatic representation of the main themes in the geologic [1] and alteration history [28] of Mars

Key related questions include: What was the nature of the hydrological system (horizontally stratified or vertically integrated) [9] and how did it change with time? What was the budget of surface/near-surface water [10] and how was it distributed? What were the conditions that led to observed fluvial, lacustrine and possibly oceanic environments (duration, periodicity, episodicity)? What were the warming greenhouse gases, their sources [e.g., 11], and the mechanisms for sustaining them in the atmosphere? What was the mean

annual temperature (MAT) as a function of time and did global temperature distribution (GTD) change? What are the atmospheric loss rates to space [12] and how did they vary with time?

THE QUESTION:

As a step in addressing these many fundamental issues, we recently posed the question: *What is the most parsimonious set of conditions that might explain a transition from a Noachian Mars atmosphere and climate to the current benchmark Amazonian conditions?* Key elements that require explanation include: 1) a P_{atm} change from potentially >1 bar to 6 mbar, 2) a MAT change from potentially >273 K to ~213 K, 3) a significant decrease in the surface-near surface global water budget from as much as ~5000 m GEL [13] to <50 m GEL [10], 4) a change in the location of the major water reservoirs (from Noachian oceans or icy highlands to the polar ice caps observed today [10]) and 5) a change in the Global Temperature Distribution (GTD) from a dominantly altitude dependent temperature distribution (ADD) to dominantly latitude dependent temperature distribution (LDD) (Fig. 2).

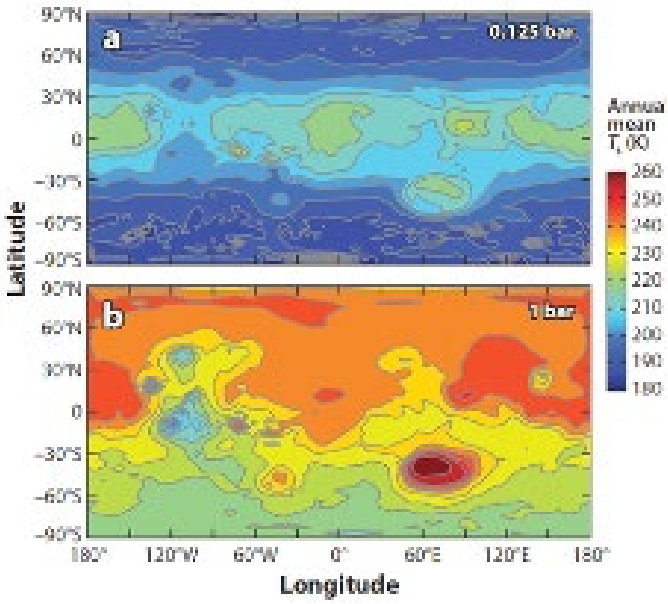

Fig. 2. The modern LDE compared to the early Mars ADE: a) MAT from 3D GCM at 125 mbar P_{atm} (Amazonian); b) MAT from 3D GCM at 1 bar P_{atm} (Noachian?) [6, 7]

THE CONCEPTUAL MODEL:

We presented what we believe might be the most parsimonious, yet potentially plausible, Noachian climate scenario and its transition to today as follows [14]: The Middle-Late Noachian atmosphere was characterized by P_{atm} of less than several hundred millibars, sufficient to cause an adiabatic cooling effect (ADD) in both 'cold and icy' and 'warm and wet' climate scenarios [5–7, 15], and preferentially sequestering snow and ice in the southern uplands, Tharsis, and the south polar cap. A modest decrease of P_{atm} (several tens of mbar?) beginning in the Late Noachian caused the altitude-dependent dominance (ADD) GTD to decay and the LDD GDT to dominate (as observed today), significantly changing the global thermal environment with geological process consequences. During this transitional period, the equilibrium line altitude (ELA; contour separating net snow and ice accumulation, above, from net ablation, below) rose in altitude in the equatorial and mid-latitude regions and appeared in the North Polar region and migrated southward (compare Fig. 2b, a). A significant part of the water budget began to accumulate to form the North Polar Cap, and Mars became "bipolar". As the ELA rose in altitude in the equatorial/mid-latitude regions, peak daily and seasonal temperatures (PDT, PST; [16]) began to exceed 273 K (as observed

today) and snow and ice in the equatorial/mid-latitude uplands was subjected to periodic top-down melting [17] of sufficient duration to produce large volumes of meltwater [18], potentially forming the observed, circum-highlands fluvial and lacustrine features. This ADD to LDD transitional climate period (compare Fig. 1b, a) continued until the North Polar Cap reached its current volume configuration and the equatorial surface water budget was depleted. This transitional period appears to have been complete by the Early Amazonian (Fig. 1); between then and today, variations in obliquity [19] dominated the Amazonian climate history, with polar ice being mobilized at higher obliquity and transported to lower latitude cold-traps to form regional mid-latitude glaciation/tropical mountain glaciers [20, 21], returning to polar cold traps as obliquity decreased toward that of today [22].

We describe this scenario as 'parsimonious' because it: 1) involves a plausible Noachian P_{atm}, 2) utilizes known global atmospheric effects (P_{atm}-dependent ADD-LDD conditions), 3) requires minimal changes in global MAT, 4) requires no major and persistent influx of warming greenhouse gases, 5) calls on a plausible global water budget throughout, 6) requires modest atmospheric loss to space, 7) provides a more plausible D/H ratio history, and 8) requires no Tharsis-induced true polar wander (TPW) to account for valley network distribution patterns [23].

TESTS OF THE MODEL:

Here we describe the significant questions that this scenario raises and how the hypothesis might be further tested, refined, or rejected:

1. Is a Noachian P_{atm} of several hundred mbar plausible and what is the geologic evidence for this?
2. What is the P_{atm} tipping point at which the ADD dominant scenario begins to decay to the LDD dominant scenario (compare Fig. 2b, a), how long does this transition take, and does it change global atmospheric circulation patterns significantly?
3. What are the effects of variations in obliquity during the transition, including potential very low obliquity-induced atmospheric collapse?
4. When did the Tharsis Rise form (including possible TPW [23]) and what effect did it have on the atmosphere and climate?
5. Are documented geologic events in the Hesperian transitional period (see Fig. 1) (e.g., volcanic resurfacing, sulfate deposits [24, 25], outflow channel formation) consistent with this scenario?
6. Are the major periods of mineralogical alteration (see Fig. 1) (phyllosilicates, sulfates, anhydrous oxidation) consistent with this scenario?
7. Are the major findings of the robotic surface exploration missions MER, MSL (Gale CBL and Jezero OBL), and Zhurong (southern Utopia Planitia) consistent with this scenario?
8. Are the predicted rates of volatile loss to space envisioned by this scenario consistent with MAVEN results [12]?
9. Are the observed characteristics, distribution and duration of fluvial and lacustrine environments (valley networks and lakes) [26] and crater degradation history consistent with this scenario?
10. Are the South polar/circumpolar deposits (Dorsa Argentea Formation [27]) and their timing consistent with this scenario?

CURRENT WORK:

We are currently exploring several of these questions using geologic observations and mapping (the Hesperian sulfate transition period [24, 25]) and climate modeling (the nature of the change from ADD to LDD; see Fig. 2).

REFERENCES:

[1] Carr M.H., Head J.W. III Geologic history of Mars // Earth and Planetary Science Letters. 2010. V. 294. P. 185-203. doi:10.1016/j.epsl.2009.06.042.

[2] The Atmosphere and Climate of Mars / eds. R.M. Haberle, R. T. Clancy, F. Forget et al. Cambridge: Cambridge University Press, 2017. https://doi.org/10.1017/9781139060172.

[3] Craddock R.A., Howard A.D. The case for rainfall on a warm, wet early Mars // J. Geophysical Research: Planets. 2002. V. 107. Iss. E11. P. 21-1-21-36. https://doi.org/10.1029/2001JE001505.
[4] Ramirez R.M., Craddock R.A. The Geological and Climatological Case for a Warmer and Wetter Early Mars // Nature Geoscience. 2018. V. 11. P. 230-237. https://doi.org/10.1038/s41561-018-0093-9.
[5] Forget F., Wordsworth R., Millour E. et al. 3D modelling of the early martian climate under a denser CO2 atmosphere: Temperatures and CO2 ice clouds // Icarus. 2013. V. 222. Iss. 1. P. 81-99. https://doi.org/10.1016/j.icarus.2012.10.019.
[6] Wordsworth R., Forget F., Millour E. et al. Global modelling of the early martian climate under a denser CO2 atmosphere: Water cycle and ice evolution // Icarus. 2013. V. 222. Iss. 1. P. 1-19. https://doi.org/10.1016/j.icarus.2012.09.036.
[7] Wordsworth R.D., Kerber L., Pierrehumbert R.T. et al. Comparison of "warm and wet" and "cold and icy" scenarios for early Mars in a 3-D climate model // J. Geophysical Research: Planets. 2015. V. 120. Iss. 6. P. 1201-1219. https://doi.org/10.1002/2015je004787.
[8] Haberle R.M., Catling D.C., Carr M.H. et al. The Early Mars Climate System // The Atmosphere and Climate of Mars / eds. R.M. Haberle, R. T. Clancy, F. Forget et al. Cambridge: Cambridge University Press, 2017. Ch. 17. P. 526-568. https://doi.org/10.1017/9781139060172.017.
[9] Head // 43rd Lunar and Planetary Science Conf. 2012. #2137.
[10] Carr M.H., Head J.W. Martian surface/near-surface water inventory: Sources, sinks, and changes with time // Geophysical Research Letters. 2015. V. 42. Iss. 3. P. 726-732.
[11] Wordsworth R., Knoll A.H., Hurowitz J. et al. A coupled model of episodic warming, oxidation and geochemical transitions on early Mars // Nature Geoscience. 2021. V. 14. P. 127-132.
[12] Jakosky B.M., Brain D., Chaffin M. et al. Loss of the Martian atmosphere to space: Present-day loss rates determined from maven observations and integrated loss through time // Icarus. 2018. V. 315. P. 146-157. https://doi.org/10.1016/j.icarus.2018.05.030.
[13] Luo S., Li He, Mo Li. Spin-momentum locked interaction between guided photons and surface electrons in topological insulators // Nature Communications. 2017. V. 8. Art. No. 2141. 7 p.
[14] Head et al. // Lunar and Planetary Science Conference. 2022.
[15] Palumbo A.M.M., Head J.W. III Early Mars Climate History: Characterizing a "Warm and Wet" Martian Climate With a 3-D Global Climate Model and Testing Geological Predictions // Geophysical Research Letters. 2018. V. 45. Iss. 19. P. 10,249-10,258. https://doi.org/10.1029/2018GL079767.
[16] Palumbo A.M., Head J.W., Wordsworth R.D. Late Noachian Icy Highlands climate model: Exploring the possibility of transient melting and fluvial/lacustrine activity through peak annual and seasonal temperatures // Icarus. 2018. V. 300. P. 261-286. DOI: 10.1016/j.icarus.2017.09.007.
[17] Head J.W., Marchant D.R. The climate history of early Mars: insights from the Antarctic McMurdo Dry Valleys hydrologic system // Antarctic Science. 2014. V. 26. Iss. 6. https://doi.org/10.1017/S0954102014000686.
[18] Fastook J.L., Head J.W. Glaciation in the Late Noachian Icy Highlands: Ice accumulation, distribution, flow rates, basal melting, and top-down melting rates and patterns // Planetary and Space Science. 2015. V. 106. P. 2-98. https://doi.org/10.1016/j.pss.2014.11.028.
[19] Laskar J., Correia A.C.M., Gastineau M. et al. Long term evolution and chaotic diffusion of the insolation quantities of Mars // Icarus. 2004. V. 170. P. 343-364. https://doi.org/10.1016/j.icarus.2004.04.005.
[20] Madeleine J.-B., Forget F., Head J.W. et al. Amazonian northern mid-latitude glaciation on Mars: A proposed climate scenario // Icarus. 2009. V. 203. Iss. 2. P. 390-405. https://doi.org/10.1016/j.icarus.2009.04.037.
[21] Forget F., Haberle R.M., Montmessin F. et al. Formation of Glaciers on Mars by Atmospheric Precipitation at High Obliquity // Science. 2006. V. 311. Iss. 5759. P. 368-371. DOI: 10.1126/science.1120335.
[22] Forget F., Byrne Sh., Head J.W. et al. Recent Climate Variations // The Atmosphere and Climate of Mars / eds. R.M. Haberle, R. T. Clancy, F. Forget et al. Cambridge: Cambridge University Press, 2017. Ch. 16. P. 497-525. https://doi.org/10.1017/9781139060172.016.
[23] Bouley S., Baratoux D., Matsuyama I. et al. Late Tharsis formation and implications for early Mars // Nature. 2016. V. 531. P. 344-347. DOI: 10.1038/nature17171.
[24] Wilson and Head // 51st Lunar and Planetary Science Conf. 2020. #2048.
[25] Kreslavsky and Head // 51st Lunar and Planetary Science Conf. 2020. #1828.

[26] Buhler P.B., Fassett C.I., Head J.W. III et al. Timescales of fluvial activity and intermittency in Milna Crater, Mars // Icarus. 2014. V. 241. P. 130-147. https://doi.org/10.1016/j.icarus.2014.06.028.
[27] Head J.W. III, Pratt S. Extensive Hesperian-aged south polar ice sheet on Mars: Evidence for massive melting and retreat, and lateral flow and ponding of meltwater // J. Geophysical Research: Planets. 2001. V. 106. Iss. E6. P. 12275-12299. https://doi.org/10.1029/2000JE001359.
[28] Bibring J.-P., Langevin Y., Mustard J.F. et al. Global Mineralogical and Aqueous Mars History Derived from OMEGA/Mars Express Data // Science. 2006. V. 312. Iss. 5772. P. 400-404. DOI: 10.1126/science.112265.

CONSTRAINING EARLY MARS GLACIAL CONDITIONS FROM PALEODISCHARGE ESTIMATES OF INTRACRATER INVERTED CHANNELS

B.D. Boatwright[1], J.W. Head[1]
[1] *Department of Earth, Environmental and Planetary Sciences, Brown University, Providence, USA; benjamin_boatwright@brown.edu, james_head@brown.edu*

KEYWORDS:
Mars, hydrology, inverted channels, glaciation, climate

INTRODUCTION:
Inverted fluvial channels are globally distributed across Mars [1–3]. Many inverted channels are interpreted as the depositional counterparts to large, regionally integrated valley networks [1–3]. These features indicate the presence of flowing liquid water in the early (Noachian) period of Mars geologic history [e.g. 4–7].

We previously identified inverted fluvial channels within the Noachian-aged crater "B" in Terra Sabaea [8, 9]. Unlike the larger inverted channels associated with valley networks, the drainage that formed these inverted channels appears to be derived from within the crater itself, i.e. a closed-source drainage basin (CSDB). Remnant geomorphic features indicative of cold-based glacial flow led us to propose that the inverted channels in crater B formed through top-down glacial melting [8] in a Late Noachian Icy Highlands climate scenario [e.g. 10–13]. These melting episodes would have generated supraglacial runoff streams that led to fluvial erosion in a proglacial outwash plain [e.g. 14–15].

The flow rate through glacial meltwater channels is directly related to the melting rate of the source glacier; thus, the estimation of water fluxes is critical to understanding the climatic conditions under which such features may have formed. Here, we follow recently described paleohydrologic reconstruction methods for Mars [16] to estimate the discharge of several inverted channel segments within the CSDB crater B. We then use these estimates to calculate the requisite melting rates of individual glacial lobes that may have fed the inverted channel networks from alcoves located upslope of the channel heads. These estimates will provide a key constraint for further early Mars climate modeling.

METHODS:
PALEOHYDROLOGIC RECONSTRUCTION:
Topographic inversion occurs when an erosionally resistant deposit (in this case, an alluvial channel bed) becomes elevated after more erodible material surrounding it is removed. The resulting deposit may either represent a single-thread channel (channel inversion) or a multi-thread channel belt (deposit inversion) [16]. Discharge Q can be expressed as the flow velocity U multiplied by the channel cross-sectional area dw, $Q = Udw$. However, the apparent width of a channel belt is many times that of an individual channel and can vary widely, leading to paleodischarge overestimates if the entire channel belt width is used to estimate Q [16].

Discharge can estimated independent of channel width by using a stream power model, $Q = 74.2 C_f^{-1/2} (Rg)^{3/8} \nu^{1/4} D_{50}^{1/8} d^2$, where C_f is a dimensionless coefficient $C_f = (gdS)^2 / U^2$; R is the specific gravity of sediment, 1.65 [16]; g is the acceleration due to gravity on Mars, 3.72 m/s^2; ν is the kinematic viscosity of water, 10^{-6} m^2/s; D_{50} is the median grain size, 0.5 mm [14]; and d is the channel depth. The bed slope S is calculated from $S = RD_{50}\tau^* / d$, where t* is the bankfull Shields stress, $\tau^* = 17 R_{ep}^{-1/2}$. R_{ep} is the particle Reynolds number, $R_{ep} = (RgD_{50})^{1/2} D_{50} / \nu$. Flow velocity U is expressed as a function of the skin friction component of the Shields stress τ_s^*, $U = (1/\kappa) \cdot \ln\left[11 (RD_{50}/Sk_s)\tau_s^*\right] \cdot \left(RgD_{50}\tau_s^*\right)^{1/2}$, $\tau_s^* = 0.06 + 0.4\tau^{*2}$, where k is von Karman's constant, 0.4; and k_s is the grain roughness length scale, $k_s = 2.5 D_{50}$ [16].

Channel depth *d* can be estimated as a proportion of caprock thickness *T* within approximately a factor of 2, with an average terrestrial *T*/*d* = 1.5 [16]. Direct measurements of caprocks from orbit are less reliable than measurements of total ridge height, so we derive a separate caprock thickness to ridge height (*T*/*z*) ratio in order to accurately determine caprock thickness for Mars. We first compiled *T*/*z* ratios from studies of terrestrial inverted channels [16, 17], finding an average *T*/*z* = 0.31 with a range of 0.13–0.57.

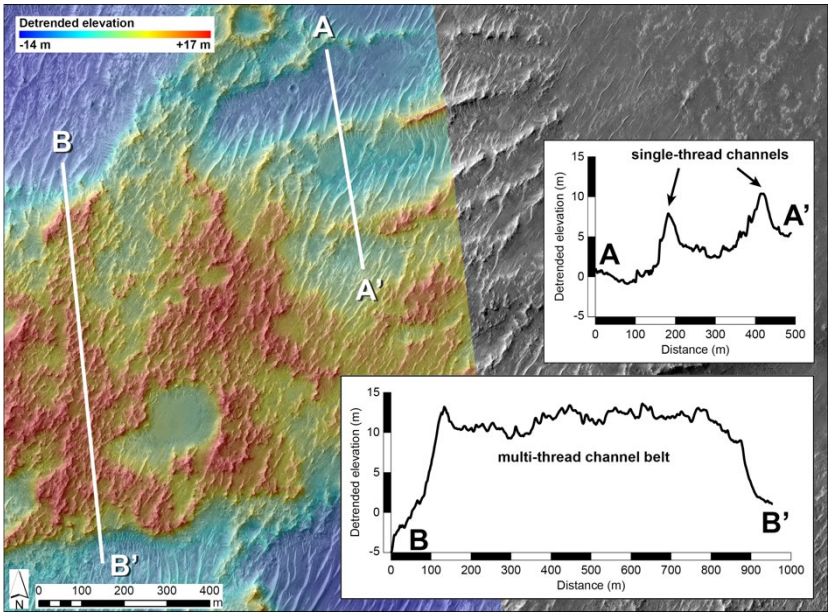

Fig. 1. Map of two sharp-crested ridges (single-thread channels, profile A–A') merging downstream into a flat-topped ridge (multi-thread channel belt, profile B–B') in the eastern crater B floor. NNW–trending transverse aeolian ridges (TARs) superposed on the larger (fluvial) ridges indicate post-depositional modification of the crater floor by aeolian processes. HiRISE visible image with detrended HiRISE stereo DEM overlay

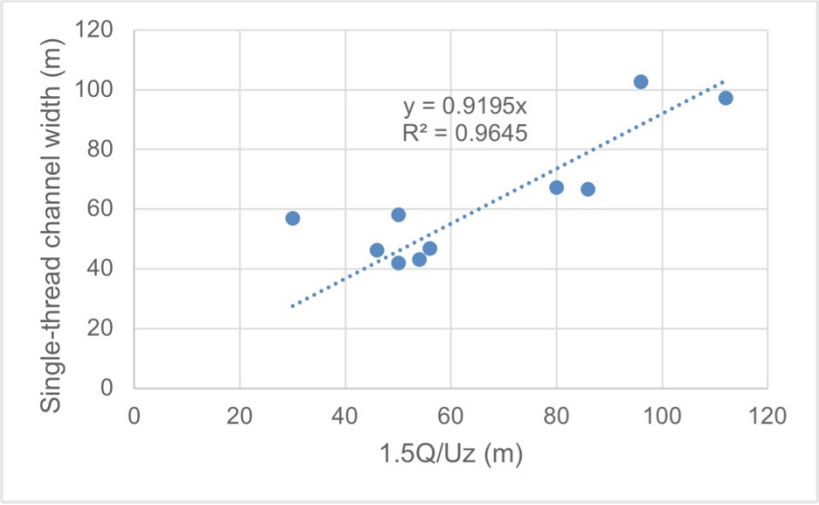

Fig. 2. Linear regression of measured single-thread channel widths vs. effective caprock thickness; slope of the regression gives best-fit *T*/*z* ratio

The inverted channels in crater B display a mixture of sharp-crested and flat-topped morphologies (Fig. 1). We interpret this difference to indicate the presence of both single-thread (sharp-crested) channels and multi-thread

(flat-topped) channel belts within the same system (Fig. 1 inset); the former have comparatively small width-to-height ratios and low stream orders. This key assumption allows us to derive an independent T/z estimate by using the ridge height z and assuming that the ridge width w for the single-thread inverted channels is close to the original channel width, $w = 1.5Q/Uz(T/z)$. We performed a linear regression on the above equation to derive a best-fit value of T/z = 0.92, R^2 = 0.96 (Fig. 2). This implies that, for crater B, the caprock makes up a much greater proportion of the total ridge height than might be expected from terrestrial measurements [16, 17].

We measured ridge heights of inverted channel segments in the crater B floor using longitudinal profiles taken from two detrended 1 m/pix HiRISE digital elevation models (DEMs) that we generated with the Ames Stereo Pipeline. Both left- and right-hand ridge base heights were recorded along with the maximum height of the ridge crest to determine an average ridge height for each segment. Ridge bases were identified using morphologic (visible transitions between ridge and crater floor units) and/or topographic (inflection point) indicators.

CONTRIBUTING AREA AND GLACIAL MELTING ESTIMATES.
The contributing area providing supraglacial meltwater and discharge to the inverted channels is assumed to correspond with individual alcoves that hosted glacial lobes along the crater walls [8]. We manually delineated individual drainage areas by considering a combination of hydrologic parameters and morphologic indicators. The shapes of the drainage areas were used to calculate an area over which glacial melting from an individual glacial lobe may have occurred. If we assume a uniform melting rate across the glacier, then the paleodischarge estimates and drainage areas can be used to determine the minimum meltwater yield that would have been necessary to supply the inverted channels with a given characteristic discharge.

RESULTS AND CONCLUSIONS:
Ridge heights were measured for 29 inverted channel segments in the eastern crater B floor and another 10 in the southern floor; among these, ridge widths were measured for 9 single-thread segments in the eastern floor and 1 in the southern floor. Average ridge heights for all segments ranged from 2.5–17.8 m with a median height of 8.6 m. Single-thread ridge widths ranged from 30–112 m with a median width of 55 m. Using our best-fit T/z = 0.92, we calculated paleodischarges of ~100–7000 m^3/s; adjusting this value to the average terrestrial T/z = 0.31, paleodischarges decrease by approximately an order of magnitude. Thus, paleodischarges calculated under the assumption of T/z = 0.92 are likely to be close to the maximum possible value, but they may be reasonable if we assume that the sharp-crested ridges represent single-thread channels.

Contributing areas within crater wall alcoves ranged from ~10–25 km^2 in size. Assuming no meltwater loss, the minimum required melting rates would range from ~300–2000 mm/hr. We previously interpreted the inverted channels in crater B to represent a single terminal event [8], such that melting rates of this magnitude would represent a peak melting extreme beyond which no further significant erosive episodes occurred.

Relative differences in discharge based upon measured ridge heights can be used to assess the hydrology of the entire system. A few key observations are noted here: 1) Discharge increases when tributaries merge; the increase is not strictly additive, perhaps due to measurement errors or differences in ridge preservation. 2) Discharge remains approximately constant or decreases slightly downstream within the same ridge; this is especially true for the longer ridges in the southern floor. 3) Discharge (~ridge height) is approximately correlated with ridge width, i.e. wider ridges generally have higher discharges. All of these observations are consistent with the expected behavior of a tributary fluvial system, namely narrow/shallow channels merging downstream into wider/deeper channels with an accompanying increase in discharge. While we previously interpreted the ridges in crater B as inverted fluvial channels based upon both morphology and topography [8, 9], our paleohydrologic approach provides another line of quantitative evidence to support our previous conclusions.

REFERENCES:

[1] Davis J.M., Balme M., Grindrod P.M. et al. Extensive Noachian fluvial systems in Arabia Terra: Implications for early Martian climate // Geology. 2016. V. 44. Iss. 10. P. 847-850. https://doi.org/10.1130/G38247.1.
[2] Davis J.M., Gupta S., Balme M. et al. A Diverse Array of Fluvial Depositional Systems in Arabia Terra: Evidence for mid-Noachian to Early Hesperian Rivers on Mars // J. Geophysical Research. 2019. V. 124. Iss. 7. P. 1913-1934. https://doi.org/10.1029/2019JE005976.
[3] Dickson J.L., Lamb M.P., Williams R.M.E. et al. The global distribution of depositional rivers on early Mars // Geology. 2020. V. 49. Iss. 5. P. 504-509. https://doi.org/10.1130/G48457.1.
[4] Carr M.H. The Martian drainage system and the origin of valley networks and fretted channels // J. Geophysical Research. 1995. V. 100. P. 7479-7507. DOI: 10.1029/95JE00260.
[5] Craddock R.A., Howard A.D. The case for rainfall on a warm, wet early Mars // J. Geophysical Research. 2002. V. 107. Iss. E11. P. 21-1-21-36. https://doi.org/10.1029/2001JE001505.
[6] Howard J.M., Moore A.D. Large alluvial fans on Mars // J. Geophysical Research. 2005. V. 110. Iss. E4. Art. No. E04005. 24 p. https://doi.org/10.1029/2004JE002352.
[7] Hynek B.M., Beach M., Hoke M.R.T. Updated global map of Martian valley networks and implications for climate and hydrologic processes // J. Geophysical Research. 2010. V. 115. Iss. E9. 14 p. https://doi.org/10.1029/2009JE003548.
[8] Boatwright B.D., Head J.W. A Noachian Proglacial Paleolake on Mars: Fluvial Activity and Lake Formation within a Closed-source Drainage Basin Crater and Implications for Early Mars Climate // The Planetary Science J. 2021. V. 2. No. 2. Art. No. 52. 9 p. https://doi.org/10.3847/PSJ/abe773.
[9] Boatwright B.D., Head J.W. Noachian proglacial paleolakes on Mars: Regionally recurrent fluvial activity and lake formation within closed-source drainage basin craters // The Planetary Science J. 2022. V. 3. No. 2. Art. No. 38. 17 p. https://doi.org/10.3847/PSJ/ac4d36.
[10] Forget F., Wordsworth R., Millour E. et al. 3D modelling of the early martian climate under a denser CO2 atmosphere: Temperatures and CO2 ice clouds // Icarus. 2013. V. 222. P. 81-99. https://doi.org/10.1016/j.icarus.2012.10.019.
[11] Wordsworth R., Forget F., Millour E. et al. Global modelling of the early martian climate under a denser CO2 atmosphere: Water cycle and ice evolution // Icarus. 2013. V. 222. Iss. 1. P. 1-19. https://doi.org/10.1016/j.icarus.2012.09.036.
[12] Wordsworth R., Kerber L., Pierrehumbert R.T. et al. Comparison of "warm and wet" and "cold and icy" scenarios for early Mars in a 3-D climate model // J. Geophysical Research. 2015. V. 120. Iss. 6. P. 1201-1219. https://doi.org/10.1002/2015JE004787.
[13] Palumbo A.M., Head J.W. Early Mars Climate History: Characterizing a "Warm and Wet" Martian Climate With a 3-D Global Climate Model and Testing Geological Predictions // Geophysical Research Letters. 2018. V. 45. Iss. 19. P. 10,249-10,258. DOI:10.1029/2018GL079767.
[14] Head J.W., Marchant D.R. The climate history of early Mars: Insights from the Antarctic McMurdo Dry Valleys hydrologic system // Antarctic Science. V. 26. P. 774-800. DOI: 10.1017/S0954102014000686.
[15] Head J.W. et al. // 48th Lunar and Planetary Science Conference. 2017.
[16] Hayden A.T., Lamb M.P. Fluvial Sinuous Ridges of the Morrison Formation, USA: Meandering, Scarp Retreat, and Implications for Mars // J. Geophysical Research. 2020. V. 125. Iss. 10. Art. No. e2020JE006470. https://doi.org/10.1029/2020JE006470.
[17] Hayden A.T., Lamb M.P. (2020) JGR 125.

FRAGMENTATION MODEL FOR IMPACT CLUSTERS ON MARS

E.D. Podobnaya[1], O.P. Popova[1], D.O. Glazachev[1]
[1] *Institute for Dynamics of Geospheres RAS, Moscow, Russia; epodobnaya@gmail.com*

KEYWORDS:
Craters, impact, meteoroids, fragmentation, numerical modelling

INTRODUCTION:
In recent years, about 1200 fresh dated meteoroid impact sites were discovered on Mars [1–3]. They resulted in the formation of single craters and crater fields (clusters), with craters up to 50 m. Mars atmosphere is more rarefied (in comparison with Earth), so falling meteoroids are less destroyed. Nevertheless, half of meteoroids fragments in the Martian atmosphere and forms clusters [2–4]. Mars surface level corresponds to about 30 km altitude in the Earth atmosphere, so crater strewn fields on Mars provide a unique opportunity to see the results of less significant fragmentation.

NUMERICAL MODELLING:
The paper is dealing with modelling of flight and fragmentation for meteoroids on Mars. Interaction of meteoroid and planet atmosphere is described by system of equations [5] supplemented by lateral spreading of fragments [6]. Fragmentation events occur when the dynamic pressure on the front face of a meteoroid exceeds its yield strength [6]. One-stage fragmentation on a number of fragments is assumed, lateral spreading of fragments occurs at a random angle to the meteoroid trajectory. The mass distribution of fragments and their number for the impactor was chosen using a truncated power law distribution [7] with fixed maximal fragment mass.

Preliminary results of numerical modeling show that developed model allows us to describe observed crater clusters, and probably in future to estimate impactor properties [8]. On the Earth atmospheric sorting of fragments is observed under conditions of the dense atmosphere, fragments are arranged along the trajectory depending on mass, as it is observed in terrestrial scattering fields of meteorites. On Mars, this effect is weak, the scattering field is mainly determined by fragmentation and lateral spreading of fragments.

REFERENCES:
[1] Malin M.C., Edgett K.S., Posiolova L.V. et al. Catalog of new impact sites on Mars formed May 1999 – March 2006 / Malin Space Science Systems. Inc., San Diego, California. 2006.
[2] Daubar I.J., McEwen A.S., Byrne S. et al. The current Martian cratering rate // 41st Lunar and Planetary Science Conf. 2010. V. 1533. Art. No. 1978. 2 p.
[3] Daubar I.J., Banks M.E., Schmerr N.C. et al. Recently formed crater clusters on Mars // J. Geophysical Research. 2019. V. 124. Iss. 4. P. 958-969. https://doi.org/10.1029/2018JE005857.
[4] Hartmann W.K., Daubar I.J., Popova O.P. et al. Martian cratering 12. Utilizing primary crater clusters to study crater populations and meteoroid properties // Meteoritics and Planetary Science. 2018. V. 53. Iss. 4. P. 672-686. https://doi.org/10.1111/maps.13042.
[5] Baldwin B., Sheaffer Y. Ablation and breakup of large meteoroids during atmospheric entry // J. Geophysical Research. 1971. V. 76. Iss. 19. P. 4653-4668. https://doi.org/10.1029/JA076i019p04653.
[6] Passey Q.R., Melosh H.J. Effects of atmospheric breakup on crater field formation // Icarus. 1980. V. 42. Iss. 2. P. 211-233. https://doi.org/10.1016/0019-1035(80)90072-X.
[7] Popova O., Borovicka J., Campbell-Brown M. Modelling the entry of meteoroids // Meteoroids: Sources of Meteors on Earth and Beyond. 2019. V. 25. P. 9-36.
[8] Ivanov B.A., Melosh H.J., McEwen A.S. HiRISE Team. Small impact crater clusters in high resolution HiRISE images // Lunar and Planetary Science Conf. 2008. No. 1391. P. 1221.

MINERALOGICAL VARIATIONS OF DEPOSITS IN THE UTOPIA PLANITIA REGION OF MARS MEASURED BY CRISM AND OMEGA SPECTROMETERS

E.D. Faber[1], M.A. Ivanov[2], I.E. Nadezhdina[3]
[1] *Lomonosov Moscow State University, Moscow, Russia, faber.cat.rina@gmail.com;*
[2] *Vernadsky Institute of Geochemistry and Analytical Chemistry of Russian Academy of Sciences, Moscow, Russia, mikhail_ivanov@brown.edu;*
[3] *Moscow State University of Geodesy and Cartography, Moscow, Russia, lorencs@mail.ru*

KEYWORDS:
Mars minerology, remote sensing, CRISM, OMEGA, imaging spectroscopy

INTRODUCTION:
This study aims to characterize the compositional variations prevailing over the southern region in Utopia Planitia. This study uses data obtained by [1], where Martian global surface types are classified based on the downsampled averaged CRISM multispectral summary product data [2]. In addition to regional characterization of the study area, a set of regions of interest in the hyperspectral resolution of TRDR CRISM dataset were consider. Principal component analysis (PCA) is carried out on the CRISM summary product data. Significant products contributing to the variance in the regions are identified, following which the regions exhibiting patterns in the PCA composites are demarcated. The spectra of the ROIs regions are analyzed. As a result, a list of principal components was obtained and graphic maps of the distribution of principal components in RGB format were constructed, as well as maps of summary parameters and browse products involved in the study. Spectral analysis of ROIs regions has revealed such interesting mineral groups as phyllosilicates, sulfates and other hydrated minerals.

REFERENCES:
[1] Kamps O.M., Hewson R.D., van Ruitenbeek F.J.A., van der Meer F.D. Defining Surface Types of Mars using Global CRISM Summary Product Maps // J. Geophysical Research: Planets. 2020. V. 125. Iss. 8. 18 p. Art. No. e2019JE006337. https://doi.org/10.1029/2019JE006337.
[2] Viviano-Beck C.E., Seelos F.P., Murchie S.L. et al. Revised CRISM spectral parameters and summary products based on the currently detected mineral diversity on Mars // J. Geophysical Research E: Planets. 2014. V. 119. Iss. 6. P. 1403-1431. https://doi.org/10.1002/2014JE004627.

LATERAL EXTENSION OF LAYERED DEPOSITS IN S-W PORTION OF HOLDEN CRATER, MARS

J. Chu[1], M.A. Ivanov[2], A.M. Nikishin[1]
[1] *Lomonosov Moscow State University, Faculty of Geology, Moscow, Russia, vladimirchujun@yandex.ru;*
[2] *Vernadsky Institute of Geochemistry and Analytical Chemistry RAS, Moscow, Russia, Mikhail_Ivanov@brown.edu*

KEYWORDS:
Mars, Holden crater, outcrop, deposits, fan, Uzboi

INTRODUCTION:
The Holden crater is located on Margaritifer Terra, which is in the Uzboi-Ladon-Morava (ULM) outflow channel system. It formed in the Noachian period and caused redistribution of water flows and deposition of a series of layers of clay-bearing materials on the crater floor [1, 5]. The existing research results generally reveal that the Holden impact crater experienced lacustrine and/or distal alluvial low-energy deposition and high-energy alluvial or glacial deposition from the Uzboi water body, these two processes correspondingly formed the lower and the upper sediment unit [2–4]. To reveal accurate geological structure and historical development process, we use HiRISE images and the digital terrain models (DTM) and stereo images generated by them to study outcrops of other layered sediments in the SW portion of the crater and assess their lateral extension and correlation.

OUTCROPS DESCRIPTION
Outcrop 1. The eastern outcrop can also be divided into lower and upper units. The lower unit, like the western outcrop [3–4], is composed of a dark in tone lower member, a light in tone middle member, and light in tone upper layer with lens of dark-toned coarse materials (Fig. 1,1). Comparing with the western outcrop, the middle member is thinner and the upper member is thicker and has a pronounced dark bedding. Four sublayers are present on the northern peninsula-like portion of the outcrop (Fig. 1,2). The upper unit is composed of dark, fine-grained material that overlies the lower unit unconformity [1–4], which is analog with the western outcrop.

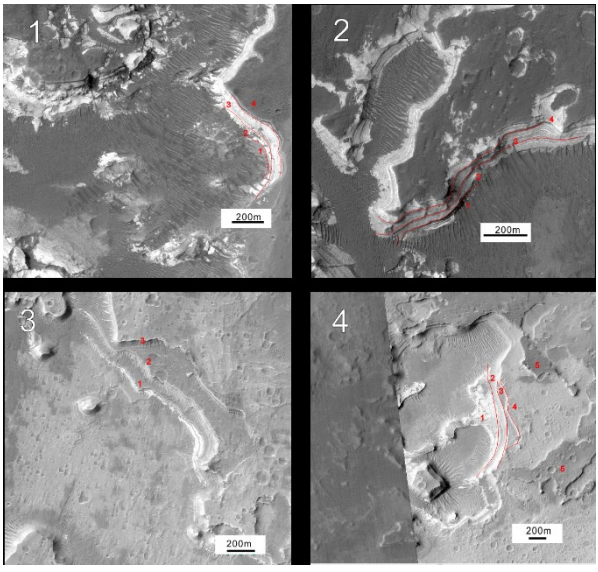

Fig. 1. Outcrops of Holden breach fan deposits: 1) HiRISE ESP_028513_1530_RED, member 1, 2, 3-lower unit, 4-upper unit; 2) HiRISE ESP_028513_1530_RED, north part of the outcrop in 1), member 3 is developed into members 1–4 in this side; 3) HiRISE ESP_019612_1535_RED, members 1, 2, 3 are correlated to members 2, 3, 4 in 2); 4) HiRISE ESP_037664_1530_RED, members 1, 2, 3, 4 — lower unit, 5-upper unit.

Outcrop 2. The outcrop shows three main members. The first member is composed of light and dark in tone interlayers from bottom to top. The light-toned interlayers have a large particle size, and the dark-toned interlayers have a small particle size. The second member is composed of light-toned coarse grains with dark-toned material interspersed between grains. The third member is like the second member, but the lighter interlayers are concentrated in the lower half. The outcrop is stepped and covered with a dark, fine-grained caprock like the upper unit of the western outcrop. According to DTM data, its bottom surface is located at –2250 m below the datum, which is like –2255 m in the western outcrop 1, so it can be estimated that the top three of four sublayers on the west side continue to the same set of strata (Fig. 1,3).

Outcrop 3. This outcrop is located to the east of the ancient impact crater and is also composed of lower and upper units. From bottom to top the lower unit can be divided into four members, which are composed, respectively, of light- and dark-toned coarse-grained materials members and dark- and light-toned members with fine-grained materials. The upper unit is composed of dark and light interlayers. The surface is dark-toned with impact craters, and the coarse-grained light-toned material buried under the dark layer is exposed at the eroded part. The bottom surface of the outcrop here is –2360 m by DTM (Fig. 1,4).

MORPHOLOGICAL UNITS

By tracing the stratigraphic units exhibited by each outcrop laterally, the Holden breach fan deposits [2–3], which is radiated from the Uzboi, can be divided into western and eastern sedimentary units. The western sedimentary unit has a waved surface and has been eroded in the south near the mouth of the Uzboi valley and buried by dark-toned eolian material in the north [2–3]. The eastern sedimentary unit is divided into northeastern and southwestern parts by a fault extending in the N–S direction. The surface of the northeastern part is roughly tongue-shaped with many craters on it. The southeastern unit has a southwest-northeast trending erosional pattern on the surface.

CHRONOLOGY:

We have performed the crater-frequency distribution (CSFD) measurements to revel the general sequence of the formation of two units of the Holden breach fan deposits. The CSFD measurement show the following absolute model ages (AMA): (1) The eastern sedimentary unit: two ages, to the east of the fault: 1.3±0.09 Ga, to the west of the fault: 1.3±0.1 Ga. (2) The western sedimentary unit: two ages, the northeastern part: 640±80 Ma, the southwestern part: 660±90 Ma.

CONCLUSIONS:

1) By the approach depth of bottom, units on outcrop 2 continue units in outcrop 1. These units apparently belong to the same sedimentary unit of the Holden breach fan deposit.
2) The upper member of the lower unit is composed of distal alluvial facies [3–4] and gradually thickens toward the center of the basin and differentiates into four layers with mixed dark and light-toned layers, indicating that the water flow intensity changes periodically.
3) Holden breach fan deposit is radially arranged in the direction of Uzboi breaches, indicating that the topography of its surface and the unconformity of the upper and lower units [3–4] are formed by the erosion of water (or glacial) [2] flow from the direction of Uzboi.
4) The AMAs of parts of depositions indicate that the renewal process was active in the Amazonian times.
5) The surface renewal process of the eastern sedimentary unit ended earlier than that of the western sedimentary unit. The eastern sedimentary unit of Holden breach fan deposit is closer to the negative topography of the center of the basin, indicating that this area has experienced surface uplift [4] and formed the present fault, which turned the inflow from the Uzboi direction to north and eroded the surface of the western sedimentary unit of Holden breach fan deposit, resulting in the formation of outcrop 2.

6) The dark sediments in the upper unit mainly come from the alluvial fan group (bajada) along the western part of the basin. At this time, the water flow from Uzboi continued in two directions to form outcrop 1, and the imbricate collapse landform to the north of outcrop 1.

ACKNOWLEDGEMENTS:
This work is supported by China Scholarship Council and represents a part of the state order of GEOKHI for MAI.

REFERENCES:

[1] Grant J.A., Parker T.J. Drainage evolution in the Margaritifer Sinus region, Mars // J. Geophysical Research. 2002. V. 107.
[2] Pondrelli M., Baliva A., Di Lorenzo S. Complex evolution of paleolacustrine systems on Mars: An example from the Holden crater // J. Geophysical Research. 2005. V. 110.
[3] Grant J.A., Irwin P.R. III, Grotzinger J.P. HiRISE imaging of impact megabreccia and sub-meter aqueous strata in Holden Crater, Mars // Geology. 2008. V. 36. P. 195-198.
[4] Grant J.A., Irwin P.R. III, Wilson S.A. Aqueous depositional settings in Holden crater, Mars // Lakes on Mars / ed. Cabrol, Nathalie A., Grin, Edmond A. Elsevier, 2010. P. 323-346.
[5] Ivanov M.A., Hiesinger H. Topographic characteristics and chronology of the Uzboi-Ladon fluvial system on Mars // The Eleventh Moscow Solar System Symposium. 2020.

ON MODEL VALUES OF CHANDLER WOBBLE PERIOD FOR MARS

E.A. Kulik[1,2], T.V. Gudkova[2]
[1] *Moscow Institute of Physics and Technology, Moscow, Russia, kulik.ea@phystech.edu;*
[2] *Schmidt Institute of Physics of the Earth, Moscow, Russia, gudkova@ifz.ru*

KEYWORDS:
Mars, interior structure, Chandler wobble

INTRODUCTION:
Chandler wobble (CW) is a free mode of the polar motion (the path of the mean rotational pole relative to the surface of a planet). For Mars, its excitation is related to the seasonal mass exchange between the Mars polar caps. The period of the Chandler Wobble was estimated in [1] and then corrected in [2], but these attempts failed to separate the signature at the Chandler frequency from the 1/3 Mars year mass redistribution term due to the small amplitude. For the first time the CW has been detected for Mars from radio tracking observations of Mars Odyssey, Mars Reconnaissance Orbiter, and Mars Global Surveyor [3]. Its period is 206.9±0.5 days. Model predictions for the Mars CW period are 203.8 to 204.8 days [4] and 201 to 208 days [5]. CW of Mars provides a measure of the body to deform at very long periods and can be used as an additional constraint on the interior structure model.

INTERIOR MODELS:
The measured geodesy parameters surve as constraints for models of the Mars interior structure. They are the normalized polar moment of inertia (MOI), which is derived from Mars' precession, and the solar tidal deformation as given by the Love number k_2. The MOI value deduced from the precession rate is 0.3640±0.0006 and the current solution for k_2 = 0.174±0.008 [3]. The interior structure models of Mars are built following the method described in [6]. A set of the interior structure models, listed in Table 1, is based on the Wanke-Dreibus mineralogy. The parameters of the models: ferrous number of the mantle Fe# (Fe# = $Fe^{2+}/(Fe^{2+}+Mg)100$) is 18–20, the crust thickness *l* is 31–50 km, while average density is varied from 2700 to 2900 kg·m^{-3}, the core radius is in the range of 1828–1860 km (in agreement with the core radius obtained by seismic data [7]). Model elastic values of k_2^e = 0.163–0.170, corresponding to 0.168–0.175 with correction to inelasticity, satisfy the data from [3].

Table 1. The parameters of interior structure models

Model	ρ crust	*L* crust	Fe# mantle	R core	I/MR^2	k_2^e	k_2
M1	2700	40	20	1828	0.3636	0.163	0.168
M2	2700	45	20	1830	0.3633	0.163	0.168
M3	2700	50	20	1836	0.3631	0.164	0.169
M4	2800	50	20	1830	0.3634	0.163	0.168
M5	2700	31	18	1857	0.3631	0.170	0.175
M6	2800	41	18	1860	0.3628	0.170	0.175
M7	2900	45	18	1855	0.3630	0.169	0.174

CHANDLER PERIOD:
The Chandler wobble had been anticipated theoretically for a long time (see for theory details, [4]). The CW period for a triaxial elastic body with a liquid core is given by

$$T_W = T_E\left(1-\frac{(A_cB_c)^{1/2}}{(AB)^{1/2}}\right)\Big/\left(1-k/k_0\right),\quad T_E=\tau_M(\alpha\beta)^{-0.5},\quad \alpha=(C-A)/A,\quad \beta=(C-A)/B,$$

where T_E is the Eulerian period; τ_M is the period of the rotation of Mars; A, B, and C are the principal moments of inertia of the planet; A_c and B_c are the principal moments of inertia of the planetary core.

The CW period depends upon both the moment of inertia of the core and the Love number k_2 at the Chandler period. Changing radius of the core gives an opposite effect. A larger core leads to a larger deformation, or larger k_2, and therefore a larger CW period, but at the same time the moment of inertia of the core is getting larger, and therefore the CW period is smaller. The CW periods for a set of models listed in Table 1 are given in Table 2.

Table 2. The Eulerian and Chandler periods for two-axial and three-axial models (k_0 = 1.290119, T_{E1} = 189.64 days, T_E = 190.03 days)

Model	I_{core}/MR^2	$A_c/((AB)^{1/2}$	$T_{w1}{}^s$, days	$T_w{}^s$, days
M1	0.02867	0.0743	201.9	202.3
M2	0.02882	0.0743	201.9	202.3
M3	0.02925	0.0752	201.9	202.3
M4	0.02880	0.0743	201.9	202.3
M5	0.03091	0.0805	201.9	202.3
M6	0.03113	0.0805	201.8	202.3
M7	0.03074	0.0796	201.9	202.3

In all calculations of the interior models only elastic models were considered. The rheological behavior of the mantle rock in tidal/rotational periods is frequency dependent. Anelastic behavior of the mantle decreases the mantle rigidity and leads to the increase of k_2 and the CW period. The growth of the Chandler period of Mars due to the inelasticity of its interior is defined as

$$\delta T_W = -T_W^t \frac{\mathrm{Re}[k(\sigma_W)]}{\sigma_W} = \frac{T_W^t}{1118}\left[\left(\frac{\sigma_t}{\sigma_W}\right)^n - 1\right]\frac{1}{\left(k_0 - k^t\right)}\cot\frac{n\pi}{2}.$$

We use the estimate based on the power law which is commonly adopted for the solid Earth tide. An open question is the choice of the exponent n in the power creep function. The exact value of n is unknown. The estimate of n for Mars is 0.07–0.35 in [3], and 0.09–0.35 in [8]. According to our model estimates, to get T_W about 206 days, we have to use n = 0.4, which gives the value δT_W = 3.5. Another possibility to satisfy the observational value of CW period for our DW composition models is introducing a partially molten layer at the bottom of the mantle (about 200 km). In this case we have n = 0.15–0.2.

CONCLUSION:

One of the tasks of obtaining a model of the internal structure of Mars is related to the cosmogonic aspects of the problem — to what extent the Mars model can be used to confirm or refute the fundamental hypothesis about the chondrite composition of the terrestrial planets. It is found that there is a discrepancy between the model and experimental values of the Chandler period of the planet for models of this type if no additional assumptions are made. The models of this type can be reconciled with the experimental value of the Chandler period if a partially molten layer is introduced at the bottom of the mantle or the value of n is higher than it is accepted for the Earth. Because of its long period, knowledge of the CW could significantly improve our understanding of the long period behavior of the mantle rheology.

ACKNOWLEDGEMENTS:

This work is financially supported by Budget funding of Schmidt Institute of Physics of the Earth RAS.

REFERENCES:

[1] Konopliv A.S., Yoder C.F., Standish E.M. et al. A global solution for the Mars static and seasonal gravity, Mars orientation, Phobos and Deimos masses, and Mars ephemeris // Icarus. 2006. V. 182. Iss. 1. P. 23-50. https://doi.org/10.1016/j.icarus.2005.12.025.

[2] Konopliv A.S., Asmar S.W., Folkner W.M. et al. Mars high resolution gravity fields from MRO, Mars seasonal gravity, and other dynamical parameters // Icarus. 2011. V. 211. Iss. 1. P. 401-428. https://doi.org/10.1016/j.icarus.2010.10.004.

[3] Konopliv A.S., Park R.S., Rivoldini A. et al. Detection of the Chandler wobble of Mars from orbiting spacecraft // Geophysical Research Letters. 2020. V. 47. Iss. 21. Art. No. e2020GL090568. https://doi.org/10.1029/2020GL090568.

[4] Zharkov V., Gudkova T. The period and Q of the Chandler wobble of Mars // Planetary and Space Science. 2009. V. 57. Iss. 3. P. 288-295. https://doi.org/10.1016/j.pss.2008.11.010.
[5] Van Hoolst T., Dehant T., Defraigne P. Chandler wobble and free core nutation for Mars // Planetary and Space Science. 2000. V. 48. Iss. 12-14. P. 1145-1151. https://doi.org/10.1016/S0032-0633(00)00099-4.
[6] Zharkov V.N., Gudkova T.V. Construction of Martian interior model // Solar System Research. 2005. V. 39. Iss. 5. P. 343-373. DOI: 10.1007/s11208-005-0049-7.
[7] Stähler S.C., Khan A., Banerdt W.B. et al. Seismic detection of the martian core // Science. 2021. V. 373. Iss. 6553. P. 443-448. DOI: 10.1126/science.abi773.
[8] Harada Y. Reconsideration of the anelasticity parameters of the martian mantle: Preliminary estimates based on the latest geodetic parameters and seismic Models // Icarus. 2022. V. 383. Art. No. 114917. https://doi.org/10.1016/j.icarus.2022.114917.

SESSION 1. MARS (MS)
POSTER SESSION

MARS MAGNETOPAUSE

O.L. Vaisberg[1]
[1] *Space Research Institute, Moscow, Russia, olegv@iki.rssi.ru*

KEYWORDS:
Mars, magnetosphere, dayside magnetosphere, magnetopause

INTRODUCTION:

Magnetosphere of Mars was first investigates by 1960th with orbiters Mars-2, Mars-3 and Mars-5. The bow shock, the dayside low-energy plasma layer (plasma cushion), and extended magneto-plasma tail of heavy ions were found. Later Phobos-2 and MEX contributed significantly to investigation of the Mars, especially to the investigation of the Martian tail.

Very important investigations of Martian envelope and solar wind-planet interaction is performing from MAVEN data starting from 2014. With comparative instrumentation of high-time resolution data very large group of scientists mage possible to achieve very interesting results.

Small IKI group draws attention to the dayside magnetosphere of Mars that became possible due to availability of high-resolution data. With previous experience in investigation of planetary objects we expected to work with interesting object which is dayside magnetosphere.

Another motivation to work with dayside of sunward side of dayside understood that no many members of MAVEN group will be busy with other topics which evidently considered more profitable. Indeed, Americans investigated and published such topics as computer models of the solar wind with upper atmosphere and ionosphere and with magnetic field and magnetic anomalies on the Mars.

Other handicaps that we haves were: 1 our experience in Mars, Venus, and outer magnetosphere of Earth, 2 strange believe in previous papers written in the statement that the solar wind interacts with magnetosphere.

MAVEN data provided excellent basis for analysis of the dayside magnetosphere and shows that dayside is exists as permanent part of all Martian magnetosphere.

OBSERVATION OF DAYSIDE MAGNETOSPHERE

Figure 1 shows the dayside of pass of MAVEN at the ~800 km to ~200 km height above the Mars. Determinate the magnetopause crossing by several criteria (see discussion in Vaisberg et al., 2022) was at about 600 as shown by vertical arrow in Fig. 1. Magnetopause crossing magnetopause was identified using several physical conditions (see Vaisberg et al., 2021): drop of shocked plasma magnetosheath pressure by about order of 10, drop of ratio $n_p/(n_p + n_h)$ to 1/2, sharp or relatively sharp ratio of proton number density to the heavy ions number density.

The data shown in Fig. 1 is typical for about 60 % crossing (in other ~40 % cases instead of relatively sharp interaction of magnetosheath plasma with magnetosphere leads to formation of the plume (Fig. 2). We will not discuss this type of magnetosheath flow interaction with magnetosphere that was shortly described in (Vaisberg et al.).

The very interesting to understand what is the nature of the structure of the magnetopause. We analyzed about 40 passed magnetosphere crossing and found that about 50 % cases show quite repeatable structure of the magnetopause. Other magnetopauses crossings quite noisy but still indicate quite resemble structure.

Minimum variance analyses of the magnetic field in the magnetopause suggests that the its magnetic field and its variations are approximately perpendicular to the magnetic current of magnetopause.

It is interesting that the current in the terrestrial magnetosheath in the case of open magnetopause (Rotational Discontinuities in the Magnetopause of an Open Magnetosphere, Yonghui Ma, Shu Wang, Chao Shen, Nian Ren, Tao Chen, Peng Shao, Peng E, Y. V. Bogdanova, J. L. Burch) shows similar structure to the one described in this paper.

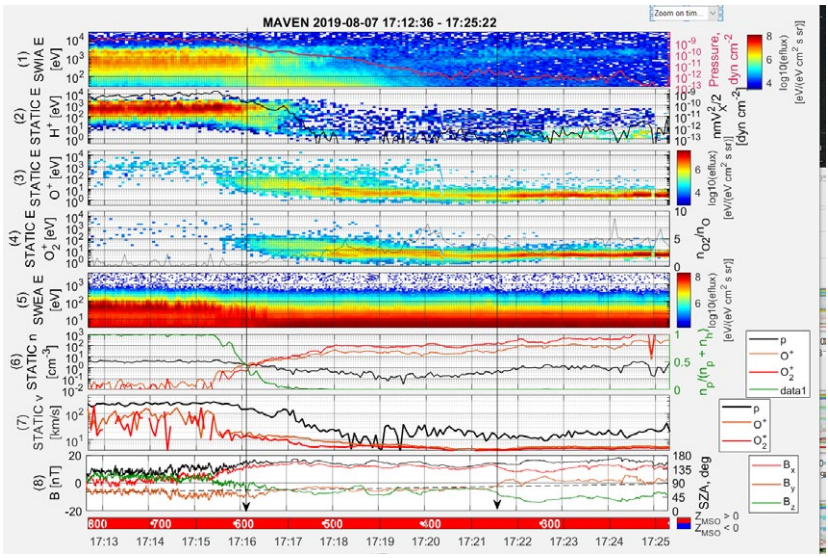

Fig. 1. The MAVEN. STATIC and MAG data in the vicinity of the subsolar point on August 17, 2019 at 12:13 to 17:25 UT. From top to bottom panels: 1 — the differential energy flux — time spectrograms of all ions; 2 — protons H^+; 3 — oxygen O^+; 4 — oxygen ions O_2^+; 5 — electrons, 6 — number densities of 3 ions and normalized ion densities as shown in green at right; 7 — velocities of 3 ions, and 8 — magnetic field components in Mars-centered Solar Orbital (MSO) coordinate system and magnitude (black line). Red color band at the bottom shows that the spacecraft is in northern hemisphere

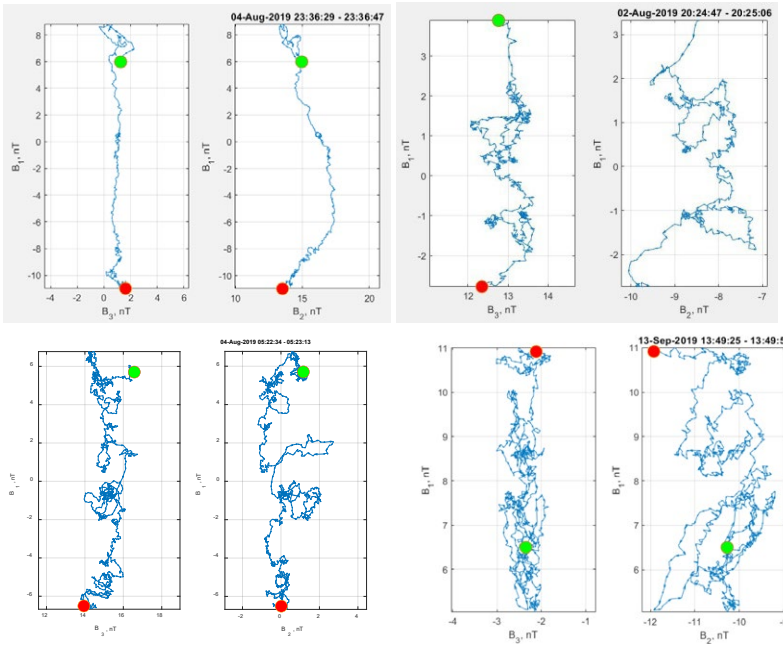

Fig. 2. 4 cases of magnetic structures within magnetopause of Mars at ~60° SZA. Different crossings of magnetopause show M and N components of the magnetic field

ACKNOWLEDGMENTS:
The work is supported to RNF “Venus and Mars in the solar wind flow”, No. 21-42-04404.

STUDY OF WAVE PHENOMENA IN THE PLASMA ENVIRONMENT OF MARS: SIMULTANEOUS OBSERVATIONS AT GROUND AND ON ORBITS

S.V. Kulikov[1], S.I. Klimov[1], N.E. Rybjeva[1], S.P. Savin[1], A.A. Skalsky[1]
[1] *Space Research Institute, Moscow, Russia; sv.kulikov93@gmail.com*

KEYWORDS:
Mars, solar wind, magnetic field, martian plasma environment, wave phenomena

INTRODUCTION:
At present, the fleet of orbiters and landers performs plasma and magnetic field measurements on orbits around Mars and at its surface. It provides a new opportunity to study magnetosphere/ionosphere dynamic in response to interplanetary medium and atmospheric conditions.

The paper presents a software package for situation analysis developed with use of the SPICE Toolkit and the available models of the Martian environment.

Based on it and statistics of available observations from landing platform and orbiters, a possible influence of disturbances originated from the solar wind, Martian foreshock and bow shock on the ionosphere /atmosphere of Mars is considered and discussed.

COMBINED APPROACH IN FINDING ANALYTICAL CONTINUATIONS OF THE MARS MAGNETIC FIELD FROM SATELLITE DATA

I.E. Stepanova[1], A.M. Salnikov[1,2], T.V. Gudkova [1], A.V. Batov [1,2]
[1] *Schmidt Institute of Physics of the Earth RAS, Moscow, Russia; tet@ifz.ru*
[2] *Trapeznikov Institute of Control Sciences of the Russian Academy of Sciences, Moscow, Russia, 117997*

KEYWORDS:
Mars, magnetic field, analytical continuation, time-dependent integral representation

INTRODUCTION:
Our work proposes a new combined method for interpreting data on planetary magnetic fields, which includes the construction of regional modified S-approximations considering ellipticity and local approximations of a nonstationary field, which is the solution of some parabolic type of equation with constant coefficients. The main provisions of the method of linear integral representations are developed as applied to time-dependent differential operators, which is of fundamental importance in solving many inverse problems of mathematical geophysics.

Models of physical fields and topography must be constantly updated to consider the rapidly changing huge amounts of data about these signals. In our opinion, methods that include the interpretation technique and mathematical formulations should differ when analyzing data of different nature. When interpreting data on the physical fields of planets, various methods and approaches are used (for example, [1–8]).

Previously we have shown that the global version of the method of linear integral representations within the framework of the structural-parametric approach can be used to construct an analytical continuation of the gravitational and magnetic fields of Mars down towards the sources [9–11].

In this paper, we attempted to construct an approximation of the magnetic field of Mars in the landing area of the Zhurong rover of the Chinese Tianwen-1 mission [12]. Approximations of the magnetic field were constructed using a combined technique, including a regional version of the method of modified S-approximations considering ellipticity and a mathematical model of the field in a three-dimensional Cartesian space, depending on time as a parameter.

MAIN RESULTS:
We have tested algorithms and programs of a new combined method for constructing analytical models of the magnetic field of Mars based on measurement data of the magnetometer MAG of the American MAVEN mission during the period from 10/10/2014 to 09/14/2021 over the area (0–50° N, 85–135° E) in the landing zone of the Zhurong rover (25.06° N, 109.54° E) of the Chinese Tianwen-1 mission.

First, we constructed a regional modified S-approximation of the three components of the magnetic field in a spherical coordinate system. At the same time, we assumed that Mars is an ellipsoid with semi-axes equal to 3376.5, 3393.5 and 3393.5 km, respectively, or a ball with a radius of 3393.5 km.

Second, we performed an analytical continuation of the magnetic field at 42, 50, 80, and 100 km towards the sources.

In addition, we applied the local variant of S-approximations without dependence on time, assuming that the field is given on the z = 100 km plane and continued this field down (towards the sources) by 10 and 20 km, as well as deep into the planet by 100.2 and 100.5 km, assuming from the average height of the satellite orbit.

After the values of the components of the magnetic induction vector in the spatial domain were determined in two ways, we solved the linear inverse

problem for parabolic type equation with constant coefficients in the upper half-space and built an approximation construction that depends on time as a parameter. At the same time, the values of this additional parameter must be set, guided by some reasonable considerations, for example, assuming that "time" is the modulus of the radius vector of the observation point, divided by some signal propagation speed. If we are dealing with real non-stationary fields, then time is an independent variable, and we obtain the statement of the inverse problem in the framework of the method of linear integral representations for an operator of parabolic or hyperbolic type.

The magnetic field was approximated by the sum of simple and double layers distributed on the surface of an ellipsoid enclosed by a ball or on the surface of a sphere located inside Mars.

When solving a system of linear algebraic equations using the improved block method, the approximation accuracy of the magnetic field of Mars at an altitude of 150 km was ~10^{-7}. Thus, a new combined method for constructing analytical models of the physical fields of planets can be used in the interpretation of satellite data obtained at different times and with different accuracy.

REFERENCES:

[1] Portniaguine O., Zhdanov M. Focusing geophysical inversion images // Geophysics. 1999. V. 64. P. 874-887. https://doi.org/10.1190/1.1444596.
[2] Portniaguine O., Zhdanov M. 3-D magnetic inversion with data compression and image focusing // Geophysics. 2002. V. 67. P. 1532-1541. https://doi.org/10.1190/1.1512749.
[3] Arkani-Hamed J. An improved 50-degree spherical harmonic model of the magnetic field of Mars derived from both high-altitude and low-altitude data // J. Geophysical Research: Planets. 2002. V. 107. Iss. E10. Art. No. 5083. P. 13-1-13-8. https://doi.org/10.1029/2001JE001835.
[4] Acuña M., Connerney J.E., Ness N.F. et al. Global distribution of crustal magnetism discovered by the Mars Global Surveyor MAG/ER Experiment // Science. 1999. V. 284. P. 790-793. DOI: 10.1126/science.284.5415.790.
[5] Mikhailov V.O., Timoshkina E.P., Kiseleva E.A. et al. Problems of the joint inversion of temporal gravity variations with the data on land and seafloor displacements: a case study of the Tohoku-Oki earthquake of March 11, 2011 // Izvestiya, Physics of the Solid Earth. 2019. V. 5. P. 746-752. DOI: 10.1134/S1069351319050070.
[6] Wang Y., Lukyanenko D., Yagola A. Magnetic parameters inversion method with full tensor gradient data // Inverse Problems and Imaging. 2019. V. 13. No. 4. P. 745-754. DOI: 10.3934/ipi.2019034.
[7] Uieda L., Barbosa V.C.F., Braitenberg C. Tesseroids: Forward-modeling gravitational fields in spherical coordinates // Geophysics. 2016. V. 81 Iss. 5. P. F41–F48. https://doi.org/10.1190/geo2015-0204.1.
[8] Schattner U., Segev A., Mikhailov V. et al. Magnetic signature of the Kinneret–Kinarot tectonic basin along the Dead Sea transform, Northern Israel // Pure and Applied Geophysics. 2019. V. 176. Iss. 1. P. 4383-4399. DOI: 10.1007/s00024-019-02211-6.
[9] Gudkova T., Stepanova I., Batov A. Density Anomalies in Subsurface Layers of Mars: Model Estimates for the Site of the InSight Mission Seismometer // Solar System Research. 2020. V. 54. Is. 1. P. 15-19. DOI: 10.1134/S0038094620010037.
[10] Gudkova T., Stepanova I., Batov A. et al. Modified method S- and R-approximations in solving the problems of Mars's morphology // Inverse Problems in Science and Engineering. 2021. V. 29. P. 790-804. https://doi.org/10.1080/17415977.2020.1813125.
[11] Salnikov A., Stepanova I., Gudkova T. et al. Analytical modeling of the magnetic field of Mars from satellite data using modified S-approximations // Doklady Earth Sciences. 2021. V. 499. Iss. 1. P. 575-579. DOI: 10.1134/S1028334X21070096.
[12] Liu J., Li Ch., Zhang R. et al. Geomorphic contexts and science focus of the Zhurong landing site on Mars // Nature Astronomy. 2022. V. 6. Iss. 1. P. 65-71. DOI: 10.1038/s41550-021-01519-5.

THE ACTIVITY OF THE YOUNG SUN AND ISOTOPIC COMPOSITION EVOLUTION OF THE ATMOSPHERES OF MARS AND VENUS

E.S.Melikhova [1], A.K.Pavlov [2], G.I.Vasilyev [2]
[1] *Peter the Great St. Petersburg State Polytechnic University, Saint Petersburg, Russia, melihova.es@edu.spbstu.ru;*
[2] *Ioffe Physical-Technical Institute RAS, Saint Petersburg, Russia*

KEYWORDS:
young Sun, solar flares, solar cosmic rays, isotopic ratios

INTRODUCTION:

An active young Sun can be described by a model that was presented in 2016 by [1]. Using the Kepler Space Telescope observations of solar-like stars [2, 3], they assumed that the frequency of Carrington-type superflares with an energy of about 10^{33} erg on the early Sun was about 250 events per day during the period of 0.7 billion years. The energy spectra of protons in solar cosmic rays are usually defined as $F = F_0 E^{-\gamma}$. The spectral index γ is assumed to be 2.15 in Airapetian's model. In our work, we consider the range of γ from 2 to 2.3 at constant total energy of solar cosmic rays. As result, solar cosmic rays can produce heavy isotopes ^{13}C and ^{15}N in nuclear reactions in the upper atmospheres of the planets. Production of these isotopes depends on the assumed value of gamma and on the composition of the early atmospheres.

CARBON RESERVOIR ON EARLY MARS AND POSSIBLE NITROGEN EARLY ATMOSPHERE:

In the early Mars's atmosphere under the influence of active young Sun the $^{13}C/^{12}C$ isotope ratio would increase by tens of percent (all carbon is assumed to be in the atmosphere). It contradicts the measurements [4]. One can assume an explanation for this discrepancy: on Mars, in addition to its atmosphere, there could be a reservoir of carbon with a mass from 0.08 M_{atm} to 8 M_{atm} (depending on γ), where M_{atm} is the mass of the modern Martian atmosphere.

However, we can also consider the ALH84001 meteorite. The age of meteorite's rocks is estimated to be about 4.1Gyr and it contains ancient Martian atmospheric gases. Isotope ratio $^{13}C/^{12}C$ in it is close to the modern one on Mars. Then to explain it, the mass of the reservoir would be an order of magnitude larger. It is also possible that the capture of atmospheric gases in the meteorite rocks occurred after the period of activity of the young Sun. Then, we can obtain agreement with measurements for carbon isotopes.

For nitrogen, the processes of selective escape from the atmosphere of Mars are essential, as well as the fact that only the atmosphere can be an exchange reservoir. This places severe restrictions on the activity of the early Sun, since the $^{15}N/^{14}N$ isotope ratio increases by several times for the parameters of solar activity specified in the model. Also, the $^{15}N/^{14}N$ isotope ratio in the meteorite ALH84001 and the modern one on Mars are noticeably different (in ALH84001 this isotope ratio is about 49% less). But ^{15}N is mainly produced in nuclear reactions involving ^{16}O. Then if we assume that the atmosphere of early Mars was dominated by nitrogen, production of ^{15}N decreases and agreement with the experimental data can be achieved. At the same time, the composition of the atmosphere has little effect on the production of ^{13}C.

ISOTOPE RATIOS $^{13}C/^{12}C$ AND $^{15}N/^{14}N$ IN THE EARLY ATMOSPHERE OF VENUS:

Similarly, we consider the production of heavy isotopes in the atmosphere of early Venus. Both planets are similar in that they do not have a magnetic field. However, shift of $^{15}N/^{14}N$ and $^{13}C/^{12}C$ isotope ratios on Venus over the 700 Myr activity of the early Sun turned out to be less than the uncertainty in measurements of this isotope ratios on Venus today. Although solar cosmic ray fluxes are greater on Venus than on Mars, the relative contribution to isotope ratios will be smaller due to the large mass of Venus's atmosphere.

RESULTS:

Thus, if the model of the active young Sun is correct, solar cosmic rays produced significant number of heavy isotopes ^{13}C and ^{15}N. Comparison with the isotopic ratios observed in the modern atmosphere and in an ancient meteorite ALH84001 shows that there should have been a reservoir of carbon on Mars. Mass of this reservoir should be an order of magnitude greater than the mass of its modern atmosphere. Also, it shows that nitrogen prevailed in atmosphere of early Mars. With an increase in the accuracy of measurements of its isotopic composition, it will be possible to obtain certain restrictions on the evolution of the Venusian atmosphere as well.

REFERENCES:

[1] Airapetian V.S., Glocer A., Gronoff G., Hébrard E., Danchi W. Prebiotic chemistry and atmospheric warming of early Earth by an active young Sun // Nature Geoscience. 2016. V. 9. P. 452-455.

[2] Maehara H. et al. Superflares on solar-type stars // Nature. 2012. V. 485. No. 7399. P. 478-481.

[3] Shibayama T. et al. Superflares on solar-type stars observed with Kepler. I. Statistical properties of superflares // The Astrophysical J. Supplement Series. 2013. V. 209. No. 1. Art. No. 5. 13 p.

[4] Webster C.R. et al. Isotope ratios of H, C, and O in CO_2 and H_2O of the Martian atmosphere // Science. 2013. V. 341. No. 6143. P. 260-263.

UPPER LIMITS OF MARTIAN ATMOSPHERE TRACE GASES BASED ON THE THERMAL SPECTRA OF ACS TIRVIM

D. Evdokimova[1], N. Ignatiev[1], P. Vlasov[1], A. Trokhimovskiy[1], A. Grigoriev[2], A. Shakun[1], O. Korablev[1]
[1] *Space Research Institute, Moscow, Russia, evd.dar@yandex.ru;*
[2] *Australian National University, Canberra, Australia*

KEYWORDS:
Mars, atmosphere, Fourier spectroscopy, minor species, ozone, methane, hydrogen peroxide

The thermal-infrared channel (TIRVIM) of the Atmospheric Chemistry Suite (ACS) on board the ExoMars Trace Gas Orbiter (TGO) is a double-pendulum Fourier-transform spectrometer operating in the 1.7–17 μm spectral range [1]. The instrument monitored the Mars surface and atmosphere in nadir and solar occultation modes with the resolution varying from 0.2 to 1.3 cm^{-1} [1] from April 2018 to December 2019. This period covered almost one Martian year (MY) and solar longitudes (LS) from 134° of MY34 to 115° of MY35. The instrument primary goals were temperature profiling and aerosol monitoring at different local times, locations and seasons [1].

The broad spectral range of TIRVIM also covers the absorption bands of trace gases in the atmosphere. Observation of minor species provide clues about the past or present of geological or probable biogenic processes on Mars, furthermore trace gases are key species for quantifying the properties of the oxidizing atmosphere. Three molecules of interest have strong absorption bands in the thermal range: ozone (O_3), hydrogen peroxide (H_2O_2) and methane (CH_4).

Ozone was discovered on Mars in the 1970s by Mariner space missions [2, 3], and then it was widely studied by spacecrafts' instruments in the ultraviolet (UV) range and ground based facilities using 9.7 μm band [4, 5]. Recently, the mid-infrared (MIR) channel of ACS also contributed to this dataset, detecting ozone absorption at ~3.3 μm [6]. Ozone is a variable gas with the clear seasonal trend, which is determined by the water vapor cycle on Mars. The reactions with odd hydrogen gases (HO_x) being H_2O photolysis products are the main net-loss pathway for the O_x species. Odd hydrogen also determines the stability of the CO_2 atmosphere; thus, ozone is a beneficial tracer of HO_x chemistry on Mars.

The first detection of hydrogen peroxide, a strong oxidant, in Mars atmosphere was reported by the JCMT sub-millimeter telescope [7]. It has also been measured with the imaging TEXES spectrometer at IRTF since 2001 [8, 9]. A seasonal trend with an increase in 150–220° of LS were obtained in correspondence with predictions of general circulation models [8,9]. The maximal observed value was 45 ppbv in the Northern Hemisphere [8]. However, the recent observational campaign took place in July 2018 during the TIRVIM observations, and it was concluded the absence of H_2O_2 with a 2σ upper limit of 10 ppbv [8]. This depletion against the seasonal trend has not yet been completely understood.

The presence or absence of methane in the Martian atmosphere has been widely debated in recent years. The Mars Science Laboratory (MSL) at Curiosity rover along with several orbital conformations has been detected CH_4 spikes and seasonally varying background in the Gale crater [10, 11]. The ACS and NOMAD spectrometers on board TGO observed solar occultations of the Mars atmosphere has not confirmed the detected abundances by MSL in global scale [12]. The methane detection limit by ACS was set to 20 pptv [13]. However, the best sensitivity of the instruments was mainly achieved at 10–30 km over the surface [13]. The discrepancy between the measurements restricts the sources of methane, perhaps even only to the Gale crater, and constrains its atmospheric propagation.

In this study we review the capabilities of the TIRVIM spectrometer for the detection of small atmospheric components in the thermal range of 600–1500 cm^{-1}. The advantage of this spectral interval is lower dust extinction, which allows us to probe trace gases of fundamental importance for photochemistry down to the surface. Moreover, H_2O_2 might be only observed by TIRVIM channel of ACS at 7.7 μm (~1280 cm^{-1}), therefore, complementing the science of TGO. The CH_4 band at 7.7 μm (1305 cm^{-1}) and the O_3 thermal band centered at 9.7 μm (1042 cm^{-1}) provide a possibility to study the gases based on millions of obtained spectra. Averaging of spectra is considered in details. It is applied to the data to increase signal-to-noise ratio and, thus, decrease trace gas detection limits, since it can be assumed that the dominant errors are random.

ACKNOWLEDGMENTS:
This work was supported by the Russian Science Foundation, grant No. 20-42-09035.

REFERENCES:

[1] Korablev O. et al. The Atmospheric Chemistry Suite (ACS) of Three Spectrometers for the ExoMars 2016 Trace Gas Orbiter // Space Sciences Rev. 2018. V. 214. No. 7.
[2] Barth C.A., Hord C.W. Mariner Ultraviolet Spectrometer: Topography and Polar Cap: Ultraviolet measurements reveal the topography of Mars and show that ozone may be adsorbed on the polar cap // Science. 1971. V. 173. No. 3993. P. 197-201.
[3] Barth C.A. et al. Mariner 9 ultraviolet spectrometer experiment: Seasonal variation of ozone on Mars // Science. 1973. V. 179. No. 4075. P. 795-796.
[4] Espenak F. et al. Ground-based infrared measurements of the global distribution of ozone in the atmosphere of Mars // Icarus. 1991. V. 92. No. 2. P. 252-262.
[5] Fast K. et al. Ozone abundance on Mars from infrared heterodyne spectra: I. Acquisition, retrieval, and anticorrelation with water vapor // Icarus. 2006. V. 181. No. 2. P. 419-431.
[6] Olsen K.S. et al. First detection of ozone in the mid-infrared at Mars: Implications for methane detection // Astronomy and Astrophysics. 2020. V. 639. Art. No. A141.
[7] Clancy R.T. et al. A measurement of the 362 GHz absorption line of Mars atmospheric H_2O_2 // Icarus. 2004. V. 168. P. 116-121.
[8] Encrenaz T. et al. Ground-based infrared mapping of H_2O_2 on Mars near opposition // Astronomy and Astrophysics. 2019. V. 627. Art. No. A60.
[9] Encrenaz T. Invited review: Infrared spectroscopy of planetary atmospheres: Searching for insights into their past and present histories // Icarus. 2022. V. 376. Art. No. 114885.
[10] Webster C.R. et al. Background levels of methane in Mars' atmosphere show strong seasonal variations // Science. 2018. V. 360. No. 6393. P. 1093-1096.
[11] Giuranna M. et al. Independent confirmation of a methane spike on Mars and a ource region east of Gale Crater // Nat. Geosci. 2019. V. 12. No. 5. P. 326-332.
[12] Korablev O. et al. No detection of methane on Mars from early ExoMars Trace Gas Orbiter observations // Nature. 2019. V. 568. No. 7753. P. 517-520.
[13] Montmessin F. et al. A stringent upper limit of 20 pptv for methane on Mars and constraints on its dispersion outside Gale crater // Astronomy and Astrophysics. 2021. V. 650. Art. No. A140.

RADIATIVE TRANSFER IN THE MARTIAN ATMOSPHERE TAKING ACCOUNT LINE-MIXING IN THE 15 μM CO_2 BAND

V.P. Ogibalov
Admiral Makarov State University of Maritime and Inland Shipping, Saint-Petersburg, Russia;
Saint-Petersburg State University, Saint-Petersburg, Russia, vpo563@mail.ru

KEYWORDS:
Radiative transfer, infrared molecular bands, vibrational non-LTE, carbon dioxide, Martian atmosphere, line-mixing

INTRODUCTION:

Radiative cooling in the 15 μm CO_2 band is the main cooling mechanism in the energy balance throughout the entire atmosphere of Mars. The exact values of the rate of this cooling are necessary to explain the observed temperature and wind structure of the Martian atmosphere, since the energy budget of this atmosphere determines its circulation system. One of the factors influencing the accuracy of calculating the non-equilibrium populations of excited vibrational states of the CO_2 molecules is the information about the values of the absorption coefficient in the infrared ro-vibrational bands of carbon dioxide**.** So, a development of more sophisticated models for estimating the values of the Martian atmosphere emissions in the IR bands of the CO_2 molecules is required.

A low density of the Martian atmosphere result in that the non-local thermodynamic equilibrium (NLTE) takes place in wide altitude intervals for populations of the excited vibrational states of the CO_2 molecules. The validity of estimating the cooling rate in the 15 μm CO_2 band depends on various input data used. In particular, spectroscopic parameters and a shape of absorption coefficient adopted for lines of the IR CO_2 bands are of great importance.

At low pressures, the Voigt contour is usually used to describe the contour of spectral lines, which is an integral convolution of the corresponding Lorentz and Gaussian contours. A more detailed study of the contours of spectral bands revealed spectral ranges that are not described by a simple sum of Voigt curves, and deviations can reach hundreds of percent. Such ranges include spectral ranges of overlapping lines in the Q-branches of the CO_2 bands, as well as ranges formed by overlapping wings of the CO_2 spectral lines. The effect of non-additivity of the spectral lines when they overlap, called the line-mixing effect, is a consequence of collisional non-radiative transitions between molecular states. This makes the LM-effect be potentially important for solving the NLTE problem of the CO_2 bands.

In the present study, the current version of computer code realizing the NLTE model for the IR emissions of CO_2 in the Martian [1, 2] has been further improved to incorporate the LM-effect. The line-mixing effect in the 15 μm CO_2 band was considered within framework of the strong collision model with adjusted branch coupling (so-called the ABC model) [3]. This method has been applied to simulate the experimental shape of the absorption coefficient within the spectral interval of the 15 μm band. For a set of atmospheric parameter models, the reference solutions of the NLTE problem of the CO_2 emissions in the atmosphere of Mars have been obtained with and without taking into account for the line-mixing.

THE MODEL:

The model used for solving the problem of radiative transfer in the ro-vibrational bands of the CO_2 molecules (near 4.3, 2.7, 2.0, 1.6, 1.4, 1.25, 1.2 and 1.05 μm) and of the CO molecules (near 4.7, 2.3, 1.6 and 1.2 μm) under conditions of the vibrational NLTE in the Martian atmosphere was developed [1, 2]. The 545 ro-vibrational bands rising between the 206 vibrational states of 7 isotopologues of the CO_2 molecules and the 10 ro-vibrational bands rising between the 8 vibrational states of 2 isotopologues of the CO mole-

cules are included into the NLTE model. The most upper state is 20^03 of the principal isotopologue with energy of about 9500 cm^{-1}. In the present study, this model has been further improved to solve the above radiative transfer problem in the following directions. 1) The radiative transfer in all the bands of CO_2 and CO within the 15–1.02 μm spectral interval is taken into account with an exact treatment of overlapping of the spectral lines in frequency. 2) A reflection of the IR radiation by the Martian surface is also taken into account. 3) The accelerated lambda-iteration technique used for solving the NLTE radiative transfer problem has been modified for the case of accounting the line-mixing effect using the ABC model.

RESULTS:

Calculations of the height profiles of non-equilibrium populations of vibrational states of the CO_2 molecules, taking into account the line-mixing effect, turn out to be very bulky. Therefore, to assess the possible effect of this effect, only 2 sets of atmospheric parameters were selected, corresponding to the equinox at the equator and the summer solstice at high latitudes. The obtained non-equilibrium populations were then used to calculate the radiative cooling rate of the atmosphere in the ro-vibrational bands of CO_2.

Despite the fact that at some frequency points, the difference in the values of the coefficient of IR radiation absorption by the CO_2 molecules, taking into account and without taking into account the phenomenon of line-mixing, reached 1–2 orders of magnitude, the analysis of the results showed that taking into account the influence of line-mixing on the values of the radiation absorption coefficient in the ro-vibrational bands of CO_2 leads to a slight difference in the values of non-equilibrium populations compared to the case when the radiation absorption coefficient at each frequency grid point within the range of the 15 μm CO_2 band is defined as a simple sum of Voigt line profiles. Obviously, the reason is that the populations depend on the integral over all frequencies, and the changes in the radiation absorption coefficient introduced by the phenomenon of line-mixing turn out to be insignificant or compensate for each other in those frequency intervals that are important from the point of view of radiation transfer.

The maximum differences for both selected sets of atmospheric parameters and for all variants of the frequency grids were observed at the level of about 2–3% for states 11101, 11102 and 03301 (according to the nomenclature of the HITRAN spectroscopic database) of the main isotopologue $C^{12}O^{16}{}_2$. For the state 01101 of the isotopologue $C^{12}O^{16}{}_2$, the difference in the values of the populations did not exceed 1% anywhere. Slightly smaller differences were observed for the $C^{12}O^{16}O^{18}$ and $C^{12}O^{16}O^{17}$ molecules (the 3rd and 4th most abundant isotopologues of CO_2): about 1.3 % for states 11101, 11102 and 03301 and less than 1% for state 01101 of both these isotopologues. As for the states of the $C^{13}O^{16}{}_2$ molecule (the 2nd most abundant isotopologue of CO_2), the maximum differences in the values of the non-equilibrium vibrational populations did not exceed 0.8% anywhere.

As a consequence, the change in the values of the radiative cooling rate of the atmosphere in the 15 μm band of CO_2 (which is also determined by integration over all frequencies) due to the line-mixing effect for all two atmospheric parameter cases studied at all altitude grid points did not exceed 1 % anywhere, which is much less at the modern time than the uncertainty introduced into the values of the radiative cooling rate due to uncertainties in the rate constants of inelastic collision processes of vibrational energy exchange between different vibrational states of the CO_2 and other atmospheric molecules.

CONCLUSIONS:

Only small differences (less than 3 %) due to the LM-effect both on the values of the populations of vibrational states excited in the $CO_2(v_1)$ and $CO_2(v_2)$ modes and on the values of the cooling rate in the 15 μm CO_2 band were found out throughout the entire atmosphere of Mars. The reasons of such negligible influence of the LM-effect are discussed.

The main conclusions of this study are as follows.

1) Taking into account the deviation of the frequency profile of ro-vibrational transitions within the range of the 15 μm CO_2 band from the sum of Voigt profiles due to the phenomenon of line-mixing leads only to insignificant changes in the values of non-equilibrium populations of vibrational states excited by the bending vibrational mode of CO_2 molecule. The influence of the line-mixing effect on the values of the radiative cooling rate of the atmosphere in the CO_2 bands is insignificant compared to its variability due to the modern time uncertainties in the values of other parameters which are important for the problem of radiative transfer in the CO_2 bands in the Martian atmosphere.
2) Based on the results obtained, it can be concluded that taking into account the phenomenon of line-mixing on the values of the IR radiation absorption coefficient by the CO_2 molecules at the modern level can be neglected both in calculations of non-equilibrium populations of vibrational states and in estimations of the radiative cooling rate of the atmosphere in the ro-vibrational CO_2 bands.

REFERENCES:

[1] Ogibalov V.P., Shved G.M. An improved optical model for the non-LTE problem for the CO_2 molecule in the atmosphere of Mars: Nighttime populations of vibrational states and the rate of radiative cooling of the atmosphere // Solar Syst. Res. 2003. V. 37. No. 1. P. 23-33.
[2] Ogibalov V.P. Non-equilibrium radiation in the infrared bands of the CO_2 and CO molecules in the planetary atmospheres (in the application to Mars) // Proc. SPIE. V. 10466. Pt. 1. 23rd Intern. Symp. Atmospheric and Ocean Optics: Atmospheric Physics. Irkutsk, Russia, 03-07 July 2017. 14 p. DOI: 10/1117/12.2292238.
[3] Filippov N.N., Tonkov M.V. Line mixing in the infrared spectra of simple gases at moderate and high densities // Spectrochimica Acta. 1996. V. A52. P. 901-918.
[4] Tonkov M.V., Filippov N.N., Timofeev Yu.M., Polyakov A.V. A simple model of the line mixing effect for atmospheric applications: theoretical background and comparison with experimental profiles // JQSRT. 1996. V. 56. P. 783-795.

MODELLING OF THE NON-EQUILIBRIUM EMISSIONS OF THE MARTIAN ATMOSPHERE IN THE NEAR-IR CO_2 BANDS TAKING ACCOUNT AEROSOL EXTINCTION

V.P. Ogibalov[1,2]
[1] *Admiral Makarov State University of Maritime and Inland Shipping, Saint-Petersburg, Russia*
[2] *Saint-Petersburg State University, Saint-Petersburg, Russia; vpo563@mail.ru*

KEYWORDS:
Radiative transfer, infrared molecular bands, vibrational non-LTE, carbon dioxide, Martian atmosphere, aerosol extinction

INTRODUCTION:
Heating due to the radiative transfer in the infrared (IR) ro-vibrational bands of CO_2 and CO molecules is an important component in the energy balance throughout the entire atmosphere of Mars. Also, the emissions in some of these bands are used for remote sensing of the Martian atmosphere. So, a development of more sophisticated models for estimating the values of the Martian atmosphere emissions in the IR bands of CO_2 and CO molecules is required.

The Martian atmosphere has a relatively low density. A high rate of absorption of solar radiation in near-infrared (NIR) spectral interval ~1.05–5 μm by these molecules and a low density of the Martian atmosphere result in that the non-local thermodynamic equilibrium (NLTE) takes place in wide altitude intervals for populations of the excited vibrational states. The altitude of the level in the Martian atmosphere, lower which one needs to take into account for the vibrational NLTE effects when assessing the populations of vibrational states of the CO_2 and CO molecules, varies depending on the wavelengths of the fundamental band in which the excitation of these states by absorption of the solar NIR radiation from the molecular ground state takes place.

On other hand, dust and water ice aerosols permanently exist in the atmosphere of Mars. The aerosol optical depth of the Martian atmosphere varies from less than 0.1 for the condition of transparent atmosphere up to about 5 during global dust storms. The optical depth of the Martian atmosphere for various ro-vibrational radiative transitions which should be considered in NLTE models for calculating the intensity of radiation in the NIR CO_2 bands, varies in very wide range. For example, for the main isotopologue of the CO_2 molecule, the optical depth for the central frequency of the most intensive line belonging to the fundamental radiative transitions of the NIR bands near 4.3, 2.7, 2.0, 1.6, 1.4, 1.25, 1.2 and 1.05 μm equals to $2.3\cdot10^8$, $2.5\cdot10^6$, $4.4\cdot10^4$, $4.9\cdot10^2$, $1.5\cdot10^3$, 87.7, 34.5 and 1.75, respectively. As for both the minor CO_2 isotopologues and the hot ro-vibrational radiative transitions contributing into the bands mentioned above, the such optical depths can be less unit. Thus, the values of aerosol optical depth are comparable to the ones of some NIR bands of CO_2 and CO. So, one needs to take into account of the extinction of the NIR radiation by the aerosol particles for accurate modeling the radiative transfer in the CO_2 and CO bands in the Martian atmosphere.

THE MODEL:
The model used for solving the problem of radiative transfer in the rovibrational bands of the CO_2 molecules (near 4.3, 2.7, 2.0, 1.6, 1.4, 1.25, 1.2 and 1.05 μm) and of the CO molecules (near 4.7, 2.3, 1.6 and 1.2 μm) under conditions of the vibrational NLTE in the Martian atmosphere was developed [1, 2]. The 545 rovibrational bands rising between the 206 vibrational states of 7 isotopologues of the CO_2 molecules and the 10 rovibrational bands rising between the 8 vibrational states of 2 isotopologues of the CO molecules are included into the NLTE model. The most upper state is 2003 of the principal isotopologue with energy of about 9500 cm^{-1}. In the present study, this model has been further improved to solve the above radiative transfer problem in the following directions. 1) The radiative transfer in all the bands of CO_2 and CO within the 15–1.02 μm spectral

interval is taken into account with an exact treatment of overlapping of the spectral lines in frequency. 2) The processes of scattering and absorption of radiation by aerosol particles at the frequencies of the IR bands of the CO_2 and CO molecules were taken into account. 3) A reflection of the IR radiation by the Martian surface is also taken into account. 4) The accelerated lambda-iteration technique used for solving the NLTE radiative transfer problem has been modified for the case of the aerosol extinction presence. This method allows to take into account the processes of scattering (with a phase function of general type) and absorption of radiation by aerosols at the frequencies belonging to the spectral ranges of the CO_2 and CO rovibrational bands.

RESULTS:

Using this model, the dependence of non-equilibrium populations of the high excited CO_2 and CO vibrational states on adopted optical properties of the Martian aerosol particles and on their vertical distribution as well as the effect of reflectance properties of the Martian surface on these vibrational state populations have been investigated.

For the daytime atmosphere of Mars and for realistic models of the mineral dust aerosols, calculations of the non-equilibrium populations of the CO_2 and CO vibrational states have been caried out.

Also the spectra of the limb radiation outgoing from the Martian atmosphere in the NIR CO_2 and CO bands were calculated taking account for the aerosol extinction of this radiation. An example of calculations of the limb radiation intensity in the 1.4 μm band for target heights of 140.9 km and 104.2 km is given below for the conditions: SZA = 60°, azimuth angle of viewing 90°, total optical depth of aerosol τd = 0.5, aerosol height scale *Ha* = 7.0 km.

An analysis of the response in the values of the limb radiation intensity to variations of some optical parameters of the aerosol model adopted has been carried out.

CONCLUSIONS:

The most variability in the values of the radiation intensity to changing the parameters of the aerosol model is found for rather optically thin ro-vibrational transitions which have the optical depth of the same order as the one of aerosols and which have no considerable overlapping in frequency with another ro-vibrational transitions. Therefore from the viewpoint of possible development of new approaches for retrieving the optical parameters of the Martian aerosols, for the short-wave NIR spectral range it is more preferable to consider a radiation in the fundamental transitions of the main CO_2 isotopologue. A radiation in the fundamental transitions of the minor CO_2 isotopologues is more preferable for consideration if it is concerned the spectral range from 2 to 5 μm.

The spectra of the NIR emissions outgoing from the Martian atmosphere with and without taking account for the aerosol extinction are simulated. Using these emissions for the retrieval of aerosol optical properties in the atmosphere of Mars is discussed.

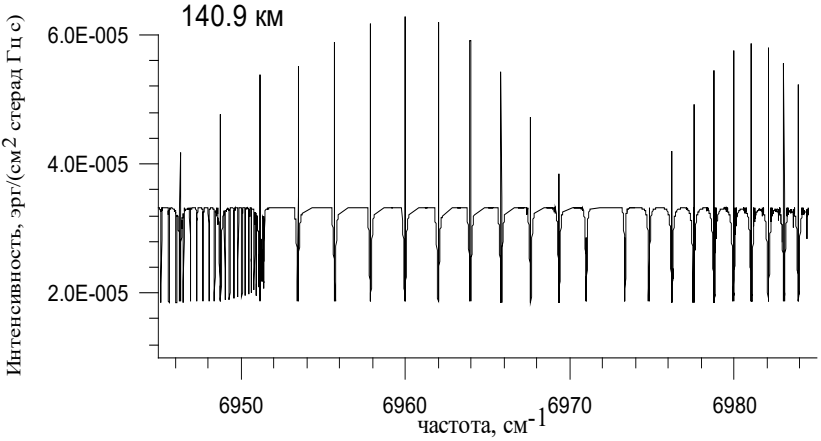

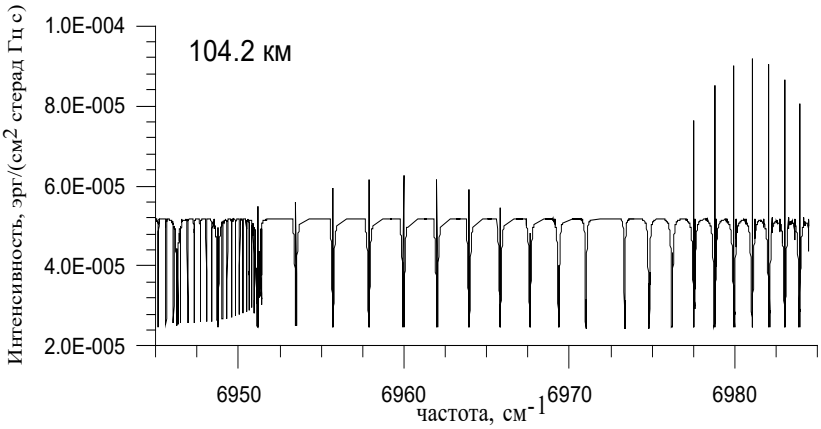

REFERENCES:

[1] Ogibalov V.P., Shved G.M. An improved optical model for the non-LTE problem for the CO_2 molecule in the atmosphere of Mars: Nighttime populations of vibrational states and the rate of radiative cooling of the atmosphere // Solar System Research. 2003. V. 37. No. 1. P. 23-33. DOI: 10.1023/a:1022343620953.

[2] Ogibalov V.P. Non-equilibrium radiation in the infrared bands of the CO_2 and CO molecules in the planetary atmospheres (in the application to Mars)// Proc. SPIE. V. 10466. 23rd Intern. Symp. Atmospheric and Ocean Optics: Atmospheric Physics. 3-7 July 2017, Irkutsk, Russia. 2017. Art. No. 1046602. 14 p. https://doi.org/10.1117/12.2292238.

ON MODEL CRUST THICKNESS VARIATIONS OF MARS AND VENUS WITH LOVE NUMBERS

A.V. Batov[1,2], T.I. Menshchikova[1], T.V. Gudkova[1]
[1] *Schmidt Institute of Physics of the Earth RAS, Moscow, Russia; gudkova@ifz.ru*
[2] *Trapeznikov Institute of Control Sciences RAS, Moscow, Russia; batov@ipu.ru*

KEYWORDS:
Mars, Venus, crust, gravity, topography, load Love numbers

INTRODUCTION:
Based on topography and gravitational field data, model variations of the thickness of the crust of Mars and Venus are calculated by the method of Love numbers. The method takes into account the adjustment of the planetary subsurface to the loads on the surface and in the subsurface. Numerical modeling is carried out using spherical harmonic expansion of topography and gravitational field data up to the 90th degree and order for Mars and up to the 70th for Venus. The relief of the crust-mantle boundary suggests partial Airy isostatic compensation. The model of the crust of Mars is consistent with the range of values of the crustal thickness beneath the InSight mission station in the southwestern part of the Elysium Planitia, obtained from the results of the seismic experiment.

DATA:
The data of the gravitational field and the topography of the planet are available on the website of the Planetary Data System (http://pds-geosciences.wustl.edu). We use the MRO120D model [1] and topography data up to 90 degrees and order, since at harmonics above 90, the correlation of the gravitational field data and the topography of Mars deteriorates markedly. For Venus, topography data (model SHTJV360u, [2]) and gravitational field data (model SHGJ180u, [3]) are used, taking into account harmonics only up to the 70th degree and order.

INTERIOR STRUCTURE MODELS:
For calculations, a model of the internal structure of Mars M_50 from the work [4] was chosen, which has an average crust thickness of 50 km with a density of 2900 kg/m^3, the radius of the core is 1821 km. This value falls within the range of determining the radius of the core of Mars by seismic methods (1830±40 km) [5]. For Venus, we will take the model of the internal structure V_16 from [6] with an average crust thickness of 30 km and a density of 2800 kg/m^3.

METHOD:
A planet is modeled as an elastic, self-gravitational spherical body. It is assumed, that deformations and stresses which obey Hooke's law are caused by the pressure of relief on the surface of the planet and anomalous density, distributed by a certain way in the crust. Numerical simulation is based on a static approach (the loading factors technique or the Green's functions method) [7–10]. We assume that there are two levels of anomalous masses — the surface and the crust-mantle boundary. Anomalous masses are a thinning or thickening of the crust on the surface and the crust-mantle boundary. Amplitudes of loads $R^j_{inm}(\varphi,\lambda)$ (which create abnormal masses) are selected in such a way as to satisfy the data of the topography C_{tinm} and the gravitational field of the planet C_{ginm} (calculated from the reference equilibrium surface):

$$C_{ginm} = \sum_{j=0}^{N} \frac{R^j_{inm}(\varphi,\lambda)}{R_0\rho_0} \cdot \frac{3\left(1+k_n(r_j)\right)}{(2n+1)} \cdot \left(\frac{r_j}{R_0}\right)^{n+2},$$

$$C_{tinm} = \frac{R^1_{inm}(\varphi,\lambda)}{R_0\rho_c} + \sum_{j=0}^{N} \frac{R^j_{inm}(\varphi,\lambda)}{R_0\rho_0} \cdot \frac{3\left(1+h_n(r_j)\right)}{(2n+1)} \cdot \left(\frac{r_j}{R_0}\right)^{n+2},$$

where ρ_0 and ρ_c — the average density of the planet and the average density of the crust; r_j — levels of occurrence of anomalous masses; N — the number of levels of occurrence of anomalous masses, load numbers $k_n(r_j)$ determining the response of the external gravitational field to an anomalous density wave with amplitude R^j_{nm}, load numbers $h_n(r_j)$ determining the deformation of the planet. The thickness of the crust consists of variations in relief relative to the leveled outer surface, the average thickness of the crust and variations in the relief of the crust-mantle boundary.

RESULTS:

By varying the average model thickness of the crust and the density jump at the crust-mantle boundary, it is possible to control the calculated variations in the thickness of the crust at the reference point — the thickness of the crust beneath the NASA InSight mission seismometer (an asterisk in Fig. 1), which is assumed to be 39±8 km [11]. Figure 1 shows a comparison of the results of modeling variations in the thickness of the crust, for the M_50 model with a lithosphere of 300 km, by the method of Love numbers (Fig. 1b), and a global map of the thickness of the crust for the same model, accor to the method described in the work [12] (Fig. 1a). For Fig. 1a ctplanet software was used [13].The difference between the models is shown in Fig. 1c. In most of the map (more than 98 % of the points when modeling with a resolution of 1×1°), the difference is less than 5 km, the largest discrepancy up to 20 km takes place under volcanic structures.

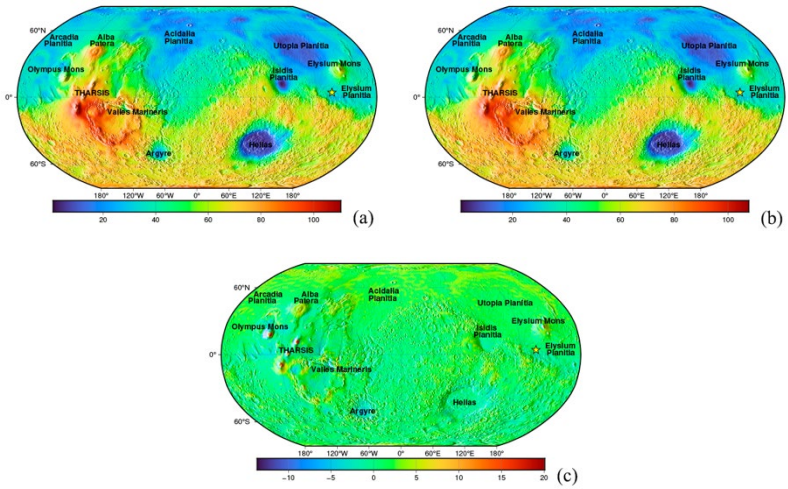

Fig. 1. A map of the crust thickness of Mars (km) (a) obtained by the method of work [12] using ctplanet software [13], (b) by the method used in this work, (c) the difference between the models. An asterisk marks the position of the InSight mission station. Meridian 0^0 is selected for the projection center.

The map of variations in the thickness of the crust for Venus is shown in Fig. 2. The thickness of the crust varies from 18.6 km (the Atlanta plain) to 82.3 km (the Maxwell Mountains on Ishtar), which is consistent with the work of other authors. The thickness of the crust on Venus is closely related to topographic structures. The crust of Venus is isostatically compensated, in the area of the lowlands the crust is thinner, and in the area of the hills its thickening is observed (the roots of the uplifts of the Ishtar, the Aphrodite, Ovda, Tethys and some others). The thickness of the crust beneath the plains is about 20–30 km, under the Atlas and Beta volcanic uplifts, the thickness of the crust reaches 48 km (Mount Maat), 47.4 km (Mount Rhea), and 46.5 km (Mount Teyi). It is assumed that dynamic support can make a significant contribution under volcanic uplifts, which is not taken into account in this work, therefore these thickness values may be slightly different than the real ones.

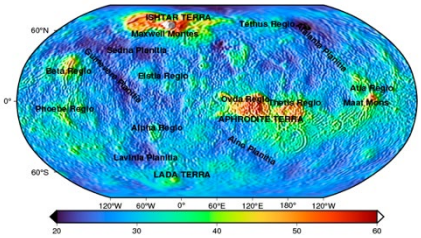

Fig. 2. The model thickness of the Venusian crust for a model with an average crust thickness of 30 km, a lithosphere thickness of 300 km, an average crust density of 2800 kg/m^3 and a density jump of 500 kg/m^3. The meridian 60° is selected for the projection center. For clarity, areas with a crust thickness of more than 60 km are marked in white.

ACKNOWLEDGMENTS:
This work is financially supported by Budget funding of Schmidt Institute of the Earth RAS.

REFERENCES:

[1] Konopliv A.S., Park R.S., Folkner W.M. An improved JPL Mars gravity field and orientation from Mars orbiter and lander tracking data // Icarus. 2016. V. 274. P. 253-260. https://doi.org/10.1016/j.icarus.2016.02.052.
[2] Rappaport N.J., Konopliv A.S., Kucinskas A.B. et al. An improved 360 degree and order model of Venus topography // Icarus. 1999. V. 139. P. 19-31. https://doi.org/10.1006/icar.1999.6081.
[3] Konopliv A.S., Banerdt W.B., Sjogren W.L. Venus gravity: 180th degree and order model // Icarus. 1999. V. 139. P. 3-18. https://doi.org/10.1006/icar.1999.6086.
[4] Gudkova T.V., Batov A.V., Zharkov V.N. Model estimates of non-hydrostatic stresses in the Martian crust and mantle: 1. Two-level model // Solar System Research. 2017. V. 51. No. 6. P. 457-478. DOI: 10.1134/S003809461706003X.
[5 Stähler S.C., Khan A., Banerdt W. B. et al. Seismic detection of the martian core // Science. 2021. V. 373. Iss. 6553. P. 443-448. DOI: 10.1126/science.abi7730.
[6] Gudkova T.V., Zharkov V.N. Models of the Internal Structure of the Earth-like Venus // Solar System Research. 2020. V. 54. No. 1. P. 20-27. DOI: 10.1134/S0038094620010049.
[7] Marchenkov K.I., Lyubimov V.M., Zharkov V.N. Calculation of load factors for deeply buried density anomalies // Doklady Earth Science Sections. V.279.1984. P. 14-16.
[8] Zharkov V.N. Marchenkov K.I., Lyubimov V.M. On long-waves shear stresses in the lithosphere and the mantle of Venus // Solar System Research. 1986. V. 20. P. 202-211.
[9] Marchenkov K.I., Zharkov V.N. Stresses in the Venus crust and the topography of the mantle boundary // Soviet Astronomy Letters. 1989. V. 16. No. 1. P. 77-81.
[10] Zharkov V.N., Koshlyakov E.M., Marchenkov K.I. Composition, structure and gravitational field of Mars // Solar System Research. 1991. V. 25. P. 515-547.
[11] Knapmeyer-Endrun B., Panning M.P., Bissig F.R. et al. Thickness and structure of the martian crust from InSight seismic data // Science. 2021. V. 373. Iss. 6553. P. 438-443. DOI: 10.1126/science.abf8966.
[12] Wieczorek M.A., Beuthe M., Rivoldini A. et al. Hydrostatic interfaces in bodies with nonhydrostatic lithospheres // J. Geophysical Research: Planets. 2019. V. 124. Iss. 5. P. 1410-1432. https://doi.org/10.1029/2018JE005909.
[13] Wieczorek M. Create crustal thickness maps of planets from gravity and topography (ctplanet). 2021. DOI: 10.5281/zenodo.4439426.

USING NEURAL NETWORKS TO SEARCH FOR INFORMATION ABOUT MARS REMOTELY

N.N. Kasatikov[1], A.D. Fadeeva[1], Sh.M. Umarov[2], O.M. Brekhov[1]
[1] *Moscow Aviation Institute, Moscow, Russia, nick925@yandex.ru;*
[2] *Moscow State Institute of Geodesy and Cartography, Moscow, Russia, shapi0890@mail.ru*

KEYWORDS:
Mars, neural networks, internet of things, craters, astrobiology

INTRODUCTION:
Neural networks and artificial intelligence work not only to provide and improve life on Earth, it has long been used to work on other planets. This happens primarily to simplify and save money, as we know the development and study of the planets calls for huge financial costs. Back in 2020, the United States (NASA) launched a system that allows remotely from the territory of our planet, from special centers, to find craters on Mars [1]. The system finds both old and new components. The conclusions that the program gives are becoming more and more accurate, and the presence of an operator, although mandatory, still greatly simplifies the work of space enterprises. In addition, Russian scientists from Skoltech [2] have developed a resource that allows remotely using artificial intelligence to process data on plants that are planned to be grown on Mars.

Having studied the previous experiences, we believe that despite the need to work further in this direction, including together with a bunch of Artificial Intelligence and IoT technologies. For example, NASA scientists trained one of the algorithms on 6830 [3] images. This is quite a reasonable indicator, showing that a normal amount of data is sufficient for digestible results. As we believe, to solve the prediction of what is happening on other planets, for example, the planet Mars, we can use the generation method using neural networks, on the open source Dalle [4], the process of generating images according to our calculations will simplify people's understanding of what is happening on Mars and will be able to make visible reports more understandable, including for professionals. In our report, we will talk about our proposals and the first results of the work done for this task.

REFERENCES:
[1] Voropaev S., Kocherov A., Lorenz C.A. et al. Features in constructing a certificate of strength of extraterrestrial material by the example of the Chelyabinsk meteorite // Doklady Physics. 2017. V. 62. No. 10. P. 486-487. DOI: 10.1134/S1028335817100111.
[2] Kameda S., Ikezawa S., Sato M. et al. Ecliptic North-South Symmetry of Hydrogen Geocorona // Geophysical Research Letters. 2017. V. 44. Iss. 23. P. 11,706-11,712. https://doi.org/10.1002/2017GL075915.
[3] Bazelyan E.M., Raizer Yu.P. Fizika Molnii i Molniezashchity. M.: Fizmatlit, 2001. 308 c. (in Russian).

SESSION 2. MOON AND MERCURY (MN) ORAL SESSION

BEPICOLOMBO STATUS

J. Benkhoff[1]
[1] *European Space Agency, ESTEC, Noordwijk, The Netherlands*

KEYWORDS:
Mercury, Space Mission, BepiColombo

BepiColombo is a joint project between the European Space Agency (ESA) and the Japanese Aerospace Exploration Agency (JAXA). The Mission consists of two orbiters, the Mercury Planetary Orbiter (MPO) and the Mercury Magnetospheric Orbiter (MIO). Both spacecraft has been launched with an ARIANE V in October 2018 for an arrival at Mercury in late 2025. From dedicated orbits the two spacecraft will be studying the planet and its environment.

On its route BepiColombo will perform flybys at Earth, Venus, and Mercury.

Especially during these flybys but also during its cruise into the inner solar system some scientific and engineering operations have been scheduled.

A status of the mission and instruments and a summary of first results from measurements taken during the first three years en route to Mercury will be given.

MERCURY MAGMATIC, TECTONIC AND GEODYNAMIC HISTORY: A COMPARATIVE PLANETOLOGY ANALYSIS

J.W. Head[1], C. Huber[1], L.H. Lark[1], S.W. Parman[1], E.M. Parmentier[1], L. Wilson[1,2]
[1] *Department of Earth, Environmental and Planetary Sciences, Brown University, Providence, USA;*
[2] *Lancaster Environment Centre, Lancaster University, Lancaster, UK*

Planetary exploration has provided insight into variation of volcanic-tectonic records, global lithospheric stress states/magnitudes, and mantle convection patterns with increasing planetary radius:

1) The Moon's tectonic-magmatic history is dominated by a thick primary crust whose magma oceanography and aftermath dictated a volumetrically insignificant secondary crust generated from deeper mantle sources through a low-density crust/thickening lithosphere that precluded formation of magmatic-volcanic-tectonic (MVT) rises; relatively rapid conductive cooling changed global lithospheric stress state to modest contraction at ~3.5 Ga; the role of subsequent mantle convection is still debated.
2) Mercury's magma oceanography suggests a distinctly different primary crust (sulfur and carbon-rich). There is little evidence of mantle convection patterns (MVT rises/mantle plumes). Regional flood basalt volcanism from now-buried fissures dominated early volcanic history. The syn-post volcanism global lithospheric stress state implies significant radial contraction over the last several BY (widely distributed wrinkle ridges, huge tectonic arches). Evolution of the lithosphere was also affected by the presence of sulfides (possibly >10 vol%), which could reduce viscosity and concentrate radiogenic heat production.
3) Mars magma oceanography suggests basaltic primary and secondary crusts; secondary crustal volcanism was near-global early on but rapidly focused to mantle-plume-like upwellings (MVT rises Tharsis/Elysium). The global lithospheric stress state implies decreasing modest contraction for the last several BY (widely distributed post-regional plains wrinkle ridges).
4) and 5) Geological records of the first 80% of Venus and Earth histories are poorly known. Venus is currently (and for the last 0.5–1.0 BY) a one-plate planet losing heat conductively, and displaying a wide range of features implying both global-scale flood volcanism (regional plains) and vigorous mantle convection at several scales (rises, rift zones, coronae, large volcanoes). Earth currently displays bimodal MVT patterns: plate recycling and vigorous mantle convection at a range of scales (mantle plumes, hot spot, rises, LIPs).

Differences in planetary core-mantle radius ratios (Moon ~0.29, to Mercury ~5.2?) are clearly an important evolutionary factor. As an endmember on this spectrum, Mercury offers insights into planetary geodynamic evolution. We currently focus on 3 questions: 1) Magma oceanography aftermath and predictions for mantle composition, fO_2, sulfide distribution, volatile content parameter space; 2) How magnitude and timing of global contraction can help constrain the nature of heat sources/timing for mantle melting (relative roles of mantle internal heating and core heat flux mantle bottom-heating); and 3) How the observed volcanic record of magma generation, ascent and eruption is related to Mercury's thin mantle, sulfur-rich lithology and convection patterns and scale.

MERCURY'S MAGNETOSPHERE VARIATIONS

A.S. Lavrukhin[1], D.V. Nevskii[1,2], I.I. Alexeev[1], E.S. Belenkaya[1]
[1] *Skobeltsyn Institute of Nuclear Physics, , lavrukhin@physics.msu.ru*
[2] *Federal State Budget Educational Institution of Higher Education Lomonosov Moscow State University, Moscow, Russia*

KEYWORDS:
Mercury, MESSENGER, magnetopause, bow shock, magnetosheath, magnetic field

INTRODUCTION:
Using data from the MESSENGER probe magnetometer describing the intersection points of the magnetopause and the bow shock of the Mercury magnetosphere, by Philpott et al. (2020) [1] we have calculated the parameters of paraboloids of revolution approximating the resulting cloud of points. For each orbit of the spacecraft, based on the obtained approximations, the coordinates of each subsolar points were obtained both at the magnetopause and at the bow shock. During all 16 Mercury years during which the MESSENGER spacecraft was orbiting Mercury, variations of global parameters of the Mercury magnetosphere and characteristics of the interplanetary magnetic field in its vicinity associated with the position of Mercury in orbit around the Sun were investigated. We refer to changes in the distances to the Sun's which control the position of the magnetopause subsolar point and the similar points at Mercury's bow shock, as well as the parameters of the interplanetary magnetic field upstream of the bow shock and in the magnetosheath upstream of the magnetosphere. The dependence of the distances to the subsolar points of the magnetopause and of the bow shock on the heliocentric distance to Mercury that we obtained is consistent with the decreasing dynamic plasma pressure and the interplanetary magnetic field module inversely proportional to the square of the heliocentring distance. The average subsolar thickness of the magnetosheath during the lifetime of the MESSENGER spacecraft and the magnitude of the magnetic field jumps during the transition from the interplanetary magnetic field to the magnetosheath for each orbit were obtained too.

REFERENCES:
[1] Philpott L.C., Johnson C.L., Anderson B.J., Winslow R.M. The Shape of Mercury's Magnetopause: The Picture From Magnetometer Observations and Future Prospects for BepiColombo // J. Geophysical Research: Space Physics. 2020. V. 125. Iss. 5. Art. No. e2019JA027544. 17 p. DOI: 10.1029/2019JA027544.

A COMPARATIVE ANALYSIS OF NEUTRON FLUX DATA MEASURED BY MGNS/BEPICOLOMBO EXPERIMENT FOR VENUS AND MERCURY FLYBYS

A.S. Kozyrev[1], J. Benkhoff[2], M.L. Litvak[1], I.G. Mitrofanov[1], S.Y. Nikiforov[1], A.B. Sanin[1]
[1] *Space Research Institute, Moscow, Russia*
[2] *European Space Agency, ESTEC, Noordwijk, The Netherlands*

KEYWORDS:
Gamma-ray burst, BepiColombo, Mars Odyssey, MGNS, HEND

INTRODUCTION:
The Mercury Gamma-ray and Neutron Spectrometer (MGNS) onboard BepiColombo's Mercury Planet Orbiter (MPO) is developed to measure the gamma-ray and neutron fluxes from Mercury's surface for the study of its elemental composition [1, 2]. Launched in October 2018, BepiColombo [3] will continue until December 2025 its cruise phase on a near-Mercurian elliptical Sun orbit. Before entering orbit around Mercury, BepiColombo will perform two flybys at Venus and six flybys at Mercury [4]. This report will present the results obtained during special sessions of MGNS measurements during flybys of Venus and Mercury. Comparison of neutron flux from the surface of Mercury during the first and second flybys, as well as from the atmosphere of Venus for the second flyby will be presented. The results of numerical simulations of neutron flux will be presented, and the models for the elemental composition of the surface of Mercury and the atmosphere of Venus will be discussed.

REFERENCES:
[1] Mitrofanov I.G. et al. The Mercury Gamma and Neutron Spectrometer (MGNS) onboard the Planetary Orbiter of the BepiColombo mission // Planetary and Space Science. 2010. V. 58. P. 116-124.
[2] Mitrofanov I.G., Kozyrev A.S., Lisov D.I. et al. The Mercury Gamma-Ray and Neutron Spectrometer (MGNS) Onboard the Mercury Planetary Orbiter of the BepiColombo Mission: Design Updates and First Measurements in Space // Space Science Reviews. 2021. V. 217. Iss. 5. Art. No. 67.
[3] Benkhoff J., Murakami G., Baumjohann W. et al. BepiColombo — Mission Overview and Science Goals // Space Science Reviews. 2021. V. 217.
[4] Mangano V., Dósa M., Fränz M., Milillo A. et al. BepiColombo Science Investigations During Cruise and Flybys at the Earth, Venus and Mercury // Space Sci Rev. 2021. V. 217. Art. No. 23.

MODELING THE ERUPTION AND THE COOLING TIMES OF THE LAVAS SAMPLED BY THE CHANG'E-5 MISSION

L. Wilson[1,2], J.W. Head[2], Y. Qian[2,3], L. Xiao[3]
[1] *Lancaster Environment Centre, Lancaster University, UK*
[2] *Department of Earth, Environmental, and Planetary Sciences, Brown University, USA; james_head@brown.edu*
[3] *Planetary Science Institute, China University of Geosciences, Wuhan, China*

KEYWORDS:
Chang'e-5, basalts, sinuous rille, Rima Sharp, Rima Mairan, turbulent flow, laminar flow, lava flow, cooling rates

INTRODUCTION:
We model the emplacement of the young [1, 2] large-volume lunar lava flow Em4/P58 [3, 4] (Fig. 1) sampled by the Chang'e-5 mission [5], and the Rima Sharp sinuous rille incised into the flow [6, 7].

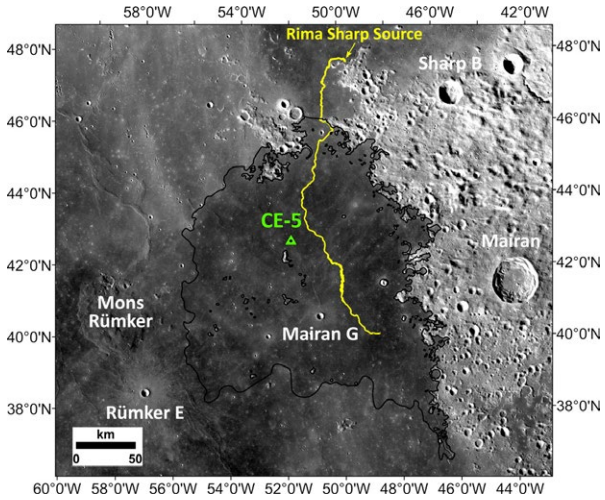

Fig. 1. Extent of the main part of the Em4/P58 flow and path of the Rima Sharp rille incised into it

We interpret the morphology [6, 7] to imply that the rille formed by thermo-mechanical erosion of the upper surface of the lava flow during the closing stage of a single eruption. The large lava volume implies a high magma eruption rate [8, 9]. The high temperature and discharge rate of low-viscosity lava leaving the vent made its motion turbulent [10]. Consequent fast cooling while turbulence persisted generated non-Newtonian bulk rheological properties very different from those of laminar lava flows. Rapid cooling during emplacement followed by much slower cooling to ambient should be reflected in returned sample petrology.

ERUPTION SCENARIO IMPLIED BY MORPHOLOGY:
The ~270 km long Em4/P58 lava erupted from a vent system at the south end of Sinus Roris [6, 7]. Its mean thickness, area and volume are ~50 m, ~33,200 km^2 and ~1660 km^3 [6, 7]. It flowed to the north and ponded around the vent before flowing south and spreading laterally to pond again as a 20 m deep flow in a depression in the Northern Oceanus Procellarum between Mons Rümker and the Mairan crater (see Fig. 1) [6, 7]. We infer that the flow then inflated to its present 50 m thickness as magma was intruded laterally into it near its base.

As the volume flux decreased, the fissure vent length decreased, and magma intrusion inflating the flow became more difficult. The magma level rose in

the conduit until lava flowed out onto the surface of the inflated flow. This late-stage overflow thermo-mechanically eroded the Rima Sharp rille channel. Figure 2 shows elevation data for Rima Sharp, measured along its meandering thalweg [6], which was used to find the slope of the surface being traversed by the rille-forming flow: 0.002 radians shallowing to 0.0004 radians in the depression. Figure 2 also shows the variation of the depth and width of the rille. The channel is 300 m deep at its source and 700 m wide, which we take to be an estimate of the width of the late-stage flow forming the rille.

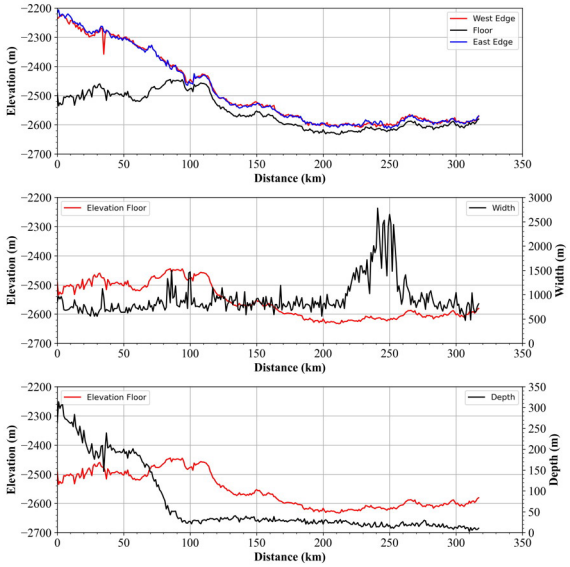

Fig. 2. Elevation, depth and width measurements for Rima Sharp [6]

The ~1660 km^3 volume of the Em4/P58 flow implies [7] that the eruption resulted from the propagation directly to the surface of a large dike that formed in the partial melt zone at the top of a deep mantle diapir [8]. Initial magma discharge rates from such dikes can be at least 3×10^6 m^3·s^{-1} [8] and are likely to decline to ~3×10^4 m^3·s^{-1} over a period of several days [9]. With rise speeds through the lithosphere of 10–20 m·s^{-1} [8], magma suffers little heat loss and erupts at near-liquidus temperature with a low viscosity. Models of eruptions of basaltic magma with these properties [8, 10–12] all show that at volume eruption rates of 10^6–10^5 m^3·s^{-1} the resulting lava flows must be turbulent.

LAVA FLOW EMPLACEMENT AND COOLING:

Our analysis shows that while the flow was turbulent, lava was typically cooling at rates of 20±10 K/hour. These rates apply to all the lava that forms the flow deposit, irrespective of where in the deposit (meaning at what depth and at what distance from the vent) it comes to rest. This is because all the lava in the deposit went through the turbulent phase. These rates apply to the lava as it cooled from its eruption temperature, assumed to be close to its 1438 K liquidus temperature, to a temperature of ~1367 K, which is the typical temperature at which turbulence ceased. In summary, this is the cooling rate experienced by all the lava during the first part of its crystallization history.

While the lava was travelling in a laminar fashion, a crust began to form at its surface as a wave of cooling propagated down into the unsheared plug created by the lava's yield strength. Cooling also occurred at the base of the flow, leaving a thin but growing layer of solidified lava on the ground beneath the flow. In all cases studied, the depth to which the upper cooling wave penetrated into the flow was less than the thickness of the unsheared plug created by the yield strength. This means that the control on the maximum length to which the lava was able to travel was a combination of the rheology preventing shearing in the upper part of the flow and the cooling wave removing lava at the base

of the flow. After coming to rest, lava in the unsheared plug continued to crystallize as its temperature continued to decrease from the end-of-turbulence temperature, 1367 K, to the solidus temperature, 1173 K. Cooling of the solid lava continued to the ambient temperature after final crystallization.

Here we update the more generalized treatment of the cooling of the stationary flow reported in [13], which gave average cooling rates for the bulk of the flow after emplacement. In this more detailed (though still approximate) treatment, we use article 2.4.iv in [14], which shows that at any given depth below the surface a wide range of cooling rates was experienced as the flow cooled. We can now be much more specific about the thermal history of crystals from different depths in the flow. Figure 3 shows three depths, 0.2, 1.5 and 3 m, and plots for each the cooling rate as a function of time, including not just the post-emplacement times but also the history during the turbulent phase. Thus, the figures show the time since lava left the vent. The times extend to 3000 days, just over 8 years. Above each cooling graph is shown the graph of the actual temperature as a function of time.

The average of all these values giving equal weight to all depths is 1693 K per year, much higher than the rate of 9 K/year reported in [13], due to the fact that the earlier estimate was weighted towards the cooling rates deep in the flow, not likely to be sampled by Chang'e-5. The new rate, 1693 K per year, is equal to 0.20 K per hour, on average 100 times smaller than the ~20 K/hour cooling rate during turbulence. So, the cooling rate after turbulence ends is still much less than the cooling rate during turbulence [13], but now by a factor of order 100 averaged over the upper part of the flow (and progressively greater factors in the deeper parts of the flow) rather than the much larger factor implied in our earlier estimates.

In this generalized treatment, we have not taken account of the fact that different crystal compositions (olivine, plagioclase, etc.) crystalize over different parts of the liquidus-solidus interval. In a more complete analysis, we plan to use MELTS to define the proportions of the different compositions at any given temperature (and their different latent heats of fusion).

IMPLICATIONS FOR CHANG'E-5 SAMPLES:

Estimates of regolith formation rates during the main formation period of mare flows are ~5 mm·Ma^{-1} [15]. With a measured age close to 2 Ga for the Chang'e-5 flow [1, 2], the regolith thickness that has been formed since the flow was emplaced is a maximum of ~10 m. Chang'e-5 will have sampled this regolith in a random fashion spatially but in a complex way vertically — we cannot assume that equal amounts of surface material were accumulated from all depths. Let us assume that the bulk of the sample was derived from depths up to 5 m. Figure 3 then shows the range of cooling rates likely to be applicable to the bulk of the mare basalts from the Em4 unit sampled by Chang'e-5.

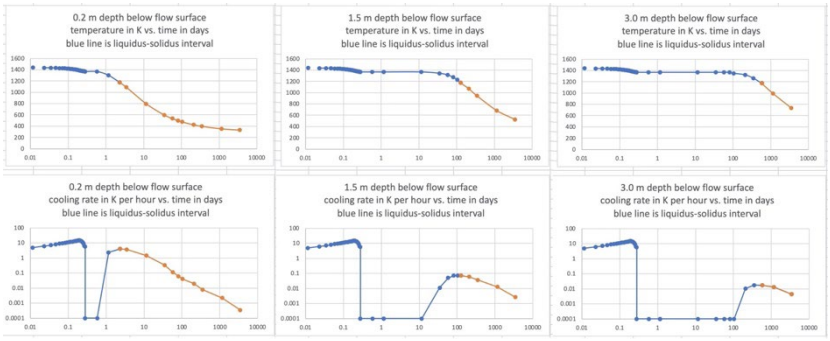

Fig. 3. Temperatures and cooling rates as a function of time for the lava emplaced at 0.2, 1.5 and 3 meters below the surface of the final lava deposit

REFERENCES:

[1] Che X. et al. (2021) Science, 374, 887-890.
[2] Li Q. et al.(2021) Nature, 600, 54-58.
[3] Qian Y. et al. (2018) JGR-Planets, 123(6), 1407.

[4] Hiesinger H. et al. (2011) Spec. Pap. GSA, 477, 1.
[5] Zhou C. et al. (2021) Adv. Sp. Res. 69, 823-836.
[6] Qian et al. (2021) GRL, 48, e2021GL092663.
[7] Qian Y. et al. (2021) EPSL, 555, 116702.
[8] Wilson L. & Head J.W. (2017) Icarus, 283, 146.
[9] Wilson L. & Head J.W. (2018) GRL, 45, 5852.
[10] Hulme G. (1973) Mod. Geol, 4, 107-117.
[11] Wilson L. & Head J.W. (1981) JGR, 86, 2971.
[12] Williams D.A. et al. (2000) JGR, 105, 20,189.
[13] Wilson et al. (2022; LPSC 43 #1624.
[14] Carslaw & Jaeger (1959) Conduction of Heat in Solids. Clarendon Press.
[15] Horz et al. (1991) Lunar surface processes. In: Lunar Sourcebook, pp. 61-120 Cambridge Univ. Press.

NORTHERN OBLIQUE IMPACT FORMATION OF THE SOUTH POLE-AITKEN BASIN

S.S. Krasilnikov[1], M.A. Ivanov[1], A.S. Krasilnikov[1]
[1] *Vernadsky Institute of Geochemistry and Analytical Chemistry RAS, Moscow, Russia; krasilnikovruss@gmail.com*

KEYWORDS:
Moon, South pole, South Pole-Aitken basin, SPA basin, impact, oblique impact, morphology

INTRODUCTION:
The South Pole-Aitken basin (SPA) is the largest and likely oldest [1, 2] basin on the Moon. The basin is highly degraded structure well described by an ellipse with axes measuring 2400 by 2050 km and centered at 53° S, 191° E [3–5].

[6] suggested an oblique impact as a reason for the elliptical shape of the basin. The formation of elliptical craters supports this hypothesis during low-angle impacts [7]. Also, laboratory experiments show that elongated structure appears only at low impact angles below ~12° [8, 9]. But the direction of the oblique impact is still unclear [5, 6, 10, 11]. In our work, we tried to understand the dependence between the direction of oblique impact and the morphology of the rim.

TOPOGRAPHICAL SINGULARITY OF THE SPA BORDER:
Our previous research [12] discovered a gradual transitional zone from the floor to the rim in the southern part of the SPA basin. This zone is characterized by a unimodal hypsogram, which indicates that the regional scarp between the rim and the floor domains is absent and topography gradually increases from the floor to the rim. In contrast, the topographic configuration of the opposite, northern edge of the SPA is characterized by a pronounced bimodality of the hypsogram [13].

The distinct differences in the topographic distributions at the southern and northern edges of the SPA have motivated us to test the topographic configuration of the SPA at its transition from the floor to the rim. For that, we have collected topographic data from the 1/64 deg./pix topographic map (resolution ~460 m/pix) at randomly selected points within large areas (5.9, 5.2 and $4.6 \cdot 10^6$ km^2, sectors 1–3 respectively) that overlay the outer ellipse defined in [5]; the density of the random points in each area were about two points per 500 km^2, which is enough to adequately describe the general topographic shape of the study areas. The sets of collected topographic data were used to construct hypsograms that characterized different SPA segments. A unimodal hypsogram characterizes a gradual transition from the floor the rim of the basin, whereas a bimodal hypsogram indicates the existence of two topographic levels (the floor and the rim) that are separated by a steep regional scarp. We prefer to use the hypsograms to characterize the general topographic characteristics of the SPA because individual topographic profiles have very complex shapes due to numerous impact structures that superpose the ancient SPA basin.

Figure 1 shows three bimodal hypsograms (1–3) at the northeastern side of the SPA basin. Hypsometry of the other sectors is unimodal. These results suggest that only at the northeast edge of the SPA a sufficiently steep scarp separate the floor and the rim of the basin. In all other parts of the basin, this transition is gradual.

At the same time, sum of the three northeastern sectors also didn't show well recognizable bimodal hypsogram (see Fig. 1, hips. 4). This point indicates a significant difference in elevation in the transitional zone of SPA.

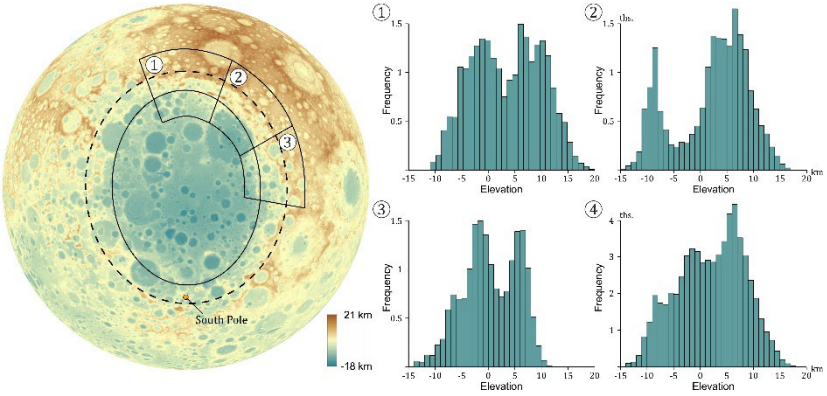

Fig. 1. Topographic configuration of the transitional zone from the floor of the SPA basin to its rim with three sectors. 1–3 histograms show topographic samples with unimodal histograms of the northeastern side of SPA. 4 — Sum of elevation values in all three sectors. Black ellipses, solid and dashed, indicate the best fit and the outer ellipses, respectively (from [5]).

DISCUSSION:

A few reasons for the lack of a distinct scarp between the floor and the rim of the SPA can be found: (1) the rim was degraded by later impact events and/or relaxation of the high topography; (2) the basin was partly filled/overlaid by later ejecta; (3) or this is a possible consequence of the original topographic configuration of the basin due to its formation by an oblique impact. The random distribution of impact craters should cause a uniform degradation of the rim by both post-formational impacts and ejecta superposition. We also believe that viscous relaxation should not selectively affect the basin configuration. Because of these reasonings, we conclude that the first two explanations of the observed large-scale topographic asymmetry of the SPA are less likely.

The oblique Craters that are formed by oblique impacts are characterized by pronounced asymmetry along the projectile trajectory with a steeper uprange wall and more gently sloping downrange wall [8]. Our results of a study of the topographic configuration of real oblique impact craters on the Moon show that they are characterized by a pronounced topographic asymmetry (see Fig. 2) established in laboratory experiments [8]. A prominent regional scarp only at the northern-northeastern edges of the SPA may suggest that this was an uprange side of the basin, whereas the southwestern portion corresponds to the downrange side.

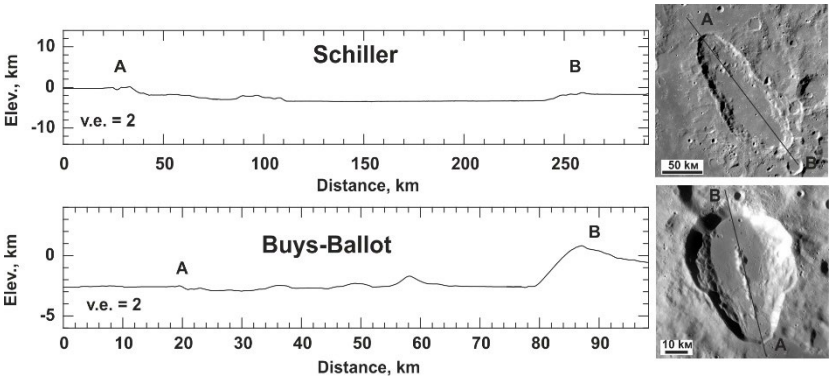

Fig. 2. Example of topographic profiles of the long axes of two oblique impact craters on the Moon. Topography from the LOLA topographic map, resolution 512 pix/deg. Steep sides of the profiles (at point B) correspond to the uprange side of the projectile trajectory.

ACKNOWLEDGEMENTS:
This work is partly supported by the Russian Science Foundation grant No. 21-17-00035: Estimates of the rate of exogenous resurfacing on the Moon.

REFERENCES:
[1] Wilhelms D.E. The geologic history of the Moon / USGS Numbered Ser. Prof. Pap. 1987. V. 1348. 302 p.
[2] Hiesinger H., van der Bogert C.H., Pasckert J.H., Schmedemann N., Robinson M.S.S., Jolliff B., Petro N. New Crater Size-Frequency Distribution Measurements of the South Pole-Aitken Basin // 43th LPSC. 2012. V. 2863. 2 p.
[3] Spudis P.D. The geology of multi-ring impact basins : the Moon and other planets. Cambridge University Press, 1993. 263 p.
[4] Shevchenko V.V., Chikmachev V.I., Pugacheva S.G. Structure of the South Pole-Aitken lunar basin // Sol. Syst. Res. 2007. V. 416. P. 447-462.
[5] Garrick-Bethell I., Zuber M.T. Elliptical structure of the lunar South Pole-Aitken basin // Icarus. 2009. V. 204. P. 399-408.
[6] Schultz P.H. Forming the south-pole Aitken basin — The extreme games // 28th LPSC. 1997. P. 1259-1260.
[7] Melosh H.J. Impact cratering : a geologic process. N.Y.: Oxford Univ. Press, 1989. 253 p.
[8] Gault D.E., Wedekind J.A. Experimental studies of oblique impact // 9th Lunar and Planetary Science Conf. Houston, Tex., March 13-17, 1978: Proc. N.Y.: Pergamon Press, Inc., 1978. V. 3. No. A79-39253 16-91. P. 3843-3875.
[9] Bottke W.F., Love S.G., Tytell D., Glotch T. Interpreting the Elliptical Crater Populations on Mars, Venus, and the Moon // Icarus. 2000. V. 145. P. 108-121.
[10] Schultz P.H. A possible link between Procellarum and the South-Pole-Aitken basin // 38th Lunar and Planetary Science Conf. 2007. V. 1839. 2 p.
[11] Schultz P.H., Crawford D. Origin of nearside structural and geochemical anomalies on the Moon // Recent Advances and Current Research Issues in Lunar Stratigraphy / ed. Ambrose W.; Geological Society of America Special Paper. 2011.
[12] Krasilnikov S.S., Krasilnikov A.S., Ivanov M.A., Head J.W. Geological mapping of the South circumpolar region of the Moon: significance for future exploration // Annual Meeting of Planetary Geologic Mappers. 22-23 June, 2022, Flagstaff, Arizona and Virtually. LPI Contribution No. 2684. Art. No. 7006.
[13] Ivanov M.A., Hiesinger H., van der Bogert C.H., Orgel C., Pasckert J.H., Head J.W. Geologic History of the Northern Portion of the South Pole-Aitken Basin on the Moon // J. Geophys. Res.: Planets. 2018. V. 123. pp. 2585-2612.

DEGRADATION OF FRESH-LOOKING CRATERS IN MARE FECUNDITATIS, MOON

K. Kochubey[1], M. Ivanov[2]
[1] *Lomonosov Moscow State University, Moscow, Russia, kochubey.ksenia@yandex.kz;*
[2] *Vernadsky Institute of Geochemistry and Analytical Chemistry RAS, Moscow, Russia*

KEYWORDS:
Moon, craters, slope, erosion, erosion rate, crater degradation

INTRODUCTION:
The morphologic degradation of smaller craters is one of the most obvious results of lunar erosion (e.g., [1, 2]). The modern high-resolution data allow detail characterization of the lunar crater degradation processes. In this report, we present our first results of a study of morphologically prominent craters in Mare Fecunditatis around the Luna-16 landing site. The goal of the study is receiving of quantitative estimates of different aspects of the crater degradation.

APPROACH:
In order to work out a methodic of the study and to pursue the main goal of our study, we have selected seven morphologically prominent craters in Mare Fecunditatis in a diameter range from ~5 km (Webb U) to 8.5 km (Taruntius H). For each crater, we have conducted crater size-frequency distribution measurements (CSFD) both on the rim and walls using the Kaguya mosaics with resolution ~7 m/pixel. On the rim, measurements were made in four polygons within a one-radius-wide zone around the crater rim crest. Inside the craters, measurements were conducted on the northern and southern portions of the wall where illumination conditions permitted confident identification of craters. Along with CSFD measurements, we also have measured steepness of the northern and southern walls of the studied craters by constructing topographic profiles and then by linear best-fit approximation of the walls. We used the LOLA gridded topography map with spatial resolution of ~60 m/pixel.

RESULTS/DISCUSSION:
As expected, the density of craters in the rim areas is larger and a ratio D_r/D_w (rim density/wall density) varies from ~1.6 up to 25 for all diameter bins (root-2 binning) excluding bins where there is no the resolution-limit turnoff. What is unexpected, is an increase of the D_r/D_w ratio as the mean crater diameter of the superposed craters increases. This tendency may suggest that the larger craters on the walls are more effectively erased compared with the smaller craters. Such an explanation does not seem plausible and we believe that an observational effect is responsible for the increase of the ratio. The mass-wasting processes on the steep-sloped walls(23-33° for the studied craters) constantly modify the older crater populations erasing the smaller craters and modifying the larger ones. The larger craters are losing their distinctive morphologies and are not recognized as impact structures. The smaller craters on the walls represent the younger crater populations that had more chances to survive as recognizable features.

Another finding of our research, which was expected, is a clear correlation between the crater ages and the steepness of the crater walls (Fig. 1). The correlation coefficient between these parameters is high (0.85) and reflects flattening of the crater walls as a function of time. Only in one case (crater Anville) we observed a landslide-like body suggesting a rapid change of the crater configuration. In all other studied craters, the flattening of the slopes appears to be gradational and we observed no talus aprons in any of these craters. The rate of the wall flattening is extremely low and is estimated as ~0.005 deg/10^6 yr. The lack of the landslides and talus aprons, and the low rate of the flattening suggest that the slopes of the crater walls were changed by their almost parallel retreat due to slow creep of the regolith.

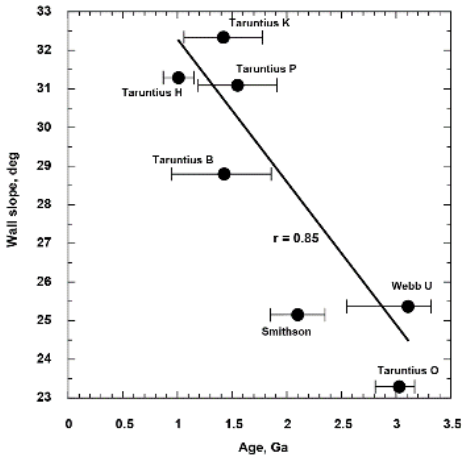

Fig. 1. Correlation between crater AMA and the slope of its walls.

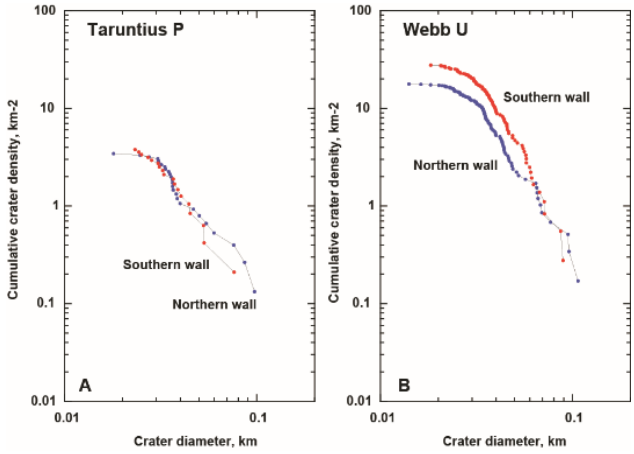

Fig. 2. Crater cumulative densities on the northern and southern walls. A: Identical densities of the younger, 1.55 Ga, crater Taruntius P. B: Cumulative crater density on the southern (poleward) wall of ancient, 3.11 Ga, crater Webb U is significantly higher for the superposed craters larger than ~60 m.

Comparison of the densities of the superposed craters on the northern (equatorward) and southern (poleward) walls of the studied craters illustrates how the wall exposition and different thermal regimes affect mass-wasting processes. The younger studied craters (Taruntius B, -K, -P, the AMAs are less than ~1.5 Ga) show no difference in the crater density on the walls (Fig. 2A). For the older craters (Webb U, Taruntius O, Smithson, the AMAs are larger than ~2 Ga) the difference is pronounced and a deficiency of the smaller craters (50–80 m diameter) is sufficient (Fig. 2B). These differences suggest that on the northern wall mass-wasting processes were more effective and removed a layer ~5-10 m thick compared with the southern wall. These estimates suggest erosion rate as high as ~5 mm/10^6 yr, which is an order magnitude higher than the rates reported earlier [3–5]. However, our estimates are related to the steep-sloped walls where the higher erosion rate is expected.

We interpret the crater density differences between the northern and southern walls by more contrast cycles of heating and cooling of the regolith that could enhance creep of the regolith on the equatorward walls. It has to be noted that despite the difference in the crater density, the slopes of the northern and southern walls are practically equal. This observation supports the model of the wall degradation by parallel retreat.

ACKNOWLEDGEMENTS:
The work is supported by the Russian Science Foundation grant No. 21-17-00035: Estimates of the rate of exogenous resurfacing on the Moon.

REFERENCES:
[1] Gault D.E. Impact craters // A Primer in Lunar Geology / eds. R. Greeley, P. Schultz. 1974. P. 137-175. NASA TMX 62359.
[2] Basilevsky A.T. On the evolution rate of small lunar craters // 7th Lunar Science Conf. Houston, Tex., March 15-19, 1976: Proc. V. 1. Art. No. A77-34651 15-91. N.Y.: Pergamon Press, Inc., 1976. P. 1005-1020.
[3] Craddock R.A., Howard A.D. Simulated degradation of lunar impact craters and a new method for age dating farside mare deposits // J. Geophysical Research. 2000. V. 105. P. 20387-20401.
[4] Fassett C.I., Combellick J.R. The rate of crater degradation and topographic evolution on the Moon: Results from the maria and initial comparisons with the highlands // 45th Lunar and Planetary Science Conf. 2014. Abstr. 1429.
[5] Fassett C.I., Thomson B.J. Crater degradation on the lunar maria: Topographic diffusion and the rate of erosion on the Moon // J. Geophysical Research. 2014. V. 119. P. 2255-2271. DOI: 10.1002/2014JE004698.

SURFACE MORPHOLOGY INSIDE THE PSR AREA OF POLAR CRATER SHOEMAKER IN COMPARISON WITH THAT OF THE SUNLIT AREAS

A.T. Basilevsky[1], Yuan Li[2], Li Gang Fang [2]
[1] *Vernadsky Institute of Geochemistry and Analytical Chemistry RAS, Moscow, Russia; atbas@geokhi.ru*
[2] *Suzhou Vocational University, SuZhou, China*

KEYWORDS:
Moon, PSR, hill-shade image, craters, rock boulders

INTRODUCTION:
Near the poles of the Moon in local depressions there are regions which are in permanent shadow, so-called PSRs [1]. They have no the day-night illumination changes and thus no the diurnal changes of the surface temperature, and inside them the regolith contains admixture of H_2O ice and ices of other volatiles [2], that may also influence geological processes and thus the surface morphology. To progress in understanding these effects we study the hill-shade images of polar crater Shoemaker (*D* ~ 51 km, *d* ~ 2,5 km) with resolution 5 m/px (Fig. 1) and compare these observations with those made in the area of work of Lunokhod-2 and Apollo-16 landing site, which have "normal" solar illumination.

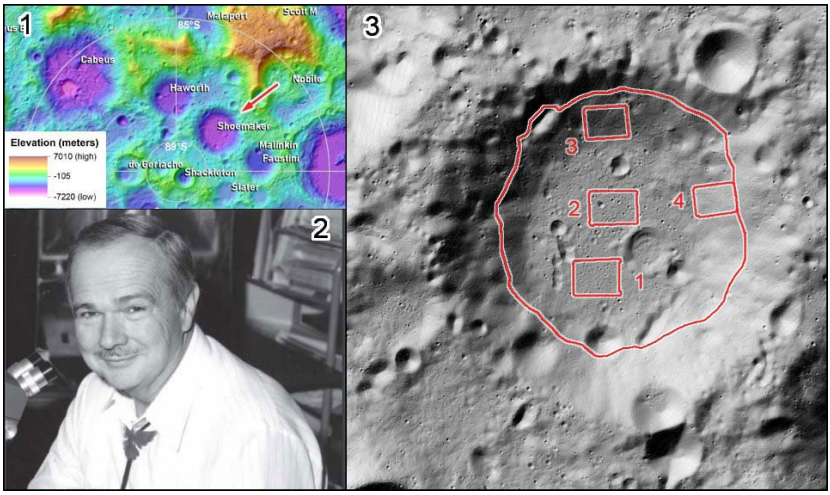

Fig. 1. 1) Part of topographic map of lunar south pole showing location of crater Shoemaker (red arrow) [3]; 2) Eugene Shoemaker, the planetary geologist, whose remains were on board of the Lunar Prospector spacecraft that impacted this crater floor [4], http://www.nasonline.org/publications/ biographical-memoirs/ memoir-pdfs/shoemaker-eugene.pdf; 3) The hill-shade image of crater Shoemaker based on the LOLA digital terrain models [5] showing the boundary of the PSR part of its interior and locations of the study areas (1–4).

SURFACE MORPHOLOGY WITHIN THE SHOEMAKER STUDY AREAS:
Figure 2 shows the hill-shade images of the ~6×4,5 km study areas on the Shoemaker floor (areas 1 and 2) and its inner slopes (areas 3 and 4). The average slope on the base of hundreds of meters for areas 1 and 2 is subhorizontal, and for areas 3 and 4 is 15 and 25° correspondingly [5].

It is seen in Fig. 2 that surface of the study areas on the Shoemaker floor (1 and 2) is covered by numerous craters with diameters up to several hundred meters. Their spatial frequency roughly corresponds to absolute age of 3,6±0,03 to 3,8±0,04 Ga that agrees with earlier results by [6] — 3,46±0,02 Ga. Images of the study areas 3 and 4 which are on Shoemaker inner slopes are

complicated by the lines of LOLA tracks that seriously worsens visibility of the surface morphology. Despite of this it is clear that on their surfaces there are craters with diameters up to a few hundred meters, but their quantity (and thus spatial frequency) is significantly smaller comparing to what is observed in the areas 1 and 2 and the apparent age there is 2,4±0,06 and 0,17±0,08 Ga. This is obviously partly due bad quality of the images, but partly to acceleration of evolution/destruction small craters on the slopes [7, 8].

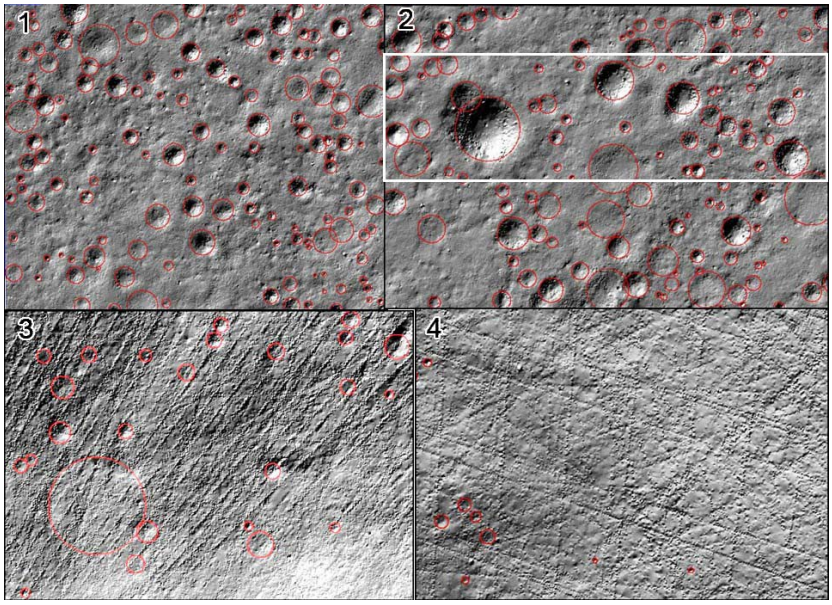

Fig. 2. The hill-shade images of the study areas (1–4) inside crater Shoemaker. White rectangular in part 2 shows position of Fig. 3.

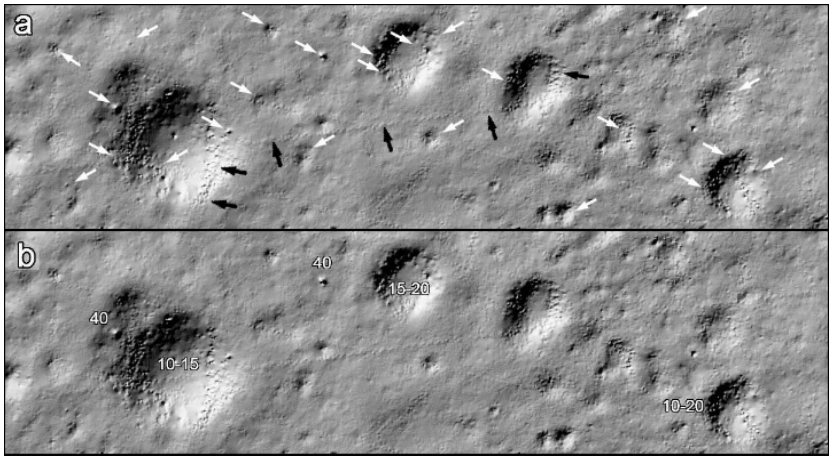

Fig. 3. a) White arrows show rock boulders and their clusters within selected part of study area 2; black arrows show boulder-like artefacts; b) Numbers in lower part of the figure are sizes of rock boulders in meters.

In areas 1 and 2 inside craters and more rarely in intercrater space are seen rock boulders of 10–15 m (= 2–3 pixels that is limit of identification) to ~40 m across (Fig. 3). In areas 3 and 4 the boulders are not reliably seen, probably because of bad quality of the images. Preferrable association of rock boulders with small craters (inside and on crater rims) was found for equatorial areas of the Moon long time ago [e.g., 9] and observations of Lunar Reconnaissance Orbiter confirmed that this is the globe-wide characteristics [10].

SURFACE MORPHOLOGY IN THE SUNLIT AREAS:

Figure 4 shows the 5 m/px hill-shade images of relatively small areas in the Lunokhod-2 working region (a) and Apollo-16 landing site (b).

It is seen in Fig. 4 that both in the Lunokhod-2 region (age is $3.2^{+0.06}_{-0.09}$ Ga) and in Apollo-16 site (~3.85 Ga) the surface is pitted by craters with diameters up to a few hundred of meters. In the image of the Lunokhod-2 region are seen the 10–20 m boulders associated with craters. In the image of the Apollo-16 site, boulders are seen only inside one looking fresh crater with diameter ~200 m. In association with presenting there several craters with diameter of several hundred meters no boulders are seen. This difference may be due to the higher mechanical strength of mare basalts comparing to that of highland fragmental breccias as it was described by [11].

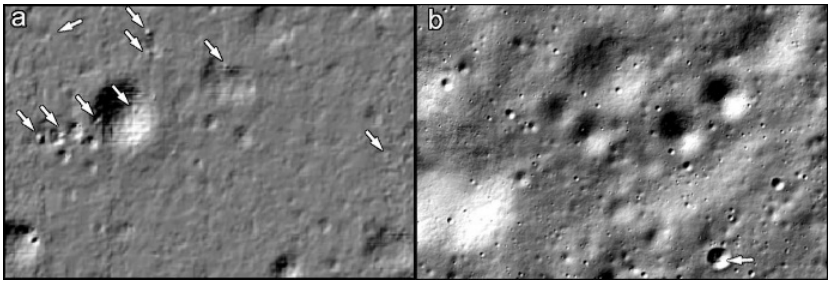

Fig. 4. Hill-shade images of selected 3×2 km areas in the Lunokhod-2 working region (a) and Apollo-16 site (b). Arrows show rock boulders.

DISCUSSION AND CONCLUSIONS:

The above consideration showed that surface morphology in permanently shadowed region (PSR) inside crater Shoemaker is generally similar to the morphologies of the sunlit areas exemplified by the Lunokhod-2 work region and Apollo-16 site: There is present population of craters up to several hundred meters in diameter, on the Shoemaker inner slopes the abundance of these craters is significantly lower than on sub-horizontal areas of the Shoemaker floor, on the Shoemaker floor inside some craters and more rarely in inter-crater space are seen rock boulders of 10–15 m to ~40 m across. The boulder abundance on the Shoemaker floor is closer to that of Lunokhod-2 region than to Apollo-16 site that is probably because the mechanical strength of the Shoemaker floor bedrock is closer to that of mare basalts than to the highland fragmental breccias. So, the permanent shadowing and presence of ices in the regolith did not significantly influence the surface geological processes comparing to the areas of the Moon with “normal” solar illumination. This agrees with absence of correlation between the water equivalent of hydrogen and the decameter-scale surface roughness found by [12] and with observations in small PSRs by [13].

ACKNOWLEDGEMENTS:

A.T. Basilevsky was supported by the Russian Science Foundation grant no. 21-17-00035: Estimates of the rate of exogenous resurfacing on the Moon, and Yuan Li was supported by the grant with no. 20KJD160001 from JiangSu education department.

REFERENCES:

[1] https://en.wikipedia.org/wiki/Permanently_shadowed_crater.
[2] Colaprete A. et al. // Science. 2010. V. 330. P. 463-468.
[3] https://www.lpi.usra.edu/lunar/lunar-south-pole-atlas/.
[4] http://www.nasonline.org/publications/biographical-memoirs/memoir-pdfs/shoemaker-eugene.pdf.
[5] http://pds-geosciences.wustl.edu/lro/lro-l-lola-3-rdr-v1/lrolol_1xxx/browse/lola_gdr/.
[6] Tye A.R. et al. // Icarus. V. 255. P. 70-77.
[7] Basilevsky A.T, Popovich V.D. // Izvestia AN SSSR. Ser. Geol. 1976. No 4. P. 56-60 (in Russian).
[8] Basilevsky A.T. et al. // Solar System Research. 2020. V. 54. No. 5. P. 361-371.

[9] Florensky C.P. et al. // Modern concepts on the Moon. M.: Nauka, 1972. P. 21-45 (in Russian).
[10] Vanga S. et al. // Geophys. Res. Lett. 2022. V. 49. Art. No. e2021GL096710.
[11] Li Yuan et al. // Planet. and Space Science. 2018. V. 162. P. 52-61.
[12] Li Yuan et al. // The 12th Moscow Solar System Symp. Abstr. 16MS3-MN-PS-16.
[13] Bickel V.T. et al. // Nature Communications. 2021. V. 12. Art. No. 5607. https://doi.org/10.1038/s41467-021-25882-z.

SITE SELECTION PROBLEMS OF THE MOON RESEARCH STATION

E.N. Slyuta[1], E.A. Grishakina[1], O.I. Turchinskaya[1], O.S. Tretyukhina[1], E.A. Feoktistova[2]

[1] *Vernadsky Institute of Geochemistry and Analytical Chemistry RAS, Moscow, Russia; slyuta@geokhi.ru*

[2] *Sternberg Astronomical Institute Moscow State University, Moscow, Russia*

KEYWORDS:
Moon, Moon base, international lunar research station, ILRS, De Gerlache crater, Shackleton crater, Slater crater, Mount Malapert, DEM, lunar resources

INTRODUCTION:

The more important real-estates in the entire Solar system are locations on the Moon, where there are the richest gas deposits, good landing sites and eternal sunlight. These are places where humanity can start production off the planet. These places are very rare and limited. The best location can forever provide a strategic advantage in the exploration of the Moon and deep space [1].

SITE SELECTION REQUIREMENTS:

Among the main requirements for the placement of lunar research base, the following can be distinguished: location and size of the site, convenient and safe terrain, maximum degree of illumination, periodic visibility of the Earth, the ability to provide direct and constant radio communication with the Earth, maximum comfortable temperature on the surface, availability of rich deposits of water ice in the lunar soil, etc.

There are three sites in the South Polar Region that meet almost all of the basic requirements for the placement of a permanent lunar research station, a lunar range and a spaceport — site #1(C) on the rim of the De Gerlache crater, site #2(B) on the rim of the Shackleton crater, and site #3(D) on the rim of the Slater crater (Fig. 1).

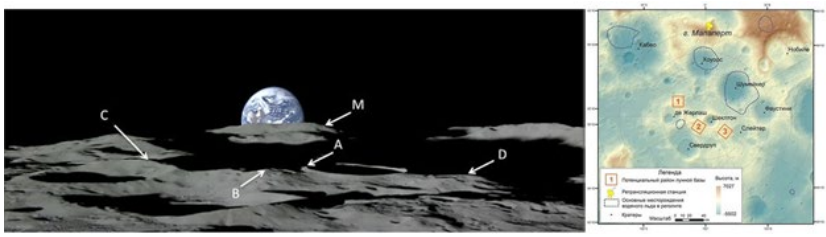

Fig. 1. Image of the South Pole according to the data of the Kaguya spacecraft [2] (left) and survey map of the South Pole (right): A — area with a high degree of illumination on the edge of the Shackleton crater; C — site #1 on the rim of the De Gerlache crater; B — site #2 on the rim of Shackleton crater; D — site #3 on the rim of Slater crater; M — Mount Malapert.

SITE SELECTION METHODS:

Comparative analysis of digital elevation models with a resolution of about 1 m for the selected three sites (Fig. 2), the distribution of safe slopes based on 5 m (Fig. 3), the degree of illumination (Fig. 4), the visibility of the Earth, average winter and summer temperatures, the availability of gas deposits showed that for the most optimal location for the lunar base is site #2(B). Relatively flat terrain and a large area of the site, approximately 10×12 km in size and with a total area of more than 100 km^2, are the most favorable for placing all the necessary zones of the lunar base at a safe and convenient distance from each other for constant maintenance and visits during one working exit.

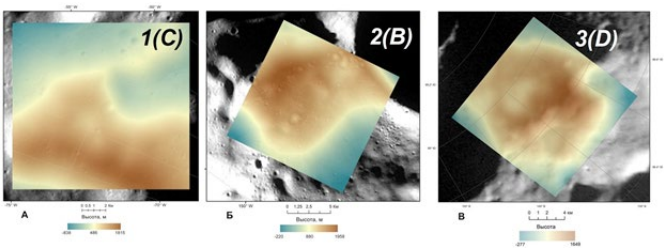

Fig. 2. Digital elevation models of sites #1, #2 and #3 by data on LRO spacecraft (NASA)

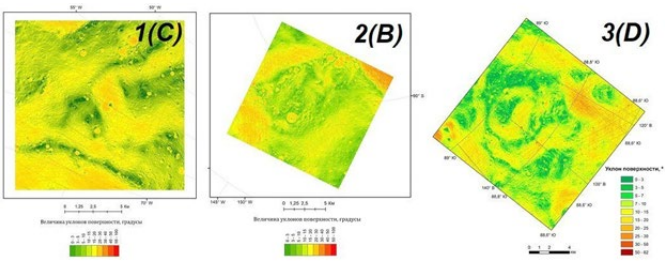

Fig. 3. Distribution of slopes based on 5 m on sites #1, #2 and #3.

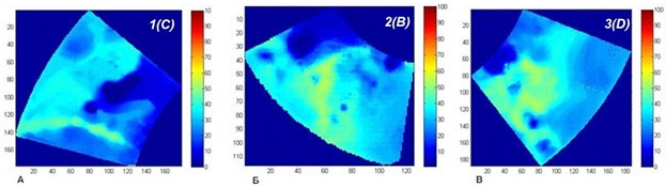

Fig. 4. Degree of illumination of sites #1, #2 and #3.

On the rim of the Shackleton crater at 7.5 km from energy zone #1 in the area with the maximum degree of illumination in antiphase with energy zone #1, it is proposed to place a backup energy zone #2 (Fig. 5). In a zone 10–15 km from the main zone on a gentle slope facing the far side of the Moon, the Earth is never visible. This zone is protected from radio interference from the Earth and is favorable for the deployment of a network of radio astronomy antennas of any scale. On Mount Malapert (M) at the meridian 2° E a repeater can be installed to provide direct and permanent communication with the Earth, a scientific station can also be located here for direct observation of the Earth and near-Earth space(Fig. 6).

Site #2(B) allows you to place at a safe distance from each other and for visiting within one working exit from the main zone a research zone, energy zones #1 and #2, a landing site, a raw material zone, recycling zones #1 and #2 (Fig. 5). The raw material zone is intended for extraction and enrichment of volatile components (water ice).

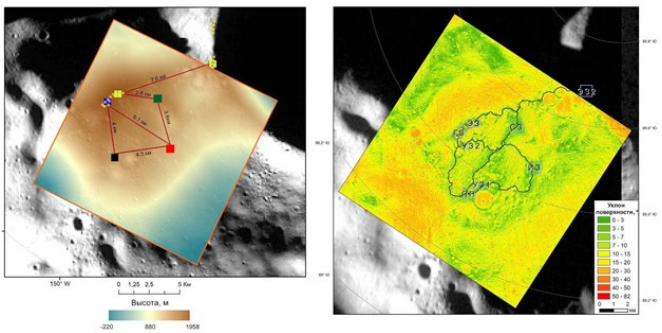

Fig. 5. Scheme of approximate placement of lunar infrastructure zones (left) and communication routes with slopes up to 5° on a base of 5 m between them at site #2: blue — main zone, yellow — energy zones #1 and #2, black — landing site, red — research zone, green — raw material zone.

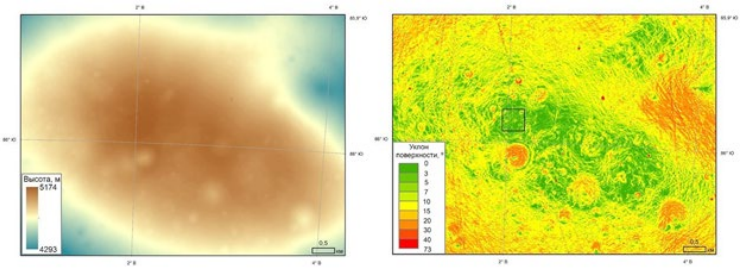

Fig. 6. Digital elevation model with a resolution of 10 m according to LOLA LRO data on the top of Mount Malapert (left) and slope distribution (right). The square size is 500×500 m.

SUMMARY:
The scenario of the lunar program and logistics, the delivery of the necessary equipment and the amount of work on the surface, the constant provision of energy and local resources, etc. will largely depend on the choice of the optimal site for the lunar base, including its location and size, comfortable and safe terrain, maximum degree of illumination etc. Such a site will significantly reduce the cost of servicing the lunar base in the future and, in fact, will forever provide a strategic advantage over other less convenient sites.

REFERENCES:
[1] Slyuta E.N. Gas fields of the Moon, key lunar technologies and pinnacles of eternal light // Znanie — Sila. 2022. No. 3. P. 13-21 (In Russian.)
[2] Bussey D.B.J., McGovern J.A., Spudis P.D., Neish C.D., Noda H., Ishihara Y., Sørensen S.A. Illumination conditions of the south pole of the Moon derived using Kaguya Topography // Icarus. 2010. V. 208. P. 558-564.

ABSOLUTE MODEL AGE ESTIMATES OF THE FECUNDITATIS BASIN AND MARE FECUNDITATIS IN THE REGION OF LUNA-16 LANDING SITE

M.A. Ivanov[1], J.W. Head[2], H. Hiesinger[3]
[1] *Vernadsky Institute of Geochemistry and Analytical Chemistry RAS, Moscow, Russia; mikhail_ivanov@brown.edu*
[2] *Brown University, Ptovidence RI, USA*
[3] *Muenster University, Muenster, Germany*

KEYWORDS:
Moon, Fecunditatis basin, Mare Fecunditatis, Luna-16, absolute age, absolute model age

INTRODUCTION:
The Fecunditatis basin represents a broad topographic depression partly filled by mare basalts. Although these features are typical of impact basins on the nearside, the other characteristics of lunar basins such as multiple rings and a pronounced topographic profile are absent. Although the basin has muted morphological and topographical signatures that provide weak evidence for its presence [1, 2], the topographic variations and crustal thickness in this region suggest that the Fecunditatis basin exists and may be among the oldest impact structures on the Moon [3–8].

Analyses of materials delivered to Earth by the Luna-16 sample return mission revealed a variety of absolute radiometric ages that appear to cluster around an ~3.4 Ga value [9–13], whereas crater size-frequency distribution measurements (CSFD) reveal a wider spectrum of absolute model ages in the Fecunditatis basin [14]. In this paper, we present our estimates of the AMAs that are related to both basin and to Mare Fecunditatis.

METHOD:
In order to estimate the AMAs of the major features and units in the region of the Luna-16 landing site we performed CSFD measurements in four key areas: 1) The region within the inferred inner ring [6] of the Fecunditatis basin that includes both the highlands (16,0002 km^2) and mare (220,000 km^2) domains. In an attempt to estimate the AMA of the basin, we conducted CSFD measurements in these domains separately. In the mare domain, some craters are overlain by mare materials but their presence is marked by specific landforms, for example, circular wrinkle ridges. These (ghost) craters have been included into the population of the mare craters. 2) An area (4×4°, ~13,000 km^2), which is centered at the Luna-16 landing point. 3) An irregular-shaped area (~9600 km^2) that has the most uniform distribution of FeO and TiO_2 determined from the Clementine data [15]. 4) The floor of crater Langrenus (~2,000 km^2) whose rays and secondary craters overlay the eastern portion of Mare Fecunditatis.

RESULTS AND DISCUSSION:
DOMAINS WITHIN THE INNER RING OF THE FECUNDITATIS BASIN.
The CSFD (diameter range 15–40 km) of the highland domain within the inner ring of the basin falls onto the lunar equilibrium curve and does not provide information for the AMA determinations.

Craters larger than ~40 km diameter deviate slightly from the equilibrium curve and their SFD suggests the AMA of $\sim 4.10^{+0.05}_{-0.07}$ Ga. The highland domain predominantly represents a portion of the rim and ejecta of the Crisium basin and the 4.10 Ga age likely reflects time of the Crisium basin formation; this age practically coincides with the earlier estimates of the Crisium formation, $\sim 4.07^{+0.016}_{-0.108}$ Ga [2]. The age of the Nectaris basin was estimated as $\sim 4.17^{+0.012}_{-0.014}$ Ga [2]. Since the ejecta of the Crisium and Nectaris basins partly overlie the topographic depression of the Fecunditatis basin, it must be older than ~4.17 Ga and thus may represent one of the oldest lunar basins.

The entire measured CSFD in the mare domain cannot be fit by a single isochron and only the distribution of the craters >15 km is poorly fit by an isochron of $\sim 3.93^{+0.04}_{-0.05}$ Ga. Because the population of craters within the mare domain includes those that predate the mare emplacement, this estimate should reflect the age of the pre-mare surfaces. In this case, an at least ~170 m.y. (up to ~240 m.y.) difference exists between the ages of the exposed (highlands domain) and hidden (mare domain) portions of the pre-mare surfaces. Such an age discrepancy requires either a single resurfacing event or a series of such events that were sufficiently extensive to partly erase the pre-mare crater population.

MARE FECUNDITATIS.

The CSFD curve for the area around the landing site shows a single AMA of $3.35^{+0.03}_{-0.04}$ Ga for craters in a diameter range from 0.6–2 km. To a large extent, this area corresponds to spectral units F7 and F8 [14], which have AMA estimates of ~3.36 and ~3.59 Ga, respectively.

In the area with the uniform concentrations of FeO and TiO_2, the entire size-frequency distribution of craters consists of two parts. The distribution of craters >~3 km corresponds to an AMA of $3.80^{+0.07}_{-0.13}$ Ga. This value is significantly smaller than the AMA of the pre-mare surfaces within the mare domain but is based on four craters only, has large error bars, and does not represent a robust age estimate.

The second part of the distribution for craters in a diameter range from 0.6–2 km is approximated by an isochron of 3.37±0.01 Ga. This value practically coincides with the AMA in the area around the landing site. Thus, counts in these neighboring areas are consistent with each other and we believe that a value of about 3.4 Ga is a good estimate of the age of a specific stage of the emplacement of the mare basalts in the landing site region.

*LANGRENUS FLOOR***.**

The crater size-frequency distribution in a diameter range 0.4–1.5 km on the floor of crater Langrenus is close to the AMAs determined in the areas near the landing site, $3.44^{+0.06}_{-0.08}$ Ga. It is, however, noticeable larger, which appears as a violation of the documented stratigraphy. This apparent AMA/stratigraphy paradox can be explained by invoking multiple phases of volcanism in Mare Fecunditatis that both predate and postdate the Langrenus impact event. The size-frequency distribution of craters in the region near the landing site may reflect the younger volcanic phases, whereas the mare surfaces in the eastern portion of the mare that are clearly older than rays/secondaries from Langrenus, is likely to represent the earlier phases of volcanic activity.

ACKNOWLEDGEMENTS:

The work of MAI is supported by the Russian Science Foundation grant No. 21-17-00035: Estimates of the rate of exogenous resurfacing on the Moon.

REFERENCES:

[1] Fassett C.I. et al. Lunar impact basins: Stratigraphy, sequence and ages from superposed impact crater populations measured from Lunar Orbiter Laser Altimeter (LOLA) data // J. Geophys. Res. 2012. V. 117. Art. No. E00H06. DOI: 10.1029/2011JE003951.

[2] Orgel S. et al. Ancient bombardment of the inner Solar System: Reinvestigation of the "fingerprints" of different impactor populations on the lunar surface // J. Geophys. Res. 2018. V. 123. https://doi.org/10.1002/2017JE005451.

[3] Spudis P.D. The Geology of Multi-ring Basins: The Moon and Other Planets. N.Y.; Cambridge: Cambridge University Press, 1993. 263 p.

[4] Rajmon D., Spudis P. Geology and stratigraphy of Mare Fecunditatis // 31th Lunar and Planetary Sci. Conf. Houston, TX. 2000. Art. No. 1913.

[5] Stoffler D. et al. Cratering history and lunar chronology // Reviews in Mineralogy and Geochemistry. 2006. V. 60. P. 519-596.

[6] Frey H. Previously unknown large impact basins on the Moon: Implications for lunar stratigraphy // Geol. Soc. Am. Spec. Pap. 477 2011. P. 53-75. DOI: 10.1130/2011.2477(02).

[7] Spudis P.D. Wilhelms D.E., Robinson M.S. The Sculptured Hills of the Taurus Highlands: Implications for the relative age of Serenitatis, basin chronologies and the cratering history of the Moon // J. Geophys. Res. 2011. V. 116. Art. No. E00H03. DOI: 10.1029/2011JE003903.
[8] Neumann G.A. et al. Lunar impact basins revealed by Gravity Recovery and Interior Laboratory measurements // Science Adv. 2015. V. 1. Art. No. e1500852.
[9] Vinogradov A.P., Artemov Yu.M. Absolute age of lunar regolith material from Sea of Fertility // Lunar soil from Sea of Feritility. M.: Nauka, 1974. P. 455-467.
[10] Papanastassiou D.A., Wasserburg G.J. Rb-Sr age of Luna 16 basalt and the model age of lunar soil // Lunar soil from Sea of Feritility. M.: Nauka, 1974. P. 471-477.
[11] Cadogan P.H., Turner G. 40Ar-39Ar dating of Luna-16 and Luna-20 samples // Philosophical Trans. Royal Society A. 1977. V. 284. P. 167-177.
[12] Cohen B.A., Snyder G.A. Hall C.M. Taylor L.A., Nazarov M.A. Argon-40-argon-39 chronology and petrogenesis along the eastern limb of the Moon from Luna-16, -20 and -24 samples // Meteoritics and Planetary Science. 2001. V. 36. P. 1345-1366.
[13] Fernandes V.A., Burgess R. Volcanism in Mare Fecunditatis and Mare Crisium: Ar-Ar age studies // Geochimica et Cosmochimica Acta. 2005. V. 69. P. 4919-4934.
[14] Hiesinger H., Head J.W., Wolf U., Jaumann R., Neukum G. New ages for basalts in Mare Fecunditatis based on crater size-frequency measurements // 37th Lunar and Planetary Sci. Conf. Houston, TX. 2006. Abstr. 1151.
[15] Lucey P.G., Blewett D.T., Jolliff B.L. Lunar iron and titanium abundance algorithms based on final processing of Clementine ultraviolet-visible images // J. Geophys. Res. 2000. V. 105. P. 20297-20305.

YUTU-2 RADAR SOUNDING OVER THE CHINESE CHANG'E-4 LANDING SITE ON THE FAR-SIDE OF THE MOON

C. Ding[1,2], S. Huang[2,3], Y. Su[4,5], J. Li[6]
[1] *Institute of Advance Study, Shenzhen University, Shenzhen, China; dingchunyu@szu.edu.cn*
[2] *Space and Earth Interdisciplinary Center, Shenzhen University, Shenzhen, China*
[3] *College of Civil and Transportation Engineering, Shenzhen University, Shenzhen, China; shaopeng@szu.edu.cn*
[4] *Key Laboratory of Lunar and Deep Space Exploration, National Astronomical Observatories, Chinese Academy of Sciences, Beijing, China*
[5] *University of Chinese Academy of Sciences, Beijing, China*
[6] *Lunar Exploration and Space Engineering Center, Beijing, China*

KEYWORDS:
Chang'E-4 mission, lunar regolith, lunar penetrating radar, chinese lunar exploration program

The Chinese Chang'E-4 mission successfully landed at the bottom of the Von Kármán crater on the far side of the Moon on January 13, 2019. Its rover Yutu-2 has been working healthily and stably for more than three years, and has obtained a large amount of scientific data from the landing area. A surface penetrating radar is carried by the Yutu-2 rover, and its main scientific goal is to detect the subsurface structure of the lunar regolith. In this paper, we will present our latest results obtained by Yutu-2 radar data, including the stratigraphy structure of the subsurface materials, the thickness of the lunar regolith and its dielectric properties inversion, the buried crater structure within the subsurface materials, and the radar observation of the lunar regolith heterogeneity around the Chang'E-4 landing site.

SOME FEATURES OF THE EARLY MOON' DEGASSING

S.A. Voropaev[1], A.P. Krivenko[1]
[1] *Vernadsky Institute of Geochemistry and Analytical Chemistry RAS, Moscow, Russia; Voropaev@geokhi.ru*

KEYWORDS:
Moon, volatiles, cracks, lithosphere, heating, stress, degassing

INTRODUCTION:
In the early stages of the Moon's development, its growing lithosphere experienced complex time-varying temperature and gravitational stress. Despite the subsequent intense impact shock transformation of the surface, during the gravimetric survey of the GRAIL space mission, the presence of relic deep faults was detected. The analysis of linear gravitational anomalies makes it possible to estimate the final deformation of the outer rigid layer of the planet due to the excess of temperature stress over gravitational compression. The obtained dependences of the time interval of the lithosphere expansion on a number of dimensionless thermal conductivity parameters allow us to refine existing models of the thermal and geochemical evolution of the early Moon.

LUNAR CRUST EVOLUTION:
The formation of the lunar crust and mantle was accompanied by the occurrence of temperature and gravitational stress in the lithosphere of the early Moon, which is associated with the features of its gravitational field, including the presence of relic faults and gravitational anomalies (mascons). The GRAIL space mission to study the external gravitational field of the Moon using mutual sensing of the motion of two satellites in low orbit has significantly improved the understanding of hidden subsurface geological structures [1]. Previous studies were limited to large-scale low-resolution photography, in which only significant objects were visible in the signal, However, this allowed us to draw a number of conclusions about the internal structure of the Moon (a small core, a relict tidal protrusion) and to detect gravitational anomalies (mascons) under the main lunar mare [2]. GRAIL made it possible to bring the expansion of the gravitational field by spherical harmonics up to 420 orders (GLA 0420A model), which corresponds to a spatial resolution of ~13 km on the surface of the planet [3]. This made it possible to study the early evolution of the Moon, since impact craters erased most of the geological record of the first ~700 million years of lunar history. At the same time, it was the pre-Nectarian and Nectarian periods that covered the critical time interval between the solidification of the lunar magma ocean and the end of the formation of large impact basins ~3.8 billion years ago.

The resulting distribution map of the horizontal gradient of the Bouge potential displays a rich set of short-wave structures in the lunar crust. A number of elongated linear gravitational anomalies (LGA) are noticeable, characterized by negative gradients that clearly stand out above the background variability. Four large LGA have a length of more than 500 km, an estimate of 22 of the most distinct LGA gives a total length of 5,300 km and another 44 possible anomalies have a total length of 8,160 km]. Such surprisingly linear structures in terrestrial geological systems are usually associated with faults or dikes. If we consider the averaged profile of the gravitational Bouge potential perpendicular to the LGA, we can show that they are associated with narrow positive gravitational anomalies. This indicates a subsurface structure of increased density, i.e. these objects are magmatic intrusions. The Bouge anomalies above a typical LGA have a bell-shaped shape with an amplitude of 90–100 mGal and a half-width of 40–50 km. The solution of the inverse problem for a model of a flat intrusion with a density contrast Δp = 550 kg/m^3 gives a width of 7–8 km, a depth of the tip of 13 km and a depth of the sole of 86 km or to contrast the density Δi = 800 kg/m^3, the width will be 5–6 km with the same vertical length and location.

It is known from terrestrial geology that flat magmatic intrusions are formed perpendicular to the direction of the tensile main stress, which leads to the formation of vertical dikes in the horizontal field of tensile stress and folds in the horizontal field of compression stress. Although local stress during the bending of the lithosphere can change the orientation of intrusions, in general, the LGA are evenly distributed throughout the Moon and do not show a clear preferred orientation or connection with the mare. This pattern indicates an isotropic horizontal expansion that can be expected as a result of global expansion. At the same time, for most of its history, the lunar lithosphere was in a state of compression as a result of internal cooling and tidal effects of the Earth [4]. During the assumed intrusive activity, the lithosphere of the early Moon should have been in a state of global horizontal stretching and, taking the total length of the LGA at 5,300 km, and the typical width of 5–10 km, the increase in the radius of the Moon can be estimated as 0.6–1.2 km.

ANALYTICAL MODEL:

To calculate elastic deformations of the Moon's lithosphere under the influence of external loads, a well-developed technique using gravitational (tidal, centrifugal, etc.) potential can be applied. The resulting force F in the volume of the body is determined using the gradient of the full potential:

$$F = \rho_0 \cdot \mathrm{grad}[V(r)],\ V(r) = V_g(r) + V_\omega(r) + V_t(r), \quad (1)$$

where ρ_0 is the average density, V_g is the gravitational, V_ω is the centrifugal and V_t is the tidal potentials. For a solid ball of radius R, in the case of spherical symmetry of all loads, the deformation vector $\mathbf{u}$ has only a radial component $\mathbf{u}(\mathbf{r})$ and the strain tensors, e_{ij}, and stresses, σ_{ij}, have radial and tangential components. The equilibrium conditions of a substance in the volume of an isotropic body under the action of a resultant force have the form

$$\mu\Delta\mathbf{u} + (\lambda + \mu)\cdot\mathrm{grad}(\mathrm{div}\ \mathbf{u}) = -\mathbf{F},\ \mu = E/2(1 + \nu);$$

$$\lambda = \nu E/(1 + \nu)\cdot(1 - \nu), \quad (2)$$

where μ, λ are the elastic Lame constants, ν is the Poisson's ratio, and E is the Young's modulus for the substance of the body. These limitations on the deformation field should be supplemented by boundary conditions of the load on the surface. If the outer surface is free from external load, as is usually the case for non-atmospheric planets and small bodies, then $\sigma_{rr}(R) = 0$ at $r = R$.

Suppose that the change in the initial temperature, T_0, by $\Delta T = T - T_0$ did not significantly affect the mechanical properties of the lunar rocks. Then the only consequence of heating will be the occurrence of additional deformations caused by a comprehensive thermal expansion with a coefficient α. These deformations are superimposed on elastic ones and should be taken into account as causing temperature stress. In this case, the relation of strain tensors e_{ij} and stresses σ_{ij} can be expressed as follows

$$\sigma_{ij} = 2\mu\varepsilon_{ij} + \lambda\varepsilon - (2\mu + 3\lambda)\alpha\cdot\Delta T,$$

and expression (1) is generalized as

$$\mathbf{F} = \rho_0\cdot\mathrm{grad}(V(\mathbf{r})) - (2\mu + 3\lambda)\alpha\cdot\mathrm{grad}(\Delta T) \quad (3)$$

Due to the linearity of the equilibrium equation (2), it is convenient to divide the solution for the radial displacement $\mathbf{u}(\mathbf{r})$ using (3) into two parts: gravitational, $\mathbf{u}_G$, — with gravity, $g(r) = dV_g/dr$, and temperature, $\mathbf{u}_T$, — with $\alpha\cdot\Delta T(r)$

$$E(1 - \nu)/(1 + \nu)\cdot(1 - 2\nu)\cdot d(1/r^2\cdot d(r^2 u_G)/dr)/dr = \rho_0\cdot g(r)\cdot r/R, \quad (4a)$$

$$d^2u_T/dr^2 + 2/r\cdot du_T/dr - 2u_T/r^2 = (1 + \nu)/(1 - \nu)\alpha d\cdot\Delta T/dr \quad (4b)$$

RESULTS AND DISCUSSION:

Figure below shows two examples of the temporal behavior of tangential stress with depth in the lithosphere at different values of the dimensionless thermal parameters, which we used earlier in assessing the behavior of temperature.

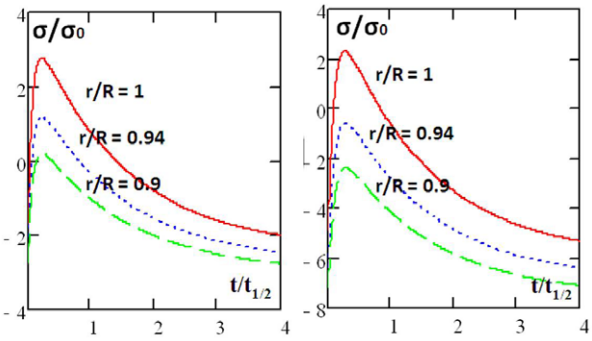

Fig. 1. It can be seen that the greater intensity of heat exchange with the cold environment (right) contributes to a faster transition from expansion to compression in the colder lithosphere.

The calculations of temperature stresses in the lithosphere of the early Moon have shown the fundamental applicability of the simple thermal model used. Based on the exact solutions possible in the spherically symmetric formulation of the thermal conductivity problem, the qualitatively correct temporal behavior of temperature and stress consistent with lunar data is obtained. For typical rock parameters: $\alpha \approx 10^{-5}$ deg^{-1}, $E \approx 60$ GPa, $\nu \approx 0.2$ and $T_0 - T_c \approx 100$ °C, the maximum total tensile stress in the lithosphere of the Moon could reach 120 MPa. This is a large amount, quite sufficient for the formation of cracks and fractures [5].

ACKNOWLEDGMENTS:
The research was carried out with the financial support of the Russian Science Foundation (project No. 21-17-00120).

REFERENCES:

[1] Zuber M.T. et al. Gravity field of the Moon from the Gravity Recovery and Interior Laboratory (GRAIL) mission // Science. 2013. V. 8. No. 339(6120). P. 668-671. DOI: 10.1126/science.1231507.
[2] Zuber M.T., Smith D.E., Lemoine F.G., Neumann G.A. The shape and internal structure of the Moon from the Clementine mission // Science. 1994. V. 266. P. 1839-1843.
[3] Andrews-Hanna J.C. et al. Ancient Igneous Intrusions and Early Expansion of the Moon Revealed by GRAIL Gravity Gradiometry // Science. 2012. V. 339. P. 675-678.
[4] Shearer C.K. et al. Thermal and Magmatic Evolution of the Moon // Reviews in Mineralogy and Geochemistry. 2006. V. 60. P. 365-518.
[5] Voropaev S.A., Dushenko N.V.et al. Relationship between the H5 chondrite composition, structure and mechanical properties from the example of NWA12370 and Pultusk // Solar System Research. 2021. V. 55. No. 5. P. 409-419.

GEOLOGICAL EXPLORATION OF THE MOON III: WATER ICE IN NEAR POLAR REGIONS OF THE MOON

A. Gusev[1a,b], Z.G. Meng[2], J.S. Ping[3]
[1a] *Geophysics&IT,* [1b] *MathMethods in Geology, Kazan Federal University, Kazan, Russia*
[2] *College of Geoexploration Science and Technology, Jilin University, Changchun, China*
[3] *National Astronomical Observatory of China CAS, Beijing, China; agusev33@gmail.com*

KEYWORDS:
core, mantle, crust, magnetic anomalies, regolith, water ice of the lunar near polar regions

INTRODUCTION:
The review discusses 1) the results of laboratory studies of the lunar regolith within the framework of the Chinese mission Chang'E-5, 2) the estimation of the water concentration in the bound state of lunar rocks, 3) the mystery of the long-term generation of a powerful thermal budget of the Moon. In the geological structure of the lunar surface, rocks of gabbro-anorthositic composition, marine basalts, and the places where the Non-KREEP-rock layer intermediate between the mantle and the crust come to the surface are of the greatest importance. The joint presence of a wide range of valuable metals in lunar rocks is an important quality that can contribute to an increase in the value of raw materials due to their complexity. The discovery of hematite in lunar rocks, the formation of which is associated with oxidation processes, makes it possible to reconsider the views on the geochemistry and features of the mineral formation under the conditions of the lunar airless surface and during its bombardment by meteorites [1, 3, 5, 9]. For years, scientists believed that the cold craters at the lunar poles contained water ice, which would be a fundamental scientific boon and an important potential resource for human missions. Hundreds of polar craters are in constant shadow due to the slight tilt of the Moon's axis of rotation to the plane of the ecliptic, 1.5° compared to Earth's 23.4°. The sun never rises over their edges, maintaining temperatures down to –250 °C [1].

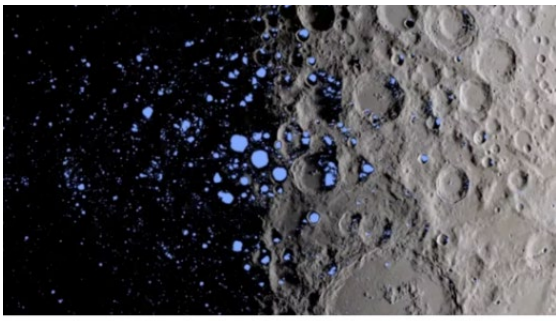

A map showing the permanently shadowed craters (blue) near the moon's shouth pole (Image credit: NASA Goddard)

Map showing permanently shaded craters (blue) at the Moon's south pole. In some of the Moon's polar craters, radar instruments on orbiting spacecraft detected reflections of water ice, possibly brought by comets. In 2018, scientists using an instrument aboard India's Chandrayaan-1 spacecraft reported measurements showing how polar ice molecules absorb infrared light, some of the most compelling evidence yet [2–4].

WATER ICE AND MAGNETIC ANOMALIES OF THE MOON:
The water ice was isolated by the eternal shadow of the crater walls and remained untouched by the sun's rays for millions or more years. However, the

discovery of water ice at the lunar poles has brought a new problem. While these polar craters are protected from direct sunlight, they are not protected from the effects of the solar wind, waves of charged particles that blast from the Sun at hundreds of kilometers per second. The ionized wind has a high erosive activity and was supposed to quickly destroy the lunar ice. But this did not happen, although the Moon does not have a permanent global magnetic field in the last billions of years! How did the polar ice of the moon survive? A new map of the Moon and the strange pockets of magnetic field anomalies located there gives the answer. These strong magnetic anomalies, first detected during the Apollo-15 and Apollo-16 missions in the 1970s, are thought to be the remnants of the Moon's ancient magnetic global shield that disappeared billions of years ago. Some anomalies are now known to be hundreds of kilometers across. Areas of magnetic anomalies on the Moon intersect with several large lunar polar craters that are in permanent shadow and may contain deposits of ancient ice. These magnetic anomalies could serve as tiny magnetic shields that keep lunar water ice from constant bombardment by the solar wind. Some anomalies are now known to be hundreds of kilometers across. While their origin is debated, one theory is that they were created over 4 billion years ago when the Moon had a magnetic field and iron-rich asteroids crashed into its surface. The resulting molten material could be permanently magnetized. It is believed that there are thousands of anomalies on the surface of the Moon. Upcoming lunar missions may shed light on dark icy deposits at the south pole of the Moon [Artemis missions and others]. Studying the ice deposits in this region can reveal how they formed and why they have been around for so long [2–10].

CHANG'E-5 MISSION ON THE MOON:

In 2021, China's Chang'E-5 mission retrieved and brought back to Earth soil samples from the visible side of the Moon weighing 1731 g, which became the first new lunar samples on Earth in more than 45 years. The Chang'E-5 mission to collect lunar soil was crowned with a tremendous scientific and technical success, and laboratory studies of the brought lunar samples shed new light on the geological evolution of the Moon. Research conducted by the research team of the Institute of Geology and Geophysics of the Chinese Academy of Sciences (IGG CAS, Beijing, China) was presented in three articles in the most prestigious scientific journal Nature in 2021 [6–8]. Chinese geologists have studied lunar soil and dated the youngest lunar sample ever brought back to be about 2 billion years old, pushing back the active period of lunar volcanism by 900 million years later than previously claimed in the theory of lunar evolution. The youngest previously dated lunar rock from the missions of the American Apollo program (1969–1972) and the Soviet lunar program: AMS "Luna-16", "Luna-20", "Luna-24" (1970–1976) — was about 2.8–2.9 billion years old [1]. However, for the completeness of the sample, it was necessary to study the age of the lunar soil in new geologically interesting regions (KREEP rocks), and one of the tasks of the Chinese Chang'e-5 mission was to study the youngest magmatic activity in the northern hemisphere of the Moon [7].

The lunar surface, riddled with craters, was formed under the influence of bombardment by numerous asteroids and comets over billions of years. For example, the Smith Sea is a special area that is one of the oldest marine basins with relatively young marine basalts and a high density of fractured crater floors [3]. Based on the numerical simulation of the radiative transfer theory, we note important results: 1) the temperature of the substrate near the Smith Sea is quite high and is provided with a special temperature structure; 2) there is an undiscovered deposit in the upper layer of regolith with a strong thermal absorption capacity; 3) the results have a strong correlation with the features of the interior, obtained from the data of the lunar radar probe and ridges on the surface [3, 7, 8].

Using a microscope, Chinese colleagues manually isolated rock fragments from 3-gram lunar capsules. Most of these dateable minerals are only one-twentieth the thickness of a hair. In total, the Chinese team analyzed 47 different rock fragments recovered from material samples and dated the youngest rock on the moon to 2.03 billion years old. A new era in the knowl-

edge of the moon prolongs the life of lunar volcanism by 900 million years longer than previously known!!! [6].

Another possible reason for the Moon's volcanic activity at such a late age is that the mantle source may have contained water to lower its melting point. The water content of the Moon's mantle is a key issue for lunar exploration, as it provides critical constraints on the formation of the Moon. Because water can significantly lower the melting point of rocks, understanding its content is important for understanding the history of lunar volcanism [1–3, 8].

WATER SATURATION OF THE LUNAR MANTLE:

The large discrepancy in estimates of the water saturation of the lunar mantle can be explained by the fact that the Apollo samples and lunar meteorites in general are quite old. Most previous lunar samples with measured water content date back to 3 billion years or earlier. Such old rocks could have undergone serious changes over a long time under the influence of asteroids and particles from the Sun. The samples recovered by Chang'e-5 were from a single basalt lava flow. Thus, in such a simple and clear geological setting, the samples provide an answer to the question of whether the mantle reservoir was wet or dry 2 billion years ago. [8]

The research team analyzed the content of water and hydrogen isotopes in melt pockets preserved in some minerals, as well as in the mineral apatite, which may contain water from the Chang'E-5 basalts. The Chinese colleagues used a nanoscale ion probe called nanoSIMS, a secondary ion mass spectrometer with ion beams up to 50 nm in diameter. The relative abundances of two hydrogen isotopes (deuterium [D] and hydrogen [H]) serve as a "fingerprint" for tracking reservoirs of water and the magmatic processes involved in them. The results indicated that the mantle source of the Chang'E-5 basalts was drier than the estimated water content based on Apollo samples and lunar meteorites [6]. This excludes the possibility that the high content of water in the mantle source was the reason for the long-term eruption of lunar volcanoes and filling the heat budget of the Moon. The mystery of late lunar volcanic activity has yet to be unraveled [1–4].

REFERENCES:

[1] Gusev A., Hanada H., Petrova N., Kosov A., Kuskov O., Kronrod V., Kronrod E. Rotation, physical librations and interior structure of the active and multi-layer Moon: Monograph. Kazan: Kazan University Publishing Co., 2015. 328 p. (Russian+English).
[2] Li J., Meng Z., Gusev A. Recent Advances in Lunar Exploration Using Radar and Microwave Techniques // Advances in Astronomy. 2019. V. 2. Art. No. 479425816.
[3] Liu C., Mei L., Meng Zh., Wang Y., Zhu K., Cheng W., Cai Zh., Ping J.-S., Gusev A. Special Thermophysical Features of Floor Materials in Mare Smythii Indicated by CE-2 CELMS Data // IEEE J. Selected Topics in Applied Earth Observations and Remote Sensing. 2021. V. 14. P. 8135-8143.
[4] Dhingra D. The New Moon: Major Advances in Lunar Science Enabled by Compositional Remote Sensing from Recent Missions // Geosciences. 2018, V. 8(12). Art. No. 498. https://doi.org/10.3390/geosciences8120498.
[5] Gusev A.V., Bakhtin A.I., Kosov A.S., Hanada H., Meng Zh., Ping J.-S., Sungatullin R. Kh., Khasanov R.R. Scientific, geological and commercial exploration of the Moon // Trans. LV Scientific Readings in memory of K.E. Tsiolkovsky, Section "Problems of rocket and space technology". Kaluga, Sept. 15-17, 2020. Kazan: KFU Publishing House, 2021. P. 161-176 (In Russian).
[6] Qiu-Li Li et al. Two-billion-year-old volcanism on the Moon from Chang'e-5 basalts // Nature. 2021. V. 600. P. 54-58.
[7] Heng-Ci Tian et al. Non-KREEP origin for Chang'e-5 basalts in the Procellarum KREEP Terrane // Nature. 2021. V. 600. P. 59-63.
[8] Sen Hu et al. A dry lunar mantle reservoir for young mare basalts of Chang'e-5 // Nature. 2021. V. 600. P. 49-53.
[9] Gusev A., Meng Zh., Ping J-S., Khanada H., Khasanov R. Geological Exploration of the Moon II: Regolith, Volatile and Trace Elements // Proc. of the 56th Scientific Readings in Memory of K.E. Tsiolkovsky. RAS – RACTs, Section "Problems of rocket and space technology". Kaluga, Sept. 21-23, 2021. Kazan: KFU Publishing House, 2022. 19 p. (In press, in Russian)
[10] Meng Zh., Qiu H., Shi Ya., Ping J.-S., Cai Zh., Gusev A. Identifying a composition-related TB anomaly in Copernicus crater using CE-2 MRM data // Intern. Geoscience and Remote Sensing Symposium (IGARSS 2022). July 17-22, 2022, Kuala Lumpur, Malaysia. 2022. Art. No. 2004. 4 p. (In press).

SALIENT RESULTS FROM CHANDRAYAAN-2 MISSION

S. Megala[1], Tirtha Pratim Das[1]
[1] *Science Programme Office, Indian Space Research Organisation (ISRO) Headquarters, Bangalore, India; megala@isro.gov.in*

ABSTRACT
Chandrayaan-2, the second Indian mission to the Moon was launched on 22nd July 2019. Though the soft-landing attempt could not be accomplished as planned, the mission life of Orbiter is extended to 7 years. The Orbiter completed three years around the Moon at 100km and all the payloads are operational. The suite of instruments on Chandrayaan-2 are providing a wealth of data to address several important questions in lunar science.

The Imaging IR spectrometer on Chandrayaan-2 was specifically designed to resolve the ambiguity in the signature of the 3-micron hydration feature used to detect wide spread presence of water-ice, first reported by our Chandrayaan-1 mission. Using the extended detection wavelength of upto 5 microns, IIRS observations showed the unambiguous detection of Lunar hydration absorption feature around 3 μm at all latitudes and surface types. Characterisation of noble gas dynamics in the sunlit lunar exosphere is done by the mass spectrometer by global mapping of Argon-40 that originate from radioactive Potassium-40 from lunar interior. Dual frequency SAR is providing full polarimetric measurements to image permanently shadowed regions and to identify water-ice deposits in the polar regions. The X-ray spectrometer on the Orbiter has mapped the abundance of sodium on the Moon for the very first time. In addition, minor elements such as Chromium and Manganese were detected due to high sensitivity of the instrument. When the Moon enters the geotail once a month, enhancement in particle environment is observed, further studies will be helpful for future human missions to the Moon. The solar X-ray monitor has detected large number of microflares occurring outside the Sun's active region which may provide clues to the coronal heating problem.

The scientific data are made available to public. Significant results from Chandrayaan-2 payloads and their value addition to lunar scientific knowledge will be discussed in this paper.

THE CONCEPT OF MOON-BASED UV SURVEY TO STUDY TRANSIENTS AND VARIABLES

A. Shugarov[1], S. Dong[2], H. Wang[3], M. Sachkov[1], N. Jiang[4], V. Shmagin[1], A. Buslaeva[1]

[1] *Institute of Astronomy RAS, Moscow, Russia; shugarov@inasan.ru*
[2] *Kavli Institute for Astronomy and Astrophysics, Peking University, Beijing, China; dongsubo@pku.edu.cn*
[3] *National Astronomical Observatories, Chinese Academy of Sciences, Beijing, China; wanghj@nao.cas.cn*
[4] *School of Astronomy and Space Science, University of Science and Technology of China, China*

KEYWORDS:
ultraviolet telescope, wide-field telescope, moon-based telescope, international lunar research station, supernovae, tidal disruption events, stellar physics, transient events, variable stars, time-domain survey

INTRODUCTION:

One of the most ambitious and promising tasks of modern astronomy is to study transient events and variables with wide-field time-domain surveys. In particular, high-energy transients have relatively high temperatures (>10000 K) at the earliest stage of the explosion/flare, and most of them have strong UV radiation.

Sky background in UV is a few magnitudes darker than in optical, making it possible to use a set of UV extra-wide small-aperture UV lenses in Space to monitor the whole sky in UV with high cadence and without interruptions to detect transients and variables. Such a UV survey will be significantly more efficient than existing similar systems that operate on the ground in the optical wavelength range.

We are motivated to study the prospect of deploying a network of wide-field, small-aperture UV telescopes on the Moon by taking advantage of its unique environment. The Moon-based multi-lens array with ~10,000 deg^2 field of view will make it possible to obtain the world's first all-sky "movie" of transients/variables in UV with high time resolution on the order of ~10 min.

The expected signature discoveries are:

- Complete samples of nearby supernovae of all types (SNe Ia and core-collapse supernovae) in UV. The high-cadence observations could detect shock breakout emissions for core-collapse supernovae (i.e., UV radiations within a few hours of the explosion), which can provide important observational clues on the unknown explosion mechanism for supernovae and enable direct measurements of the sizes of progenitors and the circumstellar environment.
- A complete sample of tidal disruption events (TDEs) in the local Universe to make a unique probe of dormant supermassive black holes (SMBHs) in nearby galaxies. The high-cadence observations could capture the UV emission at early rising stage, which is poorly explored yet crucial for understanding TDEs.
- Obtaining valuable early-time (~hr) UV information of the merger of neutron star — neutron star and neutron star – black hole, constraining the physical models.
- Potentially probing an uncharted parameter space of short and hot transients to discover hitherto unknown high-energy explosions in the Universe.

THE MOON-BASED TELESCOPE:

The first Chinese Moon-based telescope LUT (Chang'E 3 mission) demonstrated its efficiency in the near-UV wavelength range. In 2021 China and Russia signed an agreement to build a future International Lunar Research Station, which provides new exciting opportunities for Moon-based astronomy.

Recent progress in UV technologies makes it possible to design a small telescope to operate in 200–300 nm range with efficiency (system throughput) close to the optical wavelength. A combination of optical lenses made of different UV-transparent materials (fused silica, CaF_2, BaF_2, LiF_2), modern detectors with enhanced UV sensitivity and UV filters with good red leak suppression allow us to significantly improve the efficiency of a small aperture wide field UV telescope.

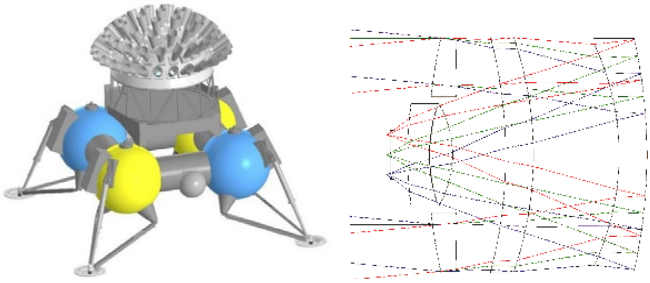

Fig. 1. Conceptual view of UV multi-lens array on Moon-lander (left), draft optical scheme of a single 160 mm aperture wide field UV telescope (right)

As a baseline for the Moon-based UV telescope, we have developed an optical scheme of a wide field of view reflector with a full aperture lens corrector (Fig. 1, right). The lens materials are fused silica, CaF_2 and BaF_2. The telescope aperture is 160 mm (central obstruction 50 %), F-Number is 1:1, wavelength range is 180–280 nm, image quality (D80) is 25-50 μm, field of view on the detector is 67 deg.^{2} (rectangular, 22.5×22.5 mm) and pixel scale is 14 arcsec on 11 μm pixel.

The main benefit of the proposed reflector design in comparison to full refractive designs is the length of the system. The main disadvantage — high central obstruction. Without serious optimization the achievable angular resolution of the system in the central part is 25 μm. There is no space for a filter wheel, if needed the filter should be deposited on the detector. Accurate focusing of the telescope can be carried out by controlled heating of some structural elements.

We propose to use the well proven CMOS GSENSE400BSI sensor, which has a radiation tolerant design and electronic shutter. The sensor format is 2048×2048 pixels of 11 μm size, temporal noise is 1.47 e^- RMS and quantum efficiency is ~40 % in 180–280 nm range (no AR coating).

To cover the whole visible sky from the ILRS we need about 100–200 of such telescopes. We can use a dedicated Moon-lander to accommodate up to 100 telescopes (Fig. 1, left) or we can distribute telescopes across different landers.

Potentially a single-lens prototype of the proposed multi-lens array can be installed on upcoming LUNA or Chang'E missions.

ACKNOWLEDGEMENTS:
The reported study was funded by RFBR and NSFC, project number 21-52-53022.

REFERENCES:

[1] Shugarov A.S., Wang H., Dong S., Sachkov M.E., Shmagin V.E., Buslaeva A.I., Jiang X., Wang J., Kanev E.N. The concept of Lunar-based astrophysical telescope for international lunar research station // Vestnik NPO Lavochkina. 2022. V. 1. No. 55. P. 3-9. (In Russian.)

[2] Shugarov A., Sachkov M., Wang H., Dong S., Jiang X., Shmagin V., Sichevskij S., Buslaeva A., Savanov I., Jianfeng W., Xiaoming Z., Chen P., Wang J. The concept of Lunar-based UV-Optical-IR Telescope for ILRS // 12th Moscow Solar System Symp. (12M-S3): Abstr. Moscow, Russia. 2021. Art. No. 12MS3-MN-19. P. 392-394.

[3] Sachkov M.E., Shugarov A.S. et al. The concept of the Moon-based astrophysical UV telescope (The Luna-UV project) // INASAN Science Reports. 2020. V. 5(6). P. 368-373.

SCIENCE OF THE LUNAR-BASED UV-OPTICAL-IR TELESCOPE FOR ILRS

H. Wang[1,2], M. Sachkov[3], S. Dong[4], X. Bai[1,2], A. Shugarov[3], X. Jiang[1,2], H. Tian[5], N. Jiang[6], Y. Deng[1,2], G. Zhao[1,2], T. Li[1], V. Shmagin[3], S. Sichevskij[3], A. Buslaeva[3], I. Savanov[3], X. Zhang[1,2], J. Wang[1,2]

[1] *National Astronomical Observatories, Chinese Academy of Sciences, Beijing, China; wanghj@nao.cas.cn;*

[2] *University of Chinese Academy of Sciences, Beijing, China; xybai@nao.cas.cn*

[3] *Institute of Astronomy RAS, Moscow, Russia; msachkov@inasan.ru*

[4] *Kavli Institute for Astronomy and Astrophysics, Peking University, Beijing, China; dongsubo@pku.edu.cn*

[5] *School of Earth and Space Sciences, Peking University, Beijing, China; huitian@pku.edu.cn*

[6] *School of Astronomy and Space Science, University of Science and Technology of China, China; jnac@ustc.edu.cn*

KEYWORDS:
UV-OPTICAL-IR telescope, Lunar-based telescope, ILRS, evolution of galaxies, transients, terrestrial exoplanet, space weather

The Lunar-based UV-Optical-IR telescope for the International Lunar Research Station (ILRS) is a science-driven payload driven by our collaborative research groups from Russia and China. Due to the advantages of the lunar-based environment, we have the opportunity to perform multi-wavelength observations with an ultra-wide wavelength coverage, especially from extreme ultraviolet (EUV) to infrared (IR).

The science of this telescope focuses on:

1) Finishing a complete UV catalog and studying the evolution of galaxies;
2) Exploring high-energy transients and variable events (supernovae, tidal disruption events, etc.) in the local universe;
3) Discovering new terrestrial exoplanets in the habitable zones;
4) Investigating the habitability of exoplanets based on space weather phenomena and the influence of small bodies in planetary systems.
   - Detecting stellar coronal mass ejections to enrich our understanding of stellar coronal activities and their impacts on the exoplanet habitability (i.e., the space weather phenomenon effects on exoplanets);
   - Discovering NEOs in the direction of the sun to support planetary defense;
5) Studying small solar system bodies (comets, asteroids, etc.), including regions close to the Sun.

These scientific drivers and some new considerations about payload requirements over the past year will be introduced in this talk, as its concept has been described in our previous talk and paper [1, 2].

REFERENCES:

[1] Shugarov A., Sachkov M., Wang H., Dong S., Jiang X., Shmagin V., Sichevskij S., Buslaeva A., Savanov I., Wang J., Zhang X., Chen P., Wang J. The concept of Lunar-based UV-Optical-IR Telescope for ILRS // 12th Moscow Solar System Symposium (12M-S3). 11-15 Oct. 2021, IKI, Moscow, Russia.

[2] Shugarov A.S., Wang H.J., Dong S.B., Sachkov M.E., Shmagin V.E., Buslaeva A.I., Jiang X.J., Wang J.Q., Kanev E.N. The concept of Lunar-based astrophysical telescope for International lunar Research Station (ILRS) // Vestnik NPO imeni S.A. Lavachkina. 2022. V. 55. No. 1. P. 3-9. (In Russia.)

INVESTIGATION OF THE LUNAR DUSTY PLASMA AND ELECTRIC FIELD DYNAMICS WITH LUNAR DUST MONITORING INSTRUMENT

I.A. Kuznetsov[1], A.V. Zakharov[1], G.G. Dolnikov[1], A.N. Lyash[1], S.A. Bednyakov[1], A.E. Dubov[1], A.A. Kartasheva[1], I.A. Shashkova[1]
[1] *Space Research Institute, Moscow, Russia; kia@iki.rssi.ru*

KEYWORDS:
Dust, lunar dust, dusty plasma, lunar lander, Luna-25, Moon

INTRODUCTION:
One of the complicating factors of the future robotic and human lunar landing missions is the influence of the dust. The upper insulating regolith layer is electrically charged by the solar ultraviolet radiation and the flow of solar wind particles. Therefore, electric charge and thus surface potential depend on the lunar local time, latitude and the electrical properties of the regolith.

These years we can see arising interest of the Moon investigation. Number of governments, space agencies and collaborations declared their intentions to build manned orbit stations or surface bases in next decades.

DUST MONITORING INSTRUMENT:
Dust analyzer instrument PmL intends for investigation the dynamics of dusty plasma near lunar surface. PmL consists of three parts: Impact Sensor and two Electric Field Sensors.

IMPACT SENSOR:
Impact sensor purpose is to investigate the dynamics of dust particles near the lunar surface (speed, charge, mass, vectors of a fluxes).

Possible detectable events may occur with:

a) high speed micrometeorites;

b) secondary particles after micrometeorites soil bombardment;

c) levitating dust particles due to electrostatic fields.

PmL instrument will measure dust particle mechanical momentum. Also Impact Sensor will measure the electrical charges of dust particles. In case the charge and impulse of a dust particle are measured with properly time-stamps of events, we can calculate the velocity and mass of the particles.

Electric Field Sensor:

Electric field Sensor will measure the value and dynamics of the electric fields near the lunar surface. The measurement technique is based on classic Langmuir probe plasma investigation method. Two Electric Field Sensors allow to measure the concentration and temperature of charged particles (electrons, ions, dust particles). Using Langmuir probes near the surface through the lunar day and night, we can obtain the energy spectra photoelectrons in various periods of time.

VERSION 2.0:
For the following missions a lot of the PmL instrument improvements proposed. One of the most important is to develop a mechanical Boom to deliver dust and plasma sensors as far as 1 m from the spacecraft body as well as to locate the dust sensors near the lunar surface and plasma sensors at the different levels above the surface.

TESTING SLM TECHNOLOGY WITH SIMULANTS OF LUNAR REGOLITH: APPLICATIONS TO LUNAR PRINTER EXPERIMENT

A.A. Kim[1], A.M. Lysenko[1], T.M. Tomilina[1]
[1] *Mechanical Engineering Research Institute RAS, Moscow, Russia*

KEYWORDS:
Moon exploration, lunar regolith, 3D printing

Report presents the results of studying the properties of lunar regolith in relation to its possible use *in situ* to create objects of complex geometry using selective laser melting (SLM) technology as the most promising additive technology for this purpose.

Today, there is already a large number of laboratory studies on the melting/sintering of lunar regolith for 3D printing in various ways. From 1973 to 2022, about fifty papers were published, and twelve of them on the application of SLM [1]. The main subject under study is the most important properties of the lunar regolith simulants which should be used for such laboratory studies.

The samples of lunar regolith have been investigated quite well, and it has been established that there are no direct analogues for them on Earth [2]. Therefore, different simulants were created for the laboratory studies, which simulate well selected parameters that are important for a specific laboratory study. This report discusses the most significant characteristics of the lunar regolith simulant in connection with the use of SLM technology. It is shown that the maximum compliance in the thermal parameters is the most important one, together with size distribution of particles.

Technological issues of SLM are also discussed. The search for a range of parameters of the melting mode for the particular simulant (such as laser power, scanning speed, scanning step, layer thickness, etc.) is shown to be necessary to obtain outprinted solid samples with acceptable mechanical properties and with the initially specified geometry. The report presents the first results of performed tests with the lunar regolith simulant [3], which allowed to determine the optimal laser power and scanning speed for 3D printing process on the used industrial printer.

ACKNOWLEDGEMENTS:
The work was supported by RSF (grant No. 22-22-00840).

REFERENCES:
[1] Farries K.W., Visintin P., Smith S.T. et al. Sintered or melted regolith for lunar construction: state-of-the-art review and future research directions // Construction and Building Materials. 2021. V. 296. Art. No. 123627. https://doi.org/10.1016/j.conbuildmat.2021.123627.
[2] Taylor L.A., Pieters C.M., Britt D. Evaluations of Lunar Regolith Simulants // Planetary and Space Science. 2016. V. 126. P. 1-7. https://doi.org/10.1016/j.pss.2016.04.005.
[3] Scientific basis for the development of the lunar 3D printer: Report RSF No. 22-22-00840. 2022.

SPACE GAMMA-RAY SPECTROSCOPY EXPERIMENT WITH TAGS OF GALACTIC COSMIC RAYS

M.I. Mokrousov[1], A.A. Anikin[1], D.V. Golovin[1], M.L. Litvak[1], I.G. Mitrofanov[1], S.Y. Nikiforov[1], A.B. Sanin[1]
[1] *Space Research Institute, Moscow, Russia; mokromax@np.cosmos.ru*

KEYWORDS:
neutrons, gamma rays, spectroscopy, spectrometer, tagged charged particles

INTRODUCTION:

One of the methods that are used to study the abundance of elements in the areas of landing on the Moon or other celestial body with a thin or no atmosphere is gamma ray spectrometry. As an evolution of this method, a promising space gamma spectrometer instrument with tagged charged particles is proposed. The telescope of GCR charged particles makes it possible to select GCR particles in a selected solid angle, i.e., particles penetrating into a selected volume of soil. Using the time correlation of the signals from the GCR charged particle counter telescope and the gamma ray spectrometer, it is possible to select gamma coming to the spectrometer only from selected volume. The proposed method makes it possible to almost completely eliminate the background of gamma radiation from the spacecraft, and significantly increase the spatial resolution when studying the elemental composition of soil along the path of the mobile spacecraft. It should be noted that the proposed method works well for measuring gamma from reactions of inelastic scattering of secondary fast neutrons, since the time before photon registration is several tens of nanoseconds. A description of the measurement method and the possibility of its application will be presented.

REFERENCES:

[1] Mitrofanov I.G., Sanin A.B., Nikiforov S.Y., Golovin D.V., Djachkova M.V., Anikin A.A., Karpushkina N.E., Lisov D.I., Litvak M.L., Mokrousov M.I., Dubasov P.A., Zontikov A.O., Starr R.D. Cosmic gamma-ray spectrometer with tagged charged particles of Galactic Cosmic Rays // Nuclear Instruments and Methods in Physics Research. Section A. 2020. V. 953.

[2] Mitrofanov I.G., Litvak M.L., Sanin A.B., Anikin A.A., Mokrousov M.I., Golovin D.V., Nikiforov S.Y., Timoshenko G.N., Shvetsov V.N. Laboratory demonstration of space experiment for spectrometry of planetary gamma-rays with tags of Galactic Cosmic Rays producing them // Nuclear Instruments and Methods in Physics Research. Section A. 2021. V. 1003.

[3] Mitrofanov I.G., Litvak M.L., Sanin A.B., Anikin A.A., Mokrousov M.I., Golovin D.V., Nikiforov S.Y., Timoshenko G.N., Shvetsov V.N. Laboratory demonstration of space gamma-ray spectroscopy experiment with tags of Galactic cosmic rays for testing different types of Martian regolith // Nuclear Instruments and Methods in Physics Research. Section A. 2022. V. 1028.

[4] Mitrofanov I.G., Litvak M.L., Golovin D.V., Nikiforov C.Y., Sanin A.B., Anikin A.A., Mokrousov M.I., Timoshenko G.N., Krylov V.A., Pavliki E.E., Shvetsov V.N., Mytsin G.V., Molokanov A.G. Gamma Spectrometry of Composite Models of Planetary Matter on The JINR Accelerator Proton Beam with Tagged Protons // Physics of Particles and Nuclei Letters. 2020. V. 17. No. 3. P. 348-357.

[5] Mitrofanov I.G., Golovin D.V., Sanin A.B., Nikiforov S.Y., Anikin A.A., Dyachkova M.V., Karpushkina N.E., Lisov D.I., Litvak M.L., Mokrousov M.I., Timoshenko G.N., Krylov A.R., Shvetsov V.N., Mitsin G.V., Molokanov A.G. First Results for Laboratory Tests of a Concept of Space Gamma-Spectrometer with Tagged Protons Method at the JINR Particle Accelerator // Physics of Particles and Nuclei Letters. 2019. V. 16. No. 3. P. 251-255.

[6] Sanin A.B., Mitrofanov I.G., Bakhtin B.N., Litvak M.L., Anikin A.A., Golovin D.V., Nikiforov S.Y. On the Study of the Spatial Variability of the Composition of the Lunar Material in Experiments on Gamma Spectroscopy Onboard a Mobile Spacecraft Using the Tagged-Cosmic-Rays Method // Solar System Research. 2020. V. 54. No. 6. P. 477-487.

[7] Anikin A.A., Djachkova M.V., Litvak M.L., Mitrofanov I.G., Mokrousov M.I., Nikiforov S.Y., Sanin A.B. A Promising Experiment with a Gamma Ray Spectrometer Onboard a Mobile Spacecraft to Study the Elemental Composition of the Moon, Mars, and Other Celestial Bodies Without an Atmosphere or with a Thin Atmosphere // Cosmic Research. 2021. V. 59. No. 1. P. 30-25.
[8] Mitrofanov I.G., Sanin A.B., Litvak M.L., Golovin D.V., Nikiforov S.Y. The concept of gamma-ray remote sensing of regolith composition onboard a Mars Rover // Acta Astronautica. 2022. V. 199. P. 134-141.

THE GROUND TESTS OF LUNAR MANIPULATOR COMPLEX FOR LUNA-25

V.A. Yakovlev[1], I.V. Dokuchaev[1], R.S. Zverev[1], T.O. Kozlova[1], M.L. Litvak[1]
[1] *Space Research Institute, , Moscow, Russia; yakovlev@rssi.ru*

KEYWORDS:
Luna-25; Moon; Robotic arm, soil sample acquisition

INTRODUCTION:
Luna-25 is the first Russian lunar mission with lunar manipulator complex (LMC), developed at the Space Research Institute, Moscow, Russia. The manipulator/robotic arm was designed to take samples of lunar regolith and deliver it for the determination of the elemental composition to the laser mass spectrometer LASMA-LR accommodated onboard Luna-25 [1–3], see also Fig. 1.

The LMC has four drives which allow to take soil in a working area on the surface around lander from a given depth (down to 25 cm). The scoop at the end of the manipulator's arm digs a trench and sample acquisition tube collects a regolith sample.

Fig. 1. The LMC installed onboard on Luna-25 mockup.

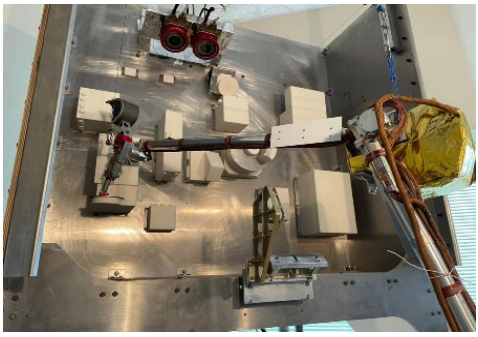

Fig. 2. The delivery of soil sample to the inlet window of laser spectrometer LASMA-LR during ground tests.

In our overview we present the design of the LMC and result of its ground tests. LMC has passed a comprehensive program of functional tests in room and lunar like conditions. As a part of this program LMC was tested at cryo-vacuum chamber imitating lunar like conditions. It was verified how the robotic arm could excavate the analog of lunar regolith mixed with different concentrations of water and frozen to the cryogenic temperatures (–100° C). It was shown that LMC is capable of excavating trenches and collecting samples in the ice rich analog of the lunar regolith homogeneously mixed with 1.5 wt% of water ice.

Another series of complex tests was carried out with the participation of the entire suite of all science instruments, including LMC. During the tests, the operation sequence (for one lunar day) of all scientific instruments was checked. It covers joint activities of LMC with IR spectrometer and stereo cameras LIS-TV-RPM installed on LMC and stereo cameras STS-L installed in the upper part of the lander. Stereo cameras observe the LMC working area in front of the lander and can navigate LMC to the desired area of soil sampling. Stereo cameras also can control and navigate LMC during the delivery of sample to the LASMA-LR inlet sample window (Fig. 2). The joint work of LMC, STS-L and LIS-TV-RPM allows to point an infrared spectrometer to study soil tails excavated during sample acquisition event. This work supports the mineralogical analysis of the lunar soil and search for subsurface water ice.

REFERENCES:
[1] Mitrofanov I.G., Zelenyi L.M., Tret'yakov V.I., Kalashnikov D.V. Luna-25: the first polar mission to the Moon // Sol. Syst. Res. 2021. V. 55. P. 485-495.

[2] Litvak M.L. et al. Ground-based testing of the lunar manipulator complex of the Luna-25 project // Sol. Syst. Res. 2021. V. 55. P. 605-619.
[3] Chumikov A.E., Cheptsov V.S., Managadze N.G. Accuracy of analysis of the elemental and isotopic composition of regolith by laser time-of-flight mass spectrometry in the future Luna-Glob and Luna-Resurs-1 missions // Sol. Syst. Res. 2020. V. 54. P. 288-294.

INDIAN LUNAR EXPLORATION PROGRAM – AN OVERVIEW

S. Megala[1], Dr. Tirtha Pratim Das[1]
[1] *Science Programme Office, Indian Space Research Organisation (ISRO) Headquarters, Bangalore, India; megala@isro.gov.in*

ABSTRACT
Indian Lunar exploration program started in early 2000's and the efforts culminated in the launch of **Chandrayaan-1** in 2008. The mission had an orbiter to map the surface topography of the moon, the mineral and elemental distribution, study volatiles and search for surface and sub-surface water-ice signatures. Using remote sensing, the orbiter discovered the wide spread presence of hydroxyl and water molecules on the lunar surface, from a 100km orbit. The spacecraft also released the Moon Impact Probe, which landed on the lunar South Pole and detected water vapour in the sunlit lunar exosphere. International payloads in Chandrayaan-1 brought in new experiences through joint instrument development, calibration, data interpretation, adopting global standards in science data formats etc.

This mission was followed in 2019 by **Chandrayaan-2**, which consisted of Orbiter, Lander and Rover. Though the landing attempt was not successful, the Orbiter is expected to have a long life of ~7 years. The unambiguous detection of water-ice signature from the IR spectrometer, is an indication of its capability to advance lunar science.

To demonstrate landing and roving on the lunar surface, **Chandrayaan-3** mission is getting ready for launch. The science instruments will carry out in-situ studies to derive the elemental composition at the vicinity of landing site. ISRO and Japan Aerospace Exploration Agency are conducting a feasibility study for a joint lunar polar exploration mission (tentatively, **LUPEX**) to characterize the volatiles and its composition in the lunar polar region. Both ISRO and JAXA have payloads on Rover to perform in-situ sample analysis.

The science outcome from Indian lunar missions provided new perspectives about the Moon. An overview of these missions and their science outcome will be presented in this paper.

DISCUSSION OF THE CONCEPT OF MOBILE ROBOTIC COMPLEXES FOR THE INTERNATIONAL LUNAR RESEARCH STATION

M.I. Malenkov[1], V.A. Volov[1], A.T. Basilevsky[2], M.A. Ivanov[2] A.N. Bogachev[1], N.K. Guseva[1], E.A. Lazarev[1], G. Haibo[3], D. Zongquan[3]

[1] *Scientific and Technical Center "ROCAD", Saint Petersburg, Russia, m.i.malenkov@gmail.com;*

[2] *Vernadsky Institute of Geochemistry and Analytical Chemistry RAS, Moscow, Russia, atbas@geokhi.ru;*

[3] *HIT, Harbin, China, jiawc911@sina.com*

KEYWORDS:
international lunar research station (ILRS), intelligent mobile platform (IMP), international space station (ISS)

INTRODUCTION:

In March 2021, a memorandum was signed between Russia and China on the establishment of the International Lunar Research Station (ILRS). On June 16, at the international conference GLEX-21 in St. Petersburg, the space agencies of the two countries presented a "road map", revealing the stages of construction of the ILRS:

- 2021–2025 — Moon exploration, design and selection of a construction site, testing of a highly accurate landing on the Moon;
- 2025–2035 — construction of ILRS.

Among the six key areas of scientific and technical research in the roadmap is "Lunar Intelligent Robotics". The report discusses possible concepts for the creation and operation of ILRS robotic systems based on universal intelligent mobile platforms (IMPs). They are necessary to carry out road, transport and installation work at the stage of creating the ILRS near the South Pole of the Moon, for example Fig. 1, on the top of Malapert Mons (84.9° S, 12.9° E, *h* = 5 km), which is known because of permanent visibility of Earth from its top [1]. This may be convenient for organization of scientific research on the far side of the Moon during the operation of the ILRS.

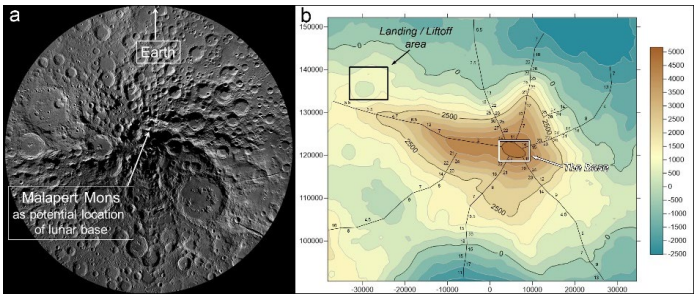

Fig. 1. a) Location of Mons Malapert at the 60-90° S LROC WAC map of the Moon; b) Topographic map of Mons Malapert based on the LOLA-based DTM LDEM80S20M_a1 with calculated values of slope steepness shown as well as the suggested positions of the base and landing/liftoff area

ABOUT THE CONCEPT OF MOBILE ROBOTS FOR ILRS:

1. DOMESTIC HISTORY OF THE PROBLEM.

In general terms, the concept and design appearance of the lunar base, on behalf of S.P. Korolev, were developed at the State Union Design Bureau of Special Machine Building (GSKB Spetsmash) under the direction of V.P. Barmin back in the 60s–70s of the last century. In particular, the concept of "lunar trains" proposed at that time, including "a tractor, a residential trailer, a power plant and a drilling station" [2], is relevant. In modern terminology, these

are mobile lunar robotic complexes (LRC) of variable structure. However, in our opinion, all the structural links of such a complex can be implemented on the basis of a universal intelligent mobile platform (IMP), capable of some independent actions and adapted to the organization of movement as part of a train as tractors. This approach makes it possible to obtain the highest traction and dynamic parameters of movement on unprepared terrain with complex geomorphology. After careful testing of prototypes, the manufacture of such IMPs can be put on the assembly line. This is an important economic factor, since the creation and operation of IRLS will require the organization of a certain fleet of mobile robotics.

2. JUSTIFICATION OF THE KEY PARAMETERS OF THE INTELLIGENT MOBILE PLATFORMS.

For work as part of a train, the authors consider the wheel formula IMP 4×4×4 to be the most appropriate, where the first digit is total number of wheels, and the next digits are the number of driven wheels and steering wheels. Such a formula makes it possible to solve all problems with the individual application of the IMP. The main difference between the IMP and the self-propelled chassis of Soviet and Chinese lunar rovers is the presence of bow and stern automatic docking devices designed to quickly change the structure of lunar trains and individual operation of individual platforms. Docking devices must ensure the freedom of rotation of each IMP about three axes (Fig. 2).

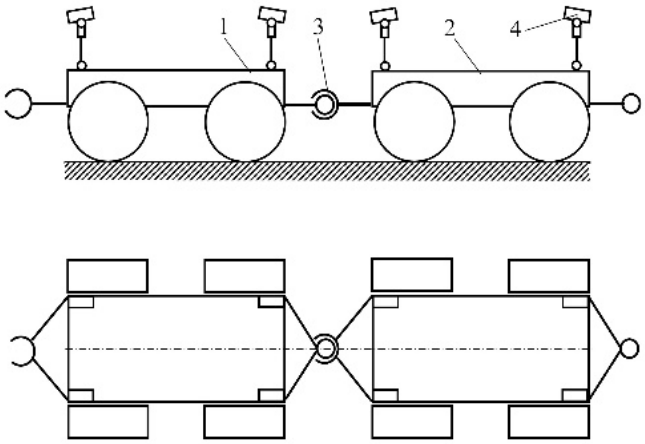

Fig. 2. A diagram of a complex of two IMPs. 1, 2 — intelligent mobile platforms; 3 — coupling automatic device; 4 — navigation cameras

The second difference is a higher level of robotization and intelligence. When used individually IMPs should provide capability of piloted control, remote and autonomous control, including docking and undocking operations in a given order. When working in conjunction, each IMP must provide maximum traversability and minimum energy costs for the movement along a given route. Focusing on the ISS modules, for the calculation of the geometrical parameters of the IMP, the authors consider the scenario of transporting a cylindrical cargo with a diameter of 4 m, a length of 8 m and mass of 18 t on the surface of the Moon, which corresponds to a fully assembled residential or laboratory ISS module. To move such a module from the landing site to the construction site of the ILRS, a two-link complex is sufficient, with a diameter of the IMP wheels of about a meter. However, in this case, the bearing capacity of the lunar regolith should be increased (relative to natural occurrence) by about 2 times, up to 46 kPa [3]. The radius of the wheels can be determined by the formula:

$$r = \sqrt{\frac{N}{kq \cdot \sin\left(2\arcsin(f)\right)}},$$

N — wheel load; q — soil bearing capacity; f — coefficient of wheel rolling resistance; $k = b/r$ — ratio of wheel width b to its radius r.

This means that the necessary road construction work must be completed on the Lunar Spaceport — ILRS route, including leveling, filling holes, soil compaction by static and vibration methods. Relevant working tools - bulldozer blades, ladles, rollers, etc. should be present on a IMP. As other autonomous attachments, one can name pressurized astronaut cabins, power plants of various types, drilling rigs, technological modules for the production of life support components, etc. Assuming the route from landing area to ILRS with slope steepness as seen in Fig. 1, and setting the freight traffic speed of 0.4 km/h, it is possible to calculate the required power of the IMP wheel traction motor – about 340° W. The required energy consumption of all IMP 4 traction drives will be approximately 1.7 kWh per 1 km. In an empty run, the complex of two IMPs can move at speed up to 2.0 km/h, thanks to the gearboxes built into the traction drives. The report also considers the option of creating IMP multilink lunar trains intended for long-range cruise (hundreds of kilometers), including manned expeditions. They will have speeds up to 5 km/h on calm terrain with elevation angles up to 5–10°. Thanks to the ability to control traction, the trains will be able to overcome slopes of at least 20° at a speed of 1.0 km/h. In order to maximize unification and reduce manufacturing costs, both versions of IMP will have the same design parameters: *L* (base) = *B* (track) = 3140 mm, *r* (wheel radius) = 550 mm. Such dimensions make it possible to inscribe the IMP in the transport position in the diameter of the launch vehicle fairing equal to 5 m. Approximately the same diameter of the head fairing is required to deliver the ILRS modules to the Moon.

3. LAYING A ROUTE AND ORGANIZING AN AUTOMATIC BRANCH OF THE ILRS ON THE FAR SIDE OF THE MOON.

Chinese specialists are successfully using the information channel they created "Earth— the far side of the Moon" with the help of the Queqiao relay satellite to transmit information from Chene-4, which landed on January 3, 2019 in crater Fon Karman. This channel is used to control Yutu-2 too, which was the first in the world to make a track on the far side of the Moon. However, to transmit information from telescopes that astronomers dream of placing on the far side of the Moon, in the shadow of ground-based radio interference, the transmission speed of such channels may not be enough. The report discusses the option of delivering a lunar telescope to the far side of the Moon from ILRS by a special expedition. The routes for such expeditions along a surface constantly illuminated by the Sun with elevation angles of no more than 15° have been found. During the expedition, an optical or relay communication line can be laid, which, in combination with the ILRS-Earth communication line, will significantly improve the reliability and quality of communication with equipment on the far side of the Moon. In fact, it is about creating a permanent branch of ILRS on the reverse side. A lunar train based on several intelligent mobile platforms must travel about 200 km to reach the vicinity of the Idelson L crater (*D* = 20 km), which is located on the far side of the Moon. On this way, it will pass through the ejecta of the Haworth and Shoemaker craters each ~50 km in diameter. These craters ejected material of the rim of the largest (*D* ~ 2500 km)) and oldest impact basin on the Moon, so observations and measurements along the way will be extremely valuable for lunar science.

ACKNOWLEDGEMENTS:

In this work M.A. Ivanov and A.T. Basilevsky was supported by the Russian Science Foundation grant no. 21-17-00035: Estimates of the rate of exogenous resurfacing on the Moon. Authors are grateful S.S. Krasilnikov for the help with preparation Fig. 1.

REFERENCES:

[1] Basilevsky A.T. et al. Potential Lunar Base on Mons Malapert: Topographic, Geologic and Trafficability Considerations // Solar System Research. 2019. V. 53. No. 5. P. 383-398.

[2] Merzhanov A.I. Lunar Base "Barmingrad": A Project Ahead of its Time // Aerospace Sphere J. 2018. No. 2(95). P. 107-117. DOI: 10.30981/2587-7992-2018-95-2-107-117. (In Rusiian.)

[3] Basilevsky A.T. et al. Estimation of the Strength of the Lunar Soil by the Depth of the Lunar Rover Wheel Tracks // Solar System Research. 2021. V. 55. No. 4. P. 283-306.

DEVELOPING THE LUNAR-BASED EARTH OBSERVATION PLATFORM

G. Liu[1,2], H. Guo[1,2], Y. Ding[1,2]
[1] *International Research Center of Big Data for Sustainable Development Goals, Beijing, China; liuguang@radi.ac.cn, guohd@radi.ac.cn, dingyx@radi.ac.cn*
[2] *Key Laboratory of Digital Earth Science, Aerospace Information Research Institute, Chinese Academy of Sciences, Beijing, China*

KEYWORDS:
lunar-based earth observation, sustainable development, large-scale geoscience phenomena, temporal consistency and spatial continuity

INTRODUCTION:

The moon is the only natural satellite of the Earth, it provides human a unique platform to deploy series of sensors so as to systematically observe the Earth for a long time to ensure the temporal consistency and spatial continuity of earth observation on the global scale. Lunar-based earth observation will provide a guarantee for the global scale multi-sphere integrated research, and it is possible to provide brand-new answers to a series of key scientific problems that are coupled with each other in the global multi-sphere from the perspective of earth system science. Constructing earth observation system on the moon will comprehensively improve the ability of earth observation, which is a revolution in the field of earth observation and will of great value to the research of earth science, space science and sustainable development.

LUNAR-BASED EARTH OBSERVATION PLATFORM AND THE ADVANTAGES:

The moon is the earth's natural satellite. Different from the artificial platforms such as the Space And aerospace Earth observation system, the lunar Earth observation platform is the utilization of the moon's natural satellite by human beings, which has a more far-reaching significance. It represents the prelude to the earth observation by using space natural resources after human beings stepped out of the cradle of the Earth. The development of lunar earth observation system is a cutting-edge innovation in the history of space earth observation technology [1, 2]. Just as the father of space science, Russian Tsiolkovsky said, "The earth is the cradle of mankind, but mankind will not live in the cradle forever" The lunar-based earth observation system is actually the intersection of the development of earth observation and space activities.

The moon is the earth's only natural satellite and the only planet that humans can and have reached. The moon is a long-term stable platform compared with the earth's space observation history which is only several decades. Compared with the current earth observing platforms, the Lunar based Earth-observation platform has a longer observation distance of 380,000 km and a much larger platform space of more than 1,730 km radius. For earth science phenomena observation, lunar-based earth observation has the following advantages: (1) the moon is always facing the earth with its front due to tide locking, and an observation station on the moon only needs a very small perspective angle (about 2°) to obtain the panoramic image of the earth facing the moon. Moreover, for different zenith angles of the sun, the lunar observatory has the ability to continuously change the viewing Angle, so the lunar observatory can obtain multi-angle parameters consistent with continuous time on the macroscopic scale. (2) Moon based synthetic aperture radar can not only achieve high spatial resolution as spaceborne radar but also reach thousands of kilometers swath. At the same time, very stable long baselines can be formed between lunar SAR, which is a powerful means to monitor the dynamic changes of the solid earth. As a natural celestial body platform, the moon has stable geological structure, various sensors can be placed to obtain the observation parameters and synchronous observe of the earth sphere from the ionosphere to the surface and sub-surface under the

same imaging conditions. (3) The life of lunar-based platforms is much longer than that of man-made earth satellites, and they can provide long-term, precisely calibrated time series data, which will greatly benefit the study of earth climate change. (4) The moon is the main source of the earth's tidal forces and an important factor shaping the earth's surface environment. The lunar base can provide a unique perspective to observe the Earth's climate system [3–5]. In conclusion, the deployment of sensors on the moon to carry out earth observation has unique advantages, in general the advantages of lunar-based earth observation can be summarized as the following four points, "Thoroughly observation, Uniform sampling, Rich angle, Comprehensive coverage", which will comprehensively improve the ability of earth observation and greatly promote the in-depth study of earth science, space science and sustainable development issues.

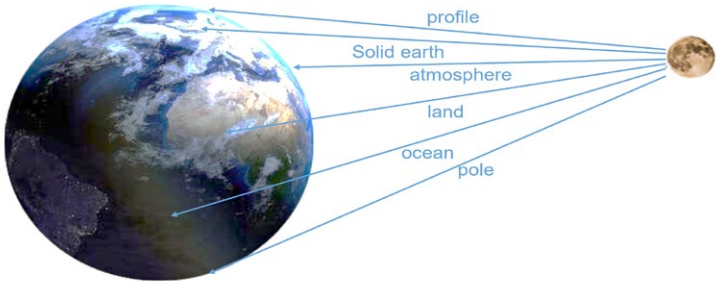

Fig. 1. Global multi-sphere observation from the perspective of Lunar-based Earth observation platform

LUNAR-BASED EARTH OBSERVATION PLATFORM AND THE APPLICATIONS:

Lunar-based Earth observation platform ensure the time consistency and spatial continuity of earth observation on the global scale, an integrated platform of active and passive multi-sensors can be set up to carry out multi-band simultaneous three-dimensional observation of multiple spheres and enhance the observation of the earth as a whole with the ability of multi-perspective, it is of great value to the research of earth science, space science and sustainable development with multi-dimensional observation.

EARTH SCIENCE

Oriented to the interaction of multi-spheres of the earth, the large-scale sea-land gas coupling phenomenon, the earth system and the outside world earth science basic problems such as energy and material exchange, collaborative rich month base sensor can be used to complete complex earth observation task and reveal the earth, the change rule of macroscopic scientific phenomenon of key elements to form the earth system on base of remote sensing observation ability, supporting earth system scientific research.

SPACE SCIENCE

Through the month of near-earth space observation, in the earth's ionosphere, magnetosphere, and natural and man-made space target as the main target of observation, reveals the magnetosphere and solar wind plasma interactions, and the earth dynamics in the process of geomagnetic storm process, based on monthly basis platform research theory and method for the system to the moon observation, forming system, high spatial and temporal coverage, the high spectrum covers the month of observation ability, the variation of the earth system is studied from the perspective of "sun-earth-moon" system.

SUSTAINABLE DEVELOPMENT

Sustainable development is a theory and strategy about the coordinated development of nature, science and technology, economy and society. It first

appeared in the Outline of World Natural Resources Conservation issued by the International Union for Conservation of Nature in 1980. Through the construction of the lunar earth observation system, the data gap can be solved in the regional coverage, timeliness and classification level of global sustainable development indicators.

PROSPECTS:

Lunar-based earth observation is an innovative new idea and a new direction in the field of earth observation, however requires the construction of lunar bases on the moon surface which puts forward high requirements on space transportation, base construction, energy supply and other technologies. Lunar-based earth observation will be a huge system engineering in human history, involving many disciplines and engineering fields, so it is difficult to achieve by the strength of a single country. International cooperation is a feasible way, through the joint efforts of relevant countries to formulate practical and feasible plans for lunar earth observation, build unmanned and manned lunar earth observation bases step by step, and eventually build a high-level lunar earth observation platform system to serve the sustainable development of mankind.

ACKNOWLEDGEMENTS:

This work was supported in part by the National Key Research and Development Program of China (No. 2020YFE0202100), and NSFC of China (No. 41590850).

REFERENCES:

[1] Guo H. et al. Moon-based earth observation for large scale geoscience phenomena // IEEE International Geoscience and Remote Sensing Symposium (IGARSS). Beijing, China, Jul. 2016. 2016. P. 3705-3707. DOI: 10.1109/IGARSS.2016.7729960.

[2] Liu G., Guo H., Wang X., Zhang L. Report on the Scheme and Key Technologies of Lunar Base Earth Observation / Chinese Academy of Sciences; Strategic Pioneer Program on Space Science of Chinese Academy of Sciences. 2016. No. XDA04077200.

[3] Guo H., Liu G., Ding Y. Moon-based Earth observation: scientific concept and potential applications // Intern. J. Digit. Earth. 2018. V. 11. N. 6. P. 546-557 DOI: 10.1080/17538947.2017.1356879.

[4] Ding Y. et al. Constructing a High-Accuracy Geometric Model for Moon-Based Earth Observation // Remote Sensing. 2019. V. 11. No. 22. P. 2611. DOI: 10.3390/rs11222611.

[5] Liu G., Guo H., Hanssen R.F. Characteristics analysis of moon-based earth observation under the ellipsoid model // Intern. J. Remote Sensing. 2020. V. 41. No. 23. P. 9121-9139. DOI: 10.1080/01431161.2020.1797220.

PRELIMINARY SCIENTIFIC OBJECTIVES OF THE INTERNATIONAL LUNAR RESEARCH STATION PROGRAM

C. Wang[1], Z.Y. Pei[2], L. Xu[1], Y.L. Zou[1]
[1] *State Key Laboratory of Space Weather/National Space Science Center, Chinese Academy of Sciences, Beijing, China, cw@spaceweather.ac.cn;*
[2] *Lunar Exploration and Space Engineer Center, China National Space Administration, Beijing, China*

KEYWORDS:
lunar research station, lunar geology, lunar-based observation; space environment, fundamental science experiments, in-situ resource utilization

The International Lunar Research Station (ILRS) is a scientific and application platform on the Moon jointly built by a number of countries, to support long-term and continuous scientific exploration and observation, fundamental science experiments and in-situ resource utilization.

According to the announced cooperation roadmap, the construction of ILRS is divided into three phases: reconnaissance, construction, and utilization.

Reconnaissance (before 2026): It is mainly to explore the Moon with the missions already planned, while selecting landing sites for subsequent missions and conducting related technical verification test.

Construction (before 2035): This phase may consist of two stages:

1) before 2030: Establishment of the command center of ILRS; Massive-cargo delivery and high-accuracy landing on the surface of the Moon; Start of joint operations;
2) from 2031 to 2035: Five missions are scheduled. Through this stage of construction, the lunar research station will be completed.

Utilization (after 2036) will use this scientific research station to carry out continuous scientific exploration and technical verification. It will support manned lunar missions, and expand and maintain the modules for each system as needed.

Preliminary scientific objectives of ILRS are as follows:

1) The geological survey of the Moon.

Through comprehensive survey of field geological, multiple geophysical measurements, and returning samples and laboratory analysis with state-of-the-art facilities, it will answer the key questions of the Moon, including its formation and evolution, the internal structure and composition, spatial and temporal distribution characteristics of the major geological events and their formation mechanisms, and the reservoirs and evolution of water and volatiles.

2) Lunar-based astronomy observations.

Performing lunar-based sky survey observations at ultralong wavelength and with an ultra-wide wavelength coverage from extreme ultraviolet (EUV) to infrared (IR); Revealing the history of the universe from the dark ages to cosmic dawn and constructing a complete image of the evolution of the universe; Exploring high-energy transients, the first light from supernovae, and new terrestrial exoplanets in the habitable zones; And then studying the formation and evolution of galaxies and the universe.

3) Space environment observation of the Sun-Earth-Moon system.

Developing the observation of the complete causal chain for the solar terrestrial lunar space-time scale based on ILRS, reveal the physical mechanisms and dynamic processes of the solar magnetic field, the Earth's upper atmosphere and high-energy radiations in the solar-terrestrial space, as well as the interaction mechanisms between the solar wind and the Moon and the Earth, build a new theoretical frame of the energy balance of the Earth's system, reveal the generation mechanisms of major space events in the Sun-

Earth-Moon system, and construct their theoretical prediction models that will further serve ILRS and geospace activities.

4) Lunar-based fundamental science experiment.

By experimentally studying the perception and response of plant-microbe coevolution and plant growth/development to lunar surface environment, and lunar soil's bioweathering improvement and plant utilization, analyze the influence of lunar surface environment on closed terrestrial ecosystem and reveal the bioavailability and biosafety of lunar soil as a plant-cultivation substrate. These results would serve the crew's activities in future lunar research station; Using lunar-based observation to search for magnetic monopoles and axion provides important demonstration for the fundamental physics research.

5) Lunar in-situ resource utilization.

A series of demonstrating experiments, such as rare gas extraction, hydrogen and oxygen production, and lunar soil material manufacturing, will provide technical support for the construction of lunar research facilities and in-situ resource utilization in the future.

THE INTERNATIONAL LUNAR RESEARCH STATION FROM SCIENCE PERSPECTIVE

A. Petrukovich[1], L. Zeleniy[1,2], I. Mitrofanov[1], V. Tretiakov[1], D. Zarubin[1]
[1] *Space Research Institute, Moscow, Russia*
[2] *Space Council of Russian academy of sciences, Moscow, Russia*

KEYWORDS:
International Lunar Research Station, space program, lunar science

INTRODUCTION:

The International Lunar Research Station (ILRS) is a space program which is aimed to provide a synergy in lunar exploration and a set of complex research facilities to be constructed with the possible involvement of international partners on the surface and/or in the orbit of the Moon.

The ILRS program is an effort co-led by Russia and China and open for international partners. It includes technical, programmatic and scientific fields of consideration.

The set of priority scientific topics was recently set by the joint working group. The team, with representatives from leading science organizations in different fields, provide opportunity for partners to discuss and plan all scientific activities for ILRS. Main areas of scientific interest have been included to the ILRS-guide for partnership [1].

A near-term science cooperation and further concepts are the two major part of the ongoing discussion and science team products development.

In this report we discuss variants of implementation of those tasks by means of ILRS infrastructure during three approved stages: reconnaissance, construction and utilization.

REFERENCES:

[1] International Lunar Research Station (ILRS): Guide for Partnership / Roscosmos; China National Space Administration. 16 p. https://www.roscosmos.ru/media/files/mnls.pdf.

SCIENTIFIC OBJECTIVES OF LUNAR EXPLORATION

L. Zelenyi[1], I. Mitrofanov[1], A. Petrukovich[1], V. Tret'yakov[1]
[1] *Space Research Institute, Moscow, Russia*

KEYWORDS:
Moon, space program, lunar science

The 21st centaury is becoming the Century of Moon Exploration. One may predict that during several next decades the Moon will become the 7th continent of human civilization (e.g. see [1]). At these days, all leading space states are developing the Moon exploration programs, both nationally and internationally. The current report discusses the main scientific and practical objectives of future space astronautics and expected results of these efforts:

MOON NATURE, ORIGIN AND EVOLUTION:
New data will be obtained on internal structure, surface evolution, processes in exosphere. The origin and evolution of the double-body Earth-Moon system will be understood, the "lunar climate" will become known for safe activity of humans on the surface.

THE PLATFORM FOR ASTRONOMICAL OBSERVATIONS:
The recent data of *James Webb* space telescope have shown that more observations in optical, IR and mm spectral ranges with high sensitivity would be very important for re-consideration of models of early Universe. Some ranges of radio waves are also still-closed window for astronomy. The Moon is the excellent platform for astronomical instruments with high efficiency, which could be too large for free space planforms.

GEOPHYSICAL/HELIOPHYSICAL MONITORING:
Space weather monitoring and forecasting is becoming more and more important for safety of complex facilities and infrastructure on Earth and in space.

LABORATORY FACILITIES FOR ASTROBIOLOGY AND SPACE MEDICINE:
Without experimental background from such studies on the Moon, human space flight to Mars would not be possible.

SPACE TECHNOLOGY DEVELOPMENT AND TESTING:
Moon is the natural field in the near space, which should become the testing site for elements of new space technology, the harbor for future deep space missions.

LUNAR NATURAL RESOURCES:
The Moon material is thought to contain elements and minerals, which are or will become useful resources for high-tech technology and manufacturing. Reconnaissance of such resources and technology of their acquisition would become the important space-based segment of future industry.

REFERENCES:
[1] The Moon is our seventh continent // In the world of science. 2018. No. 11. https://scientificrussia.ru/articles/luna-nash-sedmoj-kontinent-v-mire-nauki-11-2018-g. (In Russian.)

THE KORVET PROGRAM: INTEGRATED HUMAN AND ROBOTIC MISSIONS TO MOON

I. Mitrofanov[1], L. Zelenyi[1], V. Tret'yakov[1]
[1] *Space Research Institute, Moscow, Russia*

KEYWORDS:
Moon exploration, robotic lunar missions, human lunar missions, lunar science

There are many known sites on the lunar surface, which further studies would be very important for lunar science as well as for future Moon exploration. They are polar permanently shadowed craters, lava tubes, local regions with magnetic anomaly, regions with unusual chemical composition, etc. Visiting such sites is thought to be the goal of robotic lands with necessary instruments for in situ measurements and/or for sample acquisition.

On the other hand, future program of lunar exploration will include the humans' missions. The most likely strategy for their implementation could be linked with the permanent selected site with the most favorable natural environment, necessary infrastructure and life-support facilities. As the first step for such humans' lunar program, the orbital missions will be implemented for testing new technology in the circumlunar space.

The program Korvet (from *Corvette* in English) is proposed, as the integrated mission of human lunar orbital flight and multi-landing robotic craft. Report presents technical details of such mission and its scientific objectives.

SESSION 2. MOON AND MERCURY (MN) POSTER SESSION

EXPERIMENT MGNS ONBOARD ESA BEPICOLOMBO MISSION

M.L. Litvak[1], A.S. Kozyrev[1], I.G. Mitrofanov[1], J. Benkhoff[2]
[1] *Space Research Institute, Moscow, Russia, litvak@mx.iki.rssi.ru;*
[2] *European Space Agency, ESTEC, Noordwijk, The Netherlands*

KEYWORDS:
BepiColombo, Mercury, elemental composition, MGNS; gamma-ray spectroscopy

INTRODUCTION:
The ESA BepiColombo mission to Mercury was launched in October 2018. It carries a suite of science instruments to study Mercury interior structure, surface composition and evolution, magnetosphere and exosphere. In comparison with previous Mercury NASA mission MESSENGER BepiColombo should provide a high spatial resolution of the entire planet's surface, distribution of volatiles and to get more important data/knowledge about Mercury interior structure, gravity field, dynamic of magnetic field and exosphere [1].

The Mercury Gamma and Neutron Spectrometer (MGNS) was selected for BepiColombo mission as a fully Russian science instrument provided by Russian Federal Space Agency [2, 3]. It should determine the elemental composition of Mercury's surface and distinguish distribution of volatiles (primarily water ice) in the polar areas.

The cruise to Mercury takes about 7 years (orbit insertion is planned in December 2025). Half of this period has already passed, and in our overview we would like to summarize MGNS cruise observations including measurements of the spacecraft background (elemental composition of the spacecraft), monitoring of solar flares and gamma-ray bursts, measurements of neutron and gamma-ray flux during Mercury and Venus flybys.

REFERENCES:
[1] Benkhoff J. et al. BepiColombo — Mission Overview and Science Goals // Space Science Reviews. 2021. V. 217. Art. No. 90.
[2] Mitrofanov I.G. et al. The Mercury Gamma and Neutron Spectrometer (MGNS) on board the Planetary Orbiter of the BepiColombo mission // Planetary and Space Science. 2010. V. 58. P. 116-124.
[3] Mitrofanov I.G. et al. The Mercury Gamma-Ray and Neutron Spectrometer (MGNS) Onboard the Mercury Planetary Orbiter of the BepiColombo Mission: Design Updates and First Measurements in Space // Space Science Reviews. 2021. V. 217. Art. No. 67.

STUDYING LUNAR EVOLUTION BASED ON COMPREHENSIVE PHYSICAL FIELD EXPLORATION FOR INTERNATIONAL LUNAR RESEARCH STATION PROGRAM

Y.L. Zou[1,2], Y.Z. Jia[2], Y.T. Lin[3], A.M. Du[3], J.Z. Liu[4], J.H. Zhang[3], L. Xu[1,2], C. Wang[1,2]

[1] *State Key Laboratory of Space Weather, National Space Science Center, Chinese Academy of Sciences, Beijing, China, jiayingzhuo@nssc.ac.cn;*

[2] *National Space Science Center, Chinese Academy of Sciences, Beijing, China;*

[3] *Institute of Geology and Geophysics, Chinese Academy of Sciences, Beijing, China;*

[4] *Institute of Geochemistry, Chinese Academy of Sciences, Guiyang, China*

KEYWORDS:
lunar origin, evolution, comprehensive physical field, exploration, ILRS

INTRODUCTION:

The study of the lunar evolution history is a key scientific issue. The origin and evolution of the moon are related to the initial thermal, physical and chemical states of the Earth, and restricted the early evolution of the earth-moon system. A comprehensive study on the lunar origin and evolution is an important basis for understanding the formation and early evolution of the Earth and the key to revealing the history of asteroid impacts in the solar system. The lunar evolution is driven by both internal and external dynamics. The impact events of the moon can reflect the process of external dynamic geology, while the evolution of the magmatic ocean and the formation of the lunar crust, as well as the later magma and volcanism, can reflect the process of internal dynamic geology. These important geological processes are not only the main process of the formation of the moon, but also the formation process of other terrestrial planets in the solar system, which plays an important role in the later evolution of the moon and planets.

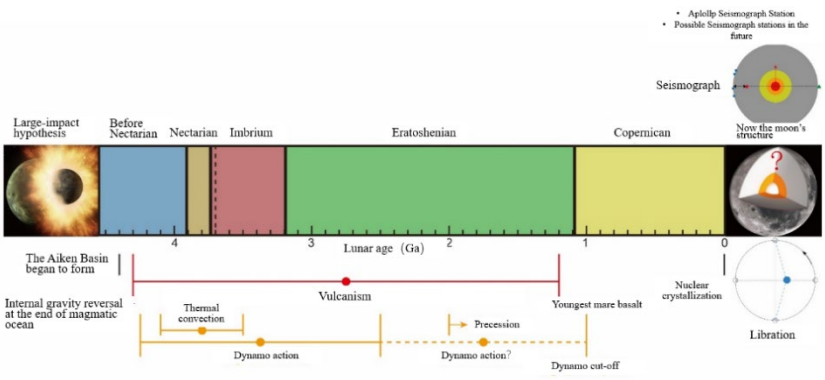

Fig. 1. The key events in the formation and evolution of the moon

The data of gravitation field, magnetic field, electric field, seismograph and heat flow contains abundant lunar internal structural information [1–3]. Based on the comprehensive study of the multi-physical fields, to study the major events in the lunar large-scale evolution and to construct the structure model of the lunar inner circle, which is of great significance to construct a new theoretical framework of the lunar evolution. A single physical field often has obvious uncertainties. New techniques and methods of multi-physical field detection can comprehensively constrain the structure of the lunar inner circle from different angles and invert its fine structure, which provide an important basis for constructing a new theoretical framework of lunar evolution.

The Apollo program completed the first comprehensive exploration of the moons physical properties such as gravity, magnetic field, electric field and seismicity, which laid the foundation for understanding the moon [4, 5]. However, due to the limitation of instrument precision and observation range, there is still a great controversy on the basic science of the moon at present, which limits our understanding of the lunar evolution [6].

With the rapid development of modern instruments and data processing methods, by installing high-precision modern physical instruments, we can detect weaker deep lunar signals and continuously record scientific data of higher quality than the Apollo era. We can well detect the deep inner sphere and local fine structures [7–9].

High-precision time-varying gravity field detection on the lunar surface is of great significance to research the density structure and rheological properties of the lunar interior. The lunar surface magnetic field reflects the remanence magnetic level of lunar rocks, and it is also the key information for understanding the distribution and formation of lunar magnetic anomalies. The lunar paleo-magnetic field records the evolution of the lunar magnetic field, and it is also the main means for understanding the evolution history and internal thermodynamic process of the moon. The lunar-seismic wave can penetrate the interior of the moon and carry key information about the lunar interior structure. By deploying multiple high-precision three-component wide-band lunar seismograph, we can break through the recognition of the one-dimensional radial structure under the lunar array during the Apollo period, which is of great scientific value to the definition of the whole lunar radial structure. The study of lunar heat flow is a necessary way to obtain the concentration of radioactive elements in the lunar interior. The research of heat transfer mechanism in the lunar interior is very important for understanding the structure and evolution of the lunar interior. The present thickness, state and composition of the lunar core, mantle and crust can be obtained by analyzing heat flow data and then lunar seismograph data, and the timeline of the lunar thermal evolution can be constructed.

The next step of Chinas International Lunar Research Station (ILRS) [10, 11] project is to set up scientific equipment of “gravity field, magnetic field, electric field, lunar seismograph and heat flux meter” on the moons South Pole. Based on the comprehensive research of the moons multi-physical field, to analyze the internal structures and the formation mechanism of major geological events, to build lunar internal fine structure model and time and space distribution and evolution model, to realize the internal structures and new breakthrough of the cognitive evolution process of the moon.

ACKNOWLEDGEMENTS:
This research was funded by the National Key R&D Program of China (Grant No. 2020YFE0202100).

REFERENCES:

[1] Grott M., Breuer D. On the spatial variability of the Martian elastic lithosphere thickness: Evidence for mantle plumes? // J. Geophysical Research: Planets. 2010. V. 115. Iss. E3. Art. No. E03005. 16 p. https://doi.org/10.1029/2009JE003456.
[2] Yoder C.F. Effects of the spin-spin interaction and the inelastic tidal deformation on the lunar physical librations // Natural and Artificial Satellite Motion/ ed. Nacozy P.E., Ferraz-Mello S. Austin: Univ. of Texas Press, 1979. P. 211-221.
[3] Williams J.G., Boggs D.H., Yoder C.F. Lunar rotational dissipation in solid body and molten core // J. Geophysical Research. 2001. V. 106(11). P. 27933-27968.
[4] Konopliv A.S., Park R.S., Yuan D.N. et al. The JPL lunar gravity field to spherical harmonic degree 660 from the GRAIL Primary Mission // J. Geophysical Research: Planet. 2013. V. 118. P. 1415-1434.
[5] Warren P.H., Rasmussen K.L. Megaregolith insulation, internal temperatures, and bulk uranium content of the moon // J. Geophysical Research: Solid Earth. 1987. V. 92. Iss. B5. P. 3453-3465. https://doi.org/10.1029/JB092iB05p03453.
[6] Nagihara S., Kiefer W.S., Taylor P.T., Williams D.R., Nakamura Y. Apollo Heat Flow Experiments: Lessons Learned for Future Lunar-Landing // 49th Lunar and Planetary Science Conference. 2018. LPI Contrib. No. 2083.
[7] Goossens S. et al. A global degree and order 1200 model of the lunar gravity field using GRAIL mission data // Lunar and Planetary Science Conference, Houston. 2016.

[8] Warren P.H., Rasmussen K.L. Megaregolith insulation, internal temperatures, and bulk uranium content of the Moon // J. Geophysical Research: Solid Earth. 1987. V. 92. Iss. B5. P. 3453-3465. https://doi.org/10.1029/JB092iB05p03453.
[9] Good A.C., Johnson A.R. NASA InSights Mole Ends Its Journey on Mars // NASA, InSight News. Jan. 14, 2021. URL: https://mars.nasa.gov/news/8836/nasa-insights-mole-ends-its-journey-on-mars/?site=insight.
[10] Wu W.R., Liu J.Z., Tang Y.H. et al. China Lunar Exploration Program // J. Deep Space Exploration. 2019. V. 6(5). P. 405-416.
[11] Pei Z.Y., Liu J.Z., Wang Q. et al. Overview of lunar exploration and International Lunar Research Station // Chinese Science Bull. 2020. V. 65. P. 2577-2586. DOI: 10.1360/TB-2020-0582. (In Chinese.)

HEAT FLOW MEASUREMENT A HIGH PRIORITY FOR UPCOMING LUNAR MISSIONS

S. Huang[1,2], Y. Liu[1], Z. Meng[3], C. Ding[4], M. Song[1]
[1] *College of Civil and Transportation Engineering, Shenzhen University, Shenzhen, China, shaopeng@szu.edu.cn, shaopeng@umich.edu*
[2] *Department of Earth and Environmental Sciences, University of Michigan, Ann Arbor, USA*
[3] *College of Geoexploration Science and Technology, Jilin University, Changchun, China*
[4] *Institute for Advanced Study, Shenzhen University, Shenzhen, China*

KEYWORDS:
planetary heat flow, Apollo, Chang'E-5, thermal structure, volcanism, heat-producing element, volatile

Heat flow density (or heat flow in short) is a parameter of fundamental importance to the study of the thermal history and inner thermal state of a planetary body. While there are about 75,000 terrestrial heat flow measurements [1], only two in-situ lunar heat flow measurements have been made by Apollo astronauts on the Moon [2]. Moreover, there have been doubts surrounding these two lunar measurements and their implications since they were first reported. The recent Chang'E-5 Mission discoveries [3–6] of unexpected young volcanism and low contents of water and heat-producing elements of the lunar basalt have further enhanced the controversy over the thermal structure of the Moon, which can only be resolved by additional high quality lunar heat flow measurements.

Planetary heat flow is determined as the product of subsurface temperature gradient and thermal conductivity of the soils/rocks. The former is typically obtained from borehole logging whereas the latter could be measured either in-situ or at laboratory. For the Apollo Lunar Heat Flow Experiment (AHFE), two boreholes were drilled by astronauts into the lunar regolith at Hadley Rille (Apollo-15 landing site) and Taurus Littrow (Apollo-17 landing site), respectively. Each borehole received an array of thermometers designed for measuring subsurface temperatures and thermal conductivity. Based on short-term in situ measurements, a 33 mWm^{-2} heat flow for Apollo-15 [7] and a 28 mWm^{-2} heat flow for Apollo-17 [8] were initially determined. The values were later lowered to 21 and 14 mWm^{-2}, respectively, based on the revised and lower thermal conductivities estimated by the analysis of long-term subsurface temperature time series [2].

The 17.5 mWm^{-2} mean of the two Apollo measured lunar heat flow values is smaller than a quarter of the global terrestrial heat flow [9]. However if the value is of global representative, it would imply a bulk Uranium concentration of 46 ppb [10] of the Moon, as opposed to 15.4 ppb of the Bulk Silicate Earth [11]. From a geochemical perspective, Warren and Rasmussen [10] believe that a regional representative lunar heat flow must be about 12 mWm^{-2}. There are other studies (e.g., [12, 13]) demanding a downward correction to the Apollo measured heat flow measurements.

However, the AHFE data demonstrated a clear warming trend at both Apollo-15 and Apollo-17 sites over the operation period from July 1971 to January 1977 at the Apollo-15 site, and from December 1972 to September 1977 at the Apollo-17 site. Nagihara et al. [14] attribute the warming to the regolith compaction effect of astronaut exploration activities. Regolith compaction would lead to an albedo reduction that would allow for absorption of more radiative heat into the subsurface. In addition to the regolith compaction effect, the Moon experienced a global warming trend due to the 18-year lunar precession and an enhanced radiation from Earth over the AHFE period [15]. The warming trend is visible in the temperature time series at all depths of the AHFE boreholes. However, it was more pronounced at shallower than at greater depths, leading to a decreasing trend in the thermal gradients. This pattern of subsurface temperature variation is consistent with

the downward propagation of surficial warming [16]. It is well known among the heat flow community that a warming on the surface will distort the subsurface steady state geothermal gradient and result in a smaller apparent heat flow [16, 17]. The surface warming transient effect demands an upward instead of downward correction to the observed lunar heat flow.

Conventional wisdom believes that the Moon is a dynamically dead planetary body, retaining little accretional heat and having ceased volcanism since around 2.8 Ga. However, the recent results [3–6] from the Chinese Chang'E-5 lunar mission show that the Moon remained volcanically active at least until 2.0 Ga and the Moon's youngest volcanism was not driven by high volatiles nor by high heat-producing element contents in its mantle source. The results from the Chang'E-5 Mission have opened new ground for the debate on the internal heat source and thermal history of the Moon.

Lunar heat flow carries rich genetic, physical, chemical, and dynamical information of the Moon. A globally representative heat flow is a cornerstone of any hypothesis and theory about the formation and development of the Moon. We urge the lunar community to make heat flow measurement a high scientific priority in the upcoming lunar missions.

REFERENCES:

[1] Fuchs S., Norden B., Artemieva I. et al. The global heat flow database: Release 2021. Intern. Heat Flow Commision, 2021. 73 p. https://doi.org/10.5880/fidgeo.2021.014.
[2] Langseth M.G., Keihm S.J. In-Situ Measurements of Lunar HEAT flow // The Soviet-American Conf. Cosmochemistry of the Moon and Planets. 1977. Pt. 1. P. 283-293.
[3] Che X.C., Nemchin A., Liu D.Y. et al. Age and composition of young basalts on the moon, measured from samples returned by Chang'e-5 // Science. 2021. V. 374. P. 887-890.
[4] Hu S., He H.C., Ji J.L. et al. A dry lunar mantle reservoir for young mare basalts of Chang'e-5 // Nature. 2021. V. 600. P. 49-53.
[5] Li Q.L., Zhou Q., Liu Y., et al. Two-billion-year-old volcanism on the moon from Chang'e-5 basalts // Nature. 2021. V. 600. P. 54-58.
[6] Liu S.J., Zhou Q., Li Q.L. et al. Chang'e-5 samples reveal two-billion-year-old volcanic activity on the Moon and its source characteristics // Science China-Earth Sciences. 2021. V. 64. P. 2083-2089.
[7] Langseth M.G., Clark S.P., Chute J.L. et al. The Apollo-15 lunar heat-flow measurement // The Moon. 1972. V. 4. P. 390-410.
[8] Langseth M.G., Chute J., Keihm S. Heat flow experiment // Apollo-17 preliminary science report. 1973. V. 9. P. 1-24.
[9] Lucazeau F. Analysis and mapping of an updated terrestrial heat flow data set // Geochemistry, Geophysics, Geosystems. 2019. V. 20. P. 4001-4024.
[10] Warren P.H., Rasmussen K.L. Megaregolith insulation, internal temperatures, and bulk uranium content of the moon // J. Geophysical Research: Solid Earth. 1987. V. 92. P. 3453-3465.
[11] Javoy M., Kaminski E. Earth's uranium and thorium content and geoneutrinos fluxes based on enstatite chondrites // Earth and Planetary Science Letters. 2014. V. 407. P. 1-8.
[12] Laneuville M., Wieczorek M., Breuer D. et al. A long-lived lunar dynamo powered by core crystallization // Earth and Planetary Science Letters. 2014. V. 401. P. 251-260.
[13] Saito Y., Tanaka S., Takita J. et al. Lost apollo heat flow data suggest a different lunar bulk composition // 38th Lunar and Planetary Science Conf. 2007.
[14] Nagihara S., Kiefer W.S., Taylor P.T. et al. Examination of the long-term subsurface warming observed at the Apollo-15 and -17 sites utilizing the newly restored heat flow experiment data from 1975 to 1977 // J. Geophysical Research: Planets. 2018. V. 123. P. 1125-1139.
[15] Huang S. Surface temperatures at the nearside of the moon as a record of the radiation budget of earth's climate system // Advances in Space Research. 2008. V. 41. P. 1853-1860.
[16] Pollack H.N., Huang S.P. Climate reconstruction from subsurface temperatures // Annual Review of Earth and Planetary Sciences. 2000. V. 28. P. 339-365.
[17] Cermak V. Underground temperature and inferred climatic temperature of the past millennium // Palaeogeography, Palaeoclimatology, Palaeoecology. 1971. V. 10. P. 1-19.

MOON-BASED SPACE WEATHER STATION FOR SUN-EARTH-MOON ENVIRONMENT INTERACTION MONITORING AND RESEARCH

B. Luo[1,2], X. Zhang[1], T. Sun[1], X. Bai[2,3], F. Wei[1], R. Lin[1], L. Li[1], S. Zhang[1], L. Kong[1], X. Wang[1], L. Xie[1], S. Peng[1], B. Tang[1], Y. Zhang[1], Q. Xu[1], S. Leng[1], P. Feng[1], Y. Su[4], W. Gan[4], L. Feng[4], H. Tian[1,5], L. Chen[1], Y. Yan[1], Y. Song[2,3], S. Liu[1,2], Y. Deng[2,3]

[1] *National Space Science Center, Chinese Academy of Sciences, Beijing, China; luobx@nssc.ac.cn, liusq@nssc.ac.cn*
[2] *University of Chinese Academy of Sciences, Beijing, China*
[3] *National Astronomical Observatories, Chinese Academy of Sciences, Beijing, China; dyy@nao.cas.cn*
[4] *Purple Mountain Observatory, Chinese Academy of Sciences, Nanjing, China*
[5] *School of Earth and Space Sciences, Peking University, Beijing, China*

KEYWORDS:
space weather, moon-based station, sun-earth-moon, solar wind, cosmic rays, solar energetic particles, bow shock, magnetopause, magnetosheath magnetotail, lunar surface

INTRODUCTION:

The Sun-Earth-Moon space environment is a complex coupled system dominated by the Sun. Solar eruptions can directly cause disturbances to the Earth's space environment. The Moon revolves around the Earth about once a month, passing through the interplanetary solar wind, the Earth's bow shock, magnetosheath, magnetopause, and magnetotail alternately (Fig. 1). Therefore, it experiences the dual influence of solar and Earth's magnetosphere activities, forming highly complex and changeable lunar surface environmental conditions, including electromagnetic radiation, particle radiation, lunar dust, electric potential and magnetic field structure, etc.

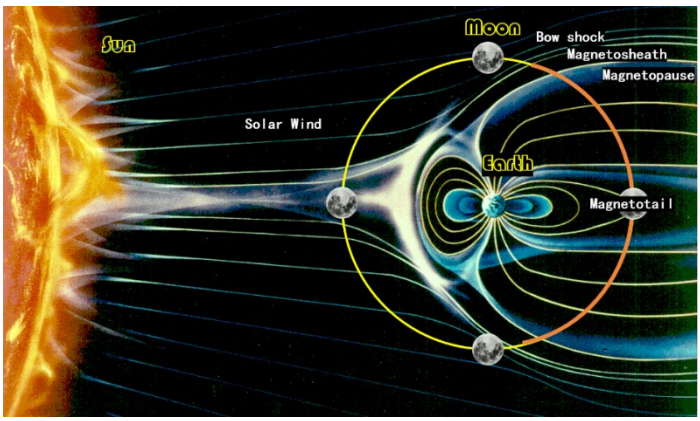

Fig. 1. The Sun-Earth-Moon system.

The stable celestial geological structure, without dense atmosphere and global magnetic field, periodic revolving around the Earth with suitable distance make the Moon a natural and excellent laboratory for the monitoring and research of the Sun-Earth-Moon space weather. The establishment of a Moon-based space weather station is of great scientific significance for studying the mechanism of solar eruptions, the coupling of the Sun to the Earth and the Moon, and the local variations of the Moon's environment. It will also promote the development of lunar space weather modeling and prediction technologies and greatly improve the capability in providing space environmental safeguard services for future lunar explorations. In the talk, I will introduce the complex Sun-Earth-Moon coupling system, review the

current research progress on space environment made by previous lunar exploration missions, survey the key scientific issues and detection requirements for future lunar space weather exploration, propose the concept of the Moon-based space weather station (Fig. 2), and finally introduce its scientific objectives and initial payload configuration.

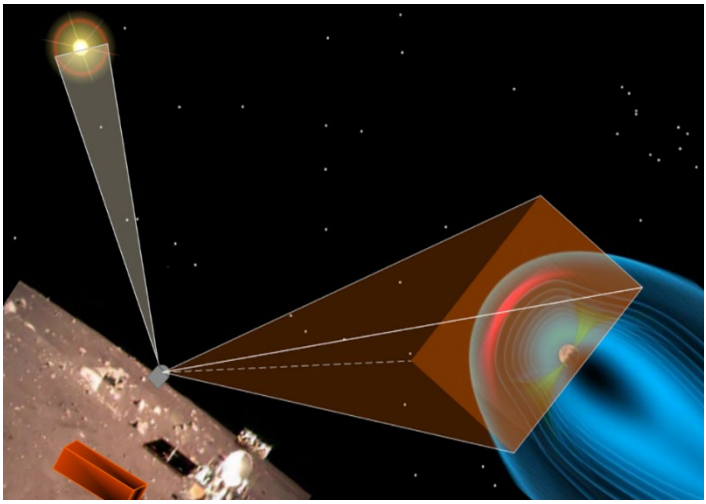

Fig. 2. The concept graph of the Moon-based space weather station, consisting of solar activity monitors, soft X-ray imager of the Earth magnetosphere, and in-situ lunar surface environment monitors.

KEY SCIENTIFIC QUESTIONS OF LUNAR LIFE SCIENCES

J. Feng[1], H. Liu[1]
[1] *Institute of Environmental Biology and Life Support Technology, School of Biological Science and Medical Engineering, Beihang University, Beijing, China; fengjiajie@buaa.edu.cn, lh64@buaa.edu.cn*

KEYWORDS:
crewed space exploration, crewed lunar exploration, bioregenerative life support system, biological effect on lunar surface, terrestrial ecosystem, plant cultivation on lunar soil, plant-microbe interaction

INTRODUCTION:

The future developing trend of crewed space exploration is crewed lunar exploration and lunar bases which accumulate technologies and experience for explorations beyond the Moon, with a further target of crewed landing on Mars. The Moon is the first station of crewed space exploration. To ensure the survival and health of the personnel on lunar surface, it is necessary to carry out biological research on lunar surface in advance to provide the scientific basis for human residency. In addition, the influence of space environment on life activities is also an important area of life sciences. Therefore, lunar life science is a very important aspect of lunar science.

"Building the Bioregenerative Life Support System (BLSS) with independent intellectual property rights, and solving key theoretical and technical problems in establishing lunar base ecological environment" is one of the strategic goals of international space science and technology development, and also a key question in life sciences. Based on principles of terrestrial ecosystem, BLSS organically combines biotechnology and engineering control technology to build an artificial ecosystem composed of plants, animals and microbes. Oxygen, water and food, which are necessary for human survival, can be recycled in the system and provide an ecological environment similar to the Earth biosphere for humans. It is an independent, complete and complex system that provides material support for astronauts' life activities [1]. Astronauts in the artificial ecosystem act as consumers of the ecosystem and also play the function of the controller. The BLSS would greatly reduce supplies from the Earth and thus the cost.

However, the integrated environment of 1/6-G gravity, low magnetic field intensity, and long-time low-dose radiation in lunar surface closed cabin is very different from the Earth. How the comprehensive environmental conditions on lunar surface would impact the biological units of the system and their interactions is unclear, which is critical to the realization of lunar surface BLSS. In BLSS, plants provide fresh food, oxygen, water and psychological comfort for astronauts and play a basic life support function, which is the core biological unit of BLSS [2]. How to achieve sustainable and efficient plant production and maintain the health and safety of plants on lunar surface is the key for BLSS. It is urgent to carry out basic research on efficient and healthy plant cultivation on lunar surface at the stage of lunar research station.

Previous space studies in low Earth orbit and ground simulation studies have confirmed that microgravity, radiation, artificial atmosphere and artificial light will all affect plant cell structure, photosynthetic physiology and material metabolism [3]. These results suggest that for plants that have adapted to 1-G gravity on the Earth over a long period of time, Extraterrestrial environment is a stress factor for plant growth and development to a certain extent. Therefore, it is necessary to carry out lunar surface experimental research to reveal the principles of the plants' perception and response to lunar surface environment, and provide an important theoretical basis for the construction of lunar surface BLSS.

The efficient production of plants in lunar BLSS must make full use of in situ lunar soil resources so as to reduce the transport supply of the Earth's resources. European and American research teams have proved the bioavail-

ability and improvement potential of lunar soil simulant [4], and China's "Lunar Palace 1" team has also studied and confirmed the feasibility of the bioimprovement of lunar soil simulant [5]. However, real lunar soil experiments and mechanism studies are still lacking. To clarify the bioavailability of lunar soil and the process of bioimprovement of lunar soil bioavailability will provide theoretical basis for in situ utilization of lunar soil.

In BLSS, it is impossible to keep plants sterile. Plants will coexist with microbes. To ensure the health of plants in lunar surface environment, it is necessary to clarify the interaction between plants and their symbiotic microbes. Current studies have demonstrated that the interactions between plants and their symbiotic microbes can maintain the health and safety of plants by regulating some metabolic and immune responses. By secreting 21 % of the photosynthically fixed carbon to the root interface, plants can provide carbon sources for the survival of related microbes. Meanwhile, they can also produce and secrete quorum sensing mimics to simulate the function of self-inducer signaling molecules generated by microbes themselves to interfere with or regulate microbial behavior [6]. However, plant microbes can accumulate and colonize the corresponding locations of plants by responding to the chemical tendency of root exudates. Through cooperation and competition, plant microbes form a stable community structure in the rhizosphere of plants, which can enhance the host's resistance to stress and disease by improving the ability of plants to tolerate abiotic stress and inducing systemic resistance to pathogenic microbes, thus promoting seed germination rate, nutrient uptake, and growth and development [7].

Previous studies have confirmed that plants growing under space flight show increased sensitivity to rhizosphere fungal diseases [8], and the health of plants is at risk of rhizosphere fungal infestation. Lunar Palace 1 team found that *Pseudochrobactrum Kiredjianiae* A4 was less effective against *Fusarium graminearum* under simulated microgravity. The contents of JA and ETH, the key regulatory factors of host ISR, which are closely related to rhizosphere microbiome, are reduced [9]. In addition, Lunar Palace 1 team also demonstrated significant changes in endophytic microbiome of wheat seedlings under simulated microgravity effect, in which the contents of *Pseudomonas* and *Bacillus*, which are closely related to plant disease resistance and resistance, significantly decreased in wheat roots [10]. These studies suggest that lunar surface environment may play an important role in the homeostasis of interactions between plants and rhizosphere microbes, thereby altering the host-microbial interactions at both genetic and physiological levels and affecting the health and safety of plants. However, the study of plant-microorganism interaction in lunar surface environment is still blank.

At the system level, BLSS is a miniature model of closed terrestrial ecosystem. Up to now, studies on the spatial effects of closed terrestrial organisms in the world have focused on the spatial carrying experiments of single species of plants or animals [11], while studies on the performance of terrestrial ecosystems with binary or multiple biological components in space have not been carried out. Only single plant seeds or individual animals have been carried out in biological experiments in lunar environment [12]. No experiment on carrying ecological systems on lunar surface has been proposed, nor has the operation experiment of lunar terrestrial ecosystem with scientific significance been carried out. Principles of material circulation and energy flow of BLSS and lunar biological effect of each biological component are not clear.

In conclusion, four key scientific questions of lunar life sciences need to be studied first: (1) How do plants perceive and respond to lunar surface environment? (2) How do plants and microbes interact in lunar surface environment? (3) What is the bioavailability of lunar soil for plant cultivation? (4) What are the effects of lunar surface environmental factors on energy and material transfer and stable operation of closed terrestrial ecosystems?

REFERENCES:

[1] Liu H., Yao Z., Fu Y. et al. Review of research into Bioregenerative Life Support System(s) which can support humans living in space // Life Sciences in Space Research. 2021. V. 31. P. 113-120.

[2] Fu Y., Liu H., Shao L. et al. A high-performance ground-based prototype of horn-type sequential vegetable production facility for life support system in space // Advances in Space Research. 2013. V. 52(1). P. 97-104.
[3] Zabel P., Bamsey M., Schubert D. et al. Review and analysis of over 40 years of space plant growth systems // Life Sciences in Space Research. 2016. V. 10. P. 1-16.
[4] Ming D., Henninger D. Use of lunar regolith as a substrate for plant growth // Advances in Space Research. 1994. V. 14(11). P. 435-443.
[5] Yao Z., Feng J., Liu H. Bioweathering improvement of lunar soil simulant improves the cultivated wheat's seedling length // Acta Astronautica. 2021. V. 193. P. 1-8.
[6] Hartmann A., Schmid M., Van Tuinen D. et al. Plant-driven selection of microbes // Plant and Soil. 2009. V. 321(1). P. 235-257.
[7] Hacquard S., Spaepen S., Garrido-Oter R. et al. Interplay between innate immunity and the plant microbiota // Annual review of Phytopathology. 2017. V. 55. P. 565-589.
[8] Foster J.S., Wheeler R.M., Pamphile R. Host-microbe interactions in microgravity: assessment and implications // Life Sciences and Space Research. 2014. V. 4(2). P. 250-266.
[9] Fu Y., Gao H., Li H. et al. Change of growth promotion and disease resistant of wheat seedling by application of biocontrol bacterium Pseudochrobactrum kiredjianiae A4 under simulated microgravity // Acta Astronautica. 2017. V. 139. P. 222-227.
[10] Qin Y., Fu Y., Chen H. et al. Microgravity effect on endophytic bacteria communities of Triticum aestivum // Acta Astronautica. 2018. V. 143. P. 297-301.
[11] Morrow R., Wetzel J., Richter R. et al. Evolution of space-based plant growth technologies for hybrid life support systems // 47th Intern. Conf. Environmental Systems. 16-20 July 2017, Charleston, South Carolina. 2017. Art. No. 301. 9 p.
[12] Vaulina E., Anikeeva I., Gubareva I. et al. Survival and mutability of Chlorella aboard the Zond vehicles // Life Sciences and Space Research. 1971. V. 9. P. 105-110.

PROBING SURFACE DEPOSITS IN HEAVILY EJECTA-CONTAMINATED MARE FRIGORIS USING CE-2 MRM DATA

Z.G. Meng[1], J.T. Lei[1], J.S. Ping[2,3], Y.Z. Zhang[2,3], A. Gusev[4]
[1] *College of Geoexploration Science and Technology, Jilin University, Changchun, China; mengzg@jlu.edu.cn (Z.M.)*
[2] *Key Laboratory of Lunar and Deep Space Exploration, National Astronomical Observatory, Chinese Academy of Sciences, Beijing, China; jsping@bao.ac.cn (J.P.); zhangyz@nao.cas.cn (Y.Z.)*
[3] *School of Astronomy and Space Science, University of Chinese Academy of Sciences, Beijing, China*
[4] *Kazan Federal University, Kazan, Russia*

KEYWORDS:
Mare Frigoris, surface deposits, dielectric properties, basaltic units, Chang'e microwave radiometer, brightness temperature

INTRODUCTION:
Mare Frigoris is the fifth largest and northernmost lunar mare on the near side of the Moon. The mare extends from about 55°W to 45° E, with an average latitudinal extent of only 7.5° (Fig. 1). Therefore, ejecta from highland craters reach its central portions and obscure the basalt deposits more easily compared to large circular maria [1, 2]. This makes it difficult to infer the pristine compositions of the basaltic deposits of Mare Frigoris using optical data.

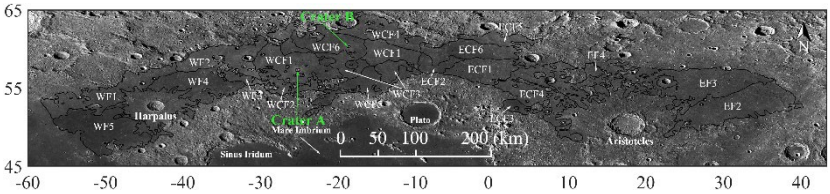

Fig. 1. A wide-angle camera image of Mare Frigoris. The black lines are the geologic boundaries mapped by Kramer et al. [2].

To reduce the influence of the impact ejecta on the surface mafic contents of basaltic units, Kramer et al. [2] proposed the small crater rim and ejecta probing (SCREP) methodology, to evaluate the pristine compositions of underlying basaltic units. Comparatively, the microwave radiometer (MRM) onboard the Chang'e-1 and -2 (CE) satellites can reflect the dielectric properties of the lunar regolith at the corresponding penetration depths [3], which provide a new potential choice to assess the basaltic units with heavy surface contamination in Mare Frigoris.

METHODOLOGY:
From 15 October 2010 to 20 May 2011, the CE-2 MRM instrument measured the lunar surface for more than 5000 earth hours and operated at 3.0, 7.8, 19.35, and 37 GHz [3]. The integration time of the CE-2 MRM instrument is 200 ms, the observation angle is 0°, and the temperature sensitivity is approximately 0.5 K. At an orbital altitude of approximately 100 km, the resolution of the MRM data is about 25 km at 3.0 GHz and 17.5 km at 7.8, 19.35, and 37 GHz. This study adopted the 2C level data after system calibration and geometric correction, obtained from the Lunar and Planetary Data Release System. For a description of the CE-2 MRM data, please see Meng et al. [3] and Zheng et al. [4].

The hour angle is introduced to ascribe the observed MRM points into twenty-four lunation hours. Then, the data points were employed to generate the brightness temperature (TB) maps using the linear interpolation method with the spatial resolution of 0.25×0.25° (Fig. 2, 37 GHz). Here, the TB performances of the surface deposits at noon and night were represented

by the observation from 12:26 to 13:08 and from 0:00 to 0:39, respectively. To clearly understand the thermophysical properties of the surface deposits, the geologic boundaries mapped by Kramer et al. [2] were vectorized and overlaid on the TB maps.

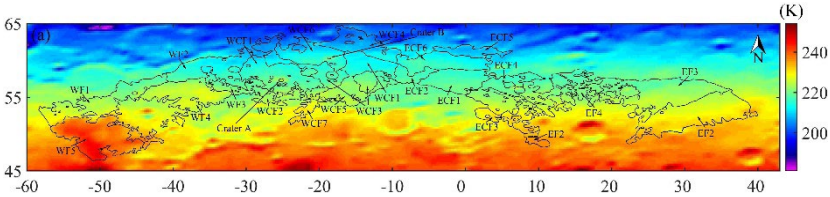

Fig. 2. TB maps of Mare Frigoris at 37 GHz, noon

To weaken the N-S trend of the TB, normalized TB (nTB) mapping and TB difference (TBD) mapping were proposed (Fig. 3 and 4). The procedure to generate nTB and TBD maps provided in reference [5].

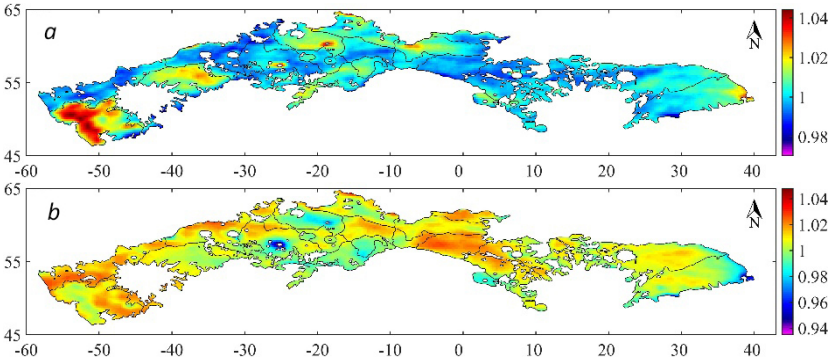

Fig. 3. Normalized TB maps of Mare Frigoris at 37 GHz: (a) noon, (b) night

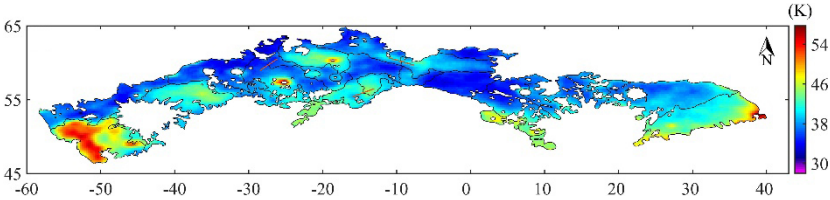

Fig. 4. TB difference maps of Mare Frigoris at 37 GHz

RESULTS:

Figures 3 and 4 demonstrate how, in the study of the basaltic units on the lunar surface, the overlay of the geologic boundaries mapped by Kramer et al. [2] on TBD maps high-lights the MRM data. Kramer et al. [2] divided Mare Frigoris into four quadrants comprising Western Frigoris (WF), West-central Frigoris (WCF), East-central Frigoris (ECF), and Eastern Frigoris (EF), which include 21 basaltic units. Here, in the WF4, WF5, WCF4, WCF6, ECF3, and ECF5 units, the TBD results correlate with the basaltic unit mapped by Kramer et al. [2] (see Fig. 4). This correlation indicates that the TBD is highly related to the SCREP-based pristine basalts.

DISCUSSIONS:

The nTB and TBD results are consistent with the basaltic units mapped by Kramer et al. [2]. Among all 21 units, most unit boundaries (in the case of 17 units) agree with the TBD results, but the boundaries of the WCF1, WCF3, ECF1, and ECF4 units do not. In particular, the TBD results for the WF4, WF5, WCF4, WCF6, ECF3, and ECF5 units strongly agree with the basaltic units obtained by Kramer et al. [2]. These indicate that the SCREP methodology and MRM data are consistent when it comes to characterizing basaltic units contaminated by impact crater ejecta.

The average Pearson correlation coefficient (PCC) is calculated, which are 0.77, 0.90, and 0.86 between the four-channel TBDs and the FeO abundances, the TiO_2 abundances, the (FeO + TiO_2) abundance of all units. Generally, the PCC results indicate that there is a very strong correlation between the TBD and the pristine basalt compositions of the units.

Therefore, compared with the optical detection results, the TB, especially the TBD, is highly related to the (FeO + TiO_2) abundance of the surface deposits and can represent the composition and distribution features of pristine basaltic units contaminated by impact crater ejecta.

ACKNOWLEDGEMENT:
This research was funded by the National Key R&D Program of China (No. 2021YFA0715104), the National Natural Science Foundation of China (No. 42071309), and the Strategic Priority Research Program of the Chinese Academy of Sciences (No. XDB 41000000).

REFERENCES:

[1] Williams N.R., Bell J.F., III; Watters T.R., Banks M.E., Daud K., French R.A. Evidence for recent and ancient faulting at Mare Frigoris and implications for lunar tectonic evolution // Icarus. 2019. V. 326. P. 151-161.
[2] Kramer G., Jaiswal B., Hawke B., Öhman T., Giguere T., Johnson K. The basalts of mare Frigoris // J. Geophys. Res.: Planets. 2015. V. 120. P. 1646-1670.
[3] Lei J., Meng Z., Wang Y., Huang S., Ping J., Cai Z., Zhang Y. Potential Applications of CE-2 Microwave Radiometer Data in Understanding Basaltic Volcanism in Heavily Ejecta-Contaminated Mare Frigoris // Remote Sens. 2022. V. 14. Art. No. 2725.
[4] Zheng Y., Chan K.L., Tsang K.T., Zhu Y., Hu G.P., Blewett D.T., Neish C. Analysis of Chang'E-2 brightness temperature data and production of high spatial resolution microwave maps of the Moon // Icarus. 2019. V. 319. P. 627-644.
[5] Meng Z., Chen S., Zheng Y., Cheng W., Zhu Y., Cai Z., Zhang Y., Cao W., Hou L. Mare Deposits Identification and Feature Analysis in Mare Australe Based on CE-2 CELMS Data // J. Geophys. Res.: Planets. 2020. V. 125. Art. No. e2019JE006330.

LOW FREQUENCY RADIO INTERFEROMETRY FROM THE LUNAR ORBIT

X. Chen[1]
[1] *National Astronomical Observatories, Chinese Academy of Sciences, Beijing, China, xuelei@bao.ac.cn*

Keywords:
Dark age, cosmic dawn, lunar orbit, ultralong wavelength, interferometer array

Introduction:

Observing the radio astronomical signal at low frequency on the ground is hindered by strong refraction, reflection and absorption by the ionosphere of the Earth, especially at frequencies below 30 MHz. There is also a large amount of naturally produced or man-made electromagnetic radiation on the Earth in this frequency band, which is reflected in the ionosphere and propagates in a wide range, further interfering with the observation of astronomical signals. This frequency band is denoted as the MF and HF frequency bands in radio engineering, but belongs to the lowest frequency band in radio astronomy (electromagnetic waves are difficult to propagate in the interstellar medium at frequencies below 0.3 MHz). Here we refer it as ultra-long wavelength. Ground observations are scarce in this band, and space observations are limited to the RAE-1, IMP-6, and RAE-2 satellites in the 1960s and 1970s, and some low frequency payloads on space probes such as WIND, Cassini, Parker, etc., the angular resolution and sky coverage are very limited. So far, little is known about astronomical radio sources in this band, and there is not a good full sky map available (see [1] for review).

In recent years, as we begin to probe the cosmic history at higher redshifts, especially the dark ages and cosmic dawn, the low end of the radio spectrum attracts great interest. The dark ages of the universe refer to the time from the end of the Big Bang and the recombination of protons and electrons to form hydrogen atoms (the age of the universe is 380,000 years, redshift ~1100), until the formation of the first generation of stars and galaxies (theoretical estimation of the age of the universe is about 100 million) year, redshift ~30) an evolutionary stage. The dark age is the initial stage of the formation of the cosmic structure. In this stage, the original density disturbance gradually grows into the seeds of galaxy formation, which contains extremely rich cosmological primitive information. Observation and exploration of this evolutionary stage are extremely important for obtaining a complete picture of the evolution of the universe, understanding the origin of the structure of the universe, and exploring the basic physical laws of the universe. However, since stars, galaxies and other celestial bodies have not yet formed during this period, baryonic matter mainly exists in the form of atomic gas of hydrogen and helium. The only direct observation method known at present is by the so called 21 cm line of the neutral hydrogen, which is generated by the hyperfine structure transition of the hydrogen atoms at 1420 MHz. The 21 cm spectral line in the dark age is redshifted to below 45 MHz, and the cosmic dawn signal is redshifted to the 45–130 MHz band. However, compared with foreground radiation such as galactic radiation, the redshifted 21 cm signal from the dark ages and cosmic dawn is very weak, and its detection is a huge challenge [2].

In order to detect the redshifted 21 cm signal, especially at the higher redshifts corresponding to lower frequencies, it is desirable to make observation from space, especially from the far side of the Moon, where the radiation from the Earth is blocked. Making radio observations from the orbit around the Moon is especially convinient to realize in near term, the part of orbit behind the Moon provides the perfect environment against the radio emissions from the Earth. The orbital period is a few hours, so the energy can be easily supplied with solar power. The data can be transmitted back to the Earth when the satellite is on the near side, without the need of another relay sat-

ellite, and the complicated landing and deployment are also avoided. Even a single lunar satellite could measure the global average spectrum, i.e. the spectrum of the radiation averaged over the whole sky. The image of the sky can also be obtained by interferometry.

The lunar orbit ultralong wavelength observation can be realized as a standalone mission. In the US, the DARE mission was proposed to probe the cosmic dawn by measuring the global spectrum, and later it has evolved to the DAPPER mission which is to measure the global spectrum at lower frequencies and to observe the cosmic dawn. A mission concept called PRATUSH was proposed by Indian scientists. In China, we have a Discovering the Sky at Longest wavelength (DSL) mission concept developed, which will not only measure the global spectrum with a single satellite, but also to map the sky at the ultralong wavelength band using interferometry with a microsatellite array [1, 3, 4].

On a smaller scale, the lunar orbit observation can also be a part of a more general lunar mission. During the Chang'e-4 mission, for example, two microsatellites, Longjiang-1 and Longjiang-2 were piggy-backed. Unfortunately, Longjiang-1 had a malfunction and was lost. Nevertheless, Longjiang-2 detected radio signals from the Earth. In the future International Lunar Science Station program, there may be further opportunities for such orbital observations.

LUNAR ORBIT INTERFEROMETRY:

It is not necessary to maintain the satellites at precise orbital locations, which would require much adjustment of their orbit. However, we do have to be able to measure the relative positions of the satellites. This can be achieved by a combination of microwave data link and optical star sensors.

The inter-satellite communication as well as ranging and clock synchronization can all be realized with one microwave link by using the dual one-way ranging (DOWR) principle, and simultaneous operation with all satellites can be achieved easily with frequency division multiplexing. The distance between the satellites can be obtained by multiplying the real time differences with speed of light. After this measurement, the clocks are also synchronized.

The direction of the vector between the satellites is determined by locating the position of one target satellite against the star background using the star sensor camera. An LED lamp is carried by the target satellite for identification. This method of measurement is not affected by the mechanical installation error of the equipment and satellite attitude error as long as they are within the range to allow normal operation. The angular accuracy is mainly determinant by the angular precision of star sensor camera.

Data communication is a major limiting factor, especially for downloading the data to ground. One of the satellites can be designated as a mother satellite, which can be larger and equipped with a high gain antenna. It is generally difficult at present to transmit the whole band. However, it should be possible to select certain frequency channels and send the interferometry data within these channels back.

Interferometry between an orbiter and ground-based telescopes have been performed before, but the lunar orbit interferometry at the Ultralong wavelength has some different characteristics. On the one hand, for the long wavelengths, it is easier to achieve stable interferometry.

The wavelength is typically longer than the antenna, so the antennas are typically electrically small, and the field of view (FoV) is large. In practice, we will see the whole sky, so the technology for realizing the interferometry is generally different. Many methods have been developed to deal with large FoV for ground based arrays, but these algorithms are not applicable. For example, in ground based observation, there is always a ground-screen (either part of the instrument or the Earth itself) that restricts the FoV to at most half of the sky. Here sources on both sides of the orbital plane are in view, resulting in a 'mirror symmetry' problem. However, as the orbital plane processes in the gravitational field of the Moon and the Earth, a 3D distribution of baselines will be formed. This will complicate the sky reconstruction process as the so

called “w-term” cannot be neglected, but the mirror symmetry is broken. Moreover, the baselines formed by the satellites depend on their position on the lunar orbit, but the Moon also blocks part of the sky as the satellites move along the orbit, so strictly speaking the visiblities for different baselines correspond to a varying sky. New imaging algorithm needs to be developed, which are likely to be computationally expensive as they will need to make use of the full 3-D distribution of *u*, *v*, *w* points [5, 6].

CONCLUSION:

The ultra-long wavelength radio signals have great potentials for scientific breakthrough, especially for the study of the cosmic dawn and dark ages. Imaging the neutral hydrogen distribution during the dark ages can provide valuable information about the primordial density perturbations and the inflationary origin of the Universe, but this requires extremely large arrays on the far side of the Moon. A useful and practical first-step is to map the foreground which is necessary for the design of future dark ages experiments, and to measure the global spectrum with high precision, which gives a first peek of the cosmic dawn and dark age. This first step can be made in the coming decade with a lunar orbit array. The technologies required by such a mission are being developed. International collaboration would enrich and advance these researches.

REFERENCES:

[1] Chen X. et al. Discovering the Sky at the Longest Wavelengths with Small Satellite Constellations // Taikong. 2019. V. 14. No. 1. 62 p. arxiv:1907.10853.
[2] Chen X.. Miralda-Escudé J. The spin-kinetic temperature coupling and the heating rate due to Lyα scattering before reionization: predictions for 21-centimeter emission and absorption // Astrophysical J. 2004. V. 602. P. 1-11.
[3] Koopmans L. et al. Peering into the Dark (Ages) with Low-Frequency Space Interferometers. 2019. 24 p. arxiv:1908.04296.
[4] Chen X.; Yan J., Deng L., Wu F., Wu L., Xu Y., Zhou L. Discovering the Sky at the Longest wavelengths with a lunar orbit array // Philosophical Trans. Royal Society A. 2021. V. 379. Art. No. 20190566.
[5] Huang Q., Sun S., Zuo S., Wu F., Xu Y., Yue B., Ansari R., Chen X. An Imaging Algorithm for a lunar Orbit Interferometer Array // Astronomical J. 2018. V. 156. Art. No. 43.
[6] Shi Y., Xu Y., Deng L., Wu F., Wu L., Huang Q., Zuo S., Yan J., Chen X., Imaging sensitivity of a linear interferometer array on lunar orbit // Monthly Notices of the Royal Astronomical Society. 2021. V. 510. Art. No. 3046.

SUGGESTION OF AN EXPERIMENT FOR MEASURING THE FLUXES OF ENERGETIC GALACTIC AND SOLAR PROTONS AND NUCLEI ONBOARD FUTURE LUNAR STATION

M.V. Podzolko[1], V.V. Kalegaev[1]
[1] *Skobeltsyn Institute of Nuclear Physics Lomonosov Moscow State University, Moscow, Russia; spacerad@mail.ru*

KEYWORDS:
Solar cosmic rays, galactic cosmic rays, energetic protons and nuclei

The fluxes of protons and nuclei of galactic cosmic rays (GCR) and solar cosmic rays (SCR) with energies from tens of MeV/nucleon to several GeV/nucleon have negative impact on the spacecraft's electronic equipment and crews; and at the same time carry the information about the physics of the Sun and heliosphere.

Measurements of these fluxes by instruments onboard the automated spacecraft were carried out during the last several decades. They allowed determining the principal quantitative and physical characteristics of these fluxes and provided the basis for developing their empirical and physical models. However, until now we still do not have the high enough quality data on the fluxes in the considered energy range, with few exceptions like measurements of proton and He fluxes by PAMELA instrument, for developing the accurate quantitative models.

To some extent, it has the objective reasons. Instruments have low series due to high cost of the high-orbit launches, it is hard to model the conditions of instrument functioning in space during its development on the ground, and provide the instrument debugging and receiving the big amount of data during its functioning onboard the automated spacecraft. Therefore, placing the instrument on the long-term regularly serviced crewed station outside the Earth's magnetosphere gives the unique opportunity to provide the precise GCR and SCR flux measurements.

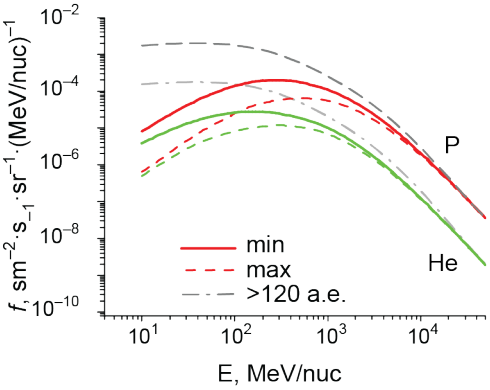

Fig. 1. GCR proton and He energy spectra outside the heliosphere and in the Earth's orbit during solar minimum and maximum. In the Earth's orbit spectra have the bell-like shape with maximum around 300–700 MeV/nucleon due to the solar modulation.

A particular problem of measuring GCR fluxes below 500 MeV is their contamination by the higher energy fluxes passing through the sides of the instrument, which are considerable due to the shape of the GCR energy spectra (Fig. 1). The high contaminated background fluxes also prevent accurate registration of the small solar proton events.

A method for distinguishing the contaminating particles is the "anti-coincidence guard" — massive scintillation detector surrounding the main "tele-

scope" (Fig. 2). But practically in many high-orbit spacecraft instruments for measuring the considered particle fluxes the anti-coincidence guard was not installed (e.g. GOES and Electro-L series geostationary satellites, proton channels on ACE spacecraft) or not working properly (e.g. IMP-8).

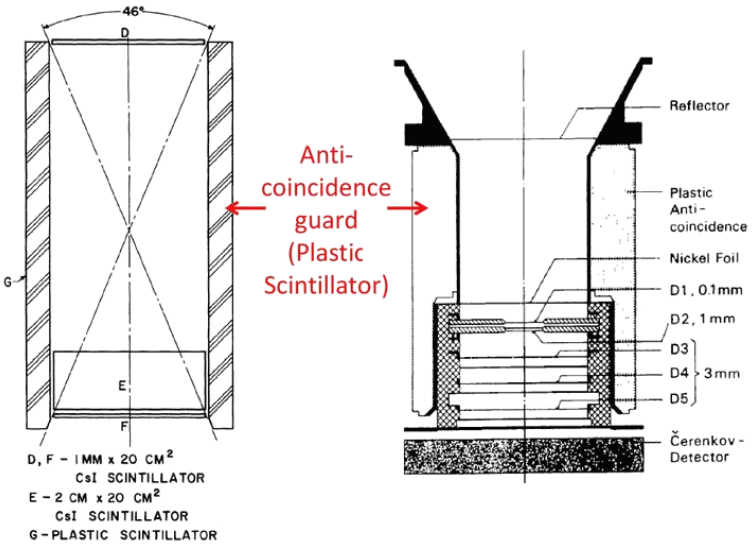

Fig. 2. IMP-8/MED and Helios/E6 instruments for measuring the fluxes of interplanetary proton and nuclei with energies of tens-hundreds MeV/nucleon. Instrument consists of a "telescope" with several semiconductor, scintillation of Cherenkov detectors, surrounded by "anti-coincidence guard".

Another method is using the matrix detectors to determine the particle's direction. But it increases the instrument complexity.

The proposed instrument for measuring the fluxes of interplanetary protons and nuclei with energies ≈10–500 MeV/nucleon for the suggested experiment onboard the future lunar station can be developed on the basis of existing SINP MSU instruments, currently functioning onboard Russian Electro-L, Meteor-M and Arctica-M Earth satellites (see e.g. [1, 2]), or a module of "NUCLON" instrument [3].

REFERENCES:

[1] Vlasova N.A., Ginzburg E.A., Kalegaev V.V. et al. Penetration of solar cosmic rays into the Earth's magnetosphere on January 28, 2012 // Cosmic Research. 2013. V. 51. No. 5. P. 319-325.

[2] Zolotarev I.A., Novikov L.S., Osedlo V.I., Tulupov V.I., Chirskaya N.P. Numerical simulation of metrological characteristics of cosmic radiation detectors // Inorganic Materials: Applied Research. 2017. V. 8. No. 2. P. 222-228.

[3] Atkin E., Bulatov V., Dorokhov V. et al. The NUCLEON space experiment for direct high energy cosmic rays investigation in TeV–PeV energy range // Nuclear Instruments and Methods in Physics Research, Section A: Accelerators, Spectrometers, Detectors and Associated Equipment. 2015. V. 770. P. 189-196.

THE NEUTRONIUM EXPERIMENTAL COMPLEX FOR THE RUSSIAN LUNAR SCIENTIFIC OBSERVATORY

A. Turundaevskiy[1], L. Kuzmichev[1], A. Panov[1], D. Podorozhny[1]
[1] *Moscow State University, Skobeltsyn Institute of Nuclear Physics; turun1966@yandex.ru*

An original idea is proposed for energy measurements. The back scattered radiation from hadron and electromagnetic cascades generated by the primary particle in the lunar regolith is registered on the Moon surface. There are three components of this radiation including gamma, neutrons and radio. It is proposed to place 100 identical autonomous modules in an area of ~100 m^2.

This technique gives new opportunities for perspective research:

- the direct study of CR in the energy range with individual particle charge resolution up to 10^{14}–10^{17} eV;
- detailed study of superheavy CR nuclei behind the iron peak;
- the increase in sensitivity in the study of gamma astronomy is almost two orders of magnitude higher than existing and planned projects.

The design and expected statistics were determined, the neutron and gamma background values were estimated. The simulation results are presented.

THE WATER ABUNDANCE AT ARTEMIS LANDING SITES

M.V. Djachkova[1], I.G. Mitrofanov[1], M.L. Litvak[1], A.B. Sanin[1]
[1] *Space Research Institute, Moscow, Russia, djachkova@np.cosmos.ru*

KEYWORDS:
Moon, water, South Polar region of the Moon, LEND, LRO, Artemis

The NASA agency has identified 13 candidate landing regions near the lunar South Pole. Each region contains multiple potential landing sites for Artemis III, which will be the first of the Artemis missions to bring crew to the lunar surface.

NASA identified the following candidate regions for an Artemis III lunar landing: Faustini Rim A, Peak Near Shackleton, Connecting Ridge, Connecting Ridge Extension, de Gerlache Rim 1, de Gerlache Rim 2, de Gerlache-Kocher Massif, Haworth, Malapert Massif, Leibnitz Beta Plateau, Nobile Rim 1, Nobile Rim 2, Amundsen Rim. Each of these regions is located within six degrees of latitude of the lunar South Pole and, collectively, contain diverse geologic features. Together, the regions provide landing options for all potential Artemis III launch opportunities. Specific landing sites are related to the timing of the launch window, so the actual landing site will be selected when the specific date is determined.

Besides the launch window criterion the criteria of a safe landing (terrain slope, possibility of communications with Earth, lighting conditions) will be considered.

To fulfill the scientific goals of the mission the study of volatiles should be performed. The most promising areas within the selected candidate regions will be evaluated based on the LEND instrument data onboard LRO.

AVAILABILITY OF LROC NAC STEREO IMAGES FOR CONSTRUCTION OF DETAILED DEMS AT THE SOUTH SUBPOLAR REGION OF INTEREST FOR RUSSIAN LUNAR MISSIONS

N.A. Kozlova[1], I.E. Nadezhdina[1], N.A. Slodarzh[1], I.P. Karachevtseva[1], A.E. Zubarev[1]
[1] *Moscow State University of Geodesy and Cartography, MIIGAiK Extraterrestrial Laboratory, Moscow, Russia; n_kozlova@miigaik.ru*

KEYWORDS:
The Moon, stereo, DEM, LROC NAC, LEND, landing site

INTRODUCTION:
Recently, with the expansion of space programs, LRO (Lunar Reconnaissance Orbiter) data is widely used in the selection of spacecraft landing sites. LRO data consists of images with the maximum spatial resolution of 0.3–1.0 m/pixel (with some possibilities of obtaining stereo) provided by the Narrow Angle Camera (NAC) and laser altimetry data obtained by the LOLA instrument. Combination of these data provides complex information about the surface. Long operation period of the LRO spacecraft (since 2009) has allowed us to accumulate a significant archive of such data and it continues increase.

However, LROC NAC camera was not constructed to provide continuous stereo cover of the lunar surface, so stereo images (which are needed to generate DEM) can be obtained only occasionally, when the spacecraft is specially tilted. Such occasions are rather seldom as they need changes in LRO orbit and influence other experiments onboard.

THE STUDY:
During the study we have made analyses of NAC stereo availability at lunar South polar region (75–87° S and 40° W–60° E). At first, we have taken a list of stereo images provided by LROC team [https://wms.lroc.asu.edu/lroc/view_rdr/SHAPEFILE_STEREO_OBSERVATIONS_SP]. It includes places with special stereo survey provided by LROC team. It shows 76 stereo images at the selected region and all of them are near 85° S and higher (see green footprints in Fig. 1). But apart from these, there are a few more images which were not planned as stereo but may have sufficient angle to provide information about heights and have enough illumination for photogrammetric processing (as it also can be a problem, especially in high latitudes). We have found 93 such images with potential stereo (red footprints in Fig. 1) in addition to ones mentioned as special stereo (green footprints).

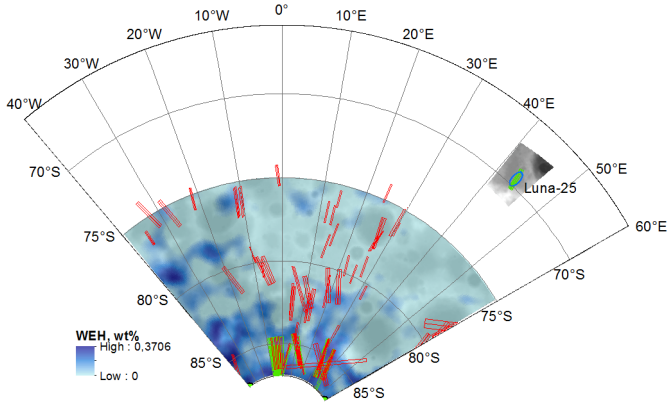

Fig. 1. Map of WEH abundance in the South polar region [2] and possible stereo coverage of LROC NAC images.

Then we wondered how the (potential) stereo covering corresponds to areas of the most interest for future exploration — regions with higher hydrogen

concentrations. For this purpose we used map of WEH (water equivalent hydrogen) abundance in the South polar region [2], obtained based on the Lunar Exploration Neutron Detector (LEND) data.

Figure 1 shows that stereo coverage at the South polar region is low even with added potential stereo footprints, however there are several areas with WEH > 0.1520.18 where we can expect to obtained detailed DEM.

CONCLUSION:

Additional stereo images are only most promising candidates for stereo processing and do not guarantee construction of high-resolution DEM for all regions. At this study we have taken into consideration images with tilts (stereo angle) more than 5°, while special stereo survey suggests 10–20°. Such small stereo angle will affect vertical accuracy of generated DEMs. This issue for the selected images will be studies in further work.

Up to date, the presented map (Fig. 1) gives the most full information on possible stereo coverage for the studying region.

REFERENCES:

[1] NAC Stereo Observations (60S to 90S) Shapefile https://wms.lroc.asu.edu/lroc/view_rdr/SHAPEFILE_STEREO_OBSERVATIONS_SP.

[2] Sanin A.B., Mitrofanov I.G., Litvak M.L., Bakhtin B.N., Bodnarik J.G., Boynton W.V., Chin G., Evans L.G., Harshman K., Fedosov F., Golovin D.V., Kozyrev A.S., Livengood T.A., Malakhov A.V., McClanahan T.P., Mokrousov M.I., Starr R.D., Sagdeev R.Z., Vostrukhin A.A. Hydrogen distribution in the lunar polar regions // Icarus. 2017. V. 283. P. 20-30. https://doi.org/10.1016/j.icarus.2016.06.002.

DRILLING OF ICE-RICH REGOLITH: VIBRATION AND BLOCKING ISSUES

S.N. Ponomareva[1], A.A. Kim[1], T.M. Tomilina[1], Sh.A. Asfandiyarov[1], T.O. Kozlova[2], M.L. Litvak[2]
[1] *Mechanical Engineering Research Institute RAS, Moscow, Russia;*
[2] *Space Research Institute, Moscow, Russia*

KEYWORDS:
Moon exploration, lunar regolith, drilling process

Drilling instrument of lunar polar regolith is now included in the payload of future mission Luna-27, which will land to the Moon in the vicinity of South pole [1]). The task of this instrument is acquisition of samples of lunar material from the 1–2 m deep shallow subsurface for further *in situ* investigation onboard the lander.

Drilling of lunar regolith has already been successfully accomplished with human and robotic instrumentation in several past missions (e.g. see [2, 3]). However, they all have landed at moderate latitudes. The regolith at landing sites was extremely dry material. The polar regolith is known might have water ice in the porosity volume between grains, which is new specific property of this material in comparison with regolith at moderate latitudes (e.g. see [4]).

Report presents the first results of studying the conditions of drilling process of a such heterogeneous material, which the polar regolith is thought to be, with the main attention to conditions of vibrational instability and blocking. The laboratory experiment is proposed to test the drill prototype for determining the requirements to space instrument for avoidance of vibrational instability and blocking during the drilling process of regolith with different content of water ice.

REFERENCES:
[1] Tretyakov V.I., Zelenyi L.V., Mitrofanovl. G. Overview of Luna-27 science instruments // 12th Moscow Solar System Symp. 2021. Art. No. 422.
[2] Basilevsky A., Ivanov B., Ivanov A., Head J. Clarification of sources of material returned by Luna-24 spacecraft based on analysis of new images of the landing site taken by lunar reconnaissance orbiter // Geochem. Int. 2013. V. 51. P. 456-472.
[3] Crouch D. Final Report for Apollo Lunar Surface Drill (ALSD) / Martin Marietta Engineering. Report No. ER 14778. Baltimore: Martin Marietta, MD, 1968.
[4] Schorghofer N., Aharonson O. The lunar thermal ice pump // Astrophys. J. 2014. V. 788. Art. No. 169.

STATIONARY AND MOBILE LUNAR GRAVIMETERS

O.O. Shevaldysheva[1,2], I.V. Lygin[1], E.N. Slyuta[2]
[1] *Lomonosov Moscow State University, Moscow, Russia;*
[2] *Vernadsky Institute of Geochemistry and Analytical Chemistry RAS, Moscow, Russia*

KEYWORDS:
Moon, gravity field, mascon, gravimeter, GRAIL

INTRODUCTION:

Currently, among all the geophysical methods that are used in the study of the deep structure of the Moon, gravimetry is the mostly supported with data for detailed analysis. The main source of information in this study was the GRAIL (Gravity Recovery and Interior Laboratory) satellite gravimetric mission, carried out in 2012 at an average altitude of 55 km from the surface of the Moon with the largest intertrack distance of 31 km [1]. The standard error of observations was estimated at ±8.92 mGal for the GRGM900C field model [2]. The accuracy and the level of details of the gravimetric data for the middle latitudes, according to our estimates, corresponds to a scale of no greater than 1:10 000 000. In the GRGM1200B model of gravitational field [3] received during the GRAIL mission it is possible to distinguish isometric (mascons) and linear (most likely of magmatic genesis [4]) anomalies, but the width of the smallest valid anomalies does not exceed 50 km.

To solve problems related to the study of the internal structure of the Moon to the depths of the first kilometers (search and exploration of minerals such as water ice, regolith, helium-3 and rare earth minerals [5], as well as the selection and research of areas eligible for the further construction of scientific bases and transfer points of spacecrafts), the received gravimetric data is not sufficient. Based on the current level of technology development, the authors believe that conducting more accurate and detailed gravimetric observations in flight over the Moon's surface in the absence of atmosphere is possible only in the long term.

For a more detailed study of the gravitational field of the Moon, including solving problems related to the study of tidal deformations, it is necessary to conduct gravimetric observations on the surface of the Moon, for example, at autonomous automatic scientific stations for long-term monitoring [6]. Mobile gravimeter is also supposed to be used in the complex of scientific equipment of the new generation lunar rover "Robot-Geologist" for lunar regional geological and geophysical survey and exploration [6]. In the past, similar work was carried out during the Apollo-17 mission, for which special gravimetric equipment was developed. The gravimetric observations made using such equipment by the Apollo-17 mission can rather be considered experimental and experimental-methodical. In this regard, there is an acute problem of developing a modern lunar gravimeter, which one will allow to carry out the profile and area gravimetric surveys, as well as long-term observations of variations in the gravitational field, including those caused by tidal deformations of the Moon.

In this research, the authors studied the structure of the gravitational field of the Moon and investigated the features of lunar gravimeters of the past years and some gravimeters that are used on Earth. Their main characteristics are presented in Tables 1 and 2. The last row of each table reflects which of the gravimeters may be the best suited for further work on the lunar surface, where number 1 means the most appropriate device.

Based on the information received, the following basic requirements for modern lunar gravimeters were proposed.

1. To calibrate the gravimeter, a large range of gravity values is required, allowing measurements to be carried out both on Earth and on the Moon.
2. Due to the large temperature difference, high-quality thermoregulation is necessary, ensuring internal temperature stability with a change of no more than 0.01–0.001 K.

Table 1. The main characteristics of the lunar gravimeters of the past years.

	Traverse Lunar Gravimeter TG	Lunar Surface Gravimeter LSG	Lunar Gravimeter Sternberg Astronomical Institute MSU
Solvable problem	Measurements of the Moon's gravitational field	Study of gravitational waves	Comparative measurements of the gravitational field
Type of measuring system	Metal string	Metal test bulk	Pendulum
Mass, kg	14,6	12,7	12
Measurement accuracy, mGal	from ±0,5 to ±5	±13	No data
Thermoregulation	Thermal insulation case, two-level oven: ensuring the desired temperature with an accuracy of 0.01 K	Thermal insulation housing, protection from direct sunlight: ensuring the desired temperature with an accuracy of 0.01 K	Thermostatic container
Ranking by suitability for further work	1	2	3

Table 2. The main characteristics of the considered Earth gravimeters.

	Scintrex CG-5, CG-6	**Gas and liquid gravimeters**	**Quantum gravimeter**	**Strapdown airborne gravimeter iCORUS**
Solvable problem	Comparative measurements of the gravitational field	Measurement of gravity increment	Absolute gravity measurements	Gravity measurement on a movable base
Type of measuring system	Test mass on quartz spring	Gas-liquid	Free fall atoms	Accelerometers
Mass, kg	5,5-8	No data	>35	14-30
Measurement accuracy, mGal	±0,0001	from±3 to ±5	up to ±0,001	±0,2
Thermoregulation	Thermostatic two-level vacuum compartment	Cold storage, Dewar vessel Revision required	Vacuum thermostatic compartment	Thermostatic, electric heaters
Ranking by suitability for further work	3	2	4	1

3. When working in space conditions without the astronauts' participation, automation of all gravimeter operations or the possibility of remote control should be ensured.
4. Sufficient strength to withstand shock and vibration during the launch, flight and landing of the spacecraft.
5. It should be possible to standardize the gravimeter in the conditions of the Moon, or the possibility of reliable data extrapolation into the gravity values ranges of the Moon for the instrument calibrated on Earth.
6. The small weight and size of the device.

7. Measurement accuracy is not worse than 1 mGal while maintaining a fairly simple and easy-to-use structure.
8. The possibility of carrying out measurements on a movable base.
9. Creation of an autonomous inertial navigation system in the design of a gravimeter, allowing to determine the position of the body without using of external landmarks, as well as the global navigation satellite system of the Moon.

As a prototype, the best option at the moment is a strapdown airborne gravimeter mounted on a lunar rover. This will allow to quickly perform area surveys with an accuracy up to 0.2 mGal. A strapdown airborne gravimeter can also be installed on autonomous jumping capsules [7], but due to the lack of their prototype, it is difficult to say with accuracy which of these vehicles is better. Gas-liquid gravimeters can be used for gravity measurements on the surface of the Moon at rover stops. Even 100 years ago, they showed measurement accuracy of about ± 1 mGal in Earth conditions with a fairly simple structure. However, whichever option is eventually chosen, it anyway requires improvements.

REFERENCES:

[1] Lehman D.H., Watkins M.M., Smith D.E., Zuber M.T. Gravity Recovery And Interior Laboratory-A (GRAIL) // NASA Space Science Data Coordinated Archive. URL: https://nssdc.gsfc.nasa.gov/nmc/spacecraft/display.action?id=2011-046A.

[2] Lemoine F.G., Goossens S., Sabaka T.J., Nicholas J.B., Mazarico E., Rowlands D.D., Loomis B.D., Chinn D.S., Neumann G.A., Smith D.E., Zuber M.T. GRGM900C: GRGM900C: A degree 900 lunar gravity model from GRAIL primary and extended mission data // Geophysical Research Letters. 2014. V. 41. No. 10. P. 3382-3389. https://doi.org/10.1002/2014GL060027.

[3] Goossens S., Sabaka T.J., Wieczorek M.A., Neumann G.A., Mazarico E., Lemoine F., Nicholas J.B., Smith D.E., Zuber M.T. High-resolution gravity field models from GRAIL data and implications for models of the density structure of the Moon's crust // J. Geophysical Research: Planets. 2020. V. 125. Iss. 2. Art. No. e2019JE006086. 31 p. https://doi.org/10.1029/2019JE006086.

[4] Andrews-Hanna J.C., Asmar S.W., Head III J.W., Kiefer W.S., Konopliv A.S., Lemoine F.G., Isamu M., Mazarico E., McGovern P.J., Melosh H.J., Neumann G.A., Nimmo F., Phillips R.J., Smith D.E., Solomon S.C., Taylor G.J., Wieczorek M.A., Williams J.G., Zuber M.T. Ancient Igneous Intrusions and Early Expansion of the Moon Revealed by GRAIL Gravity Gradiometry // Science. 2013. V. 339. Iss. 6120. P. 675-678. DOI: 10.1126/science.1231753.

[5] Alifanov O.M., Anfimov N.A., Belyaev V.S., Bodin B.V., Boyarchuk A.A., Galimov A.M., Galper A.M., Golovko A.V., Grigoryev A.I., Gubaidullin V.S., Gubertov A.M., Elkin K.S., Zaharov A.I., Zatsepin V.I., Ilyin V.K., Karabadjak G.F., Kardashev N.S., Kovkov D.V., Kovalyev U.U., Kuzhetsov V.D., Kurt V.G., Lukash V.N., Lutovinov A.A., Makarov U.N., Malchenko A.N., Manko A.S., Marov A.Y., Matafonov A.P., Milyukov V.K., Miheeva E.V., Morukov B.V., Pavlinskiy M.N., Panasyuk M.I., Panichkin N.G., Pikuz S.A., Pichhadze K.M., Popov G.A., Popovkin V.A., Prohorov M.E., Raikunov G.G., Revnivtsev M.G., Slyuta E.N., Smirnov A.V., Uspenskiy G.R., Ushakov I.B., Fortov V.E., Hartov V.V. Cherepash'uk A.M., Shevchenko V.V., Shustov B.M. Fundamental Space Research. Book 2. Solar System. M.: Physmatlit, 2014. 456 p. (In Russian.)

[6] Marov M.Ya., Slyuta E.N. Early steps toward the Lunar base deployment: Some prospects // Acta Astronautica. 2021. V. 181. P. 28-39. https://doi.org/10.1016/j.actaastro.2021.01.002.

[7] Sagitov M.U. Lunar gravimetry. M.: Nauka, 1979. 432 p.

DEVELOPMENT OF ROUTES FOR THE HEAVY ROVER LUNAR ROBOT-GEOLOGIST ON THE TERRITORY OF THE VOLCANIC PROVINCE OF MONS RUMKER

O.I. Turchinskaya[1], E.N. Slyuta[1]
[1] *Vernadsky Institute of Geochemistry and Analytical Chemistry, Moscow, Russia; olgaturch@yandex.ru*

KEYWORDS:
Moon, Mons Rumker, Lunar Robot-Geologist, rout, geology

INTRODUCTION:
The surroundings of Mons Rumker were chosen as the most optimal territory for the study of geological-diverse structures and rocks of different ages (from Lower Imbrian Series to Copernican System) for russian heavy rover Lunar Robot-Geologist [2, 3]. This territory is located in the northeast of the visible side of the Moon, in the northern part of the Oceanus Procellarum (Fig. 1). The volcanic province of Mons Rumker is an isometric uplift with a diameter of about 70 km. The excess relative to the surface of the Ocean Storms reaches 1000 m. Also, this area is located in a zone of seismic activity, which is an advantage due to the planned seismic studies carried out by the lunar rover.

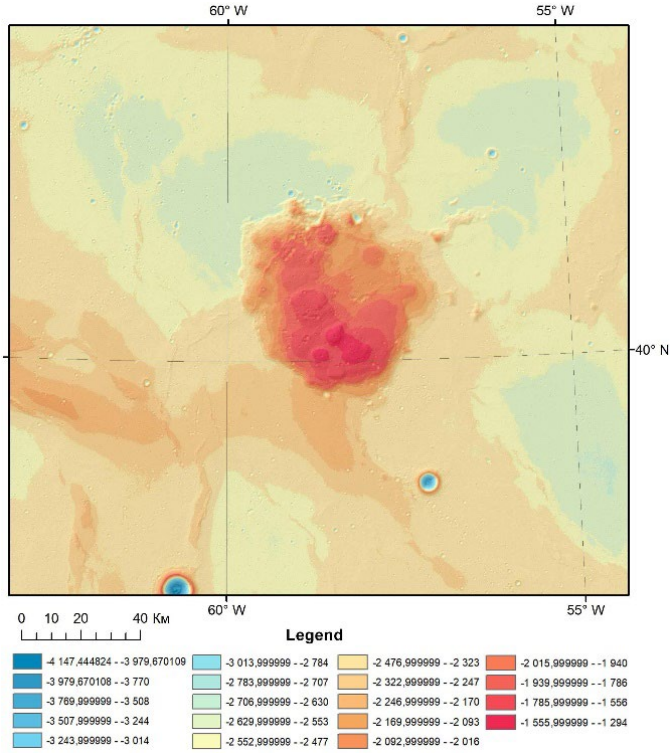

Fig. 1. Hypsometric map of the volcanic province of Mons Rumker and the adjacent plains in the Oceanus Procellarum. The map is based on data from NASA's LOLA LRO laser altimetry.

RESULTS OF MAPPING:
The source of the information was a geological map created by scientists from the United States Geological Survey (USGS) in 1987 and the latest geological map created by scientists from the USGS in collaboration with NASA and the Lunar and Planetary Institute, published in 2020 (Fig. 2).

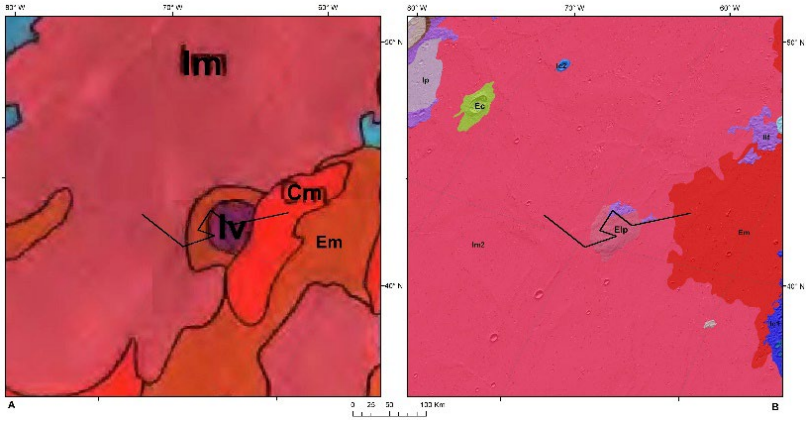

Fig. 2. Geologic maps of Mons Rumker region. A — Geologic map of Mons Rümker region [4]; Im — Imbrian Series basalts; Em — Eratosthenian System basalts; Cm — Copernican System basalts; Iv — volcanic province. B — Geologic map of Mons Rümker region [1]; Im2 — Imbrian Mare, Upper; Em — Eratosthenian Mare; Elp — Eratosthenian Imbrian Plateau; Ec — Eratosthenian Crater; Ic1 — Imbrian Crater, Lower; Ic2 — Imbrian Crater, Upper; Iif — Imbrian Imbrium Fra Mauro Formation; Ip — Imbrian Plains. The line shows the direction of the lunokhod's route of about 370 km in length.

After studying the data from different years, we chose a route for the study that crosses all age groups of marine basalts from the oldest to the youngest (Imbrian, Eratosthenian and Copernican).

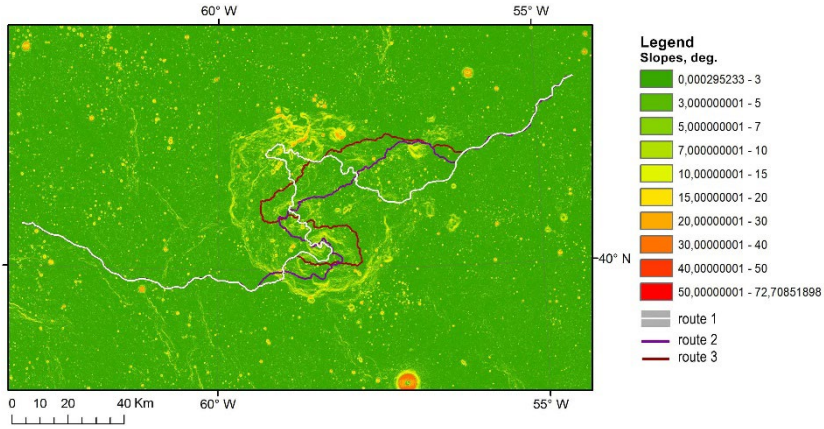

Fig. 3. Slope map of the surface of Mons Rumker and the surrounding area with the proposed routes of the robot geologist based on 60 m.

Planning the lunar rover's route should take into account a number of limiting factors for its movement. Based on the technical characteristics of a heavy geologist robot, this are the magnitude of the slope of the surface, the radius of concavity and curvature of small mesoforms of the relief, for example, craters, and the height of obstacles. The robot is able to overcome areas with a slope of 30° with a connected ground, and with a slope of 20° with an incoherent one. Variants of the proposed route of the lunar rover were compiled based on the degree of surface slopes. So, priority was given to relatively flat areas, as a result of which there were several options for laying the route of the robot (Fig. 3). As a result of the work, terrain profiles were created for each of the routes (Fig. 4).

Next, a more detailed map of the geological structure of Mons Rumker [3] was used to recreate the most detailed picture of the geological structure of the territory (Fig. 5).

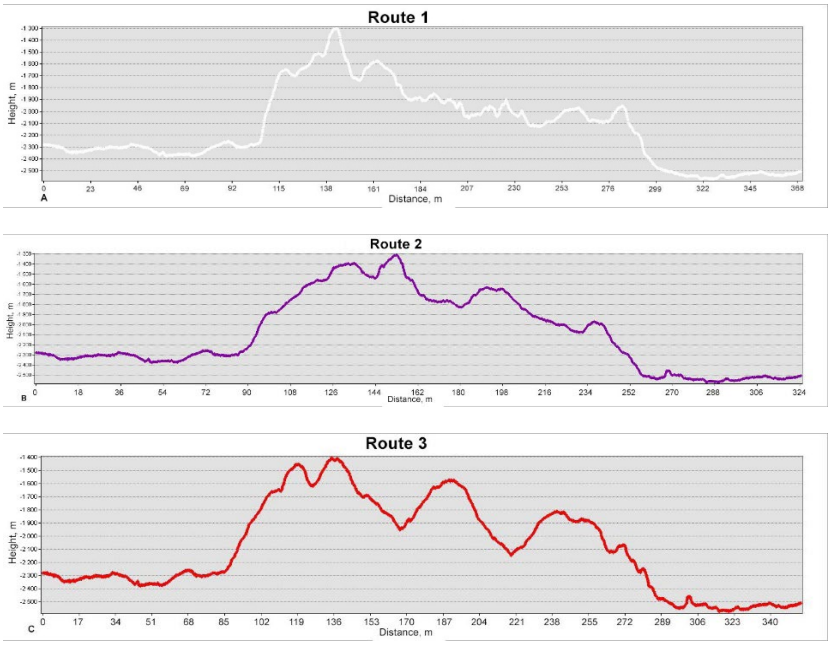

Fig. 4. A — terrain profile on route 1; B — terrain profile on route 2; C — terrain profile on route 3.

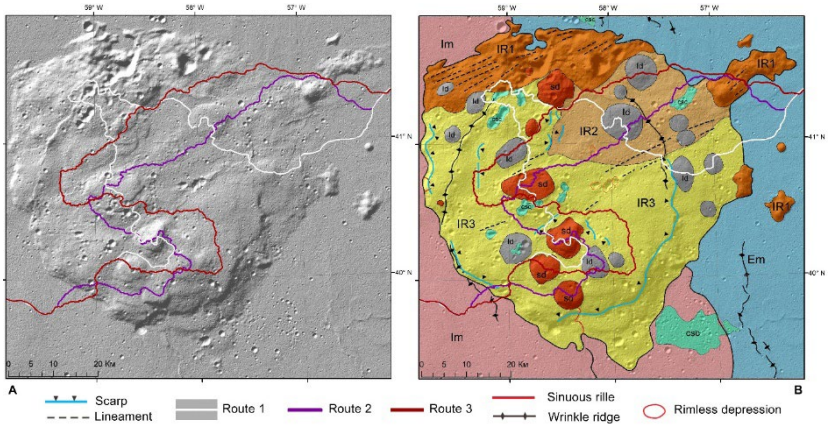

Fig. 5. A — relief map of Mons Rumker with a hillshade with the proposed routes of the lunar rover. B — geological map of Mons Rumker according to [5] with the proposed routes of the lunar rover; Im — Upper Imbrium Mare Materials; Em — Eratosthenian Mare Materials; lR3, lR2, lR1 — Upper Imbrian Rumker Plateau Materials; ld — Upper Imbrian Dome Materials; sd — Upper Imbrian-Eratosthenian Dome Materials; csc — Copernican Crater Materials.

REFERENCES:

[1] Fortezzo C.M., Spudis P.D., Harrel S.L. Release of the Digital Unified Global Geologic Map of the Moon At 1:5,000,000-Scale // 51st Lunar and Planetary Science Conf. Houston, TX. 2020.
[2] Slyuta E.N., Galimov E.M., Marov M.Ya. Thematic geological survey on the Moon // Fundamental space research / ed. G.G. Raikunov. M.: Fizmatlit, 2014. V. 2. P. 103-128.
[3] Slyuta E.N. // 7MS3 Abst. 2016. #PS-18.
[4] Wilhelms D.E. The Geologic History of the Moon // USGS Prof. 1987. Art. No. 1348.
[5] Zhao J.N., Xiao L., Qiao L., Glotch T.D., Huang Q. The Mons Rumker volcanic complex of the Moon: a candidate landing site for the Chang'E-5 mission // J. Geophysical Research: Planets. 2017. V. 122(7). P. 1419-1442.

THE SEISMO-LR IS A THREE–COORDINATE SEISMOMETER FOR MEASUREMENTS ON THE MOON

Manukin A.B[1,2], Kalinnikov I.I.[2], Sayakina N.F.[1], Tonshev A.K.[1], Chernogorova N.A.[1]
[1] *Space Research Institute, Moscow, Russia, amanukin@yandex.ru*
[2] *Schmidt Institute of Physics of the Earth RAS*

KEYWORDS:
Sensor, test mass, sensitivity, thermal fluctuations, seismic measurements, gravity, slopes, tidal processes

The issues of studying the seismic activity of the Moon, its internal structure, obtaining data on tidal fluctuations, etc. by measurements in the circumpolar region belong to the category of fundamental tasks. The issues of constructing a three-coordinate seismic accelerometer for measurements on the Moon (Luna Resource project) based on the SEM seismometer for measurements on Mars (Exo-Mars project) are considered [1, 2]. The device consists of 3 uniaxial sensing elements installed so that their axes of sensitivity are at the same angle 54° to the local gravitational vertical. In each uniaxial sensing element, along with mechanical rigidity, magnetic rigidity is introduced. By moving the permanent magnet, it is possible to change the equilibrium position of the test mass. This makes it possible, without changing the value of the test mass (as in the first version of the lunar seismometer), to adjust each sensitive element to the conditions of lunar gravity. The device must be tilted so that the projection of the Earth's gravity on the sensitivity axis of each sensor is equal to the lunar gravity. After that, the device is ready to perform measurements on the moon. The use of capacitive converters of small mechanical displacements of test masses into an electrical signal makes it possible to conduct measurements in the classical seismic frequency range (0.1–10 Hz) and in the quasi-static spectral region to measure slopes and variations in the acceleration of free fall. The ultimate sensitivity is limited by equilibrium thermal fluctuations. The sensitivity of seismic measurements by the amplitude of base vibrations in the vicinity of 1 Hz is ~$4{,}5\cdot10^{-11}$ m, the sensitivity of slope measurements is ~3·10-8 rad in the range of 0.02 rad, and the variations in the acceleration of gravity are $1{,}8\cdot10^{-9}$ m/s^2. This makes it possible to study tidal processes and libration fluctuations of the Moon. All pre-flight tests were successfully carried out on the SEM device, on the basis of which the SEISMIC-LR device is being created [3, 4]. The main difference from the SEM device is the measurement on the lander, and not on the surface of the Moon. Unlike Martian conditions, where intense winds do not allow measurements to be made on the lander, there is no atmosphere on the Moon. The high rigidity of the descent vehicle (the lower natural frequency of mechanical vibrations of at least 40 Hz) ensures the transmission of vibrations of the Lunar surface in the seismic frequency range practically without damping them.

REFERENCES:

[1] Manukin A.B., Kazantseva O.S., Kalinnikov I.I. A new version of a highly sensitive uniaxial sensor of a seismoaxelerometer // Seismic Instruments. 2018. V. 54. No. 4. P. 66-76. DOI: 10.21455/si2018.4-5.
[2] Andreev O.N., Kalyuzhny A.V., Manukin A.B. et al. Space Research: Gravitoinertial Instruments // Seismic Instruments. 2018. V. 54. No. 5. P. 557-561.
[3] Manukin A.B., Kazantseva O.S., Kalinnikov I.I., Matyunin V.P., Sayakina N.F., Tonshev A.K., Chernogorova N.A. Seismometer for observations on Mars // Space Research. 2021. V. 59. No. 5. P. 418-427. DOI: 10.31857/S0023420621050083. (In Russian.)
[4] Manukin A.B., Kalinnikov I.I., Matyunin V.P., Sajakina N.F., Tonshev A.K., Chernogorova N.A. Seismometer for measurements on Mars // 12MS3. 11-15 Oct. 2021.

APPLICABILITY OF LASMA-LR MASS-SPECTROMETER FOR THE WATER ICE DETECTION WITHIN LUNAR REGOLITH

V.S. Cheptsov[1], A.E. Chumikov[1], N.G. Managadze[1]
[1] *Space Research Institute, Moscow, Russia*

KEYWORDS:
Element analysis, laser ionization, Luna-25, Luna-27, Moon

INTRODUCTION:
Upcoming missions Luna-25 and Luna-27 are planned to be landed in the South pole region of the Moon. One of the main aims of these missions is the search of water in the regolith. The measuring of the water amount in the regolith is supposed to be carried out using active neutron sensing (ADRON-LR instrument) [1]. At the same time, to fulfill this scientific task, the possibility of using other instruments included in the complex of scientific equipment of these missions is being considered. In particular, both spacecrafts have a LASMA-LR laser ionization time-of-flight mass spectrometer onboard, whose main task is to analyze the elemental composition of lunar regolith [2]. This instrument is designed for the analysis of solid samples and is not intended for the analysis of volatiles [2, 3]. Nevertheless, we have considered some approaches for the analysis of samples during lunar missions to assess the applicability of the LASMA-LR to reveal the water in the regolith.

EXPERIMENT:
At the first step, the fundamental applicability of the laser ionization mass spectrometry method for direct analysis of a sample in the form of an ice matrix was investigated. For it, a drop of water was frozen on a Peltier element and placed in a vacuum chamber. Then a series of Nd:YAG laser shots (7 ns) with energies from 17 mJ and below was made using a LASMA laboratory instrument. When the laser radiation energy was reduced to 9–10 mJ, spectra were recorded in which only mass peaks of hydrogen and singly ionized oxygen were present. With a further decrease in the laser pulse power, the energy was insufficient to ionize the ice matrix.

In the optical scheme of the LASMA-LR flight instrument, a neutral optical filter is installed, which regulates the radiation energy to obtain an energy range in the focusing spot that is optimal for the analysis of rocks and regolith. When the energies of this range are exceeded, double and/or multiple ionization of atoms occurs in the analysis of rocks, and the attenuation of radiation only due to the attenuator is not enough to obtain spectra with single ionization, which necessitates the installation of a neutral filter in the flight instrument [2]. Thus, the energy range of the laser radiation of the flight instrument is 0.03–2 mJ. This does not allow analysis of pure water ice with a flight instrument.

However, it is unlikely to find pure ice without impurities in course of the missions [4, 5]. Impurities can play the role of sensitizers and reduce the ionization energy of ice [6]. This was confirmed by us through the analysis of water ice with an admixture of 1% TiH_2. In this case, the energy required for the ionization of the ice matrix was about 1.5 mJ, which made it possible to obtain mass spectra containing hydrogen and oxygen ions using the instrument in flight configuration.

We also carried out a series of experiments with isotope labels. Deuterated water (D_2O) was introduced into the Fe_3O_4 powder at concentrations from 0.5 to 40 % (v/w), the sample was placed in a vacuum chamber and analyzed using the instrument in flight configuration. As a result, mass spectra were obtained with deuterium and oxygen peaks, i.e. the instrument was capable of detecting heavy water in the samples (Fig. 1). During the experiments, a gradual decrease in the deuterium concentration was observed, which was recorded by the instrument, which was due to the sublimation of ice in the vacuum chamber. This creates the prerequisites for determining the state of

water in a sample (chemically bound water vs mixtures of ice with regolith) by analyzing the dynamics of the content of hydrogen ions in the sample.

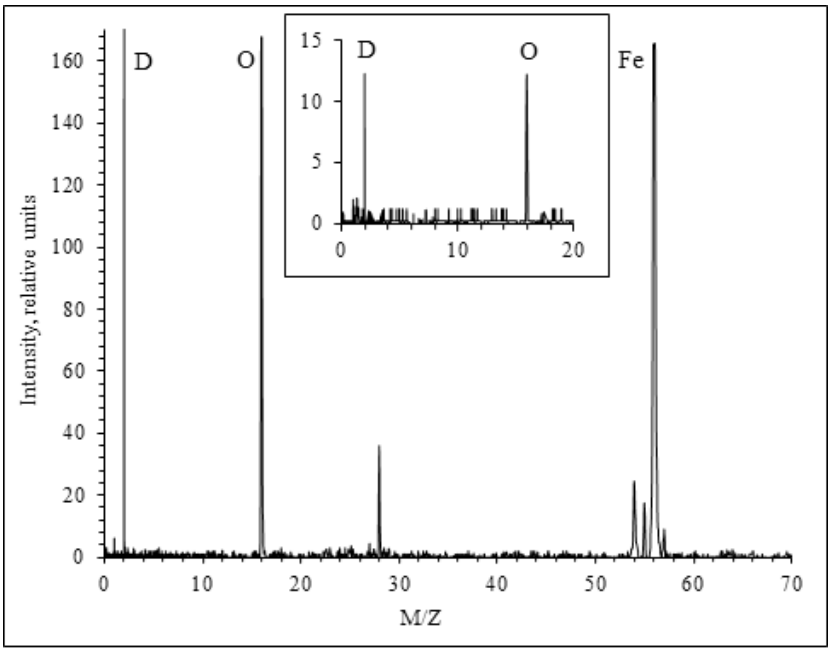

Fig. 1. Mass-spectrum of Fe_3O_4 powder with 40 % D_2O. The insert represents part of the same spectrum in the least sensitive channel.

CONCLUSION:

It was found that the LASMA-LR instrument is capable of qualitatively detect water ice in regolith. A quantitative assessment of the water content requires further research and development of methods. It is important to note that the possibility of carrying out such analyzes critically depends on the conditions of regolith sampling and its delivery to the sample receiving device of the instrument, since under the conditions of the lunar surface, sublimation of ice is possible even before the sample analysis. Nevertheless, the experiments performed testify to the fundamental applicability of the LASMA-LR for searching water in course of the Luna-25 and Luna-25 missions.

REFERENCES:

[1] Golovin D.V., Mokrousov M.I., Mitrofanov I.G. et al. ADRON-LR Instrument for active neutron sensing of the lunar matter composition // Solar System Research. 2021. V. 55. P. 529-536.

[2] Chumikov A.E., Cheptsov V.S., Wurz P. et al. Design, characteristics and scientific tasks of the LASMA-LR laser ionization mass spectrometer onboard Luna-25 and Luna-27 space missions // Intern. J. Mass Spectrometry. 2021. V. 469. Art. No. 116676.

[3] Managadze G.G., Wurz P., Sagdeev R.Z. et al. Study of the main geochemical characteristics of Phobos' regolith using laser time-of-flight mass spectrometry // Solar System Research. 2010. V. 44. No. 5. P. 376-384.

[4] Heldmann J.L., Lamb J., Asturias D. et al. Evolution of the dust and water ice plume components as observed by the LCROSS visible camera and UV–visible spectrometer // Icarus. 2015. V. 254. P. 262-275.

[5] Siegler M., Paige D., Williams J.P., Bills B. Evolution of lunar polar ice stability // Icarus. 2015. V. 255. P. 78-87.

[6] Pavlov S.G., Jessberger E.K., Hübers H.W. et al. Miniaturized laser-induced plasma spectrometry for planetary in situ analysis —The case for Jupiter's moon Europa // Advances in Space Research. 2011. V. 48. No. 4. P. 764-778.

DURABLE DIAMOND DETECTOR OF COSMIC RADIATION

K.V. Zakharchenko[1,2], A.A. Altukhov[1], V.E. Bagdatjev[1], R.F. Ibragimov[3], V.A. Kolyubin[1], V.A. Pikalov[4], E.M. Tyurin[3]

[1] *Industrial Technological Center "UralAlmazInvest", Ltd., Moscow, Russia; nanophys@mail.ru*
[2] *Moscow State Technical University of Civil Aviation, Moscow, Russia*
[3] *National Research Nuclear University MEPhI, Moscow, Russia*
[4] *Institute for High Energy Physics named by A.A. Logunov of National Research Centre Kurchatov Institute, Moscow region, Russia*

KEYWORDS:
Space radiation, electrons, protons, heavy ions, diamond, detector, high temperature

INTRODUCTION:
Diamond has ultimately high radiation and temperature hardness. This determines its prospects for development space radiation detectors [1–3] efficient for rugged service.

In previous investigations [3] new high-temperature detector has been shown to efficiently register electrons, gamma radiation and neutrons up to 200° C.

The aim of this work is the experimental testing the modified detector and the registration block that includes it under action of gamma radiation, electrons, protons, neutrons and heavy ions.

EXPERIMENTAL METHODS AND RESULTS:
Diamond detectors have been fabricated using electronic grade diamond plates with thin metal electrodes deposited on interfacial layer. The bias voltage has been applied to the electrodes. The output signals of the detectors have been applied to the charge-sensitive amplifiers and further have been registered using Greenstar digital processor.

A block of space radiation registration including the diamond detector has been developed. The registration block is designed to register space radiation on outer surface of the spacecraft. It is fabricated using only domestic components. The block has two registration channels that include the diamond detector, charge-sensitive amplifier, shaper and data processing unit. The output of the registration channel is determined by the spectrum of the energy deposited in diamond sensitive element.

The diamond detector and registration block have been tested under action of gamma radiation (^{60}Co), electrons (^{90}Sr+^{90}Y), protons, neutrons and heavy ions. To obtain the neutron radiation the isotope source (Am:Be) and deuterium-tritium generator have been used. The beam of accelerated carbon ions (400 MeV/nuclon) has been used to investigate the output of the samples under action of heavy ions. The proton radiation has been obtained by passing neutron radiation from Am:Be source through polyethylene converter and as secondary emission of the beam of accelerated carbon ions in distilled water.

The output spectrum of diamond detector under action of accelerated carbon ions is shown at the Fig. 1. The output spectrum of the registration block obtained simultaneously is shown at the Fig. 2. One can see that the spectra have similar form and we can conclude that the detector and the registration block register carbon ions efficiently. The spectra include the strongly pronounced peak associated with the ions registration and a lesser peak at higher energies is related presumably to the action of secondary particles including protons.

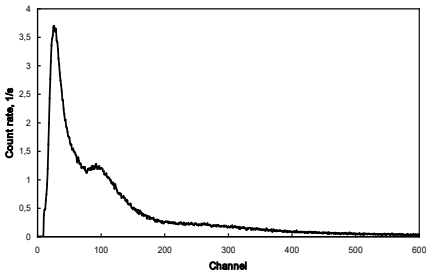

Fig. 1. Detector output spectrum under action of accelerated carbon ions.

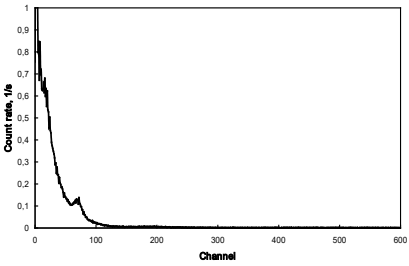

Fig. 2. Registration block output spectrum under action of accelerated carbon ions.

The differences in spectra are explained by difference in channel width and in the dimensions of diamond sensitive elements (i.e. the effective registration cross-section) and different placing of the registration block and the detector in the ion beam. The difference in first 30 channels is related to the noise correction technique in Greenstar processor. One can scale up the abscissa axis to graduate the scale of registration block. The result of scaling is shown at the Fig. 3.

The tests of the detector and registration block under action of neutron, electron and gamma radiation have shown that the samples under investigation register ionizing radiation efficiently. To register the output of the detector under action of proton radiation we have used neutron radiation with and without polyethylene converter between the source and the detector. So, the output spectra under action of protons have been obtained by subtraction of the spectra obtained without the converter from those obtained with the converter.

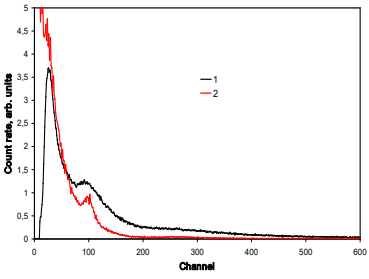

Fig. 3. Normalized spectra of the detector (1) and the registration block (2) output under action of accelerated carbon ions. Abscissa axis for registration block has been scaled up to match the peaks.

CONCLUSIONS:

The detector and the registration block for space radiation monitoring have been tested under action of different types of ionizing radiation. The samples under investigation are shown to efficiently register such ionizing radiation as gamma, electron, neutron, proton and heavy ions.

ACKNOWLEDGMENTS:
The work has been partially supported by Federal State Budgetary Institution "Fund for Promoting the Development of Small Forms of Enterprises in the Scientific and Technical Sphere" (Innovation Assistance Fund), Project No. 61893.

REFERENCES:

[1] Amosov V.N., Meshchaninov S.A., Rodionov N.B. et al. Gamma radiation radiometer on the basis of synthetic diamond // Prikladnaya fizika. 2012. No. 3. P. 79-85.
[2] Kadilin V.V., Kolyubin V.A., Lvov S.A., Nedosekin P.G., Idalov V.A., Tyurin E.M., Kolesnikov S.V., Samosadnyi V.T. The prospects of application of diamond detectors for registration of charged space radiation particles // Yadernaya fizika I injiniring. 2014. V. 5. No. 2. P. 138-144. DOI: 10.1134/S2079562914010072.
[3] Zakharchenko K.V., Altukhov A.A., Ibragimov R.F., Kolyubin V.A., Tyurin E.M. High-temperature detector of space radiation based on diamond sensitive elements // Proc. 12th Moscow Solar System Symposium (12MS^3-21). Moscow, Russia. 2021. P. 133-135.

NATURAL LUNAR TEST SITE ON EARTH

E.N. Slyuta[1], E.M. Sorokin[1], I.A. Agapkin[1], E.A. Grishakina[1], V.Yu. Makovchuk[1], D.D. Mironov[1], O.I. Turchinskaya[1], O.S. Tretyukhina, A.V.[1]
[1] *Vernadsky Institute of Geochemistry and Analytical Chemistry RAS, Kosygina str., 19, Moscow, 119991, Russia; slyuta@geokhi.ru*

KEYWORDS:
Lunar test site, lunar landscape, lunar soil, lunar regolith, volcanic tephra, Kamchatka, Tolbachik, Mutnovsky, Gorely, Khalaktyrsky beach.

INTRODUCTION:
In many countries, for testing scientific and service space equipment, landing spacecraft and all-terrain vehicles, natural test sites are used, which are characterized by landscape and soil as close to the lunar (Martian) landscape and soil, as far as possible in terrestrial conditions. There is no such test site in Russia. Previously, they were - in Kamchatka and near Evpatoria at such test sites, for example, they tested Soviet lunar rovers.

REQUIREMENTS FOR A NATURAL LUNAR TEST SITE ON EARTH:
The choice of areas suitable for creating a natural lunar test site on Earth was carried out taking into account the following requirements:

1. The soil should be predominantly of volcanic origin, which, approximately like the lunar regolith, was formed, accumulated and compacted during effusive eruptions by falling particles from above.
2. Volcanic soil should be as fresh as possible without signs of geochemical weathering and should not be displaced and redeposited by water flows.
3. The volcanic soil, like the lunar regolith, is characterized by a detrital shape and poor sorting of particles by size.
4. Volcanic soil with a significant content of fine-grained tephra (ash) should be close to the lunar soil in terms of particle size distribution.
5. The soil in terms of glass content and composition of the main rock-forming minerals and chemical composition should be close to the lunar regolith.
6. The volcanogenic landscape must be newly formed, without vegetation, and as close as possible to the lunar landscape.
7. All test sites must be within transport accessibility.

EXPEDITION TO KAMCHATKA:
Based on the above requirements, the following areas of the Kamchatka Peninsula were selected and explored in 2020: Tolbachik, Mutnovsky, Gorely volcanoes, Mount Camel in the area of Karyaksky volcano and Khalaktyrsky beach on the coast of Avachinsky Bay of the Pacific Ocean (Fig. 1).

The explored areas in Kamchatka have no vegetation, resemble a lunar landscape (Fig. 2), and have volcanic soil (tephra) with a high ash content. The rocks of Tolbachik volcano are typical basalts, tephra (ash) consists mainly of volcanic glass of basalt composition interspersed with rock-forming minerals (plagioclase, pyroxene, olivine) and ore minerals (titanomagnetite, chrome spinel). The mineral composition of tephra of Mutnovsky, Gorely, and Mount Camel volcanoes is generally close to the composition of the soil in Tolbachik.

The granulometric composition is the most important characteristic of a dispersed soil, which affects the physical, mechanical and other properties of the lunar soil [1]. The sand from the Khalaktyrsky beach turned out to be too coarse (Fig. 3), while the samples from the Mutnovsky volcano and the Gorely volcano had too low a content of particles smaller than 0.1 mm. The particle size distribution closest to the lunar soil is observed in the soil from the Gorely volcano from a height of 1390 m and from the Tolbachik volcano.

The sand of the Khalaktyrsky beach is characterized by a high degree of sorting and is composed of dark-colored minerals (pyroxenes, hornblende, olivine), feldspars and quartz are less common. Ore minerals are represented by magnetite, titanomagnetite, ilmenite, hematite, martite. The content of iron

oxides is up to 14.5% and titanium dioxide (TiO2) is up to 9.2%. Magnetic properties are strongly manifested.

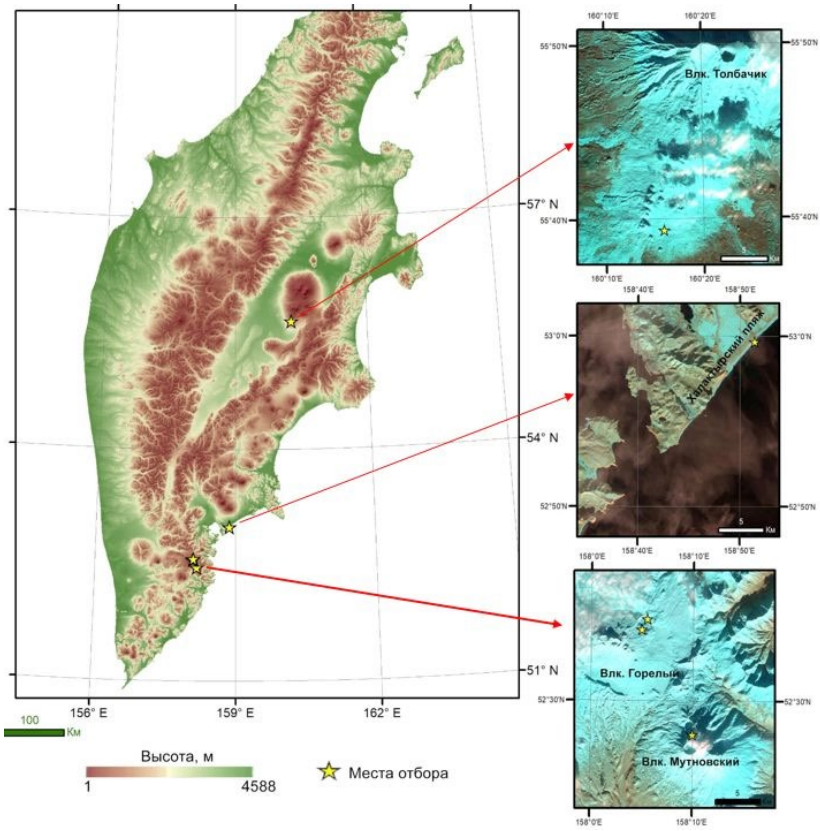

Fig. 1. Schematic map of the studied areas of Kamchatka.

Fig. 2. “Lunar” landscape on the Tolbachik volcano in the area of the Alaida hill, site coordinates 55.720588° N, 160.268339° E.

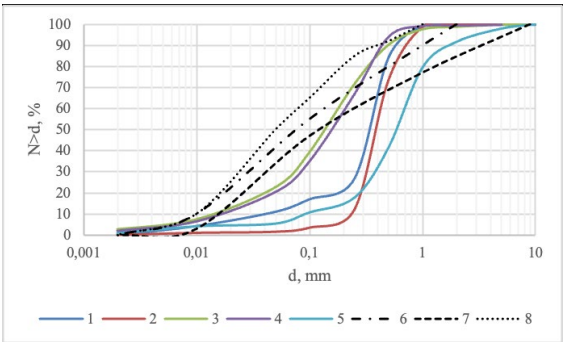

Fig. 3. Integral particle size distribution of lunar soil and studied samples from Kamchatka: 1 — Gorely; 2 — Khalaktyrsky beach; 3 — Gorely (1390); 4 — Tolbachik; 5 — Mutnovsky; 6 — "Apollo–11, –12, –14, –15, –16, –17" and "Luna–24" [4]; 7 — "Apollo 11" landing site [5]; 8 — "Apollo–17" landing site [1].

The dielectric properties of the soil depend on the chemical and mineral composition, on the particle size distribution and density, on the temperature of the soil and on the frequency of the electromagnetic pulse of the measuring equipment [2]. The dielectric constant of dry lunar soil with similar mineral and particle size distribution is almost independent of the frequency of the electromagnetic pulse of the measuring equipment and mainly depends only on its density [3].

SUMMARY:

The studied areas of Tolbachik, Mutnovsky, Gorely volcanoes and Mount Camel meet all the basic requirements for test site and are characterized by a landscape that is as close as possible to the lunar landscape. The volcanic tephra with a high content of ash and the presence of stones, does not contain vegetation. The physical properties of the soil, the granulometric, chemical and mineral composition of the soil are as close as possible to the properties and composition of the lunar soil, as far as possible under terrestrial natural conditions.

Unlike sites in the region of volcanoes, Khalaktyrsky beach is a perfectly flat area composed of black well-sorted sand, and for some properties (density, mineral composition containing magnetic minerals with iron oxide), it can also be used to test a certain scientific and service equipment of lunar landers. All the studied areas are within transport accessibility.

REFERENCES:

[1] Slyuta E.N. Physical and mechanical properties of the lunar soil (A review) // Sol. Syst. Res. 2014. V. 48(5). P. 330-353.
[2] Slyuta E.N., Marov M.Ya., Dunchenko A.G., et al. TERMO-LR experiment on the Luna–27 Lander: Study of thermophysical, physicomechanical, and electromagnetic properties of the lunar soil // Sol. Syst. Res. 2021. V. 55(5). P. 446-466.
[3] Strangway D.W., Pearce G.W., Olhoeft G.R. Magnetic and dielectric properties of lunar samples // The Soviet-American conference on cosmochemistry of the Moon and planets. NASA, Washington, D.C. 1977. Pt. 2. P. 443–446.
[4] Carrier W.D. III, Asce F. Particle size distribution of lunar soil // J. Geotech. Geoenviron. Eng. 2003. V. 129(10). P. 956-959.
[5] Preliminary examination of lunar samples, in: Apollo 11 Preliminary Science Report. NASA SP-214, 1969. P. 123-142.

CONSIDERATION OF ASHES FROM THE KAMCHATKA PENINSULA AS LUNAR SOIL- ANALOGUES ON THE BASIS OF PHYSICAL AND MECHANICAL PROPERTIES

A.V. Uvarova[1]
[1] *Vernadsky Institute of Geochemistry and Analytical Chemistry RAS, Moscow, Russia; uvarova@geokhi.ru*

KEYWORDS:
Soil-analogues, ashes, mechanical properties

INTRODUCTION:
The Laboratory of Geochemistry of the Moon and Planets of Vernadsky Institute is developing a full-scale analogue soil, which will be close not only in physical properties, but also in chemical and mineral composition to the lunar regolith. Sampling sites are also viewed as full-scale test sites for space rovers testing. The main purpose of this study is to examine the mechanical properties of several types of ashes from the Tolbachik, Gorely and Mutnovsky volcanoes, as well as the Khalaktyrsky beach and compare them with the lunar regolith. The similarity criteria are the values of density, angle of internal friction and cohesion. For this purpose, shear strength tests were performed for loose and dense compactions of material and then the angle of internal friction and cohesion were determined.

PROPERTIES OF LUNAR SOIL:
In terms of particle size distribution, a typical lunar regolith is a poorly sorted sandy-silty soil with an admixture of rubble and boulders. The median particle size ranges from 0.04 to 0.130 mm with an average value of 0.07 mm [1].

Most of the lunar regolith samples are characterized by a predominance of a coarse-grained fraction from fresh crater ejections and a finely dispersed fraction of a mature regolith, which indicates insufficient sorting of the lunar regolith in contrast to terrestrial loose soils [2].

The natural density of lunar regolith on the surface up to a depth of 15 cm, according to data from the Luna-16 and Luna-20 spacecraft missions, varies from 1.12 to 1.7 $g \cdot cm^{-3}$ with an average value of about 1.5 $g \cdot cm^{-3}$.

The average value of the density of the regolith on the surface, according to the data from the Apollo missions, is also 1.3 $g \cdot cm^{-3}$, but then sharply increases with depth with hyperbolic-like dependence. Deeper than 60 cm, the density of the regolith soil increases insignificantly, and at a depth of about 3 m it approaches 1.92 $g \cdot cm^{-3}$ [3].

An assessment of the strength characteristics showed that on the surface the lunar soil in a loose state has insignificant cohesion and a small angle of internal friction. As the soil is compacted at a depth of up to 1.5 $g \cdot cm^{-3}$, the shear resistance increases both due to an increase in adhesion forces and due to an increase in the angle of internal friction. Scientists' assessment [4] of bore hole resilience against caving from Apollo-16 and Apollo-17 missions showed that the specific adhesion at landing sites is 1.1–1.8 kPa and a ϕ value of 46.5°.

Lunokhod-2 in Lemonnier crater near the eastern coast of the Sea of Clarity also measured the following parameters: specific cohesion - 0.40 kPa, angle of internal friction – 40°° [2].

Experimental studies of the lunar soil delivered from the landing sites of the manned Apollo expeditions also showed a strong dependence of cohesion and the angle of internal friction on the density of the soil and, accordingly, on the depth of occurrence [5]. When the density changed from 0.99 to 1.87, the cohesion varied within 0.3–3.0 kPa and the angle of internal friction was 13–56° [5, 2].

Thus, the lunar regolith has a density range of 1.3–1.9 $g \cdot cm^{-3}$, the angle of internal friction, depending on the density, varies from 13 to 56°, and the cohesion is 0 to 3 kPa.

DESCRIPTION OF METHODS:
The density was determined in a cylindrical form with a known volume. The minimum density was determined by free pouring into a container, and the maximum density was determined by layer-by-layer filling and vibrocompaction. Mechanical properties were determined by shear testing (Fig. 1), it based on the Mohr-Coulomb theory: the value of the shear stress (τ) will depend on the cohesion values (c), the internal friction angle (tgϕ) and the applied normal stress (σ).

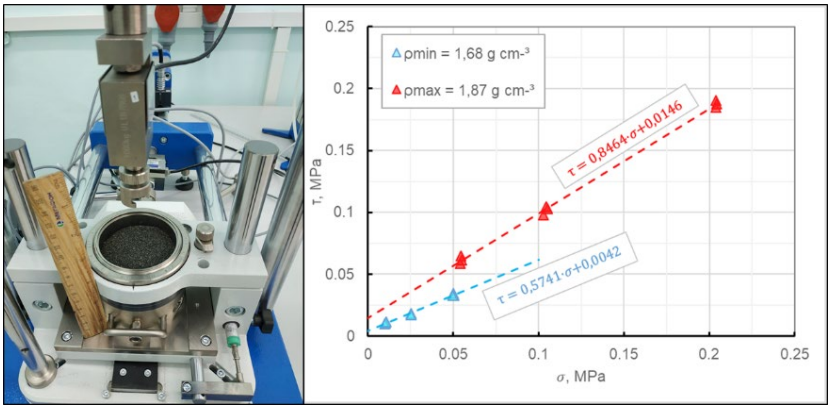

Fig. 1. Example of shear test for sand from Khalaktyrsky beach

The normal stress was set depending on the density of the samples in the range from 10 to 50 kPa for loose and from 50 to 200 kPa for dense samples. The strength value was defined as the maximum shear stress at which the sample failed. The shear speed was 2 mm/min.

RESULTS AND DISCUSSION:
Samples of Kamchatka ash are sandy soils with an admixture of dust and coarse-grained fractions in different ratios. There were 5 samples in total: Gorely volcano (lower part of the slope), Gorely vocano (upper part of the slope, 1390 m), Khalaktyrsky beach, Mutnovsky volcano, Tolbachik volcano. The last sample had a large particle size, so it was divided into two samples: screening through a sieve of 2.5 mm and a crushed part of less than 0.16 mm. The samples had a different range of density and, therefore, strength characteristics, as shown in Table 1.

Table 1. Density and strength characteristics of Kamchatka's ashes.

Samples	ρ, g·cm^{-3}	φ, grad	*c*, kPa
Tolbachik (<2,5 mm)	1.05–1.15	43.9	7.4–48.5
Tolbachik (<0.16 mm)	1.05–1.52	10–34	11–23
Mutnovsky	1.34–1.65	43.7–50.8	3.1–18.1
Gorely (foot)	1.36–1.66	34.8–33.1	3.9–16.9
Gorely (slop 1390 m)	1.27–1.57	33.8–36.1	1.7–12.8
Khalaktyrsky beach	1.68–1.87	29.9–40.3	1.7–14.6

Consideration of Kamchatka ashes as potential analogues of the lunar soil showed that they will not be able to fully imitate the lunar soil.

Samples from the Mutnovsky and Gorely volcanoes can be used to simulate the upper layer (up to a depth of 15 cm) of regolith, with a minimum density.

Preliminary studies of the mineral composition, on the contrary, show that samples from the Tolbachik volcano and Khalaktyrsky beach are close in composition, but under natural conditions they are too coarse. Crushed Tolbachik ash also does not fully correspond to the lunar one. Further research will be directed to the study of crushed samples of these samples, and possible options for mixing different samples will be considered, in order to achieve a better result.

REFERENCES:

[1] Carrier W.D. III Apollo drill core relationships // The Moon. 1974. V. 10. P. 183-194.
[2] Slyuta E.N. Physical and mechanical properties of the lunar soil: A review // Solar System Research. 2014. V. 48(5). P. 330-353.
[3] Carrier W.D. III, Olhoeft G.R., Mendell W. Physical properties of the lunar surface // Lunar Sourcebook / eds. Heiken G., Vaniman D., French B.M. Cambridge: Cambridge Univ. Press, 1991. P. 475-594.
[4] Mitchell J.K., Houston W.N., Scott R.F., Costes N.C., Carrier W.D. III, Bromwell L.G. Mechanical properties of lunar soil: density, porosity, cohesion, and angle of friction // Proc. 3rd Lunar Sci. Conf. 1972. P. 3235-3253.
[5] Jaffe L.D. Shear strength of lunar soil from Oceanus Procellarum // The Moon. 1973. V. 8. P. 58-72.

THE KAMCHATKA VOLCANIC ASHES AS A LUNAR SOIL ANALOGUE (PHYSICAL PROPERTIES)

I.A. Agapkin[1]
[1] *Vernadsky Institute of Geochemistry and Analytical Chemistry, Moscow, Russia; agapkinia@gmail.com*

KEYWORDS:
Kamchatka ashes, lunar regolith, physical properties

INTRODUCTION:
All analogues of lunar regolith are made, as a rule, in order to simulate one or two basic properties necessary for research, modelling and experiments. It is practically impossible to create a complete analogue of lunar regolith based on terrestrial rocks, corresponding to all the basic properties — physical and mechanical, thermophysical, electromagnetic, chemical and mineral composition [1].

For lunar regolith analogues of the physical and mechanical properties one of the most important characteristics is the grain size composition. The particle size of the lunar regolith is close to that of terrestrial volcanic ashes. Also, some volcanic ashes can be similar to the lunar regolith in chemical and mineralogical composition.

In this work, a comparative analysis of the grain size composition of the lunar regolith and volcanic ashes of Kamchatka was carried out.

SAMPLES:
For the study, ashes samples were taken from the Gorely, Mutnovsky, Tolbachik volcanoes, as well as sand from the Khalaktyrsky beach (Fig. 1). Two samples were taken from the Gorely volcano at the foot and from an altitude of 1390 m.

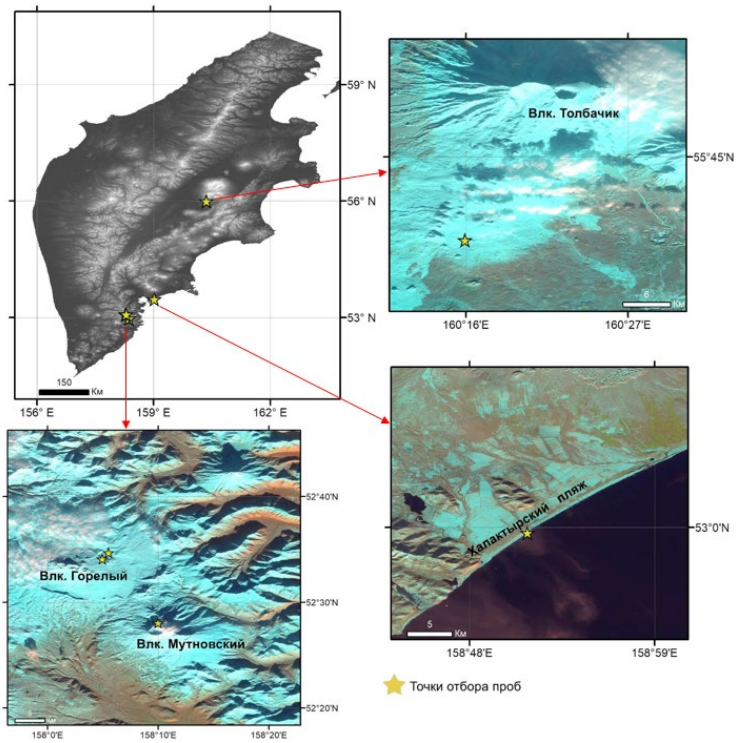

Fig. 1. Sampling sites.

All samples were examined in natural constitution, with the exception of the sample from the Tolbachik volcano. Due to the fact that the material from the Tolbachik volcano has low strength and is subject to light mechanical stress, improvised means were used to grind the material. So, during the preparation of the soil, the following technique was used: 1) Crushing the material with a hammer; 2) Screening the crushed material through sieves with a diameter of 1–0,16 mm; 3) Grinding the material with a roller-like object; 4) Sifting the crushed material through sieves with a diameter of 1–0,16 mm; 5) Abrasion of sieved material with fraction <160 μm.

It should be noted that in the lunar regolith, the total content of particles larger than 500 μm and less than 20 μm in a typical lunar regolith sharply decreases [1]; therefore, fractions in this range should prevail.

METHODOLOGY:

To determine the particle size distribution, it is necessary to know the solid particle density, which was determined using a pycnometer in accordance with GOST 5180-2015. The particle size distribution was determined using a hydrometer according to the method of GOST 12536-2014.

RESULTS:

The results of determining the density of particles are shown in Table 1. It should be noted that the data obtained for the Tolbachik and Khalaktyrsky beach samples have rather overestimated values, which is associated with the peculiarities of their chemical and mineralogical composition.

The graph (fig. 2) shows that curves (3) and (4) are the closest to the curve according to the averaged data of lunar regolith. Samples (1), (2) and (5) have too low a content of particles smaller than 0.1 mm.

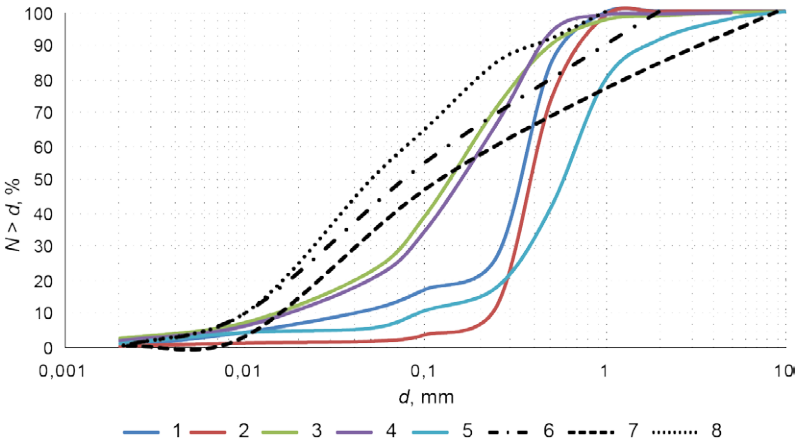

Fig. 2. Integral particlesize distribution of lunar soil and studied samples: 1 — Gorely; 2 — Khalaktyrsky beach; 3 — Gorely (1390 m) ;4 — Tolbachik; 5 — Mutnovsky; 6 — particle size distribution averaged of lunar soil (Apollo-11, -12, -14…-17 and Luna-24) [4]; 7 — Apollo-11 landing site [5]; 8 — Apollo-17 landing site [1].

Table 1.

No.	Sample	Solid particles density, $g \cdot cm^{-3}$
1	Gorely	2,60
2	Khalaktyrsky beach	3,00
3	Gorely (1390)	2,60
4	Tolbachik	2,93
5	Mutnovsky	2,72

More detailed studies of the physical and mechanical properties are needed to evaluate these samples as a physical and mechanical analogue of the lunar regolith.

REFERENCES:

[1] Slyuta E.N. Physical and mechanical properties of the lunar soil (A review) // Sol. Syst. Res. 2014. V. 48(5). P. 330-353.
[2] GOST 5180-2015 Soils. Laboratory methods for determination of physical characteristics. M.: Standartinform, 2019. (In Russian.)
[3] GOST 12536-2014 Soils. Methods of laboratory granulometric (grain-size) and microaggregate distribution. M.: Standartinform, 2019. (In Russian.)
[4] Carrier W.D. III, Asce F. Particle size distribution of lunar soil // J. Geotechnical and Geoenvironmental Engineering. 2003. V. 129. Iss. 10. P. 956-959.
[5] Preliminary examination of lunar samples // Apollo-11 Preliminary Science Report. NASA SP-214, 1969. P. 123-142.

ESTIMATES OF THE LOCAL/FOREIGN MATERIAL MIXING ON THE MOON: THE CRATER LANGRENUS CASE

A.S. Krasilnikov[1], M.A. Ivanov[1]
[1] *Vernadsky Institute of Geochemistry and Analytical Chemistry RAS, Moscow, Russia; krasilnikov_as@geokhi.ru*

KEYWORDS:
Moon, Langrenus, Mare Fecunditatis, rays, ejecta, mixing

INTRODUCTION:
Determination the material mixing factor during the fallout of impact crater ejecta is one of the most important problems, the solution of which will help to refine our understanding of the distribution of material on the Moon. However, the existing models of ejecta emplacement and their mixing differ greatly, and therefore the material mixing factor needs to be studied further.

MIXING FACTOR OF LOCAL AND FOREIGN MATERIALS:
There are a series of models [1–5] that give a representation of the thickness of ejecta deposits, but do not take into account the inevitable mixing of ejecta material with the underlying regolith. During the emplacement of ejecta deposit, materials with very broad spectrum of grain sizes fall out, forming secondary impact craters in a wide range of diameters. As the result, the local regolith of the near-surface layers is mixed with the ejecta material. An approach to the solution of the mixing problem was proposed by Oberbeck et al. [6], who used the results of experimental studies to quantify evaluation of volume ratio of the locally displaced to the introduced material of ejecta (mixing factor μ). Oberbeck et al. [6] proposed an empirical relation of the change in the value of μ as the distance from the crater increases:

$$\mu = 0.0183R^{0,87}, \quad (1)$$

where R is the distance from the middle of the crater radius to the point of interest. Oberbeck et al. [6] brought arguments that this relationship can be applied not only to determine the degree of mixing of ejecta from the Copernicus crater, but also for other large lunar craters. The R value was chosen to be equal to the distance from the middle of the crater radius to the calculation site because it is not possible to determine from which part of the crater a fragment, which caused formation of a secondary crater, was ejected.

In their work, Petro and Pieters [7] compared the results of various ejecta deposition models, including models with and without material mixing. The authors determined that the results obtained using the mixing model of Oberbeck et al. [6] are poorly comparable with the geochemical and petrographic features of the Apollo 16 soil [8]. This discrepancy led Petro and Pieters [7] to the conclusion that the mixing factor μ calculated from formula (1) should be reduced about by a factor of two.

ESTIMATION OF THE MIXING OF LOCAL AND FOREIGN MATERIALS BY THE CONTENT OF IRON OXIDE IN THE RAYS OF THE LANGRENUS CRATER:
At the moment, there is no exact confirmation of the correctness of the material mixing models. In order to refine them, the models were compared with data on the content of iron oxide in the lunar regolith, estimated from the results of the Clementine mission [9].

The objects of our study were the rays of the Langrenus crater (Fig. 1), which was selected because: (1) it is located on the border of the Mare Fecunditatis and the highlands, and part of its rays are clearly visible on the dark and smooth mare surface; (2) the age of the crater, 3.44 Ga [10], almost coincides with the age of the mare surface of the Mare Fecunditatis, 3.37 Ga [10], which minimizes the ray formation factor due to mechanical reworking of regolith by ejected particles. In our study, we used only those rays that lie on the smooth surface of the mare. Within each ray, we have selected randomly

distributed points, at which the model FeO content was determined from the Clementine FeO-map.

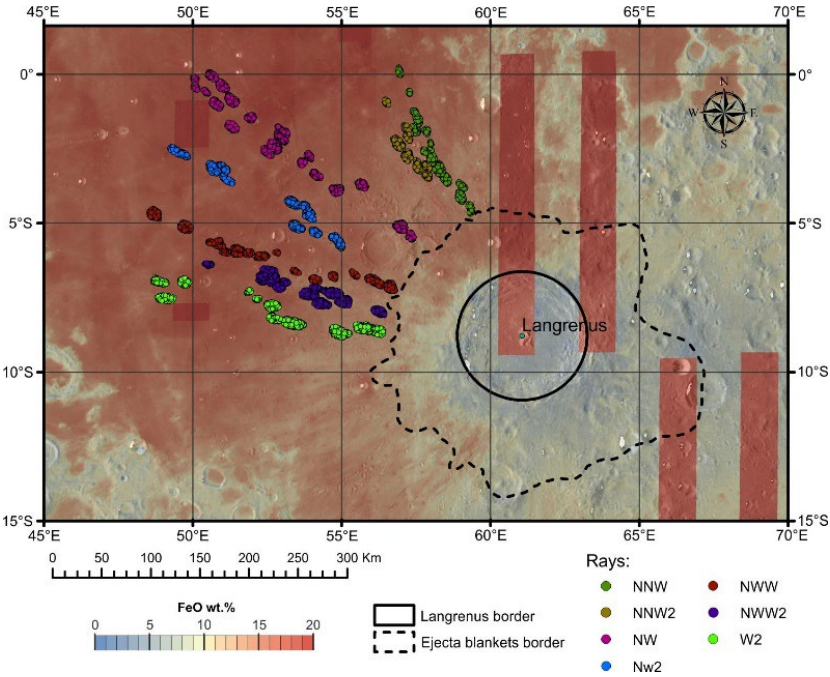

Fig. 1. Map of the FeO content in the area of the Langrenus crater and the rays used in the calculations.

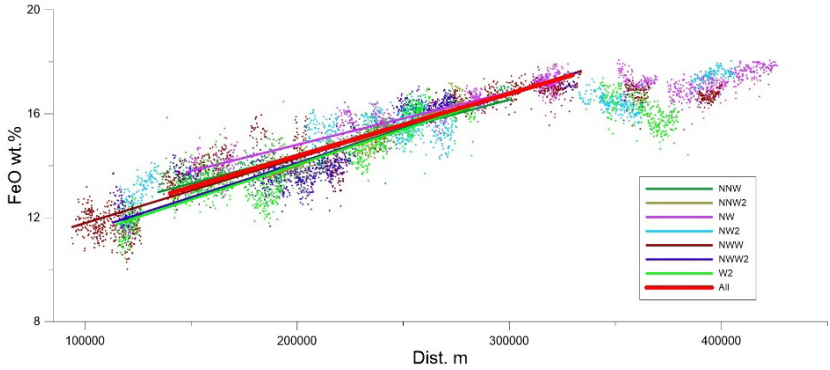

Fig. 2. Change in the amount of iron oxide in the rays of the Langrenus crater depending on the distance from its center.

The obtained estimates of FeO content form a clearly defined trend of increasing iron oxide (Fig. 2), as the distance (D) from the center of the crater increases. This trend is described by a linear function (Fig. 2):

$$FeO = D \cdot 2.36E\text{-}005 + 9.62. \quad (2)$$

At the distance of about 3 crater diameters (~300 km), the curve flattens out and no increase in iron content in the rays is observed; the local variations in the FeO content are associated with the presence of rays from Tycho crater.

We consider the increase in iron oxide as a result of the mixing of two end members, mare material with an average FeO content of 17.5 wt.%, and highland materials with an average FeO content of 5.5 wt.%. The determined function (2) shows that directly outside the zone of continuous ejecta at a distance of ~150 km from the center of the crater, the content of iron oxide is ~13.16 wt.%, which, at the indicated contents of iron oxide in the end-mem-

bers, corresponds to a mix of ~36 and 64 % of the highland and mare components. At a distance of 330 km, where the horizontal part of the trend begins, the iron oxide content is estimated to be ~17.5 wt.%, which practically coincides with the average FeO content in the Mare Fecunditatis regolith and, therefore, corresponds to almost 100 % of the mare component.

The obtained dependence (2) allows us to propose a formula for estimating the proportion of foreign material (L/F) in the range of distances from the edge of contiguous ejecta to the zone where the local regolith absolutely (~100 %) dominate at ~300 km:

$$L/F = 0.2 \cdot \exp(0.013D), \quad (3)$$

the center of the crater in kilometers. Formula (3) is not an alternative for estimating the degree of mixing, but allows one to obtain an integral estimate of the proportions of local and foreign material.

ACKNOWLEDGEMENTS:
This research was supported by the Russian Science Foundation grant No. 21-17-00035: Estimates of the rate of exogenous resurfacing on the Moon.

REFERENCES:
[1] McGetchin T.R., Settle M., Head J.W. Radial thickness variation in impact crater ejecta: implications for lunar basin deposits // Earth and Planetary Science Letters. 1973. V. 20(2). P. 226-236.
[2] Pike R.J. Ejecta from large craters on the Moon: Comments on the geometric model of McGetchin et al. // Earth and Planetary Science Letters. 1974. V. 23(3). P. 265-271.
[3] Fassett C.I., Head J.W., Smith D.E. et al. Thickness of proximal ejecta from the Orientale Basin from Lunar Orbiter Laser Altimeter (LOLA) data: Implications for multi-ring basin formation // Geophysical Research Letters. 2011. V. 38(17). Art. No. L17201.
[4] Housen K.R., Schmidt R.E., Holsapple K.A. Crater ejecta scaling laws: fundamental forms based on dimensional analysis // J. Geophysical Research. 1983. V. 88(B3). P. 2485-2499.
[5] Sharpton V.L. Outcrops on lunar crater rims: Implications for rim construction mechanisms, ejecta volumes and excavation depths // J. Geophysical Research: Planets. 2014. V. 119(1). P. 154-168.
[6] Oberbeck V.R., Hörz F., Morrison R.H., Quaide W.L., Gault D.E. On the origin of the lunar smooth-plains // The Moon. 1975. V. 12. P. 19-54.
[7] Petro N.E., Pieters C.M. Modeling the provenance of the Apollo-16 regolith // J. Geophysical Research. 2006. V. 111. Iss. E9. P. 1-13.
[8] Korotev R.L. Some things we can infer about the Moon from the composition of the Apollo-16 regolith // Meteoritics and Planetary Science. 1997. V. 32. Iss. 4. P. 447-478. https://doi.org/10.1111/j.1945-5100.1997.tb01291.
[9] Lucey P.G., Blewett D.T. Lunar iron and titanium abundance algorithms based on final processing of Clementine ultraviolet-visible image // J. Geophysical Research. 2000. V. 105. No. E8. P. 20297-20305. https://doi.org/10.1029/1999JE001117.
[10] Ivanov M.A., Head J.W., Hiesinger H. Absolute model age estimates of the fecunditatis basin and mare fecunditatis in the region of Luna-16 landing site // MSSS13. 2022. this issue.

GEOLOGICAL STRUCTURE OF THE MAIN LANDING ELLIPSES OF LUNA-25

A.S. Krasilnikov[1], S.S. Krasilnikov[1], M.A. Ivanov[1], J.W. Head[2]
[1] *Vernadsky Institute of Geochemistry and Analytical Chemistry RAS, Moscow, Russia, krasilnikov_as@geokhi.ru;*
[2] *Department of Earth, Environmental and Planetary Sciences, Brown University, Providence, RI, USA*

KEYWORDS:
Luna, Luna-25, landing sites, geological sections

INTRODUCTION:
Model distribution of the ejecta thickness in the southern subpolar region of the Moon is essential for the interpretation of the geological structure at the landing sites of Lunar missions, including the Luna-25 expedition.

This expedition is one of the highest priority projects of the Roscosmos corporation at the moment. When interpreting the results obtained at one of the selected landing sites (ellipses 1, 4 and 6, Fig. 1), it is vital to understand the geological structure of the region and the sources of the material that makes up the surface.

MAP OF THE EJECTA THICKNESSES OF LUNA-25 LANDING SECTOR:
The map of ejecta thicknesses (see Fig. 1) based on Hausen et al. [2] and Sharpton [3] models. We applied the formula of Housen et al. for craters larger than 45 km and Sharpton's formula for smaller craters. In the model of Housen et al. [2], the radial decrease in ejecta thickness is described by the formula: $T = 0.0078R(r/R)^{-2.61}$, in the Sharpton model [3]: $T = 3.95(\pm 1.19)R^{0.399}(r/R)^{-3}$. Borders of geological units (ejecta) based on the geological map at the scale of 1:300,000 [1].

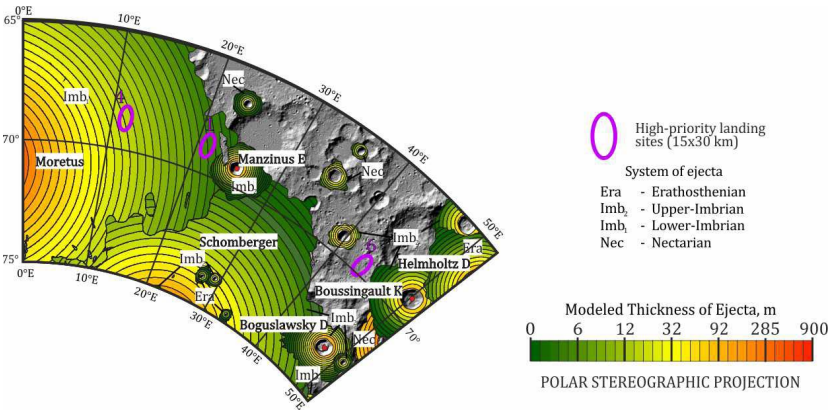

Fig. 1. Ejecta map of the Luna-25 landing area.

These maps allow us to understand the source and thicknesses of the material at the landing sites. We can calculate the source and thickness of the material at each point. This investigation could be provided not only for the exposed layer but also for overlapped. Exposed ejecta blanked overlaps a pre-Nectarian basement. Small impactors could penetrate the shallow upper layer, and older material could redeposit on the surface.

GEOLOGICAL STRUCTURE OF LANDING ELLIPSES:
Using Fassett, Housen and Sharpton models, it becomes possible to calculate the thicknesses of overlapped strata and build the series of longitudinal and transverse geological sections through the landing sites (Fig. 2).

Geological sections were built using laser altimetry data with LOLA, model ejecta thickness and geological maps compiled in this study based on works [4] and [6]. The nature of the distribution of the ejected material and data of

the morphological structure of the surface were taken into account. For better visualization of the sections, the ratio of the horizontal and vertical scales was 1:5. The ejecta thickness was calculated for all craters affecting the geological structure of the landing ellipses.

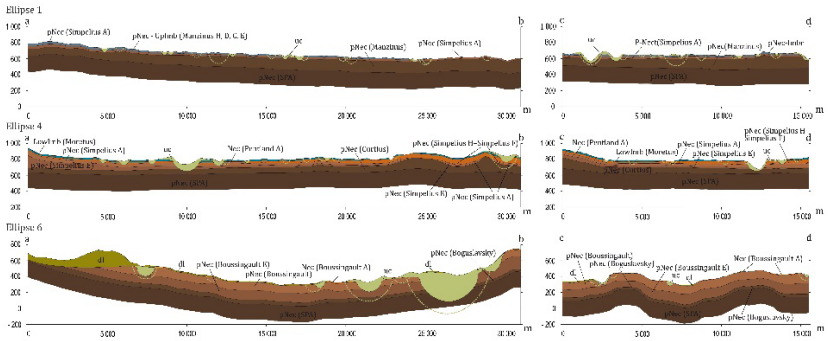

Fig. 2. Geological sections through landing ellipses 1, 4 and 6 [1]. uc — small craters. A dashed line marks the area of influence of small craters located near the section.

ELLIPSE 1:

The SPA basin ejecta represents the base of the section with an estimated thickness of about 870 m. The next layer sourced from the Manzinus crater (pre-Nectarian) with a thickness of 180 to 85 m from NE to SW, respectively. Above, sediments of the Simpelius A (pNec) crater have 35–18 m thick from the SW to NE. The near-surface zone is represented by undifferentiated deposits of pre-Nectarian (Manzinus N, 6 to 1 m thickness, W-E; Manzinus D, 22–5 m, SE–NE), Nectarian (Manzinus S, 19–2 m, S-N) and Upper Imbrian (Manzinus E, 2–1 m, E–W) ages. Upper Imbrian blanked in this ellipse have a thickness from 7 to 6 m. The section is complicated by small craters, checked by the index (uc). The excavation depth of all large craters, except for the craters Manzinus H (pNec) and Manzinus E (UpImb), is greater than the thickness of the SPA sediments, and their ejecta may contain material that comes under SPA ejecta blanked [1]. Moretus crater diameter (115 km) and approximate excavation depth of it ~12 km allow us to assume that impact could redeposit pre-SPA old material covered by SPA blanked [4] (800–1000 m, based on Fassett et al. [5] model: $T = 2900(\pm300)\cdot(r/R)^{-2.8(\pm0.5)}$).

ELLIPSE 4:

The thickness of the SPA deposit is about 850 m. The northwestern part of the section is complicated by the uneven thickness of the ejecta from the Curtius crater. The next layer is material from Curtius crater (pNec) with the variation of thickness from 90 to 52 m from NE to SW. Above layers with pre-Nectarian age: Simpelius E (95–8 m thick, from south to north), Simpelius A (48–21 m thick (SE–NW). The upper layers in the eastern part of the ellipse may contain material from Simpelius H and Simpelius F craters. Material from Pentland A crater (Nec) formed ejecta 63–10 m with the thickness (NE–SW). The overlying material of crater Pentland A (Nec) formed ejecta 63–10 m of the thickness (NE–SW). The upper layer of the ellipse is composed of ejecta from the Lower Imbrian Moretus crater with a thickness of 7–6 m from SW to NE.

ELLIPSE 6:

At the base of the geological section of ellipse 6 (see Fig. 2), there are SPA deposits with a thickness of about 1 km. They are overlain by ejecta from the Boguslawsky crater, with a thickness 74–32 m in the S–N direction. Above located the deposits of the Boussingault E (pNec) (152–95 m, NE–SW) and Boussingault (pNec) (210–85 m, E–W) craters. The Nectarian crater Boussingault A deposits are probably fragmentary and have a thickness of 20–14 m. The thickness of deposits of the youngest large craters: Boussingault F (UpImb) and Boussingault K (UpImb), inside the ellipse, does not reach 2 m in total and, apparently, did not have a significant impact on the geological structure of the territory [1].

ACKNOWLEDGEMENTS:
Input is partly supported by the Russian Science Foundation grant No. 21-17-00035: Estimates of the rate of exogenous resurfacing on the Moon.

REFERENCES:
[1] Krasilnikov S.S., Krasilnikov A.S., Ivanov M.A. Geological Details of the Main Landing Ellipses of Luna-25 // Sol. Syst. Res. 2022. V. 56. No. 3. P. 135-144.
[2] Housen K.R., Schmidt R.E., Holsapple K.A. Crater ejecta scaling laws: fundamental forms based on dimensional analysis // J. Geophysical Research. 1983. V. 88 Iss. B3. P. 2485-2499.
[3] Sharpton V.L. Outcrops on lunar crater rims: Implications for rim construction mechanisms, ejecta volumes and excavation depths // J. Geophysical Research: Planets. 2014. V. 119(1). P. 154-168.
[4] Ivanov M.A., Abdrakhimov A.M., Basilevsky A.T., Demidov N.E. et al. Geological characterization of the three high-priority landing sites for the Luna-Glob mission // Planet. Space Sci. 2018. V. 162. P. 190-206.
[5] Fassett C.I., Head J.W., Smith D.E. et al. Thickness of proximal ejecta from the Orientale Basin from Lunar Orbiter Laser Altimeter (LOLA) data: Implications for multi-ring basin formation // Geophysical Research Letters. 2011. V. 38(17). Art. No. L17201.
[6] Krasilnikov S.S., Basilevsky A.T., Ivanov M.A., Krasilnikov A.S. Geological and geomorphological characteristics of high-priority landing sites for the Luna-Glob mission // Sol. Syst. Res. 2021. V. 55. No. 2. P. 83-96.

THE NEW ANALYTICAL APPROACH FOR CALCULATION OF CRATERS EJECTA THICKNESS

V.N. Afanasyev[1,2], G.V. Pechernikova[1]
[1] *Institute for Dynamics of Geospheres RAS, Moscow, Russia*
[2] *Moscow Institute of Physics and Technology, Dolgoprudniy, Russia; vladimir.afanasev@phystech.edu*

KEYWORDS:
Ejecta thickness, ejecta, craters, Moon

INTRODUCTION:
Research of crater ejecta is important for understanding of cratering process. Thickness of ejecta is crucial characteristics of ejecta and it is usually estimated from experimental data, numerical modelling or semi-analytical dimensional analysis. Our approach is almost completely analytical, based on simple assumptions and Kepler's laws of motion. We used simple model of ejecta, which assumes:

1. Point-source ejecta.
2. Simultaneous ejection.
3. Radial symmetry of ejecta.
4. rajectories of particles of ejecta are elliptic or hyperbolic.
5. The surface of the planet is spherical.
6. Interaction between particles of ejecta is negligible.
7. Constant angle of ejecta [1, 2].

Our approach allows to use various mass-velocity distributions. We used Z-model [1], which assumes power law distribution. The best fit gives comparison of our analytical dependence with scaling law obtained by Housen et al. [2]:

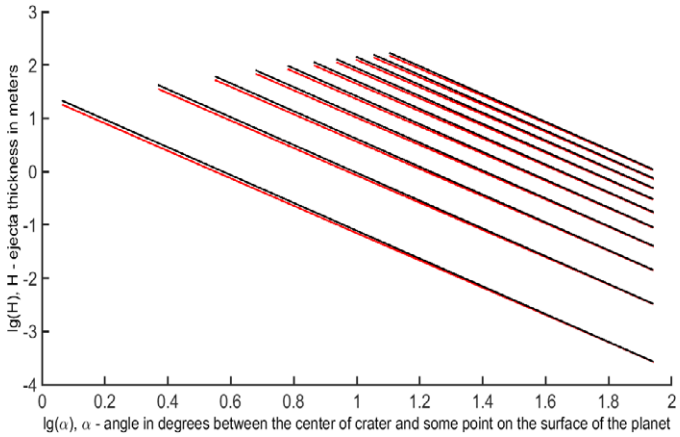

Fig. 1. Dependence of ejecta thickness on angle between the center of crater and some point on the surface of the Moon in logarithmic scale for radius of crater from 0.01 to 0.1 Moon's radius with step 0.01. Red lines are dependencies of ejecta thickness on angle calculated according our model and black lines show scaling law described in [2].

Advantage of our analytic approach is that it considers ellipticity of trajectories of ejecta particles as well as sphericity of planet's surface, therefore our formulae for ejecta thickness can be used for very large craters like Mare Orientale or Aitken basin on the Moon. In addition, our approach allows to use different mass-velocity distributions and change other initial parameters like radius or density of planet or ejection angle what makes our approach universal and applicable for wide range of craters in the Solar system.

REFERENCES:

[1] Maxwell D.E. Simple Z model for cratering, ejection, and the overturned flap // Impact and explosion cratering: Planetary and terrestrial implications. 1977. P. 1003-1008.
[2] Housen K.R., Schmidt R.E., Holsapple K.A. Crater ejecta scaling laws: fundamental forms based on dimensional analysis // J. Geophysical Research. 1983. V. 88. No. B3. P. 2485-2499.

THERMAL EVOLUTION OF THE MOON WITH GEOPHYSICAL CONSTRAINTS

E.V. Kronrod[1], V.A. Kronrod[1], O.L. Kuskov[1]
[1] *Vernadsky Institute of Geochemistry and Analytical Chemistry RAS, Moscoe, Russia, e.kronrod@gmail.com*

KEYWORDS:
Moon, thermal evolution, heat transfer, numerical modeling, temperature profile, geophysical constraints

THE MODEL OF THE MOON. GEOPHYSICAL CONSTRAINTS:
A model of the Moon consisting of a crust, upper and middle mantle, low-velocity/viscosity zone (LVZ), outer liquid and inner solid core is considered.

THE MANTLE:
It is assumed that the upper–middle mantle boundary marks the base of the lunar magma ocean (LMO), below there is a primary undifferentiated mantle, not affected by partial melting processes. The depth of the boundary between the upper and lower mantle (750 km) is set in accordance with the seismic boundary from the model [1]. The physical properties of the mantle (density, thermal conductivity, heat release) were set in accordance with the chondrite model, taking into account the heat release estimates obtained for the magma ocean model - corrections are introduced for the increased content of radioactive elements in the crust.

TRANSITION LAYER LVZ:
The existence of a partially melted LVZ layer is evidenced by selenophysical and electromagnetic data, seismic attenuation at the base of the lower mantle [2–4], as well as reanalysis of seismic data [5]. The presence of a layer of increased dissipation in the mantle base is consistent with the frequency dependence of Q-factors [4]. The outer boundary of the LVZ is set at R = 550 km, since the sources of the deepest moonquakes lie at a depth of ~1200 km [5]. Viscosity in the LVZ zone is set according to the data [6] — $3 \cdot 10^{16}$ Pa·s.

THE CORE:
The core of the Moon consists of an outer liquid core with a radius of $R_{outer\ core}$ = 350 km and a density of $\rho_{outer\ core}$ = 6700 kg/m^3 and a solid inner core with $R_{inner\ core}$ = 240 km and a density of $\rho_{inner\ core}$ = 7500 kg/m^3 [7]. The heat capacity in the core was set Cp_{core} = 800 J·kg^{-1}·K^{-1}.

RADIOACTIVE SOURCES IN THE MANTLE AND LVZ:
The content of radioactive sources in the mantle was set in accordance with the estimates obtained previously: in the range U_{crust} = 80–240 ppb for a magma ocean model with depth of 750 km, the possible concentrations of uranium in the upper (U_{upper}) and lower (U_{lower}) mantle were determined.

The restrictions on the optimal temperature gradient in the mantle dT/dH = 1.17 °C are fulfilled for $T_{crust\text{-}mantle}$ = 350 °C at a uranium concentration in the crust U_{crust} ≈ 220 ppb. These parameters correspond to: U_{bulk} ≈ 19 ppb (close to the value for silicate Earth), U_{upper} ≈ 6 ppb.

In this statement, it is assumed that the total heat release in the lower mantle and LVZ should correspond to the bulk value, and the heat release from the ilmenite-rich LVZ can be from 4 to 12 times higher than in the lower mantle [8].

CALCULATION METHOD:
The temperature distributions from 500 Ma from the formation of CAI to the present are found by numerically solving the one-dimensional non-stationary heat equation in the central symmetry approximation, which takes into account both conductive and convective heat transfer, as well as the processes of heating the mantle matter due to the energy of radioactive decay. Additional radioactive sources are included into the LVZ to ensure partial melting; there are no internal sources in the core — only conductive heat transfer is possible in the core region. The temperature profile at the initial time is set similarly [9].

RESULTS:

Calculations were carried out for a non-stationary thermal model at times from 0.5 billion years to the present for the "cold" model of the Moon — $T_{crust\ mantle}$ = 623 K (350 °C). The temperature distributions obtained as a result of calculations are consistent with geophysical data, as well as with previous estimates of the temperature distribution in the Moon, calculated from seismic data.

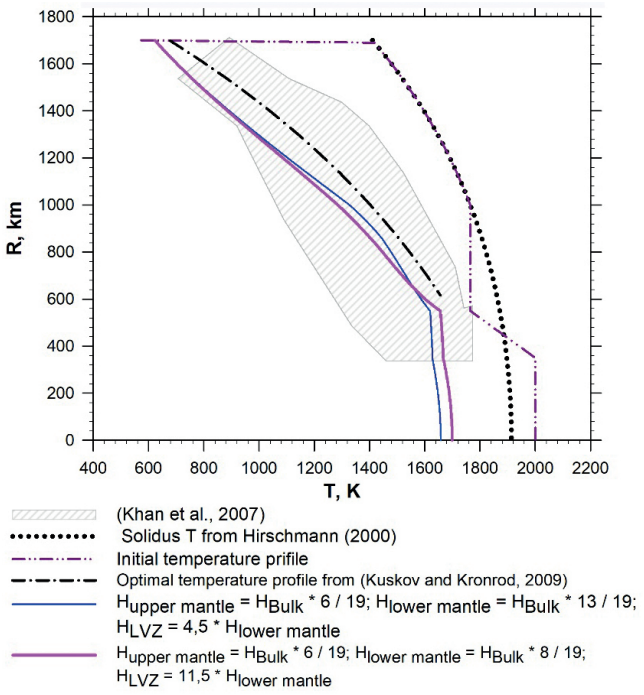

Fig. 1.

The maximum difference in heat release in the LVZ compared to the lower mantle leads to a temperature change of ~30 K in the LVZ zone and core, but does not significantly affect the temperature in the upper mantle. The temperature calculated for the present time in the liquid core in the case of a significant excess of the content of radioactive sources in the LVZ compared to the lower mantle is consistent with the melting temperature estimates.

ACKNOWLEDGEMENTS:

This study was carried out under government-financed research project for the Vernadsky Institute of Geochemistry and Analytical Chemistry, Russian Academy of Sciences.

REFERENCES:

[1] Gagnepain-Beyneix J., Lognonné P., Chenet H. et al. A seismic model of the lunar mantle and constraints on temperature and mineralogy // Physics of the Earth and Planetary Interiors. 2006. V. 159. P. 140-166.

[2] Nakamura Y. Farside deep moonquakes and deep interior of the Moon. // J. Geophysical Research. 2005. V. 110. https://doi.org/10.1029/2004JE002332.

[3] Khan A., Connolly J.A.D., Pommier A., Noir J. Geophysical evidence for melt in the deep lunar interior and implications for lunar evolution // J. Geophysical Research: Planets. 2014. V. 119. P. 2197-2221. http://dx.doi.org/10.1002/2014JE004661.

[4] Williams J.G., Konopliv A.S., Boggs D.H., Park R.S., Yuan D-N., Lemoine F.G., Goossens S., Mazarico E., Nimmo F., Weber R.C., Asmar S.W., Melosh H.J., Neumann G.A., Phillips R.J., Smith D.E., Solomon S.C., Watkins M.M., Wieczorek M.A., Andrews-Hanna J.C., Head J.W., Kiefer W.S., Matsuyama I., McGovern P.J., Taylor G.J., Zuber M.T. Lunar interior properties from the GRAIL mission // J. Geophysical Research: Planets. 2014. V. 119. No. 7. P. 1546-1578. https://doi.org/10.1002/2013JE004559.

[5] Weber R.C., Lin P., Garnero E.J., Williams Q., Lognonné P. Seismic detection of the lunar core // Science. 2011. V. 331. P 309-312. https://doi.org/10.1126/science.1199375.
[6] Tan Y., Harada Y. Tidal constraints on the low-viscosity zone of the Moon // Icarus. 2021. V. 365. Art. No. 114361. https://doi.org/10.1016/j.icarus.2021.114361.
[7] Kuskov O.L., Kronrod E.V., Kronrod V.A. Effect of thermal state on the mantle composition and core sizes of the Moon // Geochemistry Intern. 2019. V. 57. P. 605-620.
[8] de Vries J., van den Berg A., van Westrenen W. Formation and evolution of a lunar core from ilmenite-rich magma ocean cumulates // Earth and Planetary Science Letters. 2010. V. 292. P. 139-147.
[9] Laneuville M., Wieczorek M.A., Breuer D., Tosi N. Asymmetric thermal evolution of the Moon // J. Geophys. Res. Planets. 2013. V. 118. P. 1435-1452. DOI: 10.1002/jgre.20103.

AUTOMATIC METHOD TO ESTIMATE THE STEEPNESS OF WALLS OF SMALL IMPACT CRATERS ON THE MOON

M.A. Ivanov[1], E.N. Guseva[1]
[1] *Vernadsky Institute of Geochemistry and Analytical Chemistry RAS, mikhail_ivanov@brown.edu*

KEYWORDS:
Moon, impact craters, the crater wall steepness, topographic profiles, automatic and manual estimates of the steepness of crater walls, verification of data

INTRODUCTION:
Data on the variations of the slope steepness of the impact crater walls is an important component of the general task of estimation of the rate of erosional processes on the Moon. These data in combination with the estimates of the model absolute ages (AMA) of craters provide the possibility to quantify the dynamic of the crater degradation.

APPROACH:
The measurements of the steepness of the slopes is a very time-consuming procedure. In order to facilitate it and to conduct numerous measurements in craters, we have developed a simple computer program that constructs an average topographic profile of craters under study. The program collects, averages, and estimate the standard deviation of the topographic data in zones concentric relative to the geometrical center of the crater. One of the outcomes of the program is the mean value of the slope of the crater wall. This value, however, is estimated between the deepest point on the floor and highest point on the rim, which is could be a biased estimate because in many craters the slope of the wall is changed from shallower at the bottom to steeper at the wall and again to shallower near the rim. In order to be able to use the automatically collected data we have to check how adequately they describe the desirable property of the crater wall steepness.

VERIFICATION OF THE AUTOMATICALLY COLLECTED DATA:
In order to verify the data received from the automatic processing of the crater topographic data, we have mapped out small craters in the Apollo-12 landing site area (684 craters in a diameter range from 20 to 468 m) and in Apollo-15 SIVB impact areas (642 craters in a diameter range from 40 to 1000 m) using the available NAC images (spatial resolution is 2 m/px). For these craters, we have constructed the averaged topographic profiles using the NAC-based DTMs with spatial resolution of 2 m/px. During this procedure, the averaged wall steepness values of these craters were received.

At the next step, we have selected at random 10 % of the studied population, manually constructed their topographic profiles (orientation of the profiles was also selected at random), and estimated the wall steepness of the steepest (it was also the longest) portion of the wall by the least square linear approximation.

The results of the comparison of the automatic and manual measurements are shown in Fig. 1. As expected, the automatic procedure underestimates the steepness values, it is followed from the program algorithm. However, the correlation coefficient between the automatic and manual results is high. This ensures that the difference between the results has a systematic character and provide the possibility to introduce a correction coefficient for the automatically collected data in order to estimate the true steepness value.

FUTURE WORK:
We plan to apply the automatic procedure of the measurements to the secondary craters from the sources with known/inferred ages in attempt to quantitatively estimate the dynamics of the slope degradation on the Moon.

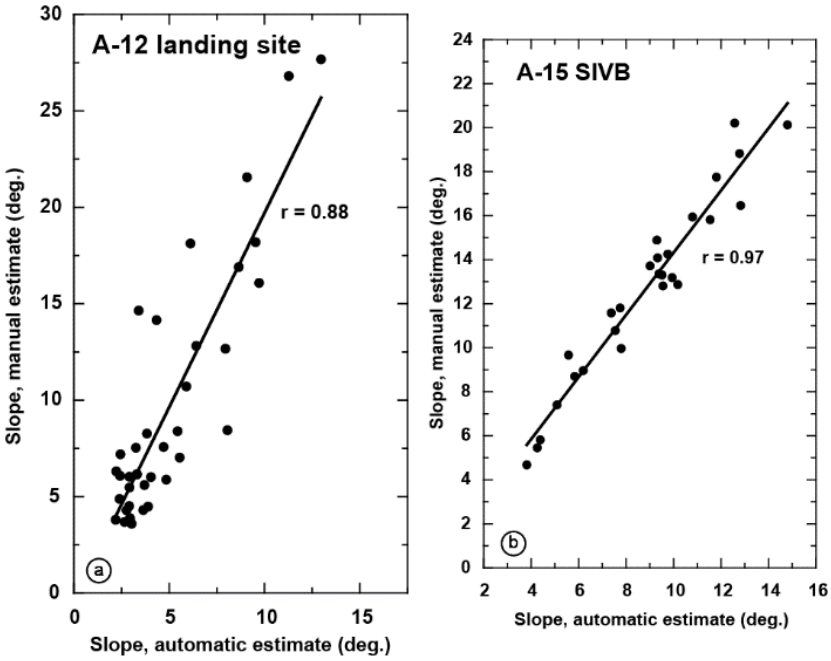

Fig. 1. Comparison of the automatic and manual estimates of the steepness of crater walls

ACKNOWLEDGMENTS:
This work is supported by the Russian Science Foundation grant No. 21-17-00035: Estimates of the rate of exogenous resurfacing on the Moon.

MORPHOLOGICAL FEATURES OF CRATERS IN THE POLAR REGIONS OF THE MOON

E.A. Feoktistova[1], Zh.F. Rodionova[1], N.A. Slodarzh[2]
[1] *Sternberg Astronomical Institute Moscow University, Moscow, Russia; jeanna@sai.msu.ru*
[2] *Moscow State University of Geodesy and Cartography, Moscow, Russia*

KEYWORDS:
Moon, impact craters, polar regions

INTRODUCTION:
The morphological characteristics of craters in the polar regions of the Moon have been studied.

For the morphological description of craters located in the polar regions of the Moon, we used the system for describing the morphological features of craters developed at the SAI MSU, which was previously used to create morphological catalogs of the craters of the Moon, Mars and Mercury [1]. The description of the crater includes coordinates and 9 morphological features: degree of preservation or degree of preservation of the rim, the presence of terraces or collapses on the slopes, the nature of the crater rim, the presence and type of the central rise (peak, hill or central ridge), the presence of fissures and chains of small craters at the bottom, the nature of the crater bottom, the presence of lava at the bottom, the ray systems, type of underlying surface. Each of these features has a number of sub-features.

Information about the coordinates and diameters of craters was obtained from the catalogs of morphometric parameters of the craters of the northern and southern polar regions of the Moon, created at the SAI MGU jointly with the Ural Federal University [2, 3]. Morphometric catalogs were created on the basis of a DEM with a resolution of 120 m/pixel according to the data of the probe "Lunar Reconnaissance Orbiter" [4]. The catalog of morphometric parameters of craters in the northern polar region of the Moon contains data on 2302 craters with a diameter of 10 km or more. The morphometric catalog of craters in the southern polar region of the Moon includes 1320 craters with a diameter of 10 km or more.

According to the data obtained, most of the craters in the polar regions of the Moon (almost 40 and 30 %, respectively) can be assigned to the 3rd and 4th classes of degree of preservation according to our classification: they have a smoothed or destroyed rim (Fig. 1). Approximately 20% of the craters can be attributed to the 2nd class of degree of preservation (craters with a clear ridge). The proportions of fresh craters (degree of preservation class 1) and ruin craters (degree of preservation class 5) in the polar regions of the Moon are approximately the same: 5 and 4.6 %, respectively (see Fig. 1).

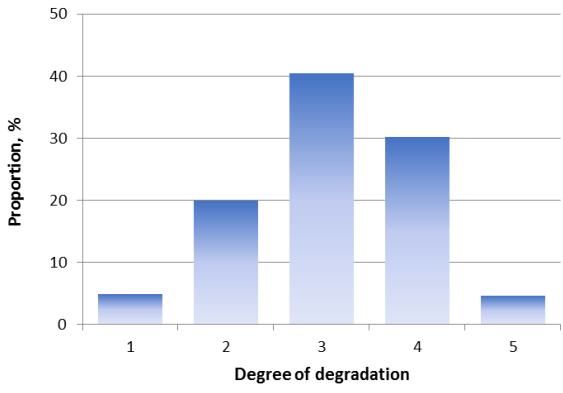

Fig. 1. Distribution of craters of the polar regions of the Moon according to the degree of preservation.

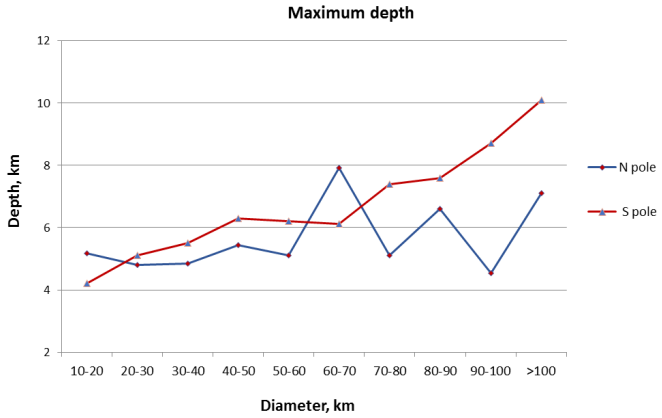

Fig. 2. Distribution of maximum crater depth of the northern and southern polar regions in dependence of craters diameters.

The graphs in Fig. 2 show that the average crater depths in the southern polar region are greater than in the northern one. This should probably be explained by the presence of lava at the bottom of many craters in the northern polar region. The greatest discrepancies are visible at diameters of 70–80 km (0.7 km) and 90–100 km (1.0 km).

An analysis of the graphs in Fig. 3 showed that the average crater depths in the polar regions of the near side and the far side are almost the same. For diameters of 50–60 km and 90–100 km, there is a discrepancy of 0.5–0.7 km.

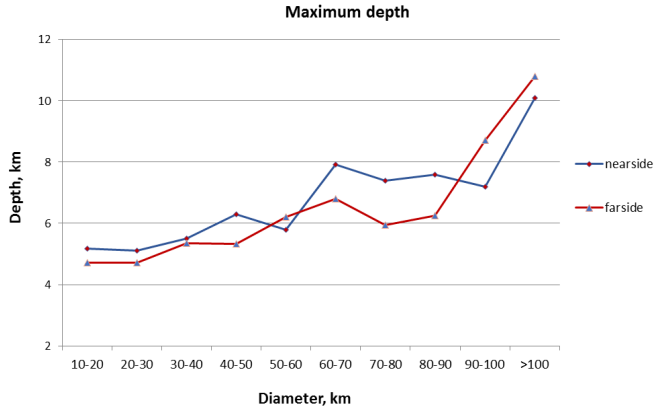

Fig. 3. Distribution of maximum crater depth on the near and far sides of the polar regions. The similar character is observed on both graphics.

REFERENCES:

[1] Feoktistova E.A., Zharkova A.Yu., Kokhanov A.A., Rodionova Zh.F., Rotaru V.A. Compilation of a new global catalog of Mercury's craters: Abstr. // The 11th Moscow Solar System Symp. 2020.
[2] http://selena.sai.msu.ru/Rod/Publications/morph-catalog-craters-moon-nord/morph-catalog-craters-moon-nord.htm
[3] http://selena.sai.msu.ru/Rod/Publications/morph-catalog-craters-moon/morph-catalog-craters-moon.htm
[4] Slodarzh N.A., Rodionova Zh.F. Comparison of the cratering of the north and south polar regions of the Moon: Abstr. // The 21 th Moscow Solar System Symp. 2021.

HERMITE A CRATER AS A COLD TRAP NEAR THE NORTH POLE OF THE MOON

E.A. Feoktistova[1], S.G. Pugacheva[1], V.V. Shevchenko[1]
[1] *Sternberg Astronomical Institute, Moscow University, Moscow, Russia; katk@sai.msu.ru*

KEYWORDS:
Moon, polar regions, crater

INTRODUCTION:
The Hermit A crater is located in the vicinity of the north pole of the moon. Data from three lunar missions (Chandrayaan-1, -2, LRO) suggest that this crater is one of the places where deposits of water ice or other volatile compounds may be present.

The Hermite A crater (87.8° N, 312.9° E) is located in close proximity to the north pole of the moon. The diameter of the crater is 20 km, the depth reaches 3 km. The average slope of the inner walls of the crater is ~37° [2]. There are no terraces or collapses on the slopes of the crater. The crater has an uneven bottom covered with slides. Figure 1a shows the height distribution in the crater area according to [1]. Most of the inner surface of the crater is never illuminated by the Sun. We calculated the illumination condition in the region of Hermite A crater. According to our estimates, the area of the permanently shaded region in the crater reaches 110 km^2 (Fig. 1b). The maximum temperatures in permanently shaded areas in the crater do not exceed 60–70 K according to our estimates. Thus, the Hermite A crater may be a cold trap for water molecules and other volatile compounds.

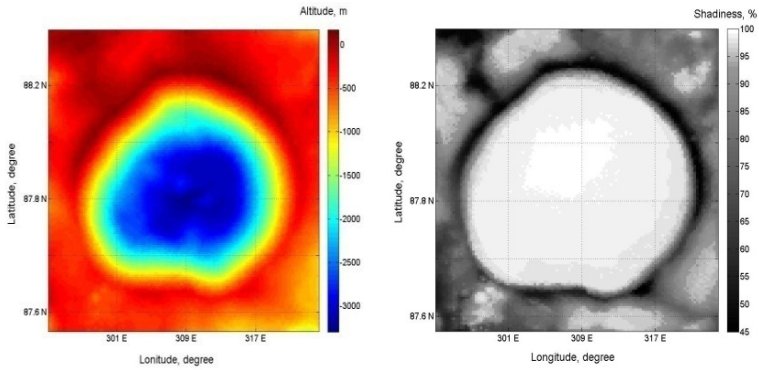

Fig. 1. Distribution of heights (a) and shading (b) in Hermite A crater

As is known, the main sources of water in the exosphere of the Moon are collisions with its surface of asteroids, meteorites and comets. We used the Monte Carlo method to estimate the amount of water that can be delivered to the Hermit A crater as a result of asteroid or comet impacts [3]. Water molecules migrated in the exosphere along ballistic trajectories. The time and place of the beginning of the movement of the water molecule on the surface of the Moon, the angle of the jump and the direction were chosen randomly. The take-off speed of the molecule was calculated on the basis of an estimate of the surface temperature at the launch site. During the flight, molecules could be destroyed during photolysis, or could evaporate from the exosphere if their speed overpassed the escape velocity for the Moon. If the molecule wasn't destroyed in photolysis and if its speed were not enough to leave the exosphere, it went down back on the surface.

We assumed that the sizes of comets lie in the range of 1–20 km, and the sizes of asteroids from 0.5 to 20 km. The proportion of water in comets is 50–70 %. The proportion of water in asteroids ranges from 5 to 40 % for carbonaceous chondrites [4]. When a comet from 1 to 20 km in size falls on the

surface of the Moon, from $1.49 \cdot 10^3$ to $1.6 \cdot 10^{13}$ g of water can be preserved in the North pole region. At the same time, from $8.3 \cdot 10^6$ to $9 \cdot 10^{10}$ g of water will fall into the Hermite A crater. When an asteroid collides with the size of 5 m to 10 km with the surface of the Moon, from 10^5 to $9.3 \cdot 0^{12}$ g of water can be saved. Our calculations show that even with a single collision of an asteroid or a comet with the Moon, from $0.8 \cdot 10^3$ to $5.3 \cdot 10^{10}$ g of water can be preserved in the Hermite A crater.

REFERENCES:

[1] https://ode.rsl.wustl.edu/moon/.
[2] http://selena.sai.msu.ru/Rod/Publications/morph-catalog-craters-moon-nord/morph-catalog-craters-moon-nord.htm.
[3] Feoktistova E.A., Zharkova A.Y., Kokhanov A.A., Rodionova Z.F. Migration of Water Molecules in the Permanently Shaded Areas of Polar Areas of Mercury // Earth, Moon and Planetsthis link is disabled. 2021. V. 125(2). Art. No. 5.
[4] Abramov O., Mojzsis S.J. // Icarus. 2011. V. 213. P. 273-279.

DYNAMICS OF THE MOON-EARTH SYSTEM AND ITS IMPACT ON CLIMATE

N.A. Chujkova[1], L.V. Zotov[1], L.P. Nasonova[1], T.G. Maksimova[1]
[1] *Sternberg Astronomical Institute Moscow University; chujkova@sai.msu.ru, wolftempus@gmail.com, nason@sai.msu.ru*

KEYWORDS:
Moon, Earth, Earth's rotation, the tidal drag, movements of the earht's crust, climate

INTRODUCTION:
Theoretical studies of the evolution of the Moon-Earth system, described in some detail in the works of Goldreich [1] and MacDonald [2], show that about 2 billion years ago the Moon approached the Earth at the smallest distance (of the order of $10R_E$), which led to an increase in tidal drag and to the dissipation of kinetic energy inside the Earth due to friction in viscous layers and to the heating of the Earth. All this could determine the processes that began at the border of the Archaean – Proterozoic.

Our analysis shows that modern uplifts of the earth's surface in the circumpolar regions are mainly associated with a decrease in the compression of the earth's surface due to a decrease in the speed of the Earth's rotation because of tidal braking due to the gravitational influence of the Moon. The Moon during the existence of the Moon-Earth system moves away from the Earth (by virtue of the law of conservation of angular momentum for the Moon-Earth system). The resulting variations in the rate of rotation of the Earth can lead to corresponding variations in the rise and fall of the surface in the circumpolar and equatorial regions of the Earth, especially noticeable in ancient geological epochs. Thus, according to paleontological data, 440 million years ago, the length of a day on Earth was 21.53 hours, i.e. the Earth has slowed down its rotation significantly since then. A similar deceleration of the Earth's rotation is fixed on the basis of an estimate of the discrepancies in the calculations of the dates of ancient eclipses, starting from the observation of an eclipse in Babylon 3022 years ago. The tidal drag increased at that time (due to a decrease in the radius of the Moon's orbit) also leads to an increase in the Earth's temperature, which contributes to the migration of fluid masses to the surface. In more ancient times, some changes in the surface of the Earth were also noted. For example, at the Archean–Proterozoic boundary 3.2–2.5 billion years ago, intensive processes of crustal melting and changes in the global fluid regime (processing of crustal material by deep fluid) were noted, which led to the formation of the modern upper crust [3]. This main stage in the formation of the earth's crust and the formation of ancient platforms ended at the turn of the Lower and Middle Proterozoic (1.9–0.1 billion years ago) [4].

Associated with a decrease in the Earth's compression, the tendency of internal fluid masses to hydrostatic equilibrium leads to their migration to the subpolar regions of the Earth, both from the deep regions of the Earth and from the equatorial regions. Such migration leads to an uplift of the Earth's surface in the polar regions, as well as to a decrease in the surface area of the equatorial regions. This can lead to compression of the crustal surface in mountain regions and to an increase in the number of faults, which increases the number of extreme events (earthquakes, tsunamis, volcanic eruptions) in equatorial regions. All these processes cause climate change both during periods of global warming (when the Moon moves away from the Earth) and ice ages (when the Moon approaches the Earth after it reaches its maximum distance ($72.5R_E$), where the role of solar tides increases). These periods are characterized by the appearance of continental ice sheets in the Lower Proterozoic, Upper Riphean, Vendian, Carboniferous-Permian [4]. Our studies based on modern data on the movement of the earth's crust [5] lead to the main conclusion that the cause of global vertical movements of the earth's surface (the rise of the polar regions and the lowering of the equatorial) is

a decrease in the speed of the Earth's rotation due to the tidal influence of the Moon. A fairly detailed modern analysis of the relationship between the Earth's rotation and climatic processes is given in Zotov's monograph [6]. The main cause of local movements, apparently, are seismic events (earthquakes, volcanic eruptions, etc.) associated with areas of maximum gradients of maximum stresses [7]. Thus, the evolution of the Moon-Earth system has a global impact on climate.

REFERENCES:

[1] Goldreich P. The lunar orbit history // Tides and resonances in the Solar system / ed. Zharkov V.N., M.: Mir, 1975. P. 97-129.
[2] McDonald G.J. Tidal friction // Tides and resonances in the solar system. M.: Mir, 1975. P. 9-96.
[3] Rodkin M.V. The role of the deep fluid regime in geodynamics and seismotectonics // Geodynamics and Seismotectonics. M., 1993. P. 86-95. P. 86-95.
[4] Monin A.S. History of the Earth. .M.: Nauka, 1977. P. 34-40.
[5] Chuikova N.A., Maksimova T.G., Chesnokova T.S., Grushinsky A.N. Vertical movements of the earth's crust according to ITRF2000, ITRF2005, ITRF2008, ITRF2014 data and their comparative analysis // Astronomy, geodesy and geophysics. M.: 2018. P. 78-89.
[6] Zotov L.V. Rotation of the Earth and climatic processes. M.: NRU HSE, 2022. 306 p.
[7] Chuikova N.A., Nasonova L.P., Maksimova T.G. A new solution of the inverse problem of gravimetry for the terrestrial planets and its verification for the Earth // Astronomy, geodesy and geophysics. M.: 2018. P. 90-113.

AUTONOMOUS ELECTRONIC YEARBOOK FOR OBSERVATIONS FROM THE SURFACE OF THE MOON

B.A. Epishin[1], M.I. Shpekin[1]
[1] *Kazan Federal University, Kazan, Tatarstan,* Russia;
epishin.boris@yandex.ru, MichaelS1@yandex.ru

KEYWORDS:
electronic lunar yearbook, physical libration, occultations and eclipses, topocentric coordinates, sunrises and sunsets, ephemerides for lunar-based observations, lunar-based observer, lunar topocenter

The return of the leading space agencies to the Moon brings closer the day when regular long-term observations will begin from its territory. Regardless of the location of the lunar observatory, as well as its scientific program, one of the important tasks is to prepare ephemeris calculations for successful observations. The ephemeris provision of a "lunar-based" observatory has a significant difference from a "ground-based" observatory: the remoteness of instruments and their management. Independent autonomous ephemeris software will be required for the lunar observer.

In this regard, we have developed a general computer program of the electronic Yearbook as the standalone multi-purpose tool for the observer on the surface of the Moon. The program was written in C# using WPF technology. The calculations were based on the barycentric coordinates of celestial bodies of the DE 440 JPL theory [1] for the time interval from 1550 to 2650. When calculating the topocentric coordinates of celestial bodies, the physical libration of the Moon was taken into account according to the algorithm from [2]. The program includes a catalog of about 800 the brightest stars [3]. The program took into account new theories of nutation and precession.

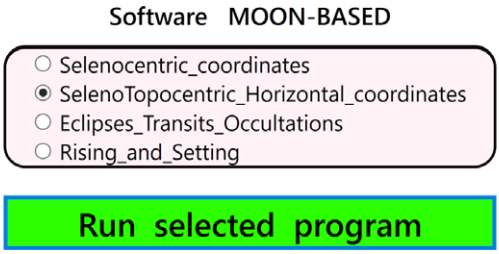

Fig. 1. The general interface of the program for lunar-based observer

The general interface of the developed program is shown in Fig. 1. It includes four subroutines. 1) Calculation of the selenocentric coordinates of celestial objects (Sun, Earth, large planets and about 800 bright stars). 2) Calculation of the horizontal coordinates of the azimuth and height of these celestial objects for a given topocenter. 3) Calculation of local circumstances of solar eclipses, transits of Mercury and Venus on the disk of the Sun, the coverage of stars and large planets by the Earth for given topocenter. 4) Calculation of the time points of sunrises and sunsets, upper and lower culminations of celestial bodies for given topocenter.

Figure 2 shows the interface of subroutine 2 for calculating the horizontal coordinates of celestial bodies in the lunar sky. A selection of celestial bodies is provided, topocenter with selenographic coordinates is set in three formats. Ephemerides are calculated with the selected step (day, hours and minutes). The option of calculating ephemerides is necessarily selected — according to dynamic or universal time. The output results are provided in two formats. In addition, the distance to the objects of the Solar system, the angular diam-

eter, the angular distance of celestial bodies from the Sun to the east or west is calculated (this is a particularly important parameter so as not to illuminate the light receiving devices of instruments). The phase and position of the "sickle" of the Earth in the lunar sky are also calculated.

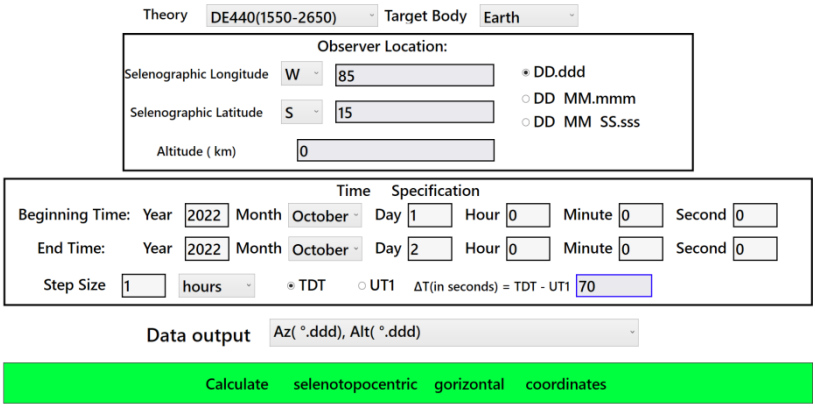

Fig. 2. The interface of the subroutine for calculating the horizontal coordinates azimuth and height of celestial bodies for given lunar topocenter

We compared the results of our azimuth and altitude calculation program with the web program of the NASA Horizon System website [5]. The results of the comparison are presented in Table 1. As can be seen from the table, the discrepancy is only 0.000 001 degrees or 0.004 arcseconds in both coordinates.

Table 1. Comparison of the horizontal coordinates of the Earth in accordance with the DE440 theory for three time points during one day on October 1, 2022 for the topocenter: Longitude = 85° W, Latitude = 15° S.

Dynamic Time	NASA		Our calculations	
	Azimuth	Altitude	Azimuth	Altitude
0 h 00 m 00 s	84.°942866	6.°580091	84.°942866	6.°580092
1 00 00	84. 892286	6. 534301	84. 892285	6. 534302
2 00 00	84. 842077	6.488336	84. 842077	6. 488336

As a result, all calculations in the developed program are independent of yearbooks. The autonomous electronic Lunar Yearbook makes it possible to obtain the necessary information about the exact position of celestial bodies in the lunar sky (the Sun, Earth, large planets and about 800 bright stars). As well as the visibility of eclipses, coverings, sunrises, sunsets and culminations for any point on the surface of the Moon and above the surface of the Moon (from the orbiter satellites of the Moon) at any time in the interval from 1550 to 2650. This will help in organizing and carrying out the astrometric observations from the surface of the Moon and from near-lunar orbits.

Currently, the developed software package is used to search for images of stars on the orbital images of the Moon delivered to Earth by the Soviet spacecraft Zond-8, as well as on the metric camera images of the American spacecrafts the Apollo series. In addition, a comparison with ephemeris calculations of the star trajectories presented by a group of authors led by [4] for a telescope mounted on one of the lunar poles will also give an idea about the reliability of the developed software package.

REFERENCES:

[1] JPL planetary and lunar ephemerides. ftp://ssd.jpl.nasa.gov/pub/eph/planets/.
[2] Taylor D.B., Bell S.A., Hilton J.L., Sinclair A.T. Computation of the Quantities Describing the Lunar Librations in The Astronomical Almanac. https://astro.ukho.gov.uk/data/tn/naotn74.pdf.

[3] Astronomical Yearbook for 2011. SPb: IAA RAS, 732 p.
[4] Petrova N.K., Nefedyev Y.A., Abdulmjanov T., Zagidullin A., Andreev A. The software complex for computer simulating the observation of stars from the lunar surface and calculating their selenographical coordinates] // Intern. Multidisciplinary Scientific GeoConferences SGEM (Survey, Geology, Ecology and Management). 2017. V. 17. No. 21. P. 687-694.
[5] Horizons System. https://ssd.jpl.nasa.gov/horizons/app.html#/.

MOON-EARTH' COMPARABLE FINE WAVE STRUCTURES CREATED BY EQUAL ORBITS (AROUND SUN AND IN GALAXY)

G.G. Kochemasov[1]
[1] *Institute of Geology of Ore Deposits, Petrography, Mineralogy and Geochemistry RAS, Moscow; kochemasov36@mail.ru*

KEYWORDS:
Chang'E-3, -4, -5, Moon, fine rippling, lunar frequencies coupling, Earth' flysch

Coupling orbital lunar frequencies (around Sun and in Galaxy) create fine centimeter-scale ripples. "Orbits make structures". In one circumsolar orbit occur two bodies-Moon and Earth. Thus, fine structures must be on both bodies. Having in mind different sizes of these bodies, fine structures in Earth are "flysch". This structure covers the whole planet, has various ages and thickness 0.1–1.5 m repeating characteristic sandstone-argillite compositions.

Orbits make structures -a main point of the new comparative wave planetology. However, any body moves in several orbits with various frequencies simultaneously. Thus, coupling orbits is a fundamental action in nature where exist together main and side frequencies and corresponding structures [1, 2]. The Moon has globally fine (centimeter size) side microwave structures and undulations, as well as much larger (e.g., 2πR, πR and πR/2) harmonic main structures. The Galaxy's rotation leaves its trace in lunar structures coupling with lunar rotations around Earth and Sun. Several Chinese lunar probes (Chang'e-3, -4, -5) and Apollo-11 images show real existence of centimeter-scale fine rippling desired explanation. The Galaxy rotation is known in science however defined approximately. We use for further calculations 1/200 000 000 y frequency [2, 3].

There are rare chances to observe fine lunar surface structures on landing sites of several probes. Among them the first was Apollo-11, and then in recent years Chang'E-3, -4 and now Chang'E 5 (Fig. 1). Landing surfaces possibly cleaned by thruster jets during landing sequences revealed clear cross-lineation of a few centimeters spacing and produced granules. This very fine granulation fortunately can be calculated by comparing it with a track of the Yutu' rover wheel (~10 cm wide) or the boot imprint of N. Armstrong (~20–25 cm long) and now with the drill or leg of the Chang'E-5. "Orbits make structures" — a main point of the wave planetology. Earth, as a scale, has a 1-year orbiting period and corresponding granule size of πR/4. Earth and its satellite both move in the Galaxy with ~1/200 000 000 y. frequency.

Calculations for the Moon: (1 y:200 000 000 y) πR = (1:200 000 000) 3.14×1738 km = 5.46 cm wavelength for the circumsolar orbiting (or 0.46 cm wavelength for around the Earth). These waves as crosscutting centimeters long ripples one observes on the above-mentioned surfaces and, as a conclusion, on the whole Moon.

Fine centimeter-scale lunar rippling must be find also in Earth, but in the larger scale (The Moon's equator radius is 1738 km, Earth's —6378 km). To find them on Earth is difficult because of the crust-atmosphere interaction and active tectonics. Mountain flysch series (thick sea sediments with characteristic repeating alternation of sandstones, aleurites and argillites) could represent fine alternation of uplifts and subsidences in area of washing away sediments (Fig. 2–5). "Fine" means decimeters-halves of meters. A solder steps long about 0,5–0,8 m can bring to ruin bridges if to step together — vibrations of the same scale.

Therefore, coupling lunar frequencies explain appearance of centimeter-scale rippling observed on the lunar surfaces. However, there is another cosmic body in the same circumsolar orbit — the Earth. One expects some structures on its surface comparable to mention above fine lunar rippling. An inspection finds them but somehow larger according to the ration char-

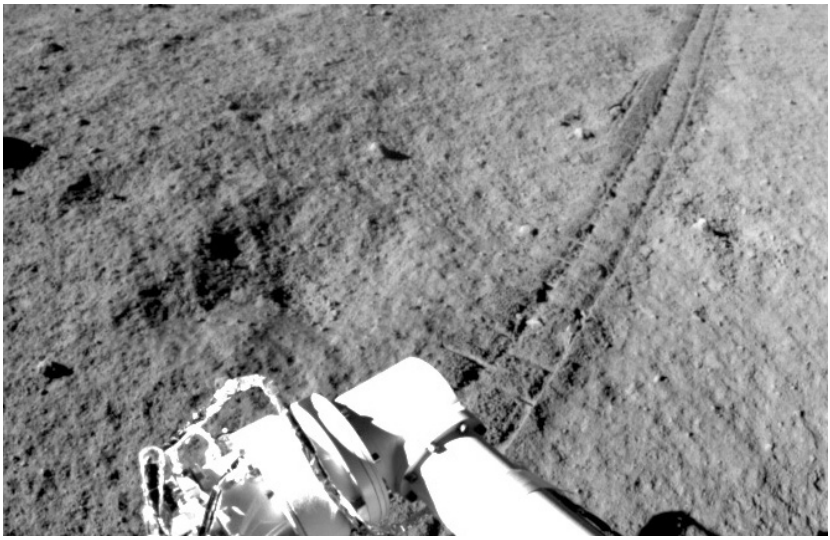

Fig. 1. Moon. Fine rippling near the Chang'e-3

Fig. 2. Earth. Flysch-in-zumaia-gipuzkoa-bask-Spain-29137506.jpg

Fig. 3. Flysch-itzurum-in-zumania-bask-Spain-r-150810483.jpg

Fig. 4. Flysch-zumania-10[2].jpg

Fig. 5. Rocks-51.jpg

acteristics of two bodies (see Fig. 2–5). It is famous but unexplained terrestrial flysch. It is developed over all terrestrial surface, like the lunar one, but have decimeter-meter sizes of repetition. It is discovered in Phanerozoic sediments (Pz-Mz-Cz) and have sizes of sandston-aleurite-argillite repetitions about 0.1–1.5 m. Sometimes aleurite is absent, sandstones are fine to course grained. In sections appear conglomerates, breccia, and organic matter. Car-

bonates and large fragments of ruined continental crust also present. Undulation of surfaces of sediment origin (washout) are proposed to explain this repetition observed on the whole terrestrial surface. Undulations of water surface were also proposed [10, 11]. Flysch origin as turbidites exists in mobilism. Characteristic features of this event is the whole Earth (compare to the whole Moon) and numerous repetition of similar sediments [4–10]. Flysch there is in Alps, Caucasus, Carpathian, Himalaya, Pyrenean, Iran, Turkey, Balkans, Tientsin, Urals, Ands, Cuba, and so on.

SUMMARY:

Several lunar landing points, including Chang'e-5, have detailed surface images showing centimeter-size intercrossing ripples. They are results of coupling lunar frequencies: around Sun and Earth and in the Galaxy. This frequency modulation process is the most common as all celestial bodies move simultaneously in several orbits with various orbital frequencies. This process [1–3] might explain various wave emissions throughout the Universe. As Moon and Earth together move in one circumsolar orbit and in Galaxy, larger Earth also has similar fine π-structures-ripples (but larger in meters).

REFERENCES:

[1] Kochemasov G.G. Gamma-ray emission in the Universe – a possible explanation by the wave modulation // Gamma-Ray Burst Symp. 2016. 4107.pdf.
[2] Kochemasov G.G. Modulated wave frequencies in the Solar system and Universe // J. Physics and Application. 2018. V. 12(4). P. 68-75. DOI: 10.13189/ujpa.2018.120402.
[3] Kochemasov G.G. Modulated lunar orbiting frequencies and corresponding them structures (Chang'E-3, -4 discoveries) // 4th LDSE. 2019. Abstr. P. 100-102.
[4] Keller B.M. Flysch Proterozoic formation in Zilair synclinory in Southern Urals and similar with it formations // GIN. 1949. V. 104. Geologic Ser. No. 34. 173 p. Ign_104_1948_geol_ser34.pdf. (In Russian.)
[5] Keller B.M., Puscharovsky Yu.M. Carboniferous flysch from river Sakmara basin // News of Academy of Sciences. Ser. Geol. 1945. No. 6. (In Russian.)
[6] Leonov M.G. Wild flysch of the Alpine region. M.: Nauka, 1975. 149 p. (In Russian.)
[7] Misens G.A. Upper Paleozoic flysch of the Western Urals. Rehab. Thesis. Inst. Geol. Geoph., Ural. Dept. Russ. Acad. Sci. Ecaterinburg: UrO RAN, 1997. (In Russian.)
[8] Sovetov Yu.K. The Upper Rifean grey wacke flisch of the Small Caratau // Flisch and flischoid complexes in various structural zones of the Earth's crust: Thesis of reports. M., 1990. P. 125-126. (In Russian.)
[9] Frolov V.T. Flisch formation- definition of understanding // Bull. MOIP. Section Geol. 1988. V. 63. Iss. 4. P. 16-32.
[10] Vassoevich N.B. Flysch and methods of its study. Leningrad: Gostoptechisdat, 1948. 240 p. (In Russian.)
[11] Vassoevich N.B. Conditions for the formation of flysch Leningrad: Gostoptechisdat, 1951. 240 p. (In Russian.)

MOON-DICHOTOMOUS AS OTHER COSMIC BODIES (FROM ASTEROIDS TO UNIVERSE)

G.G. Kochemasov[1]
[1] *IGEM RAS, Moscow; kochemasov.36@mail.ru*

KEYWORDS:
Cosmic bodies, orbits, ORCs, galaxies, planets, satellites, asteroids, fundamental wave

Orbits make structures-main point of the comparative wave planetology. Not depending sizes and compositions of celestial bodies they acquire tectonic dichotomy (two hemispheres) connected with warping action of the fundamental wave.

The main point of the wave planetology is: “Orbits make structures”. It means that movement in non-round orbits makes waves creating structures (Fig. 1, 2) However, any cosmic body moves in several orbits. They all participate in structuring [1]. Their frequencies are divided and multiplied creating new frequencies and corresponding them structures. They are (frequencies) very small and very big. Very slow but very energetic rotation of large cosmic formations (galaxies and the larger assemblies) make very fine oscillations up to microwaves, roentgen and gamma radiations infilling cosmos. From the other end, oscillations passed through fundamental wave and corresponding it tectonic dichotomy of any body. In figures are examples of bodies of various sizes from the ORC (Odd Radio Circles) and Galaxy to small asteroids (Fig. 3–9).

The row is finished with small asteroids Itokawa and Eros. Both reveal tectonic dichotomy; especially sharp in Itokawa with its convexo-concave shape (see Fig. 9). The other end of this row include giant cosmic formations like OPCs and galaxies and larger ones finishing at Universe. The Odd Radio Circles observed by radio telescopes include several galaxies and have sizes about 1 arcminute (see Fig. 3). They are not visible in X-ray, optical or infrared wavelengths. In Fig. 3 this strange radio circle shows opposition of flat and sharp ends.

The Universe also is dichotomist divided at uplifted and subsided halves. The humankind occupies the uplifted halve-in the religious sense “paradise”, the subsided halve thus is “hell”.

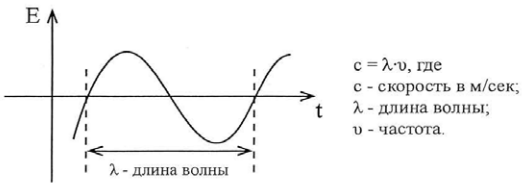

1. **2.**

Fig. 1, 2. Fundamental wave in line and circle.

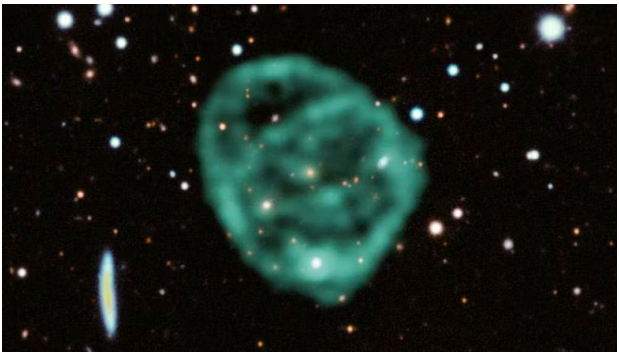

Fig. 3. ORC. Odd Radio Circles. 50548408_9e433f69754ec97cde2d87581d946275.jpg. MeerKAT observations.

Fig. 4. A spiral Galaxy. ESO 510-613. PIA04213.

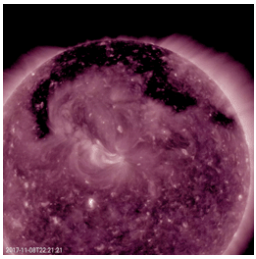

Fig. 5. Sun. PIA22113.Coronal hole all spread out.

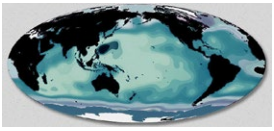

Fig. 6. Earth. Hemispheric structure.

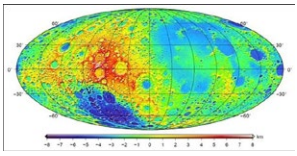

Fig. 7. Moon. Hemispheric structure.

Fig. 8. Asteroid Eros. Convexo-concave shape.

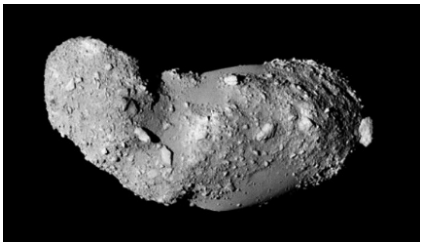

Fig. 9. Asteroid Itokawa. Convexo-concave shape.

REFERENCES:

[1] Kochemasov G.G. Modulated wave frequencies in the Solar system and Universe // J. Physics and Application. 2018. V. 12(4). P. 68-75. DOI: 10.13189/ujpa.2018.120402.
[2] Norris R. et al. Unexpected Circular Radio Objects at High Galactic Latitude // Astronomical Society of Australia. 2006. V. 38. Art. No. e003. https://doi.org/1048550/arXiv.2006.

SESSION 3. GIANT PLANETS (GP) ORAL SESSION

HYPERION (C7): CONTROL POINT NETWORK AND SHAPE MODEL. DIFFICULTIES AND SOLUTIONS

N.A. Slodarzh[1], A.E. Zubarev[1], I.E. Nadezhdina[1], N.A. Kozlova[1]
[1] *Moscow State University of Geodesy and Cartography (MIIGAiK), MIIGAiK Extraterrestrial Laboratory (MExLab), 105064, Gorokhovsky per, 4, Moscow, Russia; n_kozlova@miigaik.ru*

KEYWORDS:
Saturnian satellite, Hyperion, Control point network, Shape, Satellite rotations, Hyperion principal axis, Orthomosaic, Chaotic motions.

INTRODUCTION:
All investigations of outer planets body starting from reference frame definition or selection, because all scientific results must be referenced to the selected reference frame (one or a few with single-valued transferring). Hyperion (C7) is largest irregular satellite in Solar system and there isn't a rotation model for it yet [1, 2, 3] therefore a reference frame can't be defined. Such problem is typical for bodies with chaotic rotation. However, we can still determine shapes, surface models and figures for such satellites. This study will focus on developing a comprehensive solution to the shape of the body determination based on the results of the photogrammetric processing of space images and orbital data.

IMAGE DATA:
Frist spacecraft which had a flyby of Hyperion was Voyager in 1980–1981. This flyby gives interesting information about the body form and it raises even more questions about its rotation model. Unfortunately, Voyager`s flyby was a far away from surface and it was a short one (only 2 days of observations). Before completing its mission in September 2017, Cassini spacecraft transmitted to the Earth the latest images of Hyperion. The resolution of obtained images is up to 26 m/px. Cassini was equipped with a narrow (NAC) and a wide-angle (WAC) camera. During the mission Cassini has transmitted more than 2800 images of Hyperion and more than 50 images with medium and high resolution (500 m/pix and better). All this data was obtained in period from 2004–2016.

RESULTS:
We have developed a control point network consisting of 1954 points using 116 Cassini images from 26 m/pix to 3.3 km/pix with average errors better than 7 km. Body shape model was determined from control point network using 3D coordinates of points. In this study we determine a body shape model using two steps because there isn't a rotation model yet and body axes were determined only by the largest flyby. In the first step we pre-orient body axis to the purpose of reducing a difference between an ellipsoid model and 3D control point cloud. In the next step we process stereo pairs and improve the shape and improve the density of the point cloud (~1.6 mln points). Finally, we use all available data to determine 6 parameters (a, b, c, ω, ϕ, κ), that define the size and axis of the shape.

Model	a, km	b, km	c, km	r, km
P. C. Thomas et al., 2010	180.1±2.0	133.0±4.5	102.7±4.5	135±4
This study	177.6±0.2	128.5±0.2	105.6±0.1	141.7±0.3

REFERENCES:
[1] Tarnopolski M. Rotation of an oblate satellite: Chaos control // Astronomy and Astrophysics, 2017b, 606, A43, DOI: 10.1051/0004-6361/201731167.
[2] Thomas P., Helfenstein P. The small inner satellites of Saturn: Shapes, structures and some implications // Icarus, 2020, 344, 113355, DOI: 10.1016/j.icarus.2019.06.016.
[2] Thomas P. C., Yoder C. F., Synnott S. P., Salo H., Veverka J., Simonelli D. P., Helfenstein P., Carcich B., Black G. J., Nicholson P. D., Binzel R. P., Gaffey M. P., Zellner B. H., Bell J. F. III and Clark B.E (2021). Small Body Optical Shape Models Bundle V1.0. urn:nasa:pds:ast-sat.thomas.shape-models::1.0. NASA Planetary Data System; https://doi.org/10.26033/g5e0-kh52

UPDATED GANYMEDE CONTROL POINT NETWORK BASED ON JUNO MISSION DATA

A.E. Zubarev[1], I.E. Nadezhdina[1], N.A. Slodarzh[1]
[1] *Moscow State University of Geodesy and Cartography (MIIGAiK), MIIGAiK Extraterrestrial Laboratory (MExLab), 105064, Gorokhovsky per, 4, Moscow, Russia; fair-max@yandex.ru*

KEYWORDS:
Ganymede, 3D control points network (CPN), JUNO mission data, photogrammetric remote sensing

INTRODUCTION:
The increased interest in Galilean moons of Jupiter and especially in the largest satellite of outer planets of the solar system, Ganymede, is associated with the planned JUICE ESA mission, which is scheduled for launch in 2023. The latest data of the surface of Ganymede was obtained during the Galileo mission in 2001. In the end of August 2021, during the JUNO mission, the new imagery data with a resolution of better than 1 km/pixel was obtained, covering a significant part of the surface of Ganymede (up to 30%) and allowing a more detailed study of the surface relief and to refine the control point network [1]. Also at the end of 2021, NASA prepared and updated Galileo mission's navigation information in order to improve the accuracy of the mutual coordinate reference of JUNO and Galileo missions [2].

RESULTS:
As a result of the combining of the images of JUNO, Galileo and Voyager-1, 2 missions, the control point network was updated and now includes more than 2,050 points with mean accuracy of 0.35 pixel and a 3.5 km (RMS). The body size of Ganymede has been updated [3]. As a result of preliminary analysis of navigation information of spacecraft of different missions, it was detected that the orbits of the Galileo spacecraft and the JUNO spacecraft have good agreement at less than 10 km, however, the accuracy of the Voyager-1, 2 spacecraft orbits have significant (about 80 km) systematic shifts in the relative fixed position of the orbital data from the JUNO spacecraft. These conclusions are preliminary, but the very fact that there are significant systematic differences between Voyager missions suggests the need to adjust the orbit taking into account all available information, as was already done for Galileo. On the basis of the control point network, a mosaic was built, combined with the already available data from previous years, and local DEMs were obtained, with a vertical resolution of better than 1 km [4].

REFERENCES:
[1] Juno Participating Scientist Program // C.25 Juno Participating Scientist Program // https://nspires.nasaprs.com/external/solicitations/summary.do?solId=%7B25E361E0-C3ED-533F-6833-FE0059DFACCB%7D&path=&method=init
[2] https://naif.jpl.nasa.gov/pub/naif/GLL/kernels/spk/gll_951120_021126_raj2021.bsp
[3] Zubarev A.E., Nadezhdina I.E., Brusnikin E.S., Karachevtseva I.P., Oberst J., 2016, A technique for processing of planetary images with heterogeneous characteristics for estimating geodetic parameters of celestial bodies with the example of Ganymede // Solar System Research, 2016, Vol. 50, No. 5, pp. 352-360. ISSN 0038-0946.
[4] Melnikova M.A., Nerusin V.A., Zubarev A.E., Nadezhdina I.E., Zharkova A.Yu., Slodarzh N.A. NEW GLOBAL MOSAIC OF GANYMEDE, DETAILED DEMS AND MAPS // 13ms3. 2022. 2 p.

SESSION 3. GIANT PLANETS (GP) POSTER SESSION

ORGANIC MATTER IN THE STRUCTURE OF PARTIALLY DIFFERENTIATED TITAN

A.N. Dunaeva[1], V.A. Kronrod[1], O.L. Kuskov[1]
[1] *V.I. Vernadsky Institute of Geochemistry and Analytical Chemistry RAS, Moscow; dunaeva.an@gmail.com*

KEYWORDS:
Titan, organic matter, internal structure.

INTRODUCTION:
Organic matter (OM) is widespread in the Solar system, as well as far beyond its limits. Space spectroscopy data indicate a significant (up to 45%) content of the organic component in comets [1–4], in most main-belt asteroids and in trans-Neptunian objects, including asteroids of Kuiper belt [5-7].

In meteorite matter, the highest concentration of organic compounds (up to 4%) is found in carbonaceous chondrites CI, CM, and CR [8]. Organic matter is represented by both refractory kerogen-like material and numerous soluble forms. Depending on the class of meteorites, the proportion of the refractory organic component is 70–99% of the total OM content in chondrites [9].

Numerous astronomical observations indicate the presence of carbonaceous dust in the interstellar medium [10]. An analysis of interstellar dust particles (IDP) collected in the lower layers of the Earth's stratosphere and formed by short-period comets and main-belt asteroids [11] showed that the carbon content in such IDPs is 2-3 times higher than in the most organic-rich CI chondrites and is about 12.5% [12]. Theoretical models of rock-ice planetesimals, which are the source material for most cosmic bodies, show that their content of organic matter can reach about 30% [13].

A varied range of organic compounds (from the simplest organic molecules to complex macromolecular forms) has been found in the ice plumes of Enceladus [14]. This indicates the presence of organic matter in the satellite's interior.

In addition to Enceladus, tholin-like organic compounds are detected on the surface of Jupiter's large icy moons, Ganymede and Callisto [15], as well as on many of Saturn's icy moons [16]. However, the largest reserves of organic matter and hydrocarbons have been found on Titan in the form of organic molecules of atmospheric aerosols, solid and liquid hydrocarbons that form the satellite's topography and fill numerous lakes on its surface.

Thus, the ubiquitous distribution of organic matter in space objects allows us to consider it as a significant component of small bodies and satellites of the Solar system. In particular, models of the internal structure of Titan and Ganymede [17] show that the satellites may be composed of substance similar to carbonaceous chondrites with an addition of 23% and 16% organic matter, respectively. Models of the dwarf planets (Ceres) show that the composition of Ceres can be described by a mixture of water-altered rocks of CI-chondrite composition with 7-16% of high-molecular organic substances [18].

In this paper, we consider the structure of partially differentiated Titan at different contents of low-density organic matter. The influence of organic matter on the size and density of the rock-ice mantle and the inner core of the satellite is considered.

DESCRIPTION OF THE MODEL AND THE CALCULATION RESULTS:
The model of partially differentiated Titan assumes that the satellite consists of an outer water-ice shell with an internal ocean, an extended rock-ice mantle, and an inner rock-iron core. The rocky component of the satellite was modeled as a mixture of L/LL-chondrite substance and refractory organic material. The density of the chondritic substance under the T-P conditions of Titan changed in the range of 3370–3870 kg/m^3. The OM content varied in the range of 0–20 wt. %. The organic matter in the Titan's interior was considered to be incompressible with a constant density of 1400 kg/m^3 [17]. Model description, main parameters and calculation methods are given in [19].

The calculation results show that an increase in the content of organic matter leads to a significant decrease in the density of Titan's rocky material. In particular, with an increasing in the OM content to 20%, the density of the Titan's inner core decreases by an average of 25%, and this leads to an increase in the radius of the core by more than 2.5 times (Fig. 1). In doing so, the thickness of the rock-ice mantle decreases up to 3.5 times, and its density drops by 10%, with the thickness of the water-ice shell of the satellite practically unchanged (Fig. 2).

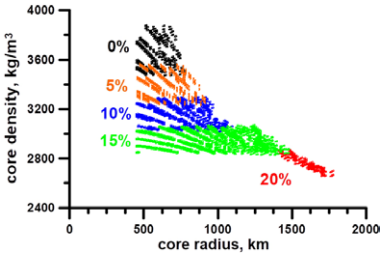

Fig. 1. Effect of organic matter on the size and density of the inner core of Titan. Here and below, the numbers show the content of the organic component in the rocky substance of the satellite.

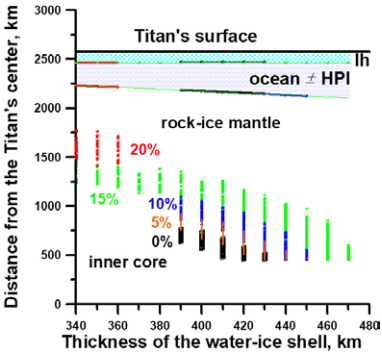

Fig. 2. Influence of organic matter on the thickness of the water-ice shell and rock-ice mantle of Titan. HPI is a layer of high-pressure water ices at the internal ocean and rock-ice mantle boundary. Ih – is the outer ice crust of Titan.

The data obtained in this work allow us to conclude that the admixture of organic matter significantly changes the structural parameters of Titan. In addition, being a low-density binder, organic matter should probably affect the viscoelastic characteristics of the Titan's rocky component, and, consequently, the rheological properties of its interior, which must be taken into account when constructing thermophysical models of the satellite.

REFERENCES:

[1] Bardyn A., Baklouti D., Cottin H. et al. (2017). Carbon-rich dust in comet 67P/Churyumov-Gerasimenko measured by COSIMA/Rosetta. Monthly Notices of the Royal Astronomical Society, 469(Suppl_2), S712-S722.
[2] Jessberger E.K., Christoforidis A., Kissel J. (1988). Aspects of the major element composition of Halley's dust. Nature, 332(6166), 691-695.
[3] Fray N., Bardyn A., Cottin H. et al. (2016). High-molecular-weight organic matter in the particles of comet 67P/Churyumov–Gerasimenko.Nature, 538(7623), 72-74.
[4] Brownlee D. (2014). The Stardust mission: analyzing samples from the edge of the solar system. Annual Review of Earth and Planetary Sciences, 42, 179-205.
[5] Gaffey M.J., Burbine T.H., Binzel R.P. (1993). Asteroid spectroscopy: Progress and perspectives. Meteoritics, 28(2), 161-187.
[6] Seccull T., Fraser W.C., Puzia T.H. et al. (2018). 2004 EW95: A Phyllosilicate-bearing Carbonaceous Asteroid in the Kuiper Belt. The Astrophysical Journal Letters, 855(2), L26.

[7] Fernández-Valenzuela, E., Pinilla-Alonso, N., Stansberry, J. et al. (2021). Compositional Study of Trans-Neptunian Objects at λ> 2.2 μm. The Planetary Science Journal, 2(1), 10.
[8] Vinogradoff V., Le Guillou C., Bernard S. et al. (2017). Paris vs. Murchison: Impact of hydrothermal alteration on organic matter in CM chondrites.Geochimica et Cosmochimica Acta, 212, 234-252.
[9] Pizzarello S., Cooper G.W., Flynn G.J. (2006). The nature and distribution of the organic material in carbonaceous chondrites and interplanetary dust particles. Meteorites and the early solar system II, 1, 625-651.
[10] Ehrenfreund P., Charnley S.B. (2000). Organic Molecules IN THE Interstellar Medium, Comets, AND Meteorites: A Voyage.Annu. Rev. Astron. Astrophys, 38, 427-83.
[11] Flynn G.J. (1989). Atmospheric entry heating: A criterion to distinguish between asteroidal and cometary sources of interplanetary dust. Icarus, 77(2), 287-310.
[12] Thomas K.L., Blanford G.E., Keller L.P. et al. (1993). Carbon abundance and silicate mineralogy of anhydrous interplanetary dust particles. Geochimica et Cosmochimica Acta, 57(7), 1551-1566.
[13] Marboeuf U., Thiabaud A., Alibert Y., Cabral N., Benz W. (2014). From stellar nebula to planetesimals. Astronomy & Astrophysics, 570, A35.
[14 Postberg F., Khawaja N., Abel B., Choblet G. et al. (2018). Macromolecular organic compounds from the depths of Enceladus. Nature, 558(7711), 564-568.
[15] McCord T.A., Carlson R.W., Smythe W.D. et al. (1997). Organics and other molecules in the surfaces of Callisto and Ganymede. Science, 278(5336), 271-275.
[16] Cruikshank D.P., Wegryn E., Dalle Ore C.M., Brown R.H. et al. (2008). Hydrocarbons on Saturn's satellites Iapetus and Phoebe. Icarus, 193(2), 334-343.
[17] Néri A., Guyot F., Reynard B., Sotin C. (2020). A carbonaceous chondrite and cometary origin for icy moons of Jupiter and Saturn. Earth and Planetary Science Letters, 530, 115920.
[18] Zolotov M.Y. (2020). The composition and structure of Ceres' interior. Icarus, 335, 113404.
[19] Kronrod V.A., Dunaeva A.N., Gudkova T.V., Kuskov O.L. Matching of Models of the Internal Structure and Thermal Regime of Partially Differentiated Titan with Gravity Field. Solar System Research, 2020, Vol. 54, No. 5, pp. 405-419.

CONVECTION IN THE ROCK-ICE MANTLE OF PARTIALLY DIFFERENTIATED TITAN

V.A. Kronrod[1], A.N. Dunaeva[1], O.L. Kuskov[1]
[1] *Vernadsky Institute of Geochemistry and Analytical Chemistry, Russian Academy of Sciences*

KEYWORDS:
Titan, rock-ice mantle, viscosity, convection

INTRODUCTION:

The possibility of the existence of an effective convective heat transfer in the mantle of partially differentiated Titan is considered for two compositions of the rocky component – without organic matter and with organic matter. It is shown that the values of heat fluxes from the core and the calculated Rayleigh numbers suggest the possibility of the existence of a convecting rock-ice mantle in Titan.

The values of the moment of inertia and the mass of Titan allow the construction of two main types of models of the internal structure of the satellite. Fully differentiated models include a water-ice shell (with or without an ocean), a hydrous silicate mantle, and possibly a silicate core. In partially differentiated models, there is no complete separation of ice and iron-rocky components. The mantle of the satellite consists of an undifferentiated rock-ice mixture (1, 2). The efficiency of heat transfer is estimated by the Rayleigh number, which in relation to the mantle of Titan can be written as follows (3):

$$Ra=\frac{\alpha\rho g q d^4}{\kappa k \eta} \quad (1)$$

where α is the coefficient of thermal expansion, ρ –the density of the mantle, k –the coefficient of thermal conductivity, κ –the coefficient of thermal diffusion, η –viscosity, d –the thickness of the mantle, q –the total heat flux passing through the mantle.

The problem of heat transfer in high-pressure (HP) ice in models of fully differentiated icy satellites and Titan was considered in detail in [4, 3]. It was shown that with heat flows from the core of $q_c \leq \approx 7$ mWm^{-2} and the thickness of the HP ice of $d \geq \approx 200$ km, there is no melting of ice at the core–rocky-ice mantle boundary, the thickness of the mantle does not change over time. The average viscosity of high-pressure ice in the mantle for these estimates is assumed to be $\eta \approx 10^{16}$ Pa s, the Rayleigh number is estimated to be $Ra \approx 10^7$–10^8 [4].

In this study, we consider heat transfer in the rock-ice mantle of partially differentiated Titan. Titan, according to the data on the moment of inertia and mass [1, 2], consists of a water-ice shell, a rocky-ice mantle and an iron- core. It is assumed that the mantle consists of a homogeneous mixture of rock and ice. The rate of "Stokes" deposition of rock particles is negligible compared to the rate of convective and turbulent motion of matter in the mantle. The composition of the rocks in the calculations was set in the form of a homogeneous mixture of substances similar in properties to silicates and organics [5]. Calculations have shown that the volume concentration of stone (Cv) in the mantle of Titan depends on the mass concentration of organic matter in the rocks and can be in the range 0.38–0.8. The viscosity of the mixture of rocks (silicates + organic matter) and ice depends to a certain extent on the volume concentration of the rocks.

Experiments [6] showed that at Cv≈0.4–0.5, the viscosity of a mixture of sand and high-pressure ice is two orders higher than the viscosity of high-pressure ice, and for Cv≈0.56, the viscosity of the composite is close to the viscosity of dry sand. As our calculations have shown, in the case of the presence of organic matter in the rocks (C_V= 0.33), the viscosity of the composite silicates + organic decreases by three orders and the resulting viscosity of the composite ice + silicates + organic is close to the viscosity of ice. Table 1 shows the

results of calculations of viscosity, Rayleigh numbers in the mantle for various variants of the composition and viscosity of the components of mantle composites.

The conducted studies suggest the possibility of the existence of a convecting rock-ice mantle in Titan.

Table 1. The number of Ra in the Titan mantle for various mantle parameters

Viscosityof HP ices, Pa s	Viscosityof organic matter, Pa s	Viscosityof silicates, Pa s	Mantle viscosity, Pa s	The number of Ra (without organic matter)	The number of Ra (with organic, x_{org}=0.15)
$1.3 \cdot 10^{17}$	-	10^{24}	$1.26 \cdot 10^{17}$	$5.8 \cdot 10^{7}$	-
$1.3 \cdot 10^{17}$	21.8	10^{24}	$6.5 \cdot 10^{16}$	-	$5.7 \cdot 10^{9}$
$1.3 \cdot 10^{16}$	$1.2 \cdot 10^{5}$	10^{21}	$8.4 \cdot 10^{15}$	-	$4.3 \cdot 10^{10}$
$1.3 \cdot 10^{17}$	$1.2 \cdot 10^{10}$	10^{21}	$1.8 \cdot 10^{17}$	-	$2 \cdot 10^{9}$

ACKNOWLEDGEMENTS
This study was carried out under government-financed research project for the Vernadsky Institute of Geochemistry and Analytical Chemistry, Russian Academy of Sciences

REFERENCES:

[1] Dunaeva A.N., Kronrod V.A., Kuskov O.L., Physicochemical models of the internal structure of partially differentiated Titan // Geochem. Int. 2016. V. 54. No. 1, P. 27-47.
[2] Kronrod V.A., Dunaeva A.N., Gudkova T.V., Kuskov O.L. Matching of Models of the Internal Structure and Thermal Regime of Partially Differentiated Titan with Gravity Field // Solar System Research. 2020. V. 54. No. 5, P. 405-419.
[3] Choblet, G., Tobie, G., Sotin, C., Kalousova, K., Grasset, O. Heat transport in the high-pressure ice mantle of large icy moons // Icarus. 2017. V. 285. P. 252-262.
[4] Kalousova K., Sotin C. Dynamics of Titan's high-pressure ice layer // Earth and Planetary Science Letters. 2020. https://doi.org/10.1016/j.epsl.2020.116416
[5] Néri A., Guyot F., Reynard B, Sotin C. A carbonaceous chondrite and cometary origin for icy moons of Jupiter and Saturn // Earth Planet. Space Sci. 2020. V. 530 (115920). https://doi .org /10 .1016 /j .epsl .2019 .115920.
[6] Durham W.B., Kirby S.H., and Stern L.A. Effects of dispersed particulates on the rheology of water ice at planetary conditions // J.Geophys Res. 1992. V. 97. P. 20,883-20,897.

NEW GLOBAL MOSAIC OF GANYMEDE, DETAILED DEMs AND MAPS

M.A. Melnikova[1], V.A. Nerusin[1], A.E. Zubarev[1], I.E. Nadezhdina[1], A.Yu. Zharkova[1], N.A. Slodarzh[1]

[1] *Moscow State University of Geodesy and Cartography (MIIGAiK), MIIGAiK Extraterrestrial Laboratory (MExLab), 105064, Gorokhovsky per, 4, Moscow, Russia; msrgo0902@bk.ru*

KEYWORDS:
Ganymede, Juno, Natural satellites, Geomosaic, Planetary cartography, Geomorphology, Ganymede map

INTRODUCTION:
First 490 images of Ganymede's surface (with resolution from 470 to 20 km/pixel) were obtained by Voyager 1 and 2 in 1979 using the Narrow Angle Camera (NAC) and Wide Angle Camera (WAC). Based on these images, the first control point network of Ganymede was created, including 370 points [1]. In 1995 Galileo spacecraft transmitted another 149 images of Ganymede (with resolution < 20 km/pixel) during 15 flybys. After that the well-known USGS mosaic was made, which can be found at The Annex of the PDS Cartography & Imaging Sciences Node [2]. A new control points network was created from updated ephemeris in 2015 [3] and formed the basis of a new mosaic [4]. At MExLab, we updated the control points network using data obtained by Juno (JunoCam) in 2021 [5]. As a result, the latest mosaic was created, which was used to map Ganymede at different scale levels.

DATA AND METHODS:
Our newest mosaic of Ganymede includes 126 Voyagers images (with resolution from 0.46 to 25.72 km/pixel), 108 Galileo images (with resolution from 0.02 to 9.14 km/pixel), and – for the first time – 44 Juno images (with resolution from 0.87 to 1.73 km/pixel).

Image orthorectification was performed in SpaceMosaic software on the basis of the DEM obtained from the points of the new control points network [6]. The radius of the sphere derived from the control points network is 2633.3 km. Radiometric correction and construction of the whole mosaic was done in the PHOTOMOD GeoMosaic software [7]. This made it possible to obtain a photosynthesized and photometrically corrected mosaic of Ganymede.

Mapping was done in ArcGIS software. We created both – a global map (with equatorial and polar regions) and detailed large scale maps of selected sites of interest – surroundings of Tros crater, Phrygia Sulcus and Enki catena. In addition to common landforms (craters, chains of craters, furrows, etc.), these sites contain more specific features: relaxed craters [8], strained craters [9], craters with central pits [10], palimpsests [11], dark terrains and areas with high albedo values [12]. The choice of sites is closely related to the current scientific research of Ganymede and accessibility of suitable data sets for DEMs creation.

RESULTS:
As a result, we present our new mosaic of Ganymede as well as DEMs and maps. Such products and their analysis are very important for understanding relief formation processes on satellites of the giant planets. The use of Juno data for study and mapping, on the other hand, makes it possible not only to supplement previous geomorphological studies, but also to compare our results with them.

REFERENCES:
[1] Davies M.E., Colvin T.R., Oberst J., Zeitler W., Schuster P., Neukum G., McEwen A.S., Phillips C.B., Thomas P.C., Veverka J., Belton M.J.S., Schubert G. The Control Networks of the Galilean Satellites and Implications for Global Shape // Icarus, Vol. 135, Issue 1, 1998, pp. 372-376, https://doi.org/10.1006/icar.1998.5982

[2] https://astrogeology.usgs.gov/search/map/Ganymede/Voyager-Galileo/Ganymede_Voyager_GalileoSSI_global_mosaic_1km

[3] Zubarev A., Nadezhdina I., Oberst J., Hussmann H., Stark A., 2015. New Ganymede point network Ganymede and global shape model // Planetary and Space Science, Vol. 117, 2015, pp. 246-249, http://dx.doi.org/10.1016/j.pss.2015.06.022
[4] Kersten E., Zubarev A.E., Roatsch Th., Matz K.-D. Controlled Global Ganymede mosaic from Voyager and Galileo images // Planetary and Space Science, Vol. 206, 2021, 105310, ISSN 0032-0633, https://doi.org/10.1016/j.pss.2021.105310
[5] Zubarev A.E., Nadezhdina I.E., Slodarzh N.A. Updated Ganymede control points network based on JUNO mission data // 13MS3, 2022, p. 2
[6] Zubarev A.E., Nadezhdina I.E., Brusnikin E.S., Karachevtseva I.P., Oberst J., 2016, A technique for processing of planetary images with heterogeneous characteristics for estimating geodetic parameters of celestial bodies with the example of Ganymede // Solar System Research, 2016, Vol. 50, No. 5, pp. 352-360. ISSN 0038-0946.
[7] https://en.racurs.ru/program-products/photomod-geomosaic/
[8] Singer K.N., Bland M.T., Schenk P.M., McKinnon W.B. Relaxed impact craters on Ganymede: Regional variation and high heat flows // Icarus, Vol. 306, 2018, pp. 214-224, ISSN 0019-1035, https://doi.org/10.1016/j.icarus.2018.01.012
[9] Pappalardo R.T., Collins G.C. Strained craters on Ganymede // Journal of Structural Geology, Vol. 27, Issue 5, 2005, pp. 827-838, ISSN 0191-8141, https://doi.org/10.1016/j.jsg.2004.11.010
[10] Alzate N., Barlow N.G. Central pit craters on Ganymede // Icarus, Vol. 211, Issue 2, 2011, pp. 1274-1283, ISSN 0019-1035, https://doi.org/10.1016/j.icarus.2010.10.015
[11] Jones K.B., Head J.W., Pappalardo R.T., Moore J.M., Morphology and origin of palimpsests on Ganymede based on Galileo observations // Icarus, Vol. 164, Issue 1, 2003, pp. 197-212, ISSN 0019-1035, https://doi.org/10.1016/S0019-1035(03)00128-3
[12] Prockter L.M., Head J.W., Pappalardo R.T., Senske D.A., Neukum G., Wagner R., Wolf U., Oberst J., Giese B., Moore J.M., Chapman C.R., Helfenstein P., Greeley R., Breneman H.H., Belton M.J.S. Dark Terrain on Ganymede: Geological Mapping and Interpretation of Galileo Regio at High Resolution // Icarus, Vol. 135, Issue 1, 1998, pp. 317-344, ISSN 0019-1035, https://doi.org/10.1006/icar.1998.5981

MEASURING THE PRECESSION PERIOD OF SOLAR SYSTEM ECLIPTIC PLANE USING GALACTIC MODEL

A.A. Barenbaum[1]
[1] *Oil and Gas Research Institute RAS, Gubkin str. 3, Moscow, 119333, Russia; azary@mail.ru*

KEYWORDS:
Galactic model, supercontinental cyclicity, precession of ecliptic plane.

Introduction:

The precession of the rotation axis of planets and stars, including our Sun, is a fact beyond doubt. Another thing is the precession of Solar System ecliptic plane as a whole. Previously, according to geology data, we found that such precession exists, and estimated it period approximately of 2.7±0.5 Ga [1]. In [2], when analyzing the supercontinental cyclicity phenomenon, using an optimized version of Galactic model [3, 4] we shown that precession of Solar System ecliptic plane is in resonance with rotation of the Galaxy and its nuclear disk. Besides, this precession period of precession is exactly equal to rotation period of Sun's orbit line of apsides in Galaxy T_E = 2.0 billion years.

GALACTIC MODEL:

The galactic model has been developed by author for more than 40 years. This model unambiguously connects the climaxes of geological processes on the Earth and on other planets with bombardments of the Solar System by galactic comets when Sun hits the jet streams and spiral arms of Galaxy. The model is based on finding parameters of Sun's orbit in Galaxy and calculating the moments of Sun's intersection of jet streams and galactic arms, which best fit the data of geology and astronomy [5].

In the model [2], our Galaxy has 4 identical arms twisted in logarithmic spirals that rotate as a whole around the center with a period of T_G=200 Ma, and 2 gas-dust jet streams twisted into an Archimedean spiral (Fig. 1). Both streams consume at a speed of 300 km/s from the rapidly rotating gas and dust disk of Galaxy. The disk is inclined to the galactic plane at an angle of 20° and precesses with a period of its rotation T_d = 50 Ma. The intersections of jet streams with galactic arms are the main sites in Galaxy for formation of young stars and comets. These processes are most active in galactic arms at a distance of the corotation radius R* from Galaxy center, at which the curvature radii of jet streams and galactic arms are equal.

From the moment of its formation in Crux-Scutum (IV) arm, Sun moves along an elliptical orbit, the line apsides of which rotates around Galaxy center with period T_a = 2 billion years. In this case, Sun either approaches the center at a distance of 5.27 Kpc, then recedes by R* = 11.47 Kpc, making low-amplitude oscillations across the galactic plane with a period T_z = 50 Ma.

This movement is in multifrequency parametric resonance [6] with rotation of Galaxy arms and nuclear disk. So, for one complete revolution of the line apsides of its own orbit, Sun makes 8 orbital revolutions and 9 revolutions around galactic center, and Galaxy itself and its nuclear disk make 10 and 80 revolutions. In this case, Sun makes 80 oscillations across galactic plane.

In the course of its movement, Sun episodically crosses galactic arms and jet streams, and at such periods during of ~2–5 Ma, the Earth and other planets of Solar System are intense bombardments by galactic comets. All these bombardments in Earth's geological history are periods of the global natural catastrophes (biotic, climatic and tectonomagmatic), the times of which are clearly fixed by geologists in stratigraphic (geochronological) scale Phanerozoic in form of its boundaries of different ranks (Fig. 2).

It has been established that the most intense cometary bombardments determine the boundaries of eras and erathems, the less intense ones determine the boundaries of systems, and the weaker ones determine the boundaries of epochs in the scale Phanerozoic. At this, the boundaries of epochs

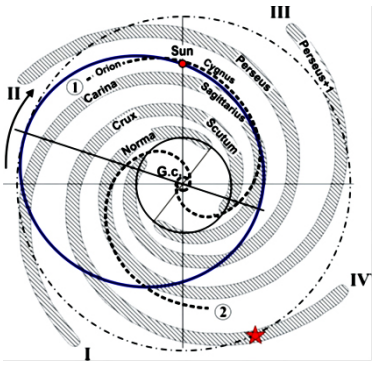

Fig. 1. The current Sun's position in orbit (ellipse) relative to 4 Galaxy arms (Roman numerals) and 2 jet streams (Arabic numerals) in projection onto galactic plane. Small circle is nuclear disk. Middle circle defines size of Galaxy isothermal core. Outer dotted ring denotes corotation radius R* of Galaxy. Arrow indicates direction of Sun's motion along orbit and rotation the line apsides (straight line) of orbit itself, which are coincided with Galaxy rotation and its nuclear disk. An asterisk is a place in Crux-Scutum (IV) arm where Solar System previously formed

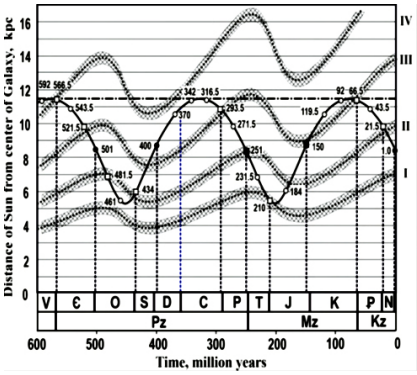

Fig. 2. The Sun's position change in time relative to Galaxy arms (bands) and distance to Galaxy center (sinusoid) in projection onto galactic plane. Roman numerals indicate the numbers of Galaxy arms in Fig. 1. Numbers show the time (in millions years) of Sun's is into jet streams (circles) and simultaneously into Galaxy arms (squares). The black icons are moments when jet streams cross galactic plane in which Sun moves. Dashed-dotted line is Galaxy corotation radius R*. Below is a time scale indicating boundaries of eras and systems of Phanerozoic

correspond to Sun's presence only in jet streams, the boundaries of systems correspond to Sun's presence simultaneous in jet streams and galactic arms, and analogous events, that occurred at a distance R* from Galaxy center correspond to the boundaries of eras and erathems.

Due to the resonant nature of the model, it was also found that since the Solar System formation, the Galaxy spiral structure and Sun's orbit have practically not changed. This circumstance made it possible to calculate with high accuracy the times of cometary bombardments of different intensity and construct a geochronological scale not only for Phanerozoic (Fig. 2), but also for Precambrian (Table 1). In contrast to Phanerozoic scale, the boundaries of Precambrian scale have the rank of eons and eras, since all they were initiated by very strong cometary bombardments when Sun was in galactic arms at a distance R * from Galaxy center.

Table 1: Relationship boundaries of Precambrian with galactic arms

Galactic arm	Event time, billion years	Precambrian boundaries of eons and eras
I. Carina-Sagittarius	1.067 3.067	Neoproterozoic -------
II. Perseus	1.567 3.567	Mesoproterozoic Paleoarchean
III. Norma-Perseus+1	2.067 4.067	------- Archaean (Eoarchean)
IV. Crux-Scutum	0.567 2.567 4.567 6.567	Phanerozoic (Paleozoic) Proterozoic (Paleoproterozoic) 2nd cycle of planet formation [5] 1st Solar System formation cycle [5]

Table 1 shows that from moment of its formation, Sun has repeatedly been into galactic arms at a distance R* from Galaxy center, where Earth and other planets were subjected to intense cometary bombardments. However, intensity of these bombardments was varied in different galactic arms. In arms Carina-Sagittarius and Norma-Perseus+1, bombardments were weaker than in Perseus arm, and even more so in Crux-Scutum arm. The galactic model also leads to conclusion [7] that bombardments by comets in Crux-Scutum arm were not only more intense than in other galactic arms, but this arm itself has twice the "width" than shown in Fig. 1 and 2.

Our other conclusion is that the cyclicity of global geological processes on Earth depends not only on powerful comet bombardments in galactic arms, repeating with a period of T_B = 500 Ma (Table 1), but also on precession the ecliptic plane of Solar System. The ecliptic plane precession affects the spatial orientation of Earth's rotation axis of relative to direction of galactic comets motion that leads to the cyclical nature of global tectonic and climatic processes with a period T_E different from T_B. The first estimate of precession period based on data of geology gave a value of T_E ~2700±500 Ma [1]. At that time, it was not possible to measure T_E value more accurately.

An analysis of the specifics of supercontinents formation and decay on basis of galactic model makes it possible to solve this problem.

SUPERCONTINENTAL CYCLICITY:

It is known that formation of lithospheric plates and their association into supercontinents began on Earth, starting from Archean. Today, with varying degrees of reliability, 10 supercontinents have been identified that arose with a period of T_S = 400 Ma [8]. In the life of each supercontinent, one can distinguish assembly stage lasting ~150 Ma, when it is formed from relatively small plates, and decay stage ~250 Ma, when it breaks up into parts. The decay can be complete or partial. In the latter case, strongly destroyed part turns out in turn, either in Northern or in Southern hemisphere of Earth. That's why supercontinental period can also be taken equal to 800 Ma [9].

On Fig. 3, we compared the periods of supercontinents existence according to [9] with periods of powerful cometary bombardments of Earth in galactic arms T_B. It is clearly seen that majority of supercontinents were formed under conditions when Sun was in Galaxy arms at a distance R* from its center. Thus, supercontinents Kenoria and Pannotia originated in powerful arm IV, Sebakwia and Gothia, in the arm II, and Vaalbara and Rodinia, in the arm I. Supercontinents Yatulia and Pangaea also originated in arm IV, but at a distance from the center R < R*.

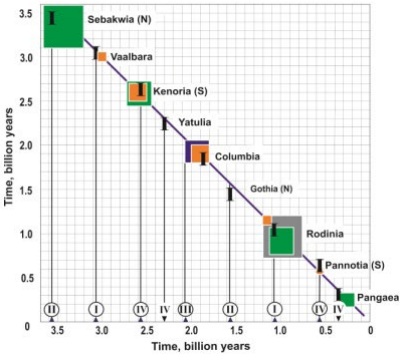

Fig. 3. Periods of supercontinents existence (vertical axis) in comparison with times of cometary bombardments in Galaxy arms (I – IV) at R = R* (circled) and R < R* (without circles). Black icons are data according [9]

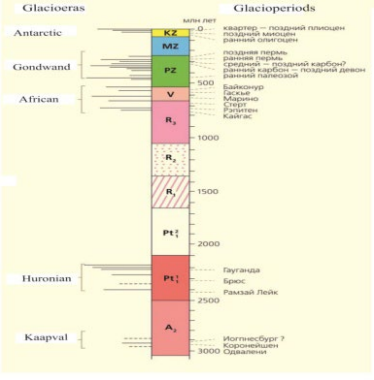

Fig. 4. Glacioeras and glacioperiods in interval from Late Archean to the present [10]. Long period of glaciation absence between Huronian and African glacioeras is "Great Ice Pause"

We note that period of supercontinental cyclicity T_S = 400 Ma does not coincide with either Sun's rotation period in Galaxy (Fig. 2) or with period T_B of strongest comet bombardments in galactic arms (Table 1). The main reason for this discrepancy is the change in Earth's axis orientation due to precession of Solar System ecliptic plane. Taking this factor as decisive, we find precession period as $T_E = (T_S^{-1}–T_B^{-1})^{-1}$ = 2.0 billion years.

The obtained value T_E coincides exactly with period rotation T_a of Sun's orbit apsidal line. This means that in resonance with Galaxy rotation and its nuclear disk, not only orbital Sun motion occurs, but also precession of Solar System ecliptic plane. It also follows from this that supercontinental cyclicity is a phenomenon primarily due to processes in Galaxy and Solar System. The main role in this phenomenon is played by the falls of galactic comets, which alternately bombard the Southern and Northern hemispheres of globe.

Taking into account the physical mechanism of high-speed galactic comets interaction with Earth and other planets [11–13], our explanation [2] for this phenomenon is that supercontinents are formed mainly in Earth's sub-polar zones at a very high falls density of galactic comets, and cease to exist at middle latitudes under conditions of a much lower density of cometary falls.

Paleoreconstruction supercontinents of Pannotia, Kenoria, Sebakwia, and Gothia indicate that during period their formation, Earth's rotation axis was oriented in direction of comets move. At that, supercontinents Pannotia and Kenoria were in Southern hemisphere, and Sebakwia and Gothia in Northern, which is noted in Fig. 3 with icons (S) and (N). As for supercontinents Vaalbara, Columbia, and Rodinia, they were in low and middle latitudes and, apparently, did not form a single supercontinent.

The periods of supercontinents existence are closely related to the occurrence of global glaciations (Fig. 4). Glaciations were the most powerful when Sun's hit into Crux-Scutum arm. The first of such glaciations ~2.5–2.2 Ga ago, which arose on Kenoria supercontinent, was called Huronian glacioera, and second ~750–540 Ma ago, on Pannotia, was called African glacioera. The time interval between these glaciations (Fig. 4) was called "Great Glacial Pause". During the "pause", according to our model, Earth's axis never exactly coincided with direction of comets move, and their bombardments in Galaxy arms, although they formed supercontinents, were much weaker than in Crux-Scutum arm.

REFERENCES:

[1] Barenbaum A.A., Khain V.E., Yasamanov N.A. Large-scale tectonic cycles: analysis from the positions of the galactic concept // Vestnik MGU. Geol., 2004, 3, 3-16.
[2] Barenbaum A.A. Bombings of Earth by galactic comets and supercontinental cyclicity // Experiment in GeoSciences. 2022. (in press).
[3] Barenbaum A.A. Geological and meteoric data as a necessary tool for developing an adequate spiral model of Galaxy // Proc. conf.: VESEMPG-2018. Moscow. Vernadsky Inst. RAS, 2018, 294-298.
[4] Barenbaum A.A, Titorenko A.S. Galactic model of geological cyclicity: parameter optimization and testing based on geology and astronomy data // Proc. conf. VESEMPG- 2020. Moscow. Vernadsky Inst. RAS, 2020, 210-215.
[5] Barenbaum A.A. Galactocentric paradigm in geology and astronomy. Moscow. PH: LIBROKOM. 2010. 544 p.
[6] Molchanov A.M. Resonances in multifrequency oscillation // Doklady AN. 1966. V. 168, No 2, 284-287.
[7] Barenbaum A.A. Analysis of the causes of glaciations and $\delta^{13}C$ anomalies of carbonates based on a galactic model // Proc. XXII Intern. conf.: Physical-chemical and petrophysical studies in Earth sciences. Inst. Experimental Mineralogy RAS. 2021. 22-26.
[8] Bozhko N.A. Supercontinental cyclicity in Earth evolution // Vestnik MGU. Geol., 2009. No 2, 13-28.
[9] Bozhko N.A. On two types of supercontinental cyclicity // Vestnik MGU. Geol., 2011. No 5, 36-61.
[10] Chumakov N.M. Glaciation of the Earth: history, stratigraphic significance and role in the biosphere. Moscow. PH: GEOS. 2015. 160 p.
[11] Barenbaum A.A. Geological structures created by falls of galactic comets // J. Phys.: Conf. Ser. 2015. 653 012073.
[12] Barenbaum A.A., Shpekin M.I. To the development of the mechanism of interaction of galactic comets with terrestrial planets // J. Phys.: Conf. Ser. 2016. 774. 012096.
[13] Barenbaum A.A., Shpekin M.I. Origin and formation mechanism of craters, seas and mascons on the Moon // J. Phys.: Conf. Ser. 2019. 1147. 012057.

SESSION 4. ASTROBIOLOGY (AB) ORAL SESSION

ELECTRON IRRADIATION OF A HOMOGENEOUS MIXTURE OF AMMONIA AND CARBON DIOXIDE (NH_3:CO_2) ICE AT SIMULATED PLANETARY TEMPERATURES

Sohan Jheeta[1]
[1] *Network of Researcher on the Chemical Evolution of Life, NoRCEL, Leeds, UK; Sohan@sohanjheeta.com*

ABSTRACT
Carbon dioxide (CO_2) and ammonia (NH_3) are two of the most abundant ices to be found in the solar system (Table 1). CO_2 ice is prevalent on Mars; on several Jovian satellites (*eg* Europa) and on Neptune's moon, Triton. NH_3 ice has recently been detected in the upper atmosphere of Saturn and on Pluto's moon Charon. Pluto has also shown a strong surface signature for NH_3 ice. Comets contain ices of both of these compounds and, in some cases, the levels of CO_2 could be as high as ~15-20% of that of water. In addition, ammonia hydrate has been identified on the surface of several Kuiper belt objects (*eg* Quaoar). The ices of CO_2 and NH_3 are also widespread in the interstellar medium (ISM). Table 1 shows the quantity of these ices in protostars and comets [1].

Table 1: Distribution of some common molecules in protostars and comets

Species	Protostars	Comets
CO	100% ~15	100% 7–20
CO_2	~23	3–6
NH_3 O_2	~8 <7	1.5 <0.5
CH_3OH	~6	~2
HCOOH H_2CO CH_4	~3 <3 ~2	~0.05 ~3 ~1
C_2H_6	<0.4	~0.5
OCS	<0.04	0.5

Measured in percentages relative to H_2O(=100%) [1]

The ices of these are regularly processed by many different types of radiation. Solar bodies are subjected to solar UV light, as well as ions trapped in the magnetosphere of large planets (eg Jupiter and Saturn). In addition, solar bodies together with molecular clouds and ISM are pervaded by UV light and cosmic rays containing a range of ions (H^+, D^+, He^+, He^{2+}). We report here electron irradiation of a homogeneous mixture of ammonia and carbon dioxide (NH_3:CO_2) ice at simulated planetary temperatures.

REFERENCE
[1] Roush, T.L. (2001). "Physical state of ices in the outer solar system." Journal of Geophysical Research-Planets 106(E12): 33315-33323.

THE COSMIC CONTEXT OF PLANET EARTH – DON'T BUY A ROADMAP THAT ONLY SHOWS A SINGLE ROAD

Martin Dominik[1]
[1] *University of St Andrews & Network of Researchers on the Chemical Evolution of Life (NoRCEL)*

The detection of about 5000 planets orbiting stars other than the Sun has changed everything, and it has changed nothing. Everything about the context of the Solar System planets, but nothing about whether there is life beyond Earth or not. The structure and formation history of planets are far more complex and diverse than those of stars, and our current planet sample appears tiny in comparison to probably hundreds of billions of planets in the Milky Way alone. We are thereby far from having a planetary equivalent to the rather simple Hertzsprung-Russell diagram, which links stellar demographics with evolutionary history. One particular feature of planet Earth is the co-evolution of life with its environment; the Earth's crust, oceans, and atmosphere. But there are substantial gaps in our understanding of how any observable features relate to life, and we might need to develop an elaborate new terminology for guiding exploration and understanding. The "NoRCEL gap map" is a community effort aiming at identifying crucial gaps of knowledge on the universality of biology and the emergence of life, fostering structured discussions across researchers with various expertise. Removing some existing road blocks probably requires inspiration and encouragement of out-of-the-box thinking.

LIFE ON VENUS: DIFFERENT CONCEPTS OF ITS ORIGIN AND EVOLUTION

O. Kotsyurbenko[1,2], D. Skladnev[2,3], V. Kompanichenko[4], A. Brushkov[5], J. Khrunyk[6]

[1] *Yugra State University, Khanty-Mansiysk, Moscow, Russia*
[2] *Network of Researchers on the Chemical Evolution of Life, NoRCEL*
[3] *Research Center of Biotechnology of the Russian Academy of Sciences, Winogradsky Institute of Microbiology RAS, Moscow, Russia*
[4] *Institute for Complex Analysis of Regional Problems RAS, Birobidzhan, Russia*
[5] *Lomonosow Moscow State University, Moscow, Russia*
[6] *Ural Federal University. Ekaterinburg, Russia*

For a long time, Venus attracted much less attention compared to Mars in the concepts of the existence of extraterrestrial life because its modern surface is heated to very high temperatures, which are unsuitable for any terrestrial organisms. However, a recent rapid increase in interest in this planet for astrobiologists has occurred due to the active discussion of the hypothesis of habitability of its cloud layer. In such an extraterrestrial ecosystem, the existence of the so-called aerochemo(photo)lithotrophic microbial community is supposed to exist, using sulfur and iron compounds as the main elements for energy production.

An important difference between the cloud layer of Venus and the Earth's cloud system is its absolute spatial isolation as a possible habitat for organisms. If the microbial biomass in clouds on Earth is constantly replenished as a result of the entry of microorganisms from the surface with air convection flows, then such a mechanism is impossible on Venus due to the apparent absence of any terrestrial-type organisms on its super-hot surface.

Despite the extremely low concentration of water vapor in the modern clouds of Venus, it is assumed that living organisms can exist in aerosols, in which the water phase can be concentrated in a small volume and contain a certain number of microorganisms capable of active life.

To date, there are various concepts of the geological past of Venus, within which the question of the existence of water on its ancient surface is discussed. This fact determines which of the hypotheses of the possible origin of life on Venus may be dominant. Moreover, the clouds themselves can also be considered as a system that meets the requirements for the emergence and further evolution of living organisms.

In general, several different scenarios for the emergence of living organisms can be considered on Venus. These include a surface or subsurface scenario in which life emerges as molecular systems becoming more and more complex, as well as a new scenario for the origin of life in clouds.

Presently, various compounds such as CO_2, CO, N, SO_2, $FeCl_2$ have been found in the atmosphere of Venus. Under certain conditions it could be the basis for the synthesis of various bioorganic macromolecules. Moreover, it is assumed that iron and sulfur compounds may play an important role in lithotrophic metabolism as the main source of energy. The cloud layer is characterized by large temperature fluctuations, the presence of all the main biogenic elements, as well as energy sources for photo- and chemosynthetic life, and is a kind of macro-scale fermenter for various biosynthesis reactions.

An alternative direction regarding the emergence of life on Venus is the concept of panspermia, which transforms the question of the origin of life into the question of its delivery to Venus from outside and its further adaptation to conditions in the Venusian clouds and subsequent evolution.

In general, Venus is a unique cosmic body, on the example of which various concepts of the origin of life and scenarios for its further evolution can be simulated.

THE SIMPLEST LAB-ON-CHIP FOR DETECTING LIVING CELLS IN THE ACIDIC ENVIRONMENT OF VENUSIAN CLOUDS

D. Skladnev[1,2], V. Sorokin[1], S. Karlov[3], O. Kotsyurbenko[2,4]
[1] *Research Center of Biotechnology of the Russian Academy of Sciences, Winogradsky Institute of Microbiology, Moscow, Russia*
[2] *Network of Researchers on the Chemical Evolution of Life, Leeds, United Kingdom*
[3] *Moscow Polytechnic University, Russia*
[4] *Yugra State University, Khanty-Mansiysk, Moscow, Russia*

The study of the Venusian clouds to find out whether they are sterile or not is complicated by the extremely high acidity of the water present. We offer using paper-based analytical devices (PADs) made of acid-resistant porous material as a simple and weightless tools and biosensors well established that rival conventional cells detection methods. Among them, gravimetry in combination with a spectrometric strategy is the most promising, since the results can be interpreted at the time of testing. Specially designed highly sensitive chips that can quickly (before the interaction with environmental acid occurs), selectively and reliably detect the only reliable evidence of the presence of Life in the clouds of Venus.

Previously, we have already proposed a concept based on the fact that a living thing is something that can be turned into inanimate by deliberately biocidal treatment - for example, to destroy cell membranes. Treatment with lysing solutions or ultrasonic irradiation have such properties. The use of paper-based biosensors makes it possible to analyze moisture samples before and after the destruction of cells presumably present in it. In particular, it is possible to distribute insoluble particles by size with subsequent spectral analysis of the corresponding chemical products of destruction.

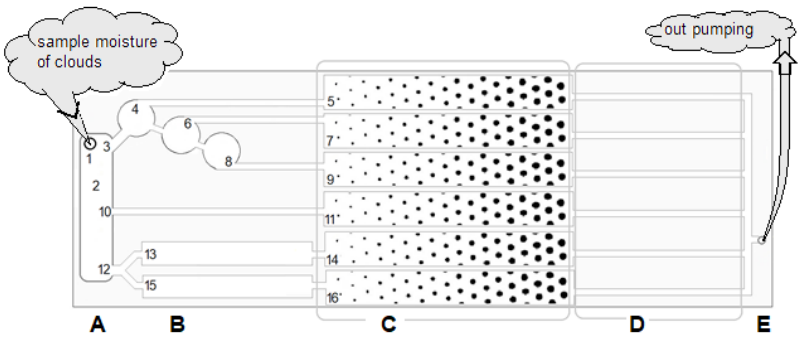

Automated multistep in a PADs format includes (A) a reservoir (2) for the sampled liquid and distribution dividing channels (3, 10, 12); (B) a zone of cell destruction by ultrasound in various modes (4, 6, 8), two type of chemical lysis (13, 15) and a control untreated sample (11); (C) a zone of particle size distribution; (D) spectrometry zone; (E) out pumping channel.

The structure of the chip allows a simple way to achieve its sealing by melting along the contour. The possibility of repeated measurements or/and delivery to the Earth remains.

THE EFFECTS OF NEARBY SUPERNOVA AND SOLAR SUPERFLARES ON EARTH BIOSPHERE EVOLUTION: MASS EXTINCTIONS AND "FLASH OF MUTATIONS"

A.K. Pavlov[1], A.A. Shepkin[2], G.I. Vasilyev[1]
[1] *Ioffe Physical-Technical Institute, Russian Academy of Sciences, 26 Politekhnicheskaya str., St. Petersburg, 194021, Russia; anatoli.pavlov@mail.ioffe.ru*
[2] *Peter the Great St. Petersburg State Polytechnic University, 29 Politekhnicheskaya str., St. Petersburg, 195251, Russia*

KEYWORDS:
Supernova, solar flares,cosmic rays, extinctions, mutations

INTRODUCTION:
Discovery of nearby Supernova explosion at 2.5 million years ago and superflares on solar-like stars [1,2] stimulated the interest to problem possible impact of high intensive cosmic rays events on terrestrial biosphere [3]. The ^{60}Fe (r-process long-lived radionuclide) was measured in deep ocean sediments with 2.5 million years age. It means the Supernova shock wave crossed Solar system. Simulations of cosmic rays (CR) acceleration on such waves [4] demonstrates, that great impulse of CR with hard energy spectrum will irradiate the Earth atmosphere and increase radiation background within several thousands years. Also, the great CR events could be produced the hypothetical solar superflares but during the several hours period.

MODELLING OF EXTERNAL AND INTERNAL RADIATION INCREASE
Calculations of CR radiation doses and ^{14}C production were carried on using the GEANT toolkit. The long-lived ^{14}C radionuclide is incorporated in all organisms and produce mutations very effectively in biosphere.

Our modelling shows the lethal doses could be reached for Supernova explosions at 5-20pc distance and solar superflares with energy 10^{37} erg. The great increase of mutations rate could be produced the Supernovas at several tenths pc and more.

REFERENCES:
[1] Fry, B.J., Fields, B.D., and Ellis, J.R. Radioactive iron rain: transporting 60Fe in SN dust to the ocean floor. //Astrophysical J. 2016. 827:48.
[2] Maehara H. et al. Superflares on solar-type stars //Nature. 2012. V. 485. №. 7399. P. 478-481 .
[3] Melott A.L., Thomas B.C., Kachelrieß M., Semikoz D.V., Overholt A.C.: A Supernova at 50 pc: Effects on the Earth's Atmosphere and Biota // The Astrophysical Journal. – 2017. – Vol. 840. – 105.
[4] Zirakashvili V.N., Ptuskin V.S.: Numerical simulations of diffusive shock acceleration in SNRs // Astroparticle Physics. 2012. v. 39-40. p. 12-21.

KINETIC MONTE CARLO MODEL OF THE AURORAL ELECTRON PRECIPITATION INTO THE N_2-O_2 PLANETARY ATMOSPHERE

V.I. Shematovich[1], D.V. Bisikalo[1], B. Hubert[2]
[1] *Institute of Astronomy of the Russian Academy of Sciences, Moscow, Russia; shematov@inasan.ru*
[2] *Laboratoire de Physique Atmosphérique et Planétaire, Université de Liège, Liège, Belgium; b.hubert@uliege.be*

KEYWORDS:
Terrestrial planet; auroral event; kinetic modeling; nitric oxide as an atmospheric biomarker

INTRODUCTION:
The study of the origin of atmospheric nitrogen and its stability gives an idea of the uniqueness of the habitat on Earth. The simultaneous existence of N_2 and O_2 in the Earth atmosphere has no analogues in the entire Solar System. This combination is closely related to the existence of aerobic life forms. The presence of nitrogen on the surface, in the ocean and in the atmosphere can contribute or hinder the habitability of a terrestrial planet, since nitrogen is vital to all known life forms. In the recent papers [1,2] the various sources of atmospheric nitrogen, the stability of nitrogen-dominated atmospheres and the development of the early nitrogen atmosphere of the Earth were discussed. In particular, it has been shown that the presence of an N_2-O_2 atmosphere is a clear biomarker for aerobic life forms. The fact is that the primary atmospheres of such planets are easily destroyed and a chemically stable mixture of N_2-O_2 can only be formed by strong secondary sources of these molecules. The only currently known complex capable of providing such massive secondary flows are aerobic life forms. Thus, the detection of an N_2-O_2 atmosphere on an exoplanet orbiting in the habitable zone around a solar-type star is a strong sign of the presence of a developed aerobic extraterrestrial biosphere [1,2].

The NO radical is a direct indicator of the atmosphere dominated by N_2 and O_2, since its formation is a consequence of the presence of molecular nitrogen and oxygen as the main components in the atmosphere of the planet. To study the chemistry and dynamics of nitrogen oxide NO in the atmospheres of terrestrial exoplanets it is necessary to use a set of numerical models (kinetic and MHD) which allow us to follow the evolution of the N_2-O_2 upper atmospheres of the sub-neptune and exo-earth families to estimate possible manifestations of life.

Two mechanisms have been identified from observations as sources of nitric oxide in the upper atmospheres of terestrial-type planets. At high latitudes, the precipitation of auroral electrons (1–10 keV) produces ionization that leads to the production of nitric oxide [3]. At low latitudes, the predominant source is now thought to be solar soft X-rays [3]. In the Earth's atmosphere the largest density of nitric oxide which occurs at 106–110 km is produced by 1–10 keV electrons precipitating into the auroral region (60°–70° geomagnetic latitude). Kinetic Monte Carlo model [4] of auroral electron precipitation was developed with an aim to interpret the UV emissions observed in the upper atmospheres of terrestrial planets. Such model provides a statistical solution of the Boltzmann integro-differential equation including sources and sinks of electrons.

Numerical kinetic Monte Carlo model allowed us to study the processes of precipitation of high-energy auroral electrons into the N_2-O_2 atmospheres of the rocky planets in the Solar and exosolar planetary systems. This model was modified and updated with an aim to calculate the source functions of suprathermal atoms formed in the electron impact dissociation of the main atmospheric molecules – N_2 and O_2. To validate model the calculations were conducted for the Earth's polar atmosphere. Calculations were performed for

two test cases of electron precipitation – a monoenergetic electron flux at the upper boundary with a givenn – monodirectional or isotropic distribution of the pitch angle. The energy spectra of downn – and upward fluxes of precipitating electrons, height profiles of the energy fluxes of auroral electrons were calculated. These data allow us to estimate the energy spectra of source functions for suprathermal nitrogen atoms formed due to the electron impact N_2 dissociation (see Figure). This modification of kinetic Monte Carlo model of auroral electron precipitation will allow us to calculate the steady-state energy distributions of suprathermal nitrogen atoms in the polar regions of the planetary atmospheres under study and to estimate the input of hot fraction into the odd nitrogen chemistry in the N_2-O_2 atmospheres of terrestrial-type exoplanets with an final aim to search for habitable worlds.

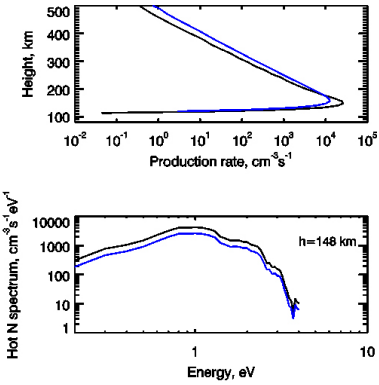

Fig. 1. (*top panel*) Height profiles of the production rate of suprathermal nitrogen atoms formed in the electron impact dissociation of atmospheric N_2 molecules. (*bottom panel*) Calculated energy spectra of suprathermal N atoms formed at height of 148 km. Auroral electrons precipitate with energy E_0= 1 keV and are characterized by monodirectional (black lines) and isotropic (blue lines) pitch-angle distributions at the upper boundary.

ACKNOWLEDGEMENTS:
We acknowledge the financial support of the Russian Science Foundation, grant # 22-12-00364.

REFERENCES:

[1] Lammer H., Sproß L., Grenfell J.L.; et al. The Role of N2 as a Geo-Biosignature for the Detection and Characterization of Earth-like Habitats// Astrobiology. 2019. V. 19. P. 927-950.
[2] Sproß L., Scherf M., Shematovich V.I., et al. Life is the Only Reason for the Existence of N2-O2-Dominated Atmospheres// Astronomy Reports. 2021. V. 65. P. 275-296.
[3] Barth C.A., Mankoff K.D., Bailey S.M., Solomon S.C. Global observations of nitric oxide in the thermosphere// J. Geophys. Res. 2003. V. 108 P. 1027-1038.
[4] Shematovich V.I., Bisikalo D.V., Gérard J.-C., et al. Monte Carlo model of electron transport for the calculation of Mars dayglow emissions// J. Geophys. Res. 2008. V. 113. P. E02011.

APPLICATION OF ACOUSTOELECTRONIC TECHNIQUES TO REGISTRATION MICROBIAL OBJECTS IN LIQUID

I.E. Kuznetsova[1], V.I. Anisimkin[1], V.V. Kolesov[1], A.V. Smirnov[1], E.S. Shamsutdinova[1], B.D. Zaitsev[2], Zh. Qian[3], T. Ma[4]

[1] *Kotelnikov Institute of Radio Engineering and Electronics of RAS, Mokhovaya str., 11, bld. 7, Moscow, 125009, Russia; kuziren@yandex.ru*

[2] *Kotelnikov Institute of Radio Engineering and Electronics of RAS, Saratov Branch, Zelyonaya str., 38, Saratov, 410028, Russia; zai-boris@yandex.ru*

[3] *State Key Laboratory of Mechanics and Control of Mechanical Structures, College of Aerospace Engineering, Nanjing University of Aeronautics and Astronautics, Nanjing 210016, China; qianzh@nuaa.edu.cn*

[4] *Key Laboratory of Impact and Safety Engineering, Ministry of Education, Ningbo University, Ningbo 315211, Zhejiang, China; matingfeng@nbu.edu.cn*

KEYWORDS:
Acoustoelectronic technique, acoustic waves, biological sensors, acoustic resonator, microbial cell, electro-physical properties.

The study of liquid media and the determination of the presence of microbiological objects in them is possible with the help of biological sensors based on the acoustoelectronic principle. In this case, the changes in the characteristics of the environment, for example, as a result of a biospecific reaction lead to the changes in the parameters (phase, amplitude, frequency) of acoustic waves propagating in a piezoactive waveguide. These devices can be implemented both on delay lines based on various types of acoustic waves, and on resonators with a lateral electric excitation field. Previously, a similar approach was used to register bioobjects in hydrogels [1], determine the presence of viruses in a liquid medium [2], and detect and identify bacteria [3]. Obviously, these devices can be adapted for research in aggressive liquid media. There is also the possibility of conducting studies without the use of sensitive films or specialized reagents. In this case, the anisotropy of piezoactive solids can be used, in which various types of acoustic waves can propagate (Fig. 1). Depending on the direction of propagation, the characteristics of these waves are different, and when the properties of the environment change, they can also change in different ways. This will make it possible to create appropriate maps for liquid media and carry out their identification.

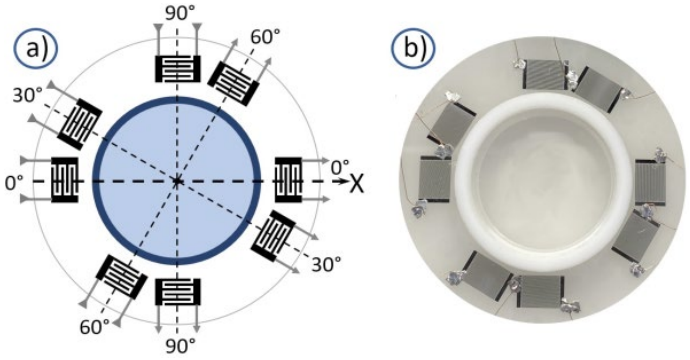

Fig. 1. Schematic view *a*) and photo *b*) of experimental sample with 4 acoustic delay lines arranged on same piezoelectric plate.

ACKNOWLEDGEMENTS:
Work is supported by RSCF grant # 21-49-00062.

REFERENCES:

[1] Anisimkin V.I., Pokusaev B.G., Skladnev D.A., Sorokin V.V., Tyupa D.V. Application of an acoustoelectronic technique to study ordered microstructured disperse systems with biological objects in a hydrogel // Acoustical Physics. 2016. V. 62. No. 6. P. 754-759.

[2] Guliy O.I., Zaitsev B.D., Semyonov A.P., Karavaeva O.A., Fomin A.S., Staroverov S.A., Burov A.M., Borodina I.A. Sensor System Based on a Piezoelectric Resonator with a Lateral Electric Field for Virus Diagnostics // Ultrasound in Medicine and Biology. 2022. V. 48. No. 5. P. 901-911.

[3] Borodina I., Zaitsev B., Teplykh A., Burygin G., Guliy, O. Sensor based on PZT ceramic resonator with lateral electric field for immunodetectionof bacteria in the conducting aquatic environment // Sensors. 2020. V. 20. No. 10. P.3003.

THE FUNCTIONING MICROBIOME AS LINK BETWEEN GENES AND MICROBIAL ENVIRONMENT

D. Smith[1]
[1] *Network of Researchers on the Chemical Evolution of Life (NoRCEL)*

The world first noticed problem of non-communicable disease in the late 1940s, when significant numbers of people, initially mostly American, started to suffer from sudden heart attack or stroke. As the medical community began to understand this puzzling new phenomenon, an influential researcher, Ancel Keys (see below and ref. 1), threw his weight behind saturated fat as the cause. Later, an equally influential British nutritionist, John Yudkin, began to demonise sugar. Whatever the cause, such disease is clearly associated with increased obesity, and subsequent researchers split into two irreconcilable camps: those that said we eat too much (too greedy), and those that said that we rely too much on mechanical aids (too lazy). Unfortunately, neither of these adequately explain the concomitant rise of immune system problems and of poor mental health. By the year 2000 the concept of the ***microbiome*** was firmly in the hands of social media influencers, with scientists refusing to engage seriously. More recently, however, both science and industry are beginning to take note of the related expression ***microbiota-gut-brain axis***. Sadly, however, modern scientific endeavour is best characterised as a Darwinian struggle for funding, with little real opportunity to take a look at the bigger picture, and the old dietary assumptions have not been seriously challenged. Interestingly, Keys' earlier "Minnesota Starvation Experiment" described a standard food intake for a young, active, male American that averaged 3,200 kcal/day in 1944, which was reduced to 1,800 in a semi-starvation regime with significant consequences [1]. Compare this with the modern reference intake of 2,000 kcal/day – with many people safely limiting themselves to 1,500 or fewer – and it can be inferred that calorie intake has indeed decreased significantly in recent decades. Alongside this, a definitive study has shown that physical activity energy expenditure has not declined between the 1980s and 2008 [2]. This dilemma can be understood by the fact that faecal weight, and therefore faecal energy excretion, has dropped by a staggering two thirds during the move from a traditional to a modern lifestyle [3], presumably a natural consequence of the lack of microbial growth within the intestine. The primary industry response has been to generate a series of probiotic products, enthusiastically received by the general public but, as Brüssow has recently described, with little validated science [4]. The aim of this talk is to provide an evolutionary and ecological rationale for the existence of the intestinal microbiome, and for its widespread failure under the influence of anti-microbial agents in the industrialised environment of the modern age. One notable point is the necessity for a double inheritance – the standard ***parental genetic*** inheritance supplemented with a ***maternal microbial*** inheritance. Both need to be working well together for the avoidance of non-communicable disease.

REFERENCES:

[1] Kalm, L.M.; Semba, R.D. (2005). They starved so that others be better fed: Remembering Ancel Keys and the Minnesota Experiment. J. Nutr. 135(6), 1347-1352. https://academic.oup.com/jn/article/135/6/1347/4663828
[2] Westerterp, K.R.; Speakman, J.R. (2008). Physical activity energy expenditure has not declined since the 1980s and matches energy expenditures of wild mammals. Int. J. Obes., 32, 1256-1263. https://cris.maastrichtuniversity.nl/ws/portalfiles/portal/73050462/westerterp_2008_physical_activity_energy_expenditure.pd
[3] Burkitt, D.P. (1973). Some diseases characteristic of modern western civilization. BMJ, 1, 274-278. https://www.ncbi.nlm.nih.gov/pmc/articles/PMC1588096/pdf/brmedj01541-0038.pdf
[4] Brussow, H. (2020). Problems with the concept of gut microbiota dysbiosis. Microb. Biotechnol. 13(2), 423-434. https://sfamjournals.onlinelibrary.wiley.com/doi/10.1111/1751-7915.13479

MONITORING OF GROWTH OF WHEAT'S HEIGHT USING TIME SERIES ANALYSIS OF SYNTHETIC APERTURE RADAR (SAR) IMAGES AND THE CORRESPONDING PARAMETERS

A. Rezaei[1]
[1] *University of Tabriz, Iran*

KEYWORDS
Radar Images, Google Earth Engine, Precision Agriculture, Time Series Analysis, Sentinel-1

In today's word, precision agriculture is one of the practical solutions in increasing agricultural products and timely monitoring to increase food security in today's world. Today, remote sensing technology and GIS are used for this purpose. Classification of various crops, especially wheat, in order to monitor its growth stages in multispectral images due to limitations such as dependence on weather conditions and lack of night imaging. At the same time, SAR images are capable of capturing images in all weather conditions, as well as day-to-day imaging, overcoming the limitations of optical images. Due to the identification of the phenomenon based on the geometry, hardness and orientation of objects, it provides us with a lot of information. Therefore, the main purpose of this study is to evaluate the feasibility of using RADAR images to monitor the growth cycle of wheat. For this study, a bipolar radar image of Sentinel 1 with polarization (VV and VH) will be used to obtain plant growth parameters such as height and biomass. Then, the parameters obtained in order to analyze the time series to understand the plant growth cycle will be performed unsupervised in the Google Earth Engine system. The results will show that band C in the early stages of wheat growth is most sensitive to wheat height and have appropriate information. Field data will then be used to assess accuracy. Final result demonstrate that VV polarization is far better indicator of Wheat growth in early stage, however, VH polarization is more sensitive to middle stage of plant growth cycle. Moreover, neither VV nor VH can detect Wheat growth cycle in their last stage. Both VV and VH showed high connection with the peak of Wheat growth in early May. In fact, it is said that it would be better way to use L band and longer wavelength for Wheat growth in its last stages.

SPECULATIVE HISTORY OF LIFE ON MARS

N.E. Demidov[1], M.A. Ivanov[2]
[1] *Arctic and Antarctic research institute, St.-Petersburg, Russia; nikdemidov@mail.ru*
[2] *Vernadsky Institute of Geochemistry and Analytical Chemistry RAS, Moscow, Russia*

KEYWORDS:
Mars, life, evolution, ecological niche

Main factors of the Noachain, Hesperian, and Amazonian periods are considered from a point of view of their influence on potential contamination/origin, protection, and evolution of microorganisms (Fig. 1). During Noachian, Mars evolved in a way that likely resembled the early evolution of Earth. This potential similarity allows origin of life on Mars. Relatively short Hesperian period was marked by intensive volcanism, fluvial, and glacial activity but conditions on the surface largely left the survival potential and microorganisms were either conserved in permafrost or migrated to deeper water-rich horizons. In Amazonian, Mars represents a frozen desert with very harsh conditions on the surface that is constantly sterilized by the cosmic radiation. The generally unfavorable conditions for the life evolution suggest that primitive organisms, which potentially could be formed on early Mars, were unable to evolve up to complex, multicellular organisms. Ecological niches of modern Mars are considered. Among these, the deep subsurface water horizons and cryopegs have the highest potential for survivability of microorganisms because conditions in these settings are independent from the condition on the surface.

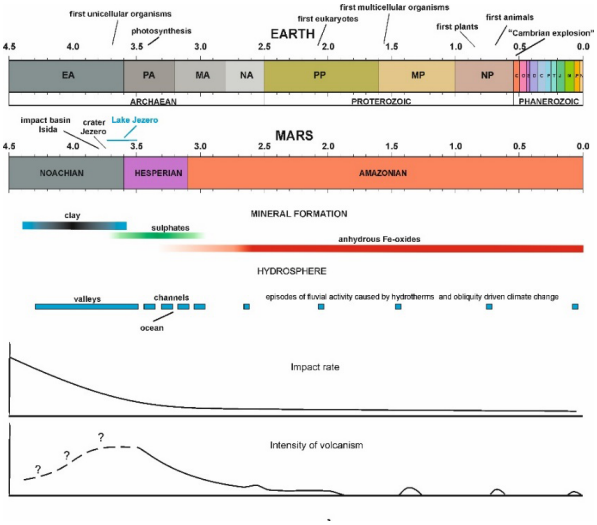

Fig. 1. Correlation of geochronological tables, main events of paleontological history of Earth and geologic history of Mars.

ACKNOWLEDGEMENTS:
This work represents a part of the state order of GEOKHI for MAI

GEOCHEMICAL INDICATION OF DESERT OVERGROWTH (BY THE EXAMPLE OF THE SARYKUM SAND COMPLEX)

D.D. Mironov[1,2]
[1] *Vernadsky Institute of Geochemistry and Analytical Chemistry, RAS, Moscow, Russia; 1032193132@rudn.ru*
[2] *Institute of Environmental Engineering, RUDN University, Moscow, Russia*

KEYWORDS:
Geochemical indicators, biogeochemistry, mineralogy, astrobiology

INTRODUCTION:
The study of arid zones and landscapes is of great importance for environmental sciences due to rapid climatic changes. Such zones are good objects for astrobiological research. A new object for astrobiology may be the Sarykum sand complex, Dagestan. The peculiarity of this complex is its gradual overgrowth. Due to this, it is possible to use this object to study biogeochemical processes of formation and development of ecosystems.

XRF methods were used to study the chemical composition of soil from different heights at different levels of vegetation. The CIA geochemical index was used to study weathering processes. However, this index is used to measure the rate of weathering of the palaeosol, so another index based on the comparison of biogenic and nonbiogenic elements, which is also given, is proposed to study the processes of overgrowth. A comparison of pH is also considered and some changes in mineralogy are described.

ACKNOWLEDGEMENTS:
The author acknowledges the support of Ministry of Science and Higher Education of the Russian Federation under the grant 075-15-2020780.

SESSION 4. ASTROBIOLOGY (AB) POSTER SESSION

PROSPECTS FOR THE APPLICATION OF MICROBIAL FUEL CELLS IN REGENERATIVE BIOLOGICAL LIFE SUPPORT SYSTEMS

V.K. Ilyin[1], D.V. Korshunov[1], A.G. Korosteleva[1], S.O. Smolyanina[1]
[1] *Institute for biomedical problems of the Russian Academy of Sciences, 76A Khoroshevskoye shosse, 123007 Moscow, Russia*

KEYWORDS:
microbial fuel cells, nitrification, denitrification, ammonification, biological nitrogen removal, biological life support systems

ABSTRACT
Microbial fuel cells (MFC) – devices for generating electric current using microorganisms – have been widely used in recent years in research for alternative energy sources search from renewable organic raw materials [1].

The origination of increased interest in this topic is connected also with an important discovery in microbiology, namely: the discovery of electrogenic bacteria that generate electric current in the process of life [2].

In the course of studying the processes occurring in MFC, new variants of "microorganism-substrate" combinations in biofuel cells are constantly being created, which is why the term "bioelectrochemical systems" has been increasingly used lately, because. it better describes the variety of designs of bioelectric cells than the classical MFC scheme.

Following the increase in the number of ways to use microorganisms that generate electricity as a by-product of their vital activity, the scope of possible application of MFCs in biotechnological processes is expanding. Currently, in particular, attempts are being made to introduce MFC in wastewater treatment technologies.

Biofuel cells that treat wastewater can also be a component of biological life support systems (BLSS) of spacecraft designed for long flights and advanced planetary bases. Such units should be of the regenerative type, i.e. to ensure the highest possible closing coefficient of the system for biogenic elements, to create a cycle of basic substances necessary for human survival. MFCs as part of the liquid organic waste treatment unit can accelerate the decomposition of organic substances, followed by the extraction from wastewater and the return to the system of such essential elements as nitrogen, phosphorus and sulfur [3].

One of the most common methods for removing phosphorus from wastewater is its precipitation as magnesium ammonium orthophosphate (struvite) NH_4MgPO_4 at high pH values. The method requires an additional consumption of reagents to maintain the required pH level. With the help of MFC, phosphorus precipitation is possible without pH correction and, therefore, additional costs [4][5]. Orthophosphate is reduced by electrons at the MFC cathode from iron phosphate; combining with magnesium and ammonium ions, it precipitates as a salt ($NH_4MgPO_4*6H_2O$). Thus, this technology makes it possible to simultaneously achieve both the extraction of nitrogen, phosphorus and organic substances from wastewater and the generation of a weak electric current [6].

The removal of sulfide from wastewater is still an urgent problem in ecobiotechnology (Pikaar et al., 2011). Standard physicochemical and biological methods are energy intensive. Sulfur multivalency – from (+6) to (–2) – creates additional difficulties in its removal [7]. A number of researchers suggest using MFC to remove sulfur from liquid media [8]. The mechanism of sulfur conversion in the MFC anode chamber is based on the interaction of sulfate-reducing and sulfide-oxidizing bacteria. The former reduce sulfate to S^{2}-, while the latter oxidize sulfide to molecular sulfur by transferring electrons to the anode [9].

Another promising area of MFC application is their use to remove nitrogen from wastewater. On Earth, the removal of nitrogen from wastewater is necessary to avoid eutrophication (oversaturation of nutrients, in particular ni-

trogen and phosphorus). Excess nitrogen in LSS can interfere with the mineralization of wastewater by biological methods; moreover, its mineral form must be available for the autotrophic link of the BLSS.

As a rule, in wastewater, nitrogen is present in the form of ammonium, and the process for its removal usually includes successive nitrification and denitrification. Standard treatment methods require a large amount of organic matter and energy to supply oxygen (nitrification process) through aeration and a large amount of activated sludge [10]. Several mechanisms of nitrogen removal in MFCs are known [11][12]:

1) Active and passive transport across the membrane, in which the ammonium ion moves through the cation-exchange membrane to the cathode passively in the uncharged form (NH_3) and/or actively in the form of an ion (NH_4+). An increase in the pH level in the cathode chamber leads to a shift in the chemical equilibrium towards the formation of ammonia and its removal from the system;
2) Microbial nitrification and denitrification at the cathode, in which ammonium is transformed into nitrate (NO_3-) and then into molecular nitrogen (N_2);
3) Conversion of ammonium into gaseous nitrogen by microorganisms in the anode chamber;
4) Absorption of ammonium by microorganisms and its accumulation (in the form of nitrogen-containing organic compounds) in microbial biomass.

For application in BLSS, nitrification at the cathode is of particular interest, since it allows you to get nitrogen in the form of nitrates dissolved in water, which are then easily absorbed by plants. A series of experiments was carried out at the Institute of Biomedical Problems of the Russian Academy of Sciences to study the processes of biological nitrogen removal occurring in MFC cells during the biodegradation of liquid organic waste. The main objectives of the experiments were:

- assessment of the electrogenic activity of the microflora of the activated sludge of wastewater and bottom sediments of fresh water bodies;
- assessment of the potential of bottom sediment microorganisms and activated sewage sludge as biological agents that transform ammonium nitrogen into nitrates and nitrogen oxides in cells of microbial fuel cells;
- assessment of the potential of bottom sediment microorganisms and activated sewage sludge as biodestructors of organic waste in cells of microbial fuel cells;

The main research methods were:

- monitoring of the power of the electric current in the external circuit of the MFC;
- measuring the pH of solutions in the cathode and anode chambers of the MFC;
- measurement of the optical density of the MFC anode chamber solution;
- measuring the concentration of nitrates and ammonium in the anode and cathode chambers of MFC cells;

The object of study and the source of electrogenic microflora for MFC were activated sewage sludge and bottom sediments of fresh water natural reservoirs (rivers, dikes) of Moscow region. The nutrient medium for activated sludge bacteria was a peptone solution. The duration of the experiments was 30 days.

According to the results obtained, the voltage in the external circuit of the MFC increased exponentially for one and two weeks for activated sewage sludge and river sludge, respectively. Subsequently, the voltage stabilized at the level of 350–370 mV until the end of the experiment. The optical density of the anode chamber solution also increased exponentially for 6–12 days, and then gradually decreased. The initial weakly alkaline pH of the anode chamber solution decreased within 5–6 days to slightly acidic (6.6), after which it gradually increased again (to the initial level?) until the end of the experiment. The concentration of ammonium nitrogen measured at the end of the experiment was approximately 100 mg/l. Under aeration conditions, nitrate nitrogen was detected both in the anode and cathode chambers at a concentration of 20 mg/l.

Based on the results of the study, the following conclusions can be drawn:

1) The maximum voltage generated by the MFC is reached after the maximum increase in the biomass of activated sludge particles in a slightly acidic medium (pH value close to 6.0);
2) The electrogenic potential of activated sludge floccules does not depend on the source of microflora (river silt or activated sewage sludge) and the presence of oxygen in the anode chamber.
3) The presence of ammonium ions in the anode and cathode chambers of the aerobic MFC indicates the diffusion of these ions through the cation-exchange membrane with subsequent conversion into a gaseous form in the cathode chamber at slightly alkaline pH (1st way of nitrogen removal using MFC);
4) The presence of nitrate ions in the anode chamber of the aerobic MFC indicates the occurrence of the nitrification process in the anode chamber. Nitrification requires a slightly alkaline reaction of the medium (pH in the range of 7.5–8.5), a reduced concentration of organic substances and a constant supply of oxygen. All these conditions are observed at the initial stage of activated sludge exposure in aerobic MFC;
5) The mechanism of electron transfer to the MFC anode, apparently, is based on the property of activated sludge particles to accumulate a negative charge on the surface at a pH of the medium from 6 to 9.

REFERENCES:

[1] Katz E., Shipway A.N., Wilner I. Biochemical fuel cells // In Handbook of fuel cells – Fundamentals, Technology and Application / Ed. by Vielstich W., Lamm A., Gasteiger H.A., John Wiley & Sons, Ltd. 2003.
[2] Bond D.R., Holmes D.E., Tender L.M., Lovley D.R. Electrode-reducing microorganisms that harvest energy from marine sediments // Science. 2002. V. 295. P. 483-485.
[3] Gowthami Palanisamy, Ho-Young Jung, T. Sadhasivam, Mahaveer D. Kurkuri, Sang Chai Kim, Sung-Hee Roh. A comprehensive review on microbial fuel cell technologies: Processes, tilization, and advanced developments in electrodes and membranes // Journal of Cleaner Production 221 (2019) 598e621
[4] Zang, G.L., Sheng, G.P., Li, W.W., Tong, Z.H., Zeng, R.J., Shi, C., Yu, H.Q., 2012. Nutrient removal and energy production in a urine treatment process using magnesium ammonium phosphate precipitation and a microbial fuel cell technique. Phys.Chem. Chem. Phys. 14, 1978e1984. https://doi.org/10.1039/C2CP23402E.
[5] Fischer, F., Bastian, C., Happe, M., Mabillard, E., Schmidt, N., 2011. Microbial fuel cell enables phosphate recovery from digested sewage sludge as struvite. Bioresour. Technol. 102, 5824e5830. https://doi.org/10.1016/j.biortech.2011.02.089.
[6] Huang, H., Zhang, P., Zhang, Z., Liu, J., Xiao, J., Gao, F., 2016. Simultaneous removal of ammonia nitrogen and recovery of phosphate from swine wastewater by struvite electrochemical precipitation and recycling technology. J. Clean. Prod. 127, 302e310. https://doi.org/10.1016/j.jclepro.2016.04.002.
[7] Sun, M., Mu, Z.X., Chen, Y.P., Sheng, G.P., Liu, X.W., Chen, Y.Z., Zhao, Y., Wang, H.-L., Yu, H.-Q., Wei, L., Ma, F., 2009. Microbe-assisted sulfide oxidation in the anode of a microbial fuel cell. Environ. Sci. Technol. 43, 3372e3377. https://doi.org/10.1021/es802809m.
[8] Izadi, P., Rahimnejad, M., 2014. Simultaneous electricity generation and sulfide removal via a dual chamber microbial fuel cell. Biofuel Res. J. 1, 34e38. https://dx.doi.org/10.18331/BRJ2015.1.1.8.
[9] Lee, D.J., Liu, X., Weng, H.L., 2014. Sulfate and organic carbon removal by microbial fuel cell with sulfate-reducing bacteria and sulfide-oxidising bacteria anodic biofilm. Bioresour. Technol. 156, 14e19. https://doi.org/10.1016/j.biortech.2013.12.129.
[10] Arredondo, M.R., Kuntke, P., Jeremiasse, A.W., Sleutels, T.H.J.A., Buisman, C.J.N., Ter Heijne, A., 2015. Bioelectrochemical systems for nitrogen removal and recovery from wastewater. Environ. Sci.: Water Res. Technol. 1, 22e33. https://doi.org/10.1039/C4EW00066H.
[11] Kuntke, P., Geleji, M., Bruning, H., Zeeman, G., Hamelers, H.V.M., Buisman, C.J.N.,2011. Effects of ammonium concentration and charge exchange on ammonium recovery from high strength wastewater using a microbial fuel cell. Bioresour. Technol. 102, 4376e4382. https://doi.org/10.1016/j.biortech.2010.12.085.
[12] Cheng, K.Y., Kaksonen, A.H., Cord-Ruwisch, R., 2013. Ammonia recycling enables sustainable operation of bioelectrochemical systems. Bioresour. Technol. 143, 25e31. https://doi.org/10.1016/j.biortech.2013.05.108.

LIFE ON MARS: WHAT CAN THE USE OF BIOSIGNATURES TELL US?

Sávio Torres de Farias[1,2]
[1] *Laboratório de Genética Evolutiva Paulo Leminski, Centro de Ciências Exatas e da Natureza, Universidade Federal da Paraíba, João Pessoa, Paraíba, Brazil; https://orcid.org/0000-0002-2997-3629*
[2] *Network of Researchers on the Chemical Evolution of Life (NoRCEL), Leeds LS7 3RB, UK*

KEYWORDS:
Biosignatures, Life concept, prebiotic chemistry.

INTRODUCTION:
Astrobiology is one of the fastest expanding scientific fields today. Among the various issues that this area of knowledge faces, the search for life outside our planet proves to be especially challenging. When it comes to identifying life beyond our planet, one of the most difficult challenges is the use of biosignatures. The choice of biosignatures that may reveal signs of life must comply with several criteria that seek to eliminate or minimize the possibility of false positives. In this essay, I hope to discuss the implications of using biosignatures considering recent advances in prebiotic chemistry, as well as new conceptual frameworks for the phenomenon of life and its implications for the development of biosignatures in a non-typological way, which could open a new way to discover life structurally distinct from what we know.

PEPTIDES PRESERVATION UNDER HIGH-DOSE IRRADIATION WITH ACCELERATED ELECTRONS

V.S. Cheptsov[1,2], A.K. Pavlov[3], D.V Belousov[4], V.N. Lomasov[4]

[1] *Soil Science Faculty, Lomonosov Moscow State University, Moscow 119991, Russia; cheptcov.vladimir@gmail.com*

[2] *Space Research Institute, Russian Academy of Sciences, Moscow 117997, Russia*

[3] *Ioffe Physical-Technical Institute, Russian Academy of Sciences, St. Petersburg 194021, Russia*

[4] *Peter the Great St. Petersburg State Polytechnic University, St. Petersburg 194021, Russia*

KEYWORDS:
Europa; Enceladus; biomarkers; ice; ionizing radiation; subsurface oceans.

Introduction:

Currently, Mars and the ice satellites of Jupiter and Saturn – Europa and Enceladus – are considered the most promising in terms of searching for traces of extraterrestrial life in the Solar System. On ice satellites, the existence of oceans under the outer ice shell is assumed. At the same time, the surface of Europa is relatively "fresh" ice, which is renewed due to the rise of water from the ocean along the observed cracks in the ice shell, and on Enceladus, water geysers were found ejecting into space not only water vapor, but also organic molecules. In the expeditions planned for these objects, one of the main tasks is to search for biomarkers (organic molecules of biogenic origin) that come to the surface in these processes – traces of hypothetical life in the subglacial oceans. One of the main factors determining the rate of degradation of biomarkers in the surface layers of ice is intense irradiation with high-energy particles (protons and electrons). In this regard, it is important to study the rate of radiolysis of biomolecules under conditions similar to those of ice satellites.

Previously, only the stability of individual biomolecules with rather small molecular weights (amino acids, nucleotides) was studied in pure form and in mixtures with model regolith. However, if there is life in the subglacial oceans of the icy bodies of the Solar System, it is likely that biomolecules will be released to the surface within microbial cells, and not in the form of pure substances. The specific composition of biomolecules and complex interactions between them (including during radiolysis) can significantly affect their stability and, consequently, the duration of their preservation and the possibility of their detection by space missions.

MATERIALS AND METHODS:

we irradiated bacterial cells (*Deinococcus radiodurans*, *Bacillus subtilis*, *Escherichia coli*) in water ice with accelerated electrons (~1 MeV) at doses up to 10 MGy under low pressure (~0.01 Torr) and low temperature (-180°C). Further, the survival of peptides after irradiation was evaluated using MALDI-TOF mass spectrometry (peptide extraction in 50% acetonitrile with 0.5% trichloroacetic acid, matrix – alpha-hydroxycinnamic acid, m/z range – 1–17 kDa).

RESULTS AND CONCLUSION:

For water ice samples with bacterial cells irradiated with accelerated electrons under low pressure and low temperature in a dose gradient 100 kGy, 1 MGy, and 10 MGy, with increasing radiation dose, a gradual decrease in the peak areas of peptides with high masses was observed. After exposure to the highest dose of radiation (10 MGy), peptides with masses up to 7.7, 6.7, and 2.4 kDa were detected in ice containing cells of *D. radiodurans*, *B. subtilis*, and *E. coli*, respectively (peptides with masses up to 15 kDa were detected in control non-irradiated samples) (Fig.1). The data obtained indicate the possibility of preserving complex organic molecules (peptides with high molecular weights) for a long time on various space objects. Thus, a dose of 10 MGy in the ice of Europe accumulates over 100 and 10,000 years at a depth of 1 cm and 10 cm, respectively, and on the surface of Mars – over 150 million years.

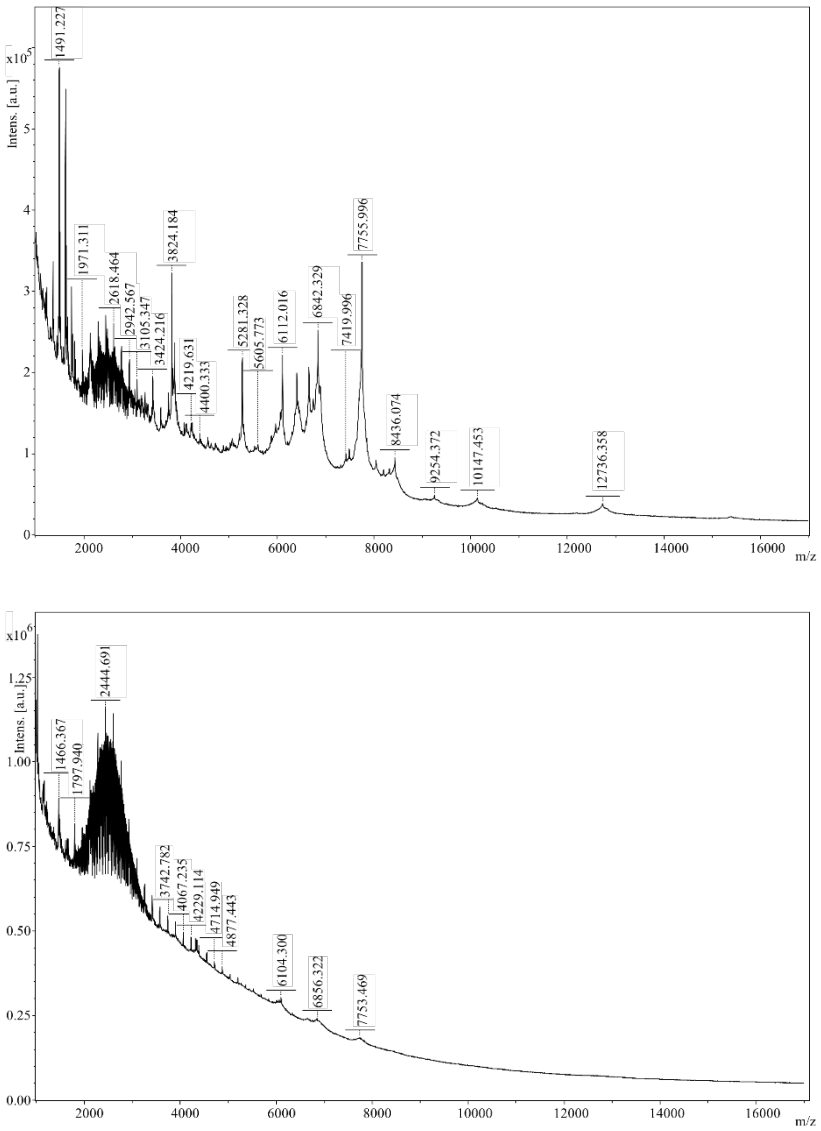

Fig. 1. MALDI-TOF mass spectra of the ice containing *D. radiodurans* cells: *top* – control sample; *bottom* – the sample, irradiated with 10 MGy dose.

ACKNOWLEDGEMENTS:
The study was supported by RFBR, grant #20-02-00470.

BIODIVERSITY OF DROUGHT-TOLERANT BACTERIA: ASTROBIOLOGICAL CONCERN

A.A. Belov[1,2], V.S. Cheptsov[1,2,3]
[1] *Soil Science Faculty, Lomonosov Moscow State University, 119234 Moscow, Russia; and.ant.be@gmail.com*
[2] *Network of Researchers on Chemical Evolution of Life (NoR CEL), Leeds 01924, UK*
[3] *Space Research Institute, Russian Academy of Sciences, 117997 Moscow, Russia*

KEYWORDS:
Water activity, oxidative stress, desert soil bacteria, metabolic activity, Actinobacteria.

INTRODUCTION:
Water plays an important role in cell metabolism and microbial communities' activity. In the extraterrestrial environments, lack of water is an important limitation factor for life expansion. However, different organisms could survive and proliferate at different levels of water availability. Moreover, not only lack of water molecules limits microorganisms' colonization of substrates, but the high concentrations of water-soluble substances (salts, sugars, amino acids etc.) also negatively affected bacteria by reduction of water availability for life support.

To estimate the potential of culturable soil bacterial communities to metabolize at different values of water availability the following experiment was performed: soil bacteria associated with Sahara (Tunisia) and Negev (Israel) deserts soils were cultured on the Reasoner 2 A medium supplemented with glycerol to set up the water activity (Aw = water vapor pressure upon distilled water/ water vapor pressure upon solution) at level of 1.0 to 0.9 (step by 0.01 Aw). After incubation unique cultures were isolated, described, identified by 16S rRNA sequencing and tested for growth at gradient of water activity (Aw) in pure cultures. After incubation and isolation 355 strains were identified and tested.

Culturable bacteria were detected down to Aw 0.95, no growth was detected on the media with lower water activity values. Numbers of culturable bacteria were decreased from 10^5 and 10^7 colony forming units per gram (CFU/g) in Sahara and Negev desert soils, respectively, to 10^4 CFU/g in both samples investigated (Fig. 1).

Representatives of *Arthrobacter, Kocuria,* and *Pseudoarthrobacter* genera were dominant in both samples analyzed at different Aw values. In total, representatives of 34 bacterial genus, predominantly from the Actinobacteria phyla were isolated during the culturing procedures. On the medium with Aw=0.95 representatives of *Arthrobacter, Corynebacterium*, and *Kocuria* genera were isolated. These bacteria are frequently found in the desert and permafrost environments and well-known as multiple-stress tolerant bacteria (Fig. 2).

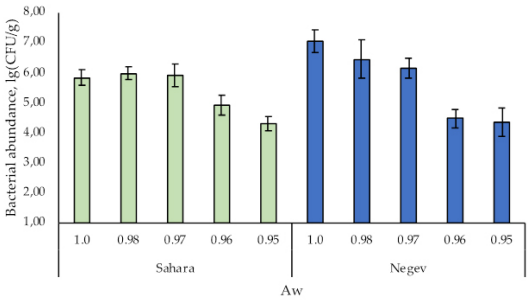

Fig. 1. Numbers of bacteria cultured from Sahara and Negev deserts soils at different water availability levels.

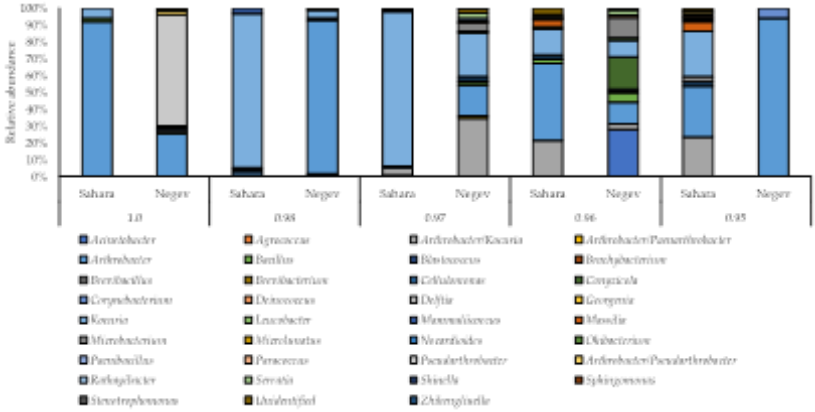

Fig 2. Culturable bacterial communities' structure on the media with low water activity (Aw).

During the isolation and identification of drought-tolerant bacteria from the samples studied 38 strains with low nucleotide sequence similarity with the databases were found. These strains could be the representatives of previously undescribed species of genera *Agrococcus, Arthrobacter, Bacillus, Brachybacterium, Cellulomonas, Conyzicola, Kocuria, Microbacterium, Okibacterium, Rathayibacter, Sphingomonas*, so it should be further investigated.

Isolated strains testing for growth in pure culture in gradient of Aw values revealed that the most strains are able to grow on the medium with Aw lower than Aw of the media, on which this strain was isolated from the native sample. In general, majority of isolated cultures were able to grow on the media with Aw from 0.1 to 0.96. At Aw = 0.95 severe reduction of strains, which are able to grow was observed. In Aw diapason 0.94–0.91 just representatives of *Arthrobacter, Kocuria, Brachybacterium, Serratia,* and *Leucobacter* genera were able to grow.

Thus, in laboratory conditions predominantly Actinobacteria demonstrates the ability to grow in conditions of water deficiency. Regarding their high tolerance to UV- and ionizing radiation, desiccation, oxidative and salt stress, fluctuations of temperature, pH, and the other environmental factors, representatives of this phyla could be considered as one of the key-taxa for further astrobiologically-oriented research. Besides, further research on the metabolic activity in native soil conditions should be performed to reveal the taxa, able to metabolize *in situ* in conditions of low water activity.

ACKNOWLEDGMENTS:

This work was supported by the grant of the President of the Russian Federation No. MK-664.2021.1.4.

INFLUENCE OF PERCHLORATES ON WATER CRYSTALLIZATION TEMPERATURE AND BACTERIAL SURVIVABILITY IN MECHANICAL SIMULANTS OF MARS REGOLITH

D.A. Vedenev[1], Z.S. Ejelev[1], V.S. Cheptsov[1,2], A.A. Belov[1]
[1] *Lomonosov Moscow State University, Moscow, 119991, Russia; den_veden@mail.ru*
[2] *Space Research Institute of Russian Academy of Sciences, Moscow, 117997, Russia*

KEYWORDS:
Microbiology; astrobiology; perchlorate tolerance; perchlorate; freezing point.

INTRODUCTION:

One of the main tasks of astrobiology is the search and study of the possibility of life beyond the Earth. The most promising extraterrestrial object in terms of habitability is Mars. In the regolith of this planet, perchlorates with a high oxidizing ability were found, which are considered as an important factor limiting the spread of living organisms. At the same time, in addition to high oxidizing ability, perchlorates are characterized by have high hygroscopicity and the ability to reduce the water crystallization temperature of water. Due to these properties, in the conditions of Mars, perchlorates can absorb the surrounding moisture and form liquid brines, which could serve as a habitat for microorganisms.

In previous studies of the effect of perchlorates on the crystallization temperature of water, only the freezing points of pure solutions of perchlorates of various concentrations were found [1], but this does not give a complete information about how the solutions will behave in a heterophase system. Also, the survival of microorganisms in such solutions is not clear, since the limit of their tolerance to perchlorates *in situ* has not yet been determined. The tolerance of microbial communities to the effects of high concentrations of perchlorates is still poorly understood, and the limits of the resistance of microbial communities have not been determined. According to the results of a number of studies, it turned out that the presence of perchlorates in a concentration of 0.5–0.6% (the concentration of perchlorates in the surface layer of Martian regolith) weakly inhibits the growth and development of many bacteria. However, perchlorates in higher concentrations (few percent and above) may eliminate diverse of microorganisms.

Identification of the limits of tolerance to perchlorates and the regularities of crystallization of perchlorate solutions in heterophase systems will allow:

- to complement the understanding of the stability of biosystems and will provide valuable information for determining the most promising potentially habitable regions on Mars
- apply the data obtained to develop planetary quarantine measures and supplement existing astrobiological models.
- to use some of the research results from the point of view of studying the processes of water crystallization in saline soils.

To study the dependence of the crystallization temperature of aqueous solutions of perchlorates depending on their concentration and the granulometric composition of mechanical analogues of regolith, experiments were conducted on freezing-thawing of 4 mechanical analogues of the Martian regolith, which are quartz with particle sizes 500–1000 μm, 250–500 μm, 100–250 μm, and <53 μm. The samples were saturated with sodium perchlorate ($NaClO_4$) solutions with concentrations of perchlorate: 3.7%, 11.2%, 18.6% and 37.2%. The freezing-thawing cycle was accompanied by a recording of the temperature course in a low-temperature freezer at a temperature of –85°C. After taking measurements, the temperature of the phase transition was determined from the data obtained, since it is accompanied by the release or absorption of energy.

To assess the tolerance of microbial communities to perchlorates, culturable heterotrophic aerobic bacterial communities were characterized, confined to native soil samples of various arid regions of the Earth (Cyprus, Tenerife, Vietnam, Russia (Voronezh Region)). According to the results of culturing procedures, a sample containing the most tolerant perchlorate-resistant microbial community was associated with Tenerife foothill soil. This soil was further used to study the effect of perchlorates on soil microbial communities *in situ*. After the experiment, the viability of microorganisms was evaluated by multisubstrate testing and plating on nutrient media.

The experimental results show that bacterial communities in a heterogeneous environment are able to survive oxidative stress caused by the presence of perchlorates, and, under favorable conditions, grow, proliferate and metabolize. Also, the dependence of the water crystallization temperature on the granulometric composition of the soil was established: the crystallization temperature decreased with increasing particle size.

At the moment, the number of studies on the effects of perchlorates on microorganisms *in situ* is few, and in the course of these studies, the effect of perchlorates on prokaryotes in concentrations up to 5% has been studied [2]. The effect of higher concentrations has not been studied yet. In our study, it was found out that microbial communities, when exposed to sodium perchlorate in concentrations up to 10%, showed high tolerance and retained a high number of viable cells. This, on the one hand, is a weighty argument in favor of the possibility of survival of terrestrial-type microorganisms in perchlorate solutions on Mars, and, on the other hand, indicates that this is not the maximal concentration at which microbial communities are able to survive *in situ*, and further studies are needed to study the effect of perchlorates in higher concentrations.

REFERENCES:

[1] Chevrier V.F., Hanley J., Altheide T.S. Stability of perchlorate hydrates and their liquid solutions at the Phoenix landing site, Mars //Geophysical Research Letters. – 2009. – V. 36. – №. 10.

[2] Cheptsov, V., Belov, A., Soloveva, O., Vorobyova, E., Osipov, G., Manucharova, N., & Gorlenko, M. Survival and growth of soil microbial communities under influence of sodium perchlorates //International Journal of Astrobiology. – 2021. – V. 20. – №. 1. – P. 36-47.

TOLERANCE OF ARID ECOSYSTEMS BACTERIA TO SODIUM PERCHLORATE: IMPLICATIONS FOR MARS' HABITABILITY

D.D. Barbashin[1], V.S. Cheptsov[1,2], A.A. Belov[1]
[1] *Soil Science Faculty, Lomonosov Moscow State University, 119234 Moscow, Russia*
[2] *Space Research Institute of RAS, 117997, Moscow, Russia*

KEYWORDS:
Astrobiology, perchlorate brines, microorganisms, soil.

INTRODUCTION:

The Phoenix mission found perchlorates on the surface of the Great Northern Plain in concentrations of 0.4–0.6% by weight [1]. It is suggested that perchlorates can contribute to liquid brines formation under Martian conditions due to high hygroscopicity of perchlorates and low freezing temperatures of its solutions [2, 3].

In recent years, a several perchlorate-resistant microorganisms have been discovered, but the limiting concentrations of perchlorates at which their growth is possible have been determined only for a relatively small set of species [2, 3, 4]. The most resistant organisms known so far have been discovered within the last few years [5, 6]. In this regard, the search for microorganisms that are more resistant than currently known is relevant, which contributes to identify habitable regions and deposits on Mars. At this, it is promising to study microorganisms of extreme habitats, since it has been shown that many bacteria from such ecosystems are highly resistant to the effects of $Mg(ClO_4)_2$ at concentrations of up to 5% [7, 8].

Bacteria (208 strains in total) isolated from the brown soil of the Sarpinskaya Lowland (Russia) and the mountain soils of the Teide volcano (Spain) were the object of the present study. Bacterial strains were cultured in liquid R3A medium supplemented with sodium perchlorate in concentrations of 0, 0.5, 1, 2.5, 5, 7.5, and 10% (w/v). Culturing was carried out at room temperature for 14 days, and the growth was determined visually.

As a result,, it was found that the majority (99.1%) of microorganisms studied was tolerant to sodium perchlorate in concentrations of up to 2.5% in the medium, and 41.8% of the strains were able to grow at the presence of 5% of perchlorate. The number of tolerant strains was 10.5% and 1.9% of all strains tested at a concentration of perchlorates in the medium equal to 7.5% and 10%, respectively.

Another part of our work was to study the tolerance of microorganisms from various microbial communities to high concentrations (7.5 and 10%) of sodium perchlorate. The object of study was bacteria (735 strains) isolated from the soils of the northern part of the Sahara Desert (Tunisia), central part of the Mojave Desert (USA), Sarpinskaya Lowland (Russia), Khrenovsky pine forest (Russia), and the mountainous soils of the Teide volcano (Spain).

The proportions of the most resistant strains for different microbial communities ranged from 3 to 17% for 7.5% sodium perchlorate and from 0 to 3% for 10% sodium perchlorate (Fig. 1). The highest tolerance to 7.5% $NaClO_4$ was observed in the microbial community of the Sarpinsky Lowland soil. Soil salinization is widespread in the ecosystem under study [9], which can contribute to the formation of halotolerant communities. The most of perchlorate-tolerant microorganisms are halotolerant [6], suggesting that the number of halotolerant microorganisms in a community correlates with the number of perchlorate-tolerant ones.

Bacteria of the genera *Nocardia*, *Pseudomonas*, *Bacillus*, *Rhodococcus*, *Arthrobacter*, *Massilia*, *Micrococcus*, and *Paracoccus* demonstrated the highest tolerance to perchlorates. High perchlorate-tolerance of the genera above, excluding *Paracoccus*, was reported previously [2].

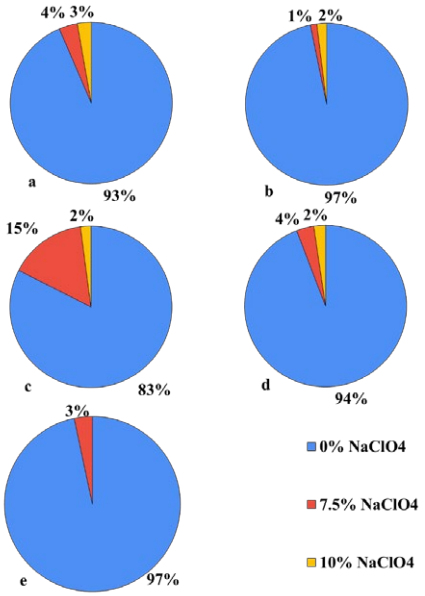

Fig. 1. Tolerance of culturable microbial communities isolated from arid ecosystems to perchlorates at various concentrations: *a* – soil of Khrenovsky pine forest, *b* – soil of the northern part of the Sahara desert, *c* – brown soil of the Sarpinskaya lowland, *d* and *e* – mountain soils of the Teide volcano.

Additional testing revealed that representatives of the genus *Paracoccus* are able to grow at a concentration of perchlorates in the medium equal to 10.5%.

Thus, the study has shown that a fairly large number of prokaryotes are resistant to sodium perchlorate even at a concentration of 10%. It testifies in favor of possibility of some representatives of the Earth's prokaryotic life (or hypothetical Earth-like extraterrestrial organisms) to survive in perchlorate brines in the Mars regolith.

References:

[1] Hecht M.H., Kounaves, S.P., Quinn, R.C., West, S.J., Young, S.M., Ming, D.W., Smith, P.H.. Detection of perchlorate and the soluble chemistry of martian soil at the Phoenix lander site // Science. 2009. V. 325. No. 5936. P. 64-67.

[2] Cheptsov, V., Belov, A., Soloveva, O., Vorobyova, E., Osipov, G., Manucharova, N., Gorlenko, M. Survival and growth of soil microbial communities under influence of sodium perchlorates //International Journal of Astrobiology. 2021. V. 20. No. 1. P. 36-47.

[3] Nuding, D.L., Davis, R.D., Gough, R.V., Tolbert, M.A. The aqueous stability of a Mars salt analog: instant Mars // Journal of Geophysical Research: Planets. 2015. V. 120. No. 3. P. 588-598.

[4] Beblo-Vranesevic K., Huber H., Rettberg P. High tolerance of Hydrogenothermus marinus to sodium perchlorate // Frontiers in Microbiology. 2017. V. 8. P. 1369.

[5] Heinz J., Krahn T., Schulze-Makuch D. A new record for microbial perchlorate tolerance: fungal growth in NaClO4 brines and its implications for putative life on Mars //Life. 2020. V. 10. No. 5. P. 53.

[6] Al Soudi, A.F., Farhat, O., Chen, F., Clark, B.C., & Schneegurt, M.A. Bacterial growth tolerance to concentrations of chlorate and perchlorate salts relevant to Mars //International Journal of Astrobiology. 2017. V. 16. No. 3. P. 229-235.

[7] Belov A.A., Cheptsov, V.S., & Vorobyova, E.A. Soil bacterial communities of Sahara and Gibson deserts: Physiological and taxonomical characteristics // AIMS Microbiology. 2018. V. 4. No. 4. P. 685.

[8] Belov, A.A., Cheptsov, V.S., Vorobyova, E.A., Manucharova, N.A., & Ezhelev, Z.S. Stress-tolerance and taxonomy of culturable bacterial communities isolated from a central Mojave Desert soil sample // Geosciences. 2019. V. 9. No. 4. P. 166.

[9] Bananova V.A., Lazareva V.G., Seratirova V.V. Natural zoning of the North-Western Caspian Sea in modern economic use // Geology, geography and global energy. 2011. No. 3. P. 42.

GROWING PEA PLANTS IN MARTIAN SOIL ANALOGUE WITH THE ADDICTION NITROGEN FIXER BACTERIA

D.D. Barbashin[1], D.D. Mironov[2,3]
[1] *Soil Science Faculty, Lomonosov Moscow State University, 119234 Moscow, Russia*
[2] *Vernadsky Institute of Geochemistry and Analytical Chemistry, RAS, Moscow, Russia; 1032193132@rudn.ru*
[3] *Institute of Environmental Engineering, RUDN University, Moscow, Russia*

KEYWORDS:
Astrobiology, Martian soil analogue, Peas, biogeochemistry.

INTRODUCTION:
Mankind aspires to become an interplanetary civilization. Roscosmos, NASA and ESA have set a goal of carrying out a manned flight to Mars in the 21st century. However, currently, Mars is not suitable for human habitation by its conditions. Therefore, it is necessary to create a source of food for a colony on Mars [1].

Therefore, work will be needed to increase the fertility of the Martian regolith. Experimentally, plant growth has been shown on lunar and Mars regolith analogues [2]. Previously, researchers conducted experiments on cultivation of Martian regolith analogues using clover and introduction of symbiotic nitrogen fixers [3]. As a result of the research, the scientists concluded that the growth of roots and shoots of legume plants increased by 95% under inoculation with symbiotic microorganisms.

During the experiment, pea (Pisum sativum) plants were grown in a chemical and mineralogical analogue of Martian soil VI-M2 with the addition of free-living nitrogen-fixers Beijerinckia fluminensis. As a control, the samples were grown in the Martian soil analog VI-M2 without the addition of microorganisms. Pea samples were grown in the Umbric Albeluvisols organogenic horizon to establish the efficiency of such cultivation compared to terrestrial conditions. At the end of the cultivation period, assays were performed to determine the differences in the microbial communities formed.

Important biogeochemical characteristics were determined using XRF analysis.

REFERENCES:
[1] Yamashita M., Hashimoto H., Wada H. Mars. Springer, Berlin, Heidelberg, 2009. P. 517-542.
[2] Wamelink, G.W., Frissel, J.Y., Krijnen, W.H., Verwoert, M.R., & Goedhart, P.W. Can plants grow on Mars and the moon: a growth experiment on Mars and moon soil simulants //PLoS One. 2014. V. 9. No. 8. P. e103138
[3] Harris, F., Dobbs, J., Atkins, D., Ippolito, J.A., & Stewart, J.E. Soil fertility interactions with Sinorhizobium-legume symbiosis in a simulated Martian regolith; effects on nitrogen content and plant health //Plos one. 2021. V. 16. No. 9. P. e0257053.

SESSION 5. SMALL BODIEIS (INCLUDING COSMIC DUST) (SB) ORAL SESSION

ONLY A QUARTER OF NEWLY OBSERVED PRIMITIVE ASTEROIDS ARE ACTIVE

V.V. Busarev[1,2], M.P. Shcherbina[2,1], S.Yu. Kuznetsov[3,1], N.P. Ikonnikova[1], M.A. Burlak[1]

[1] *Sternberg Astronomical Institute Moscow University, Moscow, Russia; busarev@sai.msu.ru*

[2] *Institute of Astronomy RAS, Moscow, Russia*

[3] *Lomonosov Moscow State University, Faculty of Space Research, Moscow, Russia*

KEYWORDS:
main-belt asteroids of primitive types, *UBVRI*-photometry, spectral reflectance, simultaneous sublimation-driven activity

INTRODUCTION:
The problem of asteroid activity arose about 20 years ago. It started from discovering a few small objects in the Main asteroid belt (MAB) with clear but *temporary* cometary features originated possibly from impact events [1]. Shortly after that, the presence of active bodies among asteroids with predominantly silicate composition was explained by supposing these bodies to be comets from the neighboring comet family of Jupiter [2, 3]. However, the result of the 20-year search for new active objects was that about half of ~40 found bodies actually are classic asteroids [4]. Therefore, the solution of this problem may be more complicated and likely associated with the presence of ice on the asteroids themselves.

OBSERVATIONS AND DATA PROCESSING:
With the aim to try answer the question posed, *UBVRI*-photometry of 29 main-belt primitive asteroids (including 4 ones of X type) was performed with the 0.6-m telescope with a CCD-photometer at the Caucasus Mountain Observatory of SAI MSU in December 2021 – February 2022. These asteroids were specially selected to have the eccentricity of orbits not less than 0.1 and to be near perihelion at the time of observations. The obtained photometric data of the asteroids were converted to reflectivity at the effective wavelengths of *UBVRI*-filters by means of observations of close solar analog stars. Then approximated normalized (at 0.55 μm) reflectance curves for each of the asteroids were calculated (some of them are presented in Fig. 1 with their available SMASS reflectance spectra [5] for comparison). Also, spectra of stable stars close to the asteroids were registered to control the stability of photometric conditions before and after the time of asteroid observations (see inserts in Fig. 1).

NEW DETECTION OF SUBLIMATION ACTIVITY OF ASTEROIDS AND DISCUSSION:
To determine which of the asteroids has signs of sublimation-driven activity, we used the spectral method. Its high effectiveness in detecting even thin dust envelope around an asteroid was substantiated in our previous papers based on observations and numerical simulations. The method allowed us to discover simultaneous sublimation activity of four primitive-type asteroids (145, 704, 779, and 1474) in September 2012 [6] and three ones (24, 449, and 704) in March 2019 [7]. Here, we analyzed new reflectance curves of 29 main-belt primitive asteroids and found spectral signs of a sublimation-driven exosphere on 7 of them: (145) Adeona, (302) Clarissa, (322) Phaeo, (435) Ella, (521) Brixia, (690) Wratislavia, and (779) Nina (302, 322, 435, 521 and 690 for the first time), which amounts to 24 % of the objects observed. So, the normalized reflectance curves only for these asteroids are given in Fig. 1. As numerical simulations show [7, 8], an unusual maximum near ~0.45 μm or/and an overall change of spectral gradient from negative to positive in spectral curves of these asteroids could appear due to the scattering of solar light by particles (including those composed of H_2O ice and with aggregate structure) in a dust exosphere. The latter could result from sublimation of ices (mainly H_2O and CO_2), which becomes more intense at

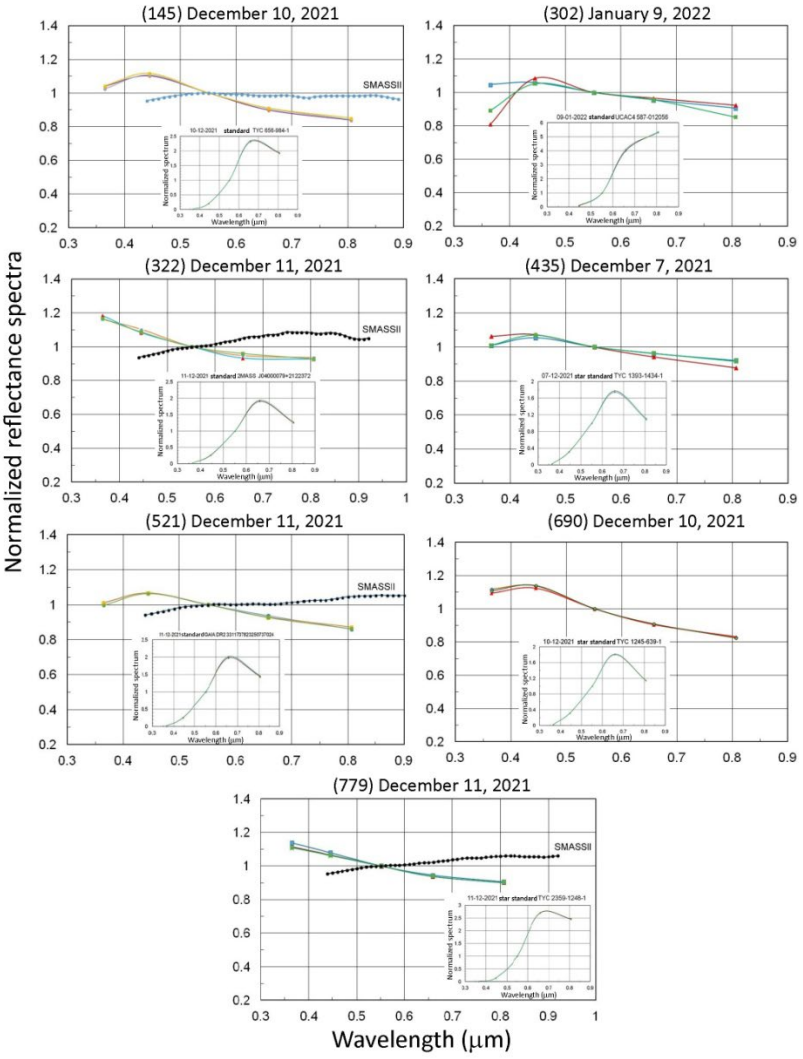

Fig. 1. The normalized approximated spectral reflectance of (145) Adeona, (302) Clarissa, (322) Phaeo, (435) Ella, (521) Brixia, (690) Wratislavia, and (779) Nina indicating sublimation-driven activity near perihelion in December 2021 – February 2022; in the insets: the spectra of close stars as reference stable standards (obtained before and after observations of asteroids)

elevated subsolar temperatures near perihelion. If so, why only about a quarter of the observed primitive asteroids demonstrate sublimation activity? If these asteroids have similar origin, e.g. beyond the snow line [9], then H_2O ice could present and survive in their interiors and active objects should be more numerous. But a very long time (~4 billion years) of depletion led to a larger occurrence depth of volatiles on primitive asteroids. On the other hand, a high porosity of the surface layers could considerably worsen their thermal conductivity [10]. Another frequent, although random, physical factor, which could make ices more exposed on main-belt asteroids, is their mutual collisions and impacts of meteoroids. High intensity of these events in the MAB at present was confirmed by detecting steady dust belts associated with it [11].

Additionally, we compared physical and dynamical parameters of asteroids observed here as active and inactive, but no features or correlations specific only to the first group were found.

CONCLUSIONS:

A search for sublimation activity signs among 29 main-belt primitive asteroids being near perihelion has shown that a dust exosphere exists around a quarter of them. This probably points to the sublimation-driven nature of an exosphere and, respectively, the presence of ices in interiors of these asteroids. A comparison of physical and dynamical parameters of the asteroids detected here as active and inactive revealed no noticeable differences. It seems that the differences, if they exist, are connected with secondary (evolutionary et al.) factors rather than the origin of the bodies.

This study is supported by the Russian Science Foundation (grant No. 22-12-00115).

REFERENCES:

[1] Hsieh H.H., Jewitt D., Fernandez Y.R. The strange case of 133P/Elst-Pizarro: A comet among the asteroids // Astron. J. 2004. V. 127. P. 2997-3017.
[2] Hsieh H.H., Jewitt D.A. Population of Comets in the Main Asteroid Belt // Science. 2006. V. 312. P. 561-563.
[3] Hsieh H.H. Haghighipour N. Potential Jupiter-Family comet contamination of the main asteroid belt // Icarus. 2016. V. 277. P. 19-38.
[4] Chandler C.O., Curtis A.M., Mommert M., Sheppard S.S., Trujillo C.A. SAFARI: Searching Asteroids for Activity Revealing Indicators // PASP. 2018. V. 130. Art. NO. 114502.
[5] SMASS reflectance spectra. http://sbntools.psi.edu/ferret/.
[6] Busarev V.V., Barabanov S.I., Puzin V.B. Material composition assessment and discovering sublimation activity on asteroids 145 Adeona, 704 Interamnia, 779 Nina, and 1474 Beira // Solar Syst. Res. 2016. V. 50. No. 4. p. 281-293.
[7] Busarev V.V., Petrova E.V., Irsmambetova T.R., Shcherbina M.P., Barabanov S.I. Simultaneous sublimation activity of primitive asteroids including (24) Themis and (449) Hamburga: Spectral signs of an exosphere and the solar activity impact // Icarus. 2021. V. 369. Art. No. 114634.
[8] Petrova E.V., Busarev V.V. Properties of particles in the exospheres of active asteroids: estimates based on the spectral features in the UV-visible range // 13MS3. 2022.
[9] V.V. A hypothesis on the origin of C-type asteroids and carbonaceous chondrites // Asteroids, Comets, Meteors 2012 Conf. 2012. Abstr. 6017. https://arxiv.org/ftp/arxiv/papers/1211/1211.3042.pdf.
[10] Schorghofer N. The lifetime of ice on main belt asteroids // Astrophys. J. 2008. V. 682. P. 697-705.
[11] Sykes M.V., Greenberg R., Dermott S.F., Nicholson P.D., Burns J.A. Dust bands in the asteroid belt // Asteroids II / eds. Binzel R.P., Gehrels T., Mattews M.S. Tucson: Univ. of Arizona Press, 1989. P. 336-367.

COLLISIONS AS A POSSIBLE REASON OF SUBLIMATION-DUSTY ACTIVITY OF MAIN BELT ASTEROIDS

B.M. Shustov[1], R.V. Zolotarev[1], M.P. Shcherbina[1,2], V.V. Busarev[1,2]
[1] *Institute of Astronomy RAS, Moscow, Russia; bshustov@inasan.ru*
[2] *Sternberg Astronomical Institute Moscow University, Moscow, Russia; bshustov@inasan.ru*

KEYWORDS:
Active asteroids, sublimation-dusty activity, asteroid collisions

it is shown in [1, 2] that the sublimation-dusty activity of a number of Main Belt asteroids (MBAs) of primitive types correlates with the location of these asteroids in the perihelion section of their orbits. This leads to the assumption that such activity is caused by a cometary mechanism, i.e. the emission of dust particles due to sublimation of ices from the surface of ice-containing layers. It was assumed that these layers are excavated by collisions between MBAs. However, expelling of dust matter can also occur during collisions themselves. We examine both mechanisms by analyzing size and velocity distributions of MBAs and considering parameters of collisional crater formation at asteroids. Fig. 1 shows size-velocity distribution of 1178752 MBAs (data of Minor Planet Center).

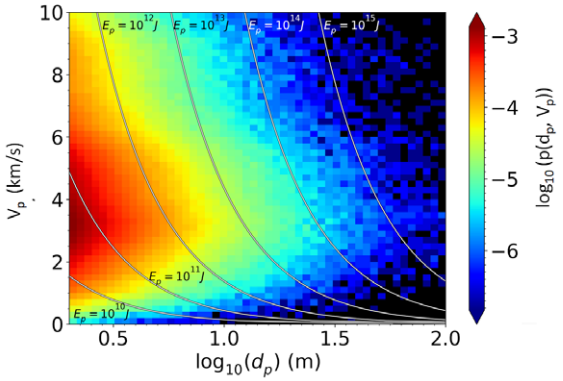

Fig. 1. An assessment of the frequency and effectiveness of collisions was carried out. It is shown that the frequency of collisions of asteroids-impactors with sufficient kinetic energy to expel a detectable amount of dust from a target asteroid (~100 km in size) is rather high, not less than $1–10 \cdot 10^{-2}$ per year. Here a size distribution of dust grains was assumed to be $dN \mu a^{-4}/da$, where a is a grain radius. The "philosophical reasons of this were presented in [3]. Life time of expelled dusty cloud is relatively short (few days to weeks).

There are about 200 MBAs larger than 100 km and current collision rate can explain dust emission in 1–10 % of all such asteroids. This estimate is consistent with the statistics of observations of ~50 studied asteroids, since manifestations of sublimation-dusty activity were detected for 4 of them.

However, this mechanism does not explain the correlation of activity manifestations with the location of asteroids in the perihelion section of orbits, which is quite natural for a cometary (sublimation) mechanism. To ensure the cometary mechanism, collisions should open ice-containing layers over a sufficiently larger area (up to several tenths of square kilometers). These collisional events seem to be much more rare. The parameters of this mechanism are discussed and it is shown that, under certain conditions, it can also explain themphenomenon of sublimation-dusty activity of some MBA asteroids.

ACKNOWLEDGEMENTS:
This work is supported by RSCF grant No. 22-12-00115.

REFERENCES:

[1] Busarev V.V., Barabanov S.I., Rusakov V.S., Puzin V.B., Kravtsov V.V. Spectrophotometry of (32) Pomona, (145) Adeona, (704) Interamnia, (779) Nina, (330825) 2008 XE3, and 2012 QG42 and laboratory study of possible analog samples // Icarus. 2015. V. 262. P. 44-57.
[2] Busarev V.V., Petrova E.V., Irsmambetova T.R., Shcherbina M.P., Barabanov S.I. Simultaneous sublimation activity of primitive asteroids including (24) Themis and (449) Hamburga: Spectral signs of an exosphere and the solar activity impact // Icarus. 2021. V. 369. Art. No. 114634.
[3] B.M., Zolotarev R.V. Mass Indices of Meteoric Bodies: I. Formation Model of Meteoroid Streams // Astronomy Reports. 2022. V. 66. No. 2. P. 179-189.

ESA MEX ASTROMETRIC OBSERVATIONS OF THE ASTEROID PSYCHE: THE TARGET OF A NASA MISSION

T.C. Duxbury[1], N.V. Seregina[1]
[1] *Fairfax, VA, USA; mars1e@yahoo.com*

KEYWORDS:
ESA, NASA, Mars Express, Super Resolution Channel, Psyche.

INTRODUCTION:
The ESA Mars Express orbiter carries the DLR High Resolution Stereo Camera that contains the Super Resolution Channel (SRC). Early in 2021, the SRC observed the main belt asteroid Psyche 33 times against a star field. These images were used to produce astrometric data of Psyche, the primary target of the NASA Discovery Psyche mission [1]. The astrometric data were used as an independent validation dataset to the Earth-based data that are being used to improve the Psyche orbit, that will be needed to navigate to this asteroid.

MEX SRC DATASET:
Between 23 February and 3 March 2021, 33 SRC images were taken of Psyche with a star background. A snippet of one of these images is shown in Fig. 1. Typically there were 3–4 stars within these images. Psyche and the stars are circled with a P identifying the Psyche image and stars identified by their visual magnitude and B-V color.

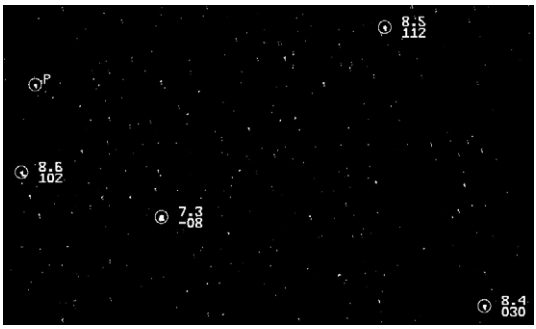

Fig. 1. Psyche imaged against a star field by the ESA MEX SRC

RESULTS:
The pass-through residuals of the reduced right ascension and declination astrometric data had a zero mean and a 1-sigma spread of about 300 km in the orbit of Psyche, giving an independent validation of the current orbit.

REFERENCES:
[1] Hart W. et al. Overview of the Spacecraft Design for the Psyche Mission Concept. URL: https://trs.jpl.nasa.gov/bitstream/handle/2014/47495/CL%2317-5366.pdf?sequence=1, 2018, CL#17-5366.pdf.

MOTION OF DUST IN COMET C/2021 A1 (LEONARD)

A. Kochergin[1], E. Zubko[2], G. Videen[2,3]
[1] *Institute of Applied Astronomy RAS, Saint-Petersburg, Russia; av.kochergin@iaaras.ru*
[2] *Humanitas College, Kyung Hee University, South Korea*
[3] *Space Science Institute, Boulder, USA*

KEYWORDS:
7Comet C/2021 A1 (Leonard), dust, motion, agglomerated debris particles, Solar-radiation pressure, temporal variation in coma

INTRODUCTION:
Comet C/2021 A1 (Leonard) (hereafter Comet Leonard) is a long-period comet discovered on January 3, 2021. This comet was studied by means of polarimetry in November-December of 2021, when the comet was approaching Earth at $\Delta = 0.234$ au [1].

The polarimetric response and modeling suggest relative stability of the dust population in the coma of Comet Leonard [1]. On 11 out 14 epochs, the observations were successfully reproduced with the model of *agglomerated debris particles* (see six examples on top in Fig. 1). These model particles have a Mg-rich silicate composition (complex refractive index $m = 1.6 + 0.0005i$) and organic-matter composition particles ($m = 1.855 + 0.45i$). Their mixture at relative volume abundance of the silicates $V_{sil} = 35.5$ % and carbonaceous materials $V_{car} = 100\ \% - V_{sil} = 64.5$ % is capable of reproducing measurements of Comet Leonard on 11 epochs. Note, such chemical composition appears in accordance with what was found in comets *in situ* (e.g., [2]), as well as, in ground-based observations of other comets (e.g., [3–6]). It also is worth noting that the agglomerated debris particles obey the power-law size distribution $r^{-2.5}$.

However, Comet Leonard also has revealed noticeable deviations in its dust population on 3 out of 14 epochs. What is even more important is that the dust population changed quite fast. For instance, in December of 2021, it occurred during only a day. In this work we simulate the motion of dust particles emanated from the nucleus of Comet Leonard in order to provide clues for better understanding the nature of the quick variations in its dust population.

MODEL:
We model the motion of particles ejected from the Leonard nucleus using an iterative time-domain approach. This approach makes it possible to account rigorously for three forces acting on a small dust particle: gravity of the nucleus F_N, gravity of the Sun F_g, and the solar-radiation pressure F_{pr}. Within this approach, a dust particle is placed at the surface of the Leonard nucleus whose location with regard to the Sun is described in terms of the position vector $\mathbf{S}_0$. At the initial time $t_0 = 0$, the particle acquires an initial velocity $\mathbf{V}_0$ that is set to be 20% of the gas-expansion velocity [7] at given heliocentric distance r_h and oriented along the normal from the surface. At this initial moment in time, we calculate the resultant of all three forces acting on the dust particle. Over the increment of time Δt, the resultant force is assumed to remain constant, implying also a constant acceleration of the dust particle $\mathbf{a}_0$. At the end of this increment, we update all three forces and their resultant for the current location of the particle and repeat the entire procedure. Clearly, at $\Delta t \to 0$, the model trajectory should converge to its exact profile. In practice, $\Delta t = 1$ s provides sufficient accuracy in determining orbits of ejected dust particles. It also is worth noting that this code has been exploited in the analysis of astronomical observations of several comets [7, 8].

RESULT AND DISCUSSION:
We apply our model to Comet Leonard on two epochs, October 7 and December 4 of 2021. In former case, the comet was located at a heliocentric distance $r_h = 1.757$ au and it appeared in ground-based observations at phase

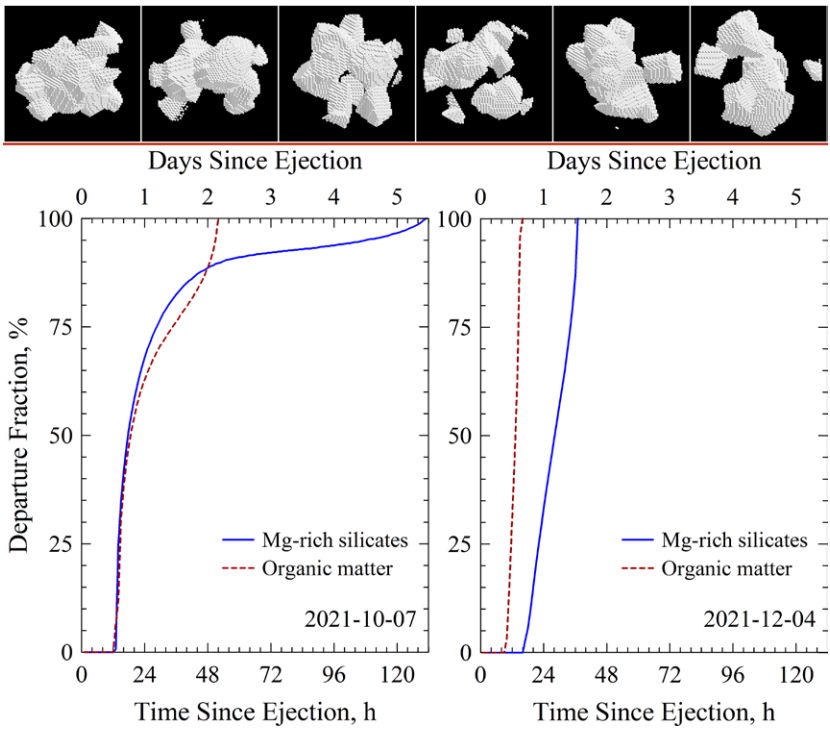

Fig. 1. On top: Six examples of agglomerated debris particles. On bottom: Fraction of particles departing from the aperture ρ = 6000 km in ground-based observations of Comet Leonard as of October 7, 2021 (left) and December 4, 2021 (right), which is shown as a function of time since their isotropic ejection from the nucleus. Blue solid line shows results for agglomerated debris particles having Mg-rich silicate composition (m = 1.6 + 0.0005i) and radius r = 1 μm, whose parameter β = 0.349. Dark-red dash line shows results for organic-matter particles (m = 1.855 + 0.45i) with r = 1 μm and β = 1.188

angle α = 24.8°; whereas, in the latter case, it was observed at r_h = 0.875 au and α = 94.4°. The velocity of the expanding gas in a cometary coma is determined by the equation: V_{gas} = (850 m/s)/sqrt(r_h) [9]. In application to Comet Leonard, it yields V_{gas} = 641.3 m/s for October 7 and V_{gas} = 908.5 m/s for December 4. Taking into account ~20 % efficiency of the momentum transfer from the expanding gas to dust, we constrain the terminal velocity of particles to be 128.3 m/s and 181.7 m/s, respectively. Since the light-scattering response in comets is governed by micron-sized particles [10], we attribute these terminal velocities to particles with radius r = 1 μm.

The effect of solar-radiation pressure on the motion of dust particles throughout the Solar System is characterized with the parameter β = F_{pr}/F_{gr} (e.g., [3]). We adapt from [3] values of the β parameter for the agglomerated debris particles having refractive indices m = 1.6 + 0.0005i and 1.855 + 0.45i. At r = 1 μm, β = 0.349 and 1.188, respectively.

There is a lack of information on the nucleus of Comet Leonard and, therefore, we put forth an assumption that it has a spherical shape with radius of 500 m, and the bulk material density is 0.6 g/cm^3. We suggest that the emanation of dust happens only from the hemisphere illuminated by the solar radiation.

Under these circumstances, we compute the fraction of dust particles released from the nucleus of Comet Leonard, which managed to leave the circular aperture having radius ρ = 6000 km (similar to what is utilized in [1]) as a function of time since their ejection. Results are shown on the bottom in Fig. 1. Here, the left panel corresponds to ejection on October 7, 2021, and the right panel on December 4, 2021. The blue solid line shows results for the

Mg-rich silicate particles with β = 0.349 and the dark-red dashed line for the organic-matter particles with β = 1.188.

As one can see, on October 7, no particle was capable of leaving the field of view during the first 12 hours. However, over the next 12 hours, up to 2/3 of all ejected particles appear already beyond the circular aperture. There is some difference here between the Mg-rich silicate particles and the organic-matter particles. This is because the effect of solar-radiation pressure is slowly accumulated at long heliocentric distances. However, at the short heliocentric distance such as on December 4, 2021, the particles move much faster. The organic-matter particles require only 16 hours in order to depart from the circular aperture. Due to a factor 3.4 smaller value of the β parameter, the Mg-rich silicate particles need a longer time (37 hours) to fully leave the aperture. Thus, it seems plausible that day-to-day variations of the polarization in Comet Leonard observed in December 2021, were caused by discontinuous emanation of the carbonaceous particles from the nucleus.

REFERENCES:

[1] Zheltobryukhov M., Zubko E., Chornaya E. et al. Microphysics of dust in Comet C/2021 A1 (Leonard) inferred by means of polarimetry // 13th Moscow Solar System Symp. 13M-S3. 2022.
[2] Fomenkova M.N., Kerridge J.F., Marti K., McFadden L.-A. Compositional trends in rock-forming elements of comet Halley dust // Science. 1992. V. 258. P. 266-269.
[3] Zubko E., Videen G., Hines D.C. et al. Comet C/2012 S1 (ISON) coma composition at ~4 au from HST observations // Planet. Space Sci. 2015. V. 118. P. 138-163.
[4] Zubko E., Videen G., Hines D.C., Shkuratov Yu. The positive-polarization of cometary comae // Planet. Space Sci. 2016. V. 123. P. 63-76.
[5] Chornaya E., Zubko E., Luk'yanyk I. et al. Imaging polarimetry and photometry of comet 21P/Giacobini–Zinner // Icarus. 2020. V. 337. Art. No. 113471.
[6] Kochergin A., Zubko E., Chornaya E. et al. Monitoring the negative polarization in Comet 29P/Schwassmann–Wachmann during quiescence // Icarus. 2021. V. 366. Art. No. 114536.
[7] Kochergin A., Zubko E., Husárik M. et al. Velocity of Dust Ejected from Interstellar Comet 2I/Borisov // Research Notes of the AAS. 2019. V. 3. Art.. No. 152.
[8] Luk'yanyk I., Zubko E., Husárik M. et al. Rapid variations of dust colour in Comet 41P/Tuttle-Giacobini-Kresák // Mon. Not. Roy. Astron. Soc. 2019. V. 485. P. 4013-4023.
[9] Budzien S.A., Festou M.C., Feldman P.D. Solar flux variability and the lifetimes of cometary H2O and OH // Icarus. 1994. V. 107. P. 164-188.
[10] Zubko E., Videen G., Arnold J.A. et al. On the small contribution of supermicron dust particles to light scattering by comets // Astrophys. J. 2020. V. 895. Art. No. 110.

MICROPHYSICS OF DUST IN COMET C/2021 A1 (LEONARD) INFERRED BY MEANS OF POLARIMETRY

M. Zheltobryukhov[1], E. Zubko[2], E. Chornaya[1], A. Kochergin[1], G. Kornienko[1], G. Videen[2,3]

[1] *Institute of Applied Astronomy RAS, Saint Petersburg, Russia; maxim.s.zheltobryukhov@gmail.com*

[2] *Humanitas College, Kyung Hee University, South Korea*

[3] *Space Science Institute, Boulder, USA*

KEYWORDS:
comet C/2021 A1 (Leonard), observation, polarimetry, dust

INTRODUCTION:

Comet C/2021 A1 (Leonard) (hereafter Comet Leonard) is a long-period comet discovered on January 3, 2021. One year later, on January 3, 2022, the comet passed perihelion at r_h = 0.615 au. In November-December of 2021, the comet approached Earth, passing by at only Δ = 0.234 au on December 13, 2021, and making possible its observations at large phase angles α. We conducted a polarimetric survey of Comet Leonard aimed at studying its maximum of linear polarization P_{max}. This light-scattering characteristic is long utilized for classification of comets [1]. It is significant that P_{max} in comets is immediately interrelated with the volume ratio of Mg-rich silicates and carbonaceous materials in dust population of their coma [2] and, hence, one can retrieve chemical composition in the Leonard coma.

OBSERVATION AND DATA REDUCTION:

We observed Comet Leonard on 14 epochs between October 7 and December 7, 2021. The observations were conducted using the *RC500* telescope (*D* = 0.5 m, *F* = 4 m) located at the Ussuriysk Astrophysical Observatory, a division of the Institute of Applied Astronomy of Russian Academy of Science (code C15). The telescope was equipped with CMOS detector *ZWO ASI 6200 pro* (resolution – 9576×6388, size of pixel – 3.76 μm) exploited in the 2×2 binning mode, the *R* filter of the *Bessell photometric system* (λ_{eff} = 0.64 μm, FWHM = 0.16 μm) and a dichroic polarization filter (analyzer). The analyzer was rotating through three position angles evenly distributed around the optical axis, allowing us to calculate the degree of linear polarization (e.g., [3]): $P = (F_\perp - F_{||})/(F_\perp + F_{||})$, where $F_\perp$ and $F_{||}$ stand for flux of the scattered sunlight that is polarized perpendicular to the scattering plane and within that plane, respectively.

At each analyzer position, we take a short exposure (from 20 to 60 s, depending on the epoch). These measurements were repeated for 8–25 complete cycles of the analyzer rotations. Each image was later processed with the *Image Reduction and Analysis Facility* (IRAF) software, including bias subtraction, removal of cosmic-ray events, and flat-field correction. Within a circular aperture having radius ρ = 6000 km centered at the photometric center of Comet Leonard, we compute the average value of the degree of linear polarization, its standard deviation and standard deviation of the mean for each epoch.

Dark red points in Fig. 1 show the average values of the degree of linear polarization in Comet Leonard, and the error bars here correspond to their standard deviation of the mean. It is worth noting that a large number of cycles of polarimetric measurements significantly increases reliability of the results, as the standard deviation of the mean in our observations does not exceed 0.5 %.

RESULT AND DISCUSSION:

As one can see on the bottom in Fig. 1, the polarization of Comet Leonard reveals a strong dependence on phase angle α that is similar to what was found in other comets. In particular, in Fig. 1 we also show the phase dependence of the degree of linear polarization measured in red light in three other comets:

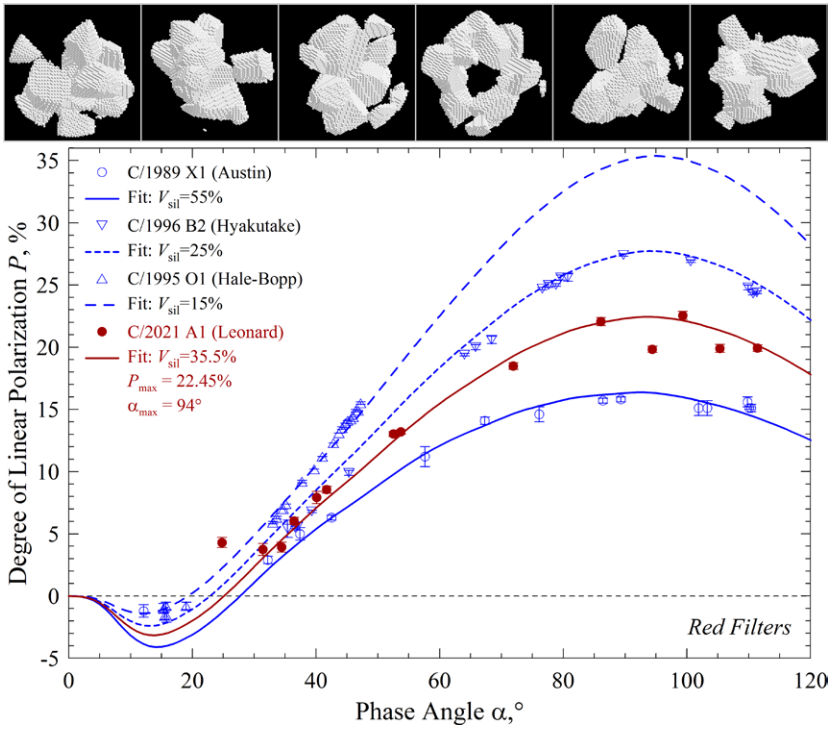

Fig. 1. Aperture-averaged degree of linear polarization as a function of the phase angle α in four different comets. Dark red dots show results of our observations of Comet Leonard with the aperture ρ = 6000 km; other symbols correspond to data adapted from the literature

C/1989 X1 (Austin), C/1995 O1 (Hale-Bopp), and C/1996 B2 (Hyakutake); these data are adapted from [4]. Near opposition, α < 30°, comets tend to reveal the phenomenon of the negative polarization, $P < 0$ (i.e., $F_{\perp} < F_{||}$); whereas, at larger phase angles, the degree of linear polarization P acquires a positive sign (i.e., $F_{\perp} > F_{||}$). Furthermore, P monotonically grows with increasing α until it achieves its maximum value P_{max} located at α_{max} = 80–100°.

What also emerges from Fig. 1 is that comets may reveal noticeable difference in their P_{max}. For instance, Comet Leonard can be unambiguously discriminated from the three other comets shown by their P_{max}. This clearly indicates difference in the microphysics of dust emanated from comets.

As demonstrated in [2], the phase dependence of polarization observed in a comet is necessarily produced by a mixture of weakly absorbing particles whose imaginary part of refractive index Im(m) does not exceed 0.02 and of highly absorbing particles with Im(m) > 0.3. The former case is compliant with Mg-rich silicates; whereas, the later one with carbonaceous materials, such as organics and/or amorphous carbon (see, discussion in [2]). Then, the dispersion of P_{max} in comets can be explained by different volume fractions of the Mg-rich silicate particles V_{sil} and of the carbonaceous particles V_{car} = 100 % – V_{sil} in their comae. This is the simplest approach that is capable of simultaneous quantitative fitting of polarization in comets with various P_{max}, using a sole free parameter, V_{sil}. The simplicity is largely caused by a highly realistic approach to modeling the shape of cometary dust, which is simulated with the *agglomerated debris particles* [2]. Six examples of these model particles are shown on top in Fig. 1. It is worth noting, however, that numerical simulations of polarization in comets involve a minimum 500 randomly generated samples of the agglomerated debris particles.

We apply the model developed in [2] to analyze our polarimetric observations of Comet Leonard. We consider a mixture of Mg-rich silicate with m = 1.6 + 0.0005i and refractory organics with m = 1.855 + 0.45i. The radius of

particles of both chemical compositions spans the range from 0.1 to 3.26 μm, which is known to dominate the light-scattering response, including polarization [5]. The response is averaged over available sizes with a power-law size distribution $r^{-2.5}$. These model parameters were chosen to be compliant with *in situ* finding in comets; see [2] for more details.

These parameters provide fits of the model to the angular profiles of polarization in all four comets considered in Fig. 1 (see solid and dashed lines). For instance, polarization in Comet C/1995 O1 (Hale-Bopp) is reproduced at the relative abundance of the Mg-rich silicate particles V_{sil} = 15 % (correspondingly, V_{car} = 85 %); in C/1996 B2 (Hyakutake) at V_{sil} = 25 %; whereas, in C/1989 X1 (Austin) at V_{sil} = 55%. When the same two-component mixture is applied to Comet Leonard, it yields a best fit (within 3σ) to 11 out of 14 data points at V_{sil} = 35.5 %; see dark-red solid line in Fig. 1. Thus, our modeling not only constrains the chemical composition of dust in the Leonard coma, but also reveals its relative stability over the course of our observations.

On the other hand, polarization measured in Comet Leonard on 3 out of 14 epochs obviously deviate from the modeling curve, suggesting different microphysics of its dust. For instance, excess of positive polarization at the smallest phase angle can be reproduced by the model at V_{sil} = 0.07; whereas, two points below the modeling curve at = 94.4° and 105.3° can be fitted at V_{sil} = 0.41. Therefore, the chemical composition of dust in Comet Leonard likely was subject to some temporal variation. This phenomenon was previously seen in other comets [3, 6]. It is worth noting, however, that other comets may reveal high temporal stability in their dust [7, 8].

Finally, unlike the sparse set of observational data, the numerical simulations allow us to characterize better the polarization maximum in Comet Leonard: $P_{max} \approx 22.5$ % occurred at $\alpha_{max} \approx 94°$.

REFERENCES:

[1] Levasseur-Regourd A.C., Hadamcik E., Renard J.B. Evidence for two classes of comets from their polarimetric properties at large phase angles // Astron. Astrophys. 1996. V. 313. P. 327-333.
[2] Zubko E., Videen G., Hines D.C., Shkuratov Yu. The positive-polarization of cometary comae // Planet. Space Sci. 2016. V. 123. P. 63-76.
[3] Chornaya E., Zubko E., Luk'yanyk I. et al. Imaging polarimetry and photometry of comet 21P/Giacobini Zinner // Icarus. 2020. V. 337. Art. No. 113471.
[4] Kikuchi S. Linear polarimetry of five comets // J. Quant. Spectrosc. Radiat. Transfer. 2006. V. 100. P. 179-186.
[5] Zubko E., Videen G., Arnold J.A., et al. On the small contribution of supermicron dust particles to light scattering by comets // Astrophys. J. 2020. V. 895. Art. ID: 110.
[6] Zubko E., Zheltobryukhov, M., Chornaya, E., et al. Polarization of disintegrating Comet C/2019 Y4 (Atlas) // Mon. Not. Roy. Astron. Soc. 2020. V. 497. P. 1536-1542.
[7] Zheltobryukhov M., Zubko E., Chornaya E., et al. Monitoring polarization in comet 46P/Wirtanen // Mon. Not. Roy. Astron. Soc. 2020. V. 498. P. 1814-1825.
[8] Kochergin A., Zubko E., Chornaya E., et al. Monitoring the negative polarization in Comet 29P/Schwassmann–Wachmann during quiescence // Icarus. 2021. V. 366. Art. ID: 114536.

ON THE CONJECTURE OF FORMATION OF THE MARTIAN MOONS PHOBOS AND DEIMOS

T.B. Salnikova[1], E.I. Kugushev[1], A.P. Pestrikov[1]
[1] *Lomonosov Moscow State University, Moscow, Russia; tatiana.salnikova@gmail.com*

KEYWORDS:
irregularly shaped satellites, interception of the cosmic masses, planar parabolic (hyperbolic) three-body problem

INTRODUCTION:
Fundamental scientific problems are the problems of the formation and evolution of Solar system and other star systems, dynamics, evolution and control of planetary satellite systems of natural and artificial origin, asteroid hazard to the Earth, with ensuring the safety of flights into space due to the presence of clouds of artificial debris in near-Earth orbits.

Among the natural satellites of the planets of the Solar system, two groups can be distinguished: the first, the largest in composition, are satellites of approximately spherical shape, the second, relatively small, are irregularly shaped satellites that can be considered as fragments of large bodies. We consider a possible mechanism for the formation of satellites of the second group. Let us assume that during the evolution of the Solar System a compact family of debris bodies was formed, consisting of a massive large body and several small debris bodies moving in its gravitational field. With a fairly close flyby of a planet, a situation is possible when one or more fragments leave the sphere of gravitational influence of a massive body and move into orbits around the planet, that is, become its satellites. We will call this phenomenon satellite interception.

PROBLEM SETTING:
We consider the possibility of capturing space objects into near-planetary space and further movement of these objects and suggest a mathematical model for the formation of non-spherical (Phobos-type) satellites of the planets. The model justify our hypothesis for the emergence of such planetary satellites. In our study, we are talking about the possible capture of cosmic masses in the framework of the plane hyperbolic three-body problem, as well as the plane parabolic three-body problem.

The results of numerical simulation within the framework of the planar restricted hyperbolic three-body problem are shown.

ELECTROSTATICALLY PRODUCED DUSTY PLASMAS NEAR THE SURFACE OF MERCURY

S.I. Popel[1], A.P. Golub'[1], L.M. Zelenyi[1]
[1] *Space Research Institute, Moscow, Russia; popel@iki.rssi.ru*

KEYWORDS:
Mercury, dusty plasmas, electrostatic processes, exosphere, future space missions, production mechanisms of the exosphere

ABSTRACT:
In spite of difficulties to obtain a satellite orbit around Mercury, there were the space missions Mariner-10 and MESSENGER which have performed some studies of Mercury. Furthermore, the European Space Agency and Japan Aerospace Exploration Agency prepared the BepiColombo mission which was successfully launched on October 20, 2018. One of the purposes of this mission is to study production mechanisms of the exosphere of Mercury. In Russia the mission Mercury-P including lander is proposed. The purpose of this work is to discuss properties of dusty plasmas near the surface of Mercury.

The illuminated surface of Mercury becomes charged as a result of the action of the solar radiation and solar wind plasma. The surface of Mercury emits electrons upon interaction with the solar wind due to the photoelectric effect, which leads to the formation of a layer of photoelectrons above the surface. Photoelectrons are also emitted from the dust particles soaring above the surface of Mercury due to the interaction of the latter with the electromagnetic radiation of the Sun. Dust particles on the surface of Mercury or in the near-surface layer absorb photoelectrons, photons of solar radiation as well as electrons and ions of the solar wind. All these processes lead to the charging of the dust particles, their interaction with the charged surface of Mercury, their liftoff, and their motion.

The distribution of dust and electrons in the near-surface layer of the illuminated part of Mercury can be calculated based on the theoretical model developed for the Moon [1, 2] that describes the dynamics of noninteracting dust particles. A significant difference between the approach applied to the Moon and that developed for Mercury is the necessity to take into account Mercury's orbital eccentricity which is the largest of all known planets in the Solar System: at perihelion, Mercury's distance from the Sun is only about two-thirds (or 66 %) of its distance at aphelion. Correspondingly, properties of dusty plasmas at Mercury differ for perihelion and aphelion. The calculations of distribution functions of photoelectrons and altitude-distributions characterizing dusty plasmas under conditions of perihelion and aphelion are performed. The contribution of dusty plasmas to the exosphere of Mercury is discussed.

ACKNOWLEDGEMENTS:
This work was supported in part by Theoretical Physics and Mathematics Advancement Foundation "BASIS" (grant "Leader").

REFERENCES:
[1] Popel S.I., Kopnin S.I., Golub' A.P. et al. Dusty plasma at the surface of the Moon // Solar Syst. Res. 2013. V. 47. No. 6. P. 419-429.
[2] Popel S.I., Golub' A.P., Zelenyi L.M., Dubinskii A.Yu. Lunar dust and dusty plasmas: Recent developments, advances, and unsolved problems // Planet. Space Sci. 2018. V. 156. P. 71-84.

ROLE OF MAGNETISM IN THE SEPARATION OF THE PARTICLES OF THE SATURN'S RINGS

V.V. Tchernyi[1], S.V. Kapranov[2]
[1] *Modern Science Institute, Science and International Business Research, Moscow, Russia; chernyv@bk.ru*
[2] *A.O. Kovalevsky Institute of Biology of the Southern Seas, RAS, Sevastopol, Russia; sergey.v.kapranov@yandex.ru*

KEYWORDS:
Saturn's rings, origin of Saturn's rings, magnetism of Saturn's rings, separation of the particles in the rings

Several theories that have been developed to date to explain the evolution and stability of Saturn's rings postulate that the orbits of the ring particles are close to the equatorial plane of the planet, but none of these approaches consistently explains this peculiarity and separation of the rings particles [1]. There are few known models of the origin of Saturn rings: a moon of the planet could have been disrupted by a passing celestial body; the rings could have been generated by the particles separated from moons of the outer planets by collision with comets or meteorites; the ring particles can be debris of a large comet tidally broken by the planet; the rings can be the relic of a protosatellite disk; the particles can be continuously forming as a result of volcanic activity on a moon of the Saturn. But none has provided a convincing explanation for rings observed peculiarities among Solar System bodies [2]. Cassini measured that the particles of rings mostly consists of water ice, 93 % [3] and 90 to 95 % [4] Also Cassini found the ratio of deuterium and hydrogen isotopes for the ice of Saturn's rings is the same as for the Earth's ice [5]. This fact indicates the similarity of ice in the rings and Earth's ice. There are 20 known types of the Earth's ice. We can choose ice XI [6], which is suitable for the environment of Saturn's rings. It has stable parameters below 73 K and is diamagnetic [7]. Taking into account these facts, we found a solution to the problem of the interaction of the gravitational field and the magnetic field of Saturn with the ice particles of the protoplanetary cloud [8]. An interesting fact is taking into account the magnetic field of Saturn explains the transformation of a protoplanetary cloud into a disk of rings as well as it accounts for strong planar structure of rings located at the magnetic equator of Saturn which is almost coincide with geographical one. Then it became clear that Saturn can create rings from the ice particles of the protoplanetary cloud with its own magnetic field due to the action of an additional third force of diamagnetic expulsion and the mechanism of magnetic anisotropic accretion [9]. An interesting fact is that under the influence of the planet, the particles of the rings remain separated, while the particles themselves try to stick together using their own gravity [10]. In this presentation we discuss how Saturn's magnetic field can contribute to the separation of particles of the rings even under the influence of periodically changing gravity of Saturn.

REFERENCES:

[1] Porco C. Cassini at Saturn // Scientific American. 2017. V. 317. P. 78-85.
[2] Crida A., Charnoz S. Solar system: Recipe for making Saturn's rings // Nature. 2010. V. 468. P. 903-905.
[3] Poulet F., Cuzzi J.N. The Composition of Saturn's Rings // Icarus. 2002. V. 160. Iss. 2. P. 350-358.
[4] Cuzzi J.N. et al. An Evolving View of Saturn's Dynamic Rings // Science. 2010. V. 327. Art. No. 5972. P. 1470-1475.
[5] Clark R.N., Brown R.H., Cruikshank D.P., Swayze G.A. Isotopic ratios of Saturn's rings and satellites: Implications for the origin of water and Phoebe // Icarus. 2019. V. 321. P. 791-802.
[6] Hemley R.J. Effects of High Pressure on Molecules // Annual Review of Physical Chemistry. 2000. V. 51. P. 763-800.

[7] Tchernyi V.V., Kapranov S.V. To the Problem of the Properties of Saturn's Rings' Ice // Research Notes of the American Astronomical Societ. 2021. V. 5. No. 10. Art. No. 255.
[8] Tchernyi V.V., Kapranov S.V. Contribution of Magnetism to the Origin of Saturn's Rings // The Astrophysical J. 2020. V. 894. No. 1. Art. No. 62.
[9] Tchernyi V.V., Kapranov S.V. How Saturn could create rings by itself. The third force of diamagnetic expulsion and the mechanism of the magnetic anisotropic accretion of the origin of Saturn's rings. 2021. 9 p. arxiv.org/abs/2104.03967.
[10] Tchernyi V.V., Kapranov S.V. The role of diamagnetism in the separation of particles and sharp edges of the Saturn's ring. 2022. 5 p. arxiv.org/abs/2204.03414.

DUSTY CLOUDS EVOLUTION IN THE MARTIAN ATMOSPHERE

Yu.S. Reznichenko[1,2], A.Yu. Dubinskii[1], S.I. Popel[1]
[1] *Space Research Institute, Moscow, Russia; nfkpb@bk.ru*
[2] *Moscow Institute of Physics and Technology, Dolgoprudny, Moscow Region, Russia; dvju@yandex.ru*

KEYWORDS:
dusty plasmas, dust structures, dust particles, electrons, ions, Martian ionosphere, charging processes

Nowadays there is a high interest in Mars exploration. Such spacecraft as Mars Express, ExoMars Trace Gas Orbiter, etc, operate successfully. In March of 2021, the rover Mars Science Laboratory Curiosity recently took photos of dusty clouds in the Martian atmosphere. These clouds, presumably, consist of solid carbon dioxide particles and are located at altitudes more than 60 km. They are similar to the noctilucent clouds (NLC) of the ionosphere of the Earth. Therefore, investigation of the Martian atmosphere is rather challenging and, furthermore, adapting Earth's theoretical models to the Martian conditions can be very effective and productive.

We perform a self-consistent model of dusty plasmas in the Martian ionosphere in our work. This model is based on theoretical models from [1–5] and is supported with comprehensive experimental data from [6–8]. We investigate formation and evolution processes of dusty plasma clouds as well as pay more attention on condensation processes near the condensation zone boundary. The solid carbon dioxide particles initially located at the upper part of the condensation zone (the zone where carbon dioxide vapor is supersaturated), gather (on their surfaces) the vast majority of carbon dioxide. Particles of different dusty layers absorb different amounts of carbon dioxide molecules. This results in a possibility of layer mixing and dusty clouds formation. The average sedimentation time is of about 400–600 seconds. All dust particles in the cloud reach sizes of about 0,3–3,5 micrometers. Our theoretical results are in agreement with the data of observations.

We also explore temporal variations of electron and ion number densities in cases of presence and absence of photoelectric effect as well as calculate the typical values of dust particle charges. Under the night conditions dust grains acquire negative charge and the electron and ion number densities decrease. Under the day conditions (in case of metal impurities in dust particles) dust grains acquire positive charge. The electron number density in this case increases because of photoelectron current appearance, the ion number density as before decreases.

ACKNOWLEDGEMENTS:
This work was supported in part by the Theoretical Physics and Mathematics Advancement Foundation "BASIS" (Grant "Leader").

REFERENCES:
[1] Reznichenko Yu.S., Dubinskii A.Yu., Popel S.I. On dusty plasma formation in Martian ionosphere // J. Physics: Conference Series. 2020. V. 1556. Art. No. 012072.
[2] Reznichenko Yu.S., Dubinskii A.Yu., Popel S.I. Formation and Evolution of Dusty Plasma Structures in the Ionospheres of the Earth and Mars // Plasma Physics Reports. 2019. V. 45. Art. No. 928.
[3] Klumov B.A., Morfill G.E., Popel S.I. Formation of structures in a dusty ionosphere // J. Experimental and Theoretical Physics. 2005. V. 100. P. 152-164.
[4] Klumov B.A., Popel S.I., Bingham R. Dust particle charging and formation of dust structures in the upper atmosphere // J. Experimental and Theoretical Physics Letters. 2000. V. 72. P. 364-368.
[5] Dubinskii A.Yu., Popel S.I. Formation and evolution of dusty plasma structures in the ionosphere // J. Experimental and Theoretical Physics Letters. 2012. V. 96. P. 21-26.

[6] Forget F. et al. Density and temperatures of the upper Martian atmosphere measured by stellar occultations with Mars Express SPICAM // J. Geophys. Res. 2009. V. 114. Art. No. E01004.
[7] Bertaux J.-L. et al. SPICAM on Mars Express: Observing modes and overview of UV Spectrometer data and scientific Results // J. Geophys. Res. 2006. V. 111. Art. No. E10S90.
[8] Delgado-Bonal A., Zorzano M.-P., Martín-Torres F.J. Martian Top of the Atmosphere 10-420 nm spectral irradiance database and forecast for solar cycle 24 // Solar Energy. 2016. V. 134. P. 228-235.

HYPERION (C7) CARTOGRAPHY: CHALLENGES AND THE FIRST SURFACE MAP

I.E. Nadezhdina[1], A.E. Zubarev[1], N.A. Slodarzh[1], N.A. Kozlova[1], M.A. Chuikin[1]

[1] *Moscow State University of Geodesy and Cartography, Extraterrestrial Laboratory, Moscow, Russia; lorencs@mail.ru*

KEYWORDS:
Saturnian satellite, Hyperion, Hyperion mosaic, mapping, shape, Hyperion coordinate system, body frame, Hyperion principal axis, orthomosaic

INTRODUCTION:
Based on the images obtained during the Cassini mission, the first map of the seventh satellite of Saturn, Hyperion, was created at the MIIGAiK MExLab. Hyperion is the largest non-spherical satellite with chaotic rotation [1, 2]. Thus, there are difficulties with not only the data processing, but also with defining the coordinate system of the body.

IMAGE DATA:
On the basis of the reference network (3d control point network) and DEM [3, 4], a global orthomosaic was created, including 43 images obtained by the Cassini narrow-angle camera (NAC) in the period from 2005 to 2016, with a resolution from 23 to 3 km. The orthorectification of the original images was performed with respect to the sphere of R 136.1 km [4] in the SpaceMosaic software (special MIIGAiK software). Global mosaic of Hyperion was created in the PHOTOMOD GeoMosaic software [5]. Next, in the ArcGIS software, the mosaic was transformed into a Mercator projection. The polar caps are given separately in the polar stereographic projection. 4 craters were mapped according to the IAU gazetteer [6]. Additionally, a hypsometric map with hillshade is shown.

CONCLUSIONS AND DISCUSSION:
There are two main problems in mapping bodies in a state of chaotic rotation:

1. Data processing: standard algorithms for creating reference networks cannot be used for such cases, the lack of initial conditions, the complexity of measurements and the subsequent creation of a basis for orthorectification and mapping;
2. Axis orientation and the position of the origin of the coordinate system (body frame) uncertainty for mapping.

In this paper, mapping is performed on the basis of a new model of the Hyperion figure [3], where the **X**, **Y**, **Z** axes coincide with the axes of the triaxial ellipsoid **a**, **b**, **c**, where **a** > **b** > **c**, and its center is placed in the center of the triaxial spheroid that best describes the body shape [4]. The plane containing the **a, c** axes defines the initial meridian plane, the plane containing the **a** and **b** axes is the "equator plane". The intersection points of the planes have coordinates (0°, 0°) and (0°, 180°). Here we can state several points of discussion:

1. According to [7], for small satellites of planets that are in chaotic rotation, the major semiaxis a is predominantly directed towards the planet. However, whether this condition is satisfied here or not, we do not know. Longitude 0 is taken as the direction of the **a** axis in the "longest" flyby of the Cassini spacecraft (OBSERVATION_ID = ISS_015HY).
2. The coordinates of the craters do not match with those given in the gazetteer. This is due to the issues of orientation of the body, there is no fixed position of the axes.
3. The Cassini mission allowed us to obtain many images that give a better idea of relief structures on the surface of the body. At the same time, no new names have been assigned to the relief forms since 1982. The new global DEM [3, 4] and orthomosaics will make it possible to better study the surface of the body and make suggestions for naming objects. However, the issue with establishing the coordinate system and its orientation remains open.

Гиперион

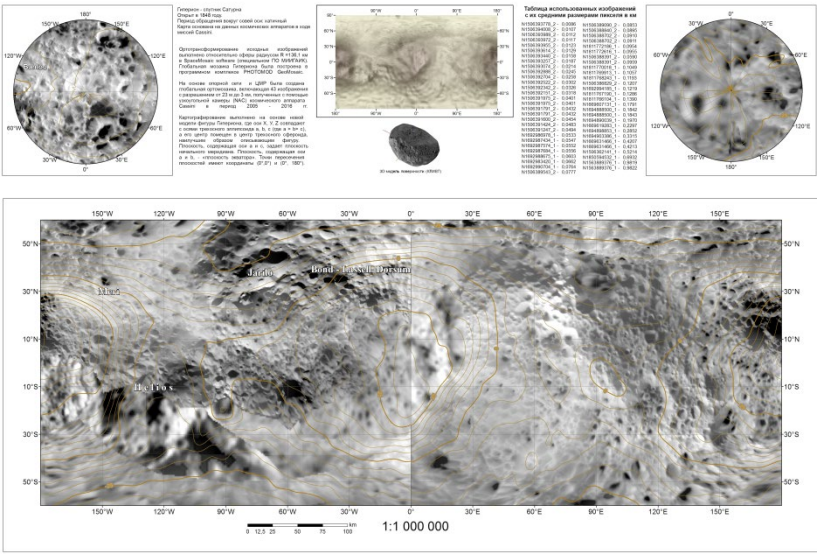

REFERENCES:

[1] Tarnopolski M. Rotation of an oblate satellite: Chaos control // Astronomy and Astrophysics. 2017. V. 606. Iss. A43. DOI: 10.1051/0004-6361/201731167.
[2] Wisdom J., Peale S.J., Mignard F. The chaotic rotation of Hyperion // Icarus. 1984. V. 58. No. 2. Art. No. 137. DOI: 10.1016/0019-1035(84)90032-0.
[3] Slodarzh N.A., Zubarev A.E., Nadezhdina I.E., Kozlova N.A. Hyperion (C7): control point network and shape model. Difficulties and solutions // 13MS3, 2022.
[4] Nadezhdina I.E., Konopikhin A.A. Prospects for an integrated approach to the study of the dynamics of the chaotic rotation of small celestial bodies // Izvestia vuzov. Geodesy and Aerophotosurveying. 2022. V. 66. No. 2. (In press. In Russian.)
[5] https://en.racurs.ru/program-products/photomod-geomosaic/.
[6] https://planetarynames.wr.usgs.gov/SearchResults?Target=75_Hyperion&Feature%20Type=9_Crater,%20craters.
[7] Mel'nikov A.V. Orientation of figures of small planetary satellites during chaotic rotation // Solar System Research. 2020. V. 54. No. 5. P. 432-441.

PROBABILITIES OF COLLISIONS OF BODIES EJECTED FROM THE EARTH WITH THE TERRESTRIAL PLANETS AND THE MOON

S.I. Ipatov[1]
[1] *Vernadsky Institute of Geochemistry and Analytical Chemistry RAS, Moscow, Russia; siipatov@hotmail.com*

KEYWORDS:
Motion of bodies, ejection of bodies from the Earth and the Moon, probabilities of collisions, planets, Moon

INTRODUCTION AND INITIAL MODEL:

The motion of bodies ejected from the Earth at collisions of bodies-impactors with the Earth was studied in [1, 2] during time interval equal to 30 Kyr. Considered initial velocities were perpendicular to the surface of the Earth. Mass m_{ej} of ejected material is smaller at greater velocity v_{esc} of ejection. According to [3], m_{ej} is proportional to $v_{esc}^{1.65}$. Therefore, more material leaves the Earth with smaller velocities (but greater than the parabolic velocity equaled to 11.2 km/s). Integrating $v_{esc}^{-1.65}$ one gets $v_{esc}^{-0.65}$. Considering $11.22^{-0.65} - x^{-0.65} = x^{-0.65} - 18^{-0.65}$, one can get $x \approx 14$ km/s. So, it is needed to consider not only velocities very close to the parabolic velocity. According to [4], the values of ejection angle i_{ej} are mainly between 20 and 55°, especially between 40 and 50°. In my calculations, the motion of bodies ejected from the Earth was studied during the dynamical lifetime T_{end} of all bodies, which was about 200–350 Myr. Such ejection was often at the stage of accumulation of the Earth. During this time interval, all bodies collided with planets or the Sun or were ejected into hyperbolic orbits. In each calculation variant, the motion of 250 bodies ejected from the Earth was studied for the fixed values of an ejection angle i_{ej} (measured from the surface plane or from other parallel plane, perpendicular to the direction from the Sun to the Earth), a velocity v_{esc} of ejection, and a time step t_s of integration. The gravitational influence of the Sun and all eight planets was taken into account. Bodies that collided with planets or the Sun or reached 2000 AU from the Sun were excluded from integration. The symplectic code from the SWIFT integration package [5] was used for integration of the motion equations. The considered time step t_s equaled to 1, 2, 5, or 10 days, and the results of calculations with different t_s were compared. For this code, a time step of integration is reducing considerably at a distance less than 3.5 Hill radii. The probabilities of collisions of bodies with the Moon were calculated based on the arrays of orbital elements of migrated bodies (stored with a step of 500 years) similar to [6–9].

In series *vf*, the motion of bodies started from the height *h* from the point of Earth's surface located most far from the Sun in the direction from the Sun to the Earth. In series *vc*, the motion of bodies started from the height *h* from the point of Earth's surface located most close to the Sun in the direction from the Earth to the Sun. In most calculations, $h = 0$, i.e. bodies started directly from the Earth. Also, some calculations were made at $h = 10$ and $h = 100$ km. There were also calculations at $h = 38500$ km $= 60r_E$, where r_E is the radius of the Earth, and $60r_E$ is the semi-major axis of the orbit of the Moon. Such calculations correspond to the motion of bodies ejected from the Moon, though the gravitational influence of the Moon and its motion about the Earth were not taken into account. In this case, real velocities of ejection of bodies from the Moon differed a little from those used in calculations. The calculations at $h = 37r_E$ correspond to the case when the Moon have not yet reached its present orbit. By mistake, results for $h = 37r_E$ were presented in some my earlier abstracts as those for bodies ejected from the Earth. In different variants, the values of i_{ej} equaled to 30, 45, 60, and 90°. v_{esc} equaled to 11.22, 11.5, 12, 12.7 or 16.4 km/s. At $h = 60r_E$, calculations

were made also for v_{esc} equal to 2.5 and 5 km/s. For the Moon, the escape velocity is 2.38 km/s. The probabilities p_E of collisions of bodies with the Earth were about the same for calculations with different t_s. For some values of i_{ej} and v_{esc}, the probabilities of collisions of bodies with Venus, Mercury, and the Sun were about the same for calculations with different t_s. For some other variants, the probabilities could differ a little for different t_s, but there was no a tendency for the probabilities of been greater or smaller at smaller t_s.

PROBABILITIES OF COLLISIONS OF BODIES WITH THE EARTH:

The values of the fraction p_E of bodies collided with the Earth were typically greater by a factor up to 2 (for $h = 0$) and by a factor up to 3 (for $h \geq 37r_E$) at $T = 100$ Myr and at $T = T_{end}$, than at $T = 10$ Myr. This factor is typically greater for greater v_{esc}. The ratio of the probability of collisions of bodies with the Earth to the probabilities of collisions of bodies with other planets and the Sun typically decreased with time. In series *vc*, the values of p_E could be equal or greater or smaller (by a factor less than 1.7) than for series *vf*, but on average for various variants of calculations were about the same. Below the results for series *vf* are presented. If it is not mentioned specially, the values of p_E are presented below at $T = 10$ Myr. For $h = 0$ and $30 \leq i_{ej} \leq 60°$, p_E was about 0.28, 0.15–0.17 and 0.06 at v_{esc} equal to 11.5, 12, and 16.4 km/s, respectively. The values of p_E at $i_{ej} = 90°$ were greater by about a factor of 1.3–1.4 than those at $30 \leq i_{ej} \leq 60°$. For $v_{esc} = 11.22$ km/s in calculations, bodies quickly collided with the Earth at $h \leq 20$ km, and about 43% of them collided with the Earth at $h = 100$ km and $T = 10$ Myr. For $v_{esc} = 11.22$ km/s, $T = 10$ Myr, $30 \leq i_{ej} \leq 60°$, and $h = 37r_E$, p_E was about 0.04–0.13. The mean value of p_E depends on distribution of bodies over v_{esc} and i_{ej}. Probably it is about 0.15–0.2 at $h = 0$ and $T = T_{end}$. For $h = 60r_E$, $T = 10$ Myr, and $30 \leq i_{ej} \leq 60°$, p_E was about 0.2–0.25 at $v_{esc} = 2.5$ km/s, 0.13–0.14 at $v_{esc} = 5$ km/s, and 0.06–0.07 at $12 \leq v_{esc} \leq 16.4$ km/s, respectively. These values of p_E show the fraction of bodies that could collide with the Earth after their ejection from the Moon moving in its present orbit. This fraction is about the same as that for the bodies ejected from the Earth if we take into account smaller minimum ejected velocities for the Moon.

PROBABILITIES OF COLLISIONS OF BODIES WITH OTHER PLANETS AND WITH THE SUN AND PROBABILITIES OF EJECTION OF BODIES INTO HYPERBOLIC ORBITS:

For $h = 0$, $30 \leq i_{ej} \leq 60°$, and $T = 10$ Myr, the ratio p_V/p_E of the probability p_V of a collision of a body with Venus to its probability p_E of a collision with the Earth was about 0.6, 1–1.2, and 0.7–1.6 at v_{esc} equal to 11.5, 12, and 16.4 km/s, respectively. The total amount of bodies delivered to Earth and Venus probably did not differed much. For $h = 60r_E$, $T = 10$ Myr, and $30 \leq i_{ej} \leq 60°$, p_V/p_E was about 0.6–0.9 at $v_{esc} = 2.5$ km/s, 0.9–1.3 at $v_{esc} = 5$ km/s, 1.3–1.5 at $11.5 \leq v_{esc} \leq 12$ km/s, 0.6–0.8 at $v_{esc} = 16.4$ km/s, respectively. In my other series of calculations with initial semi-major axes of heliocentric orbits of bodies-planetesimals between 0.9 and 1.1 AU, the ratio p_V/p_E was about 0.8 and 2 at initial eccentricities equal to 0.05 and 0.3, respectively. At small eccentricities of heliocentric orbits, more bodies collided with Earth than with Venus, but at greater eccentricities many bodies moved from the feeding zone of Earth to the vicinity of the orbit of Venus and collided Venus. About 1 % of ejected bodies could collide with Mercury and Mars at $T = 10$ Myr. In most variants of calculations, the probability of a collision of a body with the Sun was about 0.05–0.2 at $T = 10$ Myr, and it could be up to 1/2 at $T = T_{end}$. The probability p_{ej} of ejection of bodies into hyperbolic orbits during $T = 10$ Myr varied from less than 1 % at ($v_{esc} = 11.5$ km/s, $30 \leq i_{ej} \leq 60°$, $h = 0$) to 0.24–0.38 at ($v_{esc} = 16.4$ km/s, $30 \leq i_{ej} \leq 45°$, both at $h = 0$ and $h = 60r_E$).

PROBABILITIES OF COLLISIONS OF BODIES WITH THE MOON:

The Moon was not included in the integration of motion of bodies. Based on the arrays of orbital elements of migrated bodies, I calculated the probabilities of collisions of bodies with the Moon and the Earth and the ratio of probabilities of collisions of bodies with the Earth and the Moon. This ratio was mainly between 20 and 30, and the values of the probability with the Moon were often about 0.006–0.008. In considered calculations of the mo-

tion of bodies ejected from the Earth, bodies left the Hill sphere of the Earth and moved in heliocentric orbits. At some collisions of planetesimals with the Moon, the mass of the Moon could not increase due to ejection of material. With the present orbit of the Moon, the probability of collisions of the bodies ejected from the Earth with the Moon for the bodies that did not leave the Hill sphere of the Earth was even less than that for the bodies that got heliocentric orbits. Bodies ejected from the Earth could participate in the formation of the outer layers of the Moon. In order to contain the present fraction of iron, the Moon had to accumulate the main fraction of its mass from the mantle of the Earth [10]. Bodies ejected from the Earth and fallen onto the Moon embryo probably were not enough for the growth of the Moon from a small embryo in its present orbit. This result testifies in favor of the formation of a large Moon embryo close to the Earth.

CONCLUSIONS:

Bodies ejected from the Earth and the Moon at impacts of bodies-impactors could move in the zone of the terrestrial planets for up to a few hundred million years. The fraction of such bodies that fall back onto the Earth was about 0.15–0.2. The probability of collisions of such bodies with the Moon in its present orbit was about 0.006–0.008. A large Moon embryo should be formed close to the Earth in order to accumulate material rich in iron.

ACKNOWLEDGEMENTS:

The studies of falls of bodies onto planets were carried out under government-financed research project for the Vernadsky Institute. The studies of falls of bodies onto the Moon and its growth and of migration of bodies ejected from the Moon were supported by the Russian Science Foundation, project No. 21-17-00120.

REFERENCES:

[1] Gladman B. et al. Impact seeding and reseeding in the inner Solar System // Astrobiology. 2005. V. 5, p. 483-496.
[2] Reyes-Ruiz M. et al. Dynamics of escaping Earth ejecta and their collision probabilities with different Solar System bodies // Icarus. 2012. V. 220. P. 777-786.
[3] Svetsov V. Cratering erosion of planetary embryos // Icarus. 2011. V. 214. P. 316-326.
[4] Shuvalov V.V., Trubetskaya I.A. Numerical simulation of high-velocity ejecta following comet and asteroid impacts: preliminary results // Solar System Research. 2011. V. 45. P. 392-401.
[5] Levison H.F., Duncan M.J. The long-term dynamical behavior of short-period comets // Icarus. 1994. V. 108. P. 18-36.
[6] Ipatov S.I., Mather J.C. Migration of trans-Neptunian objects to the terrestrial planets // Earth Moon Planets. 2003. V. 92. P. 89-98. DOI: 10.1023/B:MOON.0000031928.45965.7. astro-ph/0305519.
[7] Ipatov S.I., Mather J.C. Migration of Jupiter-family comets and resonant asteroids to near-Earth space // Ann. NY. Acad. Sci. 2004. V. 1017. P. 46-65. DOI: 10.1196/annals.1311.004. astro-ph/0308448.
[8] Ipatov S.I., Mather J.C. Comet and asteroid hazard to the terrestrial planets // Adv. Space Res. 2004. V. 33. P. 1524-1533. DOI: 10.1016/S0273-1177(03)00451-4. astro-ph/0212177.
[9] Ipatov S.I. Probabilities of collisions of planetesimals from different regions of the feeding zone of the terrestrial planets with forming planets and the Moon // Solar System Research. 2019. V. 53. No. 5. P. 332-361. DOI: 10.1134/S0038094619050046. arXiv:2003.11301.
[10] Ipatov S.I. Formation of embryos of the Earth and the Moon from the common rarefied condensation and the subsequent growth // Solar System Research. 2018. V. 52. No. 5. P. 401-416. doi:10.1134/S0038094618050040. arXiv:2003.09925.

ASSESSING THE CONSEQUENCES OF ASTEROID AND COMET IMPACTS ON THE EARTH

D.O. Glazachev[1], O.P. Popova[1], E.D. Podobnaya[1], V.V. Shuvalov[1], N.A. Artemieva[1], V.V. Svetsov[1], V.M. Khazins[1]
[1] *Institute of Geosphere Dynamics RAS, Moscow, Russia; GlazachevD@gmail.com*

KEYWORDS:
asteroid-comet hazard, shock wave, scaling relations, overpressure distribution

INTRODUCTION:
Impacts of cosmic bodies on the Earth lead to hazardous effects that can immediately after the impact or subsequently have a harmful effect on humans, animals and plants, and on economic objects. Damage on the ground produced by pressure pulses of shock waves and radiation fluxes are most important dangerous effects of asteroid and comet impacts. The Chelyabinsk airburst resulted in little structural damage, other than broken windows, window frames and doors [1]. The thermal radiation can be strong enough to be dangerous to people, to ignite fires and even to melt rocks [2]. It may be recalled that the Chixculub crater-forming impact of an asteroid 10–15 km in size generated global wildfires, and the famous 1908 Tunguska event, caused by the entry of an object about 50 m in diameter, generated a forest fire within a radius of 10–15 km [3]. The shock wave is also the cause of seismic effects [4]. The Richter scale magnitude and Mercally scale intensity are used for determination of the instrumental characteristics of a seismic disturbance in the observational point. Atmospheric plume resulting from impact rises to high altitudes (100-300 km) and generate atmospheric disturbances expanding to distances up to thousands of kilometers [5, 6]. For crater-forming impacts, important characteristics are the size of the crater and the parameters of the layer of ejecta from crater (thickness of the ejecta blanket and fraction of melt in ejecta) [7].

A serial numerical modeling of the interaction of cosmic objects with the atmosphere has previously been performed for a large number of different scenarios under the hydrodynamic model [8, 9]. Based on these simulation results scaling relations for the most important parameters of the shock wave, radiation and seismic effects and atmospheric disturbances are constructed. Suggested scaling relations are dependent only on the properties of the entering object (size, density, velocity and entry angle). Precise impact risk assessment is a significant computational challenge. This motivates the usage of simplified approaches and fast assessment of effects, which can be based on suggested scaling relations [10]. Such calculator have been developed and is available at http://AsteroidHazard.pro/.

REFERENCES:
[1] Popova O.P., Jenniskens P., Emel'yanenko V. et al. Chelyabinsk Airburst, Damage Assessment, Meteorite Recovery, and Characterization // Science. 2013. V. 342. Iss. 6162. P. 1069-1073.
[2] Svetsov V., Shuvalov V. Thermal radiation from impact plumes // Meteoritics and Planetary Science. 2019. V. 54. No. 1. P. 126-141.
[3] Svetsov V., Shuvalov V. Tunguska catastrophe of 30 June 1908 // Catastrophic events caused by cosmic objects / eds. V. Adushkin, I. Nemtchinov. N.Y.: Springer Verlag, 2019. P. 227-267.
[4] Khazins V.M., Shuvalov V.V., Svettsov V.V. The Seismic Efficiency of Space Body Impacts // Solar System Research. 2018. V. 52(6) P. 547-556.
[5] Artemieva N., Shuvalov V.V., Khazins V.M. Upper atmosphere effects after the entry of small cosmic bodies: Dust trains, plumes, and atmospheric disturbances // Icarus. 2019. V. 327. P. 60-71.
[6] Shuvalov V.V., Khazins V.M. Numerical Simulation of Ionospheric Disturbances Generated by the Chelyabinsk and Tunguska Space Body Impacts // Solar System Research. 2018. V. 52. P. 129-138.

[7] Holsapple K. The Scaling of Impact Processes in Planetary Sciences // Annual Review of Earth and Planetary Sciences. 1993. V. 21. P. 333-373.
[8] Shuvalov V., Popova O., Svetsov V., Trubetskaya I., Glazachev D. Determination of the height of the “meteoric explosion” // Solar System Research. 2016. V. 50. Iss. 1. P. 1-12.
[9] Artemieva N., Shuvalov V. Atmospheric shock waves after impacts of cosmic bodies up to 1000 m in diameter // Meteoritics and Planetary Science. 2019. V. 54. No. 3. P. 592-608.
[10] Glazachev D.O., Popova O.P., Podobnaya E.D., Artemieva N.A., Shuvalov V.V., Svetsov V.V. Shock Wave Effects from the Impacts of Cosmic Objects with Diameters from 20 m to 3 km // zvestiya, Physics of the Solid Earth. 2021. V. 57. P. 698-709.

MODIFICATION OF TECHNIQUE OF ASTEROID OBSERVATIONS ON TERSKOL OBSERVATORY

T.Yu. Galushina[1], A.V. Shein[2], E.S. Bakanas[3], P.A. Levkina[4]
[1] *Tomsk State University, Russia; tatyana.galushina@mail.tsu.ru*
[2] *Terskol Branch of Institute of Astronomy RAS, Tyrnyauz, Kabardino-Balkaria Republic, Russi; shein.andrey.94@gmail.com*
[3] *Institute of Astronomy RAS, Moscow, Russia; oterma@yandex.ru*
[4] *Institute of Astronomy of the Russian Academy of Sciences, 48 Pyatnitskaya st., Moscow, Russian Federation; ayvazovskaya@inasan.ru*

KEYWORDS:
near-earth asteroids, observations, Terskol observatory, Zeiss-2000, 2003 MW7, (399457) 2002 PD43, 2008 MG1

INTRODUCTION:
Observations of near-Earth asteroids (NEA) is important to determine the orbits more accurately. But it is difficult problem for objects with low magnitude. So, during June session on Terskol observatory we put task to test new technique connected with moving of telescope with asteroid velocity.

OBSERVED ASTEROIDS:
We choose two objects with small perihelion distances ((399457) 2002 PD43 and 2008 MG1) and one asteroid with ill-defined orbit 2003 MW7. According to Minor Planet Center (https://minorplanetcenter.net/) magnitudes of these asteroids were 21.8, 20.5, and 20.8 correspondently. It is interesting that 2002 PD43 has been observed last time in 2018 year, and 2008 MG1 has been seen in 2015 year. The orbit of (399457) 2002 PD43 is well-defined but it is potentially hazardous asteroid that is why it need to be observed. 2003 MW7 was discovered in 2003 but after that had not observed until June, 2022.

OBSERVATIONS' CONDITIONS:
Terskol observatory is located on the Terskol peak, near Elbrus Mountain. Unfortunately, weather allowed us to observe only two nights in the second half of June: June 28 and June 29 after midnight when humidity was decreasing to 45–55°. In the second night the conditions were worse than in the first one. It should be noted that 2008 MG1 was visible just before sunrise that make observations more difficult.

OBSERVATIONS' TECHNIQUE:
The telescope Zeiss-2000 have opportunity to work in different modes. For not bright objects we use mode associated with moving of telescope with asteroid velocity that permit to accumulate light during 3–4 min.

RESULTS:
Table 1 contains statistics about observations and CCD-images' processing. Here N_o is number of received measurements, N_f is number of CCD-images with found asteroid, $(O–C)_\alpha \cdot \cos\delta$ and $(O–C)_\delta$ are mean square errors in right ascension and declination, respectively. The first string for all object corresponds to June 28 and the second matches to June 29. The images were processed with Apex II software [1].

Table 1. The results of observations and processing

Asteroid	N_o	N_f	$(O–C)_\alpha \cdot \cos\delta$, "	$(O–C)_\delta$, "
2003 MW7	10	5	0.44	0.28
	9	8	1.13	1.18
(399457) 2002 PD43	5		0.30	0.25
			4.06	3.91
2008 MG1	3		0.05	0.15
	–			

From Table 1 we see that in the first night residuals less than 0.5″. In the second night the weather conditions were worse, so the accuracy of observations is not such good: approximately half of received observations are acceptable. Nevertheless, our observations of (399457) 2002 PD43 and 2008 MG1 asteroids allows to increase arc length significantly and to decrease the uncertainties.

CONCLUSION:

Thus, our results showed that modified technique permit to observe asteroids up to magnitude 22nd but residuals depend on weather conditions. It is important that our observations for two objects are the first in the new series for the last years.

ACKNOWLEDGEMENTS:

The research was carried out within the state assignment of Ministry of Science and Higher Education of the Russian Federation (theme No. FSWM-2020-0049). The work was made with using equipment of Centre for collective use "Terskol observatory" of the Institute of Astronomy of the Russian Academy of Sciences.

REFERENCES:

[1] Devyatkin A.V., Gorshanov D.L., Kouprianov V.V., Verestchagina I.A. Apex I and Apex II software packages for the reduction of astronomical CCD observations // Solar System Research. 2010. V. 44. Iss. 1. P. 68-80.

EXPERIMENTAL INVESTIGATION OF THE DUST PARTICLES LOFTING PROCESSES

I. Kuznetsov[1], I. Shashkova[1], A. Poroykov[2], A. Zakharov[1], A. Lyash[1], S. Bednyakov[1], G. Dolnikov[1], A. Dubov[1], A. Kartasheva[1], A. Shehovtsova[3], M. Essam[1], E. Kronrod[4]

[1] *Space Research Institute, Moscow, Russia; kia@iki.rssi.ru*
[2] *National Research University "Moscow Power Engineering Institute", Moscow, Russia*
[3] *Lomonosov Moscow State University, Moscow, Russia*
[4] *Vernadsky Institute of Geochemistry and Analytical Chemistry RAS*

KEYWORDS:
dust, lunar dust, dusty plasma, dust dynamics

INTRODUCTION:

The direct observations of the lunar horizon glow that made more than 50 years ago by the Surveyor-7 automatic spacecraft [1] and Apollo-17 astronauts [2] are one of the most mysterious observations related to Moon and are still under debate. [3–5] and other authors stated that the electric potential of the lunar surface in the terminator region and in the lunar nightside can highly vary and reach as low as minus 4000 V. [6] estimated the possible electric field on the Moon up to 3000 V/cm. Levitation mechanism explanation is based on the idea that the electrically charged surface and electrically charged dust grains repel each other. A very similar phenomenon is proposed for most of the celestial atmosphereless bodies. Due to much lower gravity force, the increasing of the dust dynamics on the asteroids [7, 8] and Martian satellites Phobos and Deimos [9, 10] is predicted. [11] estimated the electric field on asteroids in the range of 500–1500 V/cm. Alongside the theoretical works, there is an experimental simulation approach [12, 13] that can help to solve the dust dynamics mystery.

In this work, we describe the experimental simulation approach to the airless dust particles dynamics.

ACKNOWLEDGEMENTS:
This work was partially funded by 10th Program of the Experimental Laboratory Astrophysics and Geophysics NCPM.

REFERENCES:

[1] Rennilson J.J., Criswell D.R. // Moon. 1974. V. 10. Art. No. 121.
[2] Zook H.A., McCoy J.E. // Geophysical Research Letters. 1991. V. 18. Art. No. 2117. URL https://doi.org/10.1029/91GL02235.
[3] Stubbs T.J., Vondrak R.R., Farrell W.M. A dynamic fountain model for lunar dust // Advances in Space Research. 2006. V. 37. Iss. 1. P. 59-66. URL: https://www.sciencedirect.com/science/article/pii/S0273117705004989.
[4] Halekas J.S., Delory G.T., Lin R.P., Stubbs T.J., Farrell W.M. // J. Geophysical Research: Space Physics. 2008. V. 113. URL https://agupubs.onlinelibrary.wiley.com/doi/abs/10.1029/2008JA013194.
[5] Farrell W., Stubbs T., Vondrak R., Delory G., Halekas J. // Geophysical Research Letters. 2007. V. 34. Art. No. L14201.
[6] De B.R., Criswell D.R. Intense localized photoelectric charging in the lunar sunset terminator region, 1. Development of potentials and fields // J. Geophysical Research. 1977. V. 82. Iss. 7. P. 999-1004. URL: https://agupubs.onlinelibrary.wiley.com/doi/abs/10.1029/JA082i007p00999.
[7] Lee P. // Icarus. 1996. V. 124. Art. No. 181.
[8] Yeo L.H., Wang X., Deca J., Hsu H.W., Horányi M. // Icarus. 2021. V. 366.
[9] Popel S.I., Golub' A.P., Zakharov A.V., Zelenyi L.M. // JETP Letters. 2017. V. 106. Art. No. 485.
[10] Krivov A.V., Hamilton D.P. // Icarus. 1997. V. 128. Art. No. 335.
[11] Rennó N., Kok J. Electrical Activity and Dust Lifting on Earth, Mars, and Beyond // Space Sciences Series of ISSI. 2008. V. 137. P. 419-434.
[12] Wang X., Schwan J., Hsu H.W., Grün E., Horányi M. // Geophysical Research Letters. 2016. V. 43. Art. No. 6103.
[13] Orger N.C., Toyoda K., Masui H., Cho M. // Advances in Space Research. 2019. V. 63. Art. No. 3270. URL: https://doi.org/10.1016/j.asr.2019.01.045.

THE 10-MICRON SILICATE FEATURE IN HETEROGENEOUS DUST PARTICLES

E. Chornaya[1], E. Zubko[2], G. Videen[2,3]
[1] *Institute of Applied Astronomy RAS, Saint-Petersburg, Russia*
[2] *Humanitas College, Kyung Hee University, Republic of Korea*
[3] *Space Science Institute, Boulder, USA*

KEYWORDS:
comets, dust, thermal emission, mid-IR spectrometry, 10-μm silicate feature, modeling, agglomerated debris particles, discrete dipole approximation

INTRODUCTION:

Comets and protoplanetary disks often reveal a series of peaks in their mid-IR spectra between 8 and 13 μm that are attributed to stretching of the Si-O bonds in silicates. In the literature, this phenomenon is referred to as the *10-μm silicate feature* [1, 2]. The position and shape of these peaks may provide important clues for better characterization of chemical composition and structure of silicates (e.g., [3]). While the 10-μm silicate feature was long attributed either to the compact silicate particles whose radius does not exceed 1 μm [2] or to an extremely fluffy aggregate consisting of submicron grains [3], recent experiments reveal the phenomenon may also appear in very large, submillimeter compact silicate particles [4]. It is worth noting that the constraint drawn in [2] emerges from using an oversimplified, spherical model of particle shape. Our modeling of the mid-IR spectra using a more realistic model of the cometary dust, the so-called *agglomerated debris particles*, unambiguously suggests the 10-μm silicate feature appears even when the particle radius exceeds 10 μm [5]. It also is significant that the agglomerated debris particles are capable of fitting polarimetric observations of various comets in the visible and near-IR [6, 7].

An important problem arising in interpretation of the 10-μm silicate feature is that the phenomenon is better reproduced with the Mg-rich silicates compared to Fe-rich silicates (e.g., [3]). It is worth noting that the Mg-rich silicate particles also play a crucial role in shaping the phase dependence of polarization in comets [6]. Due to their extremely low material absorption in the visible and near-IR, imaginary part of their refractive index Im(m) ~10^{-5}, the Mg-rich silicate particles acquire 3–5 times lower temperature compared to other species in a cometary coma [9]. However, the thermal-emission flux is strongly dependent on the temperature of particles, ~T^4, and, hence, the relative contribution of the cold Mg-rich silicate particles should be a factor of 81–625 weaker compared to the hot Fe-rich silicate particles and/or carbonaceous particles. In other words, there is little chance that the Mg-rich silicate particles would be detected in a cometary coma by means of the mid-IR spectroscopy. Yet, the 10-μm silicate feature was found in various comets. Our work is aimed at resolving this inconsistency.

MODELING THE THERMAL EMISSIVITY:

Wavelength dependence of the thermal emissivity of a target can be converted from its wavelength dependence of absorption by means of Kirchhoff's law of thermal radiation. Using the discrete dipole approximation (DDA), we compute the cross section of absorption C_{abs} in the agglomerated debris particles.

The algorithm generating the agglomerated debris particles is as follows. A spherical volume is filled with a cubic lattice. All cells are divided into two subgroups, those lying in the inner volume (i.e., having 26 neighbors) and those located at the surface of the spherical volume (otherwise). Among the surface cells, 100 cells are randomly chosen to be seeds of empty space. In the inner volume, 21 cells are randomly chosen to be seeds of a material and 20 cells are seeds of empty space. Each cell is assigned the optical properties of the nearest seed cell, either empty space or material. Six examples of the agglomerated debris particles are shown on top in Fig. 1. For more details on the algorithm of their generation and on the DDA computations, we refer to [6].

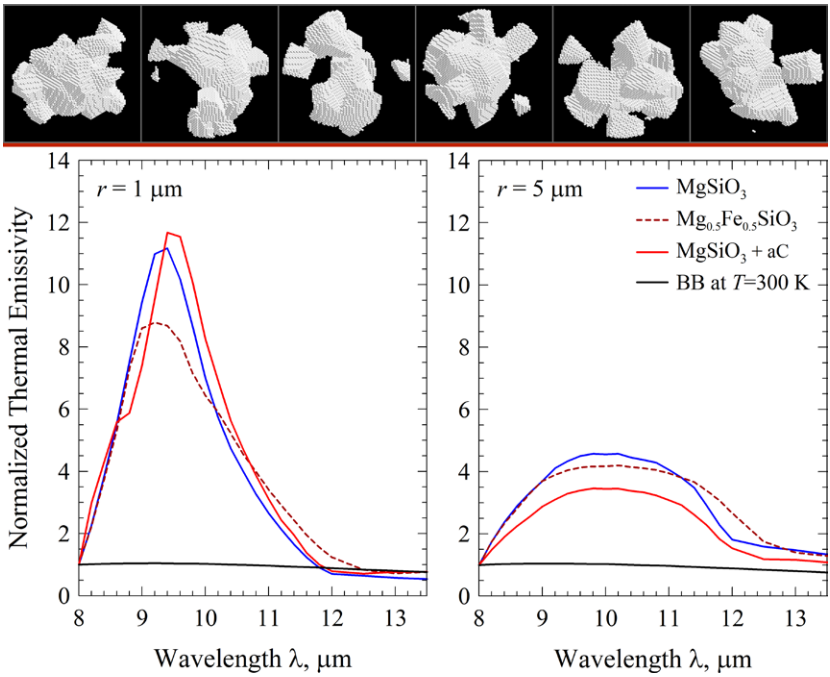

Fig. 1. Six samples of agglomerated debris particles (top) and the thermal-emission spectra of these particles having three types of chemical composition (see legend) at r = 1 μm (left) and r = 5 μm (right)

C_{abs} is determined by the ratio of the particle radius r to wavelength λ and by the complex refractive index m. In our modeling, the wavelength λ spans the range from 8 to 13.5 μm. We investigate two sizes of particles, r = 1 μm and 5 μm, and three types of chemical composition: (1) pure magnesium-rich pyroxene glass $MgSiO_3$; (2) magnesium-iron pyroxene glass $Mg_{0.5}Fe_{0.5}SiO_3$; and (3) chemically heterogeneous agglomerated debris particles generated with 20 seed cells of $MgSiO_3$ and 1 seed cell of amorphous carbon (aC). Refractive indices in silicates are adapted from [8] and in amorphous carbon from [10]. It is worth noting for each set of m, λ, and r, we consider 500 randomly generated particles for statistical reliability.

RESULTS AND DISCUSSION:

Figure 1 presents the mid-IR spectra of the relative thermal emissivity for three types of agglomerated debris particles. The left panel shows results for r = 1 μm and the right for r = 5 μm. Curves of different color result from different chemical compositions of the agglomerated debris particles (see legend). In addition, the black solid line shows the blackbody-radiation spectrum at temperature T = 300 K, corresponding to the heliocentric distance r_h = 0.865 au. All curves are normalized at λ = 8 μm.

As one can see in Fig. 1, particles having all three types of composition reveal a sharp peak at r = 1 μm and a broad surge at r = 5 μm. Smaller particles demonstrate a very strong excess in their thermal emission over what is in the blackbody, up to 12 times. For larger particles, the excess is somewhat dampened, but it still remains to significant, up to a factor of 4.5. It is worth noting that the Mg-rich silicate particles produce a stronger surge in their spectra compared to what emerges from the Mg-Fe silicate particles. This finding goes along with what is reported in [3] for particles with fluffy morphology.

Interestingly, at r = 1 μm, replacement of 1 seed cell in the Mg-rich silicate particles with amorphous carbon enhances the peak at λ = 9.4 μm and shifts it slightly toward longer wavelengths. The same does not hold, however, in

larger particles with r = 5 μm, where the amorphous-carbon inclusion dampens the surge in the mid-IR spectrum. It also is worth noting that the decrease of the surge in the mid-IR spectrum in Mg-rich silicate particles slightly contaminated with the amorphous carbon appears to be more prominent than in the Mg-Fe silicate particles.

It is significant that even a single seed cell of amorphous carbon embedded into the Mg-rich silicate particles dramatically enhances their efficiency of absorption $Q_{abs} = C_{abs}/G$, where G stands for the geometric cross section of target particles. For instance, in red light with λ = 0.7 μm, the agglomerated debris particles with r = 1 μm and having the pure Mg-rich silicate composition reveal Q_{abs} = 0.0095; whereas, the Mg-rich silicate particles contaminated with the amorphous carbon yield already Q_{abs} = 0.158. In other words, a single seed cell assigned to the amorphous carbon increases material absorption of the whole particle for ~16.6 times. It is roughly equivalent to an increase of the imaginary part from Im(m) = 0.0005 in the pure Mg-rich silicates to Im(m) = 0.01. The later one corresponds to dramatic growth of the particles temperature, significantly increasing their contribution to the thermal emission.

REFERENCES:

[1] Gehrz R.D., Ney E.P. 0.7- to 23-μm photometric observations of P/Halley 1986 III and six recent bright comets // Icarus. 1992. V. 100. P. 162-186.
[2] Hanner M.S., Bradley J.P. Physical properties of cometary dust from light scattering and thermal emission // Comets II / eds. M.C. Festou, H.U. Keller, H.A. Weaver. University of Arizona Press, 2004. 555 p.
[3] Kimura H., Chigai T., Yamamoto T. Infrared spectra of dust aggregates in cometary comae: Calculation with olivine formed by exothermic chemical reactions // Astrophys. J. 2009. V. 690. P. 1590-1596.
[4] Chornaya E., Zakharenko A.M., Zubko E. et al. Revisiting the particle-size constraint of the 10-μm silicate feature // Icarus. 2020. V. 350. Art. No. 113907.
[5] Chornaya E., Zubko E., Videen G. The 10 micron silicate feature in the agglomerated debris particles // 11th Moscow Solar System Symp. 11M-S3. 2020. P. 252-253.
[6] Zubko E., Videen G., Hines D.C., Shkuratov Yu. The positive-polarization of cometary comae // Planet. Space Sci. 2016. V. 123. P. 63-76.
[7] Chornaya E., Zubko E., Luk'yanyk I. et al. Imaging polarimetry and photometry of comet 21P/Giacobini-Zinner // Icarus. 2020. V. 337. Art. No. 113471.
[8] Dorschner J., Begemann B., Henning T. et al. Steps toward interstellar silicate mineralogy. II. Study of Mg-Fe-silicate glasses of variable composition // Astron. Astroph. 1995. V. 300. P. 503-520.
[9] Harker D.E., Wooden D.H., Woodward C.E., Lisse C.M. Grain properties of Comet C/1995 O1 (Hale-Bopp) // Astrophys. J. 2002. V. 580. P. 579-597.
[10] Preibisch Th., Ossenkopf V., Yorke H.W., Henning Th. The influence of ice-coated grains on protostellar spectra // Astron. Astroph, 1993. V. 279. P. 577-588.

THE MASS ESTIMATIONS OF FAINT METEORS

A. Kartashova[1], Yu. Rybnov[2], O. Popova[2], D. Glazachev[2], V. Efremov[2]
[1] *Institute of Astronomy RAS, Moscow, Russia; akartashova@inasan.ru*
[2] *Institute of Geosphere Dynamics RAS, Moscow, Russia*

KEYWORDS:
meteor, meteoroid mass, meteor observations

INTRODUCTION:

The problem of accurately determining the mass, density and properties of the substance of meteoroids still not unresolved. The mass of small meteors (less than ~1 cm) is often estimated based on empirical ratios using the maximum meteor brightness, velocity and the entry angle [1–4]. The variation of estimates by different ratios can be exceeding an order of magnitude.

Estimates of the mass of small meteoroids by various models strongly depend on the assumptions of the model used, in addition, these models are few. These models are also not perfect, and the accuracy of determining the mass is not very high, the spread of estimates can reach two or more times [5].

Meteor observations were used for meteor mass estimations. The analysis of infrasound registrations and their comparison with optical observations made it possible to identify several dozens of acoustic signals corresponding to optical registrations (from several points). Therefore, the mass estimations were got from two type of observations.

Methods for determining the parameters of meteor particles are presented.

REFERENCES:

[1] Jacchia L., Verniani F., Briggs R.E. An analysis of the atmospheric trajectories of 413 precisely reduced photographic meteors // Smithsonian Contributions to Astrophysics. 1967. V. 10. P. 1-139. https://doi.org/10.5479/si.00810231.10-1.1.
[2] Jenniskens P. Meteor showers and their parent comets. Cambridge: Cambridge University Press, 2006. 790 p.
[3] Verniani F. On the luminous efficiency of meteors // Smithsonian Contributions to Astrophysics. 1965. V. 8. No. 5. P. 141-171.
[4] Vida D., Brown P.G., Campbell-Brown M. Modelling the measurement accuracy of pre-atmosphere velocities of meteoroids // Monthly Notices of the Royal Astronomical Society. 2018. V. 479. No. 4. P. 4307-4319.
[5] Efremov V., Popova O., Glazachev D., Margonis A., Oberst J., Kartashova A. Small Meteor Ablation Model: Applying to Perseid Observations // Contributions of the Astronomical Observatory Skalnate Pleso. 2021. V. 51. P. 186-206.

ON THE MASS INDICES OF METEOR BODIES

R.V. Zolotarev[1], B.M. Shustov[1]
[1] *Institute of Astronomy RAS, Moscow, Russia; rv_zolotarev@mail.ru, bshustov@inasan.ru*

KEYWORDS:
meteor, meteoroid, mass index, comet, meteoroid stream

It is known that mass spectra of meteoric bodies are close to $dN \sim m^{-s}dm$, where d is the number of meteor particles whose masses is in the interval [m, m+dm], s is the differential mass index of meteoroids. According to observational data mass index is close to 2 for sporadic meteors and less than 2 at the maximum for meteor showers (which means relative lack of lighter particles) [1]. The most direct way to deal with this problem is modeling of evolution of meteoroid streams with particles of different masses. We use two-step modeling: 1) modeling of ejection of particles from parent body; 2) modeling of dynamical evolution of particles in Solar System.

Cometary activity and asteroids collisions are thought to be the main sources of meteoroid streams. We consider meteoroid streams originating from cometary activity. In [1] we construct the model of ejection of particles from the parent body during perihelion passage. The model taking into account gas outflow rate and gravity of a comet and predicts escape velocities, which are used as initial conditions for modeling of dynamics of meteoroids in Solar System. Fragmentation of comet crust and meteoroids ensemble formation is a complicated process and it can be represented as effect of some random process, which can be described as statistical noise with mass spectrum with mass index s = 2. On this basis we consider dynamics of 4 types of particles which mass distribution has initial mass index s = 2.

At the next step [2] we use numerical approach to model dynamics of meteoroid particles in Solar System taking into account gravity of the Sun and planets and also radiative forces (light pressure and Poyting-Robertson effect). Following methodic described in [3] we model two hypotetical meteoroid streams with different initial parent bodies: comets 2P/Encke and 96P/Machholz. At each model dynamics of $4 \cdot 10^5$ particles (10^5 particles per group) was integrated using rebound code with MERCURIUS hybrid scheme [4].

Figure 1 demonstrates meteoroids of different masses after 500 yr integration ejected from 2P/Encke comet.

One may note that lightweight particles spreads much more wider than others. This is effect of larger escape velocity and radiative forces.

To study mass index behavior with time, number of particles of each size was calculated with time step in near-Earth sphere with radius 0.1 AU with repeating ejections taking into account. Figure 2 shows mass index as function of time calculated for model of swarm ejected from comet 2P/Encke.

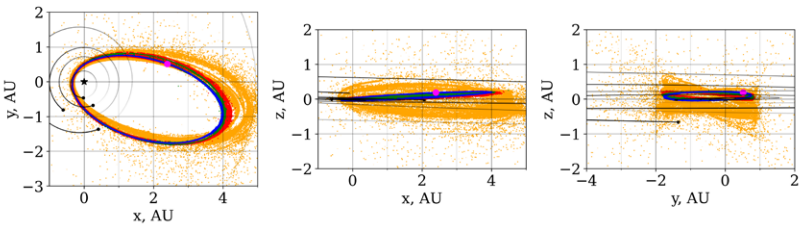

Fig. 1. Meteoroid swarm ejected from comet 2P/Encke at 500 yr. Color represents size of particle: yellow – 0.005 cm, red – 0.016 cm, green – 0.05 cm, blue – 0.16 cm. Black dots and lines are planets positions and its orbits, purple dot is parent body position

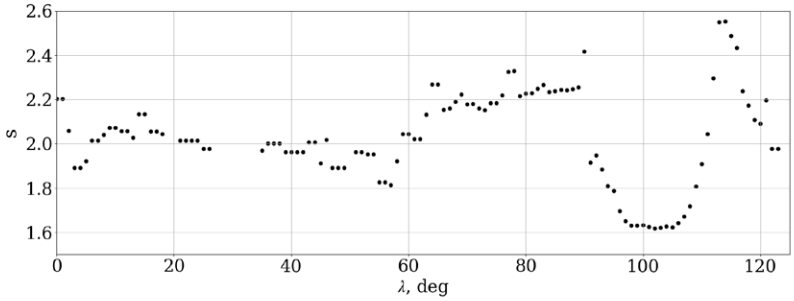

Fig. 2. Mass index in model of meteoroid swarm ejected from comet 2P/Encke as function of solar longitude. Stream age is 500 yr

Solar longitude in interval $\lambda \approx [70º, 110º]$ corresponds Earth crossing of meteoroid stream. When the Earth is far from main part of meteoroid swarm, mass index is close to 2, which corresponds initial mass index and sporadic meteors, when Earth crosses meteor stream, mass index decreases sufficiently.

The model constructed reproduces observational behavior of mass index for sporadic meteors and meteor showers. The lack of lightweight particles is concerned with its dynamics. Lighter and smaller particles have greater escaping velocities during ejection and they are more exposed to act of non-gravitational forces.

ACKNOWLEDGEMENTS:
This work is supported by RSCF grant No. 22-12-00115.

REFERENCES:

[1] Shustov B.M., Zolotarev R.V. Mass Indices of Meteoric Bodies: I. Formation Model of Meteoroid Streams // Astronomy Reports. 2022. V. 66. No. 2. P. 179-189.
[2] Zolotarev R.V., Shustov B.M. Mass Indices of Meteoric Bodies: II. Evolution of Meteoroid Streams // Astronomy Reports. 2022. V. 66. No. 3. P. 255-268.
[3] Ryabova G.O. Mathematical Modeling of Meteoroid Streams. Springer International Publishing, 2020. 68 p.
[4] Rein H., Hernandez D.M., Tamayo D. et al. Hybrid symplectic integrators for planetary dynamics // Monthly Notices of Royal Astronomical Society. 2019. V. 485. No. 4. P. 5490-5497.

ENERGY ACCUMULATION IN ICY BODIES DURING LONG-TERM IRRADIATION

D.V. Belousov[1], A.K. Pavlov[1]
[1] *Ioffe Institute, Saint Petersburg, Russia; dom.999.bel@gmail.com*

KEYWORDS:
Comets, cometary outbursts, cosmic rays, radionuclides, cryovolcanism

INTRODUCTION:
Many icy bodies in the solar system (e.g., comets and Kuiper Belt objects) demonstrate activity at large distances from the Sun, where a small body is supposed to hibernate. The examples of such an activity are ongoing internal activity of icy satellites (e.g., Enceladus), cometary outbursts at large distances and flashes experienced by Kuiper Belt objects. The source of activity at temperatures up to that of the Oort Cloud (3–10 K) remains one of the main questions of planetology. Herein, we investigate radiation effects in ice that take place in icy bodies during cosmic ray irradiation and the decay of radionuclides. The former causes physical and chemical changes [1] in the upper tens of meters beneath the surface, while the latter affects the entire volume of a body. Radicals formed by irradiation can be accumulated at low temperatures and furiously recombine during the external heating or react spontaneously with an energy release [2]. We study the accumulation of radicals followed by their recombination as a possible mechanism of cryovolcanism currently detected on icy bodies or occurring during their long-term evolution.

EXPERIMENTS:
We conducted several experiments on energy accumulation in water ice irradiated by 15 MeV protons and 0.9 MeV electrons at temperatures 80–85 K [3]. The major result is that the fast energy release of ~20 $J \cdot g^{-1}$ took place in the proton-irradiated ice at the temperature 106 K induced by external heating. A similar effect was detected in electron-irradiated ice. At lower temperatures, several scientific groups detected energy release in water ice and solid methane irradiated by protons and neutrons with the accumulated energy up to 280 $J \cdot g^{-1}$ [2]. At low temperatures, water ice with a high concentration of radicals ~1 per cent (to water molecules) is prone to experience the spontaneous recombination.

ENERGY ACCUMULATION BY COSMIC RAYS AND RADIONUCLIDES:
Galactic cosmic rays (GCRs) deposit a high dose in the upper layer of the comet, thereby leading to the number of irradiation effects, for instance, radical accumulation. Based on the experiments, ice with the high concentration of radicals is not stable and can spontaneously experience self-heating events [2]. From calculations, the critical concentration of radicals is accumulated in the upper two-meter layer of ice by GCRs within the 10-150 Myr range. Thus, the upper layer of comets in the Kuiper Belt and the Oort Cloud can be periodically active.

Since icy bodies are composed of dust, ice and frozen gases, decay of short-lived (^{26}Al and ^{60}Fe) and long-lived radionuclides (^{232}Th, ^{235}U, ^{238}U, and ^{40}K) results in the constant irradiation of internal layers. The value of accumulated radicals depends on concentration of radionuclides, which is closed to concentrations in ordinary chondrites. However, radionuclides fractions in comets can differ from that of meteorites. The final concentration of radicals also depends on the dust-to-ice ratio. In Figure 1, we plotted the number of radicals accumulated in ice at low temperatures. The irradiation of the dust component can also produce radicals, thereby contributing to overall stored energy. The mobility of radicals substantially decreases at low temperatures, and free radicals can be accumulated up to high concentrations. Internal radiation produced by radionuclides also leads to heating [4], nevertheless the certain fraction of accumulated dose can be stored in free radicals. Spontaneous recombination was detected in experiments with water ice irradiated at temperatures below 30 K. This temperature can be regarded as the critical

for sustainability of high radicals concentration. From calculations, the heating by long-lived radionuclides in bodies with a radius below ~20–40 km (depends on porosity and ice conductivity) does not result in a severe heating above the critical temperature. However, short-lived nuclides, primary ^{26}Al, causes fast heating in the yearly stages of comet evolution up to the ice melting point.

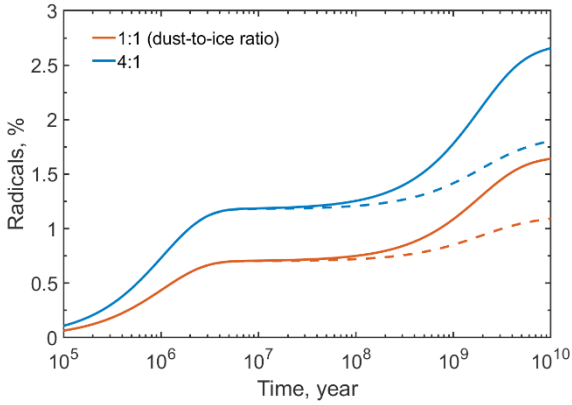

Fig. 1. Concentration of radicals accumulated in ice by the decay of radionuclides. Here, we consider the radicals stored in the water-ice component of ice in per cent (to water molecules). The blue and red curves are for ice with the dust-to-ice ratio 1:1 and 4:1, respectively. Dashed and solid curves are for the minimum and maximum mass fraction of potassium detected in meteorites, respectively

We can limit the temperatures of ice bodies during their evolution based on modern models and data on the chemical composition and physical structure. Rosetta mission detected high concentrations of molecular oxygen in the coma of comet 67P/Churyumov-Gerasimenko [5]. It is assumed that the major source of O_2 is radiolysis of icy grains during comet formation. Stability of O_2 in comet ice favors the assumption of low temperatures of comet nuclei during their evolution. The existence of volatile gas CO in comets also demands the low temperature of nuclei formation.

ACTIVITY OF ICY BODIES DRIVEN BY THE RECOMBINATION

Icy bodies with a high concentration of trapped radicals beneath the surface can experience self-heating events with gas and dust ejection during a sunward movement or a body collision. Such a mechanism could trigger

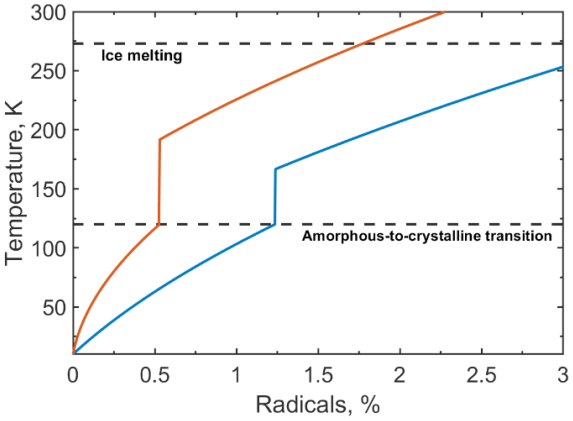

Fig. 2. The heating of the icy body by the recombination of free radicals. Concentration of radicals is presented in per cent (to water molecules). The dust-to-ice ration is 1:1. The blue curve is for ice with radicals stored only in the water-ice component. The red curve is for ice with radicals accumulated in water-ice and dust

cometary outbursts at large heliocentric distances [3]. It is also possible that the high concentration of radicals inside an icy body reacts spontaneously, thereby furiously raising the temperature. The maximum value of accumulated energy in ice strongly depends on ice structure, its composition, and the type of impinging particles. In addition, the stability of high concentrations against spontaneous recombination shows a stochastic nature at low temperatures[2]. Figure 2 shows the maximum temperature up to that ice can be heated by radicals. It is assumed that water ice in comets has an amorphous form; the amorphous-to-crystalline ice transition gives the additional source of energy. If we take into account that the dust component also has accumulated radicals, ice can reach the temperature of melting. Thus, the accumulation and recombination of free radicals play an important role in currently detected cometary outbursts and in the long-term evolution of icy bodies.

ACKNOWLEDGEMENTS:
This research was funded by Russian Foundation for Basic Research, grant No. 20-02-00470.

REFERENCES:

[1] Maggiolo R. et al. The effect of cosmic rays on cometary nuclei. II. Impact on ice composition and structure // The Astrophysical J. 2020. V. 901. Art. No. 136.
[2] Shabalin E., Kulagin E., Kulikov S., Melikhov V. Experimental study of spontaneous release of accumulated energy in irradiated ices // Radiation Physics and Chemistry. 2003. V. 67. P. 315-319.
[3] Pavlov A.K., Belousov D.V., Tsurkov D.A., Lomasov V.N. Cosmic ray irradiation of comet nuclei: a possible source of cometary outbursts at large heliocentric distances // Monthly Notices of the Royal Astronomical Society. 2022. V. 511. P. 5909-5914.
[4] Mousis O. et al. Impact of radiogenic heating on the formation conditions of comet 67P/Churyumov–Gerasimenko // The Astrophysical J. Letters. 2017. V. 839. Iss. L4.
[5] Mousis O. et al. Origin of molecular oxygen in comet 67P/Churyumov–Gerasimenko // The Astrophysical J. Letters. 2016. V. 823. Iss. L41.

SESSION 5. SMALL BODIES (INCLUDING COSMIC DUST) (SB) POSTER SESSION

STATISTIC ANALYSIS OF DYNAMIC PARAMETERS AND SIZES OF ASTEROIDS OF THE ADEONA FAMILY

S.Y. Kuznetsov[1,2], V.V. Busarev[2,3]
[1] *Lomonosov Moscow State University, Faculty of Space Research, Moscow, Russia; imarpus@gmail.com*
[2] *Sternberg Astronomical Institute Moscow University, Moscow, Russia; busarev@sai.msu.ru*
[3] *Institute of Astronomy RAS, Moscow, Russia*

KEYWORDS:
asteroids, Adeona family, active asteroid, orbits, dynamics

INTRODUCTION:
(145) Adeona is a large asteroid of the main asteroid belt with diameter 127.7 km, which belongs to the spectral class Ch (SMASSII) and has a low geometric albedo (p_V = 0.067, [1]). The additional index “h” in the notation of Adeona’s type means that its reflectance spectrum includes a specific absorption band with the center at 0.7 μm, which indicates the presence of hydrosilicates in its material [2]. Taking into account the recent detection of sublimation-dust activity of Adeona near perihelion [3], the surface material may contain some amount of water ice or some local exposition of it (possibly due to an impact event).

FAMILY DESCRIPTION:
Adeona family is a large asteroid family that formed from the supposed parent body (145) Adeona. Its spectral type is that of a carbonaceous C-type, with currently 2,236 asteroids identified as family members [4]. Based upon simulation studies, the Adeonian family is believed to be no more than 794±194 My old [5], compared to a typical asteroid family age of 1–2 billion years. The semi-major axis of the orbit (a), eccentricity (e) and orbital inclination (i) of the asteroids of the family take the following values: 2.57353 au < a < 2.69265 au, 0.15563 < e < 0.17579, 11.22 < i < 11.86°. The distribution histograms of these family parameters are shown in (Figs. 1 and 2).

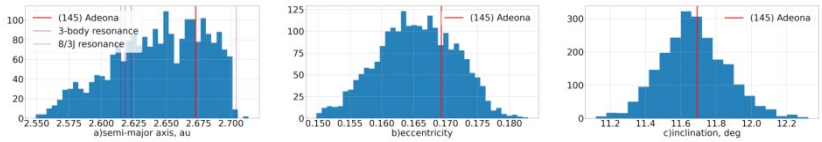

Fig. 1. Whole family distribution

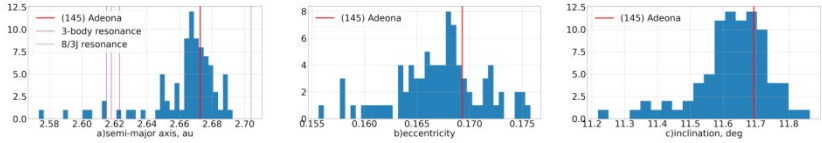

Fig. 2. A sample with diameter >10 km

ANALYSIS:
The distribution of the number of bodies as a function of their own a (see Fig. 1a, three purple vertical lines; the position of Adeona is indicated by the red vertical line) shows a sharp decrease in dynamical family membership (DFM) in the region with three resonances (on the left) caused by the interaction of 3-body resonances at $a \approx 2.623$, 2.615, 2.18 au [5]. An even stronger decrease in the DFM is observed at a ~2.704 au on the right (8/3J resonance) (see Fig. 1a, dotted vertical line). This means that a part of the family could have been removed due to resonances [5]. In the sample of large asteroids

(more than 10 km in diameter), Adeona's *a* and *e* values are quite close to the average values between the same resonances (see Figs. 2a and 2b, red line). At the same time, on the general histogram of the family, the position of Adeona by eccentricity is shifted to large values (see Fig. 1b, red line). This fact probably indicates an increase in the asteroid's eccentricity as a result of the main catastrophic event. The largest diameter of Adeona in comparison with other members of the family and their similarity in spectral type indicate that this asteroid is, with a high probability, the parent body of the family (or its surviving main part), fragmented during the catastrophic event that led to the formation of the family. The shift of the eccentricities and inclinations of the orbits of smaller members of the family towards smaller values could be caused either by the main impact event or by long-term resonant disturbances.

CONCLUSION:

Based on the distribution of the main parameters for different samples, it can be assumed that a significant part of the asteroids of the family under consideration is close in origin to (145) Adeona and should have similar properties, including the suggested presence of water ice in its composition and manifestation of sublimation activity near perihelion [3].

ACKNOWLEDGMENTS:

This work was supported by the Russian Foundation for Basic Research (grant No. 22-12-00115).

REFERENCES:

[1] https://ssd.jpl.nasa.gov/tools/sbdb_lookup.html#/?sstr=145.
[2] Bus S.J., Binzel R.P. Phase II of the Small Main-Belt Asteroid Spectroscopic Survey. A feature-based taxonomy // Icarus. 2002. V. 158. No. 1. P. 146-177.
[3] Busarev V.V., Makalkin A.B., Vilas F. et al. New candidates for active asteroids: Main-belt (145) Adeona, (704) Interamnia, (779) Nina, (1474) Beira, and near-Earth (162,173) Ryugu // Icarus. 2018. V. 304. P. 83-94. DOI: 10.1016/j.icarus.2017.06.032.
[4] Nesvorny D. NASA Planetary Data System, EAR-A-VARGBDET-5-NESVORNY-FAM-V3.0. 2015.
[5] Milani A., Knežević Z. et al. On the ages of resonant, eroded and fossil asteroid families // Icarus. 2017. V. 288. P. 240-264.

INFLUENCE OF METEOR FLARES ON THE DEVELOPMENT OF MODULATION INSTABILITY OF ELECTROMAGNETIC WAVES IN METEOROID TAILS

T.I. Morozova[1], S.I. Popel[1]
[1] *Space Research Institute, Moscow, Russia*

KEYWORDS:
meteoroids, dusty plasmas, meteoroid tail, modulational interaction, electrophonic sounds, low-frequency perturbations, dust acoustic waves, meteor flares

INTRODUCTION:
The effect of meteor flares on the occurrence of modulation instability of electromagnetic waves in meteoroid tails associated with the dust acoustic mode, which has not been done before, is considered. It is shown that the modulation instability has time to develop at lower altitudes compared to the situation without flares in paper [1].

DISCUSSION:
The mechanism of meteor flares and features of their formation are considered. It was shown in [2] that the main flare peak falls at a height of 92 km. Moreover, flares and the associated fragmentation of a meteoroid depend on the composition and configuration of the meteoroid and on its velocity and angle of entry into the Earth's atmosphere. The faster the meteor, the later flashes appear on its path. The most powerful flashes occur when the meteor body is already sufficiently heated. Different forms of meteoroid explosions are observed due to their different shapes and compositions. Including, because of the peculiarities of the structure of the meteoric body and combinations of fusible inclusions. The lower the altitude of the meteoroid, the more the meteor body heats up and the greater the probability and frequency of flares). With the constant destruction of the meteoric body, particles with sizes of 100 μm – 1 mm are separated [2].

It is shown that increments of the modulational instability higher in the case of meteor flares that leads to the faster developing of the modulational instability of electromagnetic waves. Moreover modulation instability cam develop at lower altitudes compared to the situation without flares.

ACKNOWLEDGEMENTS:
The work was supported by the Foundation for the Advancement of Theoretical Physics and Mathematics "BASIS".

REFERENCES:
[1] Morozova T.I., Kopnin S.I., Popel S.I. Modulation interaction in the dusty plasma of meteoroid tails // Geomagnetism and Aeronomy. 2021. V. 61ю No. 6. P. 794-802.
[2] Bronshten V.A. Physics of Meteor Phenomena. Dordrecht, Holland: D. Reidel Publishing Company, 1983. 16 p.

INFLUENCE OF THE INTERNAL STRUCTURE OF DUST ON THE LIGHT-SCATTERING PROPERTIES OF COMET 29P/SCHWASSMANN-WACHMANN 1

D.V. Petrov[1], E.A. Zhuzhulina[1]
[1] *Crimean Astrophysical Observatory RAS, Bakhchisaray, Nauchny, Crimea, Russia*

KEYWORDS:
comets, light scattering, computer simulation, fractal particles, scattering cross section

INTRODUCTION:

Comet 29P/Schwassmann-Wachmann 1 has attracted the attention of comet researchers and those interested in the origin of the solar system for many years. For its continuous flare activity since its discovery in 1927, the object received the comet designation. Its orbit lies entirely behind the orbit of Jupiter, at a distance of approximately 6 AU. As a result, this comet is accessible for observations from the earth only in a rather narrow range of phase angles from 0 to 10°.

A feature of comet 29P/Schwassmann-Wachmann 1 is that from time to time it shows an increase in brightness by 1–5^m. With this comet's typical brightness ranging from 16^m to 19^m, the burst of brightness can increase its brightness to 13^m, and in some cases up to 10^m, which corresponds to more than a thousandfold increase in brightness [1].

In work [2] it was shown that flares can be explained by the presence of one or several large satellites (more than a kilometer) near the comet, with the pericentric distance of the orbit approximately equal to the radius of the comet's nucleus and having a rotation period of 6 to 14 days. Due to the fact that the satellite during the passage of perihelion "rubs" against the surface of the comet, it leaves a furrow on the soft dusty surface of the comet and raises a plume of dust on both sides of the drawn furrow.

PARTICLE MODEL:

However, one should take into account the morphological changes that occur with dust grains. Based on general considerations, it is obvious that they should become more "fluffy", i.e., the size of a dust particle should increase due to the mutual separation of its constituent fragments.

Moreover, the farther from the center of a dust grain its fragment is, the further it must move away from its center.

For this purpose, a special model was developed, called a radially porous fractal particle (RPFP). It is based on a quasi-fractal particle that combines the hierarchy of roughness at all levels [3]. And then the fragments that make up the particle begin to move away from its center, and the amount of removal is directly proportional to the distance from the center. As a result, the particles shown in Fig. 1 are obtained.

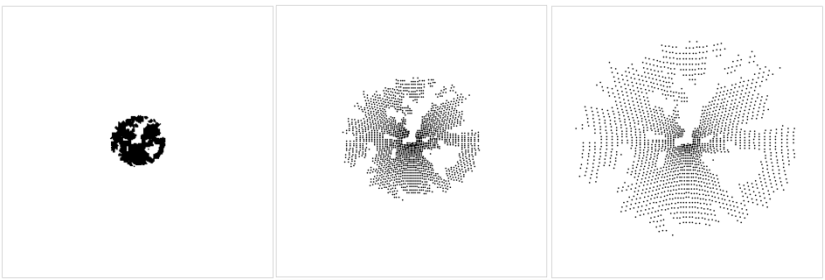

Fig. 1. Examples of RPFP

RESULTS AND DISCUSSION:

The constituent particles are assumed to consist of a mixture of silicates, metals, and carbonaceous materials that is consistent with the composition of the dust in comet Halley [4]. This composition is called Halley's dust, and refractive index of this mixture at λ = 0.45 μm is equal $m = 1.88 + i0.47$ [5]. Program DDSCAT version 7.3.3 [6] was used for computer simulation of characteristics of scattered light. Initial size of RPFP is equal 0.5 mm, and then its size increases by 4 times – up to 2.0 μm. Here, the particle size is the radius of the sphere circumscribed around the particle.

Figure 2 shows the results of the C_{sca} (scattering cross section) calculations. As can be seen from the figure, an increase in the size of a dust grain by a factor of 4 can increase the scattering cross section by 200 times. It should be noted that when the external factor that changes the structure of the particle disappears, it can return to a more compact state under the influence of gravitational forces, which explains the short-term nature of flares on the comet. Therefore, the change in the brightness of comet 29P/Schwassmann-Wachmann 1 can be explained by the change in the internal structure of dust grains under the influence of various factors, such as the gravitational influence of the comet's satellite.

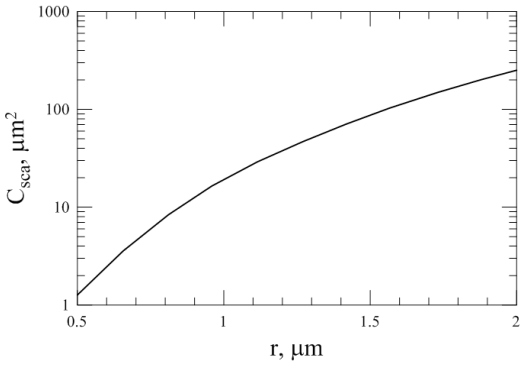

Fig. 2. Scattering cross section of radially porous fractal particle as a function of particle size

CONCLUSIONS:

To explain the comet's 29P/Schwassmann-Wachmann 1 outbursts, we developed a model of dust particles called a radially porous fractal particle, whose size and internal structure change under the influence of external factors. The calculations performed showed that an increase in the size of such a particle by a factor of 4 can increase the scattering cross section of such a particle by about 200 times, which can explain the presence and short-term nature of changes in the brightness of this comet.

REFERENCES:

[1] Trigo-Rodríguez J.M., García Melendo E., García-Hernández D.A., Davidsson B., Sánchez A., Rodríguez D. A continuous follow-up of Centaurs, and dormant comets: looking for cometary activity // European Planetary Science Congress 2008. 2008. Art. No. 811.

[2] Medvedev Yu.D., Pavlov S.R. Explanations for Periodic Comet Flares 29P/Schwassmann-Wachmann 1 // Proc. All-Russia Scientific Conference "The Multifaceted Universe: Theory and Observations – 2022". 2022. Art. No. 148.

[3] Petrov D.V., Zhuzhulina E.A. Polarization properties of quasi-fractal porous particles // J. Quantitative Spectroscopy and Radiative Transfer. 2022. V. 289. Art. No. 108298.

[4] Jessberger E.K., Christoforidis A., Kissel J. Aspects of the major element composition of Halley's dust // Nature. 1988. V. 332. No. 6166. P. 691-695.

[5] Kimura H., Kolokolova L. Mann I. Optical properties of cometary dust-Constraints from numerical studies on light scattering by aggregate particles // Astron. Astrophys. 2003. V. 407. P. L5-L8.

[6] Draine B.T., Flatau P.J. Discrete-dipole approximation for scattering calculations // J. Optical Society of America A. 1994. V. 11. P. 1491-1499.

AGE ESTIMATION OF BRUGMANSIA ASTEROID FAMILY

M.A. Vasileva[1], E.D. Kuznetsov[1]
[1] *Ural Federal University, Yekaterinburg, Russia; vasilyeva.maria@urfu.ru, eduard.kuznetsov@urfu.ru*

KEYWORDS:
asteroid family, numerical simulation, probabilistic evolution, Kholshevnikov metrics, Hill radius, escape velocity

INTRODUCTION:
The Brugmansia asteroid family was discovered by Nesvorný and Vokrouhlický in 2006 [1]. They found three asteroids with very similar heliocentric orbits: (16598) Brugmansia, (190603) 2000 UV80, (218697) 2005 TT99, and estimated the family's age from 50 to 250 kyr. Late Pravec et al. [2] estimated the age of the Brugmansia family as 170^{+60}_{-50} kyr.

METHOD:
The search for new members of Brugmansia family was carried out by calculating the values of the Kholshevnikov metrics ρ_2 and ρ_5 [3]. We found new member of Brugmansia asteroid family – 2006 SK443. At present, four members are known (Table 1).

Table 1. Osculating orbital elements of the Brugmansia family members at epoch 9 August 2022 (MJD 59800.0)

Asteroid	*a*, au	*e*	*i*, deg	Ω, deg	ω, deg
(16598) Brugmansia	2.61992	0.218767	1.625	286.769	105.046
(190603) 2000 UV80	2.62068	0.217999	1.627	286.419	105.835
(218697) 2005 TT99	2.62067	0.220783	1.622	286.225	105.791
2006 SK443	2.61860	0.221796	1.624	285.950	107.023

In the study of probabilistic evolution, 1000 orbital clones were generated for each asteroid based on the Cholesky expansion for multivariate normal distributions. For all six pairs within family, a numerical simulation of the orbital evolution in the past over the time interval of 500 kyr was carried out. We used the Mercury software [4]. We considered 10^6 combinations for each pair. We determined the minimum values of the metric ρ_2 and the minimum reachable distances between asteroids.

Distances between orbits and between bodies must be small at the moment of pair formation. We chose following limits on the physical distance and relative velocity between the clones $r_{rel} \le R_{Hill}$ and $r_{rel} \le 4v_{esc}$, where R_{Hill} and v_{esc} are the radius of the Hill sphere and the surface escape velocity, respectively.

RESULTS:
Pair (16598) Brugmansia – (190603) 2000 UV80.

Close encounters are experienced by 28.1 % pairs of asteroids clones. The minimum distance between asteroids r_{rel} = 472 km (at v_{rel} = 4.4 m·s^{-1}) is reached at the moment t_r = –144345 years. The metric $\rho_2 = 2.9 \cdot 10^{-5}$ au$^{1/2}$ is minimal at t_ρ = –145563 years.

Pair (16598) Brugmansia – (218697) 2005 TT99.

Part of pairs of asteroids clones experiencing close encounters is 22.3 %. The minimum distance between asteroids r_{rel} = 644 km (at v_{rel} = 4.7 m·s^{-1}) is recorded at time t_r = –144519 years. The metric ρ_2 reaches a minimum $2.5 \cdot 10^{-5}$ au$^{1/2}$ at t_ρ = –145745 years.

Pair (16598) Brugmansia – 2006 SK443.

The minimum distance between asteroids r_{rel} = 525 km (at v_{rel} = 5.6 m·s^{-1}) is fixed at the moment t_r = –161550 years. 10.2% pairs of asteroids clones experience close encounters. The metric ρ_2 takes on a minimum value $3.5 \cdot 10^{-5}$ au$^{1/2}$ at t_ρ = –121052 years.

Pair (190603) 2000 UV80 – (218697) 2005 TT99.

Close encounters are experienced by 99.6 % pairs of asteroids clones. The minimum distance between asteroids r_{rel} = 57 km (at v_{rel} = 0.5 m·s^{-1}) and the minimum value of the metric $\rho_2 = 7.2 \cdot 10^{-7}$ au$^{1/2}$ are achieved at t_r = –147768 years and t_ρ = –156182 years, respectively.

Pair (190603) 2000 UV80 – 2006 SK443.

Part of pairs of asteroids clones experiencing close encounters is 1,6 %. The minimum distance between asteroids r_{rel} = 831 km (at v_{rel} = 3.6 m·s^{-1}) is recorded at time t_r = –89188 years. The metric ρ_2 reaches a minimum $2.2 \cdot 10^{-5}$ au$^{1/2}$ at t_ρ = –88478 years.

Pair (218697) 2005 TT99 – 2006 SK443.

Close encounters are experienced by 0.1 % pairs of asteroids clones. The minimum distance between asteroids r_{rel} = 4321 km (at v_{rel} = 3.6 m·s^{-1}) and the minimum value of the metric $\rho_2 = 6.1 \cdot 10^{-6}$ au$^{1/2}$ are achieved at t_r = –110689 years and t_ρ = –141242 years, respectively.

Based on the simulation results, estimates of the Brugmansia family's age is about 145 kyr. This is consistent with age estimates obtained by other authors.

ACKNOWLEDGEMENTS:
The work was supported by the Ministry of Science and Higher Education of the Russian Federation via the State Assignment Project FEUZ-2020-0038.

REFERENCES:

[1] Nesvorný D., Vokrouhlický D. New candidates for recent asteroid breakups // The Astronomical J. 2006. V. 132. No. 5. Art. No. 1950.
[2] Pravec P. et al. Asteroid clusters similar to asteroid pairs // Icarus. 2018. V. 304. P. 110-126.
[3] Kholshevnikov K.V., Kokhirova G.I., Babadzhanov P.B., Khamroev U.H. Metrics in the space of orbits and their application to searching for celestial objects of common origin // Monthly Notices of the Royal Astronomical Society. 2016. V. 462. P. 2275-2283.
[4] Chambers J.E. A Hybrid Symplectic Integrator that Permits Close Encounters between Massive Bodies // Monthly Notices of the Royal Astronomical Society. 1999. V. 304. P. 793-799.

DRIFT TURBULENCE IN DUSTY PLASMA NEAR THE MOON

Yu.N. Izvekova[1], S.I. Popel[1]
[1] *Space Research Institute, Moscow, Russia; izvekova.un@mipt.ru*

KEYWORDS:
drift waves, dusty plasma, lunar exosphere, lunar magnetic anomalies

INTRODUCTION:
The environment near the Moon is a dusty plasma consisting of small particles of lunar regolith, photoelectrons, as well as electrons and ions of the solar wind. When moving around the Earth, a part of trajectory of the Moon passes through the Earth's magnetosphere. In addition, for some areas on the Moon, namely, the so-called lunar magnetic anomalies, the presence of rather intensive magnetic fields is possible: the values of magnetic fields above these areas can exceed the values of the magnetic field of the Earth's magnetosphere in the region of the lunar trajectory by one or two orders of magnitude. The existence of a magnetic field together with number density gradients of photoelectrons can result in the development of drift turbulence. The conditions for excitation of this turbulence are discussed.

PROPERTIES OF PARTICLES IN THE EXOSPHERES OF ACTIVE ASTEROIDS: ESTIMATES BASED ON THE SPECTRAL FEATURES IN THE UV-VISIBLE RANGE

E.V. Petrova[1], V.V. Busarev[2]
[1] *Space Research Institute, Moscow, Russia; epetrova@iki.rssi.ru*
[2] *Sternberg Astronomical Institute Moscow University, Moscow, Russia*

KEYWORDS:
asteroids, spectrophotometry, light scattering, aggregate particles

INTRODUCTION:
In the reflectance spectra of active asteroids (AAs) measured in the visible and near-UV range, unusual details are observed from time to time. They are apparently caused by scattering of light in the exosphere formed by sublimation processes on an asteroid. Examples of the spectra of this kind [1–3] are shown in Fig. 1. To attempt to estimate qualitatively the properties of particles in a presumed exosphere from these spectral details, model reflectance spectra of an AA enveloped by an exosphere composed of aggregates of submicron grains with different morphology and composition, as well as homogeneous submicron particles, were calculated. The particles composing aggregates were assumed to be similar in size to grains in agglomerates of cometary and interplanetary dust. To calculate the scattering characteristics of aggregates, we used the superposition T-matrix method [4].

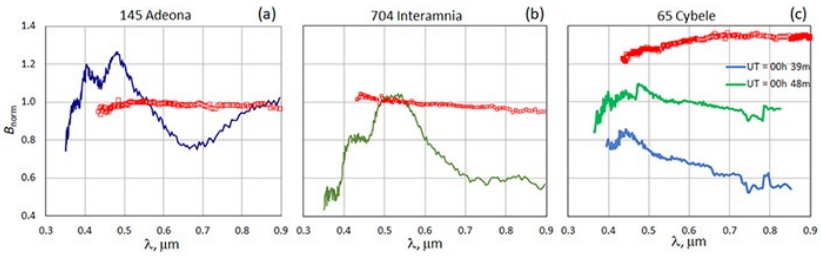

Fig. 1. The reflectance spectra (normalized at 0.55 μm) B_{norm} measured in AAs 145, 704 (in September 2012), and 65 (in September 2016). The classical SMASSII spectra [5] of these asteroids are shown by red symbols. In panel (c) the spectra are shifted in vertical relative each other

RESULTS OF SIMULATIONS:
In agreement with the results of our previous analysis [3, 6], it has been shown that the scattering on aggregates of submicron grains forms interference features at wavelengths λ < 0.6 μm, the position of which is determined by both the sizes of these particles (but not the aggregates themselves) and the real part of the refractive index (see the examples of models in Figs. 2 and 3). However, since the estimates of these parameters, which can be derived from the interference pattern, are interrelated, the shape of the measured spectrum at λ > 0.6 μm, which also turned out to be dependent on the sizes of constituent grains, should also be taken into account for the final conclusions. The position of interference features in the spectra of aggregates is insensitive to the number of aggregate's constituents (i.e., the aggregate's size), and weakly sensitive to the aggregate's structure and variations (up to 20 %) in the sizes of constituents in the aggregate. This is caused by the fact the features at short wavelengths are induced by the interference of waves scattered on individual grains in aggregates, while the interference on groups of grains in aggregates manifests itself at longer wavelengths [6].

Comparison of the model profiles with the spectra measured in asteroids Adeona and Interamnia (Figs. 1a and 1b) suggests that the particles in their exospheres were, most likely, weakly absorbing and contained grains with

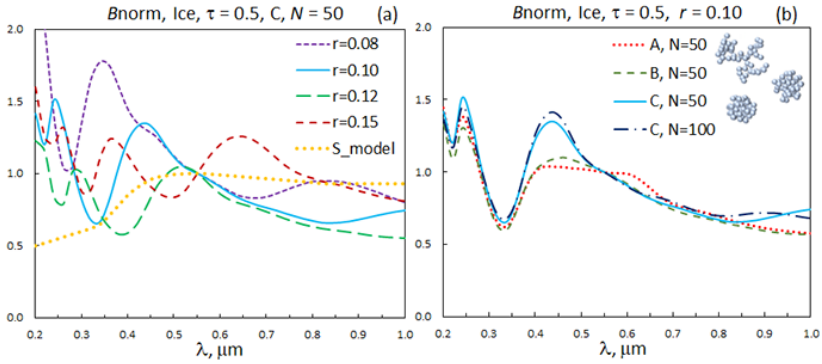

Fig. 2. The models B_{norm} for an AA enveloped by an exosphere composed of ice aggregates with an optical thickness τ = 0.5 at a phase angle of 20°. (a) Models for rather densely packed aggregates (type C shown in the inset in (b)) composed of N = 50 monomers with the radii r (in microns) indicated. The model spectra of a conditional C-type asteroid with the surface albedo $A_s(\lambda = 0.55\ \mu m) = 0.072$ is also shown (S_model). (b) Models for aggregates of different structures (shown in the inset) with N = 50 and structure C with N = 100

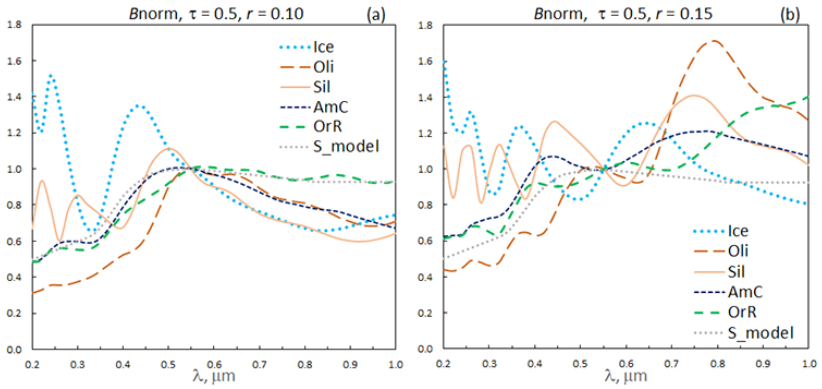

Fig. 3. The models B_{norm} for an AA with an exosphere composed of aggregates of different composition: water ice, olivine, astronomical silicates, amorphous carbon, and organic refractory material. The structures of type C contain 50 monomers of radii 0.10 μm (a) and 0.15 μm (b)

a radius of ~0.1 μm or less. This is evidenced not only by two consecutive (at ~0.4 and ~0.5 μm) maxima in the spectrum of Adeona or "steps" in the spectrum of Interamnia, but also by a steady decline in the spectrum at λ > 0.6 μm. Since the distance between these details in the measured spectra is significantly smaller than that between the interference maxima in the model spectra for any single substance, we may suppose that these details in the measured spectra were formed by scattering on aggregates of different composition, such as ices and astronomical silicates.

Calculations performed for aggregates absorbing in the short-wavelength range (which is characteristic of many matters that can be expected to be detected in AAs) show that the absorption significantly suppresses the interference pattern appeared in this range. Therefore, attempts to detect strongly absorbing particles in the exosphere and to estimate their properties from these spectral details cannot yield reliable results, in contrast to simulations for weakly absorbing particles.

The presence of homogeneous weakly-absorbing submicron particles in the exosphere causes a steady increase in intensity at λ < 0.4–0.5 μm, which may change a positive gradient of the AA spectrum to a negative one, as we see in

the spectra of Cybele (see Fig. 1c). In addition, from the maximum at 0.45 μm in the measured spectra, we may also suppose that Cybele's exosphere contained ice aggregates composed of grains with a radius of ~0.10 μm.

CONCLUDING REMARKS:

The results of the present modeling suggest that the features, which appear in the reflectance spectra of AAs, may be induced by the light scattering on aggregate structures in their exospheres and they may serve as a tool for estimating the properties of these structures in terms of the composition and size of grains composing aggregates. Spectral measurements at $\lambda < 0.35$ μm can help to estimate more confidently the properties of weakly absorbing, both aggregate and homogeneous, particles in the exospheres of AAs.

ACKNOWLEDGEMENTS:

This study is supported by the Russian Science Foundation (grant No. 22-12-00115). Computations of the light-scattering characteristics of aggregates were performed under the support of Ministry of Science and Higher Education of the Russian Federation (grant No. 075-15-2020-780 (N13.1902.21.0039)).

REFERENCES:

[1] Busarev V.V., Makalkin A.B., Vilas F. et al. New candidates for active asteroids: Main-belt (145) Adeona, (704) Interamnia, (779) Nina, (1474) Beira, and near-Earth (162,173) Ryugu // Icarus. 2018. V. 304. P. 83-94.

[2] Busarev V.V., Shcherbina M.P., Barabanov S.I. et al. Confirmation of the Sublimation Activity of the Primitive Main-Belt Asteroids 779 Nina, 704 Interamnia, and 145 Adeona, as well as its Probable Spectral Signs on 51 Nemausa and 65 Cybele // Sol. Syst. Res. 2019. V. 53. P. 261-277.

[3] Busarev V.V., Petrova E.V., Irsmambetova T.R. et al. Simultaneous sublimation activity of primitive asteroids including (24) Themis and (449) Hamburga: Spectral signs of an exosphere and the solar activity impact // Icarus. 2021. V. 369. Art. No. 114634.

[4] Mackowski D.W., Mishchenko M.I. A multiple sphere T-matrix Fortran code for use on parallel computer clusters // J. Quant. Spectrosc. Radiat. Transfer. 2011. V. 112. P. 2182-2192.

[5] http://smass.mit.edu/data/smass/.

[6] Tishkovets V.P., Petrova E.V. Spectra of light reflected by aggregate structures of submicron particles // J. Quant. Spectrosc. Rad. Trans. 2020. V. 252. Art. No. 107116.

LUNAR OBSERVATORY AIMED AT MONITORING AND STUDY OF ENERGY IMBALANCE AND CLIMATE OF THE EARTH, NEAR-EARTH ASTEROIDS AND COMETS, EXOPLANETS, SUPERNOVAE, AND NOVAE

H.I. Abdussamatov[1]
[1] *Pulkovo observatory, Saint Petersburg, Russia; abduss@gaoran.ru*

KEYWORDS:
lunar observatory, earth's energy imbalance, climate, potentially dangerous near-earth asteroids and comets, exoplanets, supernovae and novae, special optical telescope, dust-protecting cup, spectrobolometer

INTRODUCTION:
The only and most reliable way to predict the amplitude and the time of future changes in climate is to study long-term variations in the thermal state of the planet, i.e., the Earth's energy imbalance (EEI). EEI is determined as the difference between the fraction of TSI energy absorbed by the planet and the energy of intrinsic thermal radiation ejected into the space [1, 2]. Scientifically grounded long-term tracking of climate change and reliable forecast of its coming profound changes in the future should be based on highly accurate continuous representative data on the average annual EEI obtained on a constant basis over many decades and centuries. However, modern space integral radiometers on board low orbital and geostationary satellites measurement of the energy of radiation emanating only from individual parts of the planet to the upper hemisphere with large errors and practically only at a certain angle [1, 3]. In addition, all orbital spacecrafts have a relatively short service life. Continuous representative simultaneous observations of the whole Earth's surface during many decades require creation of new highly stable long-term stationary space platforms at sufficient distances from the Earth.

THE LUNAR OBSERVATORY (LO) FOR MONITORING AND STUDY OF THE EEI AND CLIMATE OF THE EARTH:
The Earth-facing surface of the Moon is the only place in space which provide reliable and long-term precise measurements (with the error ~0.1 %) the absolute values of the specific power of energies of the TSI portion reflected and scattered by the Earth and the planet's own thermal energy

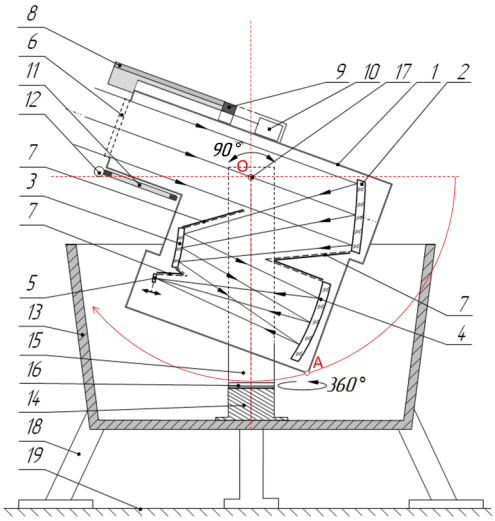

Fig. 1. General view of telescope SOTR-300V in longitudinal section

outgoing into space in all directions. Therefore, since 2012, at the Pulkovo observatory has been actively development the LO – a system of two identical special optical robotic twin-telescopes with sliding visors with primary mirror diameter 300 mm (SOTR-300V) with working field of view 2.2×2.2° in the dust-protecting cup (protecting from charged lunar dust particles). The system of two twin-telescopes, replacing each other in automatic mode, as a single telescope will sequentially survey the entire Earth's surface continuously for during more than 94 % of the time of a lunar day only at lunar nighttime [4, 5]. A matrix micro-bolometer detector of radiation (~2048×2048 pix) and spectral separated wide- and narrow-bands spectrobolometers will equip SOTR-300V for Earth observations. Twin-telescopes will be installed on the equator of the Moon at opposite its edges, on ±(81±0.1°) distance from its visible center. The climatic parameters determined by the LO will be almost an order of magnitude more accurate than the parameters measured by instruments of any modern orbiting spacecraft [1].

THE LO AIMED AT THE SOLUTION OF THE FOLLOWING MOST IMPORTANT PROBLEMS:

- Long-term monitoring and study of the energy flux of the solar radiation reflected by the planet and the outgoing intrinsic thermal radiation within the spectral ranges of 0.2–4 and 4–50 micron, respectively, continuously in the nighttime during more than 94 % of the lunar day;
- For the first time, a study of the most important climate-forming physical process based on long-term monitoring of variations of the latitude distribution of radiation energy flux and on dynamics of variations of the relation of the radiation energy flux between low and high latitudes;
- Long-term monitoring of variations in the integral flux of the intrinsic thermal radiation of the Earth within the range 8–13 micron in the primary transparency window of the atmosphere, in order to study and reveal the contribution of greenhouse gases to climatic variations;
- Studies of variations of Bond albedo of the planet and of physical parameters of the atmosphere and the surface depending on cyclical TSI variations;
- Long-term monitoring and study of the absolute value of integral annual average energy imbalance between the Earth and space – the stored heat or its deficit in the Ocean, using known TSI values; determination of their dependence on cyclical TSI variations, and also on the climate;
- Determination of physical mechanisms of the formation, reasons and regularities of climate change, of the direction and amplitude of its variations;
- For the first time, formation of the lacking extremely necessary and most important fundamental database for high-precision data on EEI and its components;
- Long-term monitoring and study of cloud and snow-ice covers, vegetation, aerosol and ozone concentrations etc., in each region and throughout the whole planet, from the monitoring data in 10 individual narrow bands within the range 0.3–3 micron;
- Continuous all-sky survey: coordinate-photometric monitoring and study of near-Earth asteroids and comets, particularly moving from the side of the Sun, and also of exoplanets, supernovae and novae in the time free of observations of the Earth, sequentially by the system of two twin telescopes within the range 0.2–2 micron.

MONITORING OF OUTGOING ENERGY WITHIN THE RANGE OF THE TRANSPARENCY WINDOW OF THE ATMOSPHERE AND GLOBAL CHANGES OF THE NATURE:

Long-term monitoring of outgoing energy variations within the range 8–13 micron in the transparency window of the atmosphere will make it possible to control and determine the relative contribution of the variation in the concentration of greenhouse gases in the atmosphere to EEI change and climate. And for local and global remote sensing of the Earth ten interference filters are additionally will mounted on the focal plane of the SOTR-300V with

narrow transmission bands cover the range 0.3–3 micron. The images of the sunlit and dark (in the IR range) regions of the planet taken over 24 hours will help survey the state of the terrestrial surface, cloudiness, vegetation, and cryosphere and the aerosol and ozone concentrations for the entire surface and atmosphere.

THE GENERAL CONFIGURATION OF THE SCIENTIFIC PAYLOAD:

SOTR-300V with lightweight mirrors in dust-protecting cup, without solar panels, batteries and soft landing engines, with the mass of one set less than 100 kg, and the dimensions less than 1500×1500×1500 mm, and with the required electric power much less than 100 W. SOTR-300V will install at a height of more than 1000 mm above a surface. A specialized dust-protecting cup of SOTR-300V will be adapted as a landing module with soft landing engines to install the telescope on a required area of the lunar surface. Four patents of the RF (No. 2613048, 2591263, 164303 and 155044 by author Abdussamatov H.I.) protect the system two robotic twin-telescopes LO located in the lunar equator. LO will provide the development of new homogeneous lacking and extremely necessary the most important fundamental database of high-precision annual average EEI value and its components over the period substantially exceeding 15 years. Such database will make it possible to calibrate and determine the dependence of the absolute value of the annual average EEI on cyclical TSI variations, which serves a reliable indicator for reconstruction EEI variations for the total period of high-precision space TSI measurements since 1978. This for the first time will make it possible to reliably and authentically reveal and state physical mechanisms of formation, reasons, and regularities of climate change on our planet for more than 70 years and to develop the most reliable methods of its forecasting. LO is a unique project, because the most important fundamental scientific and applied problems that it solves cannot be carried out with any other means: no alternative “non-lunar” solutions of this most important problem exist.

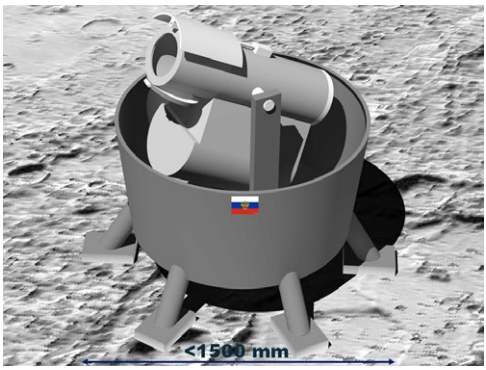

Fig. 2. General view of SOTR-300V on the lunar surface (solar panels, soft landing engines and sun lens hood are not indicated)

LO ALSO AIMED AT MONITORING AND STUDY OF POTENTIALLY DANGEROUS NEAR-EARTH ASTEROIDS AND COMETS, EXOPLANETS, SUPERNOVAE, AND NOVAE:

In the time free of observations of the Earth, the system of two twin telescopes will simultaneously and sequentially, taking turns, carry out continuous survey of the stellar field of the entire sky (within the total spectral range of 0.2–2 micron and its three individual broad bands) in the entire broad working field of view 2.2×2.2° in the mode of coordinate-photometric monitoring and study of potentially dangerous near-Earth asteroids and comets, especially those approaching the Earth from the side of the Sun, potentially habitable exoplanets, supernovae and novae with a resolution of ~1″/pixel. To protect the lens of the telescope from solar and Earth’s radiation at the angular separation of more than 15°, the hood will be used, consisting of two halves of a cylinder, fold back to horizontal sides along the tube in the course

of observations of the Earth and transportation. The telescopes will also use another exchangeable (single or mosaic) CCD matrix ~(8000×8000 pix) as the radiation detector. The system of SOTR-300V twin telescopes can carry out the complete cycle of the survey of stellar field of the entire sky in continuous observations with the exposure of 30 s for the time about 100 hours. An individual survey of an area of the sky around Sun can be carried out for about 10 hours. Since in LO telescopes direct falling of the solar radiation in the entrance pupil is shielded by the hood, the telescopes can also detect asteroids and comets approaching the Earth from the side of the Sun (at an angular separation exceeding 15°), thereby contributing very substantially into planetary defense. SOTR-300V telescopes of LO will be able to detect asteroids with the diameter more than 10 m, which present the highest hazard. LO will become a professional "Space Patrol" aimed at early detection of near-Earth asteroids and comets, especially those approaching the Earth from the side of the Sun. The continuous survey of stellar field of the entire sky will also make it possible to simultaneously continuously search and study potentially habitable exoplanets (using the transit technique). Lunar telescopes will observe planets around other stars «directly», tracking their transits across the disks of their parent stars. The telescope system will also continuously search and study supernovae and novae in all areas of the sky.

REFERENCES:

[1] Abdussamatov H.I. Comparative analysis of errors in monitoring the Earth's global energy budget by the Lunar Observatory and orbiters // Izvestiya, Atmospheric and Oceanic Physics. 2018. V. 54. No. 9. P. 1341-1352.
[2] Abdussamatov H.I. Energy imbalance between the Earth and space controls the climate // Earth Sciences. 2020. V. 9. No. 4. P. 117-125.
[3] Trenberth K.E., Fasullo J.T., Kiehl J. Earth's global energy budget // Bull. Am. Meteorol. Soc. 2009. V. 90. P. 311-323.
[4] Abdussamatov H.I. Lunar Observatory for the study of the deviation of the Earth's energy balance from the equilibrium state and the causes of climate change // Issledovanie Zemli iz kosmosa. 2016. No. 5. P. 79-88. (In Russian.)
[5] Abdussamatov H.I. Lunar Observatory for monitoring the radiation balance of the Earth and climate // IOP Conf. Ser.: Earth. Environ. Sci. 2022. V. 1040. Art. No. 012001.

ABOUT THE 11th EDITION OF THE GLOBAL TRAJECTORY OPTIMIZATION COMPETITION HELD IN 2021 – "DYSON SPHERE" BUILDING

A.S. Samokhin[1], M.A. Samokhina[1]
[1] *Institute of Control Sciences RAS, samokhin@ipu.ru, ph@ipu.ru*

KEYWORDS:
GTOC 11, Dyson sphere, asteroids moving, numerical simulations, trajectory optimization

INTRODUCTION:
The Global Trajectory Optimization Competition – GTOC was first organized by Dario Izzo of ESA in 2005 [1]. The 10th competition held in 2019 was won by the NUDT-XSCC team from China, who presented the problem for the 11th issue of GTOC held in 2021.

PROBLEM STATEMENT:
The setting was futuristic, requiring the construction of part of Dyson's sphere from the asteroids of the solar system after 100 years from the present day.

The task consisted of two big parts. In the first part it was necessary to use up to 10 ships launched from Earth with hyperbolic excess speed. These ships could, install special engines – asteroid transfer devices on the asteroids while passing them. The second part of the task was to send the asteroids to the 12 stations under construction.

The problem takes into account the attraction of the Sun only. The elliptical orbits of 83453 asteroids and their masses were given to the participants in a separate file. A total of 12 stations were required to be placed in one circular orbit around the Sun at an angular distance 30° in relation to each other.

The task of the participants was to maximize the functional J. The goal was to make the mass of the lightest station built as much as possible, so that the ring was as close to the Sun as possible and the spacecrafts carried out as little momentum as possible.

All flights must take place between 2121 and 2141.

The solution to the problem was given 4 weeks, participants who sent the solution earlier received a bonus.

RESULTS:
GTOC 11 was won by the TsinghuaLAD&509 team from China with 388 asteroids involved in the construction, the value of the functional $J = 8443$. They first used the construction of a special library of asteroid chain flyovers, beam search, genetic algorithm with the consideration of a single ship's trajectory as a gene, Lambert problem solving and greedy algorithm for pulse problems. And then used their own algorithm for optimization trajectories with low thrust.

The next GTOC 12 competition will be held in June 2023.

REFERENCES:
[1] Izzo D. 1st ACT global trajectory optimisation competition: Problem description and summary of the results // Acta Astronautica. 2007. V. 61. Iss. 9. P. 731-734. DOI: 10.1016/j.actaastro.2007.03.003.
[2] GTOC 11 Homepage. URL: http://sophia.estec.esa.int/gtoc_portal/?page_id=782 (accessed: 10/08/2022).

SESSION 6. VENUS (VN)
ORAL SESSION

GEOLOGICAL HISTORY OF THE NORTH REGION OF POLIK-MANA MONS, VENUS

V.E. Rozhin[1], R.E. Ernst[1,2], H. El Bilali[1,2]
[1] *Faculty of Geology and Geography, Tomsk State University, Tomsk, Russia; vadimroz@mail.ru*
[2] *Department of Earth Sciences, Carleton University, Ottawa, Canada*

KEYWORDS:
Polik-mana Mons, lava flow, grabens, geological history, Venus

INTRODUCTION:
The Polik-mana Mons volcano (24.8° N, 264° E) is located in the Asteria Regio lowlands along Latona Chasma which is the part of the 7000 km long Hecate Chasmata rift zone and 1500 km west of Beta Regio (Fig. 1). Polik-mana Mons is a large volcano with a diameter of 600 km.

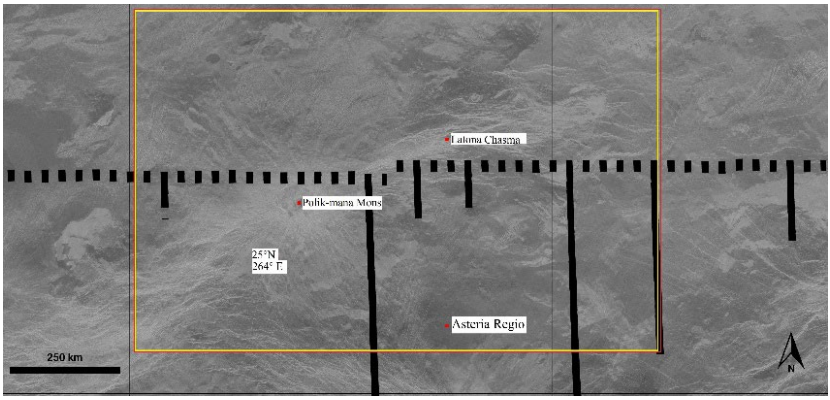

Fig. 1. Magellan SAR image of the Asteria Regio region with main features labelled

We have selected this Asteria Regio region (see Fig. 1) for the present study to characterize its volcanic history through detailed mapping (1:500 000 scale). Such Venus volcanism is analogous to Large Igneous Provinces (LIPs) on Earth [1–3] and provides a complementary view, given the absence of erosion on Venus at this time [4], when compared to the erosion that can deeply dissect terrestrial LIPs.

Our mapping of this region at 1:500 000 is 10x more detailed than previous mapping. The western part of the area of our research is in Hecate Chasma V-28 quadrangle which was mapped at 1:5 000 000 [1].

The goals of this research of Asteria Regio are: 1) detailed mapping of graben systems (interpreted to overlie dyke swarms) and linking them to specific magmatic centers; 2) detailed mapping of the lava flows and identification of the specific sources for each of them; 3) determining the relative ages of dykes and flows and developing a geological history for the area; 4) determining the geodynamic relationship with the plume-related magmatism of Beta Regio, centered about 1,000 km to the east; and 5) considering implications for improved understanding of terrestrial LIPs.

Lava flows

In our work we have distinguished three types of lava flows according to their brightness on the Magellan SAR images: dark, grey and light, reflecting the strength of radar reflection back to the spacecraft and corresponding to the orientation and roughness of the surface.

We have constructed two maps of lava flows distributions for Polik-mana Mons and the adjacent territory. The first map (Fig. 2) shows the lava flows according to their radar brightness. Figure 3 shows different lava flow groups distinguished by color.

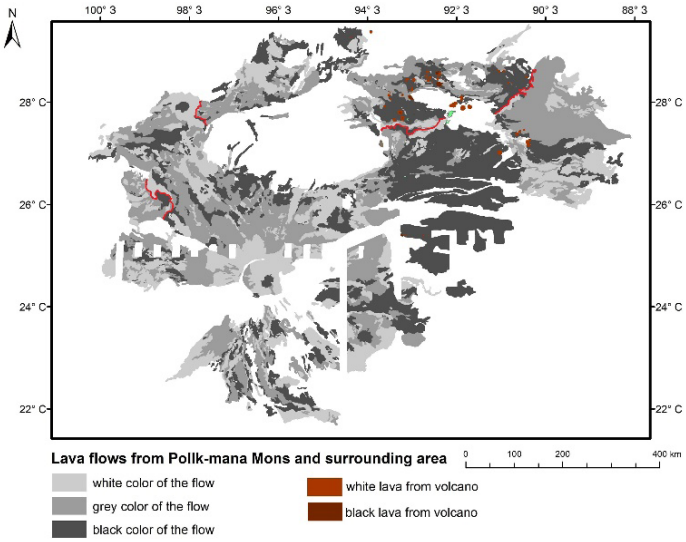

Fig. 2. Distribution of main flow units of Polik-mana Mons and surrounding area. The red lines on the map show the contacts boundaries of individual lava flows

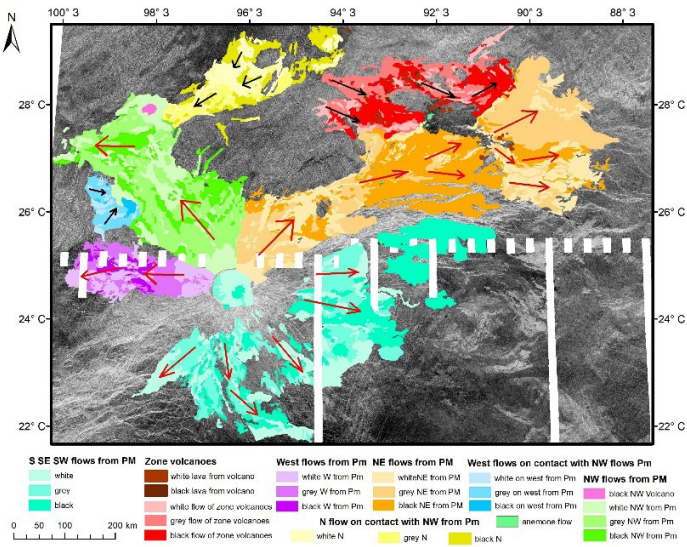

Fig. 3. Distribution of lava flow units of Polik-mana Mons and surrounding area with the main directions of flow distribution (maps in color with divisions into groups)

The lava flows in this area are dense or solidified flows of molten rocks that are predominantly basaltic in nature. The white streams have a rough surface, which tells us that this lava material has already mostly solidified and erupted much earlier than the dark-colored streams. The gray streams represent a transitional phase from a dense and viscous material to a hardened and rough one. Correspondingly, the black color represents the youngest streams, which have a viscous smooth surface.

At this stage of the mapping, 7 lava flow groups were identified, 4 belonging to Polik-mana Mons and 3 which are not related to the Polik-mana volcano (blue, red, yellow streams) (ыуу Fig. 3). Within these groups, 3 main types of flows were identified according to the properties described earlier. By carrying out zonal statistics, we were able to determine a number of basic parameters for each of the types of flows (Table 1).

Table 1. Table of zonal statistics. Characteristics of each lava flow group Colors match the units shown in Fig. 3. A thickness of 25 m was chosen to measure the volume of the lava flow

Name	Area,km^2	Max point, m	Min point, m	Range, m	Majority, m White/grey/black	V,km^3
S-SE-SW flows from Pm	92 188	5 830	-338	6 168	1 290/1 628/1 293	2 305
Zone volcanoes	37 672	2 168	392	1 776	1 275/1 470/1 359	942
West flows from Pm	21 151	4 808	1163	3 645	1 325/2 071/1 336	529
NE flows from Pm	126 501	4 824	-1856	6 680	2 049/ 647/1 018	3 163
N flows on contact with NW from Pm	26 601	2 308	469	1 839	1 176/937/1 162	665
W flows on contact with NW flows from Pm	7 538	2 041	1123	918	1 710/1 663/1 248	188
NW flows from Pm	64 984	4 766	536	4 230	963/911/975	1 625

According to the collected statistics it is possible to make some following conclusions:

1. The total volume of the lava material of northern, eastern and western directions, which source is Polik-mana Mons is – 5317 km^3 (Area = 239 840 km^2). The volume of all mapped lava material is 9417 km^3 (Area = 376 651 km^2). The volume of all mapped material, which belongs to Polik-mana Mons is 7622 km^3 (Area = 304 840 km^2). A thickness of 25 m was chosen to measure the volume of the lava flow.
2. The greatest volume of lava material is the north-east flow, which tells us that this zone has a large number of lava sources.
3. Most of the lava flows accumulate in areas with elevation values between 1200 and 1400 m.
4. The greatest concentration of the three types of lava (by radar brightness) is as follows: “white” lava in the central part of the P-m volcano and its slopes; “gray” lava in the northwestern part of the study area, and near the end of the eastern northeastern flow; and “black” lava in the northeastern and eastern sections of the study area.

REFERENCES:

[1] Head J.W., Coffin M.F. AGU Geophys. Monograph. 1997. V. 100. P. 411-438.
[2] Ernst et al. // Superplumes: Beyond Plate Tectonics. Springer, 2007. P. 537-562.
[3] Buchan K.L., Ernst R.E. Plumbing systems of large igneous provinces (LIPs) on Earth and Venus: Investigating the role of giant circumferential and radiating dyke swarms, coronae and novae, and mid-crustal intrusive complexes // Gondwana Research. 2021. V. 100. P. 25-43. https://doi.org/10.1016/j.gr.2021.02.014.
[4] Khawja S. et al. // Nature Communications. 2020. V. 11. Art. NO. 5789.

MAPPING OF LAVA FLOWS OF THEIA MONS, BETA REGIO, VENUS

A.S. Shimolina[1], R.E. Ernst[1,2], H. El Bilali[1,2]
[1] *Tomsk State University, Faculty of Geology and Geography, Tomsk, Russia; arina051299@gmail.com*
[2] *Department of Earth Sciences, Carleton University, Ottawa, Canada*

KEYWORDS:
Theia Mons, Beta Regio, volcanoes, Venus, planetary geology

INTRODUCTION:
Theia Mons is one of the most important volcanic edifices on Venus (Fig. 1). It is centered at 22.7° N, 281.0° E (101.0° W) on Beta Regio, which along with Atla and Themis Regio, define the BAT (Beta-Atla-Themis region) as a region with some of the youngest volcanic and tectonic activity of Venus. Beta Regio is thought to represent a currently active plume in that it is topographically elevated, has an associated geoid high, is the center of a triple junction rifting system [1] and is also the focus of a giant radiating dyke swarm [2].

The northern half of Theia Mons has been previously mapped at 1:5 000 000 scale as part of Beta Regio Quadrangle (V-17) [3]. The southern half of Theia Mons is located in Devana Chasma Quadrangle (V-29), and initial 1:5 000 000 mapping of this quadrangle was reported in [4]. The global compilation of [5] catalogued this as Theodora Patera (24.0° N 280.5° E) with a diameter of 1000 km [5]. In later publications [1, 3] it is referred to as Theia Mons and we use this name here.

General view and objectives:

Theia Mons consists of a volcanic edifice which is 500 km across and 2.5–3 km high with a deep central caldera (2.5 km deep) which is about 50 km across (see Fig. 1). Flows can be traced up to at least 650 km away from the central edifice. The radiating dyke swarm (recognized by their surface expression as grabens) can be linked to a regional linear N-S swarm suggesting an overall swarm length of 3,400 km [2]. The transition in the dyke swarm pattern from the radiating to linear pattern at 1000 km is interpreted to mark the outer boundary of the underlying flattened plume head [6].

The focus of this research is detailed mapping of Theia Mons at a scale of 1:500 000 with the following goals: 1) identify the sources of all mapped flow units, 2) integrate the emplacement of flows with graben system (dyke swarm) emplacement and central caldera collapse (above a central magma reservoir); 3) characterize the relationship with the triple junction rifting; and 4) develop a comprehensive geological history of Theia Mons in order to better constrain the geodynamic evolution of Beta Regio plume event. The results of detailed graben-fissure mapping were reported in [7]. Here we focus on mapping of the lava flows.

LAVA FLOW MAPPING:
Initial mapping of lava flows indicates multiple generations of lavas. The area around the volcano was provisionally divided into four sectors.

Eastern sector:

We have identified at least three large lava generations of different ages, each of which has three to five separate flows. Here and below, color filled polygons denote lava flows separated by relative age. Lava flows marked with a colored line (but not filled with color) are currently not separated by relative ages, but are presumably older than the color-filled ones. The flows highlighted in shades of yellow are interpreted to be the oldest since its flows are overlapped by younger lavas of subsequent generations. The source is the central caldera of the volcano. The next generation is highlighted in blue. We hypothesize that the lava flows here originate from a parasitic vent located to the east of the central caldera and overlap the lava of the previous generation. The last generation is represented by pink flows, the source of which is presumably the graben system in the north of the volcano. The option of their origin from the central caldera or from another vent obscured by subsequent rifting is also considered.

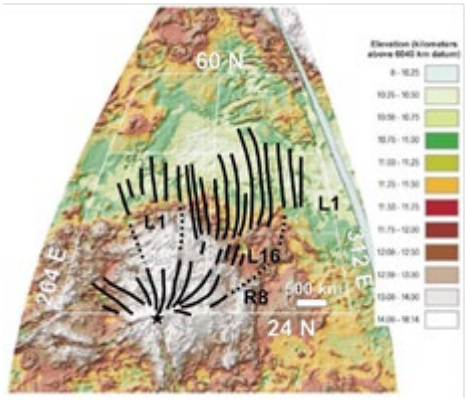

Fig. 1. Topographic map of Beta Regio showing elevated topography centered on Theia Mons (star) and associated with potential radiating swarms that swings into a common trend after 1000 km (modified after [2])

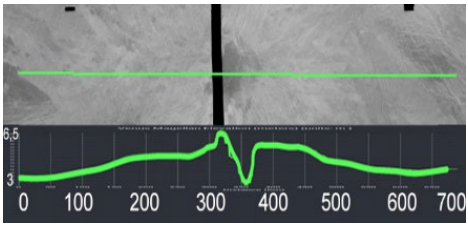

Fig. 2. W-E topographic profile across Theia Mons reveals an edifice 500 km across with a deep central caldera which is about 50 km across. Flows can be traced up to at least 650 km away from the central edifice. The SAR image of Theia Mons is 750 km across. Vertical exaggeration 15x.

Southern sector:

The lava flows here are largely damaged by Devana Chasma rifting and other various faults. For now, lava flows here are combined into one generation.

Western sector:

At the moment, one large generation of lava flows of a complex structure has been identified (poor visibility of many flow boundaries has complicated the recognition of individual flows) (Fig. 3, blue). Based on the analysis of the topography of this area and the interaction of flows with faults, it is hypothesized that the lava flows erupted here prior to the subsidence of the area, since otherwise the lava would have flowed in a southwesterly direction.

In the west, there is one large complex lava flow that changes direction from northwest to west. This change in flow direction is thought to be related to the topography of the area rather than a change in lava source.

Northern sector:

The eastern part of the sector is as difficult to map as the south of the volcano, due to the younger Devana Chasma rifting. In the eastern part there is an interesting group of lava flows. We interpret that their source was not the central caldera of Theia Mons. Rather we propose that these lava flows originated from grabens (overlying dykes) emplaced prior to the Devana Chasma rifting. The possibility of another large caldera hidden under the grabens of Devana Chasma and the lava flows of Theia Mons is also being considered. Such a cryptic caldera may be indicated by some radial and concentric swarms of dikes.

GRABENS AND FUTURE WORK:

Theia Mons is surrounded by many graben systems of different (tectonic and magmatic) origin. Preliminary mapping of these were discussed in a previous

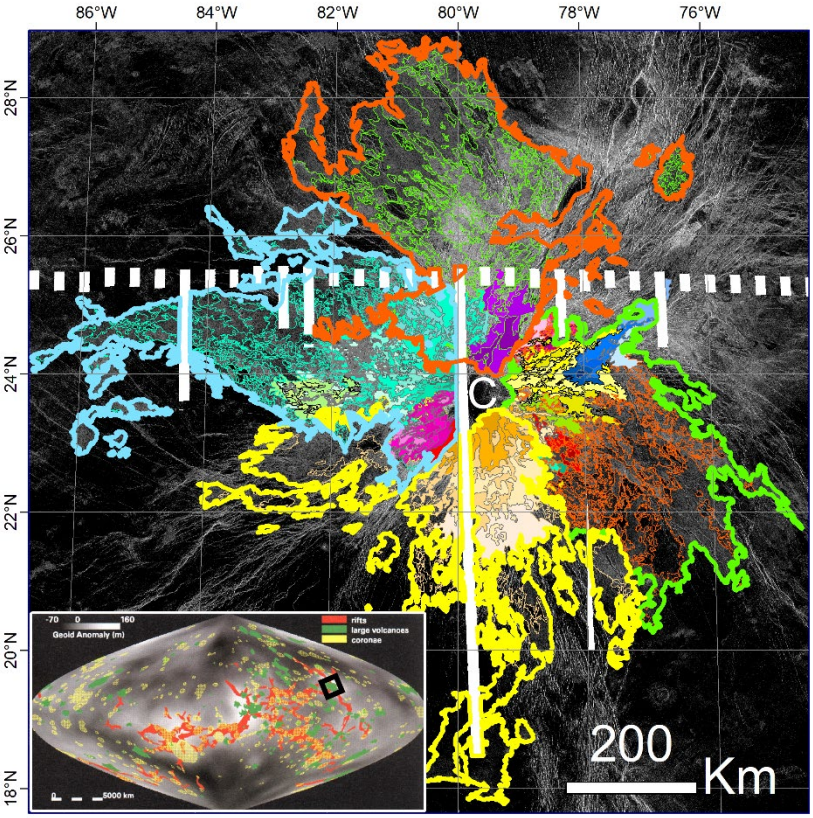

Fig. 3. Mapping of Theia Mons' lava flow units. Colored contours divide volcano into 4 sectors (green contour is for Eastern sector, yellow for Southern, blue for Western and orange for Northern). "C" is for central caldera. In the lower left is a map of Venusian rifts and volcanoes with Theia Mons marked with black box

abstract at LPSC 2022 [7]. Since graben systems are important to understanding of magmatic history, the graben systems of Theia Mons will be fully mapped and characterized in future papers, along with description of relative ages of grabens and lava flows and development of a comprehensive geological history of Theia Mons and surrounding area.

ACKNOWLEDGMENTS:
Magellan SAR images obtained from https://astrogeology.usgs.gov/search/ ?pmi-target=venus based on the data from https://pdsimaging.jpl.nasa.gov/ volumes/magellan.html#mgnFMAP.

REFERENCES:

[1] Basilevsky A., Head J.W. // Icarus. 2008. V. 192. P. 167-186.
[2] Ernst R.E. et al. // Icarus. 2003. V. 164. P. 282-316.
[3] Basilevsky A.U.S. Geological Survey Scientific Investigations Map 3023. 2008.
[4] Tandberg E.R., Bleamaster L.F. // LPSC XLI. 2010. Abstr. No. 1816.
[5] Crumpler L.S., Aubele J.C. // Encyclopedia of Volcanoes / ed. Sigurdsson H. Academic Press, 2000. P. 727-769.
[6] Ernst R.E., Buchan K.L. // Geological Society of America. 2001. Special Paper 352. P. 247-265.
[7] Shimolina A.S., Ernst R.E., El Bilali H. // LPSC LIII. 2022. Abstr. No. 1153.

GEOLOGICAL HISTORY OF SAMODIVA MONS REGION, DEVANA CHASMA QUADRANGE V-29, VENUS

D.G. Malyshev[1], R.E. Ernst[1,2], H. El Bilali[1,2], M.A. Ivanov[3,4]
[1] *Faculty of Geology and Geography, Tomsk State University, Tomsk, Russia; malyshev.danil13@gmail.com*
[2] *Department of Earth Sciences, Carleton University, Ottawa, Canada*
[3] *Vernadsky Institute of Geochemistry and Analytical Chemistry RAS, Moscow, Russia*
[4] *Department of Geological Sciences, Brown University, Providence, USA*

KEYWORDS:
Samodiva Mons, Venus, planetary geology, graben, lava flows, geological history

INTRODUCTION:
Samodiva Mons (13.6° N, 291.0° E) and surrounding area (Fig. 1) are located east of Beta Regio major plume center [1], at the southern end of Hyndla Regio, a flat-topped highland consisting mostly of tesserae [2, 3]. The Samodiva area is within Quadrangle V-29, for which some 1:5 M scale mapping has been done [4]. In the present research we focus on detailed 1:500 000 scale mapping. Overall width of the edifice is 150 km and a central summit caldera has 25 km in diameter and up to 500 m deep.

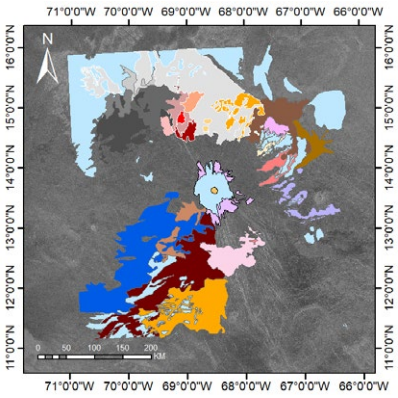

Fig. 1. Currently mapped geological units. Colors indicate different units and lava flows

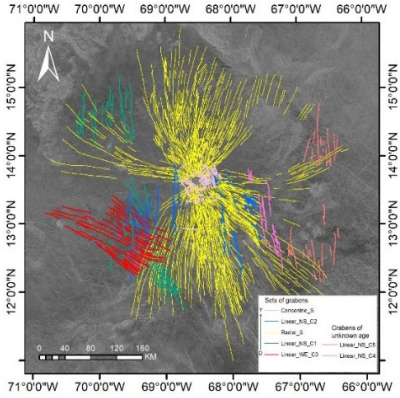

Fig. 2. Graben-fissure systems (interpreted to overlie dyke swarms). Colors represent different dyke swarms

GRABEN SYSTEM HISTORY:
From the mapping of graben systems, which can be interpreted to overlie dyke swarms [5], seven different trends of dykes were distinguished (Fig. 2). The most pervasive radial (yellow lines, **Radial_S**) and circumferential (white lines close to the center, **Concentric_S**) originate from Samodiva Mons; the sources of the five other graben systems are not yet identified. There are two north-south trends to the west of Samodiva Mons (blue and green lines, **C1–C2**). The northwest-southeast trend (red lines, **C3**) probably originates from Zhivana corona further to the west. On the east side there are three north-south trends (blue, pink, pale pink lines, **C1**, **C4–C5**), **C4** most likely has an unnamed corona to the north-east as the source. The age relationships, based on cross-cutting relationships, are (oldest to youngest): **C3**, **C1**, **Radial_S**, **C2**, **Concentric_S**. The relative ages of **C4** and **C5** are not yet constrained.

NORTH SECTOR HISTORY:
Most of this sector consists of tesserae terrain (**t**) and regional plains (**rp**) (Fig. 3). The latter group of units can be divided in several units by their

backscatter, which might indicate different covering by aeolian activity, the cause of which is probably a debris from the surrounding tesserae. There are also distinct lava flows superimposed on regional plains, five of them are probably originating from dykes underlying grabens (**fSM-N-1…-5**), another one (**fSM-N-6**) has a small shield volcano as a source. North-Northeast sector is also filled with regional plains covered by debris from the surrounding tesserae. Apart from that, the vast area is covered by flows (**fSM-NNE-1, -2**) superimposed on regional plains and originating from dykes underlying grabens. The whole area is superimposed by wrinkle ridges (**wr**), which are less abundant closer to the volcano's summit, covered by younger flows.

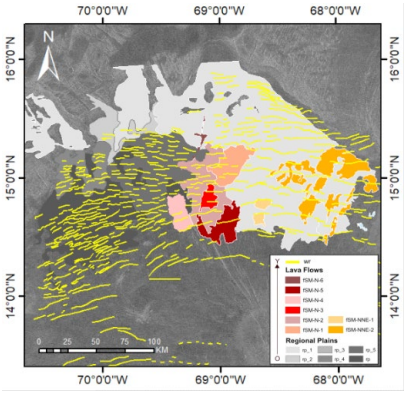

Fig. 3. Geological map of the North sector

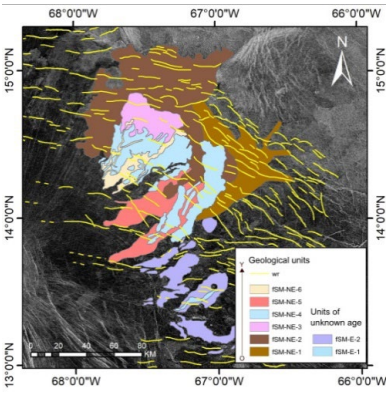

Fig. 4. Geological map of the East sector

EAST SECTOR HISTORY:

There are at least five lava flow units, all of which originated on Samodiva Mons' summit, and are distinguished by trends and radar backscatter (**fSM-NE-1…6 and fSM-E-1, -2**) (Fig. 4), which are superimposed on regional plain. Wrinkle ridges serve as a relative age marker in this area, gradually reduced to the summit and cover the whole sector. Being superimposed on **fSM-NE-1, -2** they are covered by **fSM-NE-2, -3** and **fSM-E-1, -2**. To the east-northeast, due to local topography, flows start to curve in a northern direction.

SOUTH-SOUTHWEST SECTOR HISTORY:

This sector is covered by vast lava flows, which may have been sourced from Samodiva Mons or be a part of regional plain (Fig. 5). The area is dominated by tesserae terrain, which is crosscut by various flows. This sector is also characterized by a lower density of wrinkle ridges as compared to the North and East sectors, which may indicate a younger age of South sector units.

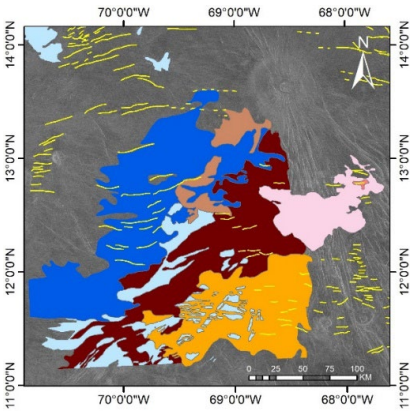

Fig. 5. Geological map of the South sector

SUMMARY:
At this stage of mapping it can be concluded that: 1) Grabens (interpreted to overlie dyke swarms) can be grouped into at least seven sets on the basis of trends and cross-cutting relationships; 2) Regional plains on the North seem to be older than lava flows and covered by aeolian debris from tesserae; 3) On the east side there are several distinct lava flows originating from Samodiva Mons, and these are interpreted to be younger than the yellow radiating graben system; 4) Most of the map area is covered by wrinkle ridges, which may serve as a marker of relative ages.

ACKNOWLEDGMENTS:
Magellan SAR images obtained from https://astrogeology.usgs.gov/search/?pmi-target=venus based on the data from https://pdsimaging.jpl.nasa.gov/volumes/magellan.html#mgnFMAP.

REFERENCES:
[1] Basilevsky A.T., Head J.W. Beta Regio, Venus: Evidence for uplift, rifting, and volcanism due to a mantle plume // Icarus. 2007. V. 192. P. 167-186.
[2] Basilevsky A.T. Geologic Map of the Beta Regio Quadrangle (V–17), Venus / United States Geological Survey. 2008. Scientific Investigations Map 3023. 36 p. https://doi.org/10.3133/sim3023.
[3] Ivanov M.A., Head J.W. Global geological map of Venus // Planetary and Space Science. 2011. V. 59. P. 1559-1600.
[4] Tandberg E.R., Bleamaster L.F. Geologic mapping of the Devana Chasma (V-29) Quadrangle, Venus: preliminary report // 41st Lunar and Planetary Science Conf. 2010. Abstr. No. 1816.
[5] Buchan K.L., Ernst R.E. Plumbing systems of large igneous provinces (LIPs) on Earth and Venus: Investigating the role of giant circumferential and radiating dyke swarms, coronae and novae, and mid-crustal intrusive complexes // Gondwana Research. 2021. V. 100. P. 25-43.

PREM-BASED MODELS OF VENUS' INTERIOR STRUCTURE

D.O. Amorim[1], T.V. Gudkova[2]
[1] *Moscow Institute of Physics and Technology, Moscow, Russia; amorim.dargilan@gmail.com*
[2] *Schmidt Institute of Physics of the Earth RAS, Moscow, Russia*

KEYWORDS:
Venus' interior, moment of inertia, tidal Love numbers, viscoelasticity

INTRODUCTION:
A better understanding of Venus' interior structure is crucial to reconstruct the planet's history and explain the unusual geologic processes that took place at its surface. In this work we have built 72 PREM-based models of Venus that differ in crust thickness, core size and density profile. The analysis of the modeled pressure distributions allowed us to conclude that Venus' core probably is entirely liquid. Moment of inertia, tidal Love numbers and the tidal phase lag have also been calculated. They provide valuable information about Venus' interior structure when compared with the experimental estimates [1, 2].

VENUS' MODELS:
Our models differ in crust thickness (30, 50 and 70 km), core radius (from 2800 to 3500 km) and density profile. As it was suggested in [3], the mantle equation of state $\rho_m(P)$ is defined as $\rho_m(P) = A\rho_0(P)$, where P is the pressure; A is a coefficient near 1 and $\rho_0(P)$ is the PREM's equation of state. Similarly, the liquid core equation of state $\rho_c(P)$ is given by the expression $\rho_c(P) = B\rho_0(P)$, where B is also a coefficient near 1. We analyze models with three values of B: 1.00, 0.99 and 1.01, representing respectfully an Earth-like core, a lighter core and a heavier core. For each model the value of A is chosen so that the mass condition is satisfied (Venus' mass = $4.8669 \cdot 10^{24}$ kg [4]). Models with large cores (3400–3500 km) have lighter mantles ($A < 1$), while models with small cores (2800–2900 km) have heavier mantles ($A > 1$).

CORE STATE:
The pressure profile is computed for all models and the obtained values at the center of Venus are shown in Fig. 1. They range from 260 to 310 GPa, which is considerably lower than the pressure at Earth's inner core boundary (328.8 GPa according to PREM [5]). This indicates that Venus' core should be entirely molten if its composition is similar to Earth's.

MOMENT OF INERTIA:
The computed values of the moment of inertia (Fig. 2) lie in the range of 0.323 to 0.347, which is in accordance with the experimental value [1]. Unfortunately, the measured value [1] is not precise enough to constrain Venus' internal structure.

TIDAL LOVE NUMBERS:
In order to account for the viscoelasticity, we use Andrade rheology as suggested in [6]. The α parameter of Andrade rheology is often considered to lie between 0.2 and 0.5. For $\alpha = 0.2$ the viscoelasticity effect on k_2 and h_2 is considerably stronger than for $\alpha = 0.5$. We compute the tidal Love numbers for both of these values.

In this work we consider two viscosity distributions:

1. Low viscosity model
   a. Crust viscosity – 10^{21} Pa·s;
   b. Upper mantle viscosity – 10^{19} Pa·s;
   c. Lower mantle viscosity – 10^{21} Pa·s;
2. High viscosity model
   a. Crust viscosity – 10^{23} Pa·s;
   b. Upper mantle viscosity – 10^{21} Pa·s;
   c. Lower mantle viscosity – 10^{23} Pa·s;

The tidal Love numbers k_2 and h_2 and the tidal phase lag have been calculated for the models with a crust thickness of 30 km and a B value of 1.00. The k_2 values are shown in Fig. 3. For a better analysis of the models, a probability distribution based on the moment of inertia and k_2 values is shown in Fig. 4.

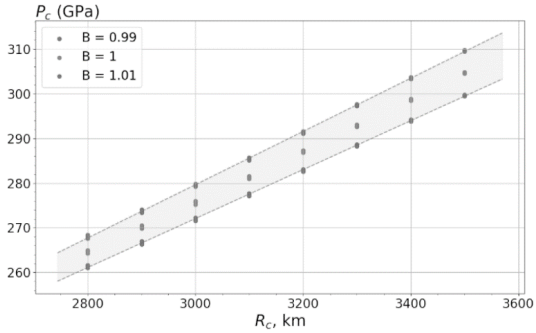

Fig. 1. Pressure at the center of Venus (P_c) in GPa for all models. The core radius and B strongly affect P_c, while the crust thickness does not

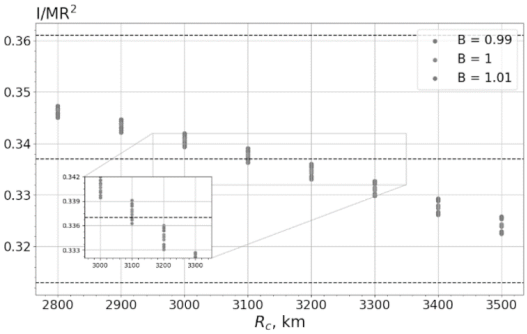

Fig. 2. Moment of inertia values of all 72 models. Dashed lines represent the measured value 0.337±0.024 [1]

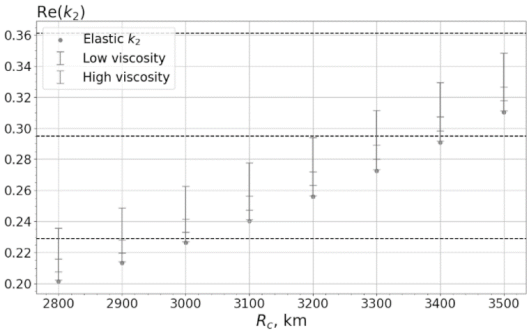

Fig. 3. k_2 values for models with a crust thickness of 30 km and B = 1.00. Bars represent the variation of k_2 due to the uncertainty of the rheological parameter α. Dashed lines represent the measured value 0.295±0.066 [2]

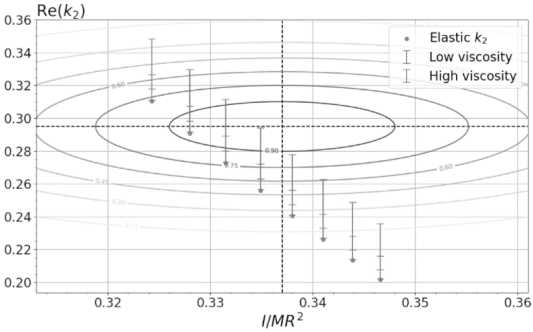

Fig. 4. Probability distribution of models (grey solid lines) based on the measured values of the moment of inertia (0.337±0.024 [1]) and tidal Love number k_2 (0.295±0.066 (2σ) [2])

CONCLUSION:

The pressure at the planet's center varies from 260 to 310 GPa depending on the model. These values are considerably lower than the pressure value at Earth's inner core boundary and indicate that Venus' core should be entirely liquid. It could only be partially solid if its composition were very different from Earth's core composition.

The comparison between the calculated values of the tidal Love number k_2 and its estimate from the Magellan mission [2] shows that a core radius in the range between 3100 and 3500 km is preferable to smaller ones. For low viscosity profiles this range could be narrowed to 3100–3400 km, while for high viscosity profiles to 3200–3500 km. Precise measurements of Venus' moment of inertia, tidal Love numbers and tidal phase lag would help us constrain the planet's structure.

ACKNOWLEDGEMENTS:

This work is financially supported by the budget funding of Schmidt institute of the Earth RAS.

REFERENCES:

[1] Margot J.-L. et al. Spin state and moment of inertia of Venus // Nature Astronomy. 2021. V. 5(7). P. 676-683.
[2] Konopliv A.S., Yoder C.F. Venusian k2 tidal Love number from Magellan and PVO tracking data // Geophysical Research Letters. 1996. V. 23(14). P. 1857-1860.
[3] Gudkova T.V., Zharkov V.N. Models of the internal structure of the Earth-like Venus // Solar System Research. 2020. V. 54(1). P. 20-27.
[4] Steinberger B., Stephanie C.W., Trond H.T. Deep versus shallow origin of gravity anomalies, topography and volcanism on Earth, Venus and Mars // Icarus. 2010. V. 207(2). P. 564-577.
[5] Dziewonski A.M., Don L.A. Preliminary reference Earth model // Physics of the Earth and Planetary Interiors. 1981. V. 25(4). P. 297-356.
[6] Castillo-Rogez J.C., Efroimsky M., Lainey V. The tidal history of Iapetus: Spin dynamics in the light of a refined dissipation model // J. Geophysical Research: Planets. 2011. V. 116. Iss. E9.

MODEL STRESS VALUES FOR VENUS: ELASTIC CASE

T.I. Menshchikova[1], A.V. Batov[1,2], T.V. Gudkova[1]
[1] *Schmidt Institute of Physics of the Earth RAS, Moscow, Russia; ms.tamm@mail.ru*
[2] *Institute of Control Sciences RAS, Moscow, Russia*

KEYWORDS:
Venus, gravity, topography, tension-compression stresses, shear stresses

INTRODUCTION:
Little is known about seismic activity of Venus and location of seismic sources. There are no seismic instruments that would be able to survive over extended periods under Venus conditions. Nevertheless, a seismic experiment is planned on the surface of Venus [1]. It is also proposed to register disturbances in the atmosphere and ionosphere of the planet caused by seismic events [2]. For forthcoming seismic experiments on Venus, it is important to know in which areas the stresses are large enough and capable of producing venusquakes. Here we study stress field of Venus starting from a simple model: a liquid core and an elastic mantle and crust with the help of a static method [3–5].

DATA:
The topography and gravity data are provided by the Magellan mission: SHTJV360u [6] and SHGJ180u model [7], respectively. We take into account harmonics only up to the 70^{th} degree and order, since for higher degrees the correlation between the gravity and topography deteriorates an effectively equilibrium figure of Venus [8, 9], which survives from an earlier epoch, is chosen as a reference surface.

INTERIOR STRUCTURE MODEL:
Models of the internal structure of Venus are insufficiently defined due to inaccuracy of the moment of inertia and Love number k_2. Here we use two models with the average thickness of the crust of 30 and 70 km, and a density of 2800 kg/m^3. These are models V_5 and V_16 of the work [10].

METHOD:
The pattern of non-hydrostatic stresses in a planet can be obtained by considering the planet as an elastic spherically symmetric body under the influence of both surface (relief on the surface of the planet) and internal (buried density anomalies) loads. A static approach (the load coefficients technique) accounting the deformation of a planet under loads was developed in [3–5]. Here we assume that there are two levels of loads (anomalous masses) – the surface and the crust-mantle boundary. Amplitudes of loads are selected in such a way as to satisfy the data of the topography and the gravitational field of the planet (calculated from the reference equilibrium surface). The system of equations defining the problem includes: the equation of equilibrium of a deformed (elastic body) in the presence of volumetric forces, the Poisson equation, the rheological equation giving the relationship between stress and displacements (Hooke's law for an ideally elastic and isotropic medium). The solution of the system determines the displacement field for each value of the harmonic degree n and a given depth, then, the harmonic series are summed up. At each point, the symmetric full stress tensor σ_{ik} is further reduced to a diagonal form by coordinate transformation and the corresponding principal stresses are determined. These additional non-hydrostatic stresses σ_1, σ_2, and σ_3 ($\sigma_3 \le \sigma_2 \le \sigma_1$) at each point are decomposed tension (positive) – compression (negative) stresses $\sigma = (\sigma_1 + \sigma_2 + \sigma_3)/3$, and shear stresses. The maximum shear stresses represent the largest of the half-differences of the main stresses $\tau=\max|\sigma_i - \sigma_k|/2$ (i, k = 1, 2, 3; $i \ne k$). The scheme of stress calculations is presented in Fig. 1.

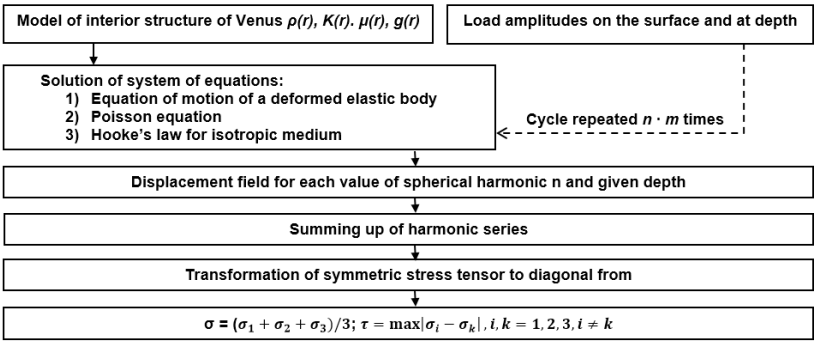

Fig. 1. The scheme of stress calculations

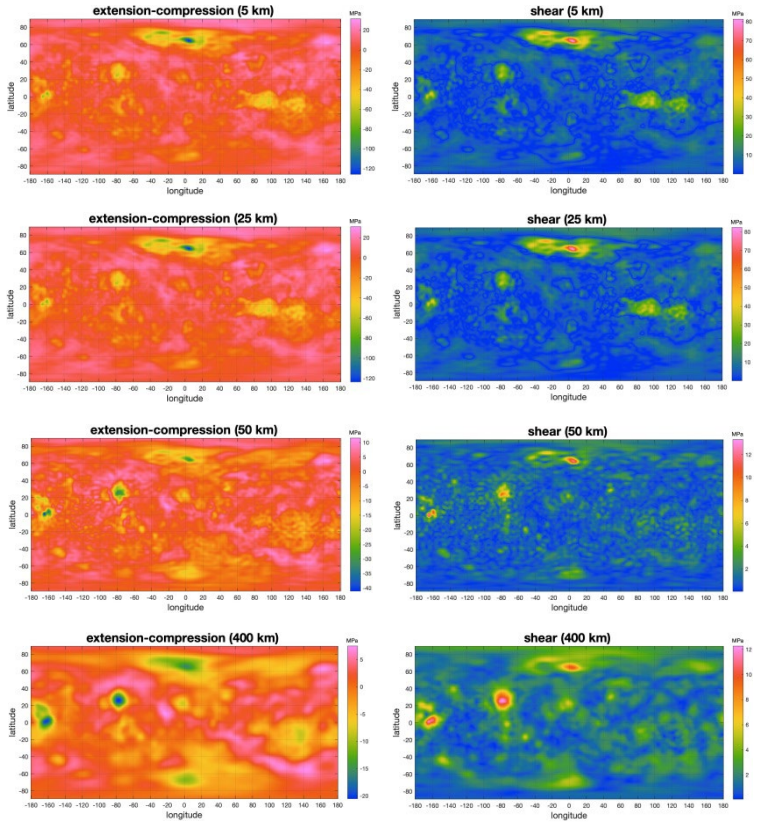

Fig. 2. Tension-compression stresses (on the left) and shear stresses (on the right) in the crust, at depths of 5 and 25 km and in the mantle, at depths of 50 and 400 km for an elastic interior structure model V_16 from [10]

RESULTS:

We have obtained stress field on the surface and at depth of Venus for an elastic model based on gravity and topography data in a frame of the static method. In general, the level of non- hydrostatic stresses on Venus is not too high. This result is in agreement with the values obtained in [5], where the calculations were performed up to 18th degree (the accuracy of the gravity field at that time). There is not significant difference for stress pattern obtained for the model with the crust thickness of 30 and 70 km. The Fig. 2 shows maps of tension-compression and shear stresses in the crust and mantle for the model with the crust thickness of 30 km. As expected, on the surface of the planet and in the crust, the largest shear stresses are manifested in the area

of the Maxwell Mountains on Ishtar Terra. Beneath the Maxwell Mountains shear stresses in the crust reach 80 MPa, compression values reach values of 120 MPa, while the tension stresses around this area are about 20 MPa.

ACKNOWLEDGEMENTS:
This work is financially supported by Budget funding of Schmidt Institute of the Earth RAS.

REFERENCES:

[1] Kremic T., Ghail R., Gilmore M., Hunter G., Kiefer W., Limaye S., Pauken M., Tolbert C., Wilson C. Long-duration Venus lander for seismic and atmospheric science // Planetary and Space Science. 2020. V. 190. Art. No. 10496.
[2] Komjathy A., Didion A., Sutin B., Nakazono B., Karp A., Wallace M., Lantoine G., Krishnamoorthy S., Rud M., Cutts J., Makela J., Grawe M., Lognonne P., Kenda B., Drilleau M., Helbert J. Remote sensing of seismic activity on Venus using a small spacecraft initial modeling results // 49th Lunar and Planetary Science Conference. 2018. No. 2083. Id. 1731.
[3] Marchenkov K.I., Lyubimov V.M., Zharkov V.N. Calculation of load factors for deeply buried density anomalies // Doklady Earth Science Sections. V. 279. 1984. P. 14-16.
[4] Zharkov V.N. Marchenkov K.I., Lyubimov V.M. On long-waves shear stresses in the lithosphere and the mantle of Venus // Sol. Syst. Res. 1986. V. 20. P. 202-211.
[5] Marchenkov K.I., Zharkov V.N. Stresses in the Venus crust and the topography of the mantle boundary // Sol. Astron. Lett. 1989. T. 16. No. 1. P. 77-81.
[6] Rappaport N.J., Konopliv A.S., Kucinskas A.B. Animproved 360 degree and order model of Venus topography // Icarus. 1999. V.139. P. 19-31.
[7] Konopliv A.S., Banerdt W.B., Sjogren W.L. Venus gravity: 180th degree and order model // Icarus. 1999. V. 139. P. 3-18.
[8] Zharkov V.N., Gudkova T.V. On Parameters of the Earth-like model of Venus // Sol. Syst. Res. 2019. V. 53. No. 1. P. 1-4.
[9] Menshchikova T.I., Gudkova T.V., Zharkov V.N. Analysis of the topography and gravity data for the Earth-like Venus // Solar Syst. Res. 2021. V. 55. No. 1. P. 11-19.
[10] Gudkova T.V., Zharkov V.N. Models of the internal structure of the Earth-like Venus // Solar Syst. Res. 2020. V. 54. No. 1. P. 20-27.

FOOTPRINTS OF ASTEROID ATMOSPHERIC EXPLOSIONS AT THE SURFACE OF VENUS

B.A. Ivanov[1]
[1] *Institute of Geosphere Dynamics RAS, Moscow, Russia; baivanov@idg.chph.ras.ru*

KEYWORDS:
Venus, asteroid impact, radar-bright surface, radar-dark surface, atmospheric shock waves

INTRODUCTION:
Thick atmosphere of Venus is able to crash km-size pace bodies like asteroids creating surface footprints of various kinds [1]. While larger space bodies are able to reach the surface creating impact craters or a kind of strewn fields, smaller bodies effectively transfer the initial kinetic energy to the atmosphere, resulting in an atmospheric burst at some altitude [1]. In these cases, the most prominent footprints at the Venusian surface are created with atmospheric shock waves and gas flow behind shock fronts, reflected at the solid surface [2]. The near-circular radar-bright and radar dark zones around the epicenter were named with a general term “splotches” [1, 3].

Discussions on the 2021 presentation [4] resulted in the re-reading of the 20-years old thesis [3] devoted to the splotch systematization and some new modeling [5]. Here we summarize our first results in a study of splotches.

SPLOTCHES AROUND VENUS:
We use Wood’s catalog [3] to start a fresh looking to splotches. The whole known splotch collection in [3] includes about 400 examples of all kinds. Typical examples are presented in [5]. Sizes of splotches vary from ~10 to 200 km. The large diameter splotches are comparable in size with the characteristic atmosphere thickness.

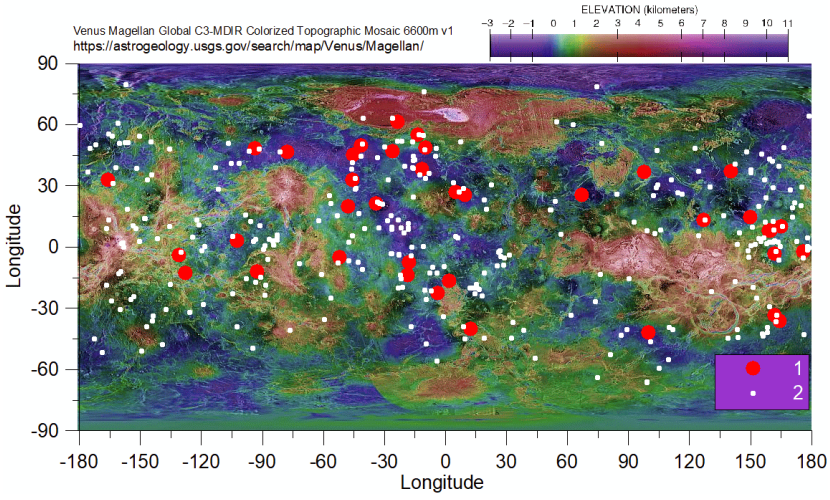

Fig. 1. Locations of splotches with a dark ring/arc (1) and all other splotches at the USGS-produced topography background

In general, the spatial splotch distribution looks random (Fig. 1), while in high altitude areas (mountain formations) splotches seem to be rare.

SPLOTCHES WITH DARK RINGS/ARCS:
Searching for methods to estimate (or to bound) airburst energy related to dark ring formation we select ~40 cases where dark rings/arcs are well seen in radar images (Fig. 2). Typically, dark surface could be interpreted as more smooth areas, reflected weaker signal to the spacecraft.

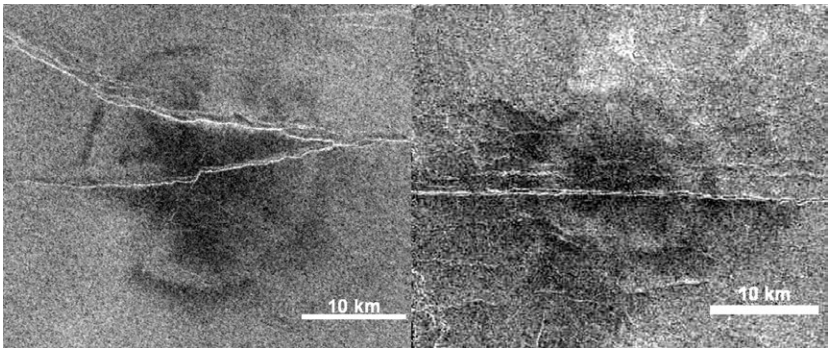

Fig. 2. Two examples of dark rings in a complex surface pattern around an impact point. The left image is centered at 267.4° E, 11.8° N, altitude ~1.3 km, the right image is centered at 314.41° E, 32.942° N, altitude –0.18 km. Images are constructed with the JMars computer tool (https://jmars.asu.edu/).

In selected 40 cases ring/arc diameters vary from 10 to ~55 km. In 30 cases (75 % of the selected population) the dark ring diameter is in the range from 10 to 30 km (Fig. 3). We hope to interpret this measured interval in terms of the effective energy release altitude, and to find possible range of asteroid's size and velocity (and may be to limit the angle of incidence).

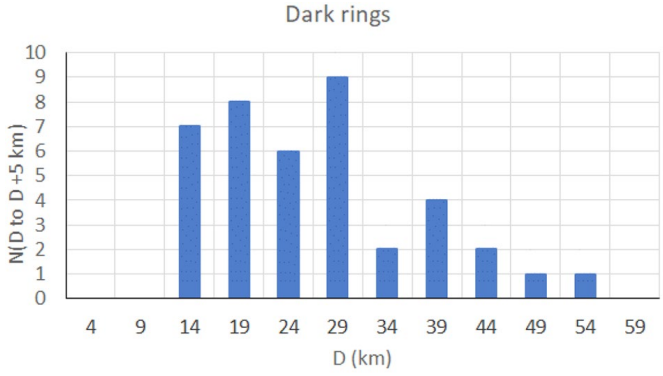

Fig. 3. Size distribution of 40 radar-dark rings/arcs remeasured after [3] – see examples in Fig. 2. Around 75 % if all identified dark rings have diameters 10 to 30 km

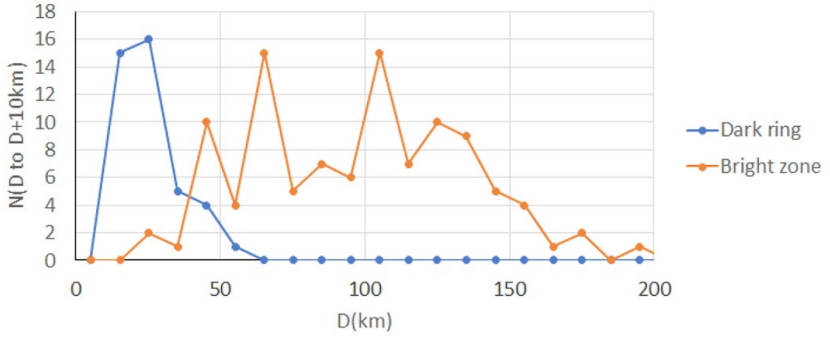

Fig. 4. Size distributions of dark rings (see details in Fig. 3) and bright splotches (106 cases)

In some cases, one can see double rings with shifted centers, possibly indicated the atmospheric breakup of the falling body into parts, aerodynamically separated before the final explosive crash in a lower atmosphere.

OTHER SPLOTCHES:

At least in one case [4] we have solid evidences of simultaneous formation of splotches from multiple body fragments formed before the atmospheric entry. For this reason, the statistics of the splotch formation should be checked before a discussion about the life-time of splotches at the surface.

Figure 4 compares size distributions for dark ring/arcs (see Fig. 3) and for more "standard" bright zone (see [5] for more details).

CONCLUSIONS AND PERSPECTIVES:

The new research interest to footprints of asteroid atmospheric break up on Venus [2, 4] prompts us to use more sophisticated tools, evolved after early publications [1]. The combination of the numerical modeling and rethinking of the Magellan data promises better understanding of small celestial body's fate in the dense Venusian atmosphere.

REFERENCES:

[1] Zahnle K.J. Airburst origin of dark shadows on Venus // JGR Planets. 1992. V. 97. No. E6. P. 10243-10255.
[2] Bondarenko N.V., Kreslavsky M.A. Surface properties and surficial deposits on Venus: New results from Magellan radar altimeter data analysis // Icarus. 2018. V. 309. P. 162-176.
[3] Wood D.A. Jr. Effects of airbursts on the surface of Venus: PhD thesis. The University of Arizona, 2000. 263 p.
[4] Antropova E.G., Braga C.H.G., Ernst R.E., Buchan K.L., El Bilali H., Head J.W. Analysis of multiple impact "splotches" in Hinemoa Planitia, NW and W of Phoebe Regio // 12th Moscow Solar System Symposium. Abstr. 12MS3-VN-02. 2021. P. 86-88.
[5] Ivanov B.A. Splotches on Venus: Models revisited // 53rd Lunar and Planetary Science Conference. The Woodlands. Texas, 2022. Abstr. 1841.

IDUNN MONS AS THE LANDING SITE OF THE VENERA-D MISSION: SCIENTIFIC RELEVANCE AND POSSIBLE OPERATIONAL TESTS ON MOUNT ETNA

P. D'Incecco[1,2], R. Ghail[3], L.V. Zasova[4], J. Filiberto[5], D.A. Gorinov[4], I. Lopez[6], G. Di Achille[1], M. Mastrogiuseppe[7], S. Aveni[6], G.L. Eggers[9], G. Komatsu[10], C. Monaco[11], N. Mari[12], M. Blackett[6], M. Cardinale[1], A. Martynov[13]

[1] *National Institute for Astrophysics – Astronomical Observatory of Abruzzo, Teramo, Italy; piero.dincecco@inaf.it*
[2] *Arctic Planetary Science Institute, Rovaniemi, Finland*
[3] *Earth Sciences, Royal Holloway, University of London, United Kingdom*
[4] *Space Research Institute, Moscow, Russia*
[5] *NASA Johnson's Space Center, Houston, TX, USA*
[6] *Departamento de Biología, Geología, Física y Química Inorgánica, Universidad Rey Juan Carlos, Madrid, Spain*
[7] *"La Sapienza" University of Rome, Rome, Italy*
[8] *Centre for Agroecology, Water and Resilience, Coventry University, UK*
[9] *Lunar and Planetary Institute, USRA, Houston, TX, USA*
[10] *International Research School of Planetary Sciences, Università d'Annunzio, Pescara, Italy*
[11] *Dipartimento di Scienze Biologiche Geologiche e Ambientali, Università di Catania, Italy*
[12] *Department of Earth and Environmental Sciences, University of Pavia, Italy*
[13] *Maana Electric, Dubai Silicon Oasis DDP, Dubai, UAE*

KEYWORDS:
Venus, volcanism, Venera-D, Idunn Mons, Mount Etna, landing site

INTRODUCTION:

Along with the recently selected NASA DAVINCI [1] and VERITAS [2] missions, and with the ESA EnVision mission [3], the Roscosmos Venera-D mission [4, 5] opens the new decade of Venus exploration. Among these missions, the Venera-D is the only one to be equipped with a lander which could drill the surface of Venus and analyze its chemical composition. For this reason, it is crucial to select a future landing site based on its scientific relevance, as well as on safety constraints.

We propose here Idunn Mons (Fig. 1a), a major large volcano of Imdr Regio, as the landing site for the Venera-D mission. We also indicate Mount Etna in Italy (Fig. 1b) as a suitable test site on Earth for drilling tests and in-situ elemental and mineralogical analyses [6, 7].

A REASONABLE BALANCE BETWEEN SCIENTIFIC RELEVANCE AND SAFETY CONSTRAINTS:

One of the major science discussions on Venus concerns whether the planet is still volcanically active today [8, 9], and if so, what is the current rate and style of resurfacing on the planet. The young volcanic rises with their related large volcanoes are considered as the geologically youngest regions of Venus. Imdr Regio and its major volcanic structure, Idunn Mons (Figure 1a) is one of the most promising areas for active volcanism [i.e., 10]. Chemical analysis of eruptive products of a recently active volcano such as Idunn Mons may tell us about the volatile content of the mantle, thus shedding light on the debate between catastrophic [i.e., 11] and equilibrium [i.e., 12] resurfacing on Venus.

During the 70s' and 80s' of the last century, ten Soviet landers successfully landed on and conducted chemical analyses of Venusian surfaces (i.e., 13,14). These landers appear to have landed on regional plains of Venus. Such regional plains are generally considered as the safest areas for landing on Venus due to their gentle topography. The geochemical composition of at least some regional plains is now known from the previous Soviet landing missions. On the contrary, the scientific relevance and unknown geochemistry of possibly active large volcanoes such as Idunn Mons make these sites

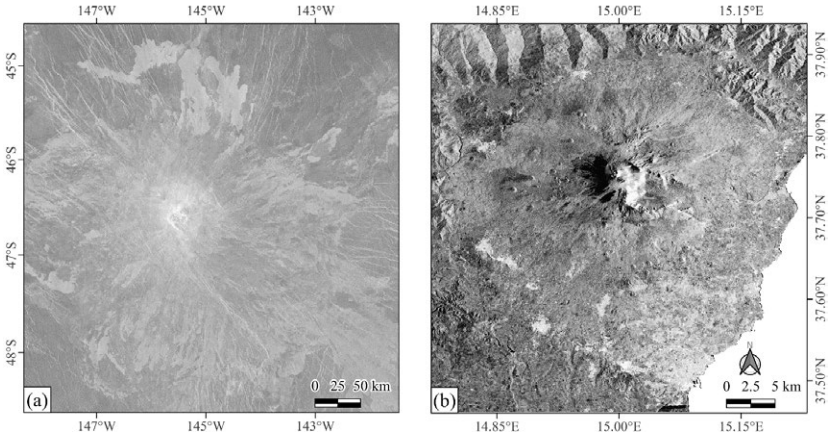

Fig. 1: *a*) Idunn Mons (46° S; 146° W), Imdr Regio – Venus. Magellan left-look SAR scene - Resolution ~75m, *b*) Mt. Etna (37.75° N, 14.99° E), Sicily – Italy. S-1 GRDH SAR Ascending – Resolution ~75m

unprecedented landing targets, which deserve more attention. While being a scientifically relevant objective, the gentle slopes of Idunn Mons as well as the expected roughness of its lava flows would keep this volcano within the safety constraints for the lander of the Venera-D mission [15]. Other areas of comparable scientific interest on Venus, such as the tessera terrains, may likely constitute a too dangerous target for the landing [15].

MOUNT ETNA AS A TERRESTRIAL LABORATORY FOR OPERATIONAL TESTS

We propose Mount Etna (Fig. 1b) in Sicily (Italy), one of the most active volcanoes on Earth, as a suitable test site for drilling operations and in-situ elemental and mineralogical analyses to be performed by the Venera-D mission lander. Unlike other potentially suitable analog sites on Earth (i.e., East African Rift), Mount Etna is more easily accessible. Moreover, given its composite nature, this volcano offers unique opportunity to perform tests on different types of eruptive products.

REFERENCES:

[1] Garvin J.B. et al. // Planet. Sci. J. 2022. V. 3. Art. No. 117.
[2] Smrekar S. et al. // EPSC2020-447. 2020. https://doi.org/10.5194/epsc2020-447.
[3] Ghail R.C. et al. // Exp. Astron.2012. https://doi.org/10.1007/s10686-011-9244-3.
[4] Senske D.A. et al. Venera-D: Expanding our Horizon of Terrestrial Planet Climate and Geology through the Comprehensive Exploration of Venus: Report of the Venera-D Joint Science Definition Team. 2017.
[5] Zasova L.V. et al. // Sol. Syst. Res. 2019. V. 53. P. 506-510. https://doi.org/10.1134/S0038094619070244.
[6] D'Incecco P. et al. // XVII Congresso Nazionale di Scienze Planetarie. 2022.
[7] Eggers G.L. et al. // 53rd LPSC. 2022. Art. No. 2255.
[8] Smrekar S.E. et al. // Science. 2010. V. 80. https://doi.org/10.1126/science.1186785.
[9] Filiberto J. et al. // Sci. Adv. 2020. https://doi.org/10.1126/sciadv.aax7445.
[10] D'Incecco P. et al. // Planet. Sci. J. 2021. V. 2. Art. No. 215.
[11] Schaber G.G. // J. Geophys. Res. 1992. https://doi.org/10.1029/92je01246.
[12] Phillips R.J. et al. // J. Geophys. Res. 1992. V. 97(E10). P. 15923-15948. DOI: 10.1029/92JE0169.
[13] Basilevsky A.T. // Geokhimia. 1985. V. 2. P. 131-141 (in Russian).
[14] Kargel J.S. et al. // Icarus. 1993. V. 103. P. 253-275.
[15] D'Incecco P. et al. // Sol. Syst. Res. 2021. V. 55. 315-32.3

WINDS IN THE LOWER CLOUD LEVEL ON THE NIGHTSIDE OF VENUS FROM IR2 (AKATSUKI) 1.74 μm IMAGES

D.A. Gorinov[1], L.V. Zasova[1], I.V. Khatuntsev[1]
[1] *Space Research Institute, Moscow, Russia; dmitry_gorinov@rssi.ru*

KEYWORDS:
Venus, atmosphere, dynamics, nightside, infrared images

INTRODUCTION:
Dynamics of lower cloud layer of Venusian atmosphere are important to understand the global circulation. Studying horizontal winds is possible through analyzing the displacement of cloud features over time. In this research we used nightside images of Venus lower clouds obtained by IR2 infrared camera onboard JAXA's orbital spacecraft Akatsuki in 1.74 μm wavelength.

METHODS:
The entire IR2 database was analyzed, which spanned across 2016, for the 1.74 μm channel of the instrument. From previous research it is known that the lower cloud layer rotates around the planet in a superrotation mode, although with zonal speeds slower than those at the upper boundary of clouds – 60 m/s compared to 100 m/s. Our study allowed a more detailed look at the distribution of zonal and meridional wind on Venus nightside at those altitudes.

RESULTS:
The zonal wind speed has a prominent jet-like feature at the equator. Diurnal variations showed strong dependence of both zonal and meridional speed, with meridional speed changing direction from equatorward (most of the nightside) to poleward at both hemispheres.

No significant correlation with surface topography was found.

EXPLORATION OF VENUS ATMOSPHERE AND SURFACE WITH THE UPCOMING NASA DAVINCI MISSION

M.Yu. Zolotov[1], J.B. Garvin[2], and the DAVINCI Science Team
[1] *School of Earth and Space Exploration, Arizona State University, Tempe, USA; zolotov@asu.edu*
[2] *NASA Goddard Space Flight Center, Greenbelt, MD, USA; james.b.garvin@nasa.gov*

KEYWORDS:
Venus, atmosphere, surface, composition, DAVINCI

INTRODUCTION:
The atmosphere of Venus has not been investigated *in situ* since the Vega-2 mission in 1985. Despite the achievements of the *Venus Express* mission [1], ground-based near-infrared (near-IR) spectroscopy, and current data from the *Akatsuki* orbiter, the chemical composition of the atmosphere below 20–30 km remains ambiguous and poorly sampled. The D/H isotopic ratio in H_2O is unknown in the sub-cloud atmosphere. Measured abundances of He, Ne, and Ar isotopes have uncertainty of 36–70 %, isotopic abundances of Kr are highly doubtful, and Xe isotopes have never been measured. Although a felsic composition of highly deformed tessera plateaus is suggested based on the *Galileo* and *Venus Express* near-IR emissivity data (e.g. [2, 3]), the composition and high spatial resolution topography of tesserae are unknown. The scarcity of information about the deep atmospheric composition, isotopes of noble gases, and properties of enigmatic tesserae regions limits our understanding of chemical and physical processes in the atmosphere, atmosphere-surface interactions, volcanic degassing, and early aqueous vs. anhydrous evolution of Venus. The Deep Atmosphere Venus Investigation of Noble gases, Chemistry, and Imaging (*DAVINCI*) Discovery class NASA mission [4] is aimed at obtaining atmospheric chemical/isotopic, and sub-cloud surface imaging data to address these outstanding questions. The plan is to launch the spacecraft in mid-2029, perform two Venus's flybys in 2030, and accomplish the descent-sphere atmospheric entry in June 2031, with potential for an extended orbital phase.

ATMOSPHERIC STUDIES:
Chemical and stable isotopic composition of the atmosphere will be investigated by means of a meter-diameter entry probe from an altitude of ~67 km down to the surface over Alpha Regio. The *Venus Mass Spectrometer* (VMS) will be used for noble gas (He, Ne, Ar, Kr, Xe) measurements in the bulk atmosphere and composition (CO_2, N_2, SO_2, H_2O, OCS, H_2S, H_2SO_4, S_n, and HCl) measurements at 50–200 m cadence in altitude from ~41 km to the surface. The *Venus Tunable Laser Spectrometer* (VTLS) is designed to obtain concentrations of SO_2, H_2O, CO, and OCS, and isotope ratios (D/H in H_2O, $^{32}S/^{33}S/^{34}S$ in SO_2 and OCS, and $^{16}O/^{18}O$ and $^{12}C/^{13}C$ in CO_2) as functions of altitude below 67 km. The accuracy of VTLS measurements is <5 %. Analyses of chemical active gases will be complemented by data on oxygen fugacity (fO_2) obtained with a solid-state Nernstian ceramic sensor, and via measurements of temperature, pressure (every 10–50 m), and wind speed acceleration during the decent. *Venus Imaging System for Observational Reconnaissance* (VISOR) will be used to obtain global dayside imaging and 1000+ frame movies of clouds in the ultraviolet (0.355–0.375 μm) with spatial resolution of 10–20 km per pixel.

DAVINCI data will resolve ambiguity about concentration gradients of SO_2, CO, OCS, and H_2O, and improve our understanding of chemical and photochemical reactions from the clouds top to the surface. Data on S-bearing gases and S isotopes will constrain the S cycle. The composition of the near-surface atmosphere will be used to check gas-gas and gas-solid type equilibrium hypothesis for some key chemical species. Concentrations of chemically active gases in the near surface atmosphere together with fO_2 data will be applied

to assess stability of exposed geological materials, directions of gas-solid type weathering reactions, and to constrain mineralogy of altered rocks and fines. The new data will test the hypothesis about control of the atmospheric redox state (CO_2/CO and SO_2/OCS ratios, fO_2) by the hematite-magnetite (Fe_2O_3–Fe_3O_4) mineral assemblage [5]. D/H measurements with precision <1% will constrain altitude distribution and improve models of water loss. Data on ^{4}He and ^{40}Ar will improve models on volcanic degassing through time. Data on Xe and Kr will be used to constrain formation and early atmospheric evolution of Venus in comparison with Earth and Mars. Data on ^{129}Xe and ^{136}Xe will constrain the long-term outgassing rate and inform about major early impacts. Data on temperature, pressure, winds, and gas composition will constrain atmospheric circulation models coupled with physical-chemical processes that affect both gases and surface materials.

SURFACE STUDIES:

Surface materials will be studied through near-IR imaging from two nightside flybys and from the atmospheric probe descending above Alpha Regio. During flybys, the VISOR camera suite will allow nighttime imaging in three near-IR bands within 0.93–1.03 μm to constrain thermal emissivity from selected regions that include tesserae (Alpha, Ovda). The emissivity data with spatial resolution of ~70 km will be correlated with surface geology to constrain origin and composition on the targeted regions. Surface studies from the entry probe with the *Venus Descent Imager* (VenDI) will begin at ~38 km with ~1 μm imaging in two bandpasses. At lower altitudes, the ~1 μm and broadband (0.74–1.04 μm) imaging interleaves to produce band-ratio composites. Only broadband imaging data will be obtained within 1.5 km of the surface. Spatial resolution of the imaging is <200 m down to 1 m per pixel. Band ratios will be used to evaluate types or surface materials: felsic and mafic (e.g., basalts) rocks will be clearly distinguished. Image processing of VenDI data obtained at altitudes <11 km will be used to constrain surface topography with meter-scale vertical precision and with spatial resolution of <10 m (<1 m at altitude <1.5 km above ground level). Overall, surface imaging will advance our knowledge about composition and high-resolution topography of tesserae materials and whether liquid water played a role in exogenic and/or endogenic processes in Venus's history.

SUMMARY:

The *DAVINCI* mission will explore Venus's atmosphere by analyzing its chemical (CO_2, N_2, SO_2, OCS, CO, H_2S, H_2SO_4, S_n, HCl) and stable isotopic (H, He, C, O, Ne, S, Ar, Kr, Xe) composition from a descent probe down to the surface. The surface will be investigated from flybys and with the atmospheric probe through sub-cloud deck near-IR imaging. For the first time, these data will provide high precision *in situ* information on the near surface atmosphere and reveal high spatial resolution topography and thermal emissivity of tessera. These data will constrain current physical-chemical processes in the atmosphere and clouds, past and present atmosphere-surface interactions, geological evolution, degassing history, fate of water, and formation of Venus.

REFERENCES:

[1] Marcq E., Mills F.P., Parkinson CD, Vandaele A.C. Composition and chemistry of the neutral atmosphere of Venus // Space Science Reviews. 2018. V. 214. Art. No. 10.

[2] Hashimoto G.L., Roos-Serote M., Sugita S. et al. Felsic highland crust on Venus suggested by Galileo Near-Infrared Mapping Spectrometer data // J. Geophysical Research. 2008. V. 113. Art. No. E00B24.

[3] Gilmore M.S., Mueller N., Helbert J. VIRTIS emissivity of Alpha Regio, Venus, with implications for tessera composition // Icarus. 2015. V. 254. P. 350-361.

[4] Garvin J.B., Getty S.A, Arney G.N. et al. Revealing the mysteries of Venus: The DAVINCI Mission // The Planetary Science J. 2022. V. 3. No. 5. Art. No. 117. 17 p. https://doi.org/10.3847/PSJ/ac63c2.

[5] Zolotov M.Yu. Gas–solid interactions on Venus and other solar system bodies // Reviews in Mineralogy and Geochemistry. 2018. V. 84. P. 351-392.

THE VENERA-D MISSION: PROGRESS IN STUDY

L.M. Zelenyi[1], L.V. Zasova[1], O.I. Korablev[1], O.Yu. Sedykh[1], N.A. Eismont[1], M.V. Gerasimov[1], D.A. Gorinov[1], N.I. Ignatiev[1], D.V. Strelnikov[1]
[1] *Space Research Institute, Moscow, Russia; lzasova@gmail.com*

The purpose of the Venera-D mission is a comprehensive study of Venus, its atmosphere, surface, and surrounding plasma, in order to advance the answer to the questions of why is the sister planet Venus so different from Earth, and what lessons can we learn from the understanding of process of evolution of the climate of Venus as applied to the Earth climate. It also has a lot to do with understanding a climate of the terrestrial planets of the Solar System and Earth-like in size exoplanets (many of which are similar to Venus) as well as with the problem of their possible habitability.

The main element of the Venera-D mission is a big Lander of the VEGA- type, which contains the scientific payload to study the elemental and mineralogical composition of the surface and near subsurface (a few cm depth, by drilling) materials, including radiogenic elements; as well as the structure and chemical composition of the atmosphere down to the surface, including the abundances and isotopic ratios of the trace and noble gases, direct chemical analysis of cloud aerosols, and the geology of the surface.

The Orbiter on the polar orbit is focused on studying the thermal structure of the atmosphere, winds, thermal tides, and solar locked structures; the dynamics and the nature of superrotation, radiative balance, and the source of greenhouse effect; the composition of the atmosphere, on the investigation the clouds, their structure, composition, microphysics and chemistry; on the analysis of composition of the low atmosphere, and on the surface emissivity on the night side. A complex of plasma instruments on the orbiter is aimed to study the upper atmosphere, ionosphere, electrical activity, magnetosphere, the atmospheric escape rate, and solar wind interaction.

Lavochkin Association is working on the inclusion of a balloon with variable altitude of floating (within 53–60 km), working up to three months. The preliminary list of scientific payload includes GC, MTLAS, Meteo, Cameras (IR, VIS and UV), UV-spectrometer etc. However, the final list of the instruments is open for consultation and approval at the next stage – Phase B.

It is also proposed to use a gravitational maneuver. Its aim is to enlarge the area available for selection as landing sites, extending it up to more than 80% of the surface of Venus.

The Venera-D project, which is planned to be launch in 2029 is an important addition to the “flotilla” of three missions (VERITAS, DAVINCHI, EnVision). Indeed, the instruments on all four missions may be complemented to each other. However, the Venera-D only possesses the additional capabilities for measurements on the surface and the long-term measurements in the cloud layer.

Venus is a difficult planet for understanding the processes and phenomena occurring on it. Although the planet is closest to Earth, it remains the most mysterious one in the solar system. A coordination of efforts and the synergy between individual missions as well as between scientific instruments is highly important.

CASE STUDY OF VENUS SURFACE STUDIES USING POLSAR

Gaurav Seth[1], Sriram Saran Bhiravarasu[1], Deepak Putrevu[1], Ch.V.N. Rao[1], Nilesh Desai[1]
[1] *Space Applications Centre, Indian Space Research Organisation*

KEYWORDS:
Synthetic Aperture Radar, Polarimetry, Venus, Ambiguity analysis,

INTRODUCTION:
Microwave remote sensing data acquired with ground-based and orbiter-based radar instruments are the major source of information about the surface of Venus.The Synthetic Aperture Radar (SAR) on Magellan mission mapped ~98% of the surface of Venus in 1990s with a resolution of 90–150 m in single polarization mode. However, due to its coarse resolution and single polarization measurements, there are several gap areas in our understanding of the geologic and resurfacing history of the planet [e.g., 1]. In this paper, we present the scientific objectives and instrument specifications of a full-Polarimetric Synthetic Aperture Radar (PolSAR) to map the surface of Venus with ground resolution as high as 40 m, onboard a proposed Venus mission by the Indian Space Research Organization (ISRO) [3]

SCIENCE OBJECTIVES:
The major scientific objectives of this PolSAR instrument are (i) To determine the presence of active/recent volcanism on Venus (e.g., detection of active volcanic hotspots, characterizing episodic volcanic events), (ii) To understand the altitude-related surface composition anomalies (e.g., anomalous radar properties from the Venusian highlands), (iii) Finer-scale geological mapping and understanding the resurfacing history (e.g., buried features, high-resolution mapping of selected targets), and (iv) To characterize impact related features in greater detail (e.g., paucity of craters, parabolic ejecta, and melt features)

SYSTEM DESIGN OF THE INSTRUMENT:
The design goals of sensitivity of -25 dB at incidence angle range of 30^{o}–33^{o} were obtained by simulating angular response of backscattering coefficient for Venusian surface model. The design of this SAR is carried out considering both an elliptical orbit (200 km X 600 km) by performing trade-off studies among parameters like power, frequency, noise equivalent sigma naught, pulse repetition frequency (PRF), altitude, look angle, pulse width, swath, and radar ambiguities. The presented PolSAR design also aims at deriving some physical parameters of the Venusian near-surface by taking the advantage of full polarimetry which provides data sufficient to measure the 2×2 complex scattering matrix of the backscattered field [e.g., 2]. Availability of such polarimetric data products leads to the extraction of all information available in the radar reflections, which complements the objectives of SAR payloads proposed on contemporary missions.

REFERENCES
[1] Ghail R.C. et al. VenSAR on EnVision: Taking earth observation radar to Venus. International Journal of Applied Earth Observation and Geoinformation, 2018, Vol. 64, 365-376.
[2] Kocher Inderkumar et al. Retrieval of Lunar Surface Dielectric Constant Using Chandrayaan-2 Full-Polarimetric SAR Data, IEEE Transactions on Geoscience and Remote Sensing, 2022, Vol. 60, 4602212.
[3] Antonita, TM. Outstanding science questions of Venus and the proposed Venus Orbiter Mission. Talk given at National Meet on Venus Science 05/04/2022, ISRO HQ, Bengaluru, India. https://www.youtube.com/watch?v=yUp6DplyPJk

NEW INSTRUMENTS, METHODS, AND EXPERIMENTS IN ASTROBIOLOGY RESEARCH: VENUS AND MARS

E. Chatzitheodoridis[1,2], S. Jheeta[2], Ch. Georgiou[3], I. Markopoulos[4], M. Holynska[5]

[1] *National Technical University of Athens, School of Mining and Metallurgical Engineering, Department of Geological Sciences, Athens, Greece; eliasch@metal.ntua.gr*

[2] *Network of Researchers on the Chemical Evolution of Life, Leeds, UK*

[3] *Department of Biology, School of Natural Sciences, University of Patras, Greece*

[4] *ZEROONE Ltd, Athens, Greece*

[5] *Materials' Physics and Chemistry Section (TEC-QEE), Technical Reliability and Quality Division (TEC-QE), ESTEC, ESA*

KEYWORDS:
biosignatures, oxygen, superoxide radicals, peroxides, hydroxyl radicals, mass spectrometry, OxR, Reactive oxygen Species (ROS), Raman, atmospheric chemistry chamber, surface chemistry, levitation experiments, exoplanet atmospheres

INTRODUCTION:

The exploration for the putative presence of life on our neighbouring planets is in this last decade more intense and focused, performed through advanced missions which employ a large array of sophisticated instrument payloads. Sample return missions are now a way forward, both from planetary bodies such as NASA's Mars2020, but also from asteroids, such as the very successful examples of Japan's Hayabusa II to asteroid Ryugu, and the mission OSIRIS-REx to asteroid Bennu from USA.

The advantage that sample return missions provide is the analysis of the samples with laboratory-grade instruments of high resolution and fidelity. However, special curation is required for samples returned to Earth. But still, instruments that operate *in situ* on the planetary and asteroid surfaces or planetary atmospheres will still continue to be necessary not only because we require a pre-examination of such samples, but mainly because possible terrestrial contamination and thus alteration by the terrestrial environment is avoided. This demonstrates the need to enhance our array of instruments for in-situ analysis, and therefore to proceed to miniaturisation so as to reduce the payload.

Currently, the focus of instrumental payloads is to understand the natural extraterrestrial environments and to search for possible biosignatures. Additionally, instruments allow for experimentation in simulated environments to provide better understanding of processes in extreme or difficult to approach space and planetary locations. Next Venus and Mars missions will profit from the proposed instrumental setup.

ANALYTICAL INSTRUMENTS AND METHODS:

The main focus of instrument development is to characterise and identify materials and their environmental conditions, and/or to simulate certain environments. Simulation of certain environments either provide information for processes occurring in areas that are difficult to approach (and for which only remote or simply theoretical data are available), or they are used to test and calibrate new analytical instruments.

Instruments that are made to fly should be designed with miniaturisation in mind. Instruments that are used for simulation can be large setups, fully monitored and automated. We will provide here some instrumental concepts that we evaluate as the most appropriate to synergistically provide adequate information for interpreting true biosignatures. We will also provide an example of a simulation chamber, employing different instrumentation, to perform atmospheric experiments without being affected by surface effects,

i.e., from chamber walls. For both cases, we will describe methods to assist in analysis and interpretation of the results.

Current missions employ payloads of instruments to perform analysis and detect biosignatures. We will ignore here all the environment-related sensors, or instruments that relate to measuring physical parameters, such as seismographs or magnetometers, but we will focus on the instruments that are made to detect signatures of extraterrestrial life or identify areas that could have potentially harboured life in the past.

The OxR device[*]

Organics, and therefore bio-organics, are potential biosignatures if they can be preserved in the harsh extraterrestrial environments, such as those on Mars or on Venus. The harshness of the environment is primarily brought on by undesirable chemistry (e.g., acidic rain); due to extreme temperatures as result of volcanic eruptions and by heating by impactors pounding the Earth; due to energetic particles such as protons, electrons and alpha-rays as well as electromagnetic radiation: UV-C, X- and gamma-rays; solar winds; and due to mechanical friction between particles, i.e., during strong winds or micrometeorite impacts. These harsh conditions induce the formation of Reactive Oxygen Species (ROS) [1], i.e., superoxide radicals, peroxides, and irradiated perchlorates. These compounds are not only toxic to life (except in rare cases that peroxides can be produced by some organisms), but they react with organics destroying them, and as a result, any evidence becomes disputable.

We have proposed the OxR instrument which can detect the ROS superoxide radicals ($O_2^{\bullet-}$), peroxides (O_2^{2-}) and hydroxyl radicals ($^{\bullet}OH$) in extraterrestrial soils, regoliths, and ices. OxR [2, 3] is a miniaturised microfluidic instrument that can be constructed as a 'lab on a small platform', a few centimetres of size. It is designed to integrate a sample chamber with exchangeable soil samples, a fluid circulation system to wet the sample and enable necessary catalytic reactions involving the release of gaseous O_2 from $O_2^{\bullet-}$ and O_2^{2-}, a very sensitive oxygen sensor to measure them, and a small spectrofluorometer to detect $^{\bullet}OH$. Briefly, soils that contain $O_2^{\bullet-}$ and O_2^{2-} react with the water of the OxR instrument's reagent and release O_2 and H_2O_2. The latter, and any existing H_2O_2 (or formed by other means) are catalysed on the surface of a MnO_2 to release again O_2, the two-step production of which is then measured by a sensitive oxygen sensor and converted to $O_2^{\bullet-}$ and O_2^{2-} concentration. The water-based solution that wets the soils contains terephthalate, which specifically reacts with $^{\bullet}OH$ to form the specific fluorescent 2-hydroxy-terephthalate, the fluorescence of which is measured by a miniaturised spectrofluorometer. A large-scale prototype of this device can produce gaseous oxygen in volumes that can be considered as a significant ISRU resource for oxygen production, i.e., on the Moon or Mars. The generated oxygen can then be used by astronauts for respiration during their stay, or as a propulsion fuel. This instrument is currently under construction and will be tested on various laboratory made soils (simulants).

The use of OxR will allow to identify soils that do not contain ROS, known to oxidise almost all organic molecules (including those of Earth's life), therefore any putative life or biosignatures are still preserved and can be detected. ROS can also form in the atmosphere on atmospheric aerosols and particles by photochemical and heterogeneous reactions and can be measured [4]. Venusian atmosphere and clouds, for example, could be easily evaluated for their ROS-based toxicity to life with such a miniaturised device. An exploration concept would be the consequent release of multiple OxR monolithic microfluidic devices to measure ROS concentration at different altitudes.

When ROS are not identified in planetary targets of interest, the secure detection on them of any existing biosignatures requires analytical techniques that can identify the molecular composition and the structure of the biocomponents. From all available techniques, we identify two that can effectively perform this task by providing rich information and distinguishing identification characteristics. These are mass and Raman spectrometry.

MEMS-based, miniaturised mass spectrometers

Mass spectrometry is based on the ionisation of atoms and molecules, usually singly charged, their acceleration with an electric potential, and their separation by a mass analyser which usually is a magnetic analyser, a Time-of-Flight (ToF) analyser, a quadrupole, or an orbitrap. The ionisation of the samples chemical or molecular components can be performed thermally, by bombardment with electron or ion beams, or by laser desorption by the use of intense pulsed lasers, such as Nd:YAG lasers. Detection is performed by special detectors that allow the release of the charge of the secondary ions, which is measured as current. Mass spectrometers are large lab-scale instruments, however relatively small instruments are already employed as payload to detect organics on comets (i.e., the COSIMA instrument aboard ESA's Rosetta mission) [5] or now the MOMA instrument [6] aboard the Rosalind Franklin rover, a payload mass spectrometer ready to fly to Mars by ESA's ExoMars mission. These instruments are small but further miniaturisation is required.

Recently, there is interest to develop MEMS-based mass spectrometers [7]. Currently, such systems can have limited mass resolution and abundance sensitivity but there is the potential to be improved with special designs. Mass spectrometers can detect elements and their isotopes, as well as low-mass or large-mass molecules. ToF, ion trap, and orbitrap analysers can detect the full series of elements and isotopes, starting from hydrogen through to a few tenths of thousands of atomic mass units (amu or Daltons) in very short time periods. Methodologies to distinguish different populations of molecular species that are represented as peaks of certain masses, can include the interpretation and plotting of all fragments of molecules, i.e., of hydrocarbons, which group in visibly distinct distributions or patterns, or similarly with computational techniques such as machine learning and artificial intelligence (ML/AI) methods. We have deployed the first method (visual plots) as the most secure one, since interpretation is based on a rich database of molecular fragments, as well as atoms and their isotopes. We have implemented this method in a sophisticated software that contains data mining tools, generalisation tools, mass calculators, formula parsers, and ion image processing tools since ToF instruments, when combined with an ion ionisation source as primary beam, can provide ion images with ultra-high spatial resolution in 2D and 3D (scanning mode). Mass spectrometry techniques therefore provide spatial distribution of chemical, isotopic and molecular information, and constitute strong interpretation tools. Therefore, mass spectrometers are almost in any mission, and miniaturised versions will enable wider information acquisition with less resources (payload volume, energy consumption, etc.).

Raman in an optical fibre

Raman is a technique that provides easily interpreted structural information of most molecules and crystals. A laser irradiates the sample and Raman scattering returns information on the strength of the chemical bonds that constitute the molecules or crystals (single or mixed phases) while symmetry information can be also extracted allowing interpretations on the 3D structure of the phase. Presently, Raman instruments have already been miniaturised to some degree (i.e., handheld devices) but further miniaturisation would be of greater value, assisting better integration.

We propose the fabrication of a "Raman in a fibre" instrument, where the irradiation laser and the gratings and sensors, as well as the control electronics, are integrated on a single optical fibre. Each fibre will allow the identification of a few substances, but a bundle of fibres in an array can perform imaging, allowing the formation of spatial distribution maps of phases, i.e., mineral grains in a powder spread on the surface of the instrument. A surface with many Raman fibres can easier collect aerosols, gas condensates, and particles to perform their analysis.

Technological advances in micro and nanofabrication [8] can produce such a device, i.e., with the use of laser machining through the cladding of a multimode fibre and towards its core to install gratings, or simply the inscribing of

gratings on the periphery of the fibre to trap certain wavelengths outside the fibre and measure them with attached sensors. Fibre lasers having an active gain medium inside their core can be exploited [9], with certain advantages if photonic crystal optical fibre technologies are combined.

Currently, such as system is not available, but if manufactured, its potential for space or terrestrial applications would be immerse, i.e., as a sensor for specific types of chemicals or minerals, integrated into instruments such as robotic arms, or in a production line, or even inside conservation chambers of foods or chemicals. Ultra-miniaturised portable devices can have additional applications, i.e., in forensics.

The Atmospheric Chemistry Chamber (*ACC*)[**]

The ACC is a large experiment chamber constructed of 316-stainless steel. The chamber needs to be one metre in diameter in order to eliminate surface chemistry. It can be used for carrying out astrochemical experiments on the simulated atmospheres of distance exoplanets, as well as the atmospheres of Venus, Mars and Titan (one of Saturn's moons). The same chamber can also be used for the investigation and study of greenhouse gases. The pressure attained in the chamber can range from as low as a few millibars through to many atmospheres, depending on the particular experiments. The effect of both UV-light and electron radiation (with the possibility of extending to also include proton radiation) can be studied on various mixtures of gases. In addition, materials (e.g., droplets) can be suspended in the chamber's centre (levitation experiments) for irradiation with the relevant radiation. For measuring real-time results both FTIR, Raman, and ToF-MS can be used.

CONCLUSIONS:

The combination of instruments proposed here is, in our opinion, the ultimate setup for searching for life on Mars and Venus. The OxR device can identify whether ROS exist or not and decide if further characterisation is necessary in a certain area. The Atmospheric Chemistry Chamber can replicate reactions in order to understand formation processes of molecules, or test and calibrate the above instruments. Together with the necessary instruments to perform optical inspection (i.e., optical microscopes and cameras) to perform targeted sampling prior to analysis, the proposed set of instruments can provide chemical analysis as well as structural molecular information. Structural information is important to allow easy and secure identification of organics and formation processes.

Miniaturisation of instruments is paramount in order to allow multiple spatially distributed systems to expand on the surfaces of planets, or in volume in the planetary atmospheres (i.e., using balloons in Venus), and work in parallel or on different tasks. This concept has never been tried, although it can certainly reduce mission costs and operational risks.

A communications and information acquisition and processing backbone can automate exploration significantly in such harsh environments, and they are very appropriate to explore the atmosphere of Venus.

[*] *The research work performed on the OxR device is done at the National Technical University of Athens and University of Patras under a programme of, and funded by, the European Space Agency (contract number 4000136482/21/NL/GLC/ov). However, the views expressed herein can in no way be taken to reflect the official opinion of the European Space Agency and are not intended to endorse particular technologies, companies, or products.*

[**] *The ACC experimental setup is under design and is funded by Dr. Sohan Jheeta.*

REFERENCES:

[1] Georgiou C.D., Zisimopoulos D., Kalaitzopoulou E., Quinn R.C. Radiation driven formation of reactive oxygen species in oxychlorine containing Mars surface analogues // Astrobiology. 2017. V. 17. No. 4. P. 319-336.

[2] Georgiou C.D., McKay C.P., Quinn R.C., Kalaitzopoulou E., Papadea P., Skipitari M. The Oxygen Release Instrument: Space mission reactive oxygen species measurements for habitability characterization, biosignature preservation potential assessment, and evaluation of human health hazards // Life. 2019. V. 9. P. 70. https://doi.org/10.3390/life9030070.

[3] Moon and Mars superoxides for oxygen farming // https://www.esa.int/. 04.03.2022. https://www.esa.int/Enabling_Support/Space_Engineering_Technology/Moon_and_Mars_superoxides_for_oxygen_farming.
[4] Zhang Z.H., Hartner E., Utinger B., Gfeller B., Paul A., Sklorz M., Czech H., Yang B.X., Su X.Y., Jakobi G., Orasche J., Schnelle-Kreis J., Jeong S., Gröger T., Pardo M., Hohaus T., Adam T., Kiendler-Scharr A., Rudich Y., Zimmermann R., Kalberer M. Are reactive oxygen species (ROS) a suitable metric to predict toxicity of carbonaceous aerosol particles? // Atmos. Chem. Phys. 2022. V. 22. P. 1793-1809. https://doi.org/10.5194/acp-22-1793-2022.
[5] Bardyn A., Baklouti D., Cottin H., Fray N., Briois C., Paquette J., Stenzel O., Engrand C., Fischer H., Hornung K., Isnard R., Langevin Y., Lehto H., Le Roy L., Ligier N., Merouane S., Modica P., Orthous-Daunay F.-R., Rynö J., Schulz R., Silén J., Thirkell L., Varmuza K., Zaprudin B., Kissel J., Hilchenbach M. Carbon-rich dust in comet 67P /Churyumov-Gerasimenko measured by COSIMA/Rosetta // Monthly Notices of the Royal Astronomical Society. 2017. V. 469, P. S712-S722. https://doi.org/10.1093/mnras/stx2640.
[6] Goesmann F., Brinckerhoff W.B., Raulin F., Goetz W., Danell R.M., Getty S.A., Siljeström S., Mißbach H., Steininger H., Arevalo R.D., Buch A., Freissinet C., Grubisic A., Meierhenrich U.J., Pinnick V.T., Stalport F., Szopa C., Vago J.L., Lindner R., Schulte M.D., Brucato J.R., Glavin D.P., Grand N., Li X., van Amerom F.H.W., the MOMA Science Team The Mars Organic Molecule Analyzer (MOMA) Instrument: Characterization of Organic Material in Martian Sediments // Astrobiology. 2017. V. 17. P. 655-685. https://doi.org/10.1089/ast.2016.1551.
[7] Syms R.R.A., Wright S. MEMS mass spectrometers: the next wave of miniaturization // J. Micromech. Microeng. 2016. V. 26. Art. No. 023001. https://doi.org/10.1088/0960-1317/26/2/023001.
[8] Conneely A.J., Bennett C., O'Connor G.M., Vollmerhausen T., O'Byrne C., Spence G., Rowe D., Victor J. Generation of side-emitting polymer optical fibres by laser ablation for use in antimicrobial applications // Intern. Congress on Applications of Lasers and Electro-Optics. 2016. Art. No. M604. DOI: 10.2351/1.5118619.
[9] Limpert J., Roser F., Schreiber T., Tunnermann A. High-power ultrafast fiber laser systems // IEEE J. Select. Topics Quantum Electron. 2006. V. 12. P. 233-244. https://doi.org/10.1109/JSTQE.2006.872729.

MISSION SCENARIO OF FLIGHT TO VENUS WITH LANDING AT ANY DESIRED LOCATION ON ITS SURFACE

V.A. Zubko[1], N.A. Eismont[1], A.A. Belyaev[1], K.S. Fedyaev[1], L.V. Zasova[1], D.A. Gorinov[1], A.V. Simonov[2], R.R. Nazirov[1]
[1] *Space Research Institute, Moscow, Russia; werrert2014@yandex.ru*
[2] *Lavochkin Research and Production Association, Khimki, Moscow Region*

KEYWORDS:
Venera-D project, resonant orbit, gravity assist maneuver, Venus, space mission

The Venera-D mission is intended to study Venus physical characteristics by scientific instruments installed on board of a spacecraft to be sent to Venus in 2029. The spacecraft will consist of two parts: the transfer and the Venus atmosphere modules. The first one fulfills all functions necessary to fly from the initial point of trajectory near the Earth after separation from the upper stage of the launcher to the point near Venus where the reentry module is detached and begins its own flight along the atmosphere entry trajectory. After that the transfer module fulfills series of maneuvers using a rocket engine and becomes a near Venus orbital satellite moving along a high elliptical orbit. After deceleration by atmospheric drag to the planned value of velocity the reentry module continues its motion with the use of parachutes. At the conclusion phase it is separated onto two parts: an atmospheric inflatable balloon and a lander. After this the lander lands onto planned site on the surface and its instruments fulfill the program of studying the Venus soil and atmosphere in the close proximity which is to last no more than 3 hours. The balloon after some descending increases its altitude to 60 km at the clouds layer in order to explore this area during several months.

For the lander the main goal for the mission scenario is to guarantee reaching any planned area of the Venus surface at the phase of the mission planning. In the earlier published papers, we have shown that this task is doable by the use of gravity assist maneuver near Venus during its first flyby when the spacecraft is transferred onto a resonant orbit with respect to Venus orbital motion. And mentioned above operations are executed after the spacecraft moving along the resonant orbit returns to Venus.

The main difficulties are generated by the necessity to satisfy demands to land the landing module in the prescribed place and simultaneously to put the orbiter on the orbit with the required period as well as other characteristics such as visibility between the lander and the orbiter during operations of landing, some minimum time of ballistic life of the orbiter and other flight dynamics characteristics requirements.

So, our mission design shows the example of compromising multipurpose requirements by the use of some new approaches for the scenario of mission development.

SCIENTIFIC GOALS OF THE VENERA-D LANDER

M.V. Gerasimov[1], and the JSDTeam
[1] *Space Research Institute, Moscow, Russia; mgerasim@cosmos.ru*

KEYWORDS:
Venera-D mission, atmosphere composition, cloud aerosols, surface mineralogy

INTRODUCTION:
The former exploration of the Venus by multiple missions gave general understanding of composition and pressure/temperature parameters of the atmosphere, atmospheric superrotation, structure of cloud layer, geological specifics of the surface, and preliminary surface chemical composition. Nevertheless, there are still a number of open scientific questions. Joint Science Definition Team (JSDT) was established about a decade ago by Roscosmos and NASA to identify science goals and Venera-D mission architecture options with enabling instrumentation for potential joint collaboration. Despite the present situation with sanctions and cancelation of cooperation, conclusions of the JSDT became the base of national Venera-D mission.

THE LANDER:
Advantage of Venera-D mission is the use of a Lander capable to perform direct analyses in the atmosphere down to the surface and about two hours at the surface.

Scientific goals of the Lander are:

- Perform chemical analysis of the surface material and study the elemental composition of the surface, including radiogenic elements;
- Study of interaction between the surface and atmosphere;
- Investigate the structure and chemical composition of the atmosphere down to the surface, including abundances and isotopic ratios of the trace and noble gases;
- Perform direct chemical analysis of the cloud aerosols;
- Characterize the geology of local landforms at different scales;
- Search for volcanic and seismic activity and search for lightning.

Capability to answer open questions will depend on the list of scientific payload of the Lander and on sensitivity and resolution of selected scientific instrumentation.

STUDY OF SULPHUROUS AND OTHER COMPONENTS OF THE VENUS ATMOSPHERE BY LASER ABSORPTION SPECTROSCOPY AT THE VENERA-D MISSION

I.I. Vinogradov[1], V.V. Barke[1], D.A. Belyaev[1], D.G. Evdokimova[1], V.A. Kazakov[1,2], Yu.V. Lebedev[1], V.V. Meshcherinov[2,1], O.Z. Roste[1], M.V. Spiridonov[1], A.A. Venkstern[1], P.A. Volkov[1]

[1] *Space Research Institute, Moscow, Russia; imant@iki.rssi.ru*

[2] *Moscow Institute of Physics and Technology, Moscow Region, Russia; meshcherinov@phystech.edu*

KEYWORDS:
Venera-D lander, atmosphere of Venus, sulfur dioxide, laser spectrometer

INTRODUCTION:
To continue studies of the atmosphere of Venus [1–3], an experiment ISCRA-V (Investigation of Sulphurous Components of Rarefied Atmosphere of Venus) have been proposed for retrieving of vertical profiles of sulphurous and of several minor gas components of the atmosphere at a descent trajectory of the Venera-D lander.

EXPERIMENT ENVIRONMENT AND METHOD OF MEASUREMENT:
An active phase of the experiment ISCRA-V [4, 5] will start up when a protective shield of the lander be dropped off at an altitude of nearly 70 km and will be continued during its decent until touching down the surface of Venus, and afterwards near the surface at the landing zone during the lander lifetime.

Multichannel laser absorption spectrometer (MLAS) is the core of the ISCRA-V instrument. The sequential operation of diode and quantum cascade lasers will make possible fine study of the ambient atmosphere composition. Probing laser beams will be coupled into a multipass optical cell analytical volume, filled in by a portion of the surrounding atmosphere, rarefied down to the work pressure of 20 mbar. Measurements are currently planned for a number of molecules and of several isotopologues (an example of model calculation is shown in Fig. 1):

- SO_2, CO_2, H_2O . . . . . at 7280 nm;
- OCS and $^{34}S/^{32}S$, CO, CO_2 . . . . . at 4823 nm;
- HCl and $^{37}Cl/^{35}Cl$ . . . . . at 3397 nm;
- CO_2 and $^{13}C/^{12}C$, $^{18}O/^{17}O/^{16}O$ . . . . at 2808 nm.

Multipass optical scheme of the MLAS concept is shown in Fig. 2. Collimated output beams of cascade lasers will be aligned into same trajectory, entering Herriot type mutipass cell at large radial input point distance from the cell center and passing over 15 m through the cell analytical volume with many reflections from the cell edge concave metallized mirrors. Output beam of a diode laser will enter the cell near its axis and will be aligned at shorter needed optical path of 1 m. MCT photodiode modules will detect laser beams as they pass through the cell volume. Same edge for optical input and output option will help for compactness of the 4-laser scheme.

Accuracy and precision of measurements are preliminary estimated to be at sub-percent level for retrieving of molecular concentrations and at percent level for isotopic ratios, in agreement with expected spectral peaks depth values of one percent to several percent and more for selected molecular absorption lines. Actual data error values will be estimated experimentally and might be reduced substantially in the case of efficient suppression of scattered light, which causes interference and fringing of highly monochromatic laser beams, giving main contribution to output signal noise and calculation errors.

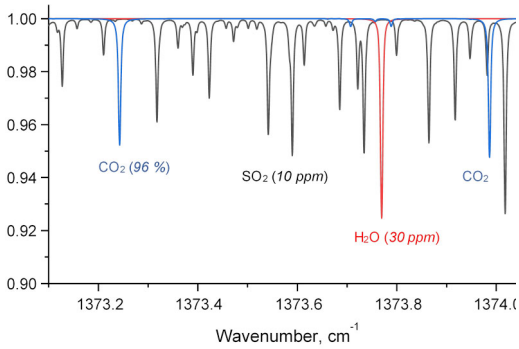

Fig. 1. Example of simulated spectral transmission for sampled atmosphere of Venus at the 7280 nm spectral region. The gas mix model total pressure is 20 mbar, temperature – 300 K, effective optical path – 15 m, and targeted gas components content: CO_2 96 %, SO_2 10 ppm, H_2O 30 ppm

Gas sampling system will take a portion of the ambient atmosphere, being injected by outside high pressure, will rarefy and insert it into the analytical cell volume and, after measurement, will rapidly pump it out in a ballast volume, setting 3–5 minutes of time for one complete measurement cycle. Sampling technique becomes challenging at low heights and near the surface of Venus, where the atmosphere main gas CO_2 approaches to and reaches its supercritical state under high values of its pressure and temperature.

General technological challenge is minimization of size, mass, power con-sumption, and other resource parameters of the ISCRA-V instrument, working under large variations of ambient gas pressure and temperature at the gas inlet and under expected wide variations of local temperature at the ISCRA-V mounting board, which may alter up by several tens of degrees during the experiment active time. Stability of opto-mechanical modules, reliability and rapidness of gas sampling should be provided by selection of original technologies and use of low thermal expansion materials, such as invar alloy and sitall ceramic, despite if they are hard ones for processing.

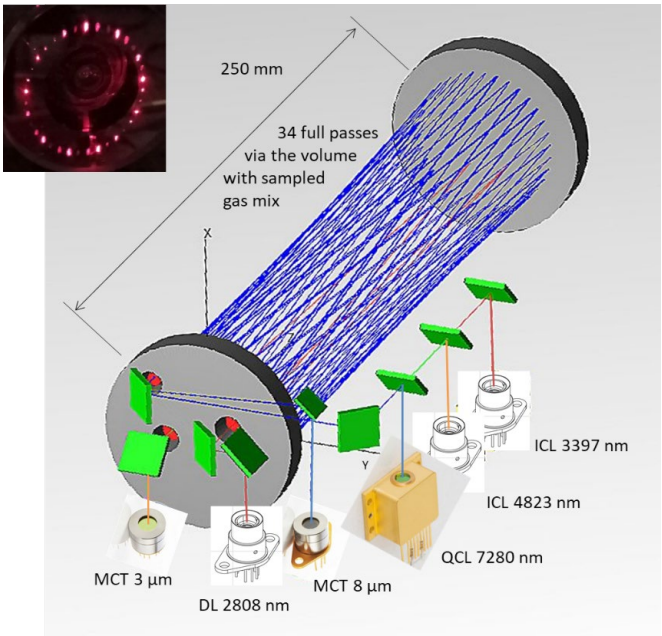

Fig. 2. An illustration of the ISCRA-V optical multipass sensor layout

SO_2 MEASUREMENTS IN THE CLOUD LAYERS:

The Venera-D lander at its descent will rapidly pass through the cloud layers of the atmosphere of Venus, leaving time for not more than two complete measurements of the ISCRA-V in the clouds. However, studies of gas mixing, phase transitions, chemical reactions, etc. in the cloud layers are of particular interest for the Venera-D mission. An optional atmospheric balloon probe module could be included into the mission for carrying out measurements in low and medium cloud levels, at heights from 53 to 60 km during several weeks of its work.

A simplified version of the ISCRA-V instrument could be proposed for measurement of molecular content variations in the clouds of Venus on board of such an atmospheric balloon-carried module. For example, leaving only one laser channel of measurements at 7280 nm spectral region (see Fig. 1) and adapting the gas sampling system to nearly "normal" pressure and temperature of the ambient atmosphere, it should be possible to monitor SO_2 content variations by a kind of a Laser Atmospheric Spectrometer (LAS) instrument with its high sensitivity to SO_2 and with its radically reduced mass and other resource requirements. In this case, carrying out regular measurements over a long time of time will help to obtain statistically accurate data and a spatial mapping of measured molecular content variations in accordance with the actual trajectory of the atmospheric module flight.

REFERENCES:

[1] Bertaux J.-L., Moroz V.I. et al. VEGA 1 and VEGA 2 entry probes: An investigation of local UV absorption (220-400 nm) in the atmosphere of Venus (SO2, aerosols, cloud structure) // J. Geophysical Research: Planets. 1996. V. 101. No. E5. P. 12709-12745.

[2] Zasova L.V. et al. SO2 in the middle atmosphere of Venus: IR measurements from Venera-15 and comparison to UV data // Icarus. 1993. V. 105. No. 1. P. 92-109.

[3] Zasova L.V. et al. Venera-D: A Design of an Automatic Space Station for Venus Exploration // Solar System Research. 2019. V. 53. No. 7. P. 506-510.

[4] Vinogradov I.I., Belyaev D.A. Experiment ISCRA-V (Investigation of Sulphurous Components of Rarefied Atmosphere of Venus) of the national project "Venera-D" // Intern. Conf. DLS-23. 27 Oct. 2015, GPI, Moscow. http://www.dls.gpi.ru/rus/sem/23/1.pdf.

[5] Vinogradov I. et al. Investigation of sulphurous components of rarefied atmosphere of Venus: ISCRA-V experiment at the Venera-D lander // Proc. VAK-2021 Conf. 23-28 Aug 2021, SAI MSU.M., 2022. P. 263. DOI:10.51194/VAK2021.2022.1.1.096.

VENUS INFRARED ATMOSPHERIC GASES LINKER (VIRAL): SCIENTIFIC CONCEPT FOR SOLAR OCCULTATION EXPERIMENT ON BOARD VENUS ORBITER MISSION

D.A. Belyaev[1], O.I. Korablev[1], F. Montmessin[2], A.V. Rodin[3], A. Trokhimovskiy[1], A.A. Fedorova[1], A.S. Patrakeev[1]

[1] *Space Research Institute, Moscow, Russia; bdenya.iki@gmail.com*

[2] *Laboratoire Atmosphères, Milieux, Observations Spatiales / Institut Pierre-Simon Laplace, Centre National de la Recherche Scientifique, Guyancourt, France*

[3] *Moscow Institute of Physics and Technology, Dolgoprudny, Russia*

KEYWORDS:
Venus atmosphere, minor species, solar occultation, infrared spectroscopy

INTRODUCTION:

In this paper, we describe a scientific concept of the VIRAL experiment (Venus InfraRed Atmospheric Linker), devoted to studing the composition and structure of Venus atmosphere at the top and above the cloud layer, on board the Venus Orbiter Mission announced by the Indian Space Research Organization (ISRO). VIRAL includes two infrared channels: an echelle spectrometer [1] and an ultra-high resolution heterodyne interferometer [2]. The instrument is designed to perform solar occultation measurements, providing an optimal photon yield combined with a superior spectral resolving power that exceeds 20 000. The high vertical resolution (with a footprint of about 1 km at the limb) allows the detailed altitude profiling of the Venusian upper atmosphere with its composition and structure.

VIRAL will provide the profiling of both the major and minor species that exist in Venus' upper atmosphere, altitudes from 65 to 150 km. The list of components in the infrared wavelength range (2.2–4.2 μm) includes CO_2 and its main isotopes (with related retrievals of the atmospheric temperature), H_2O and HDO (related to the evolution of water on Venus [3], CO, SO_2 [4]) HCl, HF, as well as H_2SO_4 droplets and aerosols. An optimized sensitivity will allow for the establishment ofrefined upper limits or new detections for a number of trace gases, such as H_2CO, OCS, C_2H_2, H_2S, and possibly phosphine. Due to the mission orbital peculiarity, VIRAL will cover the middle and near-equatorial latitudes. This will complement and improve the results of analogous experiment on board Venus Express orbiter operated in 2006–2014, which sounded mostly near the Northern Pole [5]. The VIRAL results will increase also our knowledge about the gaseous species variability and about the structure and dynamics of Venus upper atmosphere.

REFERENCES:

[1] Patrakeev A. et al. The Venus infrared atmospheric gases linker instrument concept for solar occultation studies of Venus atmosphere composition and structure onboard the Venus Orbiter Mission of the Indian Space Research Organization // Optics, Photonics and Digital Technologies for Imaging Applications VII. Proc. SPIE. 2022. V. 12138. Art. No. 1213810. https://doi.org/10.1117/12.2632371.

[2] Zenevich S., Gazizov I.S., Spiridonov M.V., Rodin A.V. IVOLGA: a high-resolution heterodyne near-infrared spectroradiometer for Doppler studies of Venus atmospheric dynamics // Optics, Photonics and Digital Technologies for Imaging Applications VII. Proc. SPIE. 2022. V. 12138. Art. No. 1213811. https://doi.org/10.1117/12.2632630.

[3] Fedorova A.A. et al. HDO and H2O vertical distributions and isotopic ratio in the Venus mesosphere by solar occultation at infrared spectrometer onboard Venus express // J. Geophys. Res. 2008. V. 113. http://dx.doi.org/10.1029/2008JE003146.

[4] Belyaev D.A. et al. Vertical profiling of SO2 and SO above Venus' clouds by SPICAV/SOIR solar occultations // Icarus. 2012. V. 217. P. 740-751.

[5] Vandaele A.-C. et al. Contribution from SOIR/VEX to the updated Venus International Reference Atmosphere (VIRA) // Adv. Space Res. 2016. V. 57. No. 1. https://doi.org/10.1016/j.asr.2015.08.012.

REANALYSIS OF INTERNAL WAVES IN THE VENUS'S ATMOSPHERE BY USING MAGELLAN RADIO OCCULTATION DATA

V.N. Gubenko[1], I.A. Kirillovich[1]
[1] *Kotel'nikov Institute of Radio Engineering and Electronics RAS, Fryazino branch, Fryazino, Moscow region, Russia; vngubenko@gmail.com, gubenko@fireras.su*

KEYWORDS:
Radio occultation measurements, Magellan spacecraft, Venus's atmosphere, vertical temperature profiles, internal gravity waves.

INTRODUCTION:
Radiative damping in the Venus's atmosphere at altitudes above ~65 km is the main process of internal wave dissipation having vertical wavelength <4 km, and this approach was used by Hinson and Jenkins [1] earlier for the wave analysis of the Magellan radio occultation (RO) temperature and signal intensity data. We used parameters of the temperature variation at altitude of ~65 km from Magellan profiles, remaining after high-pass filtering for wavelengths <4 km by Hinson and Jenkins, as the input data for our reanalysis of internal waves in the Venus's atmosphere. Internal gravity wave (IGW) characteristics in the atmosphere were inferred from the radio occultation measurements, collected on 5–6 October 1991 during three successive orbits (orbit numbers 3212–3214) of the Magellan spacecraft [1]. The results obtained by two independent methods are presented, compared, and discussed in this work.

ANALYSIS OF THE MAGELLAN RO TEMPERATURE DATA BY USING THE SATURATED WAVE ASSUMPTION (SWA-METHOD):
The estimate of intrinsic wave frequency by Hinson and Jenkins [1] (HJ-paper) is based on the assumption that the observed attenuation of wave amplitude at altitudes above ~65 km is due to radiative damping. With this aim, they analyzed the attenuation of vertical temperature oscillations in the three Magellan profiles at the full altitude range from ~65 to ~90 km.

Our SWA-method uses parameters of local temperature anomaly at altitude of ~65 km only which is connected with the monochromatic IGW. They are the amplitude of temperature perturbation $|T'|$=4 K, its vertical wavelength $|\lambda_z|=2\pi/|m|$=2.5 km, the background absolute temperature T_b = 230 K, the normalized amplitude of temperature perturbation $|\hat{T}'|=|T'/T_b|=17\cdot10^{-3}$, and the background buoyancy (Brunt-Vaisala) frequency N_b =0.021 rad/s. These experimental values were determined by Hinson and Jenkins [1] from temperature data and they are represented in table 1 (upper part) as input RO data for our reanalysis. Based on the above indicated values and equation (12) of the work [2], the values of relative wave amplitude a_e and other IGW parameters were reconstructed. Thus, our local estimates don't require temperature analysis in the full altitude range. Using equation (12) of the work [2] and indicated data about vertical wavelength, background buoyancy frequency, gravity acceleration, normalized amplitude of temperature perturbations, we have determined the relative wave amplitude a_e = 0.83. This value satisfies the IGW identification criterion ($a_e \le 1$) and wave-like temperature fluctuations in Magellan RO data may be considered as wave induced. Based on HJ-paper [1] results about wind velocity perturbation amplitude $|u'|$and intrinsic horizontal phase speed, we have also calculated relative wave amplitude ~0.82. The key ratio f/ω was determined with the aid of following equation:

$$\frac{f}{\omega}=\frac{2\sqrt{1-a}}{2-a}=\frac{2\sqrt{1-a_e/d_e}}{2-a_e/d_e}. \qquad (1)$$

Assuming that the wave saturation degree d_e = 1 = 100 % (saturated wave assumption), we have found from (1) that the ratio f/ω is equal to ~0.69.

Using value $|f|=2.7\cdot10^{-5}$ rad/s at 67° N latitude, we have determined the intrinsic frequency $\omega = 3.9\cdot10^{-5}$ rad/s and intrinsic wave period τ^{in}=44.8 hrs = = 1.9 days. The last value is ~5 times greater than the wave period ~9 hrs inferred in HJ-paper [1]. In the table 1 we have shown internal wave characteristics which were computed from the Magellan RO temperature data using SWA-method.

Comparison our results with the data found in HJ-paper [1] shows dramatic differences. So, our estimate of intrinsic horizontal phase speed $|c_{ph}^{in}|$ (~11.8 m/s) and wave amplitude of wind speed perturbations $|u'|$ (~9.9 m/s) are 1.4 more than corresponding estimates ~8.5 m/s and ~7.0 m/s inferred in [1]. We see that these estimates $|c_{ph}^{in}|$ and $|u'|$ found by two independent techniques differ from each other by ~28 and ~29 % respectively. The value of horizontal wavelength obtained by SWA-method (~1895 km) is ~7 times greater than corresponding value ~270 km found by Hinson and Jenkins [1]. One of the reasons for observed differences is possible uncertainties for methods used. Hinson and Jenkins declare that probably uncertainty of their method is of ~50 % [1, p. 322].

Taking into account the results obtained in the works [3–5], we consider that following two assumptions given in HJ-paper [1, p. 319, left column] may be reasons of significant systematic uncertainties:

1. "The wave amplitude is not sufficient to cause convective instability, an alternative damping mechanism."
2. "Similarly, wind-shear instability is not likely to be the cause of the observed attenuation, since the wave amplitude appears to be insufficient to trigger this effect."

In addition, authors of HJ-paper [1, p. 320, right column] used a simplified dispersion equation for IGWs with intermediate intrinsic frequencies: $N_b >> \omega >> f$, which excludes low-frequency internal waves in advance.

For reanalysis Magellan RO temperature data we use the saturated wave assumption and in our SWA-method. Sometimes, this assumption does not hold, thus leading to some systematic errors in the SWA-method application and aliasing of reconstructed wave characteristics [6]. Let us consider error estimates connected with the fact that the exact value of threshold amplitude a may be differ from relative wave amplitude a_e. We assume a fully saturated wave $a_e = a = 0.83$, but in the common case a threshold amplitude a may be arbitrary obeying inequality $1 \geq a \geq a_e$. So, the possible values of saturation degree are in the interval $1 \geq d_e \geq a_e$, or $83 \leq d_e \leq 100$ %. Simultaneous radiosonde studies of temperature and wind speed show that saturated IGWs are observed in most cases; however, exceptions are also possible [6]. We adopt a reasonable deviation of ~10 % for the a_e- and a-values. Points A and B in figure 1 indicate our obtained results and 10 % deviation: A ($f/\omega = 0.69$; $a_e = 0.83$) and B ($f/\omega = 0.54$; $a = 0.91$). The value $f/\omega = 0.54$ was calculated with aid of equation (1) using $a = 0.91$. So, we see that relative uncertainty for f/ω is equal of ~22 %. We have found other internal wave characteristics for given case B. Their magnitudes are: $\omega = 5.0\cdot10^{-5}$ rad/s (~28 %); τ^{in} = 34.9 hrs (~22 %); $|c_{ph}^{in}|$ =9.9 m/s (~16%), $|k_h|= 0.5\cdot10^{-5}$ m^{-1} (~52 %); λ_h = 1260 km (~34 %); $|u'|$=9.0 m/s (~9 %); $|v'|$=4.9 m/s (~28%); $|w'|=1.8\cdot10^{-2}$ m/s (~39 %). The relative errors for these parameters are shown in brackets. We see that a deviation of ~10 % for the a_e- and a-values leads to relative uncertainties from ~9 % to ~52 % for the reconstructed IGW characteristics.

Thus, the observed great differences between wave parameters reconstructed by two independent methods may be connected with erroneous assumptions and significant systematic uncertainties for methods used. There is a simple possible explanation allowing reconciling the results obtained by two independent techniques. The data obtained in work [1] can indicate that an analyzed internal wave is unsaturated. The values of the threshold amplitude a and saturation degree d, calculated on the basis of the data from [1], are ~0.99 and ~83 %, respectively. If the errors of the method allow these estimates to be considered reliable, the assumption about the saturation of the internal wave amplitude may not be fulfilled. In this case, the correction ($d_e = 0.83 = 83$ %) in equation (1) makes it possible to reconcile the results obtained by two independent methods.

Table 1. Internal gravity wave characteristics in the Venus's atmosphere inferred by two independent methods from the radio occultation temperature data collected on 5–6 October 1991 during three successive orbits (orbit numbers 3212–3214) of the Magellan spacecraft

Input radio occultation data taken from HJ-paper [1] for analysis	
Solar zenith angle (SZA)	109°
Local true solar time (LTST)	22 h 05 m
Latitude, ϕ	67° N
Longitude	127° E
Altitude, h (Venus's radius R_0 = 6052 km)	≥57 km
Acceleration of gravity[1], g	8.7 m/s^2
Angular rotation rate of the atmosphere, Ω	$-1.5\cdot10^{-5}$ rad/s (westward)
Coriolis parameter, $\lvert f\rvert=\lvert 2\Omega\cdot\sin\varphi\rvert$	$2.7\cdot10^{-5}$ rad/s (at 67° N latitude)
Inertial period, $\tau_f = 2\pi/\lvert f\rvert$	~64.6 hrs ≈ 2.7 days (at 67° N latitude)
Background absolute temperature[1,*], T_b	~230 K
Background buoyancy frequency[1,*], N_b	~$2.13\cdot10^{-2}$ rad/s
Vertical wavelength[1], $\lvert\lambda_z\rvert = 2\pi/\lvert m\rvert$	2.5 km
Vertical wave numbe[1], $\lvert m\rvert$	~$2.5\cdot10^{-3}$ m^{-1}
Amplitude of temperature perturbations[1], $\lvert T'\rvert$	4.0 K
Normalized amplitude of temperature perturbations[1,*], $\lvert\hat{T}'\rvert=\lvert T'/T_b\rvert$	~$17.4\cdot10^{-3}$
Internal wave characteristics found by two independent methods	
Relative wave amplitude[1], $\lvert a_e\rvert\equiv\lvert u'\rvert/\lvert c_{ph}^{in}\rvert$	~0.83 (our results) 0.82 (was calculated by us for HJ-paper results)
Intrinsic wave frequency[1], ω	~$3.9\cdot10^{-5}$ rad/s (our results) $2\cdot10^{-4}$ rad/s (parameter σ in HJ-paper)
Intrinsic wave period[1], $\tau^{in} = 2\pi/\omega$	~44.8 hrs ≈ 1.9 days (our results) ~9 hrs (value 2π/σ in HJ-paper)
Ratio f/ω	~0.69 (our results) ~0.14 (value f/σ in HJ-paper)
Intrinsic horizontal phase speed[1], $\lvert c_{ph}^{in}\rvert=\omega/\lvert k_h\rvert$	~11.8 m/s (our results) 8.5 m/s (value N/m in HJ-paper)
Horizontal wave number[1], $\lvert k_h\rvert=\omega/\lvert c_{ph}^{in}\rvert$	~$0.33\cdot10^{-5}$ m^{-1} (our results) ~$2.33\cdot10^{-5}$ m^{-1} (was calculated from HJ-paper)
Horizontal wavelength[1], $\lambda_h = 2\pi/k_h$	~1895 km (our results) 270 km ("meridional" wavelength in HJ-paper)
Amplitude of wind speed perturbations along the horizontal propagation vector, $\lvert u\rvert=a_e\lvert c_{ph}^{in}\rvert$	~9.9 m/s (our results) 7.0 m/s ("meridional" amplitude in HJ-paper)
Amplitude of speed perturbations transverse to the horizontal propagation vector, $\lvert v'\rvert=f/\omega\lvert u'\rvert$	~6.8 m/s (our results) 0.7 m/s ("zonal" speed amplitude in HJ-paper)
Amplitude of vertical wind speed perturbations, $\lvert w'\rvert=\lambda_z/\lambda_h\lvert u'\rvert$	~1.3 10^{-2} m/s (our results) 0.07 m/s (vertical speed amplitude in HJ-paper)

[1] At 65 km altitude;

[*] was calculated by us using data of HJ-paper [1]

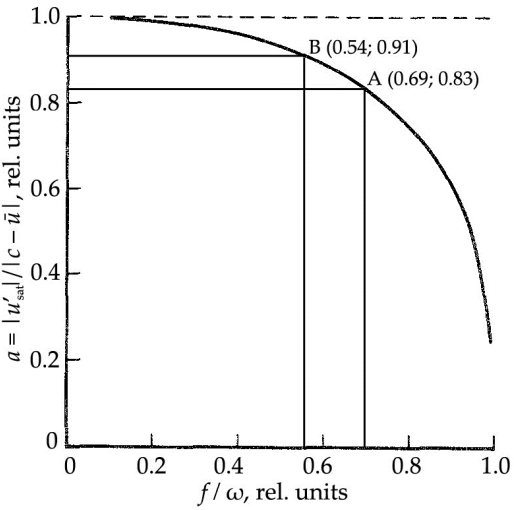

Fig. 1. Normalized wave amplitude (threshold amplitude) a required for shear wind instability ($Ri < 1/4$) as a function f/ω. The wave amplitude ($a = 1$) required for convective instability is shown by a dashed line. This plot was built by using formula (7) from the work [2]

FUNDING:
This research has been carried out in the framework of the state task.

REFERENCES:

[1] Hinson D.P., Jenkins J.M. Magellan radio occultation measurements of atmospheric waves on Venus // Icarus. 1995. V. 114. P. 310-327.
[2] Gubenko V.N., Pavelyev A.G., Andreev V.E. Determination of the intrinsic frequency and other wave parameters from a single vertical temperature or density profile measurement // J. Geophys. Res. 2008. V. 113. Art. No. D08109. DOI: 10.1029/2007JD008920.
[3] Fritts D.C. A review of gravity wave saturation processes, effects, and variability in the middle atmosphere // Pure Appl. Geophys. 1989. V. 130. P. 343-371.
[4] Fritts D.C., Rastogi P.K. Convective and dynamical instabilities due to gravity motions in the lower and middle atmosphere: Theory and observations // Radio Sci. 1985. V. 20. No. 6. P. 1247-1277.
[5] Dunkerton T.J. Inertia-gravity waves in the stratosphere // J. Atmos. Sci. 1984. V. 41. P. 3396-3404.
[6] Gubenko V.N., Kirillovich I.A. Diagnostics of internal atmospheric wave saturation and determination of their characteristics in Earth's stratosphere from radiosonde measurements // Solar-Terrestrial Physics 2018. V. 4. No. 2. P. 41-48. DOI: 10.12737/stp-42201807.

SESSION 6. VENUS (VN)
POSTER SESSION

WINDS FROM THE VISIBLE (513 nm) IMAGES OBTAINED BY THE VENUS MONITORING CAMERA ONBOARD VENUS EXPRESS

I.V. Khatuntsev[1], M.V. Patsaeva[1], L.V. Zasova[1], D.V. Titov[2], N.I. Ignatiev[1], D.A. Gorinov[1], A.V. Turin[1]
[1] *Space Research Institute, Moscow, Russia, khatuntsev@iki.rssi.ru*
[2] *Leiden Observatory, Leiden University, Leiden, The Netherlands*

KEYWORDS:
Venus, atmosphere; Atmospheres, dynamics; Visible, images

INTRODUCTION:

Here we present our last publication in Journal of Geophysical Research: Planets [1].

More than 250 000 wind vectors in the Southern hemisphere were derived from the VMC VIS image pairs using automated correlation procedure. The observations covered almost entire Venus Express lifetime (eight Venus years).

The VMC VIS channel (513 nm) sounded the lower part of the upper cloud (60±3 km) located between the layers at 70±2 km (cloud top) and 55±2 km (middle cloud) probed by two other VMC channels: UV (365 nm) and near-IR (965 nm) correspondingly. Effective altitudes of the layers depend on the cloud structure and vary with space (especially, latitude) and time.

The mean VIS zonal wind speed gradually decreases with latitude from about −85 m/s close to the equator to −35 m/s at 80º S.

We found acceleration of the mean zonal wind at 30±5° S over 5 years (8 Venusian years) by 18.5 m/s (Fig. 1a, green line).

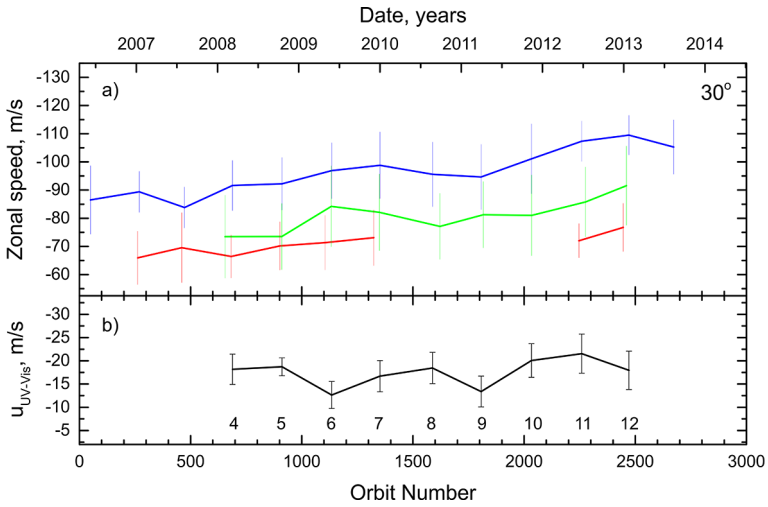

Fig. 1. Long-term variations of the mean zonal velocity at latitude 30±5° S: *a*) UV (blue), VIS (green) and near-IR (red) winds. The error bars correspond to standard deviations σ; *b*) the difference between mean zonal velocities derived from the UV and VIS channels. The numbers indicate the data sets. The error bars correspond to 99.6 % confidence interval ($3\sigma_{\bar{x}}$),shaded areas correspond to the standard deviations σ

The meridional wind derived from the VIS images has equatorward direction in the entire Southern hemisphere. The mean meridional wind speed peaks at ~10° S with +9.4±1.3 m/s (σ = 7.0 m/s) value and then gradually decreases to +1.1±0.1 m/s (σ = 7.4 m/s) at 50–55° S. Further towards the pole, the meridional component increases to +2±0.2 m/s (σ = 5.5 m/s). The VMC day

observations alone do not allow to conclude whether these motions indicate a thermal tide or a branch of a Hadley cell. However, comparisons with night observations as well as general circulation modelling suggest that the latter case is likely in the deep cloud.

Variations of the zonal and meridional wind components correlated with both local time and surface topography are observed in the cloud layer. Both zonal and meridional components have daytime maxima at low latitudes (~15° S) at 14–15 h local time.

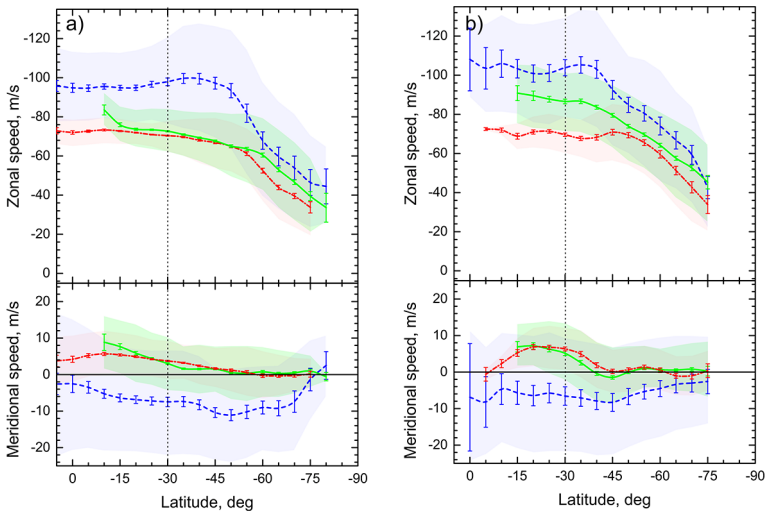

Fig. 2. Mean latitudinal profiles of the zonal and meridional winds derived for the "slow" (a) and "fast" (b) sub-sets. Error bars correspond to 99.6 % ($3\sigma_{\bar{x}}$)) confidence interval; colored shaded areas correspond to the standard deviations σ.

The latitudinal profiles of the zonal wind derived from the VIS images usually fall between those measured in UV and near-IR channels. In extreme cases they can be quite close either to UV or to near-IR wind profiles (Fig. 2). We think it would be more natural to expect VIS and near-IR wind profiles to be close since these channels sound approximately the same altitude due to similarity of the optical properties from visible through near-IR. Similarity of the VIS and UV winds is likely due to that in some cases both VMC channels "see" similar cloud features. This could, for instance, result from the UV absorption extending to the visible spectral range or presence of additional absorbers at the cloud top.

We found a tentative evidence for quasiperiodic long-term variations in the difference between the mean zonal wind speeds derived from the UV and VIS channels with a period of about 3 Venusian years and amplitude of 5–6 m/s (Fig. 1b). These quasiperiodic variations may be due to the degree of "visibility" of identical structures in the UV and VIS channels.

REFERENCES:

[1] Khatuntsev I.V., Patsaeva M.V., Zasova L.V., Titov D.V., Ignatiev N.I., Gorinov D.A., Turin A.V. Winds from the visible (513 nm) images obtained by the Venus Monitoring Camera onboard Venus Express // J. Geophysical Research: Planets. 2022. V. 127. Art. No. e2021JE007032. https://doi. org/10.1029/2021JE007032.

FROM VMC/VENUS EXPRESS TO UVI/AKATSUKI. LONG-TERM AND LONGITUDE VARIATIONS OF ZONAL WIND SPEED AT THE CLOUD TOP LEVEL NEAR NOON

M.V. Patsaeva[1], I.V. Khatuntsev[1], N.I. Ignatiev[1], D.V. Titov[2], L.V. Zasova[1], A.V. Turin[1], D.A. Gorinov[1]
[1] *Space Research Institute, Moscow, Russia; marina@irn.iki.rssi.ru*
[2] *Leiden Observatory, Leiden University, Lieden, The Netherlands*

KEYWORDS:
Venus, mesosphere, dynamics, topography.

INTRODUCTION:
UV (365 nm) images obtained by Venus Monitoring Camera (VMC/Venus Express) from 2006 to 2013 and by Ultraviolet Imager (UVI/Akatsuki) from December 2015 to August 2020 were used to study the mesosphere dynamics. Wind vectors obtained by processing 528 orbits of VMC and 86 orbits of UVI were derived by the digital tracking technique [1, 2]. We have studied changes in the longitudinal dependence of the zonal speed at the cloud top (70±2 km) in equatorial latitudes for limited time intervals of Venus Express and Akatsuki missions. Since the longitudinal position of the zonal speed minimum varies depending on local time, and the zonal speed minimum is observed at noon [3], studies were carried out for 11:00–13:00 local time (LT) interval for both missions.

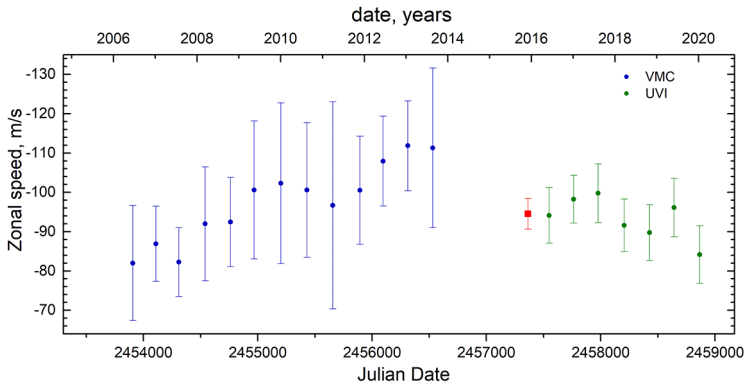

Fig. 1. Variations of the mean zonal wind speed at 20º±2.5ºS over the mission time (*X* axis – Julian Date) from 11:00 to 13:00 LT. Every point is the result of averaging over the Venusian year (224.7 days) in latitude band 20±2.5° S. Blue circles show zonal wind averaged through the Venusian year derived from VMC images, green circles are the same for UVI. Red square shows zonal wind averaged by using only two days of observation (2015.12.07–08). Error bars correspond to standard deviation σ.

RESULTS:
The VMC registered in 2006–2013 the increase of the mean zonal wind speed from 85 to 115 m/s in equatorial latitudes [1]. Figure 1 shows the zonal speed variations at 20° S, from 2006 to 2020. The trend obtained from the VMC data (2006–2014) shows the increase in the average zonal speed from 82 to 112 m/s by 2013. The results obtained from UVI images from the end of 2015 to 2020 manifest a downward trend of the mean zonal wind speed (from 95 to 84 m/s), opposite to the upward trend obtained from VMC images before 2013.

The study of the longitudinal dependence of the zonal speed on a set of limited trend intervals makes it possible to trace the evolution of the minimum

over Aphrodite Terra over time. Figure 2(a–f) shows how, as the mean zonal speed increases during the VMC/Venus Express mission, the minimum of the mean zonal speed over Aphrodite Terra transforms into a maximum. Conversely, as the mean zonal speed decreases (UVI/Akatsuki), the relative maximum observed over Aphrodite gradually transforms into a zonal speed minimum (Fig. 2(g–j)), which is then smoothed out (Fig. 2k) and, forming again, shifts in the direction of superrotation.

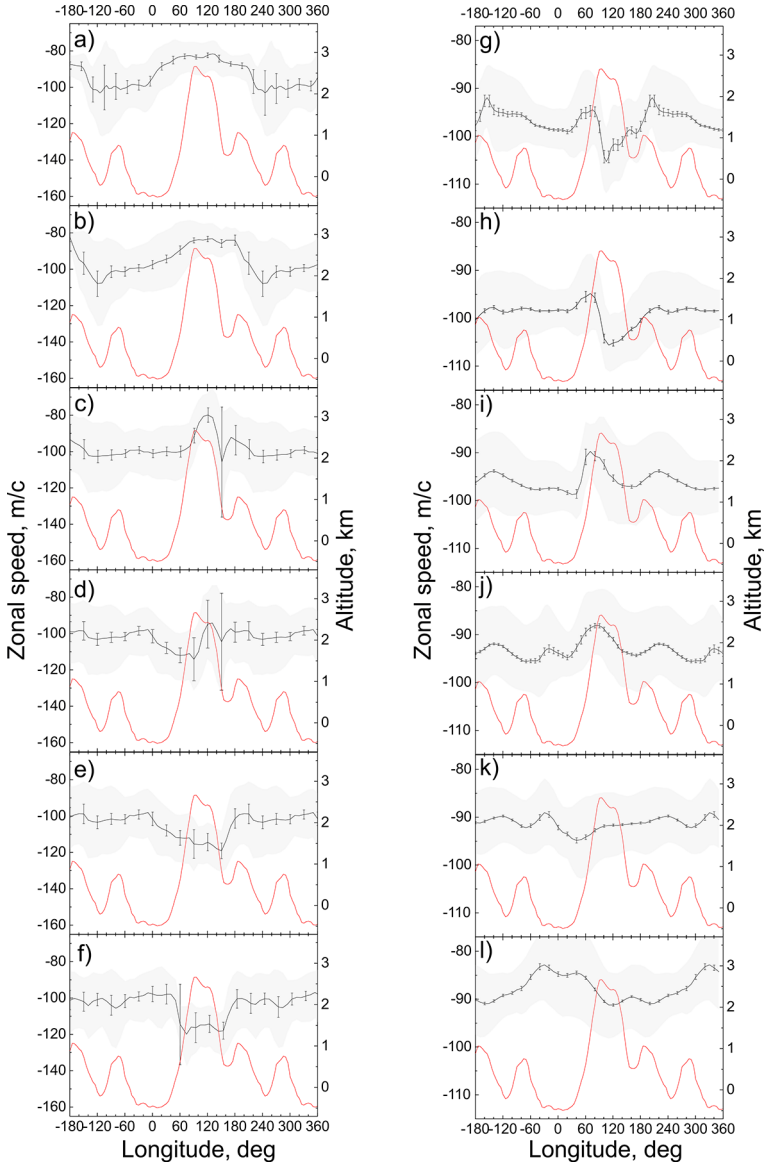

Fig. 2. Dependences of the zonal speed (black lines) on longitude in the upward part of trend (VMC) averaged for 6 Venus years: 01–06 (*a*), 03–08 (*b*), 05–10 (*c*), 06–11 (*d*), 07–12 (*e*), 08–13 (*f*). Dependences of the zonal speed (black lines) on longitude in the downward part of trend (UVI) averaged for 3 Venus years: 01–03 (*j*), 02–04 (*h*), 03–05 (*i*), 04–06 (*j*), 05–07 (*k*), 06–08 (*l*). Zonal speed is averaged in 10-deg latitude band above the highest region of Aphrodite Terra (from 5 to 15° S) in local time interval from 11:00 to 13:00 hours. The red line (all panels) shows the mean surface topography at the same latitude band. The error bars correspond to the 99.6 % confidence interval ($3\sigma_{\bar{x}}$). Grey shaded are as correspond to the standard deviations σ. Horizontal coordinate corresponds to 1.5 longitudinal period (540°) for better presentation

According to Fig. 2, the zonal speed maximum above Aphrodite Terra is observed for the first time when the results, including ones corresponding to the 11th Venusian year of the upward part of the trend (VMC), are averaged (Fig. 2d). At the beginning of the downward part of the trend (UVI), a relative maximum above Aphrodite Terra is observed only on the curve containing measurements corresponding to the 1st Venusian year (Fig. 2g). Thus, we can assume a change in the dynamics of the atmosphere of Venus from 2012 to 2015. The smoothing of the minimum (Fig. 2k), when the influence of the surface on the zonal velocity is not visible, and the subsequent appearance of the minimum, as well as its displacement (Fig. 2l), suggests some changes in atmospheric dynamics that require further study.

CONCLUSION:

The monotonous increase of the mean zonal speed at equatorial latitudes from 82 to 112 m/s during 2006–2013 changed to its gradual decrease down to 84 m/s in 2020. Change in the dynamics of the Venus atmosphere was observed from 2012 to 2015 and corresponds to high mean zonal speed in the trend.

REFERENCES:

[1] Khatuntsev I.V., Patsaeva M.V., Titov D.V., Ignatiev N.I., Turin A.V., Limaye S.S. et al. Cloud level winds from the Venus Express Monitoring Camera imaging // Icarus. 2013. V. 226. No. 1. P. 140-158. https://doi.org/10.1016/j.icarus.2013.05.018.

[2] Patsaeva M.V., Khatuntsev I.V., Patsaev D.V., Titov D.V., Ignatiev N.I., Markiewicz W.J., Rodin A.V. The relationship between mesoscale circulation and cloud morphology at the upper cloud level of Venus from VMC/Venus Express // Planetary and Space Science. 2015. V. 113-114. No. 08. P. 100-108. https://doi.org/10.1016/j.pss.2015.01.013.

[3] Patsaeva M.V., Khatuntsev I.V., Zasova L.V., Hauchecorne A., Titov D.V., Bertaux J.-L. Solar Related Variations of the Cloud Top Circulation Above Aphrodite Terra from VMC/Venus Express Wind Fields // J. Geophysical Research: Planets. 2019. V.124. P. 1864-1879. https://doi.org/10.1029/2018JE005620.

DESCENT IN THE ATMOSPHERE OF VENUS WITH THE ULTRAVIOLET SPECTROMETER (DAVUS): SCIENTIFIC CONCEPT FOR A LANDING MISSION

D.A. Belyaev[1], D.G. Evdokimova[1], N.I. Ignatiev[1], N.A. Vyazovetskiy[1], I.A. Dzuban[1], M.V. Spiridonov[1], I.I. Vinogradov[1]
[1] *Space Research Institute, Moscow, Russia; bdenya.iki@gmail.com*

KEYWORDS:
Venus atmosphere, descend probe, spectroscopy, UV absorbers

ABSTRACT:
We propose a new generation instrument, DAVUS (Descent in the Atmosphere of Venus with the Ultraviolet Spectrometer), for *in-situ* measurements of the atmospheric UV absorbers on board Roscosmos's "Venera-D" landing platform. The experiment implements active absorption spectroscopy using an integrated UV source: its light penetrates through Venusian gases in an optical cell and further is registered by a spectrometer at the wavelength range from 250 to 400 nm. This spectral interval is sensitive to the molecular absorption lines of minor species, such as SO_2, SO, ClO, which play key roles in the chemistry of the clouds and the lower atmosphere of Venus. For example, sulfur dioxide SO_2, being a volcanic gas, is a chemical precursor of H_2SO_4-acid clouds (47–70 km) enshrouding the planet. In the clouds, SO_2 mixing ratio sharply decrease with altitude: from ~10^5 ppbv at 50 km to ~10^2 ppbv at 70 km [1, 2] (Fig. 1).

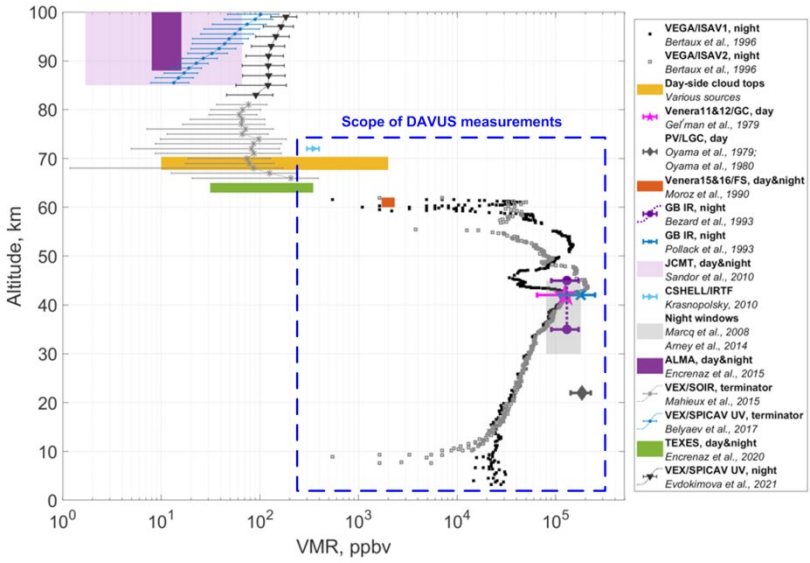

Fig. 1. Overview of SO_2 content measurements on Venus (ppbv – parts per billion in volume) at various atmospheric altitudes (adapted from Vandaele et al. [2]). The blue dashed line frames the DAVUS measurement scope

Another subject of interest is an unknown UV absorber situated at 300–400 nm when measuring the contrast albedo of Venus clouds. So far, a profound spectral characterization to define this component has been performed neither remotely nor *in situ*. Sulfurs S_x and dimeric sulfur monoxide S_2O_2, studied by Frandsen et al. [3], are also considered by DAVUS as probable candidates for the unknown absorber.

While the platform is descending from an altitude of 70 km to the surface, the gaseous and aerosol species fill the multi-pass optical cell. The spectrometer (isolated hermetically and thermally) measures the atmospheric transmission with a high spectral resolution of 0.2 nm (Fig. 2). Thus, the considered gases' concentration can be retrieved at an effective footprint length (in the cell) about 2 m with the altitude sampling of ~500 m. An analogous experiment was previously performed by ISAV/VEGA instrument [1], which retrieved SO_2 abundance at the altitude range of 5–60 km, not covering the uppermost cloud layer (see Fig. 1). With DAVUS we improve the sensitivity, spectral resolution and the altitude coverage relative to ISAV measurements. This will enlarge our knowledge about the atmospheric UV absorbers and their linkage with volcanic activity on Venus.

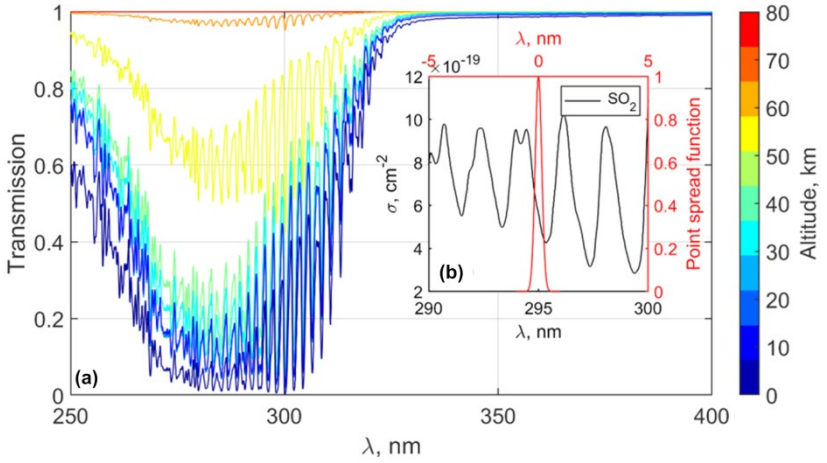

Fig. 2. Examples of SO_2 transmission spectra, modeled for DAVUS measurements at different atmospheric altitudes (a). All spectra are convolved by a point spread function of the instrument with a spectral width of 0.2 nm (b)

ACKNOWLEDGEMENTS:
Design of science concept for DAVUS experiment is supported by the grant No. 075-15-2020-780 (No. 13.1902.21.0039) of Russian Ministry of Science and Education.

REFERENCES:

[1] Bertaux J.-L. et al. VEGA-1 and VEGA-2 entry probes: An investigation of local UV absorption (220-400 nm) in the atmosphere of Venus (SO2, aerosols, cloud structure) // J. Geophysical Research: Planets. 1996. V. 101. No. E5. P. 12709-12745.
[2] Vandaele A.C. et al. Sulfur dioxide in the Venus atmosphere: I. Vertical distribution and variability // Icarus. 2017. V. 295. P. 16-33.
[3] Frandsen B.N. et al. Spectroscopy of OSSO and other sulfur compounds thought to be present in the Venus atmosphere // The J. Physical Chemistry A. 2020. V. 124. No. 35. P. 7047-7059.

DIFFRACTION PHENOMENA IN RADIO OCCULTATION STUDIES OF THE ATMOSPHERE OF VENUS BY THE SATELLITES VENERA-15 AND -16

V.N. Gubenko[1], V.E. Andreev[1], I.A. Kirillovich[1], T.V. Gubenko[1], D.A. Pavelyev[1]

[1] *Kotel'nikov Institute of Radio Engineering and Electronics RAS, Fryazino branch, Fryazino, Moscow region, Russia; vngubenko@gmail.com; gubenko@fireras.su*

KEYWORDS:
Atmosphere of Venus, Fresnel diffraction, Cornu spiral, radio occultation measurements

INTRODUCTION:

Using Venera-15 and -16 satellites, the radio occultation measurements of the Venus's atmosphere were carried out in the period from October 1983 to September 1984. The orbits of the satellites were such that the approaches to the planet were made in the Northern Hemisphere of Venus, and exits – in the Southern. As a result of radio probing of the atmosphere by satellites entering the planet, a regular drop in the decimeter (wavelength ~32 cm) signal intensity with the decreasing altitude was observed in the range from 80 to 45 km. Such a change in the signal level is due to the atmospheric refraction of radio waves. The typical behavior of the normalized radio wave intensity I_{norm} versus altitude is shown in Fig. 1 (panel a).

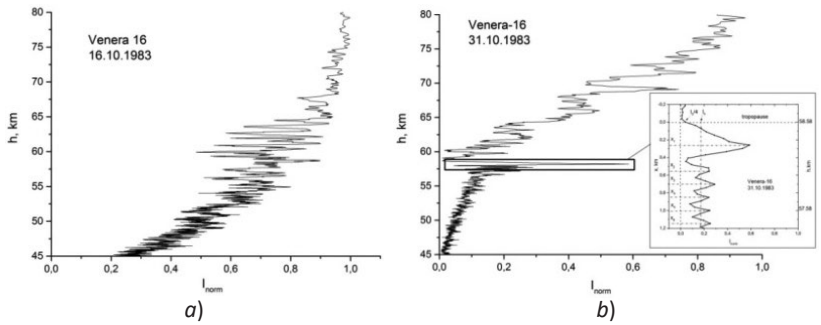

a) *b*)

Fig. 1. Examples of the behavior of the normalized radio wave intensity I_{norm} versus altitude. Panel *a*) shows typical behavior in many sessions, panel *b*) shows behavior with a striking feature that was observed in several sessions. The inset of panel *b*) shows a fragment of the selected part in magnification

In some sessions, the experimental profiles of the refractive attenuation versus the ray altitude show a sharp drop in the radio wave intensity and a bright feature is distinguished in the range from 60 to 56 km near tropopause. In this altitude interval, an alternation of deep minima and sharp maxima of the signal power is observed. The behavior of the normalized radio wave intensity I_{norm} as the ray deepens into the planet's atmosphere in sessions with a singularity is shown in Fig. 1 (panel b). It was found that strong changes in the signal level occur in the region where the transition from the isothermal to the adiabatic polar atmosphere and a sharp change in the temperature gradient are observed [1].

EXPERIMENTAL DATA:

It was noted above that during radio sounding of the atmosphere of Venus at altitudes from 60 to 56 km, strong changes in the signal level were observed on some profiles of the signal intensity. This feature manifested itself in the following: the radio wave intensity dropped to almost zero levels at an altitude of ~59 km, then, as the ray descended, it sharply increased with

the transition to a damped undulating behavior at the same level at altitudes near ~57 km. With further lowering of the ray into the atmosphere of the planet, the radio wave intensity fell in a typical way characteristic of refraction. The described behavior of the intensity at the indicated altitude interval in five radio occultation sessions is shown in Fig. 2.

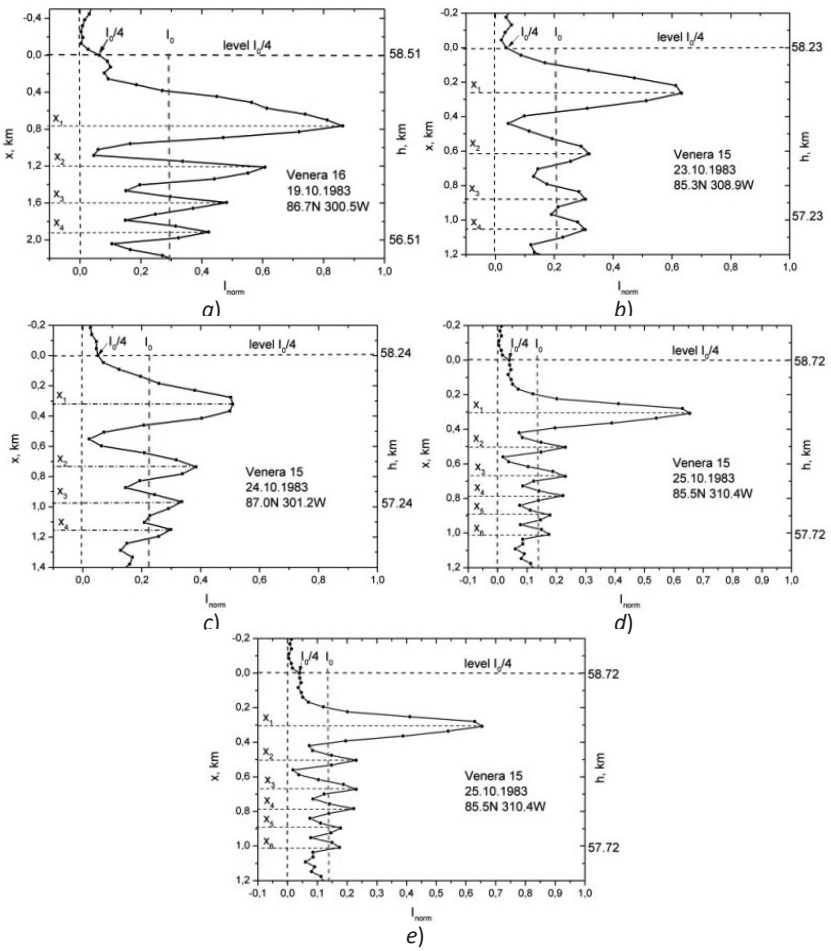

Fig. 2. Experimental data on the radio wave intensity (λ ≈ 32 cm) obtained during radio sounding in October 1983 of the Venus's atmosphere by the Venera-15, -16 satellites. The latitudes and longitudes of sounded region are shown for each session

The altitude positions of maxima for curves $I_{max} - x_1–x_6$ are shown on the left vertical axes of panels a)–e) in Fig. 2. These positions are counted from the $I_0/4$ level (shown by a horizontal dashed line in the figure). The altitude intervals from the planet's surface are indicated on right vertical axes. Vertical dashed lines mark the zero level I_{norm} and mean level I_0, where the undulating behavior of I_{norm} occurs. Values of the normalized intensity I_{norm} are plotted on the horizontal axes. In the sessions shown in Fig. 2, radio soundings were carried out at latitudes 85.3–87.0° N. It is known that the altitude of the region in the Venus's atmosphere with a changing temperature regime, including the position of the tropopause, varies greatly: from 55 km at the equator to 62 km at 75° N, and closer to the pole it again drops to 57 km from the surface.

CONCLUSION:

Analysis of the radio wave intensity (wavelength ~32 cm) profiles, obtained during radio sounding of the Venus's atmosphere and shown in Figu. 2, suggests that in these sessions the conditions were similar to the conditions for

the formation of a diffraction pattern when light is incident on the edge of an opaque half-plane. The lower edge of this opaque half-plane is located near tropopause level at altitudes of 58.2 to 58.7 km from the surface of Venus. Taking into account the influence of atmospheric refraction and using the Cornu spiral, we have shown that the observed features are due to the Fresnel diffraction of radio waves in a zone starting from the edge of opaque half-plane.

FUNDING:
This research has been carried out in the framework of the state task.

REFERENCES:

[1] Gubenko V.N., Andreev V.E., Pavelyev A.G. Detection of layering in the upper cloud layer of Venus northern polar atmosphere observed from radio occultation data // J. Geophys. Res. 2008. V. 113. Art. No. E03001. DOI: 10.1029/2007JE002940.

THE SPATIAL-GENETIC RELATIONSHIPS OF CORONAE, LOBATE PLAINS AND RIFT ZONES ON VENUS

E.N. Guseva[1], M.A. Ivanov[2]
[1] *Vernasky Inst., Moscow, Russia; guseva-evgeniya@ya.ru*

KEYWORDS:
Venus, topography, coronae, rift zones, lobate plains, rifting, volcanism

INTRODUCTION:

Coronae – large (up to 2500 km across) landforms with a characteristic annulus consisting of densely packed grooves and/or ridges [1–4]. Annulus surrounds the interior of the coronae, which is dominated by volcanic formations [4]. In some cases, lava flows extend beyond the annulus onto the surrounding plain [5]. There is a consensus that coronae are the surface manifestations of mantle diapirs [1–4, 6–13].

We have studied all cataloged coronae of Venus [4, 14] and found that three main topographic classes characterize them: D (dome-shaped), W (multiring), and U (topographic depressions) [15]. Some of these coronae may represent long-lived volcano-tectonic structures [16–19].

Coronae are often found in spatial association with rift zones, which may indicate the genetic relationship of coronae and rifts [20–27]. Sometimes coronae are spatially associated with lobate plains, and may represent the sources of the plains [28].

In this work, we have carefully analyzed regions where coronae, rift zones, and lobate plains occur together in order to establish how often or rarely the spatial associations of these formations may suggest their genetic relationships.

The results of the analysis of the spatial association of coronae with lobate plains shows that ~32 % (169 coronae out of 532) of all coronae is spatially associated with lobate plains. Among these, more commonly coronae are sources of the plains (subpopulation 1, 90 features, or ~17 % of all coronae, Table 1). Coronae of subpopulation 1 mainly belong to the D topographic class. Less often, coronae are embayed by lobate plains (subpopulation 2, 79 coronae, ~15 % of all coronae, Table 1). Coronae of subpopulation 2 more often have the W and U topographic profiles.

Table 1. Topographic and morphological characteristics of coronae spatially associated with lobate plains.

Populations of coronae spatially associated with lobate plains	Subpopulation 1, number (%)	Subpopulation 2, number (%)
	90 (17)*	79 (15)*
D class	40 (23)**	7 (4)**
W class	25 (15)**	37 (22)**
U class	25 (15)**	35 (21)**

* Percent of the entire population of coronae,

** Percent of coronae that are spatially associated with lobate plains.

The results of the analysis of the spatial association of coronae with rift zones shows that ~19 % (102 coronae out of 532) of all coronae is associated with rift zones (Fig. 1). The annulus of these coronae is either completely consist of rift structures (rift coronae, 75 features or ~14 % of all coronae), or formed by groove belts that are cut by rift structures (pre-rift coronae, 27 features or ~5 % of all coronae).

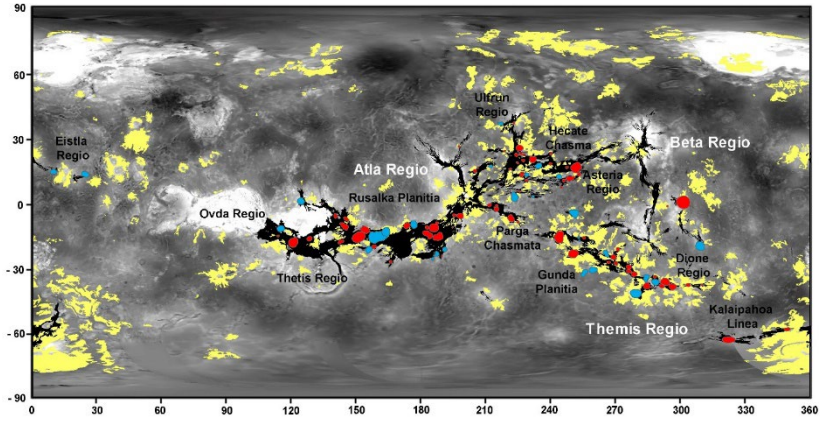

Fig. 1. Rift coronae are in red; pre-rift coronae are in blue; yellow: lobate plains; black: rift zones; geological boundaries are from [29]

Most of the rift-coronae (43, ~8 % of all coronae) are associated with lobate plains and represent apparent sources of lobate plains. The pre-rift coronae source the plains much less frequently (16 features or ~3 % of all coronae); they are mostly the W-class coronae. The rift-coronae are often spatially associated with novae (21 coronae), while the association of the pre-rift coronae with novae is less common (8 coronae). In all cases, novae postdate the corona annulae and represent sources of lobate plains.

CONCLUSIONS:

1) About 1/3 of the entire population of coronae of Venus is spatially associated with lobate plains and only ~17 % of all coronae represent apparent sources of lobate plains. These coronae mostly belong to the D (dome-shaped) topographic class, which likely represents a progressive stage of the diapir evolution accompanied by the growth of a dome-like topographic feature.
2) About 1/5 of all coronae is spatially associated with rift zones and only ~8 % of the entire corona population is formed by rift-related structures; a significant part of them are rift (~ 73 %) and a smaller part are non-rift coronae (~27 %).
3) Thus, the rate of formation of coronae during the later geologic history of Venus (the network rifting-volcanism regime during Atlian Period [30]) significantly diminished. The rift formation (in contrast to groove belts during the tectonic resurfacing regime of Giuneverian Period [30]) was not commonly accompanied by the corona formation. Instead, rifts are associated with extensive topographic swells that are characterized by abundant volcanism and large positive gravity anomalies (e.g., [31]). This may suggest that the mantle diapiric activity (development of rootless bodies) during Guineverian Period was changed by mantle plume activity (formation of bodies with deep roots or supplying channels) during Atlian Period.

REFERENCES:

[1] Barsukov V.L., Basilevsky A.T., Burba G.A. et al. The geology and geomorphology of the Venus surface as revealed by the radar images obtained by Venera-15 and -16 // J. Geophys. Res. 1986. V. 91. No. B4. P. D399–D411.
[2] Nikishin A.M. Tectonics of Venus: a review // Earth, Moon and Planets. 1990. V. 50/51. P. 101-125.
[3] Pronin A.A., Stofan E.R. Coronae on Venus: Morphology and distribution // Icarus. 1990. V. 87. P. 452-474.
[4] Stofan E.R., Sharpton V.L., Schubert G., Baer G., Bindschadler D.L., Janes D.M., Squyres S.W. Global distribution and characteristics of coronae and related features on Venus: Implications for origin and relation to mantle processes // J. Geophys. Res. 1992. V. 97. No. E8. P. 13347-13378.
[5] Ivanov M.A., Head J.W. Geology of Venus: Mapping of a global geotraverse at 30° N latitude // J. Geophys. Res. 2001. V. 106. No. E8. P. 17515-17566.

[6] Squyres S.W., Janes D.M., Baer G., Bindschandler D.L., Shubert G., Sharpton V.L., Stofan E.R. The morphology and evolution of coronae on Venus // J. Geophys. Res. 1992. V. 97. P. 13611-13634.
[7] Janes D.M., Squyres S.W., Bindschadler D.L., Baer G., Schubert G., Sharpton V.L., Stofan E.R. Geophysical models for the formation and evolution of coronae on Venus // J. Geophys. Res. 1992. V. 97. No. E10. P. 16055-16068.
[8] Koch D.M., Manga M. Neutrally buoyant diapirs: A model for Venus coronae // Geophys. Res. Lett. 1996. V. 23. No. 3. P. 225-228.
[9] Smrekar S.E., Parmentier E.M. The interaction of mantle plumes with surface thermal and chemical boundary layers: applications to hotspots on Venus // J. Geophys. Res. 1996. V. 101. P. 5397-5410.
[10] Smrekar S.E., Stofan E.R. Corona formation and heat loss on Venus by coupled upwelling and delamination // Sci. 1997. V. 277. P. 1289-1294.
[11] Jellinek A.M., Lenardic A., Manga M. The influence of interior mantle temperature on the structure of plumes: Heads for Venus, tails for the Earth // Geophys. Res. Lett. 2002. V. 29. No. 11. P. 27-1-27-4.
[12] Johnson C.L., Richards M. A conceptual model for the relationship between coronae and large-scale mantle dynamics on Venus // J. Geophys. Res. 2003. V. 108. No. E6. Art. No. 5058.
[13] Davaille A., Smrekar S.E. Tomlinson S. Experimental and observational evidence for plume-induced subduction on Venus // Nature Geosci. 2017. V. 10(5). P. 349-355.
[14] Crumpler L.S., Aubele J. Volcanism on Venus // Encyclopedia of Volcanoes // eds. B. Houghton, H. Rymer, J. Stix, S. McNutt, H. Sigurdson, Acad. Press, 2000. P. 727-770.
[15] Guseva E.N., Ivanov M.A. Coronae of Venus: geological, topographic and morphometric characteristics // Sol. Syst. Res. 2022. V. 56. No. 2. P. 76-83.
[16] Basilevsky A.T., Head J.W. Global stratigraphy of Venus: analysis of a random sample of thirty-six test areas // Earth, Moon and Planets. 1995. V. 66. P. 285-336.
[17] Basilevsky A.T., Head J.W. Geologic units on Venus: evidence for their global correlation // Planet Space Sci. 2000. V. 48. P. 75-111.
[18] Stofan E.R., Smrekar S.E. Large topographic rises, coronae, large flow field, and large volcanoes on Venus: Evidence for mantle plumes? // Geol. Soc. Am. Spec. Paper. 2005. V. 388. P. 841-861.
[19] Ivanov M.A., Head J.W. The Lada Terra Rise and Quetzalpetlatl Corona: a region of long-lived mantle upwelling and recent volcanic activity on Venus // Planet. Space Sci. 2010. V. 58. P. 1880-1894.
[20] Solomon S.C., Smrekar S.E., Bindshadler D. Venus tectonics: An overview of Magellan observations // J. Geophys. Res. 1992. V. 97. P. 13199-13256.
[21] Baer G., Shubert G., Bindschandler D.L., Stofan E.R. Spatial and temporal relations between coronae and extensional belts, northern Lada Terra, Venus // J. Geophys. Res. 1994. V. 99. P. 8355-8369.
[22] Stefanick M., Jurdy D.M. Venus coronae, craters, and chasmata // J. Geophys. Res. 1996. V. 101. P. 4637-4644.
[23] Hamilton V.E., Stofan E.R. The geomorphology and evolution of Hecate Chasma, Venus // Icarus. 1996. V. 121. P. 171-194.
[24] Stofan E.R., Hamilton V.E., Janes D.M., Smrekar S.E. Coronae on Venus: morphology and origin // Venus II / eds. Bougher S.W., Hunten D.M., Phillips R.J. Univ. Arizona Press, 1997. P. 931-965.
[25] Roberts K.M., Head J.W. Large-scale volcanism associated with coronae on Venus: implications for formation and evolution // Geophys. Res. Lett. 1993. V. 20. P. 1111-1114.
[26] Krassilnikov A.S., Kostama V.-P., Aittola M., Guseva N.E., Cherkashina O.S. Relationship of coronae, regional plains and rift zones on Venus // Planet. Space Sci. 2012. V. 68. 56-75. https://doi.org/10.1016/j.pss.2011.11.017.
[27] Piskorz D., Elkins-Tanton L.T., Smrekarr S.E. Coronae formation on Venus via extension and lithospheric instability // J. Geophys. Res. Planets. 2014. V. 119. P. 2568-2582.
[28] Romeo I. Monte Carlo models of the interaction between impact cratering and volcanic resurfacing on Venus: The effect of the Beta-Atla-Themis anomaly // Planet. Space Sci. 2013. V. 87. P. 157-172.
[29] Ivanov M.A., Head J.W. Global geological map of Venus // Planetary and Space Sci. 2011. V. 59. P. 1559-1600.
[30] Ivanov M.A., Head J.W. The history of tectonism on Venus: A stratigraphic analysis // Planetary and Space Sci. 2015. V. 113-114. P. 10-32.
[31] Konopliv A.S., Banerdt W.B., Sjogren W.L. Venus gravity: 180th degree and order model // Icarus. 1999. V. 139. P. 32-18.

DETAILED MAPPING OF LARGE SHIELD VOLCANOES ON VENUS – CHALLENGES AND PERSPECTIVES BASED ON THE STUDY OF ATIRA MONS, BAT REGION, VENUS

C.H.G. Braga[1,2], R.E. Ernst[2,3], H. El Bilali[2,3], J.W. Head[4], E.G. Antropova[2]
[1] *Faculty of Geology and Geography, Tomsk State University, Tomsk, Russia; carloshenrique_gb@hotmail.com*
[2] *Faculty of Geology and Geography, Tomsk State University, Tomsk, Russia*
[3] *Department of Earth Sciences, Carleton University, Ottawa, Canada*
[4] *Department of Earth, Environmental and Planetary Sciences, Brown University, Providence, USA*

KEYWORDS:
volcanism, Atira Mons, Venus, detailed mapping, stratigraphy, Beta-Atla-Themis Region (BAT), large shield volcanoes, geologic history

INTRODUCTION:
Geologic mapping has been used to study the Venusian surface since the first radar images were transmitted back to Earth by the Venera-15 and -16 spacecraft. Since then, and with the high-resolution global coverage provided by the Magellan mission, several efforts have been made to understand geologic processes and test hypotheses with mapping on several scales. For example, VMAP (Venus Geologic Mapping) program [1] consists of an ongoing series of 1:5 000 000 scale maps of each of Venus' 62 quadrangles (e.g., [2]). In addition, other authors compiled a global map on a scale 1:10 000 000 (e.g., [3]). These efforts provided important insights on the overall geology, major geologic units, global and regional stratigraphy and structures of Venus, as well as forming the framework for interpreting the geologic evolution of the planet.

Detailed maps of volcanic centers on a scale 1:500 000, such as the ongoing mapping of Atira Mons (Fig. 1; [4]) and [5] are less common, but are the focus of the new International Venus Research Group [6]. In the example of Atira Mons, we showcase how such efforts offer many perspectives to gain novel information using the Magellan dataset and point to several challenges that can potentially be solved by the new missions heading to Venus in the next decades [7–10].

VALUE OF DETAILED MAPPING OF A LARGE SHIELD VOLCANO:
- Developing a detailed flow history and the evolution of any summit caldera;
- Determining effusion rates and identifying cooling-limited and supply-limited flows [11-12];
- Understanding the relationship between the location of sources and timing of eruptions (e.g., mid-late flows are possibly sourced outside the summit, on the flanks);
- Estimating flow volume over time for a large shield volcano can provide constraints into the volatile release history, and its potential role for climate change on Venus;
- A thoroughly characterized large shield volcano is an important target for the future missions (for higher resolution images and a potential lander, such as Venera-D).

CHALLENGES OF DETAILED MAPPING:
- Discerning lava breakouts from isolated patches of older flows;
- Determining whether radar dark channels in the center of bright flows represent a part of the flow or a younger pulse;
- Assessing whether flow units of similar morphology and radar brightness in different sectors belong to the same flow stage;
- Determining whether downslope radar backscatter changes indicate separate flows or variations in roughness of a single flow;

- Marking and interpreting diffuse boundaries between flows;
- Dealing with data artifacts in SAR and topography data;
- Avoiding overinterpretation of subtle features, since we are mapping close to the resolution limit of the datasets.

RESULTS OF DETAILED MAPPING OF ATIRA MONS:

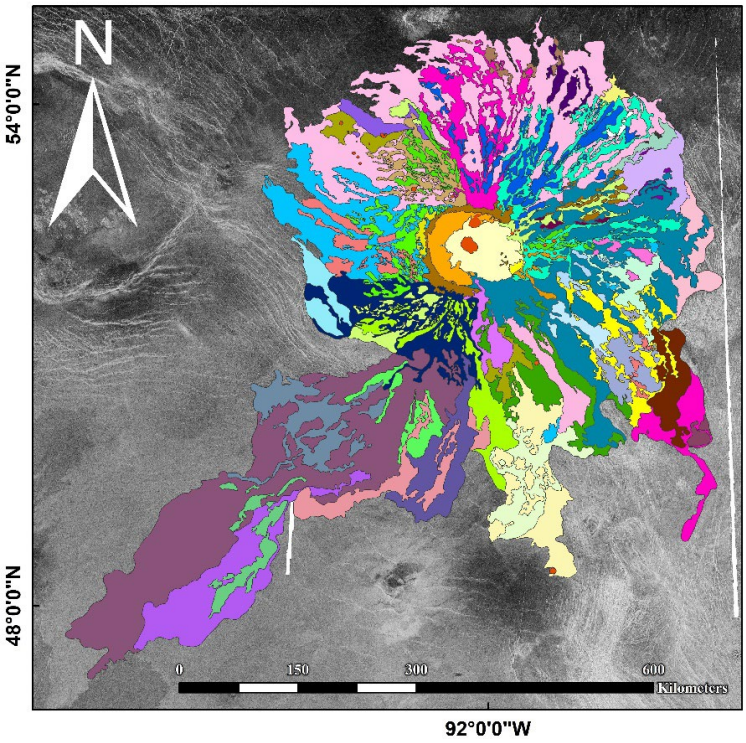

Fig. 1. Geologic map of Atira Mons. Colors indicate different generations of lava flows

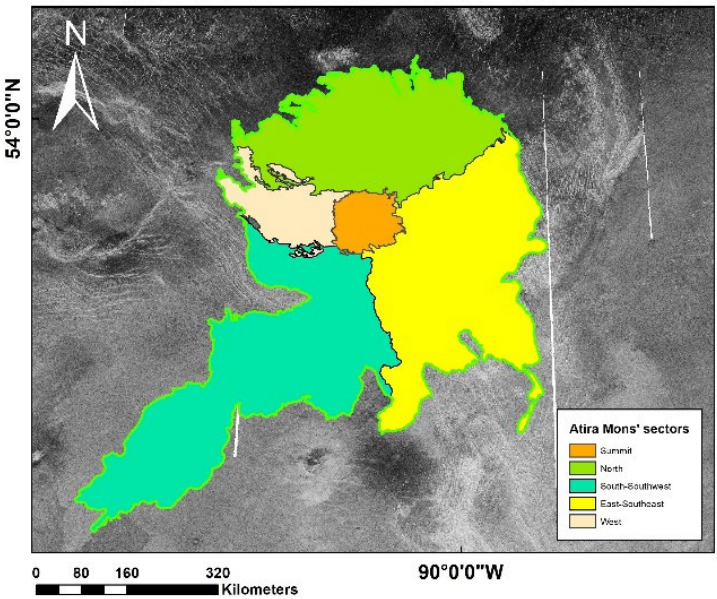

Fig. 2. Sector division of Atira Mons

Atira Mons is a large shield volcano capped by a central caldera, located on the NE portion of the Beta-Atla-Themis Region. It covers an area of ~310 000 km², has a volume of ~280 000 km³ (comparable in size to a terrestrial Large Igneous Province; [13]). Most of the flows are within ~300 km of the summit, however one flow can be traced ~700 km to the SSW (Fig. 1). Our current mapping includes 61 flow units, provisionally divided into one summit and four flank sectors (Fig. 2). It shows that 1) flow units concentrated on Atira Mons' summit are younger than the ones on the flanks and are possibly related to caldera formation; 2) larger volumes of magma were emplaced as initial stages of Atira Mons, including the ~700 km long flow in the SSW; 3) In most cases, the youngest flows in each sector can be traced back to the summit; 4) Some flows seem to be sourced from sources on the flanks (dykes?). For more details, see [4]. We are currently comparing the characteristics and sequence of Atira Mons to other large Venusian shield volcanoes in the Beta Regio area, such as the ~350–400 km diameter Tuulikki Mons [14].

REFERENCES:

[1] Tanaka K.L. The Venus Geologic Mappers' Handbook. 1994. 2nd ed. USGS OFR 94-438.
[2] Dohm J.M. et al. Venus Geologic Map of the Metis Mons Quadrangle (V-6) // USGS Sci. Inv. 2011. Map 3158.
[3] Ivanov M.A., Head J.W. Global Geological Map of Venus // Planetary and Space Science. 2011. V. 59. Iss. 13. P. 1159-1600.
[4] Braga C.H.G. et al. Geological History of the Atira Mons Large Shield Volcano, Beta Regio, Venus // LPSC LIII. 2022. Abstr. No. 1093.
[5] MacLellan L. et al. Volcanic History of the Derceto large igneous province, Astkhik Planum, Venus // Earth-Science Reviews. 2021. V. 220. Art. No. 103619.
[6] Ernst R.E. et al. International Venus Research Group (IVRG): Detailed Mapping to Develop Geological Histories of 40+ Areas of Venus // Planetary Geologic Mappers Workshop. 2022. Abstr. No. 7009.
[7] Zasova L.V. et al. Venera-D: A Design of an Automatic Space Station for Venus Exploration // Solar System Research. 2019. V. 53. P. 506-510.
[8] Garvin J.B. et al. DAVINCI+: Deep Atmosphere of Venus Investigation of Noble Gases, Chemistry and Imaging, Plus // LPSC LI. 2020. Abstr. No. 2599.
[9] Smrekar S.E. et al. VERITAS (Venus Emissivity, Radio Science, INSAR, Topography and Spectroscopy): A Selected Discovery Mission // LPSC LIII. 2022. Abstr. No. 1122.
[10] Widemann T. et al. The Envision Mission to Venus // LPSC LIII. 2022. Abstr. No. 2948.
[11] Head J.W. et al. Lava flow-field morphological classification and interpretation: Examples from Venus // LPSC XXIV. 1993. P. 627-628.
[12] Wilson L. et al. A Classification Scheme for the Morphology of Lava Flow Fields // LPSC XXIV. 1993. P. 1527-1528.
[13] Ernst R.E. Large Igneous Provinces. Cambridge: Cambridge University Press, 2014. 666 p.
[14] Ivanov M.A., Head J.W. Major Episodes of Volcanic Activity at the Large Shield Volcano Tulikki Mons, Venus // LPSC L. 2019. Abstr. No. 1272.

CHARACTERIZATION OF THE ELONGATE CLUSTER OF "SPLOTCHES" IN THE PHOEBE REGIO, VENUS

E.G. Antropova[1], C.H.G. Braga[2], R.E. Ernst[1,2], H. El Bilali[1,2], J.W. Head[3], B.A. Ivanov[4]

[1] *Tomsk State University, Faculty of Geology and Geography, Tomsk, Russia; ekatantropova@yandex.ru*

[2] *Department of Earth Sciences, Carleton University, Ottawa, Canada*

[3] *Department of Earth, Environmental and Planetary Sciences, Brown University, Providence, USA*

[4] *Institute for Dynamics of Geospheres RAS, Moscow, Russia*

KEYWORDS:
Venus mapping, bolide impact, Magellan SAR, bat region, splotches

INTRODUCTION:

The surface of Venus is characterized by the presence of numerous craters due to bolide impact, of various types seen in Magellan SAR images, which were previously classified by [1] into six main types. An additional type of bolide feature is "splotches" that are formed during the interaction of a bolide and the dense atmosphere of Venus [1, 2]. The shockwave from such an airblast can affect the surface in different ways, leading to both radar darkening and brightening [1, 3]. Shockwaves from these bolides are sufficient to form large features on the surface [2, 4].

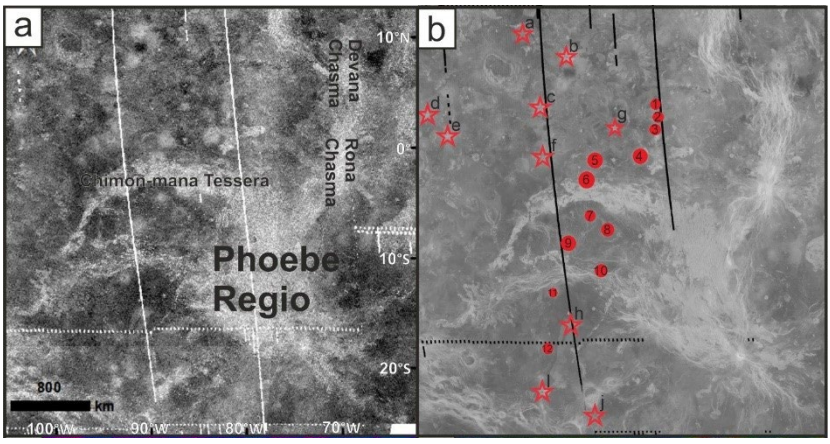

Fig. 1. *a*, *b* – Magellan SAR image of the study area showing splotches (circles) and similar appearing features (stars) that have an ambiguous origin, but are most likely volcano-tectonic

According to [5], the Phoebe Regio area is characterized by an abnormally high density of splotches. The main goal of this study is to show the main morphological characteristics of the "splotches" that were discovered as a result of the geological mapping of the Phoebe Regio on Venus, and consider their interpretation. Through our mapping, twelve well-defined bright splotches are recognized to be distributed along a SSW-NNE trend that is 3000 km long and 200 km wide (extending between the SSW end at 17,2° S and 266,8° E, and the NNE end at 6° N and 277,1° E) (circles 1–12 in Fig. 1). Additional features (marked by stars in Fig. 1b) resemble splotches, but are considered more likely of volcano-tectonic origin.

The diameters of the splotches vary from 70 to 180 km. The splotch shape is predominantly circular and the centers of these splotches are dark (which may or may not include a faint central crater) and they are surrounded by

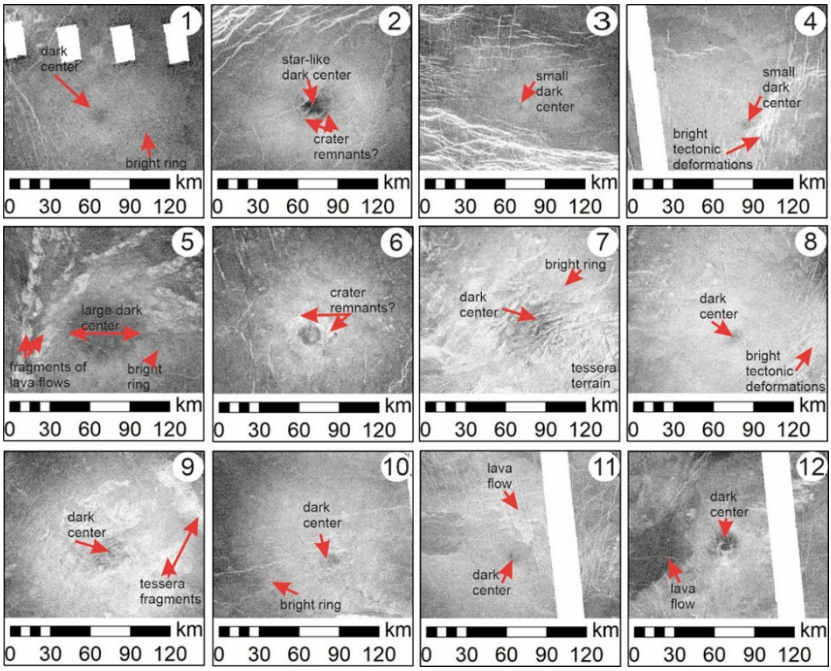

Fig. 2. Different splotches. See Fig. 1 for locations labelled by number. Key features are labelled

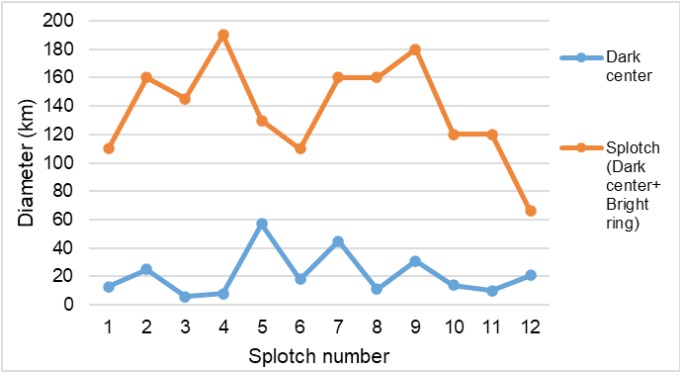

Fig. 3. Displays the diameters of splotches and their dark centers (from SSW to NNE end of the Splotch chain)

wide radar-bright annuli. The inner dark circle can vary in diameter from 10 to 35 km. The dimensions of the bright outer ring vary from ~50 to 80 km or more, and its boundaries are often quite blurred. Some particular characteristics of each of the 12 splotches are presented below (Fig. 2, 3):

According to the size of the dark center, all splotches can be divided into three main groups: splotches with a small dark center ≤20 km (1, 3, 4, 8, 10, 11 in Fig. 1), splotches with a large dark center ≥50 km (5 in Fig. 1) and splotches with a dark center ranging from 20 to 50 km (2, 6, 7, 9, 12 in Fig. 1). Some splotches have center which resemble the remains of craters in their morphology (2, 6, 12 in Fig. 1). Special attention should be paid to splotch 5 in Fig. 1. The presence of a dark center with such a large diameter is unique for this area.

As a rule, all splotches have a clear round shape, however, sometimes the definition of this characteristic is influenced by the type of surface and the presence of additional geological features. In some cases, due to the presence of rifts or grabens, which significantly increase the radar brightness of

the area, it can be difficult to determine the outer boundaries of the bright ring, as in splotches 3, 4, 8, 11, 12 in Fig. 1.

Of great importance is the type of surface on which the splotch is located. As mentioned earlier, some splotches overlap older rifts and fractures, which greatly complicates the identification of their outer boundaries. The same applies to the splotches that were found within the tessera region (splotches 7, 9). In addition to tectonic faults, in some cases we detect splotches near radar-bright volcanic flows, which also complicates correct identification (splotches 4, 5, 10, 11). Splotches are most clearly detected within the radar-dark plains (splotches 1, 2, 6, 10), because the contrast that occurs at the bright splotch-dark plain boundary allows one to correctly set the outer and inner boundaries of the splotch.

The observation of such bright splotches allows us to make an assumption about their relative age. As in the case of the halo observed in some impact craters [6], we consider "splotches" as one of the youngest units on the surface of the studied region. Our interpretation is based on the fact that the material of the splotches is rather heterogeneous, is not very thick and would be easily covered with other materials or removed by wind. The elongation direction of the splotch distribution suggests a trajectory for the arriving bolide oblique to the solar system ecliptic plane. We interpret the elongate splotch distribution to have been formed by a stream of individual fragments of a parent body that disrupted in solar orbit well before entering the atmosphere of Venus. An analogous example is the 21 fragments of Shoemaker-Levy 9 which sequentially impacted on Jupiter [7].

REFERENCES:

[1] Schaber G.G., Strom R.G., Moore H.J. et al. Geology and distribution of impact craters on Venus: What are they telling us? // J. Geophysical Research. 1992. V. 97. P. 13257-13301.
[2] Bondarenko N.V., Kreslavsky M.A. Surface properties and surficial deposits on Venus: New results from Magellan radar altimeter data analysis // Icarus. 2018. V. 309. P. 162-176.
[3] Schultz P.H. Atmospheric effects on ejecta emplacement and crater formation on Venus from Magellan // J. Geophysical Research. 1992. V. 97. P. 16183–16248.
[4] Soderblom L.A., Chadwick D.J., Schaber G.G. Surface effects of impacts into Venus' atmosphere // Lunar and Planetary Science Conference (LIPSC XXIII). 1992. Abstr. No. 1652.
[5] Kirk R.L., Chadwick D.J. Splotches on Venus: Distribution, properties and classification // Lunar and Planetary Science Conference (LIPSC XXV). 1994. Abstr. No. 1353.
[6] Ivanov M.A., Head J.W. Global geological map of Venus // Planetary and Space Science. 2011. V. 59. P. 1559-1600.
[7] Harrington J., de Pater I., Brecht S.H., Stephen H., Deming D., Meadows V., Zahnle K., Nicholson P.D. // Cambridge Planetary Science. 2004. V. 1. P. 159-184.

MOTION OF THE SUN, EARTH AND VENUS

V.A. Kotov[1]
[1] *Crimean Astrophysical Observatory, Nauchny, Crimea, Russia; vkotov@craocrimea.ru*

KEYWORDS:
Sun, pulsations, Earth, Venus, solar system

ABSTRACT
According to the long-term observations of the Sun performed in 1968–2022 by the CrAO, Stanford and five other observatories, the mean magnetic field of the Sun varies with the Hale's period P_H = 22.14(8) years; a saw-tooth shape of this variation supports the recent hypothesis [1] about a cosmological origin of the cycle. We present also arguments in favour of a tight connection between P_H and the Earth's orbital period P_E:

$P_E = (1 - 3/\pi)P_H$,

noting that motions of the Sun, Earth and Venus are involved in the close mutual resonance, since the Venusian spin period (sidereal, in days),

$P_V \approx 2P_E/3 \approx 3^2P_S \approx 3^5P_D = 243000$,

with the observed value P_V = 243025 days, P_S = 27027(7) days, synodic period of the Sun's spinning, and P_D, the mean terrestrial day. The Sun-Venus-Earth gravitational configuration, moreover, repeats each time interval P_{VE} = 243 years, while

$P_V/P_D \approx P_{VE}/P_E = 3^5$,

$P_E \approx 3^3P_S/2$, $P_S \approx 3^3P_D$ and $P_D \approx 3^2P_0$, where $P_0 \approx 3^{-2}$ days is a period of solar pulsations [2]. A hypothesis is advanced that timescales P_H, P_S, P_E, P_D and P_0 are in fact fundamental constants of the World.

REFERENCES:
[1] Kotov V.A., Sanchez F.M. Solar 22 years cycle // Astrophys. Space Sci. 2017. V. 362. No. 6. P. 1-6.
[2] Kotov V.A., Haneychuk V.I. Oscillations of solar photosphere: 45 years of observations // Astron. Nachr. 2020. V. 341. No. 6-7. P. 595-599.

THE ROLE OF RUSSIAN SCIENCE IN THE DEVELOPMENT OF PLANETARY SCIENCE OF THE SOLAR SYSTEM (FROM THE XVIII CENTURY TO THE PRESENT DAY)

N.P. Bulatova[1]
1 *Schmidt Institute of Physics of the Earth RAS; n.p.bulatova@mail.ru*

KEYWORDS:
Lomonosov M., Euler L., Venus, Moon, PANGAEA "Moving source Method", STT

Discussing the place of Russian science in the development of planetary science of the solar system, it is necessary to pay tribute to the Russian scientists of the XVIII century, whose forecasts and observations were ahead of the achievements of European ones and were succe ssfully confirmed by further scientific research of the Earth and the planets of the solar system. The laws of motion of celestial bodies, descriptions of the features of their structure and the matter of their constituents were studied in comparison with the planet Earth. Of great interest was also the verification of their compliance with the laws of physics discovered on Earth.

Let's focus on two of the most significant figures of scientists of that time: Russian scientists M.V. LOMONOSOV (1711–1765) and LEONARD EULER (1707–1783), who success – fully worked in several branches of science at once and laid the foundations of natural sciences.

Systematization of Russian science by M.V. Lomonosov (discovery of laws, definition of concepts and terms): in chemistry, physics, the sciences of the structure of matter, geography, geological surveys, astronomy, mathematics and the structure of the Earth, it allowed laying the foundation for further research. Many discoveries belong to him. In the field of astronomy, an assumption was made, later confirmed, about the nature of the Sun as a gaseous, rather than a stony incandescent formation.

M.V. Lomonosov made this discovery while observing the transit of Venus across the solar disk. It made a splash – it was the first evidence in history of the presence of an atmosphere on another celestial body near the planet Venus with the help of original scientific instruments designed by him. At the same time, Mikhail Vasilyevich himself did not consider this discovery important. Then the scientist's discovery was confirmed. Later, the effect was named after Lomonosov.

His contemporary, who also worked at the Academy of Saint Petersburg, Russia. L. Euler was focused on research in mathematics, mechanics, physics, astronomy... his works describing the motion of the Moon in differential equations are known. A special place is occupied by his work in the field of "spherical motion of bodies", in which one point of the body remains stationary. The name reflects the fact that with such a movement, the points of the body move along the spheres. More fully, this movement is called rotation around a point and the rotation of the body is set by three angular coordinates

There are several ways to choose such angles. One of them includes: – precession angle, – nutation angle, angle of proper rotation.

Laid more than 300 years ago, their foundations still serve scientists in the knowledge of nature. So, following Euler, a system of several spherical coordinate systems and angles – "Spatial-Temporal technology" – STT (Bulatova, 2000), including the "Moving source Method" MST (Bulatova, 1999) allowed solving many topical problems of navigation (determining coordinates by the signal of a found satellite), remote sensing of the Earth, geodynamics, etc.

Thus, V.P. Trubitsin calculated the process of disintegration into separate continents of the ancient supercontinent PANGAEA using the HTP algorithm and confirmed the theory of movement of modern continents constructed by him. Previously, Lomonosov believed that every 20 years it is necessary to update the maps, since the state of the planet changes during this period.

The ideas proposed by Lomonosov about the structure of the Earth, the doctrine "About the layers of the earth", where different layers of our planet (core, crust, mantle) rotate at different speeds relative to each other, and its atmosphere ("the atmosphere has three layers: the lower one, in which the main processes take place, the middle one, characterized by a consistently low temperature, and the upper one, practically independent of the Earth"). Modern concepts based on detailed studies of processes inside and on the Earth's surface and in its atmosphere (for example, the aurora – the glow of the upper structures of the atmospheres of planets that differ in the magnetosphere, as a result of contact with charged fragments of the solar wind).

Works in the field of atmospheric electricity research (together with Georg Richman) and the creation of a network of meteorological stations equipped with devices. for constant monitoring of the electricity content in the atmosphere. This made it possible to prove its presence in the air not only at the time of a thunderstorm. The device began to be used to predict thunderstorms. It was Lomonosov who first tried to explain the causes of lightning in the Earth's atmosphere by presenting his theory of atmospheric electricity. Interestingly, modern scientists confirm that he was 100 % right.

Research continues.

SESSION 7. EXTRASOLAR PLANETS (EP) ORAL SESSION

TRANSITING EXOPLANET DETECTION PROJECT AT SAO RAS

O.Ya. Yakovlev[1,2], A.F. Valeev[2] A.V. Tavrov[1,3]
[1] *Space Research Institute of RAS, Moscow, Russia; yko-v@ya.ru*
[2] *Special Astrophysical Observatory of RAS, Nizhnij Arkhyz, Russia*
[3] *Moscow Institute of Physics and Technology, Dolgoprudny, Russia*

KEYWORDS:
Exoplanets, photometry, transit method, variable stars, observations, pipeline

Small aperture ground-based telescopes are important instruments for detecting and confirming exoplanets using transit photometry (Super-WASP [1], HATNet [2]). To detect exoplanets by this method [3] it is necessary to carry out surveys of one field of the sky for a long time.

The 50-cm robotic telescope for detection of exoplanets has been in operation at SAO RAS since 2020 [4]. During 6 months (from August 2020 to January 2021) the first 2.5 degrees field was observed. As a result of these observations 8 exoplanet candidates were found, as well as more than 100 variable objects. From February 2021 to the present time observations of the second field are carried out. The data from it are now being processed, and the first results will be presented in this report.

In parallel with the process of detecting new candidates, additional photometry and spectroscopic observations of interesting objects found earlier in this program are regularly carried out since spring 2022 using the second 50-cm telescope, as well as other SAO RAS instruments.

A data processing pipeline was developed to perform photometry, light curve analysis, and parameter estimation of the found exoplanet candidates.

ACKNOWLEDGMENTS:
This work was supported by the Government of Russian Federation and Ministry of Education and Science of Russian Federation (grant No. 2020-1902-01-133).

REFERENCES:
[1] Pollacco D., Skillen I., Cameron A., et al. The WASP project and SuperWASP camera. // Astrophysics and Space Science. 2006. V. 204. P. 253–255.
[2] Bakos G., Noyes R., Kovacs G., et al.. Wide-Field Millimagnitude Photometry with the HAT: A Tool for Extrasolar Planet Detection. // Publications of the Astronomical Society of the Pacific. 2004. V. 116 P. 266.
[3] Deeg H., Alonso R. Transit Photometry as an Exoplanet Discovery Method, Handbook of Exoplanets. Springer International Publishing AG, 2018.
[4] Yakovlev O.Ya, Valeev A.V., Valyavin G.G., et al. Exoplanet Two-Square Degree Survey With SAO RAS Robotic Facilities. // Frontiers in Astronomy and Space Sciences. 2022.

UPPER ATMOSPHERES OF EARTH-LIKE EXOPLANETS AROUND LOW-TEMPERATURE STARS

S. Kameda[1], A. Nakayama[1], M. Kuwabara[1], M. Ikoma[2], N. Terada[3]
[1] *Rikkyo University, Japan; kameda@rikkyo.ac.jp*
[2] *NAOJ, Japan;*
[3] *Tohoku University, Japan*

More than 5000 planets have been discovered, and some of them are ~Earth-sized and exist in the habitable zone. However, it is difficult to characterize them as Earth-like, Venus-like, or other. Transit spectroscopy observations for the exoplanetary atmosphere have been performed to characterize larger exoplanets however require very high accuracy for small Earth-like exoplanets. A hydrogen exosphere has been detected around a Neptune-sized exoplanet [1], but exospheres of Earth-sized exoplanets have not been detected yet. Recently, Earth's hydrogen exosphere was re-investigated, and it was revealed that the Earth's exosphere is extended to ~38 Earth radii [2]. On the other hand, Venus' and Mars' hydrogen exospheres are not so extended because of the low temperatures of their upper atmosphere. This is caused by the difference in the mixing ratio of CO_2 in the upper atmosphere. Venus and Mars have CO_2-rich atmospheres with a lower exospheric temperature. On Earth, CO_2 is removed from its atmosphere by a carbon cycle with its ocean and tectonics. Translating these arguments to exoplanets in a habitable zone presents a possible marker distinguishing Earth-like planets from Mars-like or Venus-like planets.

Some theoretical upper atmosphere model results for high EUV irradiation show that the temperature of the upper atmosphere could be ~10000 K [3, 4] with EUV irradiation 10-100 times higher than that at the present Earth. We estimated the oxygen exosphere density distribution for TRAPPIST-1e. In this presentation, we show the difference in the distribution between these models and discuss their observability.

REFERENCES:

[1] Ehrenreich D. et al., A giant comet-like cloud of hydrogen escaping the warm Neptune-mass exoplanet GJ436b. Nature 522, P. 459–461, 2015.
[2] Kameda, S. et al., Ecliptic North-South Symmetry of Hydrogen Geocorona. Geophysical Research Letters 44, 11, 706–11, 712, 2017.
[3] Tian F. et al., Hydrodynamic planetary thermosphere model: 2. Coupling of an electron transport/energy deposition model," J. Geophys. Res. 113(E07), 2008.
[4] Kulikov Y.N. et al, "Comparative Study of the Influence of the Active Young Sun on the Early Atmosperes of Earth, Venus, and Mars," Space Sci. Rev. 129(1–3), 207–243, 2007

INSIGHTS FROM A NON-DETECTION OF HEI 23S ABSORPTION AT TRANSITS OF GJ436B

M.S. Rumenskikh[1], A.V. Shepelin[1], A.G. Berezutsky[1], I.F. Shaikhislamov[1]
[1] *Institute of Laser Physics SB RAS, Novosibirsk, Russia, marina_rumenskikh@mail.ru*

KEYWORDS:
Warm Neptunes, space plasma, transit spectroscopy, star-planetary interactions

INTRODUCTION:

The surface of hot exoplanets is exposed to intense radiation of host stars resulting in intense hydrodynamic escape and mass loss of hydrogen-dominated upper atmospheres. Transit absorption spectroscopy is widely used for probing exoplanetary atmospheres, providing information on composition, temperature, density, and physical processes that occur at upper layers of escaping atmospheres interacting with the stellar radiation and plasma wind.

Atmospheres of many hot Jupiters and warm Neptunes consist mostly of hydrogen, and the Ly-a spectral line is valuable for providing evidence of atmospheric escape. However, it is strongly absorbed in interstellar medium and contaminated by geocoronal emission. As it was suggested in [1] and calculated in [2], the absorption by a metastable helium in the 23S state at 10830 Å offers an alternative way to probe the evaporating exoplanetary atmospheres. Calculations by simple hydrostatical model [2] predicted for GJ-436b transit absorption in HeI(23S) line at a level of 8 %, but observations of this system have yielded unexpected non-detection at 10830 Å [3]. At the same time, extremely deep and long transit was measured in Ly-a line [4]. Such discrepancy motivates a detailed study of processes involved in populating of HeI(23S) state for the GJ436b by more developed models.

Complex and complicated models are required to interpret the spectral transit features of hot Jupiters correctly. We use in this work a 3D gas-dynamic code which takes into account the processes of recombination and plasma-photochemistry of plasma components [5, 6] and treats hydrogen and helium component as separate fluids. We found out that the main reason of discrepancy between simplest 1D calculations [2] and observations [3] was in neglecting the radiation pressure acting on metastable helium atoms. It appears that strong acceleration induced by absorption of stellar radiation at 10830 A results in a wide dispersion of HeI(23S) atoms and reduction of peak absorption by several times. Previously, we shown that radiation pressure is important for interpretation of absorption by HeI(23S) atoms for another warm Neptune – Wasp107b [7].

ACKNOWLEDGEMENTS:
This work was supported by project 075-15-2020-780 of Ministry of Science and Higher Education of the Russian Federation.

REFERENCES:

[1] Seager S.V., Sasselov D.D. Theoretical transmission spectra during extrasolar giant planet transits // The Astrophysical Journal. 2000. V. 537. №. 2. P. 916.
[2] Oklopčić A., Hirata C.M. A new window into escaping exoplanet atmospheres: 10830 Å line of helium // The Astrophysical Journal Letters. 2018. V. 855. No. 1. P. L11
[3] Nortmann, L., Pallé, E., Salz, M., Sanz-Forcada, J., Nagel, E., Alonso-Floriano, F.J., ... & Zapatero Osorio, M.R. (2018). Ground-based detection of an extended helium atmosphere in the Saturn-mass exoplanet WASP-69b. Science, 362(6421), 1388–1391.
[4] Ehrenreich D. et al. A giant comet-like cloud of hydrogen escaping the warm Neptune-mass exoplanet GJ 436b // Nature. 2015. V. 522. №. 7557. P. 459-461.
[5] Shaikhislamov I.F. et al. 3D Aeronomy modelling of close-in exoplanets // Monthly Notices of the Royal Astronomical Society. 2018. V. 481. №. 4. P. 5315.
[6] Shaikhislamov I.F. et al. Global 3D hydrodynamic modelling of absorption in Ly α and He 10830 A lines at transits of GJ3470b // Monthly Notices of the Royal Astronomical Society. 2021. V. 500. №. 1. P. 1404.
[7] Khodachenko M.L. et al. Simulation of 10 830 Å absorption with a 3D hydrodynamic model reveals the solar He abundance in upper atmosphere of WASP-107b // Monthly Notices of the Royal Astronomical Society: Letters. 2021. V. 503. № 1. P. L23.

NON-THERMAL ATMOSPHERIC LOSS FOR HOT NEPTUNE GJ3470 B

V.I. Shematovich[1], A.A. Avtaeva [1]
[1] *Institute of Astronomy of the Russian Academy of Sciences, Moscow, Russiaж shematov@inasan.ru*

KEYWORDS:
Hot exoplanets, sporadic stellar activity, atmospheric mass loss, aeronomic model, kinetic Monte Carlo model

INTRODUCTION:

Exoplanets with substantial hydrogen/helium atmospheres have been discovered in abundance, many residing extremely close to their host stars. Their atmospheres are forced by the extreme irradiation levels resulting in the formation of the extended planetary envelopes due to the thermal and non-thermal atmospheric escape. Ongoing atmospheric escape has been observed to be occurring in a few nearby exoplanet systems through transit spectroscopy both for hot jupiters and for lower-mass sub-neptunes [1].

In the recent study [2] the hydrodynamic simulations of the escaping atmospheres of 18 hot exoplanets in the solar neighborhood were performed with an aim to find ideal observational targets. It was found that the hot Neptune GJ 3470b should have one of the largest mass-loss rates due to its low mass (M_p = 0.04M_J, R_p = 0.37R_J) close orbit (a = 0.0336 a.u) and relatively high activity of the host star, M1.5 dwarf (M_{st} = 0.54M_{Sun}, R_{st} = 0.55R_{Sun}). The first Lyα observation [3] of GJ 3470b indeed revealed the large absorption depth of 35±7 % in the blue wing [-94; -41] km/s of the line and, moreover, the absorption at the level of 23±5 %, was also measured in the red wing [23; 76] km/s, as well as a relatively short transit duration of ~2 hours without any distinct early ingress and extended egress phases. Similarly to hot Neptune GJ 436b the exoplanet GJ 3470b appears to be the next hot exoplanet with a large hydrogen envelope extending far beyond the Roche lobe. Existing models of the upper atmosphere of the planet GJ 3470b predict a significant outflow of atmospheric matter [2–4].

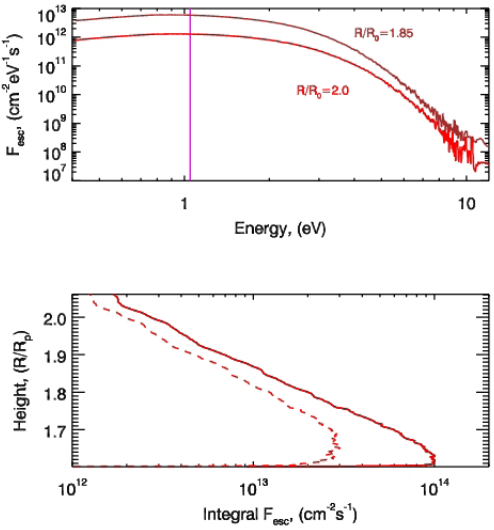

Fig. 1. (*top panel*) The energy spectra of the atomic hydrogen flux escaping from the upper atmosphere of hot Neptune GJ 3470 b due to exothermic photochemistry are shown at the upper boundary of H2→H transition region. The vertical line indicates the escape energy of hydrogen atoms at the upper boundary of the model atmosphere at distance of ~2 planetary radii. (*bottom panel*) Height profiles of the upward moving (solid line) and escaping (dashed line) fluxes of suprathermal H atoms formed due to the exothermic photochemistry.

Results of calculations of the effect of the extreme ultraviolet (UV) stellar radiation on the production of the suprathermal fraction of atomic hydrogen in the $H_2 \rightarrow H$ transition region in the upper atmosphere of hot Neptune GJ 3470b are given in this report. The formation of the escaping flux of H atoms created by this effect was also studied and the production rate and energy spectrum of the hydrogen atoms with excess kinetic energy due to the exothermic photochemistry were calculated. Using the numerical stochastic model for a hot planetary corona [5, 6], we had investigated the kinetics and transport of suprathermal hydrogen atoms in the upper atmosphere and the flux of H atoms escaping from the atmosphere was calculated (see Fig. 1). The latter is estimated as 2.0×10^{13} cm^{-2} s^{-1} at distance of $1.85R/R_p$ for a moderate stellar activity level of UV radiation, which is an indication of the non-thermal atmospheric loss due to the exothermic photochemistry. This estimate corresponds to the non-thermal mass-loss rate of 4.4×10^{9} g s^{-1} and is comparable to the estimates [2–4] of the thermal atmospheric mass-loss rates calculated with aeronomic models for GJ 3470b.

ACKNOWLEDGEMENTS:
We acknowledge the financial support of the Russian Science Foundation, grant #22-22-00909.

REFERENCES:

[1] Owen J.E. Atmospheric Escape and the Evolution of Close-In Exoplanets // Annu. Rev. Earth Planet. Sci. 2019. V. 47. P. 67–90.
[2] Salz M., Czesla S., Schneider P.C., & Schmitt J.H. M.M. Simulating the escaping atmospheres of hot gas planets in the solar neighborhood // Astronomy & Astrophysics. 2016. V. 586. P. A75–86.
[3] Bourrier V., Des Etangs A.L., Ehrenreich D., et al. Hubble PanCET: an extended upper atmosphere of neutral hydrogen around the warm Neptune GJ 3470b // Astronomy & Astrophysics. 2018. V. 620. P. A147–153.
[4] Shaikhislamov I.F., Khodachenko M.L., Lammer H., et al. Global 3D hydrodynamic modeling of absorption in Lyα and He 10830 A lines at transits of GJ3470b // MNRAS. 2021. V. 500. P. 1404–1413.
[5] Avtaeva A.A., Shematovich V.I. Non-thermal atmospheric loss for exoplanet GJ 436b due to the H2 dissociation processes // Sol. Syst. Res. 2021. V. 55. P. 150–158.
[6] Avtaeva A.A., Shematovich V.I. Non-thermal atmospheric loss for sub-neptune Pi Men c due to the exothermic photochemistry // Sol. Syst. Res. 2022. V. 56. P. 67–75.

ACTIVITY OF THE YOUNG STAR KEPLER-1627 WITH EXOPLANET

I.S. Savanov[1]
[1] *Institute of Astronomy, Russian Academy of Sciences, Moscow, 119017 Russia, igs231@mail.ru*

KEYWORDS:
Stars, exoplanets, activity, spot, flares

INTRODUCTION:
The properties of forming planets in young planetary systems are largely a reflection of the ongoing infall of planetosimals and the magnetic activity of the young star that manifests itself in its excess ultraviolet and X-ray emissions. The series of studies that are combined by the ZEIT (Zodiacal Exoplanets In Time) and THYME (TESS Hunt for Young and Maturing Exoplanets) programs based on the photometric observations of the Kepler Space Telescope (mainly the extension of its mission K2) and the TESS mission are devoted to searching for and studying the properties of young planetary systems. Until recently, there were no young planets among those discovered by the primary mission of the Kepler Space Telescope. The situation changed after the appearance of an extended study of the Kepler-1627 (KIC 6184894) planetary system by Bouma et al. [1].

KEPLER-1627:
Based on data from the Kepler Space Telescope archive, in [2] we have studied the photometric variability of the young solar analog Kepler-1627, a G8V-type star with a planet of 3.777 Earth radii in size and an orbital period 7.2 days. Kepler-1627 is a member of the δ Lyr cluster with an age of 38 Myr and is currently the system with the youngest planet with a precise age detected by the Kepler primary mission. We have found the stellar rotation period P = 2.606±0.020 days, the differential stellar rotation parameter $\Delta\Omega$ = 0.066±0.011 rad day^{-1}, and the photometric variability amplitude as well as estimated the spottedness parameter of Kepler-1627 (in the range 1.1 – 6.5 %) of the stellar surface area. In absolute measure the spot area on the surface of Kepler-1627 exceeds the maximum spot area on the Sun and varies from 11 700 to 68 200 m.s.h. We suggest that during the interval of its observations the spot area on the stellar surface had cyclic variations similar to the Rieger periodicity on the Sun. High flare activity (88 flares with an energy log$E$ in the range from 33.41 to 35.25 have been recorded) and spot activity have been detected in the star. Possible manifestations of the cyclicity in the flaring activity of Kepler-1627 are considered. We have found the chromospheric activity indices logR_HK(Teff) for Kepler-1627, which independently suggest that the object is young.

ACKNOWLEDGEMENTS:
I am grateful to the Government of the Russian Federation and the Ministry of Higher Education and Science of the Russian Federation for their support through grant no. 075-15-2020-780 (N13.1902.21.0039).

REFERENCES:
[1] Bouma L.G., Curtis J.L., Masuda K., Hillenbrand L.A., Stefansson G., Isaacson H., et al. A 38 Million Year Old Neptune-sized Planet in the Kepler Field // The Astronomical Journal. 2022. V. 163. P. 121.
[2] Savanov I.S. Activity of the Young Star with an Exoplanet Kepler-1627 // Astronomy Letters. 2022. V. 48. No. 4. P. 267–274.

SPACE WEATHER AROUND HOT EXOPLANETS INFERRED FROM TRANSIT OBSERVATIONS

I.F. Shaikhislamov[1], M.L. Khodachenko[2], M.S. Rumenskikh[1], A.G. Berezutsky[1]
[1] *Institute of Laser Physics SB RAS, Novosibirsk, Russia, ildars@ngs.ru;*
[2] *Space Research Institute, Austrian Academy of Sciences, Graz, Austria*

KEYWORDS:
Hot exoplanets, planetary wind, transit absorption

INTRODUCTION:
Close orbiting hot exoplanets possess a unique feature of hydrodynamic outflow of upper atmospheres. It was revealed for a number of hot Jupiters and warm Neptunes through observations of transit absorption in VUV lines of such elements as H, C, O, Mg, Si as well as in infrared lines of H and He. The planetary wind is driven by such important factor of space weather as intensity of ionizing radiation. The multicomponent and partially ionized atmospheric material overflowing with a supersonic velocity the Roche lobe comes into direct interaction with another important factor of space weather — surrounding plasma of the Stellar Wind. This interaction principally differs from the processes in tenuous planetary exospheres in the Solar system. The escape of upper atmospheres of hot exoplanets is a complex phenomenon, and quantitative interpretation of observational data requires numerical simulations. The comparison of spectrally resolved transit measurements of particular exoplanets and 3D simulations of their dynamical environments gives a tantalizing evidence of planetary and stellar winds interaction, enabling to draw important conclusions about both the atmosphere of an exoplanet and the parameters of a stellar wind plasma.

SIMULATION RESULTS:
Using the 3D aeronomy self-consistent global MHD code [1] we modeled several hot Jupiters and warm Neptunes for which various spectrally resolved observations have been made – HD209458b, HD189733b, Wasp107b, Wasp80b, GJ436b, GJ3470b, TOI421b&c, PiMenC [2, 3 and references there in]. For the two of them (GJ436b, GJ3470b) simulations show that the observed strong absorption in Lya line can be explained only by the interaction of planetary outflow with SW having parameters compatible with the Solar Wind. The non-detection of absorption by PiMenC in Lya line requires either a strong radiation flux or a very weak SW. The modeling of HD189733b [3] confirms that variability of observations can be explained by variability of space weather conditions. Transit data on HI, OI, CII, HeI lines available for HD209458b allowed us to estimate the upper limit on the possible magnetic field of this planet [1]. For the double planetary system TOI421 we predicted [2] strong blue-shifted absorption in Lya line and marginally observable absorption in HeI line.

These simulations of different systems give grounds for general conclusions on how diverse a space weather can be around other stars and what observations are required to constrain its parameters.

ACKNOWLEDGEMENTS:
Supported by project 075-15-2020-780 of Ministry of Science and Higher Education of the Russian Federation.

REFERENCES:
[1] Khodachenko M.L., Shaikhislamov I.F., Lammer, et al. // MNRAS 2021. 507(3). 3626.
[2] Berezutsky A.G., Shaikhislamov, I.F., Rumenskikh M.S., et al. // MNRAS. 2022. stac1633.
[3] Rumenskikh M.S., Shaikhislamov I.F., Khodachenko M.L., et al. // ApJ. 2022. 927(2). 238.

SIMULATION OF AERONOMY AND TRANSIT ABSORPTION OF TRACE ELEMENTS IN ATMOSPHERE OF HOT EXOPLANETS: DEVELOPMENT OF GENERAL KINETIC NON-LTE MODEL

A.V. Shepelin[1], M.S. Rumenskikh[1], I.F. Shaikhislamov[1], L.I. Mashonkina[2]
[1] *Institute of Laser Physics SB RAS, Novosibirsk, Russia; 4.shepelin@gmail.com*
[2] *Institute of Astronomy RAS, Moscow, Russia*

KEYWORDS:
Hot exoplanets, trace elements, non-LTE, simulation

The most widespread elements in the Universe are hydrogen and helium. It is known that such objects as Warm Neptunes' and Hot Jupiters' atmospheres and surfaces mostly consist of these elements. So, our observational data and modelling techniques can extract the most valuable information from their spectral lines. Currently, there is a search for other lines suitable for observation and research. It is expected that atmospheres contain mixture of heavier elements including carbon or oxygen. Absorption of stellar radiation and emission by trace elements, especially Mg and Fe may significantly influence the heating and cooling balance of planetary atmosphere.

Aeronomy modelling is a complex field for which many phenomena and processes need to be taken into account. In many cases LTE approximation is not viable. For example, modelling stellar atmospheres requires non-LTE approach to calculate level populations of elements [1]. The general kinetic approach, realized as independent module in aeronomy and hydrodynamic codes may allow trace elements to be included in the consideration. At the moment there are a number of ready-made solutions for kinetics modelling [2–5], but they have a number of features that do not allow them to be included in the general aeronomic codes for the implementation of fast and optimized calculations - slow languages/runtimes, lack of API, or dependence on simplified descriptions such as LTE.

We are developing a non-LTE model containing the following atomic transitions: collisional excitation and ionization, photoexcitation, photoionization, and radiative transitions between a large set of levels of any given element. The project is developed in C++, and intended primarily as a module for the code described in [6], but it can also be connected as a static or dynamic library to other C++ projects, or as a Python module thanks to the Cython extensions. Also, a universal format for describing elements and corresponding encoding/decoding and serialization/deserialization modules have been developed. Another important element of the project is the visualization of atomic diagrams of levels and transitions, since this allows to optimize calculations and generate appropriate computational configurations. To do this, the TypeScript language is selected, which is transpiled to JavaScript, and executed in the web browser (frontend) and on the server Node.js (backend).

The project aims to implement accounting for arbitrary elements (first of all, O, C, Mg, Fe) using data and methods of previous extensive research of stellar atmospheres [1]. At this stage, the main emphasis is on oxygen atom in order to simulate the absorption at 777.4. A line of OI recently detected at transits of Kelt-9b [7].

ACKNOWLEDGEMENTS:
This work was supported by project 075-15-2020-780 of Ministry of Science and Higher Education of the Russian Federation.

REFERENCES:
[1] Sitnova T.M., Mashonkina L.I., Ryabchikova T.A. Influence of Departures from LTE on Oxygen Abundance Determination. 2013 doi:10.48550/ARXIV.1302.1048.
[2] Cloudy. https://trac.nublado.org/.

[3] MOOG. https://www.as.utexas.edu/~chris/moog.html.
[4] STARLIGHT Project. http://www.starlight.ufsc.br/.
[5] TARDIS-SN. https://tardis-sn.github.io/.
[6] Shaikhislamov I.F. et al. Atmosphere expansion and mass loss of close-orbit giant exoplanets heated by stellar xuv. I. Modeling of hydrodynamic escape of upper atmospheric material. Apj 795, 132 (2014).
[7] Borsa, F. Fossati L., Koskinen T., Young M.E., Shulyak D. 2022. High-resolution detection of neutral oxygen and non-LTE effects in the atmosphere of KELT-9b. Nature Astronomy, 6(2), 226—231.

SCATTERING OF PLANETESIMALS FROM THE FEEDING ZONE OF PROXIMA CENTAURI C

S.I. Ipatov[1]
[1] *V.I. Vernadsky Institute of Geochemistry and Analytical Chemistry of RAS, Moscow, Russia, siipatov@hotmail.com*

KEYWORDS:
Proxima Centauri planetary system, exoplanets, planetesimals, probabilities of collisions

INTRODUCTION AND INITIAL MODEL:

The Proxima Centauri planetary system consists of the star with a mass equal to 0.122 of the solar mass, and of three exoplanets. In my calculations of the motion of planetesimals, the gravitational influence of planets *b* (a_b = 0.04857 AU, e_b = 0.11, m_b = 1.17m_E, m_E is the mass of the Earth) and *c* (a_c = 1.489 AU, e_c = 0.04, m_c = 7m_E) was considered. Other values of m_c (0.7m_E, 3.5m_E, 12m_E) were also considered. The probabilities of collisions of planetesimals with planet *d* (a_d = 0.02895 AU, m_d = 0.29m_E, e_d = i_d = 0) were calculated based on the arrays of migrated planetesimals and planets. The motion of planetesimals and exoplanets was calculated with the use of the RMVS3 version of the symplectic code from Levison and Duncan [1]. In most calculations, the integration time t_s equaled to 1 day. The integrations with t_s equaled to 0.5 day and 0.2 day have been also made. The obtained results were about the same for different considered t_s.

Initial orbits of planetesimals were located in the feeding zone of planet *c*. The considered time interval usually exceeded 100 Myr, and sometimes reached 1000 Myr. Planetesimals were excluded from integration, if they collided with planets or the star or were ejected into hyperbolic orbits. In [2] planets and planetesimals were considered as material points, and probabilities of collisions with planets were calculated based on the arrays of orbital elements of planetesimals and planets. Schwarz et al. [3] studied the motion of exocomets with initial eccentricities between 0.95 and 0.9999 considering Proxima Centauri *c* with a semi-major axis a_c from 0.06 to up to 0.3 AU. In my calculations, initial eccentricities e_o of planetesimals equaled to 0.02 or 0.15. Greater initial eccentricities correspond to the case of mutual gravitational influence of planetesimals. Calculations showed [4–6] that even for the feeding zone of the terrestrial planets the mean eccentricity of planetesimals could exceed 0.2 during evolution and reach 0.4 at the late stages. In each calculation variant, initial semi-major axes a_o of orbits of planetesimals were in the range from a_{min} to a_{max} = a_{min}+0.1 AU. The considered values of a_{min} varied from 0.9 to 2.2 AU. The number of planetesimals with a_o was proportional to $a_o^{1/2}$, i.e. surface density was proportional to $a_o^{-1/2}$. For the (*i*+1) th planetesimal, the value of a_o was calculated with the use of the formula $a_{o(i+1)} = (a_{oi}^2+[(a_{min}+d_a)^2-a_{min}^2]/N_o)^{1/2}$, where a_{oi} is the value of a_o for *i*th planetesimal, d_a = 0.1 AU, N_o = 250 is the number of planetesimals in one variant. Initial inclinations of the planetesimals were equal to e_o/2 rad.

THE MOTION OF PLANETESIMALS IN PROXIMA CENTAURI PLANETARY SYSTEM AND PROBABILITIES OF THEIR COLLISIONS WITH PLANETS:

The results of calculations showed that the probability of a collision of a planetesimal during its dynamical lifetime with planet *c* was about 0.05 at 1.1≤a_o≤1.2 AU, 0.4-0.55 at 1.2≤a_o≤1.7 AU, 0.3 at 1.7≤a_o≤1.8 AU, 0.02 at 1.8≤a_o≤1.9 AU for e_o = 0.02. This probability was about 0.15 at 1.0≤a_o ≤1.1 AU, 0.3 at 1.1≤a_o≤1.9 AU, 0.04-0.05 at 2.0≤a_o≤2.2 AU for e_o = 0.15. Most collisions with planet *c* took place during the first 10 Myr. For e_o = 0.02, the ratio of the number of planetesimals collided with planet *c* to that ejected into hyperbolic orbits was about

2 at $1.1 \le a_o \le 1.2$ AU, 1.2 at $1.2 \le a_o \le 1.4$ AU, 0.85-1 at $1.4 \le a_o \le 1.6$ AU, 1.3 at $1.6 \le a_o \le 1.7$ AU, 0.5 at $1.7 \le a_o \le 1.8$ AU, 0.2 at $1.8 \le a_o \le 1.9$ AU. For e_o=0.15, this ratio was about 0.9 at $1.0 \le a_o \le 1.2$ AU, 0.5-0.6 at $1.2 \le a_o \le 1.4$ AU, 0.4 at $1.4 \le a_o \le 1.8$ AU, 0.05 at $2.0 \le a_o \le 2.2$ AU, and 0.02 at $2.2 \le a_o \le 2.3$ AU. At time T = 100 Myr the fraction of initial planetesimals that were left in elliptical orbits was not more than 0.06 at $1.2 \le a_o \le 1.7$ AU and $2.0 \le a_o \le 2.1$ AU, not more than 0.3 at $1.1 \le a_o \le 1.2$ AU, not more than 0.2 at $1.7 \le a_o \le 1.9$ AU, and not more than 0.1 at $2.1 \le a_o \le 2.2$ AU for e_o = 0.15. It was not more than 0.25 at $1.2 \le a_o \le 1.8$ AU for e_o = 0.02. The ratio of the fraction of planetesimals ejected into hyperbolic orbits to that collided with exoplanets is greater for a greater mass of a planet moving in the orbit of planet *c* and for greater initial eccentricities of orbits of planetesimals. Based on estimates of the amount of planetesimals ejected into hyperbolic orbits, it is possible to conclude that during the growth of the mass of planet *c* from $3.5m_E$ to $7m_E$, the semi-major axis of its orbit could decrease by at least a factor of 1.5.

After hundreds of millions of years, some planetesimals could still move in elliptical orbits inside the feeding zone of planet *c* that had been mainly cleared from planetesimals. Often such planetesimals could move in some resonances with the planet, e.g. in the resonances 1:1 (as Jupiter trojans), 5:4, and 3:4. The number of such left planetesimals was greater at small eccentricities. For some (typically resonant) subregions of a_o located outside the main feeding zone of planet *c,* planetesimals could be ejected into hyperbolic orbits or could collide with planets.

Only one of several hundred planetesimals, which migrated from the feeding zone of Proxima Centauri *c,* reached the orbits of Proxima Centauri *b* and *d*. The probability of a collision of a planetesimal initially located in the feeding zone of planet *c* with planets *b* or *d* (averaged over all considered planetesimals) was ~10^{-4}-10^{-3} at initial eccentricities of planetesimals equal to 0.02 or 0.15. The probability was greater for greater initial eccentricities. Such probabilities are greater than the probability of a collision with the Earth of a planetesimal migrated from the zone of the giant planets in the Solar System [7]. The latter probability is typically less than 10^{-5} per one planetesimal. A lot of icy material and volatiles could be delivered to planets *b* and *d*. Depending on initial eccentricities of planetesimals (such variations correspond to possible mutual gravitational influence of planetesimals), the total mass $m_{c\text{-}b}$ of material delivered from the feeding zone of planet *c* to planet *b* was estimated to be in the range from $2\times10^{-3}m_E$ to $2\times10^{-2}m_E$. The temperature of planet *c* is considered to be much below zero, and the feeding zone of planet *c* was located farther from the star than the snow line. At fraction k_{ice} of ice in the planetesimals between 0.05 and 0.5, the values $m_{ice} = k_{ice} \cdot m_{c\text{-}b}$ of the amount of water ice delivered to planet *b* are between $10^{-4}m_E$ to $10^{-2}m_E$. Probably, the amount of water delivered to Proxima Centauri *b* exceeded the mass of water in Earth's oceans, which is $2\times10^{-4}m_E$. The amount of material delivered from the feeding zone of planet *c* to planet *d* could be a little less than that delivered to planet *b.*

The duration of the motion of ejected planetesimals from 500 to 1200 AU (the Hill radius of Proxima Centauri) from the star was studied. For the present mass of Proxima Centauri *c*, about 90 % of ejected planetesimals moved from 500 to 1200 AU in less than 1 Myr, and not more than 1 % moved in such region for more than 10 Myr (but during less than a few tens of millions of years). For the mass of the planet embryo equal to a half of the mass of planet *c*, the fraction of planetesimals moved from 500 to 1200 AU in less than 1 Myr was about 70–80 %. The consideration of the gravitational influence of the star binary system (Alpha Centauri AB) would not change the above conclusions, because the motion of planetesimals was considered inside (mainly deep inside) the Hill spere of Proxima Centaury and ejected planetesimals have very small chances to return to the Hill sphere of Proxima Centauri.

CONCLUSIONS:

During the growth of the mass of planet *c* by a factor of 2, the semi-major axis of its orbit could decrease by at least a factor of 1.5. After hundreds

of millions of years, some planetesimals could still move in elliptical orbits inside the feeding zone of planet *c* that had been mainly cleared from planetesimals. The amount of water delivered to Proxima Centauri *b* probably exceeded the mass of water in Earth's oceans.

ACKNOWLEDGEMENTS:
The work was supported by the grant 075-15-2020-780 of Ministry of Science and Higher Education of the Russian Federation.

REFERENCES:

[1] Levison H.F., Duncan M.J. The long-term dynamical behavior of short-period comets // Icarus. 1994. V. 108. P. 18–36.
[2] Ipatov S.I. Delivery of water and volatiles to planets in the habitable zone in the Proxima Centauri system // Abstracts of the AASTCS Habitable Worlds 2021 Workshop (22–26 February 2021, a virtual conference). Open Engagement Abstracts, Bulletin of the American Astronomical Society, 2021a, Vol. 53, No. 3 e-id 2021n3i1126, 5 pages. https://baas.aas.org/pub/2021n3i1126/release/2.
[3] Schwarz, R. Bazso A., Georgakarakos N., Loibnegger B., Maindl T.I., Bancelin D., Pilat-Lohinger E., Kislyakova K.G., Dvorak R., Dobbs-Dixon I. Exocomets in the Proxima Centauri system and their importance for water transport // Mon. Not. R. Astron. Soc. 2018. V. 480. P. 3595–3608. doi: 10.1093/mnras/sty2064.
[4] Ipatov, S.I. Solid body accumulation of the terrestrial planets // Solar Syst. Res. 1987. V. 21. P. 129–135.
[5] Ipatov, S.I. Migration of bodies in the accretion of planets // Solar Syst. Res. 1993. V. 27. P. 65–79.
[6] Ipatov, S.I., Migration of celestial bodies in the solar system, Editorial URSS Publishing Company, Moscow, 2000 (also 2021). 320 P. doi: 10.17513/np.451, in Russian.
[7] Ipatov, S.I. Migration of planetesimals from beyond Mars' orbit to the Earth // 14th Europlanet Science Congress 2020. EPSC2020-71. doi: 10.5194/epsc2020-71.

SESSION 7. EXTRASOLAR PLANETS (EP) POSTER SESSION

POSSIBLE TRANSIT FEATURES OF THE TOI-421B AND TOI-421C IN Lyα AND HEI 10830 A LINES

A.G. Berezutsky[1,2], I.F. Shaikhislamov[1,2,3], M.S. Rumenskikh[1,2,3], M.L. Khodachenko[4], H. Lammer[4], I.B. Miroshnichenko[1,3], M.A. Efimov[1]
[1] *Institute of Laser Physics SB RAS, Novosibirsk, Russia;*
[2] *Institute of Astronomy, Russian Academy of Sciences, Moscow, Russia;*
[3] *Novosibirsk State Technical University, Novosibirsk, Russia;*
[4] *Space Research Institute, Austrian Academy of Sciences, Graz, Austria,*
a.berezuckiy@yandex.ru

KEYWORDS:
Exoplanet, plasma, stellar wind, absorption, numerical simulations

We simulate with a global 3D aeronomy code two warm Neptunes in the TOI-421 system and show that both planets experience significant escape of their upper atmospheres. The code solves continuity, momentum, and energy equations for all considered species, which are H, H+, H_2, H_2+, H_3+, He, He+, and He_2+. Along with that, the metastable HeI(2^3S) atoms are treated as a separate fluid with its own velocity and temperature, which are determined by those of the species from which they originate, namely He+ or HeI, depending on whether recombination or excitation from the ground state, respectively, generate the HeI in the metastable (2^3S) state. Elastic collisions with other species also affect the macroscopic physical parameters of the HeI(2^3S) fluid. The ENAs are also treated as a separate fluid, which is crucial for calculation of Lyα absorption.

The double shock structures, generated around the planets in course of their interaction with the stellar wind (SW) plasma flow are revealed. Further details of the PW and SW interaction are given in the Figure 1, where the spatial profiles of velocity, temperature and density of most important molecular, atomic and ionic species are shown along the star-planet line. The X axis starts at the star and is broken from 0.065 to 0.11 a.u. The temperatures of thermospheres of TOI-421b and TOI-421c reach the maxima 8000/7000 K at the distance of about $3R_p$, and gradually decrease then with the distance due to the adiabatic cooling caused by the expansion. Similar to other simulated warm Neptunes, such as GJ-436b and GJ-3470b, the molecular hydrogen population extends rather far from the planets and strong outflows with the integral mass loss of about (2-3)·10^{10} g/s.

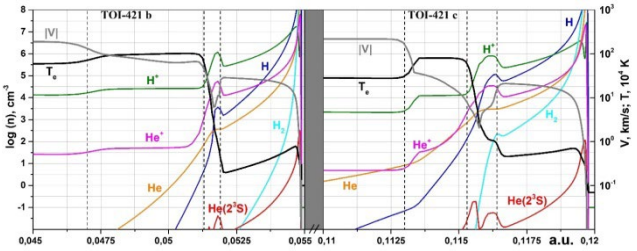

Fig. 1. Profiles of spatial distribution of the main physical quantities along the star-planet line, obtained for TOI-421b (left panel) and TOI-421c (right panel). Integral XUV flux is 20 erg/cm^2/s at 1 a.u. and stellar integral mass loss M'_{SW} is 2×10^{12} g/s. Star is positioned at zero coordinate. Right boundaries of the panels correspond to the position of each respective planet. The scaling of vertical axes (left — for the log of density, and right — for the speed and temperature) is common for both panels. Black line shows the electron temperature in units of 10^4 K, grey line shows the proton velocity, and other colored lines depict densities of the main species. Black dashed vertical lines indicate, from left to right, the position of SW shock, ionopause, PW shock. Note that planets radii in terms of a.u. are 1.14×10^{-4}/2.16×10^{-4}, while the star radius is 4×10^{-3} .

The calculations of stellar Lyα transit absorption by the planets reveal that it reaches a detectable level only for a moderate or strong SW, with a suf-

ficiently high density. In this case, the energetic neutral atoms provide significant absorption at the high velocity blue wing of the *Ly*α line, whereas the corresponding transit light curves exhibit an early ingress and extended egress features. With the same code, we modeled also the absorption at the position of the 10830 Å line of the metastable helium, showing that it can be detected only for the farthest planet of the considered two, if the helium abundance is comparable to the solar value. The increased absorption in the blue wing of Lyα for the decreasing F_{XUV} is caused by two factors.

The increase of HeI(2^3S) absorption with the increasing stellar XUV flux is caused by the growing HeI(2^2S) population, because the photoionization increases the amount of He+ ions, from which the HeI(2^2S) is produced. We found that the HeI(2^2S) absorption at both TOI-421b and TOI-421c is produced within small regions <3*Rp* around the planets. This explains why the expected absorption level remains relatively low, being marginally detectable only for larger TOI-421c, if the He/H ratio is not significantly below the solar value.

ACKNOWLEDGEMENTS:
The work was supported by the Ministry of Science and Higher Education project No. 075-15-2020-780.

MIXING OF PLANETESIMALS IN THE TRAPPIST-1 EXOPLANETARY SYSTEM

S.I. Ipatov[1]
[1] *V.I. Vernadsky Institute of Geochemistry and Analytical Chemistry of RAS, Moscow, Russia, siipatov@hotmail.com*

KEYWORDS:
TRAPPIST-1 exoplanetary system, exoplanets, planetesimals, probabilities of collisions

INTRODUCTION AND INITIAL MODEL:

The exoplanetary system TRAPPIST-1 consists of a star with a mass equal to 0.0898 of the mass of the Sun and 7 planets (from *b* to *h*) with masses from 0.33 to 1.37 Earth's masses. The semi-major axes of the planets' orbits are in the range from 0.012 to 0.062 AU. The orbital elements and masses of the planets are presented in Table 1. The motion of planetesimals under the gravitational influence of the star and seven TRAPPIST-1 planets (from *b* to *h*) was calculated with the use of the symplectic code from [1]. The late gas-free stage of formation of almost formed planets was studied. Planetesimals collided with planets or the star or ejected into hyperbolic orbits (reached 50 AU from the star) were excluded from integration. In each variant of the calculations, the initial values of semi-major axes of orbits of 250 planetesimals varied from a_{min} to a_{max}, initial eccentricities of their orbits were equal to e_o = 0.02 or e_o = 0.15, and their initial inclinations equaled to $e_o/2$ rad. The values of a_{min} and a_{max} are presented in Table 1. The considered disk of planetesimals was located near the orbit of one of the considered planets. Earlier I studied [2–3] the migration of planetesimals during formation of the terrestrial planets. The considered model of mixing of bodies in the zone of the TRAPPIST-1 planets can also characterize the migration of bodies ejected from some planets after collisions of these planets with some planetesimals or other bodies.

Table 1. Orbital elements, masses *m* (in Earth masses m_E) of exoplanets in the TRAPPIST-1 system, and the values of a_{min} and a_{max} for the considered disks near planets *b, c, d, e, f, g, h*.

	m/m_E	*a*, AU	*e*	a_{min}, AU	a_{max}, AU
b	1.37	0.0115	0.0062	0.0094	0.0137
c	1.31	0.0158	0.0065	0.0137	0.0190
d	0.39	0.0223	0.0084	0.0190	0.0258
e	0.69	0.0292	0.0051	0.0258	0.0339
f	1.04	0.0385	0.0101	0.0339	0.0427
g	1.32	0.0468	0.0021	0.0427	0.0544
h	0.33	0.0619	0.0057	0.0544	0.0694

PROBABILITIES OF COLLISIONS OF PLANETESIMALS WITH DIFFERENT PLANETS:

The results of calculations showed that, as the Earth and Venus, several planets in the TRAPPIST-1 exoplanetary system accumulated planetesimals initially located at the same distance. The conclusions are the same for calculations with the step t_s of integration equaled to 0.1 day and 0.01 day (the step can decrease for the motion near a planet). Times of evolution of disks *b, c, d, e, f, g, h* varied from 12 Kyr to 63 Myr (see Table 2). The numbers of collisions of planetesimals with planets (from *b* to *h*) for different disks (from *b* to *h*) are presented in Table 3 for the considered time intervals. The total number of such collisions of all planetesimals with planets *c* - *h* was greater than that for 100 Kyr (the numbers for 100 Kyr were presented in [4]) by not more than 4 %. Not more than 3 % of planetesimals were ejected into hyperbolic orbits. There was no ejection for disks initially located near orbits of the planets *b* and *c*. There were no collisions of planetesimals with the host star. More than a half of planetesimals from disks

near orbits of planets from *b* to *g* collided with planets in less than 1000 yr, and for disks *b* - *d* even in 250 yr. Planetesimals with a dynamical lifetime greater than 100 Kyr typically were ejected into hyperbolic orbits or collided with planet *h*. The fraction of planetesimals collided with the 'host' planet (compared to collisions with all planets) typically decreased with the considered time interval. In each calculation variant, there was at least one planet for which the number of collided planetesimals was greater than 25 % of the number of collisions of planetesimals with the 'host' planet. The fraction of collisions of planetesimals with the 'host' planet was usually smaller for disks located farther from the star. For the initial disk near the orbit of the planet *h*, the number of collisions of planetesimals with the planet *g* was about that with the planet *h*. Planetesimals migrated from distances greater than 0.7 AU could collide with all planets, but most of their collisions (>70 %) were with planets *g* and *h*. Planetesimals could collide with all planets for disks near orbits of planets from *d* to *h*. Therefore, outer layers of neighbouring planets in the TRAPPIST-1 system can include similar material, if there were a lot of planetesimals near their orbits at the late stages of the accumulation of the planets.

Table 2. Times of evolution of disks *b, c, d, e, f, g, h* (until collisions of all planetesimals with planets or their ejections into hyperbolic orbits) in Kyr for initial eccentricities of planetesimals equaled to e_o at the step t_s of integration equaled to 0.1 day (first values) or 0.01 day.

e_o	*b*	*c*	*d*	*e*	*f*	*g*	*h*
0.02	1504, >6200	12.0, 52.3	32.4, 11.1	6446, 367.4	6282, 1815	212, 1106	63135, 1133
0.15	20.1, 41.4	24.5, 13.7	355, 282.3	437, 394.2	128, 229.7	119, 467.6	3391, 933.5

Table 3. The number of collisions of planetesimals with planets (from *b* to *h*) in the TRAPPIST-1 system for different disks (from *b* to *h*). Initial eccentricities of planetesimals equaled to e_o. There were 250 planetesimals in each initial disk. Variants with an integration step t_s = 0.01 day are marked by bold letters in the left column, for other variants t_s = 0.1 day.

	e_o	*b*	*c*	*d*	*e*	*f*	*g*	*h*	*ejected*
b	0.02	**199**	47	2	2	0	0	0	0
b	0.02	**187**	54	2	3	2	1	0	0
b	0.15	**188**	55	6	1	0	0	0	0
b	0.15	**180**	63	5	2	0	0	0	0
c	0.02	49	**153**	32	9	3	4	0	0
c	0.02	56	**148**	26	11	3	5	0	0
c	0.15	77	**140**	13	10	6	2	2	0
c	0.15	73	**141**	23	7	0	5	1	0
d	0.02	13	42	**120**	43	18	11	3	0
d	0.02	13	47	**128**	29	16	14	3	0
d	0.15	28	69	**68**	45	16	19	3	2
d	0.15	30	71	**59**	43	23	19	5	0
e	0.02	5	20	31	**110**	38	39	3	3
e	0.02	7	27	24	**105**	46	34	4	3
e	0.15	11	38	32	**69**	53	32	12	3
e	0.15	7	29	22	**72**	57	53	3	7
f	0.02	6	11	10	37	**98**	75	11	2
f	0.02	4	7	14	43	**108**	58	14	2
f	0.15	6	21	26	42	**61**	77	12	5
f	0.15	7	20	23	45	**57**	80	10	8
g	0.02	3	12	12	33	45	**110**	31	4
g	0.02	1	11	16	20	48	**114**	33	7
g	0.15	2	12	20	36	62	**94**	18	6
g	0.15	5	16	16	26	68	**95**	22	2
h	0.02	1	10	7	15	43	79	**90**	**5**
h	0.02	6	3	6	24	31	71	**105**	**4**
h	0.15	6	9	8	22	48	83	**66**	**8**
h	0.15	1	6	14	31	51	86	**54**	**7**

CONCLUSIONS:

Outer layers of neighbouring exoplanets in the TRAPPIST-1 system can include similar material, if there were a lot of planetesimals near their orbits at the late stages of the accumulation of the exoplanets.

ACKNOWLEDGEMENTS:

The author acknowledges the support of Ministry of Science and Higher Education of the Russian Federation under the grant 075-15-2020-780.

REFERENCES:

[1] Levison H.F., Duncan M.J. The long-term dynamical behavior of short-period comets // Icarus, 1994, V. 108, P. 18–36.

[2] Ipatov S.I. Migration of bodies in the accretion of planets // Solar System Research, 1993, V. 27, P. 65–79.

[3] Ipatov S.I. Probabilities of collisions of planetesimals from different regions of the feeding zone of the terrestrial planets with forming planets and the Moon // Solar System Research, 2019, V. 53, P. 332–361. http://arxiv.org/abs/2003.11301

[4] Ipatov S.I. Migration of planetesimals in the TRAPPIST-1 exoplanetary system // Abstracts of 53nd Lunar and Planetary Science Conference. 2022, #1182, 2 pages, https://www.hou.usra.edu/meetings/lpsc2022/pdf/1182.pdf

ON THE TRANSIT SPECTROSCOPY FEATURES OF WARM MINI-NEPTUNES IN THE HD-63433 SYSTEM, REVEALED WITH THEIR 3D NUMERICAL SIMULATIONS

M.A. Efimov[1], A.G. Berezutsky[1], I.F. Shaikhislamov[1], I.B. Miroshnichenko[1], M.S. Rumenskikh[1]
[1] *Russia, Novosibirsk, Akademika Lavrentiev ave., 15B, efim.sci@gmail.com*

KEYWORDS:
Exoplanets; Stars: G-type; Spectra: ultraviolet; Spectra: optical; Spectra: infrared; Transit Spectroscopy; Numerical Simulation; Warm mini-Neptune.

With an 3D aeronomic model, we have numerically modeled Lyα and He (10830 Å) absorption from the escaping atmosphere of HD 63433c ($R = 2.67R_0$, $P = 20.5$ day), mini-Neptune orbiting a young (440 M_{yr}) solar analog in the Ursa Major Moving Group [1]. To compare the obtained numerical calculations with the transit spectral data, we varied the extreme ultraviolet radiation (XUV) and the mass loss of the stellar wind. With the calculated mass loss of the stellar wind $M_{sw} = 2 \cdot 10^{12}$, the mass loss of the planet was $2.13 \cdot 10^{10}$ g/s, which is 3.2 times less than for the nearby planet HD 63433b.

ACKNOWLEDGEMENTS:
The work was supported by the Ministry of Science and Higher Education project No. 075-15-2020-780.

REFERENCES:
[1] Michael Zhang et al, 2022, Astronomical Journal 163 68.

SEARCH FOR CHAINS OF RESONANCES IN THE COMPACT PLANETARY SYSTEM K2-72

E.D. Kuznetsov[1], A.S. Perminov[2]
[1] *Ural Federal University, 620000, 51 Lenin Avenue, Yekaterinburg, Russia, eduard.kuznetsov@urfu.ru;*
[2] *Ural Federal University, 620000, 51 Lenin Avenue, Yekaterinburg, Russia, perminov12@yandex.ru*

KEYWORDS:
Compact planetary system, resonance chains, tides, dynamic evolution, stability

INTRODUCTION:

At present, several dozen compact planetary systems containing more than two planets with masses of the order of the Earth's mass are known [1]. It is shown that the stable evolution of compact planetary systems requires the presence of resonances that prevent close encounters of planets moving in neighboring orbits (see, for example, the five-planet systems Kepler-80 [2], K2-138 [3] and the seven-planet system TRAPPIST-1 [4]). In this case, resonances between pairs of planets can form chains. The longest resonance chain known to date is realized in the TRAPPIST-1 system: 8:5 – 5:3 – 3:2 – 3:2 – 4:3 – 3:2 [4]. In the K2-138 system, five planets form the longest chain consisting of identical 3:2 resonances [3]. On the other hand, simulation results show that in wide systems with massive planets, chains of high-order resonances can lead to the destruction of planetary systems [5].

We consider the compact planetary system K2-72 and search for resonance chains within the errors of determining the semi-major axes of orbits from observations. For compact systems, an important factor affecting evolution is tidal interaction; therefore, when analyzing the feasibility of the proposed resonance chains, we will model dynamic evolution taking into account tides.

RESONANT ANGLES:

When analyzing the resonant properties of planetary systems, the behavior of resonant angles is studied. For two planets *i* and *i*+1, which are in resonance of mean motions $\frac{k_i}{k_i - l_i}$, the resonant angle can be set as follows [6]:

$$\varphi_{i,i+1,i+s} = (k_i - l_i)\lambda_i - k_i\lambda_{i+1} + l_i\varpi_{i+s}, \quad (1)$$

where is the resonance order, λ_i, λ_{i+1} are the mean longitudes of planets *i* and *i*+1, ϖ_{i+s} is the longitude of the periapsis of planet *i* (*s* = 0) or *i*+1 (*s* = 1) orbit. For the next pair of planets *i*+1 and *i*+2, which is in resonance $\frac{k_{i+1}}{k_{i+1} - l_{i+1}}$, the resonant angle

$$\varphi_{i+1,i+2,i+1+s} = (k_{i+1} - l_{i+1})\lambda_{i+1} - k_{i+1}\lambda_{i+2} + l_{i+1}\varpi_{i+1+s} \quad (2)$$

Instead of two resonances between two neighboring pairs of planets, three-body resonances can be considered. In this case, the three-body resonance is a chain of two two-body resonances $\frac{k_i}{k_i - l_i}$ and $\frac{k_{i+1}}{k_{i+1} - l_{i+1}}$ with a resonant angle that does not depend on the periapsis longitude [6]:

$$\Phi^{p,p+q,q}_{i,i+1,i+2} = p\lambda_i - (p+q)\lambda_{i+1} + q\lambda_{i+2} \quad (3)$$

where $p = l_{i+1}(k_i - l_i)$, $q = l_i k_{i+1}$

SEARCH FOR POSSIBLE CHAINS OF RESONANCES:

The search for chains of resonances was carried out for the values of the semi-major axes of the orbits of the planets, which varied within the standard deviation $a_i = a_{0i} + \sigma_{ai}$. Here a_{0i} is the nominal value of the semi-major axis of the orbit, σ_{ai} is the standard deviation of the determination of the

semi-major axis. To determine the resonant combinations of the semi-major axes of the orbits, the ratio of the mean motions n_i and n_{i+1} was represented as a segment of a sequence of convergent fractions

$$\frac{n_i}{n_{i+1}} = \left\{ \frac{b_1}{d_1}, \frac{b_2}{d_2}, ..., \frac{b_j}{d_j} \right\}, b_j < b_{\max} \quad (4)$$

We obtain a rational approximation of the real ratio of mean motions

$$\frac{n_i}{n_{i+1}} = \frac{k_i}{k_i - l_i} = \frac{b_j}{d_j} \quad (5)$$

After the sets of relations of the form (5) are obtained for all pairs of neighboring planets, possible chains of resonances are formed (if the resonance values of the major semiaxes of the outer and inner orbits in neighboring pairs coincide). The final selection of potential resonance chains is based on an estimate of the frequency of the resonant angle

$$v_{i,i+1,i+2}^{p,p+q,q} = \left| pn_i - (p+q)n_{i+1} + qn_{i+2} \right| < \varepsilon \quad (6)$$

where the values are chosen as a criterion $\varepsilon \sim 10^{-4}$–10^{-5} day^{-1}.

POSSIBLE CHAINS OF RESONANCES IN A COMPACT PLANETARY SYSTEM K2-72:

In table 1 shows the parameters of the K2-72 system. The masses of the planets *m* are expressed in solar masses M_S and calculated from the radii of the planets *R*, assuming that they have the same average density as the Earth. Star radius is given in solar radii R_S, and planetary radii are given in Jupiter radii R_J. The orbital elements *a*, *e*, *i*, *g* are the semi-major axis, eccentricity, inclination, periapsis argument, respectively. The moment T_{conj} corresponds to the conjunction of the planet with the star.

Table 1. Parameters of the planetary system K2-72 [1].

Parameter	K2-72	K2-72 b	K2-72 c	K2-72 d	K2-72 e
m, M_S	0.27 +0.08 –0.09	3.797×10^{-6}	4.705×10^{-6}	3.106×10^{-6}	6.471×10^{-6}
R, R_S, R_J	0.33 ±0.03	0.096 ±0.010	0.103 ±0.012	0.090 ±0.011	0.115 ±0.012
a, au		0.040 ±0.005	0.078 +0.007 –0.010	0.050 +0.004 –0.006	0.106 +0.009 -0.013
e		0.11 +0.20 –0.09	0.11 +0.20 –0.09	0.11 +0.20 –0.09	0.11 +0.20 –0.09
i, deg		0.85 +0.59 –0.86	0.46 +0.32 –0.44	0.74 +0.50 -0.70	0.32 +0.22 –0.32
g, deg		7.49 +120 –134	16.83 +113 –138	14.28 +114 –137	11.39 +117 –136
T_{conj}, JD – 2450000		7010.376 ±0.002	6989.465 ±0.005	6984.788 +0.008 –0.007	6987.054 ±0.005

The application of the described technique made it possible to obtain sets of possible resonance chains. Table 2 lists for each chain the resonant values of the semi-major axes of the orbits, two- and three-body resonances, and the frequencies of resonant angles of three-body resonances (6). The planets are numbered in order of increasing semi-major axis of the orbit: 1 — K2-72 b, 2 — K2-72 d, 3 — K2-72 c, 4 — K2-72 e.

Table 2. Possible chains of resonances in the K2-72 system

Resonance chain	1	2	3
a_1, au	0.03905	0.04079	0.04271
a_2, au	0.05117	0.05345	0.05345
a_3, au	0.07193	0.07004	0.07004
a_4, au	0.11418	0.11118	0.11118
1–2	3:2	3:2	7:5
2–3	5:3	3:2	3:2
3–4	2:1	2:1	2:1
1–2–3	$p = 4$, $q = 5$	$p = 2$, $q = 3$	$p = 5$, $q = 6$
ν_{123}, day^{-1}	5.23×10^{-5}	1.55×10^{-5}	3.71×10^{-5}
2–3–4	$p = 3$, $q = 4$	$p = 2$, $q = 2$	$p = 2$, $q = 2$
ν_{123}, day^{-1}	1.86×10^{-5}	2.88×10^{-5}	2.88×10^{-5}

We considered a number of scenarios for the evolution of the K2-72 system over 100 Myr using the Posidonius software [7], which takes into account tidal interactions. At nominal values of the semi-major axes, the simulation ended with the decay of the system 3 Myr after the start of integration. Under the initial conditions corresponding to the chains of resonances 3:2 — 5:3 — 2:1 and 7:5 — 3:2 — 2:1, the system decayed in less than 55 Myr. In the vicinity of the chain of resonances 3:2 — 3:2 — 2:1, the system remains stable over the entire interval under consideration. A detailed study of the dynamic evolution of the planetary system in the vicinity of the resonance chain 3:2 — 3:2 — 2:1 will be carried out.

ACKNOWLEDGMENTS:
The work was supported by the Ministry of Science and Higher Education of the Russian Federation via the State Assignment Project FEUZ-2020-0038.

REFERENCES:

[1] The Extrasolar Planets Encyclopaedia. http://exoplanet.eu/catalog/.
[2] MacDonald M.G., Ragozzine D., Fabrycky D.C. et al. Dynamical Analysis of the Kepler-80 System of Five Transiting Planets // The Astronomical Journal. 2016. V. 152. Id. 105. P. 18.
[3] MacDonald M.G., Feil L., Quinn T., Rice D. Confirming the 3:2 Resonance Chain of K2-138 // The Astronomical Journal. 2022. V. 163. Id. 162. 12 p.
[4] Luger R., Sestovic M., Kruse E. et al. A seven-planet resonant chain in TRAPPIST-1 // Nature Astronomy. 2017. V. 1. Id. 0129. 8 p.
[5] Murphy M.M., Armitage P.J. Instability from high-order resonant chains in wide-separation massive planet systems // Monthly Notices of the Royal Astronomical Society. 2022. V. 512. P. 2750–2757.
[6] Huang S., Ormel C.W. The dynamics of the TRAPPIST-1 system in the context of its formation // Monthly Notices of the Royal Astronomical Society. 2022. V. 511. P. 3814–3831.
[7] Blanco-Cuaresma S., Bolmont E. Studying Tidal Effects In Planetary Systems With Posidonius. A N-Body Simulator Written In Rust // EWASS Special Session 4 (2017): Star-planet interactions (EWASS-SS4-2017). 2017. doi:10.5281/zenodo.1095095.

INFORMATION

address:
Space Researh Institute (IKI)
Profsoyuznaya street 84/32
post code 117997
metro station: Kaluzhskaya
Moscow, Russia

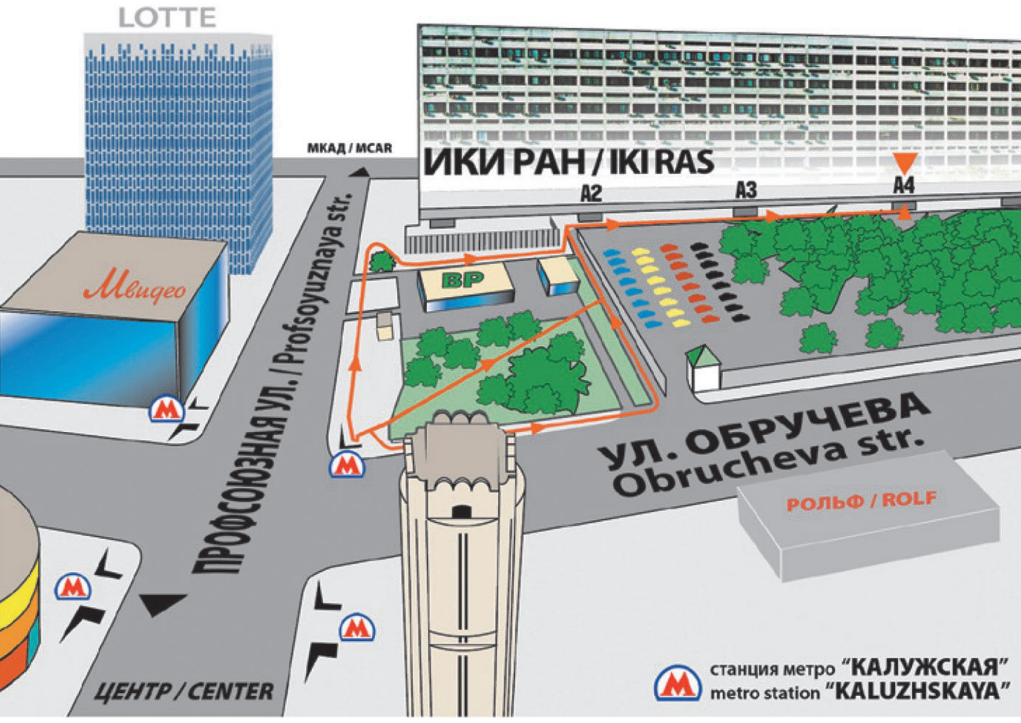

ИКИ РАН

площадь академика Келдыша
метро «Калужская», первый вагон из центра, по тоннелю – прямо,
по второму поперечному тоннелю – направо, выход на площадь,
далее по стрелкам на схеме

IKI RAS

You should get off at “Kalyzhskaya” metro station using the southern exit.
After leaving a station lobby through glass doors you should go straight
to the end of the tunnel, then take right and use the stairs to get to the surface.
From this point you may follow either arrow on this map

MOSCOW METRO SCHEME

СХЕМА МОСКОВСКОГО МЕТРОПОЛИТЕНА

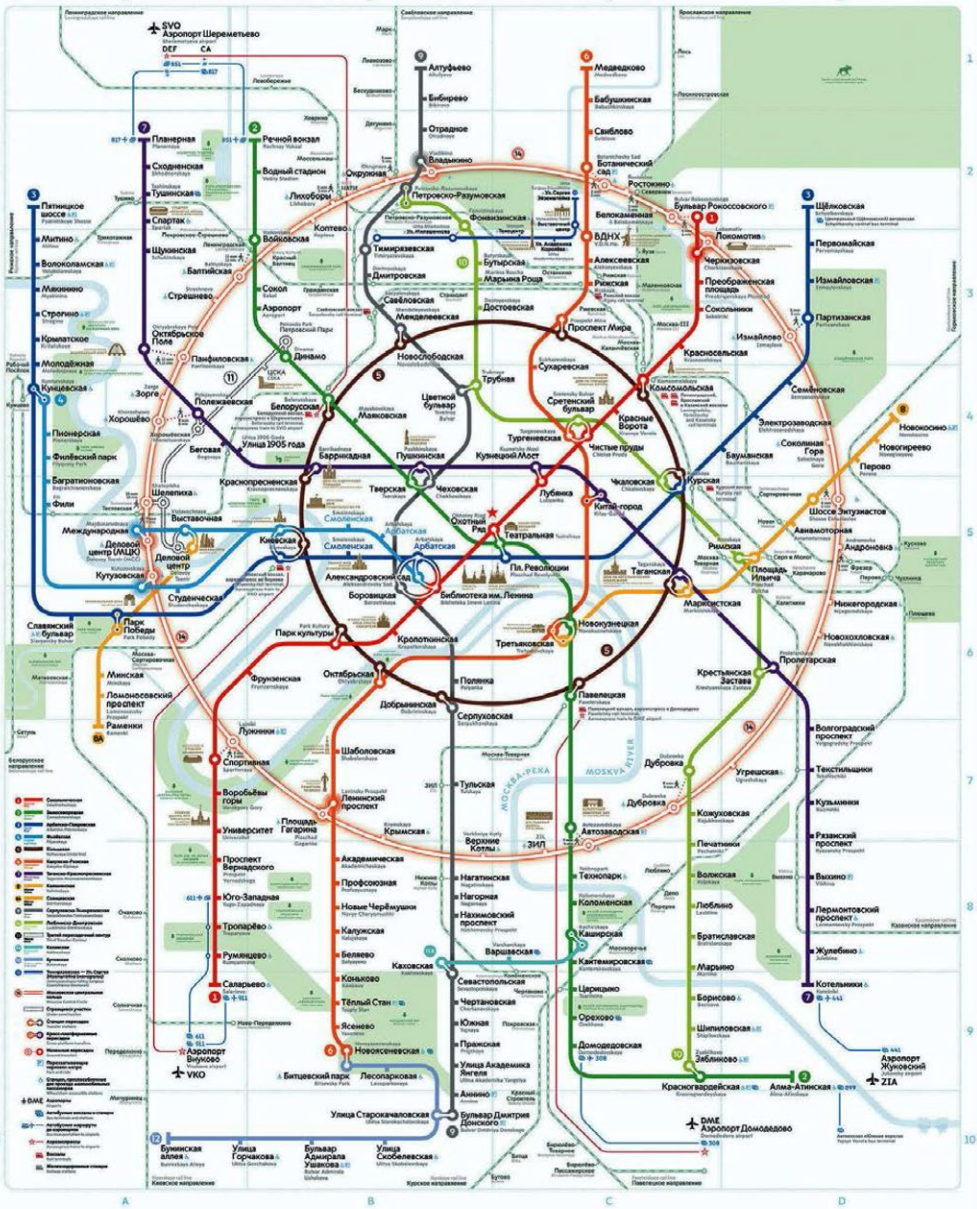

REGISTRATION AND INFORMATION DESK

location: IKI, entrance A-4

time:

10 october, 9:00–18:00

11–14 october, 10:00-18.00

ORAL SESSIONS

location:

- IKI conference hall, second floor
  Sessions:Mars, Moon and Mercury, Giant Planets, Astrobiology, Small Bodies, Venus
  11–14 october
- IKI Room 200, second floor
  Session Extrasolar Planets
  14 october

POSTER SESSIONS

online discussion

COFFEE BREAKS, WELCOME PARTY, RECEPTION

location:

- IKI conference hall, second floor
- IKI exhibition hall, ground floor

INTERNET ACCESS AND WIFI

there is Internet access in and near the conference hall

SOCIAL PROGRAM

	BOLSHOI	OPERETTA	HELIKON	MMDM	NOVAYA OPERA	KREMLIN
9.10	**14.00** Historic Stage, ballet **LEGEND OF LOVE** **14.00** opera, new stage **DON GIOVANNI, V. MOZART** **14.00** Chamber Stage (Nikolskaya, 17/1) **MADDALENA. L'HEURE ESPAGNOLE, S. PROKOFIEV, M. RAVEL**	**13.00, 19.00** Operetta **THE BAT**		**15.00** Svetlanov Hall **GRAND WALTZ** **19.00** Consert **RELAX IN THE BIG CITY**		**18.00** **MUSICAL FESTIVAL GRAND FINAL "BIG STAGE"**
10.10						**19.00** Ballet **SPARTAK, ARAM KHACHATURIAN**
11.10		**19.00** Musical **ANNA KARENINA**			**19:00** Opera **LIUCHIYA DI LAMMERMUR, GAETANO DONIZETTI**	**19.00** Ballet **ZOLUSHKA, S. PROKOFIEV**
12.10	**19.00** Opera, Historic stage **DON CARLO, G. VERDI** **19.00** One-act ballets, New stage **MADE IN BOLSHOI, LES SAISONS, DANCEMANIA**	**19.00** Musical **ANNA KARENINA**		**19.00** Consert, Svetlanov Hall **FLYING OVER TIME, E. ARTEMIEV**		
13.10	**19.00** Opera, Historic stage **DON CARLO, G. VERDI** **19.00** One-act ballets, New stage **MADE IN BOLSHOI: LES SAISONS, DANCEMANIA** **19.00** Chamber Stage (Nikolskaya, 17/1) **LES PÊCHEURS DE PERLES, G. BIZET**	**19.00** Musical **ANNA KARENINA**	**19.00 , 20.30** White-Columned Hall of Princess Shakhovskaya **COFFEE CANTATA, J.S. BACH**	**19.00** Svetlanov Hall **HOLLYWOOD MASTERPIECES**		
14.10	**19.00** Opera, Historic Stage **DON CARLO, G. VERDI** **19.00** Chamber Stage (Nikolskaya, 17/1) **LES PÊCHEURS DE PERLES, G. BIZET**	**19.00** Musical **ANNA KARENINA**			**19.00** Opera **LOENGRIN, R. WAGNER**	

BOLSHOI	**https://bolshoi.ru**	BOLSHOI THEATRE
OPERETTA	**https://mosoperetta.ru/**	OPERETTA THEATRE
HELIKON	**https://www.helikon.ru/**	HELIKON OPERA
MMDM	**https://www.mmdm.ru/**	MOSCOW INTERNATIONAL PERFORMING ARTS CENTER
NOVAYA OPERA	**https://novayaopera.ru/**	NOVAYA OPERA
KREMLIN	**https://kremlinpalace.org/**	STATE KREMLIN PALACE

lUNCH POINTS NEAREST TO IKI

1. **ИНСТИТУТ КОСМИЧЕСКИХ ИССЛЕДОВАНИЙ РАН**,
   столовая, 1 этаж, секция А3
   SPACE RESEARCH INSTITUTE,
   Food center, Ground Floor, Section A3
2. **ТЦ “КАЛУЖСКИЙ”**,
   ул. Профсоюзная, 61А, зона ресторанов, 2 этаж
   “KALUZHSKIY” Market Center,
   Profsoyuznaya Street, 61A, 2 Floor
3. **КАФЕ”АНДЕРСОН”**,
   ул. Обручева, 30/1
   CAFÉ “ANDERSON”,
   Obrucheva street, 30/1
4. **ИНСТИТУТ ПРИКЛАДНОЙ МАТЕМАТИКИ РАН,**
   столовая, 1 этаж
   INSTITUTE OF APPLIED MATHEMATICS,
   Food center, Ground Floor